ACOUSTIC MEASUREMENT OF SNOW

A Thesis Submitted to the College of

Graduate Studies and Research

In Partial Fulfillment of the Requirements

For the Degree of Doctor of Philosophy

In the Department of Geography & Planning

(Centre for Hydrology)

University of Saskatchewan

Saskatoon

By

NICHOLAS JOHN STANISLAUS KINAR

Permission to Use

In presenting this thesis in partial fulfilment of the requirements for a Postgraduate degree from the University of Saskatchewan, I agree that the Libraries of this University may make it freely available for inspection. I further agree that permission for copying of this thesis in any manner, in whole or in part, for scholarly purposes may be granted by the professor or professors who supervised my thesis work or, in their absence, by the Head of the Department or the Dean of the College in which my thesis work was done. It is understood that any copying or publication or use of this thesis or parts thereof for financial gain shall not be allowed without my written permission. It is also understood that due recognition shall be given to me and to the University of Saskatchewan in any scholarly use which may be made of any material in my thesis.

Requests for permission to copy or to make other use of material in this thesis in whole or part should be addressed to:

Head of the Department of Geography & Planning

University of Saskatchewan

Room 125 Kirk Hall

117 Science Place

Saskatoon, Saskatchewan

S7N 5C8 Canada

ABSTRACT

Instrumentation commonly used to measure snowpack stratigraphy, snow density, Snow Water Equivalent (SWE), temperature and liquid water content is usually invasive and requires disruption of the snowpack. Most measurement techniques modify the snow medium and more than one sample cannot be taken at the same location. This does not permit continuous monitoring of these parameters using a single measurement instrument. An acoustic wave sent into the snowpack was used to measure snow. To provide the theory required to make acoustic measurements, the Biot-Stoll model of sound wave propagation in porous media was modified using a mixture theory so that it was applicable to a multiphase porous medium. The combined model is called the Unified Thermoacoustic Model (UTAM) for snow. An acoustic measurement device, the System for the Acoustic Sensing of Snow (SAS2), was designed to send sound waves into snow and to receive the reflected sound waves using a loudspeaker and a microphone array. A stationary version of the SAS2 was deployed on a met station and a portable version of the SAS2 was placed on a roving ski-based platform. The systems were deployed at field sites in the Canadian Rocky Mountains, Alberta. The results showed that the SAS2 was able to measure snow density, temperature, and liquid water content and serve as a replacement technology for snowtube and snowpit measurements. Snow density was estimated more accurately by the SAS2 than from commonly-used snow tube techniques.

ACKNOWLEDGEMENTS

I would like to thank my supervisor, Dr. John Pomeroy, for supporting my endeavors and for patiently waiting while I explored new conceptual territories. I will always remember that you gave me the opportunity to have a number of great learning experiences.

I am also thankful of the advice offered by my committee: Dr. Doug Degenstein, Dr. Xulin Guo, Dr. Phil Marsh and Dr. Bing Si. The suggestions of the external examiner, Dr. Hans-Peter Marshall, were greatly appreciated.

Dr. Kevin Shook encouraged the use of Free and Open Source Software (FOSS) at the Centre for Hydrology and is to be thanked for his tireless efforts.

I thank Joni Onclin, research assistant at the Centre for Hydrology, for logistical support.

The University of Saskatchewan Libraries supported my learning. Many librarians and library staff at the Engineering, Main (Murray), and Science libraries helped to obtain journal articles and other documents. I would especially like to thank the Interlibrary Loan staff for help with obtaining obscure papers.

I am appreciative of Jeff Scheller (Commutron Industries, Elbow, Saskatchewan) for helping with the placement of some electronic components on earlier prototype circuit boards. Brian Husnik, Norine Wilson and associates (SED Systems, Saskatoon, Saskatchewan) fixed damaged traces and soldered some parts on a few circuit boards. I am also appreciative of access to an x-ray machine at Vecima Networks (Saskatoon, Saskatchewan) that helped to track down difficulties with BGA chips on a prototype circuit board; I would like to thank the engineering staff, managers and technicians for this opportunity.

Lazer-Tech Inc. (Toronto, Ontario, Canada) manufactured the SAS2 circuit boards that I designed. I soldered parts on circuit boards, drilled holes in enclosure cases, designed, programmed and tested the SAS2 systems documented in this thesis.

May Guan—field assistant and hydrologist with the Centre for Hydrology—helped with the fieldwork. The assistance of Mike Demuth, Tracey Hammer, Daniel Gunther, and Dr. Charles Maule at some of the field sites is greatly appreciated.

Lynn Martel—Rocky Mountain writer extraordinaire—wrote about this research. I will always remember your description of the big red button on the SAS2. I hope that I will be able to provide you with other stories of adventure in the future.

TABLE OF CONTENTS

	Page
PERMISSION TO USE	i
ABSTRACT	ii
ACKNOWLEDGEMENTS	iii
LIST OF TABLES	viii
LIST OF FIGURES	ix
NOMENCLATURE	xi
1. INTRODUCTION	1
1.1 Importance of Snow	1
1.2. Snow Measurement Parameters	13
1.3. Near-Surface Snowpack Measurement Instrumentation	18
1.3.1. Depth Rod	19
1.3.2. Snow Sampler Tubes	20
1.3.3. Snowpits	22
1.3.4. Pressure Sensors	24
1.3.5. Dielectric	26
1.3.6. Radar	29
1.3.7. Laser-Ranging	31
1.3.8. Near-Surface Photography	32
1.3.9. Radioactivity	33
1.3.10. Chemical	36
1.3.11. Calorimetric and Centrifugal	37
1.3.12. Acoustic Measurement of Snow Depth	39
1.3.13. Acoustic Measurement of Snow	40
1.3.14. Heat Pulse Probes	41
1.3.15. Temperature Sensors	42
1.4. Automation of Snow Property Measurements	45
1.5. Problem	48
1.6. Objectives	49
2. LITERATURE	50
2.1. Introduction	50
2.2. Overview of Processes	50
2.2.1. Precipitation	50
2.2.2. Wind Transport	51
2.2.3. Interception	52
2.2.4. Radiation	52
2.2.5. Snow Surface Heat Fluxes	54

2.2.6. Heat and Vapour Transport at the Snow-Soil Interface 55
2.2.7. Heat and Vapour Transport in Dry Snow 57
2.2.8. Dry Snow Metamorphism 59
2.2.9. Heat and Water Transport in Wet Snow 60
2.2.10. Wet Snow Metamorphism 64
2.2.11. Approximation of Snow Particles as Spheres 64
2.3. Acoustics 65
2.4. Mechanical Properties 67
2.5. Snow Acoustics Research 68
2.5.1. Invasive Snow Sample Extraction Experiments 69
2.5.2. Invasive Snowpack Experiments 71
2.5.3. Non-invasive Experiments 72
2.5.4. Biot-Stoll Model 73
2.6. Mixture Theory Models 75
2.7. Sonar and Seismology 76
2.8. Acoustic Scattering and Mode Conversion 76
2.9. Signal Processing 77
2.10. Maximum Length Sequences 79
2.11. Imaging of Snow and Snowpits 80
2.12. Comparison of Observations to Models 80

3. THEORY 81
3.1. Introduction 81
3.2. UTAM Model 81
3.2.1. Biot-Stoll Constitutive Equations 81
3.2.2. Multiphase Modifications 84
3.2.3. Percolation Theory (PT) Model 85
3.2.4. Consolidation Theory (CT) Model 88
3.2.5. Mechanical Parameters 95
3.3. High Frequency Approximation Model (HFA) 99
3.4. Application of Forward and Inverse Models 100
3.4.1. PT Model 101
3.4.2. CT Model 103
3.4.3. HFA Model 105
3.4.4. UTAM Model 108
3.4.5. Inverse Model 112
3.5. Acoustic Measurement Model 113
3.6. Maximum Length Sequence (MLS) Measurements 117
3.6.1. Overview 117
3.6.2. Measurement of Snowpack Filter Kernel 119
3.6.3. Production of the MLS 121
3.6.4. Reconstruction of PDM Sound Wave 123
3.7. Attenuation Analysis 126
3.7.1. Introduction 126
3.7.2. Q-Analysis Techniques 127
3.7.3. Forward and Inverse Gabor Transforms 129

3.7.4. Forward and Inverse Q Filters 132
3.7.5. The Vanishing Constant Filter (VCF) 134
3.7.6. Differentiation and Integration Using FFTs 139
3.7.7. Zero-Offset Q 141
3.8. FBS Analysis 141
3.9. Speed Analysis 141
3.10. Signal Processing Flow 144
3.11. Computation of Parameters 145

4. APPARATUS 147
4.1. Introduction 147
4.2. Initial Prototype Systems 147
4.3. Final Prototype Systems 150
4.3.1. Hardware 150
4.3.2. Mounting Platforms 153
4.3.3. Electronic Circuits 155
4.3.4. Microphone Selection 164
4.3.5. Microphone Sampling Rate 171
4.3.6. DAC Output and MLS Signal Amplitude 172
4.3.7. Sound Pressure Level 172
4.3.8. Length and Sampling Rate of MLS 173
4.3.9. Loudspeaker 175
4.3.10. Loudspeaker and Microphone Array Separation 175
4.3.11. Array Design and Footprint 176
4.3.12. Snowpack Layer Resolution 179
4.4. Anechoic Chamber Measurements 180

5. FIELD LOCATIONS AND DATA COLLECTION 184
5.1. Introduction 184
5.2. Sites and Deployment 185
5.2.1. Upper Clearing Stationary (UCS) Site 185
5.2.2. Upper Clearing Portable (UCP) Site 191
5.2.3. Boulton Campground (BC) Site 193
5.2.4 Sawmill Creek (SC) Site 195
5.2.5 Black Prince Cirque (BPC) 197
5.2.6 Bow Summit (BS) 198
5.2.7 Bow Meadow (BM) Site 199
5.2.8 Bow Lake (BL) Site 202
5.2.9 Nakiska Ski Hill (NSH) Site 203
5.2.10 Icefields Parkway Forest (IFPF) Site 204

6. RESULTS 206
6.1. Introduction 206
6.2. Snowpack Measurements 206
6.2.1. Ultrasonic 206
6.2.2. Ultrasonic and SAS2 209

6.2.3. Density 209
6.2.4. Thermal 219
6.2.5. Liquid Water Content 225
6.2.6. Acoustic 229
6.3. Acoustic Imaging Example 234
6.4. Seasonal Snowpack Changes 237
6.5. Repeatability of Successive Measurements 247
6.6. Influence of Wind on SAS2 Measurements 250
6.7. Example of Portable SAS2 Observation Site 252
6.8. Error Comparisons 265
6.9. Effect of Signal Cutoff Time on Inverse UTAM Model Results 268

7. CONCLUSIONS 270
7.1. Non-invasive Measurement of Snowpack Variables 270
7.2. Unified Thermoacoustic Model (UTAM) 271
7.3. Signal Processing Techniques 272
7.4. System for the Acoustic Sensing of Snow (SAS2) 273
7.5. Deployment of SAS2 275
7.6. Snowpack Measurements 275

LIST OF REFERENCES 280

APPENDIX A 318
CIRCUIT DIAGRAMS

APPENDIX B 353
ADDITIONAL FIELD SITE OBSERVATIONS

LIST OF TABLES

	page
1.1. Internal parameters explicitly used in snowpack models	15
2.1. Measured heat fluxes between the ground and snowpack.	56
5.1. Names, acronyms, geographic locations of acoustic sampling points	186
6.1. Overall comparisons between gravimetric and acoustic densities	214
6.2. Overall comparisons between gravimetric and acoustic SWEs	215
6.3. Comparisons between gravimetric and acoustic measurements $\bar{\rho}$ (field sites)	217
6.4. Descriptive statistics of density $\bar{\rho}$ (kg m^{-3}) measured using the SAS2	218
6.5. Comparisons between snowharp and SAS2 measurements over observation periods	219
6.6. Overall comparisons of snowharp temperature over the entire time of observation	219
6.7. Comparisons between snowpit and acoustic measurements of temperature $\bar{T}$	225
6.8. Descriptive statistics of snow temperature $\bar{T}$ measured using the SAS2	225
6.9. Comparisons between dielectric and acoustic measurements of $\bar{\theta}_w$	229
6.10. Descriptive statistics of liquid water content $\bar{\theta}_w$ measured using the SAS2	229
6.11. Descriptive statistics of the speed of sound in snow c_s	231
6.12. Descriptive statistics of sound attenuation a_c measured using the SAS2	231
6.13. Descriptive statistics of snow depth $\bar{y}$ measured using a depth rod	232
6.14. Descriptive statistics of Ψ coefficient measured using the SAS2	232
6.15. Descriptive statistics for repeated measurements of $\bar{\rho}$	249
6.16. Descriptive statistics for repeated measurements of $\bar{T}$	249
6.17. Descriptive statistics for repeated measurements of $\bar{\theta}_w$	250
6.18. Comparison between meaurements for the SC site	257

LIST OF FIGURES

page

2.2. Diagram showing the effect of a system on an input signal 78
3.1. Diagram of two snow particles used for the CT model 90
3.2. Sensitivity analysis for the Young's modulus E calculated using the PT model 102
3.3. Sensitivity analysis for the shear modulus G calculated using the PT model 103
3.4. Sensitivity analysis for the CT model 105
3.5. Sensitivity analysis for the HFA model outputs 107
3.6. Sensitivity analysis for the HFA model cutoff frequency 107
3.7. Sensitivity analysis for the UTAM model (1) 110
3.8. Sensitivity analysis for the UTAM model (2) 111
3.9. Conceptual diagram showing the acoustic measurement model 114
3.10. Diagram showing the Linear Feedback Shift Register (LFSR) 122
3.11. Signal processing flow diagram for the lowpass Butterworth filter 125
3.12. Frequency response of the lowpass Butterworth filter 125
3.13. Zeros and poles for the Butterworth digital filter 126
3.14. Signal processing flowchart 146
4.1. Pictures of the two initial prototype devices 148
4.2. Picture of the first stationary prototype device 150
4.3. Side view of SAS2 in an enclosure box 151
4.4. Front view of SAS2 152
4.5. Mounting attachment situated on the top side of the portable SAS2 154
4.6. Portable version of the SAS2 mounted in a child chariot carrier 154
4.7. Stationary version of the SAS2 mounted on a boom arm 155
4.8a. PCBs designed for the SAS2 system 156
4.8b. Block diagram of the system 157
4.9. Physical system used for conducting a sensitivity analysis 165
4.10. Sensitivity analysis of model parameters 170
4.11. Planar microphone array 176
4.12. Beam pattern of the array 178
4.13. Picture of the SAS2 measurement setup in the anechoic chamber 181
4.14. Plot of the sound wave detected by one of the microphones 182
4.15. Plots of the magnitude and phase of the reference signal 183
4.16. Plots of the magnitude and phase of all signals collected in the anechoic chamber 183
5.1. Stationary SAS2 setup at the UC site 188
5.2. Position of snowharp thermocouple array 189
5.3. Frame with thermocouples referred to as a "snowharp" 189
5.4. Portable measurements being made at the UC site 192
5.5. Snowpit being sampled at UC site 193
5.6. Picture of the BC site 194
5.7. Picture of the SC site on the ridge looking toward Mount Inflexible 195
5.8. Picture of the SC site taken in the forest 196

5.9. Ecotone between the forest and the open ridge for the SC site 196
5.10. Picture of the BPC site showing the clearing and the forest 197
5.11. Picture of the BS site 198
5.12. Picture of the BM site 200
5.13. Acoustic and gravimetric samples being taken along the transect (1) 201
5.14. Acoustic and gravimetric samples being taken along the transect (1) 202
5.15. Picture of the Bow Lake site situated on the frozen ice of Bow Lake 203
5.16. Picture of the NSH site showing the slope with artificial old-season snow 204
5.17. Picture of the IPFS, showing the road and the nearby forest 205
6.1. Upper Clearing Stationary (UCS) site time-series data of $\bar{y}$, $\bar{\rho}$, SWE and $\bar{\theta}_w$ 207
6.2. ESC30 and acoustic density comparisons 213
6.3. ESC30 and snowpit density comparisons 214
6.4. Acoustic and snowpit density comparisons 215
6.5. Temperature measurements at UCS site 220
6.6. UCS site time series data of temperature and heat flux 221
6.7. Acoustic and snowpit temperature comparisons 224
6.8. Acoustic and dielectric liquid water content comparisons 228
6.9. UCS site acoustic parameters 233
6.10. Example of acoustic image sampled by SAS2 235
6.11. Acoustic image observed on 2 February 239
6.12. Acoustic image observed on 16 February 246
6.13. Acoustic image observed on 18 April 241
6.14. Acoustic image observed on 18 April 242
6.15. Acoustic image observed on 2 May 243
6.16. Acoustic image observed on 10 May 244
6.17. Acoustic image observed on 12 May 245
6.18. Acoustic image observed on 14 May 246
6.19. Histogram of repeated measurements 248
6.20. Absolute temperature error and windspeed relationship 251
6.21. Sawmill Creek (SC) site transect of $\bar{\rho}$, SWE and liquid water content 255
6.22. Sawmill Creek (SC) site transect temperature, speed, attenuation and Ψ 256
6.23. Snowpit #1 stratigraphy at SC site 258
6.24. Snowpit #2 stratigraphy at SC site 259
6.25. Snowpit #3 stratigraphy at SC site 260
6.26. Snowpit #4 stratigraphy at SC site 261
6.27. Snowpit #5 stratigraphy at SC site 262
6.28. Example of acoustic scattering due to buried conifer tree 263
6.29. Example of acoustic image taken near a tree well 264
6.30. Error comparisons between acoustic and non-acoustic parameters (1) 266
6.31. Error comparisons between acoustic and non-acoustic parameters (2) 267
6.32. Error comparisons showing effect of an assumed t_{max} on the absolute error 269

NOMENCLATURE

Acronyms

CE	Common Era of historical time
RMSD	Root Mean Squared Difference
MB	Mean Bias
LWC	Liquid Water Content (%)
MLS	Maximum Length Sequence
SNR	Signal-to-Noise Ratio
DAC	Digital-to-Analog Converter (DAC)
ADC	Analog-to-Digital Converter (ADC)
LTI	Linear Time-Invariant (LTI)
FFT	Fast Fourier Transform
IFFT	Inverse Fast Fourier Transform
LFSR	Linear Feedback Shift Register
SOS	Second Order Sections
IIR	Infinite Impulse Response
FIR	Finite Impulse Response
STFT	Short Time Fourier Transform
ISTFT	Inverse Short Time Fourier Transform
OLA	Overlap-Add
FBS	Filter-Bank Summation
PCB	Printed Circuit Board
SAS2	System for the Acoustic Sensing of Snow
FET	Field -Effect Transistor
DC	Direct Current
IC	Integrated Circuit
V	Volt
A	Amp
LED	Light Emitting Diode
USB	Universal Serial Bus
FPGA	Field-Programmable Gate Array
I2C	Inter-Integrated Circuit bus
SPL	Sound Pressure Level

Roman

SWE	Snow Water Equivalent (mm or $\mathrm{kg\ m^{-2}}$)
$\mathbf{u}$	Vector that describes movement of the porous frame
$\mathbf{U}$	Vector that describes movement of the fluid in the porous frame
$\mathrm{div}(\ )$	Divergence
t	Time (s)
k_p	Permeability of porous medium ($\mathrm{m^2}$)
κ	Effective thermal conductivity of porous medium ($\mathrm{W\ m^{-1}\ K^{-1}}$)

q_F	Heat flux ($\mathrm{W\ m^{-1}}$)
A_s	Area of snow pillow ($\mathrm{m^2}$)
K_r	Bulk modulus of snow particles comprising the frame (Pa)
K_b	Bulk modulus of the porous medium frame (Pa)
f	Frequency (Hz)
m_f	Inverse fluid mobility ($\mathrm{Pa\ s\ m^{-2}}$)
m_s	Mass of snow ($\mathrm{kg\ m^{-3}}$)
$F(\kappa)$	Dimensionless correction factor as function of $\kappa \in \mathbb{R}$
$\mathrm{Ber}(\kappa)$	Real part of Kelvin function
$\mathrm{Bei}(\kappa)$	Imaginary part of the Kelvin function
$i = \sqrt{-1}$	Imaginary number
E	Young's modulus of snow (Pa)
G	Shear modulus of snow (Pa)
E_0	Young's modulus of material comprising the frame (Pa)
G_0	Shear modulus of material comprising the frame (Pa)
l_k	Complex root of Biot solution equation
$c_{s,k}$	Speed of sound in snow ($\mathrm{m\ s^{-1}}$) corresponding to complex root k
f_c	Percolation theory exponent (dimensionless)
T	Temperature (°C or Kelvin, as noted in text)
$\mathbf{F_t}$	Surface tension force vector
L_s	Distance over which surface tension force acts (m)
C	Curve over which the surface tension force acts
$\lvert\mathbf{F_{t,y}}\rvert$	Magnitude of surface tension force acting in the vertical direction (N)
$\lvert\mathbf{F_{ac}}\rvert$	Magnitude of the force vector holding the snow particles together (N)
$\lvert\mathbf{F_p}\rvert$	Magnitude of the downward-acting force of the snow particles (N)
V_a	Volume of air occupying the pore spaces of the control volume ($\mathrm{m^3}$)
V_i	Volume of ice occupying the pore spaces of the control volume ($\mathrm{m^3}$)
V_w	Volume of water occupying the pore spaces of the control volume ($\mathrm{m^3}$)
V_T	Total control volume of porous medium ($\mathrm{m^3}$)
S_w	Water saturation (dimensionless) in control volume
g	Acceleration due to gravity ($\mathrm{m\ s^{-2}}$)
R_g	Ideal gas constant for air ($\mathrm{J\ kg^{-1}\ K^{-1}}$)
R	Radius at air-water interface (m)
K_a	Bulk modulus of air (Pa)
K_f	Bulk modulus (Pa) of pore space fluid

P	Air pressure (Pa)
K_w	Bulk modulus (Pa) of water
c_w	Speed of sound in water ($\mathrm{m\,s^{-1}}$)
c_{sh}	HFA speed of the second Biot P-wave in the pore space of the medium ($\mathrm{m\,s^{-1}}$)
c_s	Speed ($\mathrm{m\,s^{-1}}$) of the second Biot P-wave at frequency ω (rad)
c_0	Speed of sound in air ($\mathrm{m\,s^{-1}}$)
a_p	Mean diameter of pore spaces in snowpack (m)
b_k	Cumulative sum of terms (real number)
n_T	Number of terms added during summation
$\{f_1,\ldots,f_N\}$	Frequencies (Hz)
$\{c_{s,1},\ldots,c_{s,N}\}$	Speeds of sound in snow ($\mathrm{m\,s^{-1}}$) corresponding to known frequencies
$\{c'_{s,1},\ldots,c'_{s,N}\}$	Speed outputs of the forward model ($\mathrm{m\,s^{-1}}$)
$s[t]$	Digital (discrete) source signal as a function of discrete timestep t.
$r_k[t]$	Signal received by microphone k
$n[t]$	Measurement noise signal
$m_k[t]$	Microphone k frequency response
$p[t]$	Frequency response of the loudspeaker
$e[t]$	Electronic circuit frequency response
$d[t]$	Direct air-coupled wave travelling from loudspeaker to microphones
$c[t]$	Enclosure case effect on the acoustic signal
L_M	Length of the MLS (integer number)
$L_{\min}$	Minimum length of MLS
f_{ds}	DAC sampling rate (Hz)
t_{mls}	Time duration of the MLS (s)
P_s	Signal power (W)
P_{MLS}	MLS signal power (W)
B	MLS Bandwidth (Hz)
$\mathrm{F}(\,)$	Discrete Fourier Transform operator
$\mathrm{IF}(\,)$	Inverse Discrete Fourier Transform operator
$\mathrm{Rev}(\,)$	Operator that reverses a discrete signal
L_{lag}	Lag (number of samples)
$\mathrm{conj}(\,)$	Complex conjugate transform operator
$x_w[t], y_w[t]$	Discrete signal buffers
$B_k^*[t]$	Raw bitstream from a microphone
$B_k[t]$	Binary signal from microphone

f_s	Microphone sampling rate (Hz)
Q	Coefficient representative of attenuation in medium (dimensionless)
Q_0	Zero-offset Q value
a	Attenuation coefficient (Nepers m^{-1})
$A[t,\omega]$	Discrete attenuated signal spectrum at discrete time t and frequency ω
$A_0[t,\omega]$	Source signal spectrum
$M_Q[t,\omega]$	Function relating Q, ω and c variables
$G[t,\omega]$	Discrete Gabor transform
$g[t,t']$	Inverted Gabor transform
$w[t]$	Time-domain windowed trace
$W[f]$	Frequency-domain windowed trace
$h[t]$	Input signal
t_k	Discrete timestep at element k
$x[t]$	Discrete signal in time domain
$x'[t]$	Reconstructed estimate of discrete signal
$w_f[t]$	Gaussian window function
$G'[t,\omega]$	Regularized Gabor transform
$G_{\lim}$	Gain limit (dB)
$Q[t]$	Discrete Q-values as a function of time
$\mathbf{x_{os}}$	Discrete vector of microphone offset distances (m)
m_s	Slope of offset line
$H_k[t,\omega]$	Gabor transform of attenuation-corrected traces for microphone k
$U[Z_t,Z_x]$	Z-transform of $u[t,x]$ signal
$\{Z_t,Z_x\}$	Time-shift and spatial-shift operators
$v[t,x]$	Moveout velocity as a function of time t and offset x
t_0	Offset time (s)
S_w	Water saturation (dimensionless or %)
$\bar{\theta}_w$	Depth-averaged water content (dimensionless or %)
$\bar{T}$	Depth-averaged snow temperature (°C or Kelvin)
$\bar{y}$	Snow depth measured using a depth rod (cm or m)
$\bar{\rho}_s$	Depth-averaged snow density ($\mathrm{kg\ m}^{-3}$)
ρ_s	Snow density ($\mathrm{kg\ m}^{-3}$)
L_n	Input noise level for microphone (dB)
a_c	Attenuation coefficient at maximum MLS frequency (Nepers m^{-1})
P_0	Reference RMS pressure (Pa)
P	Sound power of source (W)

S_0	Directionality factor (m^2)
c_a	Speed of sound in air ($\mathrm{m\ s}^{-1}$)
y_a	Distance from the SAS2 microphones to the snow surface (m)
y_s	Snow depth used in SAS2 design calculations (m)
p_a	Barometric air pressure (Pa)
$\{p_1, p_2, p_3\}$	Pressure at interfaces (Pa)
$\{L_1, L_2, L_3\}$	SPL at interfaces (dB)
p_{ref}	Reference pressure (Pa)
L_n	Microphone noise level (dB)
$f_{\max}$	Maximum frequency component in signal (Hz)
d	Diameter of loudspeaker (cm or m)
x_a	Inter-element microphone array spacing (cm or m)
f_a	Frequency of wave incident on array (Hz)
$D_{dB}(\theta)$	Beam pattern magnitude (dB)
x_s	Footprint of sound wave on snow surface (cm or m)
Δy	Minimum resolvable acoustic layer width (cm or m)
a_s	Sound source dimension (m)
d_r	Longest room dimension (m)
l_w	Length of sound-absorbing wedges in anechoic chamber (m)
T	Period of sound wave (s)
dH / dt	Internal energy change of snowpack ($\mathrm{W\ m}^{-2}$)
$K\downarrow$	Downward shortwave radiation flux ($\mathrm{W\ m}^{-2}$)
$K\uparrow$	Upward shortwave radiation flux ($\mathrm{W\ m}^{-2}$)
$L\downarrow$	Downward longwave radiation flux ($\mathrm{W\ m}^{-2}$)
$L\uparrow$	Upward longwave radiation flux ($\mathrm{W\ m}^{-2}$)
H_s	Sensible heat flux ($\mathrm{W\ m}^{-2}$)
H_L	Latent heat flux ($\mathrm{W\ m}^{-2}$)
H_P	Heat flux due to blowing snow or precipitation ($\mathrm{W\ m}^{-2}$)
G	Ground heat flux ($\mathrm{W\ m}^{-2}$)
K^*	Net shortwave radiation flux ($\mathrm{W\ m}^{-2}$)
L^*	Net longwave radiation flux ($\mathrm{W\ m}^{-2}$)
Q^*	Net radiation flux ($\mathrm{W\ m}^{-2}$)

Greek

ξ	Effective fluid content increment (dimensionless)
∇^2	Laplacian
ρ	Total density of the control volume ($\mathrm{kg\ m^{-3}}$)
ρ_f	Fluid density in the pore spaces of the medium ($\mathrm{kg\ m^{-3}}$)
m_f	Inverse fluid mobility ($\mathrm{Pa\ s\ m^{-2}}$)
η	Dynamic viscosity of pore space fluid ($\mathrm{Pa\ s}$)
μ	Shear modulus of the porous medium (Pa)
ϕ	Porosity (dimensionless)
α	Tortuosity (dimensionless)
$\omega = 2\pi f$	Angular frequency of sound wave ($\mathrm{rad\ s^{-1}}$)
ϕ_c	Critical porosity (dimensionless) used in percolation theory
σ_s	Surface tension coefficient for water ($\mathrm{N\ m^{-1}}$)
θ_F	Angle over which surface tension force acts (rad)
ϕ_i	Ice fraction (dimensionless) in control volume
θ_c	Contact angle (rad)
σ_{iw}	Surface tension between snow particle and water ($\mathrm{N\ m^{-1}}$)
σ_{wa}	Surface tension between water and air ($\mathrm{N\ m^{-1}}$)
ρ_i	Ice density ($\mathrm{kg\ m^{-3}}$)
ρ_w	Water density ($\mathrm{kg\ m^{-3}}$)
ρ_s	Snow density ($\mathrm{kg\ m^{-3}}$)
ε_a	Volume fraction (dimensionless) of air in the pore space of the medium
ε_w	Volume fraction (dimensionless) of water in the pore space of the medium
χ_g	Dimensionless gas constant; heat capacity ratio of air (1.402)
η_a	Dynamic viscosity of air ($\mathrm{Pa\ s}$)
η_w	Dynamic viscosity of water ($\mathrm{Pa\ s}$)
δ	Dimensionless loss tangent
γ_s	Berryman coefficient (dimensionless)
$\tilde{\omega}$	Angular frequency above which speed of the P-wave is constant in snow (rad)
$\Psi = \psi_G = \psi_G$	Dimensionless scaling coefficient
$\varepsilon_T = 1.0\text{e-}10$	Small number used in loop iteration
$\varphi[t]$	Filter kernel of the snowpack
$\mu_k[t]$	Total measurement response of the system for microphone k

$\odot$	Hadamard multiplication operator
$\varphi_k^*[f]$	Truncated filter kernel in Fourier domain
$\varphi_k[t]$	Truncated filter kernel in time domain
Υ	Datatype (container) that holds the LFSR
π	Pi constant (3.1415…)
$\Delta[t,\omega]$	Filter kernel
σ_p	Stabilization parameter (dimensionless)
ω_h	Highcut frequency (Hz)
$\beta_1[t,\omega]$	Gabor transform of attenuated signal passed through snowpack
$\Gamma[t,x,\omega_\ell]$	Discrete matrix used for speed analysis
Ω	Parameter used in the application of the plane wave destruction filter
$\Gamma_M[t,x]$	Time-remapped matrix
$\bar{\rho}$	Depth-averaged snow density ($\mathrm{kg\ m^{-3}}$)
$\{\Lambda_1,\Lambda_2\}$	Transmission coefficients (dimensionless)
Γ_r	Reflection coefficient (dimensionless)
ς	Reflection/transmission coefficient parameter (dimensionless)
λ	Wavelength of sound pressure wave incident on array (m)
θ	Sound wave incidence angle (rad or degrees)
θ_m	Half-width angle (rad)
λ_{sr}	Longest wavelength that can be measured in an anechoic chamber (m)

CHAPTER 1
INTRODUCTION

1.1. Importance of Snow

Snow has long been recognized as an important component of the hydrologic cycle (King et al., 2008; McKay and Adams, 1981). The production of water from snowpack runoff and the influences of snow on regional and global climates have always been of extreme importance to the stability of human societies. For example, in the Middle East, the Tigris and Euphrates rivers are dominated by snowmelt from the Taurus and Zagros Mountains (Beaumont, 1998; Özdoğan, 2011; Şensoy et al., 2005). To ancient societies situated near these mountains, floods and the effects of climate change may have been associated with snowfall. Perhaps the earliest mention of this relationship can be found in the Avesta, a sacred Zoroastrian religious text recounting the story of Yima, a shepherd instructed to create an enclosure of land to protect humans, plants and animals from a great flood. The story portrays the flood occurring due to snowmelt (Darmesteter, 1880, pp. 15-16):

> And Ahura Mazda spake onto Yima, saying: 'O fair Yima, son of Vîvanghat! Upon the material world the fatal winters are going to fall, that shall bring the fierce, foul frost; upon the material world the fatal winters are going to fall, that shall make snow-flakes fall thick, even [fourteen fingers] deep on the highest tops of mountains. And all the three sorts of beasts shall perish, those that live in the wilderness, and those that live on the tops of the mountains, and those that live in the bosom of the dale, under the shelter of stables. Now with floods that stream, with snows that melt, it will seem a happy land in the world, the land wherein footprints even of sheep may still be seen.'

Snow may have been mentioned in an Egyptian temple inscription attributed to Ramesses II that is associated with travelling difficulties in cold regions (New York Times, 18 October 1906). The Greek historian Herodotus wrote on snowmelt contributions and climate to the Danube River in Central Europe. Considering that snowmelt would contribute negligible amounts of water to the discharge of the Nile River due to the climate of Egypt and Africa (Beloe 1812, Euterpe XXII, pg. 75), Herodotus later reasoned in a similar fashion that snowmelt comprised the flow of the Danube River in Central Europe (Beloe 1812, Melpomene, L, pg. 203). During Roman rule of Asia Minor, contemporary writers recounted that large amounts of

snowfall would often disrupt the life of people living on the Cappadocian plateau (Van Dam, 2002, p. 14). Snowmelt caused flooding in this region, endangering homes and livelihoods. An example is the Lycus ("Wolf") River that often raged with snowmelt (Van Dam, 2002, p. 42).

Snow had major economic importance in the past. As recounted by Needham (1959), quantitative measurements of snow were made as early as 1247 CE by Chinese investigators, who trapped snow in containers to estimate the amount of water entering rivers as runoff (Peck, 1972). Since Medieval times up to the invention of refrigeration, "snow merchants" would collect snow from mountains bordering the Mediterranean Sea. The snow would lucratively be sold for consumption in drinks and deserts or for the preservation of imported food during transport (McNeill, 1992, pp. 124–125). In 1836, the chief engineer of Chanago Canal in the state of New York, John B. Jervis, may have conducted one of the first snow surveys in the United States. Jervis was concerned that not enough snow would fall to provide water for canal transportation (Harrington, 1953). From 1850 to 1900, settlers in the Sacramento Valley of California realized that much of the water in the region was from snowmelt. Snow depth was also measured in the nearby Sierra Nevada mountains to ascertain the amount of water available from runoff (Powell, 1987). Historical accounts may suggest that runoff from snowmelt contributed to the great flood of 1862 in the Sacramento Valley, indicating that snow has long affected the hydrology and agriculture of this region (Kattelmann, 1996). J. E. Church popularized snow surveying in California and the United States during the early part of the 20th century (Church, 1933). Welsh settlements in Wales and North America from 1170 CE to 1902 CE were dependent on snowmelt for farming and agriculture (Pomeroy and Jones, 1996).

In a modern context, snow is a major contribution to the water balance, climate and economy of many geographic regions. Approximately 33% of precipitation in Canada originates as snow (Brown, 1995; Pomeroy and Goodison, 1997) and "is a primary source of Canadian water supplies" (McKay and Findlay, 1971). Snow contributes more than 80% of water to streams located in the Prairies (Barnaby, 1980; Gray and Landine, 1988; Gray et al., 1970; McKay and Blackwell, 1961), Arctic (Marsh, 1990), and western United States (Daly et al., 2000; Marks et al., 2001; Rice et al., 2007).

Nearly all streamflow in the High Arctic is derived from snowmelt (Prowse, 1990; Woo, 1980). Snow is present in the High Arctic for more than 8 months per year. The hydrology of the High Arctic is completely dependent on snow (Woo, 1982a) and climate change in this

region will affect vegetation, animals, and well as biogeochemical cycles, influencing human lifestyles and forestry operations. Because snow covered area influences energy exchange with the atmosphere, global climates will also be affected by changes in the Arctic snowpack (Callaghan et al., 2011).

The Arctic is characterized by snowpacks that are dense, extremely variable, and cold. Snow temperatures can remain less than -15 °C until the month of June, thereby depressing snowmelt and the production of liquid water for most of the winter season (Woo and Sauriol, 1980). Moreover, ground heat flux contributes negligible energy for snowmelt in the Arctic due to the presence of extensive permafrost underlying ice layers at the base of the snowpack (Woo et al., 1982). When the snowpack becomes isothermal, reaching 0 °C due to higher levels of net radiation and increasing day length, snowmelt occurs rapidly. Hilltop areas with lower snow depth become snow-free before valleys with greater snow depth that retain snow until late in the ablation season. Preferential flow channels occur through the snowpack, diverting water to lakes and streams (Woo, 1980; Woo and Sauriol, 1980). The high density and hardness of snowpacks in valleys contribute to the formation of these flow channels (Woo and Sauriol, 1980), creating "snow dams" that impede runoff and rupture due to seepage of liquid water through the snow (Xia and Woo, 1992). The movement of liquid water through snow-covered catchments in the Arctic is thereby dependent on the density, liquid water content, and temperature of the snowpack in these environments. Because the magnitude and timing of snowmelt governs the hydrology of the Arctic, understanding of these processes is important to predict flooding and adequate apportionment of water supplies (Marsh and Woo, 1985, 1984a, 1984a, 1984b; Woo and Marsh, 1978).

Snowmelt is a major contribution to discharge in rivers situated within the United States. Examples include Oregon (Harr, 1981); Washington (Koch and Fisher, 2000; Pelto, 2004); Colorado (Fassnacht et al., 2001); and California (Davis et al., 1999). Snowfall from the Catskill Mountains provides water to the city of New York (Matonse et al., 2010; Pierson and Kick, 1995). The contribution of snow to the water supply of this city has been monitored for decades (Porter and Horton, 2010). Snowmelt contributions from the San Juan Mountains and Sangre de Cristo mountains contribute runoff to the Rio Grande Basin of New Mexico that provides water to the city of El Paso, Texas and parts of the country of Mexico (Rango et al., 2010). Snow provides more than 50% of runoff in California (Mount, 1995) and more than 75% of water for

agricultural use in this state (Rosenthal and Dozier, 1996). Reservoirs on streams draining from the Sierra Nevada Mountains of California do not hold significantly more water than annual snowmelt runoff (Rittger et al., 2011). Much of the water supply of agriculture-producing state Idaho is derived from snowmelt, leading Abramovich (2007) to refer to snow as "Idaho's frozen liquid gold." In a similar fashion, snow is considered to be "white gold" in California (Roos, 1991).

Population increase in the western United States will place increasing demands on water use in the near future. Accurate knowledge of the amount of water available from snow and the timing of runoff is required to manage water in this region (Bryant and Painter, 2010; Harshburger et al., 2005). Barnett et al. (2008) have indicated that due to a reduction in snowfall, an increase in precipitation falling as rain, and snowmelt occurring earlier in the spring, smaller amounts of water will be available during the summer in the western United States. This foretells water shortages for the region and implies that careful planning is necessary to mitigate the effects of these changes.

Further south in the Sierra Nevada of California, higher air temperatures during the winter months have resulted in an increase in snowmelt and an increase in streamflow during the winter season (Johnson et al., 1997). From April to July, snowmelt from the Sierra Nevada contributes 18 billion cubic meters of water. This represents 35% of annual flow used for urban and agricultural water use (Roos, 2006). Hydroelectric power generation using water from 25 rivers in California is also dependent on snowmelt. Adequate apportionment, use and competitive pricing of electricity is dependent on measuring the amount of water that enters these rivers in the form of snowmelt (Freeman, 1997). Reservoirs providing water to the City of San Francisco are dependent on snowmelt for normal operation (Mazurkiewicz et al., 2011).

More than 90% of electricity from hydroelectric power generation in British Columbia is derived from snowmelt (Assaf et al., 1995). A depth of 1 mm runoff from snowmelt produces $1 million worth of hydroelectric power in Quebec (Brown and Tapsoba, 2007). In the Mount Megantic area of the Quebec Eastern Townships, snow is a vital resource for tourism involving skiing and fishing and also provides water for human consumption (Fourtier, 2009). Snow provides water for hydroelectric power generation in the Grand Lake watershed of Newfoundland. Snow surveys are conducted in this watershed to assess the amount of water available for hydroelectric power generation and the potential for flooding (Banfield, 1991).

Hydroelectric power generation is also dependent on snowmelt in the mountains of France (Duband and Lallement, 1992) and the Swiss Alps (Martinec and Rango, 1995).

In areas where snowmelt is a major contribution to the hydrological cycle, large amounts of runoff can result in flooding. Flooding has occurred in watersheds draining into the Peace River of Alberta (Sampson, 1961) and the St. Lawrence River of eastern Canada (Bruce, 1962). In 1967 flooding due to snowmelt occurred along the Chena River near Fairbanks, Alaska (Gray, 1968), leading the United States government to establish a regional early flood warning system. In 1969 excessive snowmelt contributions to the Souris River caused downstream flooding in the city of Minot, North Dakota (Pomeroy et al., 2007a). Extensive flooding also occurred during 2011 in the same area. This led government officials in both Canada and the United States to begin cross-boundary border talks in March 2013 following the ablation of large amounts of snow that increased water levels in the Alameda and Rafferty reservoirs situated near Estevan, Saskatchewan (The Star Phoenix, 23 March 2013). Flooding from snowmelt is an environmental hazard in New Brunswick, where forest thinning may influence the timing and amount of runoff (Daugharty and Dickison, 1982).

The southern part of the state of Wyoming has been subjected to flooding from snowmelt originating in the Sierra Madres and Snowy Range mountains (Dietrich and Rieman, 2001). The rapid melting of large amounts of snow deposited in Arizona during the Labor Day storm of 1970 caused extensive flooding, the destruction of roads and infrastructure by debris, and the loss of 22 lives (Thorud and Ffolliott, 1972). In the western Cascades of Oregon (Christner and Harr, 1982) and the Rocky Mountains of British Columbia (Toews, 1991), landslides were triggered by snowmelt flooding. Landslides influenced by snowmelt were found to damage fish habitat by the addition of sediment to Quesnel Lake, British Columbia (Cheng, 1987). Despite the presence of the Folsom Dam, flooding due to snowmelt occurred in 1995 within the American River basin near the city of Sacramento, California (Kattelmann, 1996). Extensive flooding occurred throughout most of the northeastern United States due to rapid snowmelt during January 1996. The flooding caused the deaths of 30 people and $1.5 billion in damages (Anderson and Larson, 1996).

Rain-on-snow events increase snowmelt and the potential for flooding (Osterhuber, 1999) Harr (1981) identified rain-on-snow events as the major contributing factor to flooding caused by snowmelt in northern Oregon. Rain-on-snow events commonly occur in the Pacific Northwest

from British Columbia to Idaho and south to northern California (Brunengo, 2007), and are often observed during the winter in the mountains of California (Kattelmann, 1997; McGurk et al., 1993), in the Coquitlam River Basin of the British Columbia Coast Mountains (Solano, 2008), and in the Alps of Switzerland (Collins, 1988). Most severe floods in United Kingdom are caused by rain-on-snow events (Blyth et al., 1974). Rain-on-snow was the causal factor of the January 2005 flood in the Santa Clara River basin of Utah that destroyed 20 homes (Bardsley and Julander, 2005).

In the Sierra Nevada, high flow rates are significantly increased by mid-winter rain-on-snow events that flush nutrients and pollutants into Lake Tahoe, thereby influencing the ecology of the lake. The floods also transport sediment into the lake due to stream bank erosion that occurs during high-magnitude discharge rates (Kattelmann, 1999). Large amounts of snowmelt that enter rivers are often passed through spillways instead of dams, causing supersaturation of water with air (Speers, 1972). This can cause death of fish from gas bubble disease, and has been an issue in the Columbia River Basin (McGrath et al., 2006) where water from snow is used for hydroelectric power generation (Speers and Versteg, 1982).

Large amounts of snowmelt due to heat transport by pyroclastic flows can also cause excessive flooding, necessitating the monitoring of snow on Mount St. Helens in Washington State (Lea, 2007). Flooding occurred along the Toutle River when Mount St. Helens erupted in 1980 (Lea and Reid, 2006). Volcanic ash from the volcano reduced the albedo of snowpacks in the vicinity of the mountain and increased the rate of snowmelt (Crook et al., 1981; Tangborn and Lettenmaier, 1981).

The 2013 Alberta floods that affected the city of Calgary, the Kananaskis Valley and the town of Canmore were exacerbated by rain-on-snow events. Due to large amounts of sediment transported during the flood, as well as landslides and stream bank erosion, the hydrology and ecology of the Rocky Mountains was irrevocably changed. The cross-sectional area of stream channels in the region must be re-measured to accurately determine discharge and fish species such as trout that spawn in gravel river bottoms may be affected by sediment transported during the flood (Davison and Powers, 2013; Martel, 2013; Weber, 2013). The flooding in Alberta displaced more than 10 000 people and will likely cost more than $256 million to rebuild infrastructure (CBC, 2013). The flooding may eventually cost the city of Calgary more than a billion dollars (Kaufmann, 2013).

On the Canadian Prairies, frozen soils during the time of ablation and fast melt rates ensure that most water from snowmelt enters the prairie hydrological cycle as surface runoff (Gray and Landine, 1988; Gray et al., 1985; Shook and Pomeroy, 2012). Snowmelt on the prairies contributes runoff to areas of internal drainage, such as sloughs and wetlands, where high rates of evapotranspiration due to vegetation exceed rates of infiltration to groundwater reservoirs (van der Kamp and Hayashi, 1998). Snowmelt in this region provides water for irrigation, farming, hydroelectric power and human consumption (Steppuhn et al., 2003). The rate and timing of snowmelt is important for the proper design of hydrologic structures in this region (Gray et al., 1970).

Along with low rainfall rates, the occurrence of drought is an aspect of the prairie environment influenced by these runoff processes. The Prairies have shown significant increases in temperature and decreases in precipitation and streamflow since the 1950s (Gan et al., 1997). The reduction of snowfall during drought can reduce snowmelt contributions to a wetland up to 79% (Fang and Pomeroy, 2008). The depletion of snow from wetlands consequently reduces runoff to rivers. During the recent drought of 1999-2005, snowmelt contributions to prairie rivers from both mountain snowpacks and prairie wetlands remained low, along with lower than average precipitation (Pomeroy et al., 2011). Due to reduced water availability for agriculture, the recent drought caused the loss of 41 000 jobs in 2001-2002 and was also associated with a drop in national agricultural production of $3.6 billion (Stewart et al., 2011).

Climate change and drought in California also necessitates the need for efficient snow management systems to ensure adequate snowmelt water supply (Davis et al., 1999). During the 1976-1977 drought in California (Hannaford and Howard, 1979), 8000 wells were drilled to provide adequate water for agricultural use, fish spawning was affected due to low water levels, the reuse of irrigation water exposed ecosystems to toxic chemicals, a drop in hydroelectric power generation led to an increase in fossil fuel consumption, aquatic recreational businesses were pushed close to bankruptcy, and forests were affected by disease and fire (Brown, 1978). Another drought affected California for six years from 1987 to 1992 (Roos, 1995).

The amount of snowfall on the prairies decreased by 17.2% from the 1960s to the early 2000s (Steppuhn et al., 2003). Climate change models for the Canadian Prairies predict future increase in surface temperature, a decrease in available soil moisture during the summer months,

a decrease in the water available from snowmelt due to a smaller amount of precipitation falling as snow, and an earlier snow ablation season (Barnett et al., 2005).

Gan (2000) suggests that on the prairies, snow trapping and water storage management techniques should be used to locally mitigate the effects of climate change to increase the amount of water from snowmelt. The trapping of snow is accomplished by snow fences (Cooley et al., 1981; Pomeroy and Gray, 1995; Tabler, 1971), controlling the height of stubble left on a field during the winter season (Steppuhn et al., 2009), planting trees, and by moving snow or soil using earth-moving equipment (Stepphun, 1980). Stubble height control and the trapping of snow allows for farmland with saline soil to increase grain yield due to dilution of the salt by runoff (Stepphun, 2005). Approximately 30 million hectares of farmland on the North American Great Plains are affected by saline soils (Steppuhn and Miller, 1998). Stepphun and Wall (1996) found that trapping snow on alfalfa fields increased the water content in the top 1.2 m of the soil by 78% and increased forage yield by 40%. Snow can increase the survival of winter wheat by providing insulation against colder temperatures during the winter (Stepphun and Nicholaichuk, 1986). Trapping of snow also prevents snowdrifts from forming on roads and highways (Tabler and Jairell, 1980) and can be used to provide water for animals (Jairell and Schmidt, 1995; Sturges, 1989). "Snow harvesting" involves the trapping of blowing snow by pits situated in the lee of obstructions. This can be significantly cheaper than drilling wells to provide water for agriculture (Jairell and Schmidt, 1992).

Snowmelt in the Rocky Mountains provides most of the water in major rivers on the Prairies due to extensive non-contributing areas in Alberta, Saskatchewan and Manitoba, making water use in this region reliant on mountain hydrology (Harlan, 1969; Pomeroy et al., 2007a). An example is the Saskatchewan (Curry and Mann, 1965) and Athabasca River (Pomeroy et al., 2009) systems that provide water to major cities in the provinces of Alberta and Saskatchewan as well as oil sand development regions.

As the "world's natural water towers," mountain chains are estimated to globally provide more than 80% of fresh water to human populations (Viviroli et al., 2003). Due to sensitivity of hydrologic systems in the mountains, monitoring of snow and climate in these regions is similar to "canaries in the coal mine" (Diaz, 2007). The mountains thus provide early warning of changes in natural resources. Rather than using empirical relationships, physically-based models driven by measurements of snow in mountain catchments are required to properly assess changes

in water resources (Cline et al., 1997). However, as argued by Viviroli et al. (2003), there is a lack of research on hydrological processes in the mountains, making mountain hydrology a scientific priority.

In the Rocky Mountains, a decrease in river discharge due to a decrease in snow accumulation, an earlier snow ablation season, and an increase in water consumption by stakeholders in Alberta will contribute to reductions in future water availability (Bonsal et al., 2003; Byrne et al., 2006; Lapp et al., 2005; St. Jacques et al., 2010). Decreases in snow accumulation have been observed for the past two decades over the entire region of the Rocky Mountains (Ingersoll et al., 2009). The understanding of climate change in and near mountain regions is hampered by the relative sparcity of meteorological observations (Freeman, 2009; Lundquist and Rochford, 2007; Smith, 2009).

To estimate the rate, timing and volume of snowmelt in the Rocky Mountains, various researchers have contributed to an understanding of the processes in this region. The Cold Regions Hydrological Model (CRHM) was tested to ascertain the applicability of this model for prediction of hydrological processes in ungauged basins (Fang et al., 2013). Turbulent energy transport in the near-surface boundary layer at meteorological observation sites situated in valley bottoms are affected by wind gusts, necessitating the use of modelling techniques beyond simple mass and energy-balance equations (Helgason and Pomeroy, 2012a). Due to the complexity of terrain in the mountains, shading of solar radiation can influence snowmelt, necessitating the development of snowmelt energetics models using algorithms from computer graphics (Marsh et al., 2012). Reba et al. (2012) estimated sublimation from snowpacks using eddy covariance techniques. Debeer and Pomeroy (2009) modelled snowmelt and snowcover ablation in an alpine cirque.

Forest-gap thinning treatments will increase the amount of runoff from snow, but this is influenced by energy balance and microclimate in complex terrain (Ellis et al., 2013). Thinning of forests reduces interception of snow, decreases evaporation and sublimation, and increases the amount of water available from snowmelt (Ffolliott and Gottfried, 2003). Forest thinning experiments have been conducted to increase snowpack runoff for human use (Bernier and Swanson, 1986; Swanson and Stevenson, 1971). At the Marmot Creek Research Basin (MCRB) in Alberta, Canada, Swanson and Golding (1982) created a thinned forest in a “honeycombed”

pattern, showing that this treatment increased runoff by 20% to 30%. However, Chinook winds in Alberta can sublimate snow in clearings, reducing snowmelt runoff (Swanson, 1980).

Reduction of forest canopy by fire can increase overland flow from snowmelt and cause flooding. An example of this was the 2009 Mill Flat Fire near Harmony, Utah (Julander et al., 2011). Skidmore et al. (1994) found that burned areas of a forest had 9% more runoff from snowmelt and an ablation rate 57% greater than unburned areas. Burning of vegetation by wildfire can reduce forest canopy cover and change snow accumulation patterns, influencing the amount of snowmelt produced during ablation (Drake et al., 2008).

The mountain pine beetle epidemic in western Canada has affected the hydrology of the Rocky Mountains (Pomeroy et al., 2012). Infestation of Lodgepole pine trees by the mountain pine beetle causes tree morality. This is due to infection of trees by blue-strain fungi transmitted by the beetle as an epidemiological vector (Solheim, 1995). The death of trees in a forest reduces canopy cover, decreases the amount of water available from snow (Winkler and Boon, 2009) and increases the rate of snowmelt (Teti, 2009). Hydrological modelling of mountain catchments affected by the mountain pine beetle has been conducted to assess the influence of attacks on water availability from mountain catchments (Borden et al., 2010; Pomeroy et al., 2012).

Snow acts as an insulator for tree species such as Yellow Cedar (*Chamaecyparis nootkatensis*) by protecting the roots from freezing and moderating soil warming during the spring. Changes in snowpack melt rate and distribution due to climate change has led to the decline of yellow cedar in Alaska. This decline has commercial and ecological ramifications (Hennon, 2007). Snowcover affects the distribution of mountain hemlock (*Tsuga mertensiana*) since this plant thrives on the additional moisture from snowmelt (Nachlinger and Berg, 1988). Melting snow affects the composition and spatial distribution of plants in mountain communities (Billings and Bliss, 1959).

Measurement of snow depth and hardness has been used to assess the ability for reindeer to forage for food during the winter in western Alaska (Clagett, 1978). The amount of snow on the ground is associated with the movement patterns of animals. For example, it has been observed that elk are found in areas with less than 70 mm SWE from snowmelt (Farnes and Romme, 1993). Snow also provides a home for algae (Hoham et al., 1993; Takeuchi, 2001), bacteria and fungi (Brooks et al., 1993) that help to comprise a snow ecosystem (Hoham, 1989).

Snow protects animals from cold temperatures during the winter since it is a thermal insulator (Kalliomaki et al., 1984).

Snow deposited on lake ice influences the timing and rate of ice development and melt-out. The formation of lake ice shows spatial patterns of thickness over the entire water body. Thicker ice formation as "black ice" initially occurs near the lake edges. Wind-redistributed snow accumulates near the lake edges, insulating the ice surface and reducing ice growth. Over time, ice growth becomes thicker near the lake center, but snow deposited at the lake edges increases in mass. The heavier snow near the edges can crack the ice, causing water to seep into the bottom of the snowpack. Refreezing of the water produces "white ice" on top of the black ice, thereby increasing the strength of the black ice areas (Adams, 1982). Understanding the interactions between snow, ice formation and melt on lakes can be of importance to establishing the rate and timing of nutrient release from the ice into the lake (Adams and Lasenby, 1982). Physical measurements of snow are required for models of ice formation on lakes (Ménard et al., 2002).

Snow accumulation affects the mass (Pelto and Brown, 2011), energy balance (Sloan, 1986) and chemical composition (Winski et al., 2011) of glaciers, thereby influencing the magnitude of runoff (Krimmel and Tangborn, 1974), the timing of the spring freshet during ablation, and the rate of glacial retreat. Meltwater from glaciers was found to contribute up to 50% of the discharge to the Bow River above Banff during the month of August (Hopkinson and Young, 1997). Due to a rise in global temperatures over the past 150 years, the area of glaciers has been shrinking. The meltwater from glacier wastage increases discharge in rivers situated within the glacial basin watershed (Hopkinson, 1997). In the Hood River basin of Oregon, glacier wastage provides ~75% of water to the Upper Middle Fork River, with a 31% decrease in discharge occurring over the next 50 years due to climate change and glacier retreat (Nolin and Phillippe, 2008). Most of the flow in the Yukon River above Whitehorse is derived from snowmelt. This river provides hydroelectric power and water for the City of Whitehorse. Climate change may affect the future availability of water from this river (Janowicz and Ford, 1994). Glacier melt contributions to runoff will change stream temperatures and influence fish spawning (Nolin and Phillippe, 2008).

Avalanches develop due to the formation of a weak layer of snow with low shear strength that causes structural instability in the snowpack, thereby resulting in the movement and

transport of snow under the influence of gravity (Perla, 1981). The development of a layer of weak snow in the snowpack is coincident with a temperature gradient and the presence of facetted crystals of depth hoar (Scheler et al., 2003), low density, brittle forms of snow particles with large grains (Pfeffer and Mrugala, 2002). Avalanches are a major threat to human life in mountainous terrain (McClung and Schaerer, 2006). For example, avalanches killed 24 people in western Canada and the United States in 2008 (CBC, 2008). Avalanches can also destroy buildings and are hazardous to roads that travel through mountainous terrain (Armstrong, 1981, 1973), necessitating the development of early warning systems (Judson, 1977). These warning systems are effective when dependent on physically-based models of snowpack evolution that require accurate measurement of snowpack parameters (Bartelt and Lehning, 2002; Lehning et al., 2002a, 2002b, 1999).

Avalanches play a significant role in mountain hydrology. The redistribution of snow by avalanches can contribute between 19% and 57% of snow to the mass balance of a glacier, increasing the amount of snowmelt during ablation. Because snow deposited at higher elevations is redistributed to lower elevations, this permits glaciers to develop up to 1600 m below the regional snowline. The redistributed snow may have a quicker melt rate at lower elevations due to higher temperatures (de Scally, 1996). Alternately, snow redistributed to lower elevations can accumulate in areas where topographic shading influences snowmelt, thereby changing the timing and duration of streamflow in mountain catchments (de Scally, 1995). Sediment deposited by the avalanche can also affect the energy balance of the glacier by reducing the albedo (de Scally, 1996).

Avalanches can dam rivers, reducing discharge and increasing the potential for flooding during ablation. The mass of snow from an avalanche deposited on an ice-covered water body can either break up the ice or depress the ice enough to cause the development of a flood wave at the lake outlet. Sediment and other organic debris transported by the avalanche will be deposited in the lake, reducing water depth and affecting fish that spawn in gravel beds. The sediment is also a source of gravel required by these fish species, indicating a long-term relationship between avalanche activity and fish spawning (de Scally, 1996). Williams and Clow (1990) reported that an avalanche on the ice of Emerald Lake, California, produced a flood wave that lowered the survival rate of brook trout embryos from 90% to 2.5%. Avalanches also remove soil from mountain regions, influencing the hydrologic response of watersheds (de Scally, 1996).

The geographic presence or absence of snow affects the location and operations of ski resorts (Crowe and Baker, 1983; Mote et al., 2007). For example, projected climate change in Ontario (Harrison et al., 1986), Colorado (Lazar et al., 2006) and the Columbia River basin (Mote and Hamlet, 2009) will increase regional temperatures and decrease the number of days available for skiing. Birkeland (1996) found that snow density and SWE of snow was greater on artificial ski runs cleared from forest than under the forest canopy due to the presence of artificial snow and the mechanical packing of the snowpack by skis, thereby influencing the amount of water available for runoff. Compaction of snow will influence metamorphism and snow thermal properties affecting the timing of snowmelt runoff (Kattelmann, 1986). Extensive runoff from snow can occur in ski areas due to deep snowpacks resulting from the removal of vegetation and the creation of buildings and roads that increase overland flow (Osterhuber et al., 2007).

1.2. Snow Measurement Parameters

Mathematical models of snowpack evolution require energy and mass flux inputs. From these inputs, energy and mass balance equations are used to calculate internal state variables. Internal state variables of some snowpack evolution models are listed in Table 1.1.

Not all of these models have a "detailed" development of snowpack physics. The internal state variables of the models are updated at model timesteps and show temporal changes in snowpack properties. The internal state variables are not directly measured by instrumentation due to a lack of deployed observation technologies and the inability to measure these variables at all locations where the model is applied.

The models of snowpack evolution are used to predict climate, the amount of water available for runoff during the time of ablation, or the potential for avalanche activity in a particular area. The importance of these processes has been discussed in the previous section. The predictive ability of the model is related to the accuracy of the inputs and internal state variables. Table 1.1 shows that six variables are often used in models of snowpack evolution.

The snow depth $\bar{y}$ is a measure of the vertical length of snow determined with respect to a reference datum normally taken as the ground. The density ρ_s of snow is the mass of snow m_s in a reference volume V_T. Together these variables are used to define Snow Water Equivalent (SWE), a point measurement of the depth of water created by the melting of the snow.

Assuming that water spread over an area of $1\,\mathrm{m}^2$ has a depth of $1\,\mathrm{mm}$ and a mass of $1\,\mathrm{kg}$ and that snow depth $\bar{y}$ is reported in centimeters, snow density and SWE is defined by (Pomeroy and Gray, 1995):

$$\rho_s = m_s / V_T \tag{1.1}$$

$$\mathrm{SWE} = \left(0.01\,\mathrm{cm}^{-1}\ \mathrm{m}^3\ \mathrm{kg}^{-1}\ \mathrm{mm}\right)\bar{y}\bar{\rho} \tag{1.2}$$

SWE is the mathematical product of snow depth and density, and is commonly reported in units of mm or $\mathrm{kg\,m}^{-2}$. Using Equation (1.2) to obtain up-scaled estimates of SWE over an area requires the addition of a term that models the covariance between depth $\bar{y}$ and density $\bar{\rho}$ (Pomeroy and Gray, 1995; Stepphun, 1975). For prairie snowpacks with depth less than 60 cm, the covariance term is small (Shook et al., 1993). As given by Pomeroy and Gray (1995), Equation (1.2) uses a unit conversion factor for historical purposes, since snow depth is often reported in centimeters rather than meters.

The measurement of depth alone is not sufficient to obtain SWE since density can vary over an area (Gray et al., 1970) and must be measured rather than assumed to be a particular value such as $100\,\mathrm{kg\,m}^{-3}$ for freshly-fallen snow (Pomeroy and Gray, 1995). Judson and Doesken (2000) found that new snow density ranges between $10\,\mathrm{kg\,m}^{-3}$ and $350\,\mathrm{kg\,m}^{-3}$ at sites in the United States. Nominal snow densities are between $80\,\mathrm{kg\,m}^{-3} \le \rho \le 600\,\mathrm{kg\,m}^{-3}$ (Pomeroy and Gray, 1995).

Model	ρ_s	ϕ	θ_w	α	κ	T	Note	Reference
2LM	X	X	X		X	X	a	(Yamazaki, 2001; Yamazaki et al., 2004)
CLASS	X	X	X		X	X	b	(Bartlett et al., 2006; Verseghy, 2000, 1996, 1991; Verseghy et al., 1993)
CLIM2-TOP	X	X	X		X	X	c	(Bonan et al., 2002; Yang and Niu, 2003)
CLM3	X	X	X		X	X	d	(Oleson et al., 2004)
COLA-SSib					X	X	e	(Mocko and Sud, 2001; Mocko et al., 1999; Sud and Mocko, 1999, 1999)
CoupModel					X	X	f	(Gustafsson et al., 2001)
CRHM	X	X	X		X	X	g	(Pomeroy et al., 2007b)
CROCUS	X	X	X		X	X	h	(Brun et al., 1992, 1989)
ISBA	X	X	X		X	X	i	(Douville et al., 1995; Noilhan and Mahfouf, 1996)
MATSIRO					X	X	j	(Takata et al., 2003)
MOSES	X	X	X		X	X	k	(Cox et al., 1999)
SAST	X	X	X		X	X	l	(Jin et al., 1999)
SNOWPACK	X	X	X	X	X	X	m	(Bartelt and Lehning, 2002; Fierz and Lehning, 2001; Lehning et al., 2001, 1999)
SNTHERM	X	X	X		X	X	n	(Gustafsson et al., 2001; Hardy et al., 2000; Jordan, 1991)

Table 1.1. Internal parameters explicitly used in snowpack models. The snow density is given by ρ_s, the porosity by ϕ, the water content by θ_w, the tortuosity by α, the thermal conductivity by κ and the temperature by T.

a. Explicitly includes the presence of depth hoar
b. Snow density is initially considered to be 100 kg m^{-3} and increases with time
c. The porosity is used in calculating the mass balance of liquid water
d. Implicitly includes the water saturation as changes in the mass of snow and liquid water
e. Thermal conductivity is noted as being one of the most sensitive of all parameters
f. The model does not parameterize the movement of liquid water through the snowpack
g. CRHM provides a selection of algorithms for modeling snowpack evolution and uses SWE as an input
h. Snow metamorphism affects albedo and heat fluxes through the snowpack
i. Models heat transport between vegetation and the snowpack
j. Directly calculates for SWE using a balance equation
k. Snow modifies the thermal conductivity, temperature and saturation of the soil layer
l. Includes the water saturation in the effective snow density
m. Includes the effects of snow metamorphism and vapor exchange in snow pore spaces
n. Uses a mixture to model the water saturation of snow

Snow is a porous medium consisting of pore spaces of air and a frame comprised of ice from snow particles sintered together by metamorphic processes (Buser and Good, 1986). Due to thermal gradients in the snowpack created due to mass and energy fluxes and the production of water by melting snow, a snowpack is an uneven mixture of air, ice and water (Colbeck, 1976a). Assuming that the volumes of air (V_a), ice (V_i) and water (V_w) are fractional constituents of a medium with control volume V_T, the air porosity θ_a, liquid water content θ_w and ice fraction θ_i are given by (Bartelt and Lehning, 2002):

$$\theta_a = \frac{V_a}{V_T}, \theta_w = \frac{V_w}{V_T}, \ \theta_i = \frac{V_i}{V_T} \tag{1.3}$$

$$\theta_a + \theta_w + \theta_i = 1$$

Equation (1.3) is subjected to a continuity constraint since the fractional constituents of the medium cannot exceed unity. Liquid water content θ_w is a measure of the fractional amount of liquid water in the pore spaces of the snowpack. This is distinct from Snow Water Equivalent (SWE), which is the resulting depth of water after the snowpack has completely melted.

The density of snow ρ_s is related to the density of air ρ_a, water ρ_w and ice ρ_i by (Bartelt and Lehning, 2002):

$$\rho = \rho_s = \rho_a\theta_a + \rho_w\theta_w + \rho_i\theta_i \tag{1.4}$$

The porosity is the volume fraction of pore spaces in the medium:

$$\phi = \frac{V_a + V_w}{V_T} \tag{1.5}$$

The water content θ_w and water saturation S_w are measurements of snow wetness and are often reported as a percentage calculated from a volume fraction. Whereas the water content θ_w is the volume fraction of water per total volume V_T, the water saturation S_w as used by authors

such as Colbeck (1976) is the volume fraction of water in the pore space of the snowpack (Marsh, 1991):

$$S_w = \frac{\theta_w}{\phi}$$

The irreducible water content θ_e is the residual fraction of water per unit volume that cannot be removed from the pore spaces of the snowpack (Marsh, 1991). This is also expressed as the irreducible water saturation S_e (Colbeck, 1976a). Let V_e be the volume of irreducible water in a control volume. Then,

$$\theta_e = \frac{V_e}{V_T}$$

$$S_e = \frac{\theta_e}{\phi}$$

From the definition of irreducible water saturation, the effective water saturation S^* as the total amount of water held by the pore spaces of the snowpack and the effective porosity ϕ_e is defined as (Colbeck and Anderson, 1982):

$$S^* = \frac{S_w - S_i}{1 - S_i}$$

$$\phi_e = \phi\left(1 - S_e\right)$$

The diffusion of gas into a snowcover in the absence of wind is dependent on the tortuosity α, which is a dimensionless number quantifying the straight-line deviation of the pore spaces in a medium. The tortuosity is a measure of the convoluted nature of the pore spaces. The tortuosity is always $\alpha \geq 1$, with $\alpha = 1$ for cylindrical pores oriented parallel to the direction of fluid motion (Stoll, 1989). Tortuosity is one of the parameters used to model gas diffusion in snow using Fick's Law (Jones et al., 1999). It can be measured using x-ray tomography (Kaempfer et al., 2005).

Since tortuosity cannot be easily measured in the field, Sommerfeld et al. (1996) assumed that $\alpha = 1$. For a model of CO_2 transport through snow, Massman et al. (1995) assumed that $\alpha \approx 0.7$ and that α varies weakly with density. Assuming that the range of tortuosity in snow is $0.75 \leq \alpha \leq 0.92$, Mast et al. (1998) related tortuosity to porosity by $\alpha = \phi^{1/3}$ using the theory of Millington (1959). However, according to Bear (1972, pg. 111), the assertion that $\alpha < 1$ for all porous media is incorrect, since this neglects the effect of tortuosity on the speed of flow through the porous medium. Moreover, the $\alpha \geq 1$ assumption has been used in the Buser (1986) model of sound propagation through snow, where $1.0 \leq \alpha \leq 1.25$ (Arons and Colbeck, 1995). In this thesis, it is assumed that $\alpha \geq 1$ in accordance with the definition given by Bear (1972).

The temperature T is a measure of heat present in a substance. For a snowpack, temperature measures the effective heat of the air, ice and water that comprises the porous medium. Assuming that the effective thermal conductivity of the porous snow medium is κ and the temperature gradient over a depth of snow is $\partial T / \partial y$, the heat flux q_F for steady-state heat flow is given by Fourier's Law (Langham, 1981):

$$q_F = -\kappa \frac{\partial T}{\partial y} \tag{1.6}$$

Snow density has been related to thermal conductivity by an empirical equation developed from gravimetric and heat pulse probe measurements of snow (Sturm et al., 1997; Usowicz et al., 2008).

1.3. Near-Surface Snowpack Measurement Instrumentation

The following review discusses snowpack measurement instrumentation deployed near the earth's surface. Although snowpack properties have been measured by sensors mounted on satellites (Frei et al., 2012; König et al., 2001; Lucas and Harrison, 1990) and airplanes (Rees, 2006), these applications are outside of the scope of this review.

The purpose of the review is to describe measurement instrumentation that determines similar snowpack properties to the sensing system developed in this thesis. This includes commercial devices used for snowpack measurement. These devices obtain snowpack

measurement parameters that were described in the previous sections. The purpose of these measurement devices is to obtain data for input into models of snowpack evolution and for validation of the internal state variables.

1.3.1. Depth Rod

Measurements of snow depth along a transect are commonly made using a snow ruler. The ruler is a graduated aluminum rod or stick with markings indicating a measurement scale (Goodison et al., 1981). On a 1 m snow depth rod (Snowmetrics Inc., Fort Collins, Colorado), markings are engraved every 1 cm, with a number scale given in 10 cm increments. Screw threads on each rod permit multiple rods to be coupled together so that snow depths greater than 1 m can be measured. The rod is pointed on the measurement end to ensure that the ground surface can be contacted and the measurement rod remains upright when snow depth is determined. Snow sampling rod design is discussed by Woo (1997).

Snow depth rulers are also installed in permanent locations along a snow course. The numbers on the ruler are manually read by snow surveyors. In geographic areas that are not easily accessible during the winter season, the numbers are large enough to be read from an airplane using binoculars. Snowmelt around the base of the ruler can cause inaccuracies in the measured snow depth (Pomeroy and Gray, 1995). Some early snow course markers did not have numbers but markers spaced every two feet along a twenty-foot long post (Henderson, 1953).

Because measurement of snow depth is time-consuming, Sturm (1999) devised a self-recording snow depth probe (Snow-Hydro Inc., Fairbanks, Alaska). Similar to a ski pole, the device uses a sliding electromechanical attachment that coincides with the snow surface when the tip of the pole contacts the ground surface. A switch is closed when a depth measurement is to be made, and a circuit logs the distance between the tip of the pole and the ground surface.

Changes in snow depth were determined by Elder et al. (1999) using GPS measurements of elevation. A GPS receiver was placed on the snow surface next to a marker and the elevation recorded. The measurement was repeated at the maker at various times over the snow accumulation season and changes in snow depth were determined. A similar measurement principle was used to determine changes in snow depth when the GPS receiver was placed on a moving snow machine.

Determining snow depth using a measurement ruler can be inaccurate if vegetation, logs or ice layers are situated beneath the snow surface and the ruler cannot easily contact the ground. If the soil under the snowpack is unfrozen and consists of organic matter, the rod can penetrate the soil and an inaccurate measurement of snow depth is obtained (Elder et al., 1999). During each measurement, care must be taken to ensure that the rod is inserted parallel to the ground surface. This can produce inaccurate measurements of snow depth if the ground surface under the snowpack is not flat due to the presence of undulating topography or bedrock near the snow surface. The snow ruler creates a hole in the snowpack at every sampling location. This does not permit multiple samples to be taken at the same sampling point. Blyth et al. (1974) indicate that snow depth measured using a conventional measurement rod is often inadequate for forecasting snowmelt runoff due to the inability and labour required to sample at a large number of points over a landscape.

1.3.2. Snow Sampler Tubes

A snow sampling tube ("snowtube") is used to extract gravimetric samples of snow to measure Snow Water Equivalent (SWE) and depth-integrated snow density (Goodison et al., 1981). Snowtubes and snow surveying were initially popularized by Church (1933) in the early 1900s. The snowtube is made of metal or non-opaque plastic with a serrated cutting end (Crook and Freeman, 1973; McKay and Blackwell, 1961). The plastic tube allows the snow surveyor to visibly see the snow sample after it has been extracted. A sample is extracted by pushing the tube through the snowpack until the serrated cutting end reaches the ground surface. Handles on the top side of the tube allow the sampler to be turned so that the serrated cutting end extracts a plug of soil. The sampler is carefully removed from the snowpack and placed on a calibrated scale to measure SWE. Depth measurements taken with a measurement ruler permit the calculation of depth-averaged snow density from SWE measurements made by the tube (Goodison et al., 1981). The snow sampling tube accuracy can show high correlations with snowpit measurements of SWE (Fassnacht et al., 2010). Snow sampling tubes are used along snowcourses by snow surveyors to measure areal estimates of SWE for streamflow forecasting and runoff modelling (Goodison, 1975; Tabler, 1982).

Farnes et al. (1980, 1982) tested 22 different snowtube designs against gravimetric snowpit measurements of SWE. Ensuring that snow was not lost from the tube, they found that

smaller-diameter snowtubes without a sharpened cutting end overestimated SWE by 9% to10%, whereas snowtubes with sharper cutting ends had an overestimation of 3% to 6%. This finding coincides with Peterson and Brown (1975), who compared "Federal" snow sampling tubes to samples of snow carefully extracted from the snowpack, finding that the snow tube overestimated SWE. For shallow snowpacks with less than 1 m depth, the error in measurement was found to be 1% to 3% (Goodison, 1978). Farnes et al. (1980, 1982) found that increasing the snowtube diameter decreased the overestimation of SWE. Snowtubes with a sharpened cutting end area > 20 cm^2 had the least error and the ESC-30 snowtube with a cutting end area of 30 cm^2 showed the least measurement error when used to sample snowpacks with a depth of less than 1 m. Turčan and Loijens (1975) present a simple model of snow tube insertion into snow, showing that compression of the snow as the snowtube moves through the snowpack can be an source of error in the application of this technique.

A complete mechanical design and blueprint for the ESC-30 snowtube and calibrated weighting scale is presented by Farnes et al. (1982). The total length of the snowtube is 126 cm and the tube body is made out of clear plastic. This allows for the snow sample contents to be visible to the snow surveyor so that the presence of vegetation in the extracted sample can be determined. The inner diameter of the snowtube is 69.85 mm and markings are placed on the tube in centimeter increments. The cutting end is comprised of 16 slanted teeth. The spring scale has calibrated markings to report the amount of SWE in centimeter increments.

The snow sampling tube is invasive since it destroys the snowpack at each sampling location (Smith et al., 1967). Davis (1973) refers to snow sampling as "archaic, inefficient, and hard work." If a plug of soil is not extracted to cap the bottom of the tube, the extracted snow sample can fall out and the measurement will have to be repeated. When the snow temperature is colder than the air temperature, snow can freeze to the inside of the tube (Goodison et al., 1981). The snow will have to be extracted before another measurement is made. The presence of buried vegetation and logs beneath the snow surface will often interfere with the collection of a snow sample. Ice crust formation inside of the snowpack can cause difficulties with the extraction of a sample. (Powell, 1987). Due to the relative size of the snowtube, it can be difficult to carry over long distances. To allow for easier transportation of the snowtube, Gluns and Rose (1992) designed a special backpack referred to as the "Kootenay Cruiser."

1.3.3. Snowpits

A snowpit is created when measurements of snow stratigraphy are required, invasive instruments (as discussed in the following sections) are used to measure the snowpack, or when visual observations of snowpack properties or processes are being made. The snowpit is simply a hole in the snowpack that is dug using a shovel down to the ground surface. The ground surface is taken as the origin of the depth reference datum, with a ruler used to measure the distance of each layer from the bottom. Layers are classically identified by an observer in the field using visual interpretation (Fierz et al., 1999).

To reduce the subjectivity of layer identification, infrared imaging and image processing algorithms has been used to identify layers after the snowpit is created (Shea et al., 2012; Tape et al., 2010). The size of snow particles in the snowpack can be measured by microscopy or spectroscopy (Painter et al., 2007). By photographing the snow surface, the snow surface profile can also be determined (Fassnacht et al., 2009; Kinar and Pomeroy, 2008a; Rees, 1998).

Marsh and Woo (1984) measured the propagation of water in a melting snowpack by injecting a red-colored dye tracer into the side of a snowpit. Photographs of the snowpit side revealed preferential flow paths for meltwater. A similar experiment was conducted by Peitzsch et al. (2008) at a field site using red food coloring as the dye tracer.

McGurk and Kattelman (1988) and McGurk and Marsh (1995) used a "cutter box" to extract horizontal slices out of a snowpit wall. The slices were photographed and then observed for melt channel formation.

Williams et al. (2010) injected a blue dye tracer into a snowpack and then used a large "snow guillotine" to progressively shave away vertical sections from the snowpit wall. The instrument created by Williams et al. (2010) is similar to but much larger than a microtome utilized to prepare biological specimens for mounting on a microscope slide (Hodge et al., 1954). The Visible Human Project also created a large microtome (referred to as a "cryomactrotom") for thin-sectioning a frozen human cadaver so that medical imaging techniques could be tested (Sachse, 2004). In a similar fashion to the Visible Human Project, Williams et al. (2010) photographed the side of the snowpit after each snow slice was removed and then used commercial software to recombine the camera images into a 3D image of meltwater flow in snow.

Fortin et al. (2002) injected artificial ice layers with a florescent dye tracer and inserted the ice layers into the side of a snowpit. Interaction of water with the ice layers was revealed by movement of the dye tracer.

The density of each layer in the snowpit is normally estimated using a measurement scoop with a known volume. Samples are extracted from a pit wall not facing the sun to mitigate the effects of solar insolation on changes in snowpack properties. A sample from each snowpack layer is extracted using the measurement scoop. The mass of the measurement scoop is determined using a weight scale and the density of each layer calculated by dividing mass by volume (Fierz et al., 1999).

Triangular measurement scoops (RIP Sampler – from Ronald Ivan Perla, a Canadian snow scientist) are used to determine snow density. The triangular measurement scoop (Snowmetrics Inc., Fort Collins, Colorado) is ideal for density measurement since a metal cutter fits into a slide on the top of each scoop. The triangular scoop is inserted into a snowpack layer and the cutter is used to extract a snow sample. Two types of triangular scoops are available: a small scoop with a volume of $250\ cm^3$ and a large scoop with a volume of $1000\ cm^3$.

The "CRREL" snow sampler is a $500\ cm^3$ cylinder with a serrated metal edge that is inserted into the side of the snowpit (Crook and Freeman, 1973). The length of the CRREL sampler is 20 cm long. Alternately, the "Canadian" snow sampling scoop has a volume of 250 cm^3, is only 19 cm in length and may contain serrated cutting teeth for sampling high-density snow. Both types of snow tubes can be capped for sample extraction. Snow density samples collected using both types of tubes show high correlations between datasets, indicating that the samplers perform in a similar fashion (Gary, 1967).

Snowpit sampling is time-consuming and the creation of a snowpit is labour-intensive (Pomeroy and Gray, 1995). In a similar fashion to the other measurements discussed in this section, the digging of a snowpit is an invasive procedure that destroys the snowpack structure. After the snowpit is created, heat transport from the surrounding landscape and insolation from the sun will cause melting of the snow. This is the reason why the snowpit is covered with a tarp (Marsh and Woo, 1985) if further experiments are required hours after the snowpit is dug. If the snowpit is not backfilled with snow after experiments are completed the snowpit creates a safety issue at backcountry locations and presents a hazard to skiers.

1.3.4. Pressure Sensors

The most common pressure sensor used to measure SWE is a snow pillow. The classic snow pillow (i.e. SP 3 from Sommer Messtechnik GmbH, Austria) is an oval (Beaumont, 1965) or rectangular (Molnau, 1971) pressure transducer buried in the ground surface under the snowpack. The pressure transducer is filled with an antifreeze chemical. A manometer senses the mass of snow on top of the pillow by measuring changes in fluid pressure (Beaumont, 1965). The mass of the snow is related to SWE by:

$$\text{SWE} = \frac{m_s}{A_s} \tag{1.7}$$

In the above Equation (1.7), A_s is the area of the snow pillow computed using simple geometry.

Snow pillows are only suitable for permanent installation at a field site and cannot be moved. This adds logistical and cost considerations to the selection of a snow pillow site (Farnes, 1967). Moreover, because the pressure transducer is filled with a liquid, mechanical abrasion can cause leakage (Ord, 1968), damage can be inflicted by animals (Davis, 1973; Shannon, 1968) and air bubbles can develop in transducer lines (Cox et al., 1978). Frost-heave processes and the presence of bears in high-latitude environments necessitates the need for snow pillows in Alaska and the Yukon Territory to be installed on top of a specially-designed frame (Clagett and McClure, 1994). Because the antifreeze chemical mixture commonly used in the snow pillow is hazardous to animals, some research has been conducted to find suitable mixtures that are less toxic (McGurk, 1992).

The size of the pillow is related to the maximum SWE that can be measured. Pillows with larger area are required for sites with greater snow depth and SWE (Beaumont, 1965). A recommended minimum diameter for the snow pillow is 3 m (Farnes and Rompel, 1969). The development of ice layers between the pillow and the ground surface and uneven melt rates between the ground and the top of the snow pillow (Johnson and Schaefer, 2002) can cause measurement errors. Julander (2007) noted that snow pillows can be manufactured from steel or Hypalon, a black synthetic rubber compound. Julander (2007) found that the steel pillows accumulated more SWE than the Hypalon pillows, suggesting that the black color of the Hypalon rubber influenced snowmelt rates. The snow pillow is often painted white to reduce heating by solar insolation (Beaumont, 1965).

Snow pillows are tested in the field by a laborious procedure of removing all of the snow from the top of the pillow. The mass of removed snow is then carefully determined by bagging and weighing (Davis, 1973). Smith and Boyne (1981) installed a snow pillow in a laboratory test chamber, finding that the response of the transducer did not show a linear relationship with applied pressure. They also presented a mathematical model of changes in snow pillow pressure with environmental temperature. Johnson (2004) realized that most snow pillow designs rely on "rule-of-thumb" engineering estimates. To quantify errors in snow pillow measurements, Johnson (2004) used mathematical modelling to show that SWE pressure sensor errors occur due to: (1) a shear stress exerted from the side of the snow pillow caused by a difference in compressibility between the adjacent snow and the pillow; (2) differences between thermal properties of the pillow and the surrounding snowpack causing an uneven melt rate; and (3) sensors with a high compressibility that influence measurement of the snowpack's mass. A mathematical procedure for correction of these errors has been proposed by Johnson and Marks (2004).

Modern snow measurement devices that are similar to snow pillows use load cells in lieu of antifreeze. This reduces the possibility of mechanical breakdown. The load cell is a transducer that changes in resistance with a change in applied pressure. Moffitt (1995) designed a load-cell device referred to as a "snow plate." A circular plate with 1.1 m diameter was suspended on three load cells. Due to the smaller area of the sensor relative to most snow pillow designs, ice-bridging effects were observed to be a major influence on sensor results. Johnson et al. (2007) describe a load-cell based SWE measurement device that consists of eight aluminum plates with dimensions of 3.2 m by 3.0 m (i.e. SSG from Sommer Messtechnik GmbH, Austria). In a similar fashion to a snow pillow, the plates are installed during the snow-free season in a frame flush with the ground surface to ensure that measurement errors do not occur due to uneven settling of the snow. The plates are perforated with holes to reduce the ponding of meltwater on the surface of the device. Load cells are situated on each corner of the center plate to measure the mass of the snow on each of the surrounding plates. The idea is similar to a much older design that arranges triangular plates around a weighing scale (Beaumont, 1966).

1.3.5. Dielectric

Dielectric measurement techniques relate the complex dielectric constant (relative permittivity) of snow to the porosity ϕ and/or volumetric water content θ_w. For most of these techniques, the relationship between the quantities is empirical. Dielectric instruments generally measure snowpack wetness as volumetric water content θ_w instead of water saturation S_w.

The Finnish snow fork consists of two parallel stainless-steel prongs with sharpened ends that act as a transmission line (Sihvola and Tiuri, 1986; Tiuri and Sihvola, 1986; Toikka, 1992). Although popularized by Finnish investigators, similar methods involving three prongs (Gerdel, 1954) and four prongs (Kendra et al., 1994) have also been proposed.

A triangle wave generator connected to a Voltage Controlled Oscillator (VCO) sends an RF wave into one of the prongs of the Finnish snow fork via a coaxial cable (Denoth et al., 1984). After inserting the prongs into the snowpack, the snow medium acts as a load that terminates the transmission line (Sihvola and Tiuri, 1986). Adjusting the frequency of the VCO from 500 MHz to 900 MHz (Toikka, 2010) enables measurement of the real and imaginary parts of the snow dielectric constant by determining the resonant frequency of the snow. The resonant frequency of the air medium must also be determined since the ratio of these frequencies is related to the dielectric constant (Sihvola and Tiuri, 1986). Assuming that the snow has a neutral pH level of 7, an empirical relationship developed for snow at a frequency of 1 GHz is then used to calculate porosity and water content. All snow samples used to develop this relationship were collected in Finland. For snow with impurities and a known pH level, another empirical relationship can be used to calculate these quantities (Tiuri et al., 1984).

The Finnish snow fork is normally used in a sampling configuration where the prongs are inserted horizontally into the side of a snowpit. However, the prongs can be placed on the snow surface for a dielectric half-space measurement, or inserted into the snow surface at a 30° or 45° angle. This requires the snow fork measurements to be multiplied by a correction factor (Moldestad, 2005).

The effective measurement volume of the Finnish snow fork has been estimated as 47 cm^3 (Techel and Pielmeier, 2011). Alternately, assuming that the volume of measurement is comprised of a cylinder with 1 cm radius and 7.5 cm height, the volume is 24 cm^3 (Moldestad, 2005). The effective sampling area has been estimated as 15 cm^2 (Techel and Pielmeier, 2011).

The Finnish snow fork can measure snow with a maximum liquid water content of 10% and a maximum snow density of $600\ \mathrm{kg\ m^{-3}}$ (Toikka, 2010), with a minimum of ~0% liquid water content (Techel and Pielmeier, 2011). The water content measurement error of the Finnish snow fork is reported as ±0.5% (Sihvola and Tiuri, 1986) but has been claimed to be as low as ±0.3% (Moldestad, 2005). Mechanical compression of the snow as the snowfork is inserted into the snowpack will cause snow density to increase by 1% to 2%, adding another source of error to the measurement (Techel and Pielmeier, 2011). The error in determination of density is $\pm 5\ \mathrm{kg\ m^{-3}}$ (Moldestad, 2005). The Finnish snow fork was estimated by Harper and Bradford (2003) to have a density measurement error of 5%. A possible disadvantage of the Finnish snow fork is that the empirical relationship developed for snow at a frequency of 1 GHz may not be valid for snow at tuning frequencies of 500 MHz to 900 MHz.

Two other resonant-frequency sensors have been proposed. The saw resonator consists of a saw blade with a parallel wire. Designed for hard snow such as melt-crusts and ice layers, the sensor operates using a sensing principle where the RF wave creates a mirror image of the saw blade in the snowpack. In a similar fashion to the snow fork, the ratio of resonant frequencies is used to calculate the dielectric constant. The coaxial resonator sensor is placed on the snow surface. The sensor is pushed slightly into the snow surface to ensure proper coupling of the sensor to the snow medium. A dielectric half-space calculation is used to determine the complex dielectric constant of the snow surface layer (Denoth et al., 1984).

Free-space measurement sensors require the extraction of a snow sample from the snowpack (Denoth, 1989). The sample is placed in a Styrofoam holder between a transmitting and a receiving horn antenna. An electromagnetic wave at frequencies greater than 10 GHz is sent between the two horns. Measurements made in the air medium without a sample present allow for determination of the complex transmission and reflection coefficients of the snow sample. The reflection coefficients are related to the dielectric constant of the snow (Hallikainen et al., 1986). An alternate "ellipsometric" measurement places the two horns at an angle to the surface of the snow sample. Measurement of the reflection coefficient is related to the dielectric constant by an empirical relationship (Denoth, 1999).

Capacitor cell sensors are comprised of two parallel metal plates, between which is placed a snow sample. Similar to the measurement of an unknown capacitor on a circuit board, an impedance bridge is used to measure the capacitance of the snow using frequencies in the 10

kHz to 10 MHz range. The ratio of snow capacitance to the empty-cell capacitance is used to calculate the dielectric constant of the snow (Perla, 1991). An alternate design uses an aluminum pipe. The snow sample is placed inside of the pipe (Camp and LaBrecque, 1992; Perla and Banner, 1988). A parallel plate capacitor sensor can be placed on the end of a rod and the rod used to penetrate the snow surface to obtain snow profile measurements (Louge et al., 1998).

The Denoth capacitive sensor (referred to in this thesis as a "Denoth meter") consists of a flat plate antenna that is inserted into the snowpack (Denoth, 1994). The volume of measurement of a flat plate antenna sensor is 900 cm^2 corresponding to a 4 cm by 15 cm by 15 cm cuboid (Boyne and Fisk, 1990). The area of measurement has been estimated as 176 cm^2 (Techel and Pielmeier, 2011). This is a larger measurement area than the Finnish snow fork.

The Denoth sensor is similar to a printed circuit board (PCB) antenna. Three types of antennas can be used. Two of these antennas have an effective measurement depth of 1.5 cm and 1 cm respectively, whereas another antenna is used for snow surface measurements in the top 5 mm of the snowpack (Denoth and Wilhelmy, 1988). The first two sensors can also be placed on top of the snow surface to make half-space measurements of snow surface wetness.

A 20 MHz oscillator and the flat-plate Denoth sensor are connected to a twin-T bridge. The bridge is balanced by turning a potentiometer or can be automatically balanced by an electronic circuit connected to the bridge. The current across the balanced bridge is determined and related to the dielectric constant of snow by an empirical equation. Gravimetric measurements of snow density and the dielectric constant of snow are used to calculate the liquid water content of snow by this empirical equation. The balancing of a twin-T bridge is also used as the operating principle of a seven-plate air-gap condenser sensor (Denoth et al., 1984).

The flat plate sensor can be buried in the snowpack and used to measure diurnal cycles in snowpack wetness (Denoth, 1994). Techel and Pielmeier (2011) have shown that when compared to snow wetness measurements made with the Denoth capacitive sensor, the Finnish snow fork overpredicted water content by 1%. Although Denoth et al. (1984) found that the Finnish snow fork had a slightly higher standard deviation of measurements as compared to Denoth meter measurements, Williams et al. (1999) showed that there is no statistically significant difference between Denoth meter and Finnish snow fork measurements.

The Snow Pack Analyzer (SPA) system (Sommer Messtechnik GmbH, Austria) uses a flat coaxial cable antenna installed at an angle to the ground surface. The antenna is used by the

system to measure density and liquid water content of snow. A measurement of snow depth using an acoustic ranging sensor permits the calculation of SWE. A number of ribbon sensors situated parallel to the ground surface can be used to measure snow densities and liquid water contents throughout the snowpack. The sensor assembly needs to be installed during the snow-free season so that snowfall can accumulate over the antenna, which is buried in the snowpack in a similar fashion to a thermocouple assembly.

The theory of operation of the SPA sensor is given by Niang et al. (2003). It is assumed that the snowpack is comprised of a mixture of air, ice and water. Three equations (one serving as a constraint function) are used to solve for the volume fractions of the constituents. Substitution of the constraint function equation into one of the other equations provides two equations relating the dielectric constant of the snow to the dielectric constants of the air, ice and water comprising the snowpack. This does not require the use of empirical equations directly relating the snow dielectic constant to snow density.

The SPA sensor measures the dielectic constant of snow using Time Domain Reflectometry (TDR). This relates the speed of the pulse in the antenna to the snow dielectic constant (Jones et al., 2002). Determination of the snow dielectic constant using 6 kHz and 50 kHz electromagnetic waves permits two equations to be solved for two unknowns. The error in the measurement associated with a change in dielectric constant at the air-snow interface is corrected using a mathematical model. Niang et al. (2003) determined that the sensor could measure snow density with a maximum RMSD of 5% between gravimetric and dielectic measurements. The RMSD was 3% during the ablation period when the snowpack was isothermal.

1.3.6. Radar

Radar snow measurement systems operate by sending electromagnetic waves into snow and receiving the reflections. Two different types of radar measurements have been used for snowpack sensing applications.

Pulse radar sends a short impulse into the snowpack and the time difference between the sent and received pulses is used to determine snowpack stratigraphy (Harper and Bradford, 2003). The disadvantage of pulse radar is that the resolution is limited by the duration of the pulse. Pulses of smaller duration will give better resolution of layered media (Klauder et al.,

1960). However, the minimum pulse duration is limited by the transmitter and receiver circuits at frequencies in the GHz range. This in turn limits the operating resolution of pulse radars (Meikle, 2008). A unique application of pulse-based radars is tomographic imaging of a snowpack (Fortin and Fortier, 2001).

Frequency-Modulated Continuous Wave (FMCW) radar uses a frequency-swept pulse (chirp) to determine the distance to a reflector. Two horn antennas are situated at an offset distance. One horn produces an electromagnetic wave, whereas the other receives reflections (Stove, 1992). This is a bistatic radar system (Willis, 1991). The sent and received waves are homodyned by a time-domain analog mixer, creating a waveform that is low-pass filtered and digitized by an Analog-to-Digjtal Conveter (ADC). The difference waveform frequency spectrum is related to the snowpack layer distances and snow stratigraphy using an assumed snow density or dielectric constant of snow (Yankielun et al., 2004). The bandwidth of the chirp is commonly situated in the 2-6 GHz, 8-12 GHz, and 14-18 GHz ranges. Higher frequencies have better ability to resolve layers in the snowpack, but greater attenuation and less depth penetration (Koh et al., 2002). Lower frequencies are more appropriate for wet snowpacks due to attenuation created by high liquid water contents (Marshall et al., 2004).

FMCW radars are deployed above the snow surface and the antennas are moved over a short distance (less than 3 m) to obtain images of snowpack stratigraphy (Marshall et al., 2004). Moverment of the radar system enables a measurement of SWE to be made over a large area (Marshall et al., 2005). The FMCW radar can also be set up to measure snowpack stratigraphy at a point location (Ellerbruch and Boyne, 1980). FMCW radars have been mounted on a sled towed behind a snow machine to measure snowpack stratigraphy along a transect (Gubler and Hiller, 1984; Holmgren et al., 1998; Pomeroy and Gray, 1995). Mounted on a gondola situated ~30 m above the snow surface, the FMCW system has measured snowpack stratigraphy along a transect ranging over ~500 m (Yankielun et al., 2004). Upward-looking FMCW radar has been used to measure snowpack stratigraphy in avalanche-prone areas by burying the system in the ground (Gubler and Hiller, 1984). Snowpack density and SWE can be determined from FMCW radar using an empirical relationship between the radar-measured dielectric constant of snow and these two parameters (Lundberg et al., 2006). Further applications and a review of FMCW radars are given by Marshall and Koh (2008).

The high cost of the measurement system and the attenuation of electromagnetic waves by liquid water in snow are two disadvantages of the FMCW method. The cost of the measurement system could be mitigated by building the system using coffee-can antennas and simple electronics (Charvat et al., 2013).

Using radar, overestimation of SWE by 20% can occur if the liquid water content of the snowpack is 5% by volume (Granlund et al., 2007). An upward-looking FMCW radar system can be used to determine liquid water content by measuring the attenuation of radar waves in snow and using an empirical relationship to relate attenuation to water content (Mitterer et al., 2011). The attenuation of electromagnetic radiation in snow was recently investigated by Sundström et al. (2013) using Ground-Penetrating Radar (GPR) and a path-dependent attenuation function. Sundström et al. (2013) found that liquid water content was underestimated by ~50% but the mean error in determining SWE was reduced from 34% for a dry snowpack to 16% when the snowpack was wet.

Williams and Knoll (2002) used tomographic imaging of radar waves sent between two antennas to determine the dielectric constant of snow and measure snow wetness. One antenna was placed at the bottom of the snowpack, whereas the other antenna was placed at the top. Assuming that the snowpack had a constant density of $500\ \mathrm{kg\ m^{-3}}$, a mixture theory equation was used to determine liquid water content. The 250 MHz frequency used for the radar waves enabled penetration of the snowpack with a depth of 1.5 m.

1.3.7. Laser-Ranging

The use of laser-ranging equipment to measure snow depth relies on two observations. One observation is made during the snow-free season, whereas the other observation is made when snowcover is present. The laser range-finder is placed at a fixed location that is the same for all measurements. An observation is made by sending a short laser pulse toward the ground or snow surface. The pulse is reflected, and the time-of-flight between the sent and received pulse is used to measure distance from the range-finder to the ground or snow surface. The difference between the snow-free and snow-covered measurements is used to determine snow depth. Due to the similarity of laser-ranging to monopulse sonar and radar, the same limitations related to pulse width is also present in the application of this method.

Osterhuber et al. (2008) used a ground-based LiDAR system (Optech Inc., Ontario, Canada) with a depth measurement accuracy of ± 4 mm to determine snow depth at the Central Sierra Snow Laboratory in California. The LiDAR scanner was able to obtain a three-dimensional volume of the snowcover by moving the laser beam over the snow surface using a computer-controlled mirror. Gravimetric measurement of snow density permitted computation of SWE. The 1.5 μm laser wavelength did not penetrate the snowpack and was suitable for use with wet snow. Hood and Hayashi (2010) used a hand-held laser rangefinder (Lasercraft Contour XLRIC, Earth Vector Systems) with a 0.905 μm wavelength, finding that snow depth in complex mountain terrain could be measured with an accuracy of 12% compared to manual depth measurements.

1.3.8. Near-Surface Photography

Photogrammetry is the use of two cameras situated at a known offset distance to determine the depth of objects in a scene. This method has been applied to measure snow depth using cameras situated near the ground surface. Although having similar principles of operation, near-surface photogrammetry is to be distinguished from conventional photogrammetry (Mikhail et al., 2001) conducted using downward-looking cameras mounted on airplanes (Cline, 1993; Smith et al., 1967). In a similar fashion to the laser-ranging method, images of the landscape before and after snow accumulation are required. The cameras are situated so that there is overlap between the images. Depth in the image pair is determined using linear algebra equations that relate points on each image to the camera positions.

Blyth et al. (1974) took photographs at two locations facing the side of a hillslope in an upland area near Plynlimon, Wales. The camera locations were situated 30 m apart on a vertical line and 2.5 m high markers were used to delineate the corners of a trapezoidal area spanning 4 hectares. A stereo-plotter normally used to measure depth from air-photo pairs was used to determine distances to the snow surface. Comparison with depth rod measurements revealed that this method could determine snow depth within 10% error.

Vallet (2001) and Skaloud et al. (2005) described a single-camera system used to measure snow depth. The system was mounted on the side of a helicopter for deployment near the ground and in Alpine areas. Placed near the single camera was a high-accuracy differential GPS system, inertial measurement sensors and a laser-ranging device. The position of the

camera relative to a Digital Elevation Model (DEM) was used to obtain estimates of the volume of snow for an avalanche control application.

Essery et al. (2008) used a digital camera fitted with a hemispherical (fisheye) lens to calculate the fraction of the sky (expressed as the "sky-view factor") not obscured by a forest canopy so that longwave radiation incident on snow beneath the canopy could be calculated. Debeer and Pomeroy (2009) used near-surface photography to measure snow covered area (SCA). The investigators set up a single camera facing a cirque on the side of Mount Allen in the Rocky Mountains. Using a DEM of the area and the known position of the camera, a software tool developed by Corripio (2004) was used to extract SCA from the single camera image.

1.3.9. Radioactivity

Measurement of snow density or SWE by radioactivity can be classified by sensor type: active or passive. The classification scheme is similar to that of sonar (Lurton, 2002). An active sonar device sends and receives acoustic waves, whereas a passive device only detects acoustic waves. Devices that use radioisotopes to measure snowpack properties either send and detect radioactive particles (active) or only detect radioactive particles (passive).

Active measurements often use a radioisotope such as ^{60}Co or ^{137}Ce to produce gamma radiation (Goodison et al., 1981). The advantage of using ^{60}Co over other isotopes such as ^{65}Zn is that this isotope has a greater penetration of snow (Gerdel et al., 1950), thereby allowing for a larger sampling area to be sensed (Armstrong, 1976). The ^{60}Co isotope also emits a narrow wavelength spectrum of radiation that can be empirically related to snow density with less error than an isotope with a broader wavelength spectrum (Gerdel et al., 1950). The source is collimated so that the radiation escapes from a slit in a lead box. A complete design for the collimator is presented by Gerdel (1952).

Two common active designs exist: either the source and a detector are situated above and below the snow surface (Gerdel et al., 1950), or in two parallel metal tubes installed perpendicular to the ground so that snow density can be measured by moving the source and detector vertically (Armstrong, 1976; Smith and Halverson, 1969). Movement of the source and detector is accomplished using an electric motor and mechanical assembly (Paulin, 1978; Smith and Willen, 1966). The disadvantage of using the above-and-below configuration is that snow

profiles cannot be recorded (Smith et al., 1967). Davis (1973) noted that the above-and-below configuration was used at a field site in California with a radioactive source buried under the snowpack and a detector situated on an airplane passing over the site.

Portable versions of active sampling gauges were once utilized by the Division of Hydrology at the University of Saskatchewan (Pomeroy, 1988), and the parallel tube device was deployed at the Bad Lake research site near Rosetown, Saskatchewan (Gray et al., 1970). Laboratory testing and calibration of the parallel tube device at the University of Saskatchewan was reported by Olfert (1970) and Gray et al. (1970). The spacing between the parallel tubes can range from 30.5 cm to 61 cm center-to-center (Gray et al., 1970).

An increase in the SWE and density of snow results in a decrease of the number of particles per unit time transmitted through the snowpack from the radioactive isotope to the detector. Empirical equations are used to relate particle counts to SWE or snow density. Gerdel et al. (1950) used Beer's Law with an empirically-determined extinction coefficient. Smith et al. (1965) used a simple logarithmic relationship.

Geiger-Muller tube (Armstrong, 1976) and sodium iodide tube (Smith et al., 1965) detectors have been used to detect the particles. The advantage of using a Geiger-Muller tube is operational stability (Blincow and Dominey, 1974) due to temperature shifts in sodium iodide tubes. Cosmic background radiation particle counts are required to completely correct for errors in received counts (Gerdel, 1952). Empirical calibration may be necessary before each run to correct for temporal changes in the system (Howe and Houghton, 1968). Gray et al. (1970) found that calibration is essential at least once every five readings. An empirical calibration procedure to correct for temperature changes in the metal tubes of the active gauge was proposed by Gray et al. (1970).

The accuracy of such active gauges is within 1% to 7% of SWE measured using gravimetric techniques (Blincow and Dominey, 1974; Pyper, 1962; Smith et al., 1965). Inherent difficulties in the deployment of the system arise due to temperature shifts in the electronics and snowmelt occurring around tubes buried in the snow (Smith et al., 1967). Uneven snow drifts can also form around the tubes, influencing the accuracy of the measurement and making detection of the snow surface more difficult. For an active gauge with two tubes, misalignment of the source and receiver can also occur (Kattelmann et al., 1983). Compared to snow pillows, daily estimates of SWE using active radioisotope gauges show greater variability in

measurements (Ord, 1968). Due to environmental and human health hazards associated with radioisotopes, active gauges are presently not used in an operational context (Pomeroy and Gray, 1995) despite "acceptable-risk" arguments once used to rationalize the deployment of such instrumentation (Gerdel et al., 1950; Morrison, 1976).

The backscattering method is an active measurement method that uses only one tube containing a source and receiver (Anderson et al., 1965; Morris, 2008a). A gauge of similar design was once available commercially as the Digiray Portable Profiling Snow Gauge PSG-1 (Blincow and Dominey, 1974). Initially, a core of snow is extracted from the snowpack (Young, 1976). The single-tube device is then inserted into the hole created by removal of the snow sample. A source containing ^{85}Kr (Blincow and Dominey, 1974), ^{187}Cs (Anderson et al., 1965) or ^{241}Am (Hawley and Morris, 2006; Morris and Cooper, 2003) produces radioactive particles that escape through slits in a lead collimator into the snowpack (Blincow and Dominey, 1974). The backscattered particles from the snowpack are sensed by a Geiger-Muller tube receiver. For the PSG-1, the sampling volume is a torus situated around the tube with a vertical extent of 5 cm and a horizontal extent of 30 cm (Young, 1976). Insertion of the single-tube device into a provided "calibration can" containing a substance of known density allows for counts of backscattered particles to be related to snow density (Blincow and Dominey, 1974) or empirical calibration is performed using gravimetric samples at a field site (Schytt et al., 1962). Recently, Morris (2008a; b) presented a non-empirical model for determining snow density using the back scattering method. The model is based on the physics of backscattered particles from snow and does not require empirical relationships.

The back-scattering method was tested in the mountains of California (Anderson et al., 1965; Gay, 1962) and on glaciers in Sweden (Schytt et al., 1962). The investigators found that errors in snow density determination were greatest near air-snow (Anderson et al., 1965; Schytt et al., 1962) and ground-snow (Anderson et al., 1965) interfaces. Young (1976) tested the PSG-1 device on Peyto Glacier in the Canadian Rockies, finding that depth-averaged densities agreed to within 5% of gravimetric measurements. The densities of individual layers in the snowpack did not necessarily coincide with gravimetric measurements due to the sampling volume of the detector and lags in particle counts associated with vertical movement of the sensing apparatus. Gerland et al. (1999) used the back-scattering method to measure snow density in Antarctica, finding an error of 2% comparison with gravimetric estimates of snow density. Measurements of

snow density on the Devon Ice Cap (Morris and Cooper, 2003) and the Greenland Ice Sheet (Hawley and Morris, 2006) in Nunavut, Canada showed that a disadvantage of the back-scattering method was "smoothing" of the density profile due to the size of the back-scattered sampling volume.

Passive radioactivity gauges work in a similar fashion to the active gauges, but rely on the natural background radiation in the soil to provide a source of gamma radiation. The passive radioactivity gauge is situated in the air above the snow surface. Although this technique is very safe, background radiation counts at the same field site during the snow-free season are required and the gauge must count the number of particles accumulated over daily time periods. This does not permit "on-demand" measurements of SWE. As the SWE and snow depth increases, particle attenuation increases and the signal-to-noise ratio decreases. The gamma radiation particles are often highly attenuated by the snow, thereby limiting the snow depth and SWE that can be determined by this measurement technique (Bissell and Peck, 1973). Morrison (1976) briefly describes a passive radioactivity gauge being developed for prairie hydrology applications. The gauge was able to measure snow with SWE less than 50 mm and a depth less than 150 cm.

The CS725 SWE gauge (also referred to as the "GMON," from Campbell Scientific Canada, Edmonton, Alberta) can measure up to 600 mm of SWE using the passive radioactivity method. The SWE measurement is limited due to attenuation of radioactive particles by the snow and the sensitivity of the detector. The CS725 was initially developed by Hydro Québec. When suspended 3 m above the ground, the effective measurement area of the gauge is 500-100 m^2 due to collimation of the detector. Aside from particle count rates during the snow-free season, the empirical equation used to determine SWE also requires measurements of soil moisture prior to winter freeze-up (Wright et al., 2011).

1.3.10. Chemical

Chemical measurement of liquid water content θ_w relies on physical changes in the concentration of ions in a snow sample. These methods involve the extraction of a sample of snow from a snowpit or from the snow surface.

Davis and Dozier (1984) added a florescent dye (Rhodamine WT) to a snow sample and then measured the florescent intensity of the mixture using a chemical fluorometer. The

intensity of the sample was related to water saturation of snow using an empirical curve and chemical mixing formulae.

Perla and LaChapelle (1984) and Davis et al. (1985) conducted experiments in the Canadian Rockies to develop an acid dilution technique. A solution of 0.01-N hydrochloric acid was added to a snow sample and an electrolytic conductivity meter was used to measure the conductivity of the resulting solution. The conductivity was then related to snow wetness. Because the acid dilution technique does not involve the use of empirical curves, it can be used to calibrate capacitor cells (Perla and Banner, 1988).

The error in dilution methods is ±1.5% liquid water content (Davis et al., 1985). Although these methods can be used to measure snow wetness in a snow pit at a field site, the preparation and mixing of chemicals at a remote location can be tedious and time-consuming.

1.3.11. Calorimetric and Centrifugal

Calorimetry is used to measure the liquid water content θ_w of snow. A calorimeter consists of an insulated container into which is placed a snow sample. The insulated container is fitted with a temperature sensor to measure internal temperature. The mass of the snow sample is determined before a liquid is added to the insulated container. Stirring of the sample occurs over the time of measurement to ensure that heat is evenly distributed between the liquid and the snow sample. A change in heat content due to a change in phase of the mixture is related to the liquid water content of the snow sample using a heat-balance equation. Empirical calibration coefficients in the heat balance equation can correct for heat loss by the insulated container. Freezing, melting and chemical calorimeters have been used to measure snow (Boyne and Fisk, 1990; Jones et al., 1983). In a similar fashion to the chemical methods, the time taken for measurement and the equipment used creates logistical problems at field sites.

Freezing calorimetry requires a liquid freezing agent that is held at a temperature between -40 °C and -50 °C. This is accomplished by keeping the freezing agent in a portable cooler that is packed with dry ice and taken to the field site. Toluene has been used as a freezing agent, but this is a hazardous chemical and so silicone oil can be used instead. After addition of the freezing agent to the insulated container, the container is shaken by hand and a change in temperature is recorded in 30 second intervals for approximately 10 minutes. The error in determination of liquid water content θ_w using freezing calorimetry is ±1% to ±2% (Jones et al.,

1983), but the method can be inaccurate due to uneven transfer of heat between the snow sample and the freezing agent (Fisk, 1986a). Moreover, the specific heat of the silicone oil will often change between purchased bottles and must be measured before use in the calorimeter (Boyne and Fisk, 1990). The presence of snow chunks in the sample can affect the measurement due to liquid water contained inside the snow chunk (Boyne and Fisk, 1987).

Melting calorimetry involves the addition of hot water to the snow sample. The hot water serves as a melting agent. The hot water can be directly added to the snow sample (Akitaya, 1985; Halliday, 1950; Yosida, 1967), or the water can be heated using an electric coil, which has an advantage of controlling the rise in temperature of the sample (Brun, 1989; Halliday, 1950). Brun et al. (1989) describe a melting calorimeter that uses a combination of calorimetry and dielectric techniques to measure liquid water content. The melting calorimetry method has better transfer of heat between the snow sample and the melting agent and is quicker than freezing calorimetry (Fisk, 1986a). The absolute measurement error in liquid water content ranges from ~1% to ~5% (Akitaya, 1985; Halliday, 1950; Morris, 1981).

Chemical methods involve the addition of a chemical to a snow sample. The chemical breaks intermolecular bonds holding the snow particles together and disperses ions and molecules into the solution, causing a resulting change in temperature. The use of methanol (alcohol) as a chemical agent has an absolute liquid water content measurement error of ~1% (Fisk, 1986b). Because methanol is hygroscopic, a drying agent must be used to prevent water contamination during storage of the methanol solution (Boyne and Fisk, 1987). Morris (1981) used a NaCl (salt) solution, finding that the measurement error in snow liquid water content was ±4% when the salt dissolved in solution did not exceed 5% by volume. Bader (1950) reported on the use of a NaOH (sodium hydroxide) solution as the chemical agent. Boyne and Fisk (1990) compared the alcohol and freezing calorimetry methods to dielectric techniques, finding that all methods had a maximum ±2% measurement error.

Centrifugal methods involve the spinning of a snow sample to separate out liquid water from the snow. Drawbacks of this method include melting that occurs due to friction and the incomplete extraction of all liquid water from the sample (Colbeck, 1978; Jones et al., 1983). The irreducible liquid water content θ_e can be obtained by soaking a snow sample in water, draining the snow sample in an insulated chamber that is kept at an isothermal temperature by an ice bath, and then measuring θ_e using a freezing calorimeter (Coléou and Lesaffre, 1998).

1.3.12. Acoustic Measurement of Snow Depth

Most acoustic measurements of snow depth have been made using ultrasonic devices that determine the distance to the snow surface. The measurement device is fixed to a mast of known height situated above the snowpack. An ultrasonic sensor produces an inaudible (> 20 kHz) acoustic pulse that is reflected from the snow surface. Measuring the time between the sent and received pulses enables calculation of snow depth using kinematics. This is a "time of flight" measurement. Concomitant measurements of air temperature are used to calculate the speed of sound in air. The measurement system principle is similar to pulse sonar and radar systems, and the range is limited by the pulse duration.

Gubler (1981) designed a snow depth measurement system using separate sending and receiving piezoelectric transducers. The transducers were situated next to each other in a bistatic sonar configuration. The sending transducer was driven at its resonant frequency of 40 kHz. Drifting and blowing snow caused scattering of the acoustic wave due to the small signal-to-noise ratio of the pulse. Gubler (1981) also observed that soft surface layers of snow would not cause strong reflections of the pulse, implying that some penetration of the snowpack by the ultrasonic wave may have occurred. This was recognized by Caillet et al. (1979) as occurring due to changes in the porosity and roughness of the snowpack surface.

Goodison et al. (1984) adapted an acoustic rangefinder from the Polaroid Corporation to measure the distance to the snow surface. This approach was later followed by Earl et al. (1985).

An improved sensing system was proposed by Goodison et al. (1988). Only a single transducer was used in this system operating at a frequency between 50-60 kHz with a range of 27 cm to 10.7 m, an accuracy of ~3 mm for distances ranging up to 3 m, and an overall accuracy of ±1% (Mims, 2000). Increasing the speed of the microcontroller increased the time resolution and permitted the measurement of snow depth to within 1 mm depth error (Goodison et al., 1988). The air temperature was automatically measured at the same time that the acoustic pulse was sent toward the snowpack. The ultrasonic sensor device was able to detect drifting and blowing snow events. The system was observed to underestimate snow depth by 6 cm relative to snow ruler measurements (Goodison, 1985). Goodison et al. (1984) remarked that this bias may be due to partial penetration of the snow surface by the acoustic wave. This may occur if the snow is of relatively low density.

Acoustic scattering of the sound wave at the snow surface and temperature gradients near the air-snow interface were also considered by Goodison et al. (1984) to influence the accuracy of the gauge. Measurement test details of the gauge are given by Edey (1985) and Metcalfe et al. (1987). Osterhuber et al. (1994) present an empirical calibration procedure for removing the influence of temperature changes on spurious fluctuations in determined snow depth.

Snow depth was measured by Lahtinen (2011) using an ultrasonic sensor situated on the top of a post inserted into the snowpack. Since the length of the post was known, the distance to the snow surface could be determined using a time-of-flight measurement in a similar fashion to the measurement sensors previously discussed. The portability of the system enables it to be considered as being similar to the mechanical measurement system developed by Sturm (1999).

Acoustic measurement gauges are available commercially from several companies. Ryan et al. (2008) tested commercially-available ultrasonic snow depth gauges, finding that the maximum RMSD between ultrasonic and snow ruler measurements was less than 3 cm for 17 sites in the USA. Anderson and Wirt (2008) examined the factors that contribute to errors in ultrasonic snow depth measurement, finding that contamination of the transducer by dirt or insects, tears in the transducer surface, and obstruction of the transducer or snow surface under the transducer were major influences. Bergman (1989) found that heating of the thermocouple used to measure air temperature could affect the resolution of the depth measurement by up to ±3 cm, indicating the need to ensure adequate shielding of the thermocouple.

1.3.13. Acoustic Measurement of Snow

Smith (1965) and Smith (1969) sent sound waves through cylindrical snow samples extracted from a snowpack and related the speed of the sound wave to density using semi-empirical equations. Buser (1986) and Buser and Good (1986) placed snow in an impedance tube and used the Zarek porous media model (Zarek, 1978) to explicitly determine snow density. Lee and Rogers (1985) set up a loudspeaker and microphone above a snow surface. The loudspeaker was used to send a 30 ms impulse into a 2 cm snow layer that had accumulated on a roof. Selecting the parameters of the Zarek porous media model allowed for generation of a synthetic waveform. The synthetic waveform was compared with the waveform recorded by the microphone. The measurement method used by Lee and Rogers (1985) was not systematic and was not applied to a seasonal snowpack.

In a similar fashion to Vertical Seismic Profiling (VSP) in seismology, Moore et al. (1991) created a probe microphone that was inserted beneath the snow surface on a rod. A loudspeaker situated above the snow surface produced white noise. The porous media model proposed by Attenborough (1983) was used to predict porosity from the transfer function measurement within < 20% error.

Using a seismic array and acoustic models of snow, Albert (1998) used an inversion procedure (Albert, 2001) to determine snow depth and permeability. The acoustic inversion procedure was similar to Lee and Rogers (1985) but fully automated.

SWE has been measured using a loudspeaker and microphone situated above the snow surface in a similar fashion to bistatic radar or sonar. In an analogous fashion to FMCW radar, the measurement system sent a frequency-swept sound wave into snow. The frequency-sweep was between 20 Hz and 20 kHz. The reflection was homodyned and related to SWE using a recursive acoustic model (Kinar and Pomeroy, 2007). Later work used a Maximum Length Sequence (MLS) as the source signal and another recursive acoustic model relating geometric spreading and reflection of the sound wave beneath the snow surface (Kinar and Pomeroy, 2008a, 2008b).

1.3.14. Heat Pulse Probes

A heat-pulse probe measurement apparatus consists of a number of needles inserted into a medium such as a soil to measure the thermal conductivity and density. There are two major types of heat pulse probes that have been used to measure snow. These can be classified using the number of needles: single-needle or multiple-needle heat pulse probes.

The heat pulse probe measurement begins by applying an electrical current to a heater wire looped inside of one of the needles. The heater needle warms up, and a rise in temperature is sensed by a thermocouple. The thermocouple is either placed inside of the heater needle (single-needle), or inside another needle situated at a radial distance to the heater needle (multiple-needle) (Mori et al., 2003). The change in temperature during heating or cooling of the needle is related to material properties by a mathematical model (Carslaw and Jaeger, 1959; Kluitenberg et al., 1993; Liu and Si, 2010; Morin et al., 2010).

Most heat pulse probes used to measure the thermal conductivity of snow utilized a single needle (Jaafar and Picot, 1970; Riche and Schneebeli, 2013; Sturm and Johnson, 1992; Sturm et

al., 1997). Fowler (1974) and Sturm et al. (1997) measured the thermal conductivity of snow using a single needle heat pulse probe and related this measurement to density using an empirical relationship. Single-needle probes have been buried in a snowpack and used to measure effective thermal conductivity of snow over a three-month period (Morin et al., 2010). Heating of cylinders, spheres, plates and wires have been used since 1886 to measure the thermal conductivity of snow (Sturm et al., 1997).

Liu and Si (2008) showed that both the density and thermal conductivity of snow could be measured using a multiple-needle heat pulse probe. Care must be taken to ensure that the strength of the heat pulse is not high enough to melt snow and that the radial distance between the heater needle and temperature sensing needle is calibrated in a medium with a known thermal conductivity. Although the multiple-needle heat pulse probe is an invasive measurement apparatus, the investigators realized that the probe could measure snow density and thermal conductivity in a snowpit. Alternately, the probe could be buried in the snowpack to make continuous measurements (Liu and Si, 2008).

Ross and Picot (1975) describe a heat-pulse probe where the surface responsible for thermal transfer of heat to the snowpack was a circular plate with a diameter of 15 cm. The entire probe was buried in the snowpack. The temperature change of the plate in contact with the snow was related to Fourier's Law of heat transport and used to measure the thermal conductivity of snow. Comparisons between measurements made with a single-needle heat pulse probe, a heat flux plate and a model related to snow microstructure have been reported by Riche and Schneebeli (2013). Microtomography images of snow structure and a mathematical model of heat transport have been used to measure snow thermal conductivity (Calonne et al., 2011).

1.3.15. Temperature Sensors

Temperature sensors are used to record snow temperature. The temperature sensor most often used by snow surveyors is a dial thermometer (Fierz et al., 1999; McGurk, 1983) or a thermocouple with a digital readout (digital thermometer) (Koh and Jordan, 1995). The thermometer is inserted into the snowpit wall at successive depths beneath the snow surface (Crook and Freeman, 1973). The temperature of the thermometer sensing surface is allowed to equalize with snowpit temperature before a measurement is read from the dial.

Brandt and Warren (1997) inserted a tube with 3 mm diameter into the side of a snowpit and used the tube to extract a small core of snow. The tube was removed and a thermocouple was placed into the hole created by the tube. Snow was then placed by hand over the thermocouple leads to retain the thermocouple in the snowpack. The process was repeated for layers at various depth in the snowpack to obtain a temperature profile. Back-shovelling of snow into the snowpit allowed for thermocouples to be buried under snow and temperature profiles to be determined over an extended period of time.

Infrared thermometers and IR cameras have been used to record the spatial distribution of snow temperature in a snowpit (Shea et al., 2012); to record the spatial distribution of temperature in snow and shrubs (Pomeroy et al., 2006); and to measure the temperatures of snow and tree trunks in a forest (Pomeroy et al., 2009). IR thermometers and cameras measure longwave radiation emitted by a surface (Bates and Gerard, 1989). Thermal imaging devices can have an absolute measurement error of 2 °C, but a measurement error of only 0.2 °C between pixels in an image (Pomeroy et al., 2006). Correction and calibration of IR imagers for measuring snow temperature has been discussed by Shea et al. (2012). Snowpit-based measurement of snow temperature is laborious, invasive and time-consuming due to the creation of a snowpit (Sauter and Tanner, 1992).

Swanson (1968) described a system for measuring snow surface temperature using a thermocouple. The thermocouple was mounted on a plastic frame suspended above the snow surface on a vertical metal wire fastened to the ground. The plastic frame was held motionless by a nylon cord. To drop the frame onto the snow surface, a circuit was used to warm up a section of Nichrome heating wire that severed the nylon cord, thereby allowing the frame to drop under the influence of gravity. The output signal of a 2 kHz oscillator was applied to the top and bottom of the wire. A reservoir filled with mercury was mounted on the plastic frame. The reservoir made contact with the metal wire and a grounding point, modifying the oscillation frequency. The change in the oscillation frequency was then related to the position of the frame along the wire and the snow depth. The disadvantage of this system was that more than one plastic frame was required to make measurements of the snow surface over time. Modern implementations of this system would not use mercury due to the environmental hazards associated with its use.

Thermocouple arrays have been buried in the snowpack to measure temperature distribution throughout the snow. The basic setup of this apparatus is a series of thermocouples situated over a vertical distance. Installation of the stationary version of this apparatus occurs during the snow-free season so that snow can accumulate around the thermocouples. The vertical extent is selected to be higher than the maximum depth of snow over which temperature is to be measured.

Bowles (1967) suspended thermocouples on a post supported by a triangular frame. The post was 3 m high and the spacing between thermocouples was 10 cm. McGurk (1983) suspended thermocouples on a wire stretched between the ground and a boom arm situated at a distance of 3.4 m above the ground. The spacing between thermocouples was 30.5 cm.

Desrochers and Granberg (1986) used a system of thermocouples installed on a vertical post to measure snow temperatures in a woodland area. They describe a portable version of this system where a single thermocouple situated on the end of the vertical post is used to measure snow temperature profiles throughout the snowpack. The observer pushes the post through the top of the snow surface. Desrochers and Granberg (1986) recount that a disadvantage of the portable version of the system is that the temperature measurement is invasive, destroying the snowpack. A similar system was used by Metcalfe and Buttle (1998), where the thermocouples were placed along a wooden stick situated vertical to the ground surface. The stick was painted white and installed at a stationary location to measure vertical temperature distributions throughout the snowpack.

Tanner and Gaza (1990) suspended a rod between two pipe tripods. The rod was placed at a distance of 160 cm above the ground and was used to suspend thermocouples at 10 cm intervals along a wire. Tanner and Gaza (1990) found that heat conduction along the wires suspending the thermocouples in the upper 35 cm of the snowpack caused recorded temperatures to be significantly greater than 0 °C during ablation, despite the use of low-thermal conductivity wire intended to minimize these effects. Tanner and Gaza (1990) also used chromel-constantan thermocouples instead of copper-constantan thermocouples to reduce thermocouple self-heating. Moreover, snow settling around the thermocouple supports may have influenced temperature measurements.

To minimize these effects, Sauter and Tanner (1992) created a ladder-type structure to suspend the thermocouples throughout the snowpack. The ladder was comprised of nylon

fishing wire. The vertical height of the wire was 2 m above the ground and thermocouples were spaced at distances of 10 cm along the ladder. Despite these precautions, Sauter and Tanner (1992) found that temperature conduction errors affected measurements at distances up to 20 cm beneath the surface of the snowpack, but snow temperatures measured during ablation were closer to 0 °C than the measurements made by Tanner and Gaza (1990).

Sturm and Johnson (1991) suspended a two-dimensional network of thermocouples on strings between two posts before the snow accumulation season. Four rows of vertical thermocouples over an 80 cm horizontal distance were used to record temperature gradients throughout the snowpack. The vertical thermocouple spacing was every 5 cm over a 60 cm distance. The thermocouple array setup was able to detect convection plumes under the snowpack surface. Conway and Benedict (1994) later used a similar setup to measure temperature changes caused by meltwater propagation through snow. The network of thermistors spanned a 2 m vertical distance and a 1.5 width. The spacing between thermocouples was 15 cm.

Albert and McGilvary (1991) progressively laid down rows of thermocouples on the snow surface before a snow deposition event. Over the winter season, this caused the thermocouples to be buried inside of the snowpack without the need for a supporting structure. Although this method would have minimized the effects associated with heat conduction apparent in application of the other methods, the thermocouples could only be buried at depths related to snow deposition events. Albert and McGilvary (1992) later suspended thermocouples on nylon fishing wire between wooden dowels. Arranging thermocouple arrays in two separate directions allowed for a three-dimensional measurement of snowpack temperature.

Luce and Tarboton (2001) used nylon fishing wire to place thermocouples vertically along a line at distances of 5, 12.5, 27.5 and 35 cm from the ground surface. Temperature measurements made by the thermocouples were used to test a model of heat transport through snow.

1.4. Automation of Snow Property Measurements

Although many environmental scientists and hydrologists use commercially-available instrumentation such as dataloggers, some investigators have measured snowpack properties

with custom-built automated systems. As is apparent from the previous section of this thesis, hydrologists have a long-standing tradition of building instrumentation to make observations.

Researchers at the University of Saskatchewan's Division of Hydrology pioneered automated measurement systems in the 20th century, building dataloggers that recorded hydrologic observations of snow to cassette tapes (Gray, 1972) and measuring radiation fluxes to snow using instrumentation situated on the ground (O'Neill and Gray, 1973a) and on aircraft (O'Neill and Gray, 1973b). The mass flux of blowing snow was autonomously measured using particle detectors developed at the same research institute (Brown and Pomeroy, 1989). These detectors have been utilized to measure blowing snow in prairie (Pomeroy, 1988; Pomeroy et al., 1993), sub-Arctic (Pomeroy et al., 1999), Arctic (Savelyev et al., 2006) and Antarctic (Leonard and Cullather, 2008) environments. An improved version of the system with a collimating lens and on-board signal processor was reported by Sato et al. (1993).

Active profiling radioactivity gauges have been remotely controlled at field sites over telephone communications (Armstrong, 1976) or the pulses from such gauges have been transmitted to a base station using radio communications (Gerdel et al., 1950). Meteorological and hydrological instrumentation have been remotely controlled and data collected at various field sites since the 1960s (Bowles, 1967; Fletcher, 1967; Gray, 1967; Maxwell et al., 1960; Shannon, 1968; Weaver, 1967). In the United States, more than 600 SNOTEL (SNOwTelemetry) sites automatically measure SWE with an average error of ~3 mm using snow pillows (Cooley and Palmer, 1997).

Painter et al. (2000) describe a system to automatically measure the angular distribution of snow reflectance using a spectroradiometer mounted on the end of a robotic arm controlled in the field using a program running on a portable computer. Further tests and field deployment of the system was reported by Painter and Dozier (2002).

Lundquist et al. (2003) describe the development of a metrological sensor network deployed in Yosemite National Park consisting of instrumentation specifically designed for the measurement application. The network utilized a custom-designed electronic circuit serving as a datalogger that conveyed environmental measurements over wireless distribution networks. The purpose of this device was to provide high-resolution measurements of snow properties for predictive hydrological applications.

Hubbart et al. (2005) suggested that iButtons (Maxim Integrated Circuits Inc., California) could be used for environmental temperature measurements at locations where dataloggers are not available or are too difficult to deploy. The iButton is an environmentally-sealed module measuring ~16 mm in diameter. It contains an integrated circuit, battery, and data storage for observations. The iButton can be programmed to automatically take temperature measurements on a set time schedule. Lundquist and Rochford (2007) used iButtons to automatically log temperature measurements at different locations in the mountains of California and Colorado. They suggested that temperature differences between sensors could be empirically related to the surface albedo of snow. The iButton sensors were also deployed in the Andes mountains of Peru and used to monitor temperatures for glaciological studies (Hellström and Mark, 2006). PVC pipe shielded the iButton temperature sensors from sunlight.

Rice and Bales (2008) discuss the development of an embedded sensor network to measure snow depth and meteorological parameters. Skalka et al. (2009) and Moeser et al. (2011) report the development of the "Snowcloud" sensor network. The sensor network was comprised of nodes linked together using mesh radio communications. This permitted transmission of data to a base station using inter-node communication. The network was "self-healing" so that failure of one node would not disrupt the flow of communications. The loss of a node would cause the network to intelligently route communications to another node, eliminating the need for a high-powered radio transmitter or antenna towers. Each node was used to obtain data from an ultrasonic sonar receiver/transmitter used to measure snow depth. Processing of sonar data was not performed in the field. The sensor network was deployed at the Sagehen Creek Field Station near Truckee, California.

Koh et al. (2010) mounted an FMCW radar system on a sled and used an autonomous robot to pull the sled over a 150 m transect in Antarctica. The reflection data from the FMCW radar was used to detect crevasses. FMCW radar systems have been designed by investigators who have used these devices to measure snow (Marshall et al., 2007).

Lahtinen (2011) described preliminary tests of an instrument by which profiles of light extinction, reflectance and temperature in snow were determined using sensors mounted on the end of a pole. In a similar fashion to the backscattering active radioisotope method (Section 1.3.9) or the dielectric instrument described by Louge et al. (1998), the pole was pushed beneath

the snow surface and profiles automatically logged. An ultrasonic depth sensor situated on the top of the pole enabled measurement of snow depth.

1.5. Problem

The previous sections of this thesis have shown that snowpack processes are of major environmental and human importance. Models used to understand these processes and predict runoff from snowmelt require quantitative measurements of snow as model inputs. Internal state variables commonly used by these models are not directly measured and are computed by mass and energy flux inputs. These models are validated using quantitative measurements of snow.

Researchers have long recognized that snow surveying using snow sampling tubes and the creation of snowpits to measure snow properties is a laborious process that is time-consuming and prone to human error. This fact has been explicitly stated by many authors (Davis, 1973; Marsh, 1991; Pomeroy and Gray, 1995; Sturm, 1999).

Any device that requires the creation of a hole in the snowpack is invasive and does not allow for multiple measurements to be performed at the same location. Moreover, these devices require the presence of a human observer. The skill of the human observer affects the measurement error. The human observer cannot be present at locations that are difficult to access or where dangerous conditions such as avalanches are present during the snow accumulation and ablation season.

Electronic instrumentation can be deployed at a field site and set up to make automatic measurements on a time schedule. This has been attempted using some of the electronic devices described in the review section of this thesis. Devices that require installation during the snow-free season are not portable and cannot be ubiquitously deployed without prior preparation of a field site.

Devices that rely on empirical relationships between instrumentation outputs and snowpack variables may not work at field sites where environmental conditions are different than the conditions used to derive the relationships. However, some of the devices described in the previous sections do not rely on empirical relationships. Models used to process data from these devices have been proposed to reduce the reliance on empirical relationships.

Variables commonly used in models of snowpack evolution (Table 1.1) are estimated using multiple measurement devices. There is not a single device currently available that can

simultaneously measure snow density ρ_s, water content θ_w as a measurement of snow wetness, and temperature T. Different devices can be used to obtain measurements of these variables.

Non-destructive measurements of snow wetness would be useful to fully understand processes of water transport through snow (Marsh, 1991). A few decades ago, Colbeck (1978) presented a review identifying snow density and wetness as being two crucially important variables measured in snow hydrology. These two variables govern the rate, timing and amount of meltwater produced by snow. Colbeck (1978) suggested that acoustics might be used to obtain measurements of these quantities. Techel and Pielmeier (2011) suggested that a portable device would be useful for field measurements of snow wetness.

1.6. Objectives

The previous sections suggest objectives for the research described in this thesis. An overall objective is to use a non-invasive measurement system to determine snow (1) density, (2) liquid water content, and (3) temperature by the use of acoustics, which can be used to obtain all of these variables simultaneously in a non-invasive fashion. Under this overall objective, the following sub-objectives are:

1. To develop and test a model of sound wave propagation in snow as the Unified Thermoacoustic Model (UTAM);

2. To develop novel signal processing techniques and use these to design an electronic system—the System for the Acoustic Sensing of Snow (SAS2)—that sends sound waves into snow and receives the reflected waves; and

3. To deploy the electronic device at field locations in order to show how the electronic device can report data indicative of snowpack measurements.

CHAPTER 2
LITERATURE

2.1. Introduction

This chapter of the thesis provides an overview of the literature required to provide a necessary background for the following chapters. The review is limited in scope to provide an understanding of developments presented in this thesis. A review of snow acoustics research and models of sound propagation through snow places the research reported in this thesis in the context of experiments conducted by other investigators. Because the System for the Acoustic Sensing of Snow (SAS2) is similar to sonar, these acoustic sensing systems are also reviewed. Signal processing techniques required for the development of the theory are discussed.

2.2. Overview of Processes

2.2.1. Precipitation

In this thesis, a "snow particle" is considered to be the smallest visible unit of snow that comprises the snowpack. This is similar to the definition of a "snow grain" given by Colbeck (1986) and follows the terminology used by Pomeroy and Schmidt (1993).

The formation of a snow particle begins in the atmosphere (Pruppacher and Klett, 2010). The particle falls as precipitation on the land surface. Successive snowfall events create a snowpack that is a layered snow medium. However, layers can be created and destroyed by metamorphic processes (Colbeck, 1991). Metamorphic processes are discussed in Sections 2.2.8 and 2.2.10 below.

The amount of snow deposited as precipitation is strongly influenced by global atmospheric circulation as well as by the land surface and oceans (Intihar and Stewart, 2005). Fitzharris (1987) studied the climatology of the Rogers Pass area in the Rocky Mountains, finding that cold and dry Arctic air masses depressed temperatures. Frontal systems from the Pacific Ocean were responsible for raising temperatures and bringing moisture resulting in snowfall. Cullen and Marshall (2011) state that continental air masses from the southwestern United States also influence the climate of this area of the Rocky Mountains. The direction of travel of these three air masses is influenced by the polar jet stream and topography. Claus et al. (1984) note that snowfall is higher on the western side of the Rocky Mountains but lower in

semi-arid valleys. As air masses move further east over the Rocky Mountains, they lose moisture and precipitation rates are lower. As noted by Cullen and Marshall (2011), Chinook winds will develop in the lee of the Rocky Mountains of Canada. This makes climate on the eastern side of the mountains more arid and reduces precipitation.

2.2.2. Wind Transport

Falling snow or snow that is deposited on the ground can be subjected to transport by the wind. Snow particles that have not contacted the snow surface can be entrained into preferential flow paths due to changes in surface topography that constrain air flow (i.e. valleys or gullies). Preferential flow paths are also created by turbulent eddies resulting due to surface topography. The eddies cause local acceleration and de-acceleration of air flow (Kind, 1981). When snow particles reach the snow surface, wind transport occurs due to processes of creep, saltation and suspension. The snow particles that fall on the ground comprise a "bed" of particles that are subjected to these three processes (Pomeroy and Gray, 1995).

For snow particles to be transported, mechanical and cohesive forces between snow particles at the bed must be overcome. Moreover, rougher surfaces and surfaces with vegetation stalks will have greater shear strength, requiring shear stresses of higher magnitude to dislodge particles. This is why wind transport over a hard snow surface and denser snow is more efficient than wind transport over a freshly-deposited snow layer. Vegetation with greater height and exposed stalk area will be more efficient at increasing the strength of the snow surface and reducing the mobility of snow particles, thereby trapping snow and increasing snow depth. Snow particles that are subjected to saltation and suspension are mechanically disaggregated, reducing snow particle size (Pomeroy and Gray, 1995). Sublimation will occur during transport of snow particles in the air. This causes loss of mass from the snow particles and the production of latent heat that is advected by the airflow (Pomeroy and Essery, 1999).

In areas of complex topography such as the mountains, wind will remove snow from ridges and transport snow by turbulent eddies occurring due to disruption of airflow by mountain peaks. Snow mass transport is constrained by topography and mountain barriers (Mott et al., 2010). Wind-scouring of snow can occur on a ridge and transport snow into forests situated on the slope leading up to the ridge (Pomeroy et al., 2009). Despite the interception of snow by a forest canopy (Pomeroy et al., 2002), wind can transport snow into forests, increasing snow

depth in the forest relative to an open clearing. The forest can be considered as a porous medium that resists air flow (Miller, 1964). Turbulent eddies in forest clearings can redistribute snow in both the clearing and the surrounding forest (Golding and Swanson, 1978).

2.2.3. Interception

Snow particles are retained by the canopy due to the collection efficiency of the tree branches. This is dependent on the tree species and canopy structure (Pomeroy et al., 1998), with an increase in Leaf Area Index (LAI) and canopy density coincident with an increase in interception efficiency (Pomeroy et al., 2002). Coniferous trees have greater collection efficiencies than deciduous trees due to the greater area spanned by the branches during the winter season (Pomeroy and Schmidt, 1993).

Interception influences the distribution of snow in a forest. Due to snow interception by the canopy, "tree-wells" form around the base of coniferous trees. This is distinct from a "snow cone" that forms at the base of a deciduous tree. Whereas the tree-well is a depression with an increase in snow depth away from the tree trunk, the snow cone shows an increase in snow depth at distances closer to the tree trunk. Snow cone formation occurs because the deciduous tree has less interception efficiency than the coniferous tree (Sturm, 1992). Snow depth as a function of distance from the tree trunk can be determined by empirical models (Hardy and Albert, 1995; Sturm, 1992; Woo and Steer, 1986).

2.2.4. Radiation

Electromagnetic shortwave radiation with wavelengths between $0.1\,\mu m$ and $4\,\mu m$ is provided to the land surface by the sun. The sun provides the majority of downward shortwave radiation flux ($K\downarrow$) in the net shortwave radiation balance (K^*). These wavelengths of radiation are important for providing energy for photosynthesis and for warming the land surface (Oke, 1992; Petty, 2006). Shortwave radiation is a dominant term in the snowpack energy balance and contributes large amounts of energy required for snowmelt (Link and Marks, 1999; Male and Gray, 1975). Topographic shading in mountain regions reduces the magnitude of shortwave radiation incident on the snowpack (Marsh et al., 2012). South-facing slopes are oriented toward the sun and tend to receive more shortwave radiation than north-facing slopes

(Pomeroy et al., 2003), but this is moderated by trees providing canopy cover that attenuates shortwave radiation and reduces air temperatures under the canopy (Ellis and Pomeroy, 2007; Ellis et al., 2011; Essery et al., 2008; Metcalfe and Buttle, 1998).

Outgoing shortwave radiation ($K\uparrow$) is radiation that is reflected from the snowpack. The reflection of a land surface is modelled by the albedo. The albedo is the ratio $K\uparrow/K\downarrow$. Higher albedos imply that a greater magnitude of shortwave radiation is being reflected, whereas lower albedos imply that more shortwave radiation is being absorbed. The albedo ratio is dependent on the magnitude of incoming shortwave radiation. Vegetated surfaces and bare ground have a lower albedo than snow (Oke, 1992). The albedo of snow has a high magnitude (>0.80) over shortwave radiation wavelengths (Wiscombe and Warren, 1981) for most of the snow accumulation season, decreasing during the time of ablation (Gray and Landine, 1988) due to metamorphism (Warren, 1982) and the presence of dust from aerosol particles (Conway et al., 1996; Painter et al., 2007; Warren and Wiscombe, 1981). An increase in snow particle size over time due to snowpack metamorphism is the primarily mechanism for reducing the albedo of snow. For wet snow, the presence of water will have little influence on the albedo, but water can accelerate the growth of snow particles by metamorphism. An increase in snow particle size will increase the probability that a photon will collide with the snow particle, thereby causing scattering, absorption of photons by ice comprising the snow particle, and a consequent reduction in the albedo (Warren, 1982; Wiscombe and Warren, 1981).

Longwave radiation has wavelengths between $4\,\mu m$ to $100\,\mu m$ (Oke, 1992; Petty, 2006). Radiation fluxes with these wavelengths are emitted from the sky, clouds, snow, vegetation and the land surface as a consequence of heating by shortwave radiation. Direct longwave radiation from the sky can be modelled using the Stefan-Boltzmann law, treating the sky as a grey body emitter with an emissivity coefficient dependent on temperature and humidity (Sicart et al., 2004). Semi-empirical relationships take into consideration geographic location and an increase in the magnitude of longwave radiation by cloud cover (Granger and Gray, 1990; Granger et al., 1978). Longwave radiation is also produced by the snow surface. This is modelled using the Stefan-Boltzmann law. The assumption can be made that snow without the presence of surface impurities is a nearly-perfect blackbody emitter (Geiger et al., 2003).

Snowmelt is strongly influenced by the net radiation flux Q^* (Ellis et al., 2011; Male and Granger, 1981; Oke, 1992; Pomeroy et al., 2003; Sicart et al., 2006). Net radiation often shows a

strong correlation with the net shortwave radiation flux. This is because net shortwave radiation is a dominant contribution to the net energy balance (Granger and Gray, 1990). When the net radiation balance is positive, the snowpack is warming, whereas when the net radiation balance is negative, heat is being lost from the snowpack to its surroundings and the snowpack is cooling. The net radiation flux is negative during the night, when shortwave radiation contributions to the energy balance are negligible. The negative energy balance will increase the cold content of the snowpack. The cold content is defined as the energy required to raise the temperature of snow to the melting point of 0 °C. Because snow is a thermal insulator (Sturm et al., 1997), it has low thermal conductivity and retains energy. This results in a time lag between rising levels of net shortwave radiation, an increase in the temperature of the snowpack, and a decrease in the cold content (Bengtsson, 1982; Gray and Landine, 1988; Marks et al., 2008).

2.2.5. Snow Surface Heat Fluxes

Due to uneven spatial distribution of radiation over natural land surfaces, transfer of heat occurs from areas with an excess of thermal energy to areas with a deficiency of thermal energy. In the energy balance taken at the snow surface, sensible heat is heat that causes a change in temperature, whereas latent heat occurs due to a phase change associated with the melting or sublimation of snow. In high-latitude environments where shortwave radiation inputs are of small magnitude during the pre-ablation winter season, energy required for snowmelt can be mostly provided by sensible heat from warm air masses (Male and Granger, 1981). However, low magnitudes of sensible heat flux can contribute negligible energy to snowmelt, causing ablation of snow to be primarily driven by net radiation fluxes (Pomeroy et al., 1998). Ablation of snow by high-magnitude net radiation fluxes tends to occur earlier in the snow accumulation season before snowmelt, when advection of heat between snow patches is a dominant contribution to the energy balance (Marsh and Pomeroy, 1996). When the snow temperature reaches 0 °C, further energy inputs produce additional latent heat as a result of phase changes (Rowlands et al., 2002).

In the mountains, turbulent fluxes of sensible and latent heat are strongly influenced by forests and complex topography (Helgason and Pomeroy, 2005). At a clearing site in the Rocky Mountains, intermittent wind gusts were found to be responsible for half of the sensible and latent heat fluxes to the snowpack (Helgason and Pomeroy, 2012).

2.2.6. Heat and Vapour Transport at the Snow-Soil Interface

During the snow-free season, heat is transferred to the land surface. Some of the heat is retained by the soil. This is due to the soil's heat capacity (Ronda and Bosveld, 2009). When snow is deposited on the ground, the low thermal conductivity of the snow medium ensures that the snowpack acts as a thermal insulator (Sturm et al., 1997). This traps heat in the soil. When the soil loses heat during the winter season and the air temperature above the snow surface is colder than the soil, there is heat flux from the ground into the snowpack. Most of the heat flux is due to latent heat produced due to gradual freezing of the soil and sublimation of water vapour from the soil to the basal layer of the snowpack (Sturm and Benson, 1997). Some of the heat can be from geothermal sources (Powers et al., 1985). Vapour transport from the soil into the snowpack causes depth hoar formation in the basal layer (Sturm and Benson, 1997; Woo, 1982b).

Due to a difference in temperature between the ground and the snow surface, a temperature gradient occurs in snow. This temperature gradient is responsible for driving snow metamorphic processes. By the end of the winter season, the presence of a temperature gradient destroys much of the snowpack layering due to the development of extensive depth hoar throughout the snowpack (Sturm and Benson, 1997). This extensive depth hoar is also observed in snow deposited on an ice-covered lake, where the water beneath the ice has a higher temperature than the snow surface (Adams, 1981). This temperature gradient may not always be of high magnitude. Temperature gradients of lower magnitude occur in snowpacks that form at lower latitudes due to differences in regional energy balances.

The heat flux magnitude is moderated by frozen ground. At locations where the soil contains permafrost, the perennially-frozen ground reduces soil temperatures and heat is transferred from the snowpack into the ground. However, when the ground is incompletely frozen, soil temperatures are higher and heat is transferred from the ground into the snowpack (Marsh and Woo, 1984b). Diurnal cycles in heat flux are observed before ablation. During the time of ablation, heat cycles are strongly suppressed (Granger and Male, 1978).

Heat Flux G ($\mathrm{W\,m^{-2}}$)	Reference	Description
-5 (early snow season) to -1 (late snow season)	(Marks et al., 2008)	Measurements made in a sub-alpine watershed in Colorado from early to late snowmelt
-10	(Gold, 1957)	Measurement made during the time of early ablation at a site near Ottawa, Ontario
-5.3 (minimum) to 4.4 (maximum)	(Male and Granger, 1979)	Three years of observations at a prairie site (Bad Lake Research Basin near Rosetown, Saskatchewan)
-20 (early snowmelt) to 80 (late snowmelt)	(Pomeroy et al., 2003)	Measurements made at a subarctic site (Wolf Creek Research Basin, near Whitehorse, Yukon Territory) during the time of ablation
4	(Sturm and Benson, 1997)	Average value of measurements made over the winter season before ablation at a site near Fairbanks, Alaska
80	(Marsh and Woo, 1984a)	Meltwater flux at the bottom of a snowpack measured at a site in the High Arctic

Table 2.1. Measured heat fluxes between the ground and snowpack.

Table 2.1 shows example ground-snow heat fluxes measured before and during the time of ablation at field sites situated in the Arctic to mid-continental United States. Using the convention of this thesis, heat fluxes are negative when there is transfer of heat toward the snow surface and positive when there is transfer of heat toward the ground.

During ablation, when meltwater is transported through the snowpack and reaches the ground, the higher temperature of the water transitions the ground heat flux toward positive values. This indicates that heat is being transferred to the ground from the snowpack. Heat is also transported into the ground as the soil thaws and meltwater infiltrates into the soil. Latent heat is released in the snowpack due to re-freezing of the meltwater in the snowpack or at the base of the snowpack, and refreezing of meltwater in the soil is the soil is permeable. These processes warm the snowpack and the ground (Marsh and Woo, 1984a, 1984b).

2.2.7. Heat and Vapour Transport in Dry Snow

Heat fluxes at the snow surface act along with ground heat fluxes to transport heat in dry snow. Heat transport within the snowpack occurs due to five processes: radiation (Brandt and Warren, 1993), conduction (Mellor, 1977), free convection, forced convection (Albert and McGilvary, 1992b; Albert, 1993) and vapour transport (Adams and Sato, 1993; Mellor, 1977).

The absorption of light causes heating in the near-surface layer of the snowpack when the rate of warming exceeds the rate of cooling (Colbeck, 1989a). This causes a temperature maximum to occur beneath the snow surface. Heat flow occurs toward the snow surface because the snow surface is cooler than the temperature maximum (Brandt and Warren, 1993). Heat is transported in and away from this near-surface layer (Town et al., 2008). The development of the near-surface layer commonly occurs in natural snowcovers (Koh and Jordan, 1995; Shea et al., 2012).

Conduction of heat takes place in the ice matrix frame of the snowpack and in the pore spaces of the frame. Heat transport by conduction occurs primarily in the frame of the snowpack because the ice has a higher thermal conductivity than air in the pore spaces and the snow particles are in contact (Singh, 1999). The rate of conduction increases with snow density and is dependent on the bond contact area and geometry of snow particles (Arons et al., 1998). This makes a temperature gradient less pronounced in a dense layer of snow within a snowpack (Colbeck, 1991). Bonds with larger surface area conduct greater amounts of heat than bonds with less surface area due to more efficient transfer of heat over a larger area (Adams and Sato, 1993). When the bonds between snow particles have smaller area, water vapour becomes a dominant aspect of heat transport (Mellor, 1977), making the thermal conductivity of snow more dependent on temperature (Adams and Sato, 1993). Conduction is a significant heat transfer process in cold and dry environments such as the Antarctic ice sheet where water vapour fluxes are negligible and air transport is limited to surface snow of higher permeability (Brandt and Warren, 1997, 1993; Town et al., 2008).

Free convection (Albert and McGilvary, 1992b) is heat transport due to thermally-driven movement of air in the snowpack. This process has been observed in sub-Arctic snowcovers, where convection plumes develop. Heating of the snowpack due to ground heat flux and solar radiation causes warm air to rise to the snow surface whereas cold air is transported into the snowpack. The development of a convection plume causes “warm spots” to develop in the

snowpack at locations where air is rising (Sturm and Johnson, 1991). When thermal diffusivity in the snowpack is greater than mass diffusivity from vapour fluxes, free convection of heat will be accelerated in the snowpack. When vapour fluxes have greater magnitude, free convection of heat will be suppressed (Powers et al., 1985). Small trees buried beneath the snow can also serve as conduits for heat transport, where warm air rises in a "chimney" surrounding the tree. Ground temperatures are colder in the area surrounding the tree (Sturm, 1992).

Forced convection of heat occurs when wind pushes air into the porous snowpack. This is referred to as "windpumping" and occurs due to variations in pressure caused by surface relief (i.e. hills and gullies) or turbulence-induced transfer over a rough snow surface (Colbeck, 1997; Colbeck, 1989b). Ice layers and changes in snow permeability disrupt the flow of air, causing most of the induced pressure flow to travel horizontally along layer boundaries (Colbeck, 1997). Dissipation of pressure gradients by the porous snow medium can act as a significant source of heat near the surface of the snowpack (Clarke and Waddington, 1991). Alternately, temperature gradients that are already present in the snowpack can be modified by windpumping when colder air is forced into the pore spaces. Higher air flow rates will disrupt temperature gradients at lower depths in the snowpack. High-magnitude temperature gradients will be less disrupted by windpumping than low-magnitude temperature gradients (Albert and McGilvary, 1992b). The rate of water vapor transport in snow will be significantly enhanced by windpumping, causing regions of sublimation and condensation to develop in the snowpack (Albert, 2002).

Vapour transport in snow occurs due to diffusion of water vapour (Mellor, 1977). A source of water vapour is near the basal layer of the snowpack due to the presence of a ground heat flux. In the absence of windpumping, vapour diffusion occurs from the bottom to the top of the snowpack in the direction of the temperature gradient from warmer to colder areas (Sturm and Benson, 1997). The temperature gradient induces a corresponding gradient in saturation vapour pressure (Mellor, 1977). Vapour fluxes diffuse in a "hand-over-hand" fashion within this gradient (Yosida, 1955) and can be modelled using a mass-balance approach (Colbeck, 1991). The diffusion process begins by condensation of water vapour on the bottom of a snow particle. Due to conservation of energy, sublimation concomitantly occurs on top of the snow particle. Water vapour is progressively transferred in this fashion throughout the snowpack (Sturm and Benson, 1997). The rate of diffusion is dependent on the size of the pores in the snowpack. Greater rates of diffusion are predicted for smaller pore sizes (Colbeck, 1993)

2.2.8. Dry Snow Metamorphism

Metamorphic processes create and modify the structure of the porous media frame. Snow crystals that are situated close together undergo sintering, where "necks" or bonds form between adjacent crystals in the snowpack due to vapor transport (Brown and Edens, 1991) caused by vapour pressure differences between surfaces (Colbeck, 1997). This results in the linking together of particles to form a frame (Gubler, 1978). As the size of the bonds increase, the bond growth rate is a self-limiting process (Johnson and Hopkins, 2005), but when the snow is placed under compression, there is no relationship between the compressive force applied and the length of the bonds (Edens and Brown, 1991). However, the rate of bond formation can be increased by application of an external pressure force to the snow (Mahajan and Brown, 1993).

Snow particles deposited at lower depth in the snowpack are subjected to pressure from overlying snow layers. The mechanical compression increases the density. As snow metamorphism proceeds over time, the number of bonds between adjacent particles increases, strengthening the snow structure, reducing porosity and increasing density (Anderson and Benson, 1963). Where snow ablation does not occur due to cold conditions, the increase in density will transition the snow to glacial firn and then ice (Kawashima et al., 1993).

Colbeck (1986) proposed a process-based classification of snowpack metamorphism that is physically accurate. The scheme does not classify snow particles based solely on morphological properties but also takes into consideration the physics describing changes in particles. This supersedes other classification schemes (Sommerfeld and LaChapelle, 1970) due to a better understanding of the processes that operate over time in the snowpack. In the following paragraphs and sections of this thesis, the various stages of this classification scheme are given in brackets.

Surface hoar (Colbeck IVA) develops on the surface of the snowpack when longwave radiative cooling establishes a temperature difference at the air-snow interface, causing mass transport of water vapour from the air to the snow. Growth of the surface hoar occurs in a parasitic fashion from a particle already on the snow surface. Rapid growth of the surface hoar in a direction away from the snow surface causes facetted striations to develop and an expansion of particle area. When particles are redistributed by the wind, mechanical disaggregation will break the particle up, reducing the surface area and causing the formation of a windcrust as a hardened layer of snow (Colbeck IVB). The smaller particles are subjected to rapid

metamorphism that causes the particles to become rounded and bonded together. The bonding process is referred to as "sintering." A sun-crust (Colbeck IVD) develops when radiation from the sun melts snow, causing the production of meltwater. The meltwater then refreezes, creating a hardened layer on the snow surface. When water from rain refreezes on the surface of the snowpack, a freezing rain crust is created (Colbeck IVe).

Snow particles can develop into low density, brittle forms (Colbeck II3C) with large grains (Pfeffer and Mrugala, 2002). When these types of crystals form beneath the snow surface due to an upward flux of heat and vapor, the snow layer is referred to as "depth hoar." The bonding of depth hoar occurs in the preferential direction of the temperature gradient, causing the depth-hoar to migrate upwards toward the surface of the snowpack (Armstrong, 1980). It is possible for extensive depth-hoar formation to occur anywhere in the snowpack due to local temperature gradients (Fukuzawa and Akitaya, 1993). The vapor fluxes move in a layer-to-layer fashion (Sturm and Benson, 1997). The presence of a strong temperature gradient within an area of a snowpack is indicative of the formation of a weak layer of depth hoar (Adams and Brown, 1982). Weak layers that develop in snow are often the genesis of slab avalanches (Arons et al., 1998; Marbouty, 1980; Pfeffer and Mrugala, 2002). However, when depth hoar snow particles are bonded together, the snowpack becomes more structurally cohesive and less prone to avalanche failure (Pfeffer and Mrugala, 2002). The strength of depth hoar is dependent on the initial snow density before temperature-gradient formation. Snow with low density (~100 kg m^{-3}) will form weakly-cohesive depth hoar, whereas higher-density snow (~300 kg m^{-3}) will form a hard-crusted layer of depth hoar (Perla and Ommanney, 1985). Due to intense temperature gradients in most seasonal snowcovers, a large volume of the snowpack can be classified as depth hoar by midwinter (Sturm, 1992).

2.2.9. Heat and Water Transport in Wet Snow

Warming of the snow surface will decrease the cold content of the snowpack and cause the production of meltwater. In the near-surface layer of the snowpack, where warming occurs due to extinction of radiation, the liquid water content and temperature of the snowpack will initially increase near the surface. The meltwater can either re-freeze when the snowpack becomes colder and the cold content increases, thereby forming an ice layer, or the meltwater can percolate through the snowpack under the influence of gravity (Das and Alley, 2005; Koh

and Jordan, 1995; Techel and Pielmeier, 2011). Another source of heat and water transport through snow is rain (Fortin et al., 2002) that is at a greater temperature (>0° C) than the snow. The rain transfers sensible heat to the snowpack and will also transfer latent heat when the water re-freezes (Conway and Benedict, 1994; Marks et al., 2001).

The production of meltwater in a snowpack can be divided into three major temporal stages: the warming phase, the ripening phase, and the melting phase (Dingman, 2002). During the warming phase, the snowpack increases in temperature. The end of this phase occurs when the melting point of snow (0 °C) is reached and the cold content is numerically close to zero. In the ripening phase, the snowpack is isothermal and "ripe" but water transport does not occur until the output phase. At the output phase, the snowpack cannot hold any more water. Energy that is added to the snowpack during the output phase will drive snowmelt processes (Dingman, 2002; Marks et al., 2001).

Melting snowpacks can be spatially divided into three separate regions before meltwater reaches the ground surface. The uppermost region consists of an isothermal layer of wet snow. The lower boundary of the uppermost region is referred to as a "wetting front." Under the wetting front is a transition layer of mixed wet and dry snow. Following this transition layer is a layer of dry snow (Marsh and Woo, 1984a).

Net movement of the wetting front occurs due to the amount of meltwater available for transport and the microstructure of the snowpack. The meltwater produced in the region of wet snow must exceed the irreducible water saturation S_e of the snow immediately ahead of the wetting front before movement occurs. Moreover, enough water must be frozen at the wetting front to release latent heat sufficient to raise the temperature to 0° C so that additional meltwater is produced (Colbeck, 1976a). This causes temperatures in the uppermost region to rise and heat to be transported away from the wetting front into the colder snow at greater depth in the snowpack (Conway and Benedict, 1994).

The re-freezing of meltwater at the wetting front increases the mass of snow particles but will not create an ice layer unless the wetting front is stationary and there is sufficient heat flux for water freezing (Marsh and Woo, 1984a). Ice layer growth can also occur in the absence of melting and freezing due to temperature differences caused by sensible and latent heat fluxes. Ice layers can be wetted by meltwater and will gradually disappear (Colbeck, 1991). The

formation of ice layers is a major contribution to the heat balance of the snowpack (Marsh and Woo, 1984a).

The wetting front arrival at the base of the snowpack results in the development of a layer of wet snow overlying a layer of wet and dry snow (Marsh and Woo, 1984a). Freezing of the water at the base of the snowpack creates a basal ice layer. The basal ice layer will only develop when the ground is frozen. Because the basal ice layer has a low permeability, additional meltwater will be impeded by the ice layer and frozen ground. This causes ponding of the meltwater (Woo and Heron, 1981). On a sloping land surface, movement of the meltwater will occur in a downhill direction without infiltration into the soil (Colbeck, 1974a).

On an ice-covered lake, water from a melting snowcover will interact with water rising by capillary action through cracks in the ice, forming a slush layer at the snow-ice interface. When the ice cover melts, water from snowmelt will enter the lake (Adams and Lasenby, 1982; Adams, 1981).

The spatial variability of water transport through snow ensures that liquid water content θ_w is highly variable in both time and space over distances spanning 50 cm (Techel and Pielmeier, 2011) and over areas of 7 m^2 (Kattelmann, 1989). Water transport through snow follows three-dimensional flow paths, with more continuity between flow fingers in a snowpack layer than flow fingers in vertically lower layers (McGurk and Marsh, 1995; Williams et al., 2010). A larger number of meltwater drains have been found on south-facing slopes than north-facing slopes due to greater magnitude of shortwave radiation from the sun (Williams et al., 2000).

In the Colorado Rocky Mountains, Williams et al. (1999) took dielectric measurements of liquid water content at the snow surface. Using semivariogram analysis, they found at distances less than 6 m that liquid water contents were strongly correlated due to preferential flow of meltwater beneath the snow surface. Moldestad (2005) measured the liquid water content of snow on a cross-country ski track, finding higher liquid water contents in the top 5 cm of the snowpack due to friction heating by skiing. The liquid water content on the ski track decreased with ambient temperature.

Over the winter season, climate and geographic location causes distinctive differences in the liquid water content θ_w of snow due to variation in mass and energy balances (Jarosch and Denoth, 2004). At a study site in the Sierra Nevada, Kattelman (1990) measured the liquid water

content using a Denoth meter and averaged the values over snowpit depth. The liquid water content was found to be negligible when snow temperatures were less than -2° C earlier in the winter season. However, the liquid water content increased to an average value of 3% to 5% for snowpits sampled in mid-May. Fierz and Fohn (1994) also found higher values of liquid water contents at later times in the winter season, with a diurnal increase in water content close to solar noon owing to higher magnitude of shortwave radiation from the sun.

Colbeck (1974) states that the irreducible water saturation S_i of snow is approximately 7% ($S_i = 0.07$). However, values of S_i measured from a ripe snowpack have been reported between 2% to 4%, which corresponds to an irreducible water content θ_e of 1% to 2% (Marsh, 1991).

Dielectric measurements of snow have shown that the liquid water content θ_w can range from ~0% for dry snow to ~10% for a wet snowpack (Denoth and Wilhelmy, 1988; Denoth, 1994; Denoth et al., 1984; Sihvola and Tiuri, 1986).

For dielectric measurements, Techel and Pielmeier (2011) proposed a wetness classification scheme. In the context of this classification scheme, a water content θ_w of <1.3% by volume is dry or "barely moist" snow and > 1.3% by volume is wet snow.

Another alternate classification scheme is given by Techel and Pielmeier (2011) and referred to as the "Martinec" classification scheme after the author of an unpublished report. The scheme shows a water content of < 0.5% as corresponding to dry snow, 0.5% to 2% as corresponding to moist snow, 2% to 4% as corresponding to wet snow, 4% to 5% as corresponding to very wet snow, and > 5% as wet snow.

The classification scheme proposed by Fierz et al. (1999) defines dry snow as having a water content of ~0%, moist snow as having a water content of 0% to 3%, wet snow as having a water content of 3% to 8%, very wet snow has having a water content of 8% to 15%, and "soaked" snow as having a water content of > 15%.

Using the Colbeck classification scheme, the degree of water saturation S_w in the snowpack is classified by two different stages: the pendular and funicular regimes. In the pendular regime of saturation (< 7% to 14% of water saturation S_w), air has a continuous pathway through the pore space surrounding the snow particles (Colbeck, 1982a,b). The water is contained in a film around each particle (Denoth, 1982). The transition between the pendular

and funicular regimes of saturation occurs above 14% of water saturation S_w. This transition region was measured using dielectric techniques by Denoth (1980) as occurring from 11% to 15% (Colbeck, 1982a,b). The funicular regime of saturation is from 14% to 25% of water saturation S_w (Denoth, 1980), where the water is continuous throughout the pore space of the snowpack and the air is only found as bubbles in localized areas of the liquid (Colbeck, 1982a,b).

2.2.10. Wet Snow Metamorphism

The addition of water to snow causes wet snow metamorphism. The processes of wet snow metamorphism are significantly different from dry snow metamorphism (Colbeck, 1997).

Grain clusters (Colbeck IIIA) develop when multiple snow particles coalesce in the presence of small amounts of liquid water. The grain clusters develop due to the minimization of surface free energy. The growth of snow particle grains in the presence of water is referred to as "grain-coarsening." Smaller snow particles tend to form small spherical grains. The smaller grains are then merged to form larger grains (Colbeck IIIA). Merging of the grains occurs at a constant rate until all of the particles are approximately the same size. Although some studies have found that the mean grain size increases rapidly after the start of metamorphism and that a decline in the growth rate occurs shortly thereafter, it is possible for grain growth rate to be approximately linear over time (Marsh, 1987). When the water is found in a continuous layer without air inclusions around the snow particle (Colbeck IIIC), grain clusters cease to exist and the snow particles are found as isolated grains (Denoth, 1982) that have a spherical shape and are cohesionless (Colbeck, 1986b; Colbeck, 1982a,b). When ambient environmental temperatures drop below freezing and freeze-melt cycles occur, clusters of snow crystals are produced (Colbeck IIIB). These clusters are attached together with large bonds (Colbeck, 1986a). Re-freezing of melt water in the snowpack forms ice layers (Colbeck IVC).

2.2.11. Approximation of Snow Particles as Spheres

In lieu of measuring snow particle morphology using photogrammetry and visual inspection (Jamieson and Schweizer, 2000; Perla, 1985, 1982), snow particles comprising the snowpack are approximated as spheres in the UTAM theory presented in this thesis. However, snow particles have a wide variety of shapes and are facetted (LaChapelle, 1977; Libbrecht,

2005). Since the assumption that snow crystals are spheres may not always be valid, all snow crystals in a control volume over which the UTAM model is applied are assumed to have an effective radius that is approximated by a sphere.

Other investigators have assumed that snow particles are spheres. Partially to explain the cohesion of snow particles in a snowball, Michael Faraday (Faraday, 1859) conducted a series of experiments to pry apart spherical adhering ice particles (Hobbs, 1974; Kingery, 1960). Kuroiwa (1961) set up an experiment with two ice spheres to study sintering of snow particles during metamorphism. Colbeck and Parssinen (1978) proposed a model of sintering of wet snow using two adjacent spherical grains. This model was later elaborated on by Morris and Kelly (1990). Raymond and Tusima (1979) used an effective snow particle radius to describe the growth of snow particles in water-saturated snow. Brown (1980) proposed a constitutive model for snow with particles having effective radii. The model predicted sintering and the growth of bonds between adjacent snow particles. Similar models were also described by Edens and Brown (1991) and Mahajan and Brown (1993). The Watanabe (1993) and Dent (1993) models assumed that snow crystals in a snowpack are spheres packed in a "net-like" configuration within 3D space. Pomeroy and Schmidt (1993) assumed that snow particles were spheres to calculate sublimation rates of intercepted snow. Gay et al. (2002) used an effective radius when measuring snow crystal size with image analysis techniques.

The assumption of spherical snow particles can be eliminated by using Finite Element Methods (FEM) to model changes in the mechanical properties of snow (Dandekar and Brown, 1986), but this requires additional inputs that cannot be measured during application of the UTAM model proposed in this thesis. As noted by Bear (1972, pp. 445-446, cf. Figure 9.2.4) an "idealized model" of spherical grains is used to reduce the complexity of porous media so that it can be successfully modelled.

2.3. Acoustics

Acoustics is the science of sound. Sound waves are mechanical waves that propagate in matter. The sound wave has a phase velocity that is also referred to as a speed. The speed c as a scalar quantity is the rate at which a peak or a trough of the wave with a frequency f travels in a medium (Raichel, 2006). For porous media comprised of void spaces filled with a fluid, the

speed of a sound wave propagating in a medium is a function of frequency (Allard and Atalla, 2009).

The frequency f is the number of peaks or troughs of a waveform that occurs in a certain amount of time. The angular frequency ω is defined as $\omega = 2\pi f$. The period $T = 1/f$ is the distance between successive peaks or troughs (Raichel, 2006).

Sound waves are often linear combinations of waveforms with different frequencies. The magnitude of each frequency can be expressed as a spectral distribution of waveforms, with some frequencies having greater power. A broadband sound source is comprised of waves with a larger number of frequencies than a narrowband source (Raichel, 2006).

Power P is a measure of the acoustic energy carried by a wave per unit time. This is to be distinguished from the instantaneous root-mean-square pressure p of an acoustic wave, which is a measure of the force per area of the sound wave at an instance of time at a position within the medium (Raichel, 2006).

The Sound Pressure Level (SPL) is a measure of the instantaneous pressure of an acoustic wave expressed in units of decibels (Raichel, 2006):

$$L_p = 20\log_{10}\left(\frac{p_{\text{rms}}}{p_{\text{ref}}}\right) \text{dB} \tag{2.1}$$

In Equation (2.1), the reference pressure is $p_{\text{ref}} = 20\ \mu\text{Pa}$. The SPL is reported in decibels since this is a logarithmic scale that allows for wide-ranging values to be more easily represented (Waite 2001).

Waves that travel in a medium by compressions and rarefactions are P-waves. Alternately, transverse waves that travel in an elastic medium are referred to as S-waves. Because a gas such as air is incapable of shear, S-waves can only travel in a solid (Gadallah and Fisher, 2005).

Audible sound waves are considered to have frequencies between 20 Hz and 20 kHz and can be heard by human beings with normal hearing, although this is dependent on age, location to a source, room acoustics and noise. Infrasound is sound waves with frequencies < 20 Hz. Ultrasound is sound waves with frequencies > 20 kHz (Raichel, 2006).

The attenuation coefficient a_c of a medium is a measure of the rate at which sound is attenuated. Attenuation occurs when sound waves are gradually reduced in amplitude passing through a medium (Meyer and Neumann, 1972).

The attenuation of sound in porous media is exponential over the distance of wave travel and is a function $a_c(f)$ or $a_c(\omega)$ of the sound wave frequency, with greater attenuation present at higher frequencies (Allard and Atalla, 2009). The attenuation of sound in air is negligible at audible frequencies of sound, with a reduction in wave amplitude only occurring due to spherical spreading (Rossing and Fletcher, 1995).

Attenuation is distinguished from spherical spreading, a reduction in amplitude that occurs when sound waves spatially move outward from a source. When sound waves are produced by a hemispherical source, the waves propagate over a $180°$ sector of a sphere (Raichel, 2006).

Assuming that air is an ideal gas, the speed of sound in air is related to the air temperature T_a (Kelvin) by (Raichel, 2006):

$$c_0 = \left(\chi_g R_g T_a\right)^{1/2} \tag{2.2}$$

In Equation (2.2), the dimensionless ratio of the specific heats for air is χ_g and the ideal gas constant for air is R_g.

2.4. Mechanical Properties

The mechanical properties of a medium are referred to as the "elastic constants" (Schreiber et al., 1974). The propagation of sound in snow is dependent on these constants (Johnson, 1982).

By definition, the Young's modulus E of an isotropic material is the ratio of tensile stress σ_{stress} to tensile strain σ_{strain} and the shear modulus G is the ratio of shear stress γ_{stress} to shear strain γ_{strain}, as shown by Equations (2.3) and (2.4) below.

$$E = \frac{\sigma_{\text{stress}}}{\sigma_{\text{strain}}} \tag{2.3}$$

$$G = \frac{\gamma_{\text{stress}}}{\gamma_{\text{strain}}} \tag{2.4}$$

The tensile stress σ_{stress} is the force exerted over an initial cross-sectional area, and the tensile strain σ_{strain} is the fractional change in length of the medium resulting from the applied force. Qualitatively, the Young's modulus E is a measure of how easily a material can be stretched or compressed. As $\sigma_{\text{strain}} \to \infty$, $E \to 0\,\text{Pa}$. The material can be more easily stretched or compressed for a lower value of E as compared to higher values of E.

The shear stress γ_{stress} is the force exerted over a cross-sectional area of the material, and γ_{strain} is the fractional lateral displacement of the medium resulting from the applied force. The shear modulus can be considered as a measure how easily a material can be deformed by a shearing force. In a similar fashion to the Young's modulus, as $\gamma_{\text{strain}} \to \infty$, $G \to 0\,\text{Pa}$. For materials where $G \to 0\,\text{Pa}$, a shearing force can more easily deform the material.

The bulk modulus K of an isotropic material is calculated from the Young's modulus and the shear modulus as:

$$K_b = \frac{EG}{3(3G - E)} \tag{2.5}$$

2.5. Snow Acoustics Research

The propagation of sound in snow has been studied by investigators so that physics of sound waves can be related to snow material properties or acoustic emissions from snow can be related to avalanche processes (Sommerfeld, 1982). Using the same terminology as sonar (Lurton, 2002), devices that send sound waves into snow are classified in this thesis as active acoustic devices, whereas devices that only detect sound waves from snow are classified as passive acoustic devices. The classification is similar to the scheme given in Section 1.3.9 of this thesis for radioactive snow measurement devices. The scope of the following review is limited to acoustic research performed using active devices since these are similar to the device

described in this thesis. Passive devices are described and reviewed by Sommerfeld (1982), O'Neel et al. (2007), and Lacroix et al. (2012).

Invasive snow acoustics experiments can be classified as sending sound waves through a snow sample (Section 2.5.1), or the sending of sound waves through a snowpack (Section 2.5.2). Non-invasive experiments involve the sending of sound waves above the snow surface (Section 2.5.3) in a similar fashion to the experimental apparatus reported in this thesis. This review excludes research conducted on the propagation of shock waves through snow with amplitudes high enough to cause permanent deformation of the snowpack (Albert, 1983; Brown and Hansen, 1987; Brown, 1979; Johnson, 1990).

2.5.1. Invasive Snow Sample Extraction Experiments

Nakaya (1959) extracted snow samples from the Greenland ice sheet and measured the Young's modulus and attenuation of sound in snow using flexural vibrations. Lee (1961) showed that the speed of sound in snow samples increased with the density. Smith (1965) sent sound bursts with microsecond duration into a cylindrical snow sample, using a time-of-flight measurement between two transducers to determine the speed of the pulse. The speed of sound in the snow sample was then related to the density and elastic constants of the snow using empirical and semi-empirical relationships. Smith (1969) conducted a similar experiment, but used a continuous-wave source signal and the theory proposed by Lee (1963) to measure the attenuation of sound in snow and elastic constants of snow by finding the resonant frequency of a snow sample. The range of frequencies used in the experiment was less than 5 kHz.

Bogorodskii et al. (1974) measured the speed of ultrasound pulses in Arctic snow samples placed between two transducers (Bogorodskii and Dobrotin, 1963), finding that the speed of sound was independent of frequency but changed with snow density in the 25 kHz to 800 kHz frequency range. This was a repeat of an experiment initially conducted by Kuz'min (1957) at lower latitudes. Bogorodskii et al. (1974) used the Zwikker and Kosten (1949) rigid-frame theory of sound propagation in porous media to qualitatively explain these results, indicating that coupling of the motion of the fluid and the frame was important at higher frequencies. This finding can be interpreted using the high frequency approximation of Johnson and Plona (1980) and Johnson et al. (1982), and the Biot theory of sound propagation in porous

media (Biot, 1956a). These theories predict that the speed of sound is independent of frequency above a high-frequency threshold.

Impedance tubes have been the most common apparatus used to measure the impedance of sound in snow samples. The impedance tube determines the characteristic acoustic impedance of a material, which is a measure of flow resistance to air pressure waves. This measurement can then be related to the speed and attenuation of sound in snow. An impedance tube measurement is made by placing the material inside of the tube. A loudspeaker is placed at one end of the tube, whereas the other end of the tube is closed.

Two methods are used to measure the acoustic impedance of a material placed in the impedance tube. (1) The standing wave method uses the loudspeaker to produce a sound wave with a single frequency. This sets up a standing wave in the tube. The standing wave is spatially sampled using a probe microphone that is translated down the length of the tube. To obtain the acoustic impedance at a different frequency, the frequency of the source must be changed. Alternately, the length of the tube or the sound wave frequency can be changed until acoustic resonance occurs. (2) The two-microphone method uses two microphones placed on the walls of the impedance tube. A broadband sound wave is sent from the loudspeaker. Signal processing and spatial differences between the microphones are used to obtain the impedance of the material as a function of frequency.

Oura (1952a, b) used the standing wave method to measure snow impedance at frequencies from 500 Hz to 6 kHz. The speed of sound in snow was found to be dependent on the air temperature inside of the tube, with a decrease in the speed of sound in snow apparent with a decrease in temperature. Since the speed of sound in ice will increase at lower temperatures, Oura reasoned that most of the sound wave propagated in the pore spaces of the snowpack medium. Oura also found that the speed of sound in snow was less than the speed of sound in air. This finding is in agreement with Tillotson (1966), who made impedance tube measurements on a snow sample with density 185 kg m^{-3}, finding that the speed of sound in the sample was 60% of the speed of sound in air.

Buser (1986) and Buser and Good (1986) also used a standing wave method with source frequencies ranging from 100 Hz to 4 kHz . They quantitatively applied the Zwikker and Kosten (1949) rigid-frame theory, showing that their experimental results agreed with the theory within a 10% error. Attenborough and Buser (1988) later used this data to apply Attenborough's rigid-

frame model (Attenborough, 1987, 1983) based on the Zwikker and Kosten (1949) rigid-frame theory. In agreement with Oura (1952a, b), these investigators found that sound pressure waves were mostly propagated in the pore spaces of the snow.

Marco et al. (1996) and Marco et al. (1998) used the two-microphone method to measure snow density using a broadband source with frequencies between 100 Hz and 4 kHz. They recognized that snow density may control sound wave propagation in the pore spaces of snow or the ice matrix of the frame. Wave propagation in the ice matrix was postulated to become more important for snow with densities $> 500\ \mathrm{kg\ m^{-3}}$. The results obtained by these investigators showed a deviation from rigid-frame theory for snow with densities $> 500\ \mathrm{kg\ m^{-3}}$ and frequencies < 2.5 kHz.

2.5.2. Invasive Snowpack Experiments

Oura (1952) buried two microphones within a snowpack. The microphones were separated by an offset distance. An explosive sound source provided an impulse that allowed Oura to determine that the speed of sound in snow observed during the experiment ranged between $190\ \mathrm{m\ s^{-1}}$ and $240\ \mathrm{m\ s^{-1}}$. Oura also noted that the explosion created an air wave in the air medium above the snowpack and passed through an ice layer in the snowpack. The speed of sound in the ice layer was from $700\ \mathrm{m\ s^{-1}}$ to $1000\ \mathrm{m\ s^{-1}}$.

Ishida (1965) created a reverberant "room" out of snow by digging into the snowpack. A loudspeaker was installed in one of the walls of this room and a snow sample was placed at the opening of the room. A white noise generator was attached to the loudspeaker. The generator was used to produce broadband white noise with a frequency distribution between 100 Hz and 8 kHz. This allowed for the transmission loss of the snow sample to be determined using the reverberant room method (Mariner, 1961). Transmission loss is the reduction in amplitude of the sound wave passing through the snow sample. The transmission loss increases with an increase in the distance travelled by the sound wave. Cummings and Holliday (1983) performed a similar experiment, where tones with frequencies ranging from 105 Hz to 10.510 KHz were used to determine attenuation of sound through a model seal layer created out of snow on the ice near Prudhoe Bay, Alaska.

Lang (1976) created a snowpit and placed a loudspeaker facing the snowpit wall. Two microphones pushed through the side of the snowpit measured sinusoidal tones sent from the loudspeaker at frequencies between 100 Hz to 30 kHz. Lang found that sound with frequencies less than 3 kHz could propagate in snow for at least 3 m, with greater attenuation of sound at higher frequencies. Sound waves with frequencies from 100 Hz to 200 Hz showed the least attenuation.

Iwase et al. (2001) suspended a loudspeaker in the air above the snow surface and buried microphones in the snowpack at depths of 30 cm, 40 cm, 55 cm and 78 cm. A broadband sound wave was sent from the loudspeaker. Sound waves at frequencies between 100 Hz and 10 KHz were able to penetrate snow to be detected at these depths.

Moore et al. (1991) placed a loudspeaker on the snow surface and pushed a microphone mounted on a probe beneath the snow surface. Although the method was invasive, Moore et al. (1991) were able to determine snow porosity by application of the Attenborough model.

2.5.3. Non-invasive Experiments

Reynolds (1873) recognized that audible sound is attenuated by snow. Since the time of this early paper, researchers have measured the attenuation of sound propagating horizontally over snow between a loudspeaker and microphone pair. Kaye and Evans (1940) measured the attenuation of sound in snow within a reverberation chamber. Watson (1948) sent sound waves with frequencies ranging from 100 Hz to 2 kHz above snow, finding that the wave attenuation was greater for higher frequencies. This attenuation was also apparent in the experiments reported by Takada et al. (1954). Tillotson (1966) found that a source with SPL 100 dB to 105 dB could be detected by a microphone placed at horizontal distances greater than 10 m from the source. Tillotson (1966) used the theory proposed by Rudnick (1947) to calculate the characteristic impedance of a ground surface with a snow layer.

Hess et al. (1990) used curve-fitting to fit the semi-empirical Delany and Bazley (1970) model as well as the Attenborough model to attenuation data of sound waves propagating horizontally over snow. The curve-fitting procedure was not unique for all experimental data. Iwase et al. (2001) showed that attenuation of sound waves passing over snow was greater for fresh snow than for compressed snow.

Impulsive acoustic sources have been used to send sound waves into snow. These sound sources were provided by: military vehicles (Albert, 1987), explosives (Albert and Hole, 2001), as well as handguns and sledgehammers (Albert and Orcutt, 1990, 1989; Albert, 2003, 2001, 1998; Albert, 1993a; Boeckx et al., 2004; Moran and Albert, 1996). Experiments performed with these sound sources showed that acoustic waves originating in the air medium can be transferred to the snowpack by acoustic-to-seismic coupling. The air-coupled waves were detected by geophones placed on the snow surface and microphones placed near the surface of the snowpack. Snow depth and permeability were determined using a rigid-frame model (Albert, 2001, 1998). Seismic surveys with geophones and sledgehammers have been used to determine snow porosity using geophysical methods (Booth et al., 2013). Using impulsive sources, Albert (2003) showed that waves originating in the air medium can also propagate along the snow surface.

Some investigators have sent sound waves directly into snow using loudspeaker and single microphone pairs situated parallel to the snow surface. The loudspeaker was situated at an offset distance to the microphone. Lee and Rogers (1985) sent impulsive sound waves into a 2 cm snow layer that had accumulated on a roof using a loudspeaker and microphone pair. The source signal was impulsive and the rigid-frame Zarek porous media model (Zarek, 1978) was used to create a synthetic waveform that was compared to the measured waveform. Kinar and Pomeroy (2007; 2008a, b; 2009) used non-impulsive source signals sent from loudspeaker and microphone pairs to determine SWE.

2.5.4. Biot-Stoll Model

In a series of papers, Biot (1956a; b; c, 1962) established a theory of sound propagation through porous media. The theory considers the porous medium to be comprised of a fluid that completely saturates a sedimentary frame with pore spaces. The theory was later modified by Stoll (1989) to make the mathematics physically reasonable. This Biot-Stoll model was experimentally tested by Holland and Brunson (1988). Biot theory was first applied to snow by Johnson (1982) and Albert (1993), assuming that the snow sedimentary frame is comprised of snow particles and the pore spaces are filled with air.

Despite the presence of small amounts of liquid water as an irreducible water saturation (Colbeck, 1972), the Biot theory provides an approximate description of dry snow, with the fluid

as air and the frame comprised of ice (Buser and Good, 1986). Petrovic (2003) further classifies snow as a cellular solid form of ice. Although the densities of individual snow particles can differ from the density of ice (Ishizaka, 1993; Pruppacher and Klett, 2010), in the absence of any additional information the assumption that the snow particles are comprised of ice is used to apply the Biot theory to snow in this thesis. Scaling coefficients are later introduced to model differences between ice and snow particles.

The classical Biot theory predicts that three different waves propagate through a porous medium. The first wave is a pressure wave (P-wave) that travels through the porous frame. This is referred to as the "fast wave." The second wave is a P-wave that propagates through the pore spaces of the medium. This is referred to as the "slow wave." The speed of the second wave is often slower relative to the fast wave. The third type of wave is a shear wave (S-wave) that propagates only through the frame. The speed of sound changes with the frequency of the wave. The attenuation of the sound wave is dependent on the pore space geometry, grain size and permeability. Due to viscous damping forces, porous media comprised of coarse granular materials can have higher rates of sound attenuation than fine granular materials (Stoll, 1989).

Investigators have directly applied the Biot theory to model acoustic properties of snow (Albert, 1993b; Johnson, 1985). Since the frame is rigid an assumption can be made that it does not move during propagation of the sound wave. Simplified theories based on this assumption have been tested (Albert, 2001; Attenborough and Buser, 1988; Marco et al., 1998, 1996), but may not be applicable for snow due to a deviation from rigid-frame theory for densities > 500 kg m^{-3} and frequencies < 2.5 kHz when small movements of the frame may occur (Marco et al., 1998, 1996).

Because of this consideration, the full Biot theory is being applied in this thesis to measure snowpack properties of interest to hydrologists. However, the full Biot theory does not take into consideration the presence of a mixture of air and water in the pore spaces of snow. This necessitates the development of the Unified Thermoacoustic Model (UTAM) presented in this thesis (Section 3.2).

The High Frequency Approximation (HFA) model presented in a later section of this thesis (Section 3.3) uses the rigid-frame approximation for sound with frequencies > 2.5 kHz. The HFA model is then coupled with the UTAM (Section 3.4.4). This reconciles the full Biot theory with the rigid-frame models.

Sound pressure waves that travel from air into snow are conveyed in the pore spaces of the medium (Boeckx et al., 2004). The acoustic-to-seismic coupling of air waves into snow (Albert and Orcutt, 1989; Albert, 2001) is important in the context of UTAM theory since this physical process is being used to determine the snowpack properties. Because air as a gas is incapable of shear wave propagation, the S-wave that propagates in the frame will not be detected in the air medium. Moreover, the P-wave that travels through the frame will be of relatively low amplitude due to the frame stiffness. This implies that sound propagation into the snowpack and reflections of sound waves travelling from the snowpack back into the air medium will be conveyed by the second P-wave (Boeckx et al., 2004).

The pore spaces of snow are mostly interconnected (Buser, 1986), indicating that propagation of the second P-wave as described by the Biot model will occur. As noted by Stoll (1989) and Albert (1993), the second P-wave propagation mode cannot be neglected in media where the pore space fluid is air.

2.6. Mixture Theory Models

The UTAM model presented in this thesis (Section 3.2) is a modified version of the Biot-Stoll model. To modify the Biot-Stoll model for snow, an approach is taken using "effective" parameters. The effective parameter approach replaces model parameters by substitution of mathematical expressions. These expressions represent changes in the parameters that model sound wave propagation in multiphase media. Similar ideas have been used in other models of wave propagation in unsaturated media. These are mixture theory models (Corapcioglu and Tuncay, 1996).

For example, modelling the propagation of water waves over a porous bed using Biot theory, Yamamoto et al. (1978) define an effective volume compressibility coefficient that includes a mixture of air and water in the bed. Colbeck and Anderson (1982) define an effective porosity to take into consideration the irreducible water saturation of snow. Corapcioglu and Tuncay (1996) mention that closed pores in a medium can be modelled by an effective porosity. Carcione et al. (2004), in the derivation of a model for partially-saturated porous media, introduce an effective permeability that takes into consideration the solid, liquid and gas phases of the medium.

2.7. Sonar and Seismology

Sonar is an acronym for "SOund Navigation and Ranging" (Chevalier, 2002). The principles of sonar were used to design ultrasonic snow depth sensors (Section 1.3.12). Sonar devices are commonly deployed in ocean environments and are used to obtain images of bathymetry as distance to the bottom of an ocean, lake or river. Models of the speed of sound in saline water are used for the calculation of depth. Sonar has been used to detect underwater objects including submarines, the hull of ships, mines and fish. Sonar can obtain estimates of underwater sediment transport (Lurton, 2002). The physical properties of sediment have been determined using empirical relationships (LeBlanc et al., 1991). The Biot-Stoll theory has been applied to model sound wave propagation through sediment at the bottom of an ocean (Stoll, 1989).

Reflection of sound will only occur when there is a change in the acoustic impedance of a medium (Lurton, 2002). Changes in the acoustic impedance of sediment will cause these reflections to occur (Ewing et al., 2013).

Sonar devices can be active or passive, either sending sound waves that are bounced off of objects or receiving sound waves from propellers or underwater animals (Waite, 2001). Although sonar devices are commonly designed with a single piezoelectric transducer that sends and receives sound waves at a single frequency, bistatic sonar devices have also been created with a separate source and receiver (Cox, 1989) or many multiple sources and receivers in an array (Wilson, 1989). The device described in this thesis is similar to bistatic sonar.

Seismology is the use of sound waves to obtain images of layered rocks (Claerbout, 1992). A seismic survey uses a number of transducers (geophones) (Burger et al., 2006). Seismology is often performed on the land surface and has been used to measure snow (Section 2.5.3). However, seismic surveys can also be performed in water using an airgun (implosive) sound source and a number of transducers situated at an offset distance from the source. The offset distances between transducers are on the order of meters (Claerbout, 1992).

2.8. Acoustic Scattering and Mode Conversion

When sound from acoustic sources such as sonar contacts a rough surface such as a seabed with facets, acoustic scattering occurs. Volume backscattering also occurs within the sediment of the seabed. Scattering is a diffusion effect where sound is reflected in a number of

directions from an acoustic reflector, reducing the amplitude of the detected sound wave. The scattering is most prevalent for a surface with larger-amplitude facets and vegetation (Lurton, 2002). Attenuation and scattering will occur within porous media when the medium is incompletely saturated (Dutta and Odé, 1979). Scattering of sound waves has been observed in the atmosphere due to atmospheric turbulence (Wilson et al., 1999) and is also present in medical ultrasound (Insana et al., 1992). Scattering of sound waves will occur in suspended sediment in the ocean (Richards et al., 1997).

As shown by Kinar and Pomeroy (2008a,b), acoustic scattering of sound waves from snow can be modelled using the V-cavity paradigm (Torrance and Sparrow, 1967) and the Rayleigh parameter from wave-scattering theory (Brekhovskikh and Lysanov, 2003), but an estimate of surface slope angles is required. Acoustic scattering by snow occurs due to uneven snow surface topography and buried vegetation that causes diffusion of sound waves. The refraction of sound by tree wells will also occur and acts similar to acoustic scattering when sound waves travel directly though the snowpack into the tree well space. The effect of acoustic scattering and refraction causes higher errors to occur between acoustic and measured (gravimetric) snowpack properties (Kinar and Pomeroy, 2009, 2008a, 2008b).

Mode conversion occurs when a sound wave is incident at an angle on an interface between materials with different acoustic impedances and there is a resulting conversion from P-waves into S-waves. This causes a change in the energy conveyed by the P-waves and is a potential source of error in acoustic measurements (Furukawa and Date, 1995). Mode conversion occurs in unsaturated porous media when sound waves interact with a two-phase fluid (Chen et al., 2012).

2.9. Signal Processing

Signal processing is mathematical manipulation of sampled data. Data is sampled in the time domain and stored as a sequence of numbers. Let $s[t] \in \mathbb{R}$ denote a discrete time-domain signal as a function of time $t \in \mathbb{Z}$. In a computer program, the values of $s[t]$ are normally stored in an array. Digital signals are represented by square brackets [ ]. When square brackets are used, $t \in \mathbb{Z}$ is a counting number that is used to identify a discrete element ($t = 0,1,2,3,\ldots$) of the

signal. This is to be distinguished from a continuous function $s(t) \in \mathbb{R}$ where $t \in \mathbb{R}$ (Lyons, 2004).

The convolution of two time-domain functions $s[t]$ and $g[t]$ is an operation that results from translating and adding the two functions. Continuous and discrete convolutions are represented by the following (Smith, 2002):

$$s(t) * g(t) = \int_{-\infty}^{\infty} s(t-u)g(u)d\tau$$

$$s[t] * g[t] = \text{IFFT}\left(\text{FFT}\left(s[t]\right) \odot \text{FFT}\left(g[t]\right)\right) \tag{2.6}$$

$\text{FFT}(\,)$ represents the discrete Fourier transform operator (numerically implemented as the Fast Fourier Transform), $\text{IFFT}(\,)$ represents the inverse discrete Fourier transform (numerically implemented as the Inverse Fast Fourier Transform), and following Hansen (2002), the $\odot$ symbol represents Hadamard (point-by-point) multiplication between the complex signals in the frequency domain. To prevent circular convolution from occurring, $s[t]$ and $g[t]$ must be padded with zeros so that the length of both signals are $L = M + N - 1$, where M is the number of elements in $s[t]$ and N is the number of elements in $g[t]$.

The convolution operation can be used to model the response of a system. For example, if $s[t]$ is an acoustic wave passing through a medium, then $g[t]$ is the effect of the medium on the wave (Claerbout, 1985). Using systems theory $g[t]$ can be represented as a black-box system, $s[t]$ as the input, and the convolution $s[t] * g[t]$ as the output (Figure 2.2).

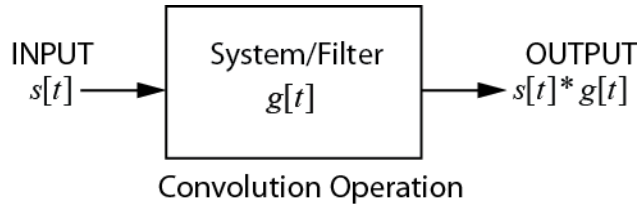

Figure 2.2. Diagram showing the effect of a system on an input signal $s[t]$.

If $g[t]$ is a filter kernel, then $s[t]$ can be filtered by convolution. A filter kernel is a signal that is constructed to modify the frequency response of $s[t]$ by convolution. Low-pass, band-pass and high-pass filters can be used to eliminate unwanted noise or signals, but many other types of filters exist (Claerbout, 1985). A Finite Impulse Response (FIR) filter can be applied by direct multiplication in the frequency domain (Equation (2.6)), whereas an Infinite Impulse Response (IIR) filter must be applied in the time domain. Although FIR filters are normally stable, an IIR filter can often exhibit numerical instability due to an inherent feedback effect (Smith, 2002).

Deconvolution is the operation that removes the filter kernel $g[t]$ from $s[t]*g[t]$ to get $s[t]$ given an estimate of $g[t]$ (Jansson, 1996). Blind deconvolution is the operation where an estimate of $g[t]$ is not available and $s[t]$ is estimated (Campisi and Egiazarian, 2007; Kundur and Hatzinakos, 1996).

2.10. Maximum Length Sequences

Maximum Length Sequences are used as source signals for acoustic observations involving signal processing. Applications of MLS signals include: hearing aid testing (Schneider and Jamieson, 1993); determining the response of loudspeakers (Atkinson, 1997); measuring the acoustics of architectural spaces (Bradley, 1996; Chu, 1984; Vanderkooy, 1994); and exciting control systems for determining system response (Pintelon and Schoukens, 2012). MLS measurements have also been used to determine the electrical impedance of a biological cell (Gawad et al., 2007).

Other investigators have used the MLS for sonar applications. Farina (1998) used MLS measurements to determine the profile of an underwater object placed in a pool. Farina performed the MLS measurements using a waterproof loudspeaker and microphone set up in a bistatic sonar arrangement. Morgan and Watts (2003) placed a loudspeaker and microphone on a trailer at the back of a vehicle and used MLS sequences to measure the absorption coefficient of porous road surfaces. Xiang and Chu (2004) set up a bistatic sonar experiment to measure the backscattered waves from a copper sphere in a water tank. An ultrasonic transmitter produced the MLS at a sampling rate of 200 kHz, and the reflection from the sphere was detected by a receiver set up at an offset distance to the transmitter.

2.11. Imaging of Snow and Snowpits

In an extensive study conducted on a 20 m by 20 m plot on the Pika Glacier, Alaska, Harper and Bradford (2003) compared 600 point measurements of snow density and stratigraphy collected in 19 snowpits to images of snow obtained from ground penetrating radar transects. Density measurements were made using gravimetric and dielectric techniques. They concluded that images of snowpit stratigraphy recorded by human observers did not always coincide with the radar profile images and dielectric profiles. The radar images and dielectric profiles showed more fine scale variability than the snowpit observations due to changes in the dielectric constant of snow over the depth of the snowpack.

Marshall et al. (2007) compared snow micro-penetrometer data collected in snowpits to FMCW radar data. The penetrometer recorded changes in snow hardness over the depth of snow. A probability density function (PDF) was applied to the FMCW radar data to show the positions of major reflections in the radar image.

2.12. Comparison of Observations to Models

The Root Mean Squared Difference (RMSD) is a comparison between model outputs and observed data reported in the same physical units. The higher the RMSD, the higher the overall differences between the datasets. RMSD is defined as (Patil et al., 2010):

$$\text{RMSD} = \sqrt{\frac{1}{N}\sum_{i=1}^{N}\left(x_i - \hat{x}_i\right)^2} \tag{2.7}$$

In the above Equation (2.7), the number of observations is N, the index is $i \in \mathbb{Z}$, the modelled value is x_i, and the measured value is $\hat{x}_i$.

The Mean Bias (MB) is a measure of the under-prediction or over-prediction of a model reported in the same units of measurement as the model and data (IEC and CIE, 1987). If the MB is positive, then the model over-predicts relative to the observed data. If the MB is negative, then the model under-predicts relative to the observed data. The MB is calculated as:

$$\text{MB} = \frac{1}{N}\sum_{i=1}^{N}\left(x_i - \hat{x}_i\right) \tag{2.8}$$

CHAPTER 3
THEORY

3.1. Introduction

The following sections of this thesis develop and apply the Unified Thermoacoustic Model for Snow (UTAM). Starting with the Biot-Stoll theory of sound wave propagation in porous media, solutions of the constituent equations were modified to take into consideration the presence of liquid water in the pore spaces of the snowpack and the mechanical and thermal properties of the snow porous medium. Consolidation theory is proposed in this thesis to predict when the snowpack will cease to act as a solid and become an equivalent fluid. A High Frequency Approximation (HFA) model was also proposed and coupled with the UTAM. To apply the UTAM and to measure snowpack properties by the use of acoustics, a signal processing procedure was developed. The vanishing constant filter (VCF) was proposed as a method of blind deconvolution to remove attenuation from the signal. Speed analysis algorithms obtained the speed of the sound wave in the snowpack. A spectrogram bandpass filter bank analysis (SBFA) was proposed to couple the signal processing with the UTAM.

3.2. UTAM Model

3.2.1. Biot-Stoll Constitutive Equations

Stoll modified Biot's theory so that it could be physically realizable (Stoll and Bryan, 1970; Stoll and Kan, 1981; Stoll, 2002, 1985, 1980, 1979). This is the Biot-Stoll theory. For a control volume of the porous media used in the UTAM model, coupled equations governing the motion of the frame (Equation (3.1)) and the fluid (Equation (3.2)) are given by (Stoll, 1985):

$$\nabla^2\left(He - C\xi\right) = \frac{\partial^2}{\partial t^2}\left(\rho e - \rho_f \xi\right) \tag{3.1}$$

$$\nabla^2\left(Ce - M\xi\right) = \frac{\partial^2}{\partial t^2}\left(\rho_f e - m_f \xi\right) - m_f \frac{\partial \xi}{\partial t} \tag{3.2}$$

$$H = \frac{\left(K_r - K_b\right)^2}{D - K_b} + K_b + \frac{4\mu}{3} \tag{3.3}$$

$$M = \frac{K_r^2}{D - K_b} \tag{3.4}$$

$$C = \frac{K_r\left(K_r - K_b\right)}{D - K_b} \tag{3.5}$$

$$D = K_r\left(1 + \phi\left(\frac{K_r}{K_f} - 1\right)\right) \tag{3.6}$$

$$m_f = \frac{\alpha\rho_f}{\phi} \tag{3.7}$$

$$\xi = \phi\,\mathrm{div}\left(\mathbf{u} - \mathbf{U}\right) \tag{3.8}$$

In the above Equations (3.1) through (3.8), ξ is an effective fluid content increment that occurs when the sound wave propagates through the porous medium; $\mathbf{u}$ is a vector with small magnitude that describes the motion of the frame; $\mathbf{U}$ is a vector that describes the movement of the fluid; $\mathrm{div}(\ )$ is the divergence; ∇^2 is the Laplacian; t is a time variable; ρ is the density of the control volume; ρ_f is the density of the fluid saturating the pore spaces of the medium, $e = \mathrm{div}(\mathbf{u})$; the inverse fluid mobility (also given by Equation (3.7)) is $m_f = \eta / k_p$, where η is the dynamic viscosity of the fluid saturating the pore spaces of the medium and k is the permeability; K_r is the bulk modulus of the sediment (snow particles) comprising the frame; K_b is the bulk modulus of the frame; μ is the shear modulus; ϕ is the porosity; and α is the tortuosity.

For application of the UTAM, the "control volume" is an arbitrary volume of the medium over which the constituent equations are applied (Wylen et al., 1993). All of the parameters in the UTAM model are assumed to be average values that are constant within the control volume. The control volume is thereby assumed to be isotropic.

Equations (3.1) and (3.2) have solutions given by the matrix determinant (Stoll, 1989):

$$\begin{vmatrix} Hl^2 - \rho\omega^2 & \rho_f\omega^2 - Cl^2 \\ Cl^2 - \rho_f\omega^2 & m_f\omega^2 - Ml^2 - i\omega F(\kappa)m_f \end{vmatrix} = 0 \tag{3.9}$$

$$l_k = c_{s,k} + a_{s,k} i$$

Grouping terms and re-writing Equation (3.9) as a polynomial, it follows that:

$$\left(Hl^2 - \rho\omega^2\right)\left(m_f\omega^2 - Ml^2 - i\omega F(\kappa)m_f\right) - \left(Cl^2 - \rho_f\omega^2\right)\left(\rho_f\omega^2 - Cl^2\right) = 0$$

$$\begin{aligned}&(C^2 - HM)l^4 + (\rho\omega^2 M + H(m_f\omega^2 - i\omega F(\kappa)m_f) - 2\rho_f\omega^2 C)l^2 \\ &-\rho\omega^2(m_f\omega^2 - i\omega F(\kappa)m_f) + \rho_f^2\omega^4 = 0\end{aligned} \tag{3.10}$$

In Equation (3.10), $\omega = 2\pi f$ is the angular frequency of the sound wave, f is the frequency, $F(\kappa)$ is a correction factor that models the frequency-dependent fluid flow resistance through the pore spaces of the medium, $i = \sqrt{-1}$, and l_k is one of the complex roots k of Equation (3.9), with $1 \le k \le 4,\ k \in \mathbb{N} \setminus \{0\}$. The speed of sound in snow is $c_{s,k}$ and the attenuation is $a_{s,k}$ for one of the roots $\{l_1, l_2, l_3, l_4\}$ at a frequency f. In addition, $l_1 = -l_2$ and $l_3 = -l_4$, with the order of the roots being unimportant. This implies that the absolute values of two of the four roots are the same, giving two complex numbers corresponding to the speed and attenuation of the slow and fast P-waves travelling in the pore spaces of snow. For purposes of nomenclature, the speed of the second P-wave is denoted as c_s, whereas the attenuation of the second P-wave is a_s.

The correction factor $F(\kappa)$ is a complex number given by (Stoll, 1989):

$$F(\kappa) = \frac{1}{4}\frac{\kappa\Lambda(\kappa)}{1 - 2\Lambda(\kappa)/i\kappa} \tag{3.11}$$

$$\Lambda(\kappa) = \frac{\frac{\partial \mathrm{Ber}(\kappa)}{\partial\kappa} + i\frac{\partial \mathrm{Bei}(\kappa)}{\partial\kappa}}{\mathrm{Ber}(\kappa) + \mathrm{Bei}(\kappa)} \tag{3.12}$$

$$\kappa = \alpha\left(\frac{\omega\rho_f}{\eta}\right)^{1/2} \tag{3.13}$$

In the above Equations (3.11) to (3.13), $\mathrm{Ber}(\kappa)$ is the real part of the Kelvin function, $\partial\mathrm{Ber}(\kappa)/\partial\kappa$ is the derivative of the real part of the Kelvin function, $\mathrm{Bei}(\kappa)$ is the imaginary part of the Kelvin function, $\partial\mathrm{Bei}(\kappa)/\partial\kappa$ is the corresponding derivative, η is the viscosity of the pore

fluid, and all other parameters are as previously defined. In addition to the Biot correction factor above, Albert (1993) has tested other correction factors proposed by Attenborough (1983) and Attenborough (1987), finding that all of these expressions give similar results. Due to this finding and for simplicity, only the Biot-Stoll correction factor given by Equation (3.11) above is used in the UTAM.

The Kelvin functions are defined as infinite series (Abramowitz and Stegun, 1964) that are only calculated for a finite number of terms required to approximate each function:

$$\mathrm{Ber}_{\nu}(x) = \left(\frac{1}{2}x\right)^{\nu} \sum_{k=0}^{N} \frac{\cos\left(\pi\left(\frac{3}{4}\nu + \frac{1}{2}k\right)\right)}{k!\Gamma\left(\nu + k + 1\right)} \left(\frac{1}{2}x^{2}\right)^{k} \tag{3.14}$$

$$\mathrm{Bei}_{\nu}(x) = \left(\frac{1}{2}x\right)^{\nu} \sum_{k=0}^{N} \frac{\sin\left(\pi\left(\frac{3}{4}\nu + \frac{1}{2}k\right)\right)}{k!\Gamma\left(\nu + k + 1\right)} \left(\frac{1}{2}x^{2}\right)^{k} \tag{3.15}$$

In the above Equations (3.14) and (3.15), $\nu = 0$ for $\mathrm{Ber}(x)$ and $\mathrm{Bei}(x)$, $N \in \mathbb{N} \setminus \{0\}$ is the number of terms for the series expansion, and $x \in \mathbb{R}$ is a real-valued argument. The derivatives of the Kelvin functions are given by the reflection formulae (Spanier and Oldham, 1987):

$$\frac{\partial \mathrm{Ber}_{\nu}(x)}{\partial x} = \frac{1}{\sqrt{8}}\left[\mathrm{Ber}_{\nu+1}(x) + \mathrm{Bei}_{\nu+1}(x) - \mathrm{Ber}_{\nu-1}(x) - \mathrm{Bei}_{\nu-1}(x)\right] \tag{3.16}$$

$$\frac{\partial \mathrm{Bei}_{\nu}(x)}{\partial x} = \frac{1}{\sqrt{8}}\left[\mathrm{Bei}_{\nu+1}(x) + \mathrm{Ber}_{\nu+1}(x) - \mathrm{Bei}_{\nu-1}(x) - \mathrm{Ber}_{\nu-1}(x)\right] \tag{3.17}$$

3.2.2. Multiphase Modifications

The Biot-Stoll equations do not completely describe an acoustic model of snow. Naturally-occurring snow is a multiphase porous medium comprised of a frame filled with a mixture of air as a gas and water as a fluid (Colbeck, 1997). This is a "mixture theory" approach that has been used in models of snowpack evolution. The snowpack is considered as being comprised of a fraction of these three constituents (Morland et al., 1990; Morris and Kelly, 1990).

From the definitions given in Section 1.2 of this thesis, the volume fraction of air ε_a, the volume fraction of water ε_w and the effective fluid density ρ_f in the pore spaces of the snow medium can be calculated using the following derivation:

$$\phi = \frac{V_a + V_w}{V_T}$$

$$\varepsilon_a + \varepsilon_w = 1$$

$$\varepsilon_a = \frac{V_a}{V_a + V_w}$$

$$\frac{1}{\varepsilon_a} = 1 + \frac{V_w}{V_a}$$

$$\varepsilon_a = \frac{1}{1 + \frac{\theta_w}{\theta_a}} \tag{3.18}$$

$$\varepsilon_w = \frac{V_w}{V_a + V_w} = S_w$$

$$\frac{1}{\varepsilon_w} = 1 + \frac{V_a}{V_w}$$

$$\varepsilon_w = \frac{1}{1 + \frac{\theta_a}{\theta_w}} \tag{3.19}$$

$$\rho_f = \varepsilon_a \rho_a + \varepsilon_w \rho_w \tag{3.20}$$

3.2.3. Percolation Theory (PT) Model

Percolation theory (Grimmett, 1999) is used to relate the shear modulus and bulk modulus to the porosity of snow. Percolation theory provides a macroscopic model of

connectivity in a porous medium that is mathematically rigorous. Based on the work of Phani and Niyogi (1987), the Young's modulus E and shear modulus G of a porous material was related to porosity by Kováčik (2001), who proposed Equations (3.21) and (3.22).

$$E = E_0 \left(\frac{\phi_c - \phi}{\phi_c} \right)^{f_c} \tag{3.21}$$

$$G = G_0 \left(\frac{\phi_c - \phi}{\phi_c} \right)^{f_c} \tag{3.22}$$

In the above, E_0 is the Young's modulus of the solid material comprising the porous frame, G_0 is the shear modulus of the solid material comprising the porous frame, ϕ is the porosity of the medium, ϕ_c is a critical porosity at which $E \approx 0$ Pa and $G \approx 0$ Pa, and f_c is the percolation theory exponent. Equations (3.21) and (3.22) imply that if $\phi \le \phi_c$, then $E = 0$ Pa and $G = 0$ Pa. Kováčik and Emmer (2013) later related the speed of shear waves in the porous media frame to the porosity using Equation (3.22).

In the context of the UTAM model for snow, E_0 is the Young's modulus of the snow particles, the corresponding shear modulus for the snow particles is G_0, the shear modulus of the porous snow medium is G, and ϕ is the porosity representing the volume fraction of air in the snowpack. Following Kováčik (2001), in lieu of any additional information on the percolation theory exponent f_c for snow, $f_c = 2.1$ for the UTAM model. This is the theoretical value of f_c that is assumed to be the same for all continuous porous media (Sahimi, 1994). The value is applicable because snow is a porous medium that has continuous pore spaces (Buser and Good, 1986). In addition, as proposed by Kováčik (2001), f_c is the same exponent used to calculate the Young's modulus and the shear modulus of the porous material.

The Young's modulus and shear modulus for ice are calculated using formulae developed by investigators who have measured the speed of shear wave propagation in ice and related this measurement to the density of the ice at different temperatures. This provides an empirical equation for determining $\{E_0, G_0\}$ as a function of temperature T (Celcius). The equation has to

be empirical due to the lack of available theory relating inter-molecular forces to macroscopic measurements of $\{E_0, G_0\}$ (Magnanimo et al., 2008).

Ashton (1986) reviews Young's modulus measurements made on ice samples without bubbles, ice samples collected from freshwater locations, and ice samples taken from an ice shelf. Godbout et al. (2000) provide a similar review, also adding an equation developed from measurements on ice extracted from snow. Due to the small number of measurements used to develop these equations and since the shear modulus G_0 must be calculated as well, other formulae were used to compute parameters $\{E_0, G_0\}$.

The elastic constants of ice have been measured by a number of investigators (Hobbs, 1974). Arguably the most complete dataset was the one collected by Dantl (1968), who determined elastic moduli over the range of $-140°\text{C} \le \text{T} \le 0°\text{C}$ (Petrenko and Whitworth, 2002). Gammon et al. (1983) note that the elastic moduli data of Dantl (1968) are 5% lower than the elastic moduli data collected by other investigators. Although Dantl (1968) explains this discrepancy as occurring due to the use of ice crystals grown in a water bath and then aged for eight months before acoustic measurements were made, Gammon et al. (1983) disagree with this claim, postulating that experimental discrepancies may be associated with ice impurities or systematic laboratory error.

Gammon et al. (1983) measured the elastic moduli of ice using Brillouin spectroscopy, but their measurements were only made at -16 °C. Although Petrenko and Whitworth (2002) state that the Gammon et al. (1983) measurements supersede the measurements made by Dantl (1968), empirical formulae published by Dantl (1968) are used for the UTAM since they provide a way to calculate the temperature dependence of elastic moduli.

Assuming that the ice is an isotropic medium, the coefficients $\{S_{11}, S_{12}\}$ are given by Dantl (1968), and the equations for the Young's modulus and shear modulus of ice (E_i and G_i) are given by Petrenko and Whitworth (2002), with the temperature T in units of Celsius:

$$S_{11} = 10.40\left(1 + \left(1.070 \times 10^{-3}\right)T + \left(1.87 \times 10^{-6}\right)T^2\right) \tag{3.23}$$

$$S_{12} = -4.42\left(1 + \left(0.463 \times 10^{-3}\right)T - \left(2.06 \times 10^{-6}\right)T^2\right) \tag{3.24}$$

$$E_i = \frac{1}{S_{11}} \tag{3.25}$$

$$G_i = \frac{1}{2\left(S_{11} - S_{12}\right)} \tag{3.26}$$

The bulk modulus of the ice K_i is computed from $\{S_{11}, S_{12}\}$ by (Petrenko and Whitworth, 2002):

$$K_i = \frac{1}{3\left(S_{11} + 2S_{12}\right)} \tag{3.27}$$

To calculate the elastic constants of the snow particles from the elastic constants of ice, Equations (3.25) to (3.27) are scaled using coefficients $\{\psi_E, \psi_G\}$:

$$E_0 = E_i / \psi_E \tag{3.28}$$

$$G_0 = G_i / \psi_G \tag{3.29}$$

The scaling coefficients model the differences between the elastic constants of ice and the elastic constants of the snow particles. Due to a lack of reported measurements on the Young's modulus and the shear modulus of individual snow particles, the scaling coefficients cannot be directly measured and must be found using an optimization procedure described in Section 3.4.5 below.

3.2.4. Consolidation Theory (CT) Model

For application of percolation theory, the critical porosity ϕ_c is calculated using a model referred to in this thesis as a "consolidation theory." This theory predicts when the Young's modulus and shear modulus of snow will be effectively zero, such that $E \approx 0$ Pa and $G \approx 0$ Pa.

By definition, the Young's modulus E of a material is the ratio of tensile stress σ_{stress} to tensile strain σ_{strain} and the shear modulus G is the ratio of shear stress γ_{stress} to shear strain γ_{strain}, as shown by Equations (2.3) and (2.4) below.

$$E = \frac{\sigma_{\text{stress}}}{\sigma_{\text{strain}}} \tag{3.30}$$

$$G = \frac{\gamma_{\text{stress}}}{\gamma_{\text{strain}}} \tag{3.31}$$

The tensile stress σ_{stress} is the force exerted over an initial cross-sectional area, and the tensile strain σ_{strain} is the fractional change in length of the medium resulting from the applied force. Qualitatively, the Young's modulus E is a measure of how easily a material can be stretched or compressed. As $\sigma_{\text{strain}} \to \infty$, $E \to 0\,\text{Pa}$. The material can be more easily stretched or compressed for a lower value of E as compared to higher values of E.

The shear stress γ_{stress} is the force exerted over a cross-sectional area of the material, and γ_{strain} is the fractional lateral displacement of the medium resulting from the applied force. The shear modulus can be considered as a measure how easily a material can be deformed by a shearing force. In a similar fashion to the Young's modulus, as $\gamma_{\text{strain}} \to \infty$, $G \to 0\,\text{Pa}$. For materials where $G \to 0\,\text{Pa}$, a shearing force can more easily deform the material.

In lieu of measuring snow particle morphology using photogrammetry and visual inspection (Jamieson and Schweizer, 2000; Perla, 1985, 1982), snow particles comprising the snowpack are approximated as spheres in the context of consolidation theory (Figure 3.1).

The spheres shown in Figure 3.1 are assumed to have an effective radius, and are joined by an inter-particle contact referred to as a "neck" (Brown, 1980) created due to sintering, compaction and metamorphism (Colbeck, 1982a,b). In a similar fashion to Figure 9.2.4 of Bear (1972) and Colbeck (1982), water occupies the neck space between the two snow particles. The effective radius of this water bridge is R. When a P-wave travels through the pore spaces of the snowpack over a control volume of the UTAM, the snow particles are assumed to be in static equilibrium, and are not changing in shape or moving due to mechanical compression or metamorphism. Although compression and metamorphism causes changes in snow particle geometry, radii, volume, and density, the time scale of these processes are on the order of minutes to hours, whereas the time of P-wave propagation through the snowpack is on the order of seconds.

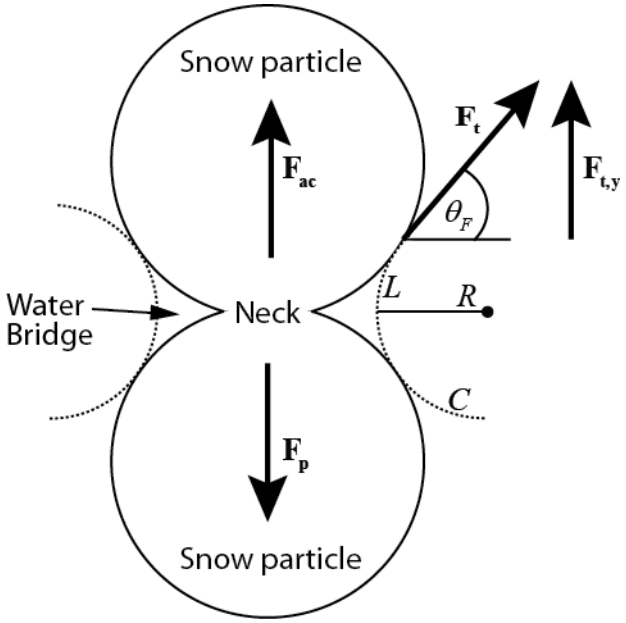

Figure 3.1. Diagram of two snow particles used for the CT model. The two particles are joined by a neck created due to sintering, compaction and metamorphism. A water bridge with radius R is situated outside of the neck. The distance L over which the surface tension force acts is the arc length of the water bridge circle with radius R. Curve C is part of the water bridge circle. The surface tension force vector is $\mathbf{F_t}$, the surface tension force vector acting in the vertical direction is $\mathbf{F_{t,y}}$, the angle over which the surface tension force acts is θ_F, the adhesive and cohesive force vector is $\mathbf{F_{ac}}$, and $\mathbf{F_p}$ is the downward-acting force of the snow particles and the water.

Treating the particles as a physical system, a statics problem is written to predict when $E \approx 0$ Pa and $G \approx 0$ Pa. In a similar fashion to Colbeck and Parssinen (1978), the statics problem resolves the forces acting on a single snow particle joined by a neck to another snow particle. The forces exerted on the sides and top of the snow particle pair by other snow particles are assumed to cancel.

The shear modulus $G \to 0$ Pa when the medium is a fluid (Adam et al., 2006). This also occurs when $E \to 0$ Pa. For a snow particle shown in Figure 3.1 to undergo this transformation, the net sum of the inter-particle forces acting on the snow particle pair must be non-zero and consequently the snowpack medium becomes "unconsolidated" and acts as an effective fluid. This physical process is similar in principle to loose snow avalanches caused by cohesionless snow that is either dry and unsintered or wet (Perla, 1981).

In the proposed consolidation theory, four different forces are assumed to act on a snow particle shown in Figure 3.1. In the coordinate system shown, the magnitude of all forces acting in the upward direction is positive, whereas all forces acting in the downward direction have negative magnitude.

(1) The surface tension force of the water acts at the air-water interface (Potter, 2002). The forces between molecules in the water are equal in all directions and thereby cancel, but the surface tension force acts toward the air medium tangent to the snow particle. Let $\mathbf{F_t}$ be the surface tension force vector, and σ_s be the surface tension coefficient for water. The force $\mathbf{F_t}$ acts over a distance L at an angle θ_F measured normal to the interface of the water in contact with the air. Let C be the curve over which the $\mathbf{F_t}$ force acts. The magnitude of the force $\mathbf{F_t}$ acting in the vertical direction is written as:

$$\left|\mathbf{F_{t,y}}\right| = L\sigma_s \cdot \int_C \frac{d\mathbf{F_{t,x}}}{d\ell} d\ell = 2L\sigma_s \sin\left(\theta_F\right) \tag{3.32}$$

In the above Equation (3.32), the dot signifies the dot product, and the integral represents an integration over the curve C.

For consolidation theory, the angle θ_F over which the surface tension force acts is related to the water content θ_w by the following Equation (3.33). This equation assumes that as θ_w increases, the surface tension force angle $\theta_F \to (\pi/2)$ rad, as the water completely fills the neck space between the two particles.

$$\theta_F = \frac{\theta_w \pi}{2} \tag{3.33}$$

Combining Equations (3.33) and (3.32) results in Equation (3.34) for the surface tension force as a function of water content θ_w.

$$\left|\mathbf{F_{t,x}}\right| = 2L\sigma_s \sin\left(\frac{\theta_w \pi}{2}\right) \tag{3.34}$$

Using geometry, the distance L over which the surface tension force acts is the arc length $L = \theta_F R$ of the circle with radius R at the air-water interface. Substituting this expression into Equation (3.34) yields Equation (3.35).

$$\left|\mathbf{F_{t,x}}\right| = 2\theta_F R\sigma_s \sin\left(\frac{\theta_w \pi}{2}\right) \tag{3.35}$$

The surface tension force coefficient σ_s as a function of temperature T_k (Kelvin) was computed using the empirical interpolating Equation (3.36) given by Vargaftik et al. (1983), developed from measurements made on water at temperatures $0°\text{C} \le T \le 185\ °\text{C}$.

$$\sigma_s = B\left[\frac{T_k - T}{T_c}\right]^a \left[1 + b\left(\frac{T_k - T}{T_c}\right)\right] \tag{3.36}$$

In the above Equation (3.36), $B = 235.8 \times 10^{-3}$ N m^{-1}, $b = -0.625$, $a = 1.256$, and $T_c = 647.15$ K as a reference temperature. For free water in the snowpack, $T = 0\ °\text{C}$ and $T_k = 273.15$ K, so $\sigma_s = 7.57 \times 10^{-2}$ N m^{-1}.

(2) The adhesive force between the water and a snow particle and the cohesive force between snow particles occurs due to differences in surface energy and molecular attraction. These two forces are modelled using a version of the Young-Dupre equation that calculates the work required to keep the two surfaces together. A similar approach was used by Meuler et al. (2010) to model ice accretion on surfaces. The magnitude of the force $\mathbf{F_{ac}}$ holding the particles together is given by Equation (3.37) derived in this thesis from an equation modelling surface tension between two surfaces (Tas et al., 1996). The force is assumed to be positive, and acting in an upward direction.

$$\left|\mathbf{F_{ac}}\right| = 2L\left(\sigma_{iw} + \sigma_{wa}\left(1 - \cos\left(\theta_c\right)\right)\right) = 2\theta_F R\left(\sigma_{iw} + \sigma_{wa}\left(1 - \cos\left(\frac{S_w \pi}{2}\right)\right)\right) \tag{3.37}$$

In the above Equation (3.37), the contact angle θ_c is taken to be the same as the surface tension angle $\theta_c = \theta_F$, the surface tension between the snow particle and the water is σ_{iw}, the surface tension between the water and the air is σ_{wa} and all other variables are as previously defined.

Measurements of σ_{iw} and σ_{wa} have been reported by Van Oss et al. (1992) for water at $T = 0$ °C, and are given below as Equation (3.38) and (3.39).

$$\sigma_{\mathrm{iw}} = 4.0 \times 10^{-4} \ \mathrm{N\ m^{-1}} \tag{3.38}$$

$$\sigma_{\mathrm{wa}} = 7.58 \times 10^{-2} \ \mathrm{N\ m^{-1}} \tag{3.39}$$

(3) The net force resulting from the weight of the snow particles and the water in the snowpack is calculated by Equation (3.40) for the porosity ϕ expressed as a function of the snow density ρ_s and the ice density ρ_i comprising the particles. The specific weight of the water is given by Equation (3.41), with ρ_w as the water density.

$$\phi = 1 - \frac{\rho_s}{\rho_i} \tag{3.40}$$

$$\gamma_w = \theta_w \rho_w g \tag{3.41}$$

The density of ice ρ_i as a function of temperature T is calculated using empirical equations given by Fukusako (1990), developed from ice density measurements made using X-ray diffraction:

$$\rho_i = 917\left(1 - 1.17 \times 10^{-4} T\right)\left(\mathrm{kg\ m^{-3}}\right), \qquad \text{-140°C} \le \mathrm{T} \le \text{0°C} \tag{3.42}$$

$$\rho_i = 930\left(1 - 1.54 \times 10^{-5} T\right)\left(\mathrm{kg\ m^{-3}}\right), \qquad \text{-260°C} \le \mathrm{T} < -140\text{°C} \tag{3.43}$$

Re-arranging Equation (3.40), adding Equation (3.41), multiplying by the gravitational acceleration $g = 9.81\ \mathrm{m\ s^{-2}}$ and dividing by the total volume V_T gives Equation (3.44) below as the specific weight of the snow particles and the water in the pore space of the snow medium. Equation (3.44) is the magnitude of the downward acting force $\left|\mathbf{F_p}\right|$ of the snow particles per volume V_T:

$$\frac{\left|\mathbf{F_p}\right|}{V_T} = g\left(\phi \rho_i + \theta_w \rho_w\right) \tag{3.44}$$

Summing the forces acting in Figure 3.1 and assuming that the net force is zero gives the following Equation (3.45) from Equations (3.35), (3.37) and (3.44).

$$\sum \mathbf{F} = \left|\mathbf{F_{t,y}}\right| + \left|\mathbf{F_{ac}}\right| - \left|\mathbf{F_p}\right| = 0$$

$$\sum \mathbf{F} = \theta_w \pi R\left[\sigma_s \sin\left(\frac{\theta_w \pi}{2}\right) + \left(\sigma_{iw} + \sigma_{wa}\left(1 - \cos\left(\frac{\theta_w \pi}{2}\right)\right)\right)\right] - \left|\mathbf{F_p}\right| = 0 \tag{3.45}$$

Dividing (3.45) by V_T, re-arranging, and substituting in Equation (3.44) gives Equation (3.46).

$$\frac{\theta_w \pi R}{V_T}\left[\sigma_s \sin\left(\frac{\theta_w \pi}{2}\right) + \left(\sigma_{iw} + \sigma_{wa}\left(1 - \cos\left(\frac{\theta_w \pi}{2}\right)\right)\right)\right] - g\left(\phi\rho_i + \theta_w \rho_w\right) = 0 \tag{3.46}$$

Equation (3.46) can be re-written as Equation (3.47):

$$\frac{V_w \pi R}{V_T^2}\left[\sigma_s \sin\left(\frac{\theta_w \pi}{2}\right) + \left(\sigma_{iw} + \sigma_{wa}\left(1 - \cos\left(\frac{\theta_w \pi}{2}\right)\right)\right)\right] - g\left(\phi\rho_i + \theta_w \rho_w\right) = 0 \tag{3.47}$$

By multiplying both sides of Equation (3.47) by Equation (3.48), the force-balancing equation becomes Equation (3.49).

$$\frac{1}{\theta_w \theta_a} = \frac{V_T^2}{V_w V_a} \tag{3.48}$$

$$\frac{\pi R}{V_a}\left[\sigma_s \sin\left(\frac{S_w \pi}{2}\right) + \left(\sigma_{iw} + \sigma_{wa}\left(1 - \cos\left(\frac{S_w \pi}{2}\right)\right)\right)\right] - \frac{g}{\theta_w \theta_a}\left(\phi\rho_i + \theta_w \rho_w\right) = 0 \tag{3.49}$$

Assuming that the volume of the air V_a is the volume of a sphere, substituting an alternate expression for θ_a and taking $\phi = \phi_c$:

$$V_a = \frac{4\pi R^3}{3}$$

$$\phi = \frac{V_w + V_a}{V_T} = \theta_w + \theta_a$$

$$\theta_a = \phi - \theta_w$$

$$\frac{3}{4R^2}\left[\sigma_s \sin\left(\frac{S_w\pi}{2}\right)+\left(\sigma_{iw}+\sigma_{wa}\left(1-\cos\left(\frac{S_w\pi}{2}\right)\right)\right)\right]-\frac{g}{\theta_w\left(\phi_c-\theta_w\right)}\left(\phi_c\rho_i+\theta_w\rho_w\right)\cong 0 \quad (3.50)$$

The two unknowns $\{R,\phi_c\}$ are found by taking values such that the RHS of Equation (3.50) is equal (or approximately equal) to zero using optimization techniques.

3.2.5. Mechanical Parameters

Assuming that E and G are the mean values over a control volume of the UTAM, the bulk modulus K_b of snow is calculated using Equation (2.5).

$$K_b = \frac{EG}{3(3G-E)} \quad (3.51)$$

The density of water ρ_w used in the consolidation theory calculations in the previous section and in the mixture theory approach below is computed using an empirical expression developed by Tanaka et al. (2001) for water in the temperature range $0°\text{C} \le \text{T} \le 40°\text{C}$. Because naturally-occurring surface water found in rivers and snow contains dissolved oxygen, a correction factor can be added. Moreover, another equation is also used to correct for small changes in density due to compressibility of water at an atmospheric pressure P. Combining these three equations from Tanaka et al. (2001) yields the following Equation (3.52).

$$\rho_w = \left[1+\left(k_0+k_1T+k_2T^2\right)\left(P-101325\text{ Pa}\right)\right]\left[a_5\left[1-\frac{(T+a_1)^2(T+a_2)}{a_3(T+a_4)}\right]+\left[s_0+s_1T\right]\right] \quad (3.52)$$

In the above, $\{k_k, a_k, s_k\}$ with $k \in \mathbb{Z}$ are constants given by Tanaka et al. (2001), the temperature is T (Celcius) and the atmospheric pressure is P. The constants are chosen to ensure that Equation (3.52) is dimensionally correct. For free water in the snowpack $T = 0°\text{C}$.

The density of the fluid ρ_f in the pore spaces of the medium is calculated using a mixture theory approach using Equations (3.18) to (3.20).

To calculate the density of air ρ_a in the pore spaces of the medium, the air is assumed to be an ideal gas. Although water vapour and the mole fraction of gases in air will influence ρ_a, the ideal gas assumption is applied in the UTAM model since it is useful in the absence of any other information. Given the air pressure P and the temperature T (Kelvin), the ideal gas law equation is:

$$\rho_a = \frac{P}{R_g T} \tag{3.53}$$

In Equation (3.53), the ideal gas constant is $R_g = 287.058 \text{ J kg}^{-1} \text{ K}^{-1}$.

Using the same mixture theory approach, the effective density ρ of the entire snowpack medium is calculated:

$$\rho = \rho_s = \rho_a \theta_a + \rho_w \theta_w + \rho_i \theta_i \tag{3.54}$$

$$\phi = \theta_w + \theta_i \tag{3.55}$$

$$\theta_a = 1 - \theta_w - \theta_i \tag{3.56}$$

Taking the bulk modulus of air K_a as the mean value in the pore spaces of the control volume and using the same ideal gas assumption as given above:

$$K_a = \chi_g P \tag{3.57}$$

In the above Equation (3.57), $\chi_g = 1.402$ as a dimensionless constant and P is the air pressure. Once again using the mixture theory approach and assuming that the bulk modulus of the mixture is related in a similar fashion to parallel resistors (Rau and Chaney, 1988), the effective bulk modulus of the pore space fluid is given by:

$$\frac{1}{K_f} = \frac{1}{\varepsilon_a} \frac{1}{K_a} + \frac{1}{K_w} \tag{3.58}$$

In the above Equation (3.58), K_w is the bulk modulus of water, and all other parameters are as previously defined.

The bulk modulus of water K_w is calculated from the Newton-Laplace equation (Raichel, 2006) that is used in acoustics to determine the speed of sound c_w in water given the water density ρ_w. Re-arranging the equation to calculate the bulk modulus of water:

$$K_w = c_w^2 \rho_w \tag{3.59}$$

For water temperatures in the range $0°\text{C} \le \text{T} \le 100°\text{C}$, the speed of sound in water is calculated using the empirical equation (Bilaniuk and Wong, 1996, 1993):

$$c_w = \sum_{k=0}^{5} \varphi_k T^k \tag{3.60}$$

In Equation (3.60), $k \in \mathbb{Z}$, $0 \le k \le 5$, the temperature is T (Celcius), and φ_k is a coefficient given in Table I, Part 2 of Bilaniuk and Wong (1993, 1996). For water in the snowpack, $T \approx 0°\text{C}$ and so $c_w = 1402.39 \text{ m s}^{-1}$. Then the bulk modulus of water K_w is computed using Equation (3.52) and (3.59).

The viscosity η of the pore space fluid is used to compute the correction factor $F(\kappa)$ given by Equation (3.13). Once again using the mixture theory approach:

$$\eta = \varepsilon_a \eta_a + \varepsilon_w \eta_w \tag{3.61}$$

In Equation (3.61), the viscosity of the air is η_a and the viscosity of the water is η_w.

The viscosity of air η_a is computed using the Sutherland formula as a function of temperature (Anderson, 1991). Assuming that the air is an ideal gas, the Sutherland formula predicts that for air at a temperature T (Kelvin):

$$\eta_a = \eta_0 \left(\frac{T}{T_0} \right)^{\frac{3}{2}} \left(\frac{T_0 + C_c}{T + C_c} \right) \tag{3.62}$$

In Equation (3.62), the constants for air are taken as $\eta_0 = 1.7894 \times 10^{-5}$ Pa s, $T_0 = 288.16$ K, and $C_c = 110$ K.

The viscosity of water η_w is calculated using an empirical equation derived from the paper of Huber et al. (2009). An assumption is made that the temperature T of the water is much lower than the temperature at which water as a substance enters the critical region where it ceases to exist as a liquid or a gas, and that $T < 900$°C and $P < 1$ GPa. Then, the viscosity is calculated as:

$$\eta_w = \frac{100\left(\hat{T}\right)^{1/2}}{\sum_{i=0}^{3} \frac{L_i}{\hat{T}^i}} + \exp\left[\hat{\rho} \sum_{i=0}^{5} \left(\frac{1}{\hat{T}} - 1 \right)^i \sum_{j=0}^{6} H_{ij} \left(\hat{\rho} - 1 \right)^j \right] \tag{3.63}$$

$$\hat{T} = T / 647.096 \text{ K}$$

$$\hat{\rho} = \rho_w / 322.0 \text{ kg m}^{-3}$$

In Equation (3.63), the $\hat{T}$ and $\hat{\rho}$ are the normalized temperature and water density, L_i and H_{ij} are dimensionless coefficients given by Huber et al. (2009).

To compensate for viscoelastic losses in the porous medium, the shear modulus μ is taken as a complex value, defined by Albert (1993) as:

$$\mu = G\left(1 + i\delta\right) \tag{3.64}$$

In Equation (3.64), the real-valued shear modulus is G, a complex number is represented by $i = \sqrt{-1}$, and δ is the dimensionless loss tangent that models the dissipation of acoustic waves in the porous medium (Stoll, 1989).

For application of the UTAM, the tortuosity α of the snowpack was estimated using the theory of Berryman (1980). To validate Biot's theory, Berryman (1980) derived a relationship between the tortuosity α and porosity ϕ of a porous medium using a theoretical dimensionless shape factor γ_s. Starting from the Biot constitutive equations, Berryman (1980) showed:

$$\alpha = 1 - \gamma_s \left(1 - 1/\phi\right) \tag{3.65}$$

Considering the particles comprising the porous medium as spheres, $\gamma_s = 1/2$, whereas if the particles are randomly-oriented needles, $\gamma_s = 2/3$ (Berryman, 1983).

3.3. High Frequency Approximation (HFA) Model

A simplified model for calculating the porosity ϕ and snow density ρ_s of the snowpack medium is proposed in this section. The model uses a high-frequency approximation (HFA) for the speed of the slow P-wave. The HFA model is coupled with the UTAM model. For this purpose, the HFA model is referred to as a "primer" model in analogy to priming an engine before use.

Similar to other acoustic models applied to snow (Albert, 2001; Attenborough and Buser, 1988; Marco et al., 1998, 1996), the porous frame is assumed to be rigid. This implies that compressibility of air in the pore spaces of the snowpack is orders of magnitude greater than compressibility of the frame. Given this assumption, the speed of the P-wave c_{sh} in the porous medium is approximately constant above an angular frequency $\tilde{\omega}$, and does not show large changes with an increase in frequency (Le et al., 2010). In a series of papers, it was shown that (Johnson and Plona, 1980; Johnson et al., 1982):

$$c_{sh} = \frac{c_0}{\alpha^{1/2}}, \quad \text{for } \omega > \tilde{\omega} = \frac{2\eta_a}{\rho_a a_p^2} \tag{3.66}$$

In Equation (3.66), $\tilde{\omega}$ is the theoretical angular frequency above which the expression is valid, (referred to as a cutoff frequency), c_0 is the speed of sound in air, a_p is the mean diameter of pore spaces in the snowpack, and all other parameters are as previously defined. Equation (3.66) has been experimentally validated by Allard et al. (1994), Allard and Atalla (2009) and Le et al. (2010).

Assuming that air in the pore spaces of the snowpack is an ideal gas, the speed of sound in air is related to the air temperature T_a (Kelvin) by (Raichel, 2006):

$$c_0 = \left(\chi_g R_g T_a\right)^{1/2} \tag{3.67}$$

In Equation (2.2), the dimensionless ratio of the specific heats for air is $\chi_g = 1.402$ and the ideal gas constant for air is R_g as defined in the previous section.

Combining Equations (3.65), (3.66) and (2.2) gives Equation (3.68). Assuming that χ_g is as defined in the previous section and that the speed of sound c_{sh} in the snowpack is known above a highpass frequency $\tilde{\omega}$, the snow density and porosity $\{\rho_s, \phi\}$ are determined from Equation (3.68) and (3.69). The density of ice ρ_i is calculated using Equations (3.42) and (3.43) above.

$$\phi = \frac{c_{sh}\gamma_s}{c_{sh}^2(\gamma_s - 1) + \chi_g R_g T_a} \tag{3.68}$$

$$\phi = 1 - \frac{\rho_s}{\rho_i} \tag{3.69}$$

Assume that the snowpack is an effective medium and the air in the pore spaces of the snow is in thermal equilibrium with the snow particles comprising the porous frame. This assumption is also used when measuring the temperature of the snowpack using thermocouples. Then, to couple the HFA model with the UTAM model, Equation (3.68) is re-arranged with $T_a = T$, and Equation (3.70) is then used to calculate the temperature T_k for the UTAM model.

$$T = \frac{c_{sh}^2}{\chi_g R_g}\left(1 - \gamma_s\left(1 - \frac{1}{\phi}\right)\right) \tag{3.70}$$

3.4. Application of Forward and Inverse Models

The five models (PT, CT, HFA and UTAM) can be considered as forward models. A forward model is a set of mathematical equations that provide model outputs, given known model input parameters. The forward model is well-posed, indicating that model outputs are unique for fixed inputs. Alternately, an inverse model is a reconstructed approximation of the forward model inputs, given only the forward model outputs. The inverse model is ill-posed, indicating that further assumptions are required to reconstruct the forward model inputs.

The following sections show how the forward and inverse models are calculated using numerical methods and also present a sensitivity analysis of model parameters. The

programming language used for model calculations was C++, with plots created in Matlab. The sensitivity analysis being used is the one-at-a-time (OAT) design, with a baseline parameter held constant while the other parameters are varied (Saltelli et al., 2009).

3.4.1. PT Model

The effective input parameters for the percolation theory (PT) model are the porosity of snow ϕ, the water content θ_w, the temperature T, and the scaling coefficients $\{\psi_E, \psi_G\}$ used to calculate the elastic constants of snow particles from the elastic constants of ice. The outputs of this model are the Young's modulus and the shear modulus of the porous snow medium $\{E, G\}$. A sensitivity analysis uses the following parameter ranges:

- The porosity of snow ranges between $0.35 \le \phi \le 0.91$. This corresponds to snow densities between $80 \text{ kg m}^{-3} \le \rho \le 600 \text{ kg m}^{-3}$ and is inclusive of the density range observed for fresh snow, shallow prairie snowcovers and deep mountain snowpacks (Pomeroy and Gray, 1995). The baseline porosity is $\phi = 0.67$ corresponding to an average snow density of 300 kg m^{-3}.

- The water content of snow ranges between $0.01 \le \theta_w \le 0.25$. This range includes the volume fraction of irreducible water held in the pore spaces of the snowpack and the volume fraction of a fully saturated wet snowpack. The baseline parameter value for the water content of snow is 0.05 for 5% water content.

- $-40\ ^\circ\text{C} \le T \le 0\ ^\circ\text{C}$ for the temperature range. The lowest temperature is coincident with the minimum operating temperature of the electronics used for acoustic sensing of snow in this thesis, and the highest temperature is set at the melting point of snow. The baseline temperature is -20 °C. This temperature range also includes the range of snow temperature observations reported in this thesis.

- $1.0 \times 10^{-3} \le \psi_E \le 2.0$ and $1.0 \times 10^{-3} \le \psi_G \le 2.0$ for the scaling coefficient range. This range produces physically-reasonable outputs. The baseline parameters are $\psi_E = 2.0$ and $\psi_G = 2.0$.

As shown by Figure 3.2 and Figure 3.3, the PT model predicts that the porosity ϕ is the most sensitive parameter for calculations of the Young's modulus E and shear modulus G.

Both $\{E,G\}$ exhibit an approximately hyperbolic decrease with an increase in porosity. Because an increase in porosity is associated with a decrease in snow density, the model predicts that the Young's modulus and shear modulus parameters are of greater magnitude for more dense snow. For the Young's Modulus E, this behavior is supported by measurements reported by Mellor (1974) and Keeler (1969). The measurements conducted by Perla et al. (1982) also show a similar increase in a shear strength index with an increase in density. The predictions given by the PT model are of similar order of magnitude as the Young's modulus and shear modulus values given by Albert (1993a).

The water content parameter θ_w is not as sensitive as porosity (Figure 3.2 and Figure 3.3), exhibiting a gradual reduction in $\{E,G\}$ with an increase in θ_w. However, when $\theta_w > 0.10$, both $\{E,G\}$ exhibit drops in magnitude. This indicates a lack of cohesion between snow particles for wet snow. The lack of cohesion is most apparent for $\theta_w > 0.15$, corresponding with the 15% "soaked" snow in the Fierz et al. (1999) classification.

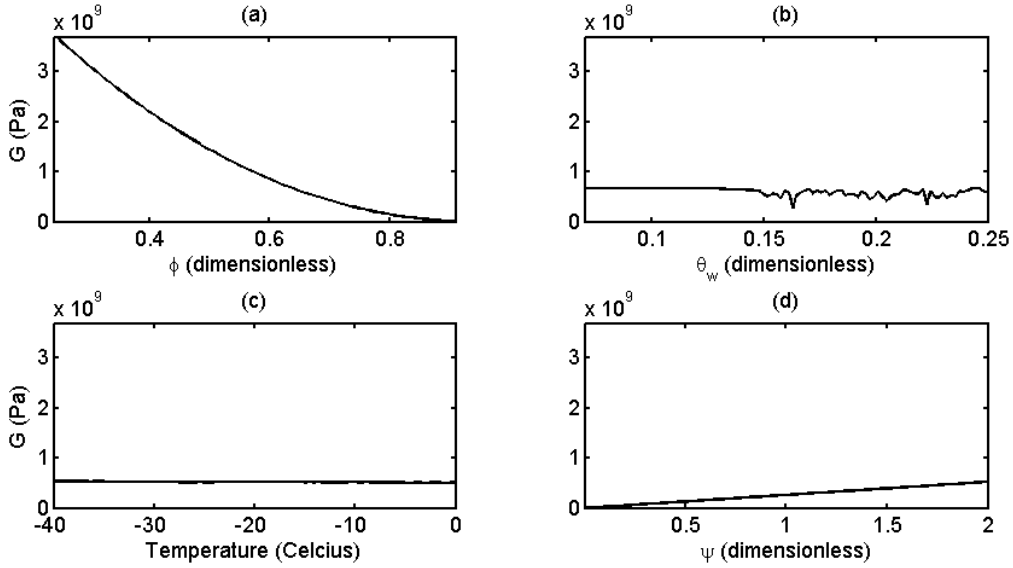

Figure 3.2. Sensitivity analysis for the Young's modulus E calculated using the PT model. The porosity ϕ, water content θ_w, temperature T and scaling coefficient Ψ are used in the sensitivity analysis. Figure 3.2b shows drops in magnitude for $\theta_w > 0.10$.

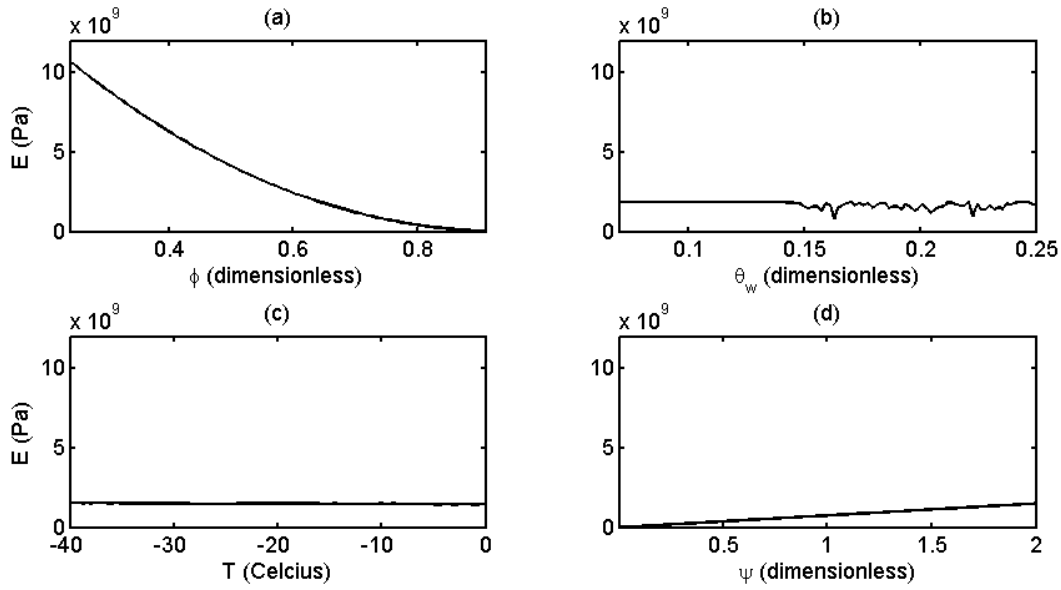

Figure 3.3. Sensitivity analysis for the shear modulus G calculated using the PT model. The porosity ϕ, water content θ_w, temperature T and scaling coefficient Ψ are used in the sensitivity analysis. Figure 3.3b shows drops in magnitude for $\theta_w > 0.10$.

A gradual reduction in $\{E, G\}$ is also exhibited when the temperature increases (Figure 3.2c and Figure 3.3c). However, an increase in temperature does not cause large changes in $\{E, G\}$. For E, this behavior is supported by observations given by Mellor (1974) and for G by Schweizer and Camponovo (2002). The scaling parameters exhibit linear increases over the parameter range (Figure 3.2d and Figure 3.3d) as is expected from Equations (3.28) and (3.29).

3.4.2. CT Model

The inputs for the CT model are the water content θ_w of snow and the temperature T. The parameter ranges are the same as those given for the PT model. The outputs of this model are the two unknowns $\{R, \phi_c\}$ in Equation (3.50) that make the LHS of the equation approximately equal to zero. To determine $\{R, \phi_c\}$, a Nelder-Mead optimizer (Nelder and Mead, 1965) as implemented by the NLopt library[1] was used for the minimization process. C++ bindings were used for interfacing the library with the model code. Box constraints (Box, 1965)

[1] Steven G. Johnson, The NLopt nonlinear-optimization package, http://ab-initio.mit.edu/nlopt

were placed on the outputs $\{R, \phi_c\}$ such that 5×10^{-5} m $\leq$ R $\leq$ 2.5×10^{-3} m and $0.1 \leq \phi_c \leq 1.0$. Because the water radius R cannot be measured, the parameter ranges were chosen to ensure that the CT model gave physically-reasonable outputs when coupled with the other models presented in this thesis. For expository purposes, the ϕ_c parameter was converted to equivalent snow density ρ_c when preparing the sensitivity analysis plots (Figure 3.4).

For water contents $\theta_w < 0.15$, the snow density (Figure 3.4a) corresponding to ϕ_c is less than $\rho_c = 100$ kg m^{-3}. This indicates that only fresh or cohesionless snow of low density that does not correspond to the "soaked" snow in the Fierz et al. (1999) classification will act as an equivalent fluid when $E \to 0$ Pa and $G \to 0$ Pa. However, for water contents $\theta_w \geq 0.2$, the density at which snow acts as an equivalent fluid will approach $\rho_c = 300$ kg m^{-3}. As predicted by the CT model, this is due to an increase in the surface tension force angle θ_F as the water completely surrounds the snow particles. Consequently, the forces keeping the particles together are weakened, decreasing ϕ_c and increasing ρ_c.

The snow density corresponding to ϕ_c remains under $\rho = 100$ kg m^{-3} over the range of T selected for the sensitivity analysis (Figure 3.4b), indicating that ϕ_c is relatively insensitive to temperature. Although a decrease in temperature will strengthen the bonds between snow particles, the presence of liquid water will encourage snow particle growth and decrease cohesion, thereby making θ_w the more sensitive parameter. The insensitibity to temperature indicates that when using the CT model as a part of the UTAM model to compute an inverse solution (Section 3.4.5), the inversion is not sensitive to temperature as well. This decreases the accuracy of the temperature determined from the inverse model.

As shown in Figure 3.4c, the water bridge radius R exhibits a linear increase between 2×10^{-4} m to 8×10^{-4} m with a corresponding increase in θ_w. The R parameter shows almost no sensitivity with temperature (Figure 3.4d). This demonstrates that changes in temperature do not influence the geometry of the water bridge between snow particles. The water bridge can still be present at low temperatures due to the presence of a quasi-liquid layer on the ice of the particles comprising the snowpack.

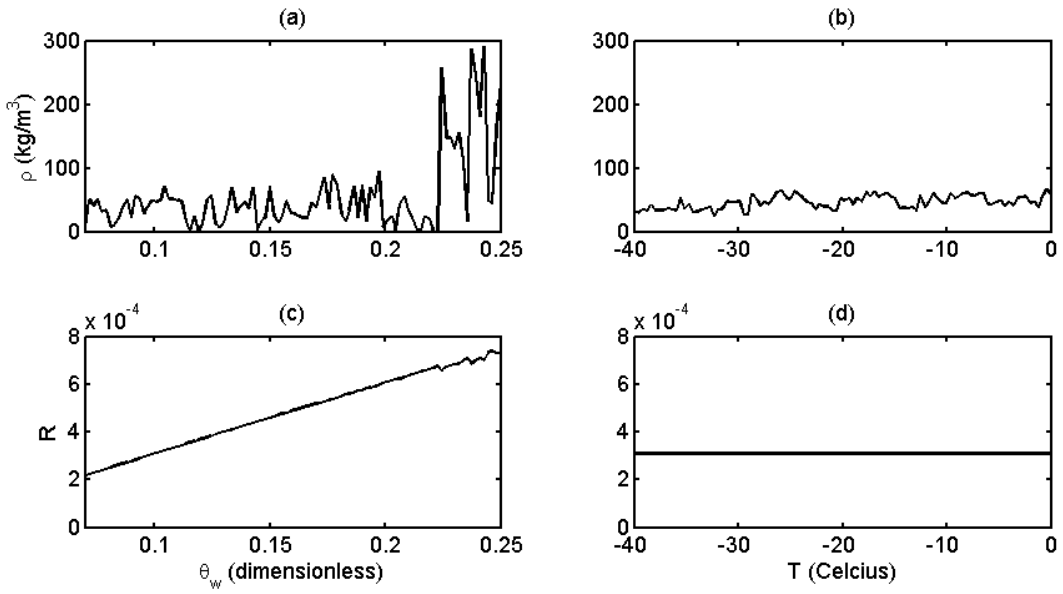

Figure 3.4. Sensitivity analysis for the CT model. The water content θ_w and the temperature T are the two parameters being used in the sensitivity analysis.

3.4.3. HFA Model

The inputs for the HFA model are the speed of sound in snow c_{sh} at a frequency greater than $\tilde{\omega}$, the temperature T and the Berryman shape parameter γ_s. The air pressure P and the mean pore space diameter a_p are used to calculate the cutoff frequency $\tilde{\omega}$. Calculation of $\tilde{\omega}$ is only done for the sensitivity analysis performed in this section, and is not required for application of the HFA model coupled with the UTAM. The outputs of the HFA model are the porosity ϕ and the angular frequency $\tilde{\omega}$ above which the HFA assumption is valid. The temperature range is taken to be the same as the range used in the sensitivity analyses for the other two models above. In the same fashion as the sensitivity analysis given in the previous section, the ϕ parameter was converted to equivalent snow density ρ. The $\tilde{\omega}$ parameter was converted from angular frequency to frequency expressed in units of Hertz. The other parameter ranges were taken as the following:

- $10\ \mathrm{m\ s^{-1}} \le c_{sh} \le 325\ \mathrm{m\ s^{-1}}$ as the range of the P-wave in the pore spaces of the snowpack used for this sensitivity analysis. This range is based on the observations made in this thesis and by Oura (1952) and Johnson (1982). For the purposes of the HFA model sensitivity analysis, the baseline parameter is selected as $300\ \mathrm{m\ s^{-1}}$.

- $30\ \mathrm{kPa} \le p_a \le 120\ \mathrm{kPa}$ as the normal range of barometric air pressures. This range is inclusive of barometric air pressures at locations in Canada (Hare and Thomas, 1979) and the low barometric air pressures observed on mountain tops (CRC, 1981). The baseline air pressure is 100 kPa, a typical value at sea level.

- The shape parameter γ_s is varied over the range of $0.5 \le \gamma_s \le 0.67$. This assumes that $\gamma_s = 0.5$ for spherical parameters and $\gamma_s = 0.67$ for randomly-oriented needles (Berryman, 1983). The baseline parameter is $\gamma_s = 0.5$.

- The mean pore space diameter a_p can be estimated from Good (1986) as ranging between 2 mm for large-grained snow such as depth hoar and 0.7 mm for fine-grained snow ($7\times10^{-4}\ \mathrm{m} \le a_p \le 2\times10^{-3}\ \mathrm{m}$). The baseline parameter is taken as being near the center of this range at 1 mm.

Figure 3.5a below shows that the speed of sound c_s in the pore spaces of the snowpack is the most sensitive parameter of the HFA model. As c_s increases, the calculated snow density ρ shows a parabolic decrease. For speeds $c_s \to 10\ \mathrm{m\ s^{-1}}$, the calculated density of snow approaches the density of ice. As $c_s \to 325\ \mathrm{m\ s^{-1}}$, the calculated snow density decreases and is similar to the density of air. This behavior is similar to the acoustic observations on snow made by Ishida (1965), Lang (1976) and Johnson (1982).

The second most sensitive parameter of the HFA model is the snow temperature T. Figure 3.5b shows a hyperbolic increase in calculated snow density that is nearly linear. This demonstrates that the HFA model incorporates the influence of temperature on the speed of the P-wave in the pore spaces of the snowpack. Changes in temperature from –40°C to 0°C will cause a change of $210\ \mathrm{kg\ m^{-3}}$ in the calculated density ρ.

The Berryman shape parameter γ_s is the least sensitive of all model parameters (Figure 3.5c). As γ_s increases over the range $0.5 \le \gamma_s \le 0.67$, the calculated snow density drops by only

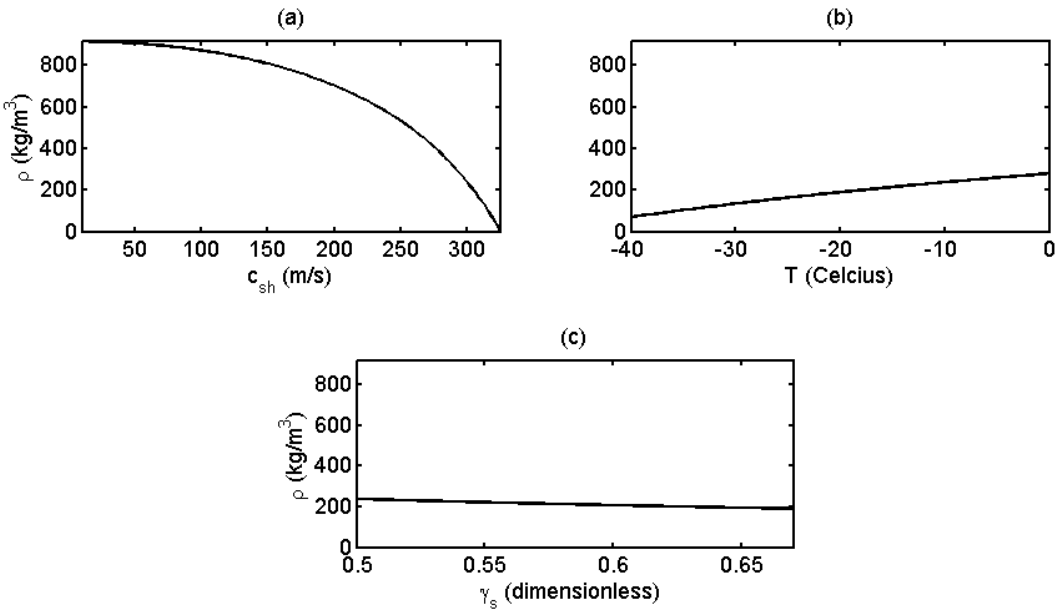

Figure 3.5. Sensitivity analysis for the HFA model outputs. The snow density is ρ, the temperature is T, and γ_s is the Berryman shape factor.

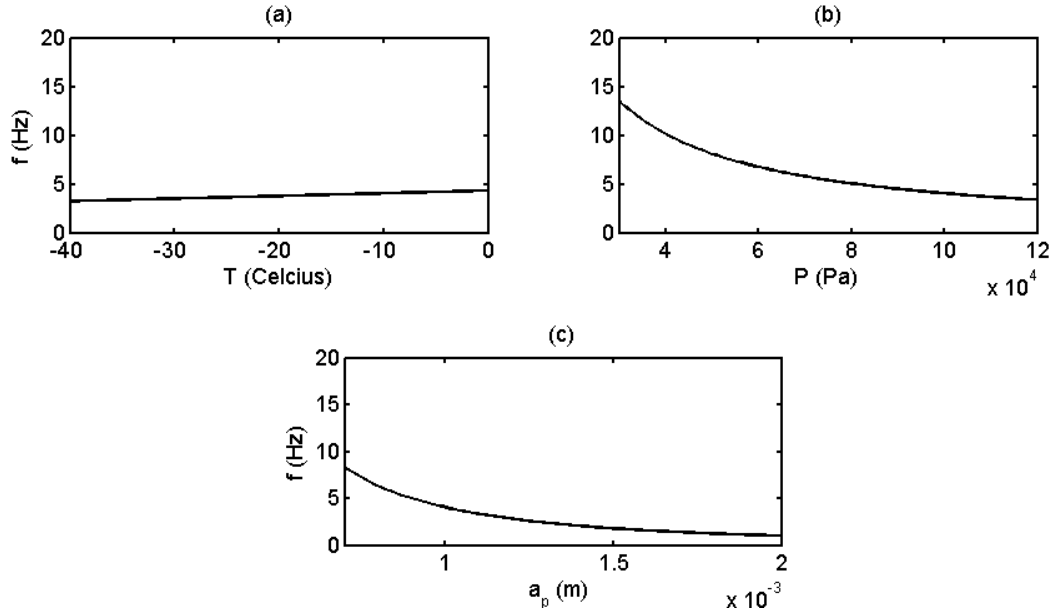

Figure 3.6. Sensitivity analysis for the HFA model cutoff frequency f. The temperature is T, the air pressure is P and a_p is the mean pore space diameter.

$48\ \text{kg m}^{-3}$. Due to the low sensitivity of γ_s, this analysis shows that $\gamma_s = 0.5$ can be taken as a fixed number for all applications of the HFA model. For all applications of the UTAM model, $\gamma_s = 0.5$. The $48\ \text{kg m}^{-3}$ change in density over the range of γ_s is smaller than the measurement differences between snow tube and snow pit measurements of density (Fassnacht et al., 2010), and is likely adequate for operational use of the HFA model.

Figure 3.6 shows that the theoretical cutoff frequency can be lower than 5 Hz, with the pore space diameter a_p being the most sensitive of all parameters. The cutoff frequency (Figure 3.6a) exhibits a linear relationship with temperature. The cutoff frequency drops with an increase in air pressure (Figure 3.6b). The relationship between air pressure and cutoff frequency is slightly hyperbolic and almost linear. As the pore space diameter increases (Figure 3.6c), the cutoff frequency decreases, indicating that pores with larger diameter in the snowpack have a lower cutoff frequency.

3.4.4. UTAM Model

The PT, CT and HFA models are coupled with the UTAM model. These three models provide estimates of parameters for the UTAM model that cannot be easily measured. Consequently, the required inputs for the UTAM model are the frequency f of the sound wave, the dimensionless loss tangent δ, the Berryman shape factor γ_s, the air pressure P, the scaling parameters $\{\psi_G, \psi_E\}$, the high frequency approximation speed c_{sh}, the porosity ϕ, and the water content θ_w. The UTAM model outputs used for the inverse model are the speed c_s and the attenuation α_s of the slow P-wave travelling in the pore spaces of the snowpack. Because only the speed c_s is used in the inverse model, the sensitivity analysis presented in this section shows the c_s parameter as an output. When the HFA model is coupled with the UTAM model, the c_s parameter is constrained so that $c_s \le c_{sh}$. Since there is a high frequency limit to the speed of the sound wave in the snowpack, this ensures that the UTAM model outputs are physically accurate.

For application of the UTAM model, the scaling parameters are assumed to be such that $\Psi = \psi_G = \psi_E$. The ranges for $\{\gamma_s, P, c_{sh}, \phi, S_w\}$ are the same as those given in the sections above, with the following parameters also used:

- $1.0\times10^{-3} \leq \Psi \leq 2.0$ for the scaling coefficient range. This range produces physically-reasonable outputs. In a similar fashion to the HFA sensitivity analysis given above, the baseline parameters are $\psi_E = 2.0\times10^{-3}$ and $\psi_G = 2.0\times10^{-3}$.

- $20\ \text{Hz} \leq f_a \leq 10\ \text{kHz}$ for the range of frequencies being used. This is dependent on the range of sound wave frequencies sent into snow. Further information on the selection of this frequency range can be found in Chapter 4 of this thesis.

- $1.0\times10^{-3} \leq \delta \leq 2.0$ for the range of loss tangents. This range is selected with recourse to the acoustic observations on snow made in this thesis. The range includes the range of physically-reasonable loss tangents identified by Stoll (1989). The baseline parameter for this range is $\delta = 0.1$.

Direct numerical evaluation of Equations (3.11) and (3.12) requires the use of multiple-precision floating-point arithmetic (Nikolaevskaya et al., 2012) due to the large number outputs of the Kelvin functions for argument κ calculated using Equation (3.13). IEEE floating- point types native to any processor cannot be used due to numerical overflow. To directly compute these equations, the MPIR[2] and MPFR[3] "big number" libraries with the MPFR C++ binding[4] were used to calculate Equations (3.11) through (3.17).

Because the Kelvin functions Equations (3.14) and (3.15) are infinite series, the maximum number of terms required for calculating these functions using a computer program was set at $N_T = 100$, with the following early termination criterion. Let b_k be the cumulative sum of terms of either Equation (3.14) or (3.15) calculated using a loop. The loop iteration number is $k \in \mathbb{N}$. Taking $\varepsilon_T = 1.0\text{e-}10$ as a small number, the loop used for the summation is terminated if the following inequality holds for $n_T = 10$ consecutive b_k:

$$|b_k - b_{k-1}| < \varepsilon_T \tag{3.71}$$

The $\{N_T, n_T, \varepsilon_T\}$ values were chosen to ensure that the Kelvin functions could be calculated for all values of argument κ computed using Equation (3.13).

[2] http://www.mpir.org/
[3] http://www.mpfr.org/
[4] http://www.holoborodko.com/pavel/mpfr/

To speed up the calculation of Equation (3.11), the κ argument was evaluated from $\kappa_1 = 150\ \mathrm{m}^{-1}$ to $\kappa_2 = 3\times10^6\ \mathrm{m}^{-1}$ and non-linear curve-fitting was used to determine Equation (3.72) below. For $\kappa \le \kappa_1$ or $\kappa \ge \kappa_2$, the direct numerical calculation using Equation (3.11) was used. For Equation (3.72), the R^2 correlation value was $R^2 = 1.0$, with the Root-Mean Squared Error (RMSD) as RMSE = 7.2×10^{-3}. The imaginary part of the expression is $\mathrm{Im}\{\ \}$ and the real part is $\mathrm{Re}\{\ \}$.

$$\mathrm{Im}\{F(\kappa)\} = 0.0006281\kappa^2\ \mathrm{m}^2, \quad \text{for } 150 \le \kappa \le 3.0\times10^6 \tag{3.72}$$

$$\mathrm{Re}\{F(\kappa)\} = 25.25, \qquad \text{for } 150 \le \kappa \le 3.0\times10^6$$

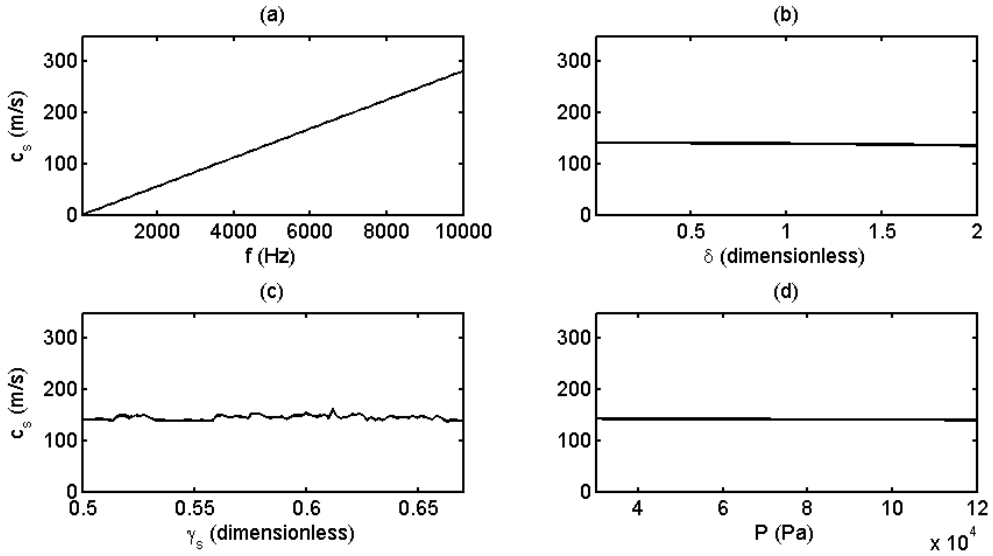

Figure 3.7. Sensitivity analysis for the UTAM model. The frequency of the sound wave in the pore space of the snowpack is f, the loss tangent is δ, the Berryman shape factor is γ_s, and the air pressure is P.

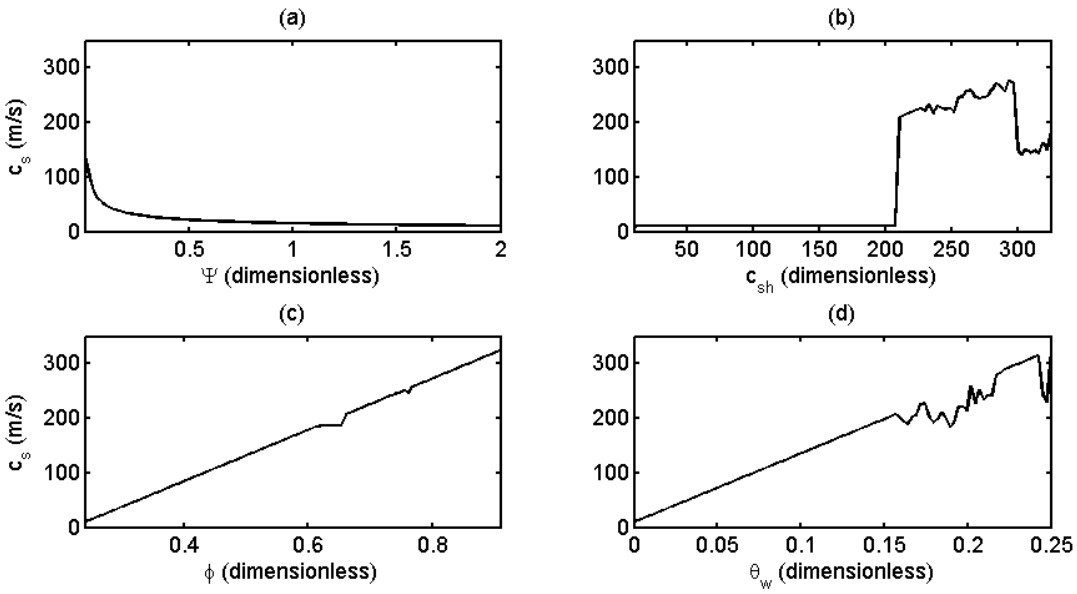

Figure 3.8. Sensitivity analysis for the UTAM model. The scaling parameter is Ψ, the speed of the sound wave at frequencies greater than $\tilde{\omega}$ is c_{sh}, the porosity of snow is ϕ, and the water content is θ_w.

The sensitivity analysis of the UTAM model is shown by Figure 3.7 and Figure 3.8. The speed of the sound wave in the snowpack c_s shows a linear increase with frequency (Figure 3.7a) indicating that P-waves waves with higher frequencies will travel through snow at a greater speed than waves at lower frequencies. This is physically-accurate behavior for sound wave propagation in porous media (Allard and Atalla, 2009). The loss tangent δ shows very little sensitivity (Figure 3.7b), dropping only $5\ \mathrm{m\,s^{-1}}$ over its range. Although the Berryman shape parameter γ_s shows some small variability over its range (Figure 3.7c), the speed of sound in snow c_s is approximately constant. This suggests that the choice of $\gamma_s = 0.5$ is good for operational use of the UTAM model, and does not need to be varied by sampling location. The air pressure P shows very little sensitivity and is approximately linear, with the speed of sound dropping by only $1\ \mathrm{m\,s^{-1}}$ over its range (Figure 3.7d). Figure 3.8b shows that the model is not stable for frequencies greater than the highcut frequency of c_{sh}.

The scaling parameter Ψ shows a hyperbolic decrease over $1.0\times10^{-3} \le \Psi \le 2.0$ (Figure 3.8a). The rate of change of this decrease is greatest for lower values of Ψ. This indicates that selection of lower values of Ψ has a greater potential for introducing error into the UTAM

model output c_s value than higher values of Ψ. Figure 3.8b demonstrates that the speed of the sound wave c_{sh} must be appropriately determined. This is because the UTAM model output c_s is constant until c_{sh} exceeds a threshold frequency. The sensitivity of the porosity ϕ is comparable to the sensitivity of the sound wave frequency f, with the porosity showing a linear increase over its range (Figure 3.8c). The water content θ_w shows a similar linear increase, with some additional variability for $S_w > 0.18$ (Figure 3.8d).

3.4.5. Inverse Model

The inverse model inputs assumed to be known are the Berryman shape factor γ_s, the atmospheric air pressure P, the dimensionless loss tangent δ, and the speed c_{sh} measured above a highpass frequency $\tilde{\omega}$. For operational application of the inverse model, the shape factor γ_s is taken as $\gamma_s = 0.5$. The air pressure P is taken as a known value at each field site, whereas the loss tangent δ and the speed c_{sh} is measured using acoustics.

Although the pressure of air within the pore spaces of the snowpack is dependent on snow permeability and is less than the atmospheric air pressure (Colbeck, 1997), the sensitivity analysis (Figure 3.7d) shows that P is an insensitive parameter in the UTAM model relative to the other parameters. In lieu of any additional information on the air pressure within the pore spaces of the snowpack, the pressure used for P in the inverse UTAM model calculations is taken as the air pressure above the snow surface. This assumption is later justified by application of the UTAM model to make measurements of snowpack physical properties.

The four unknowns determined using the UTAM inverse model are the porosity ϕ, the water content θ_w, the temperature T and the scaling parameter Ψ. These parameters are estimated using the following numerical procedure. The idea is similar to the use of the Knott–Zoeppritz equations to determine the speeds of P- and S-waves in a layered earth medium, given angle-dependent reflection coefficients computed from a seismic dataset (Bruin et al., 1990; Chavent, 2009). The inversion procedure uses the following steps:

1. Let $\{f_1,\ldots, f_N\}$ be known frequencies at which speeds $\{c_{s,1},\ldots,c_{s,N}\}$ of the slow P-wave are determined using signal processing. There are $N \in \mathbb{Z}$ frequencies in total at which speeds in the snowpack medium have been determined using signal processing.

2. The forward model is computed using known parameters at frequencies $\{f_1,\ldots,f_N\}$, with the $\{\phi,\theta_w,T,\Psi\}$ parameters taken to be initially unknown. The starting values of the $\{\phi,\theta_w,T,\Psi\}$ parameters are $\phi=0.58$, $\theta_w=0.07$, $T=0^{\circ}\mathrm{C}$ and $\Psi=1$. These parameters are limited to the ranges used in the sensitivity analyses using Box constraints (Box, 1965). The outputs of the forward model are the speeds $\{c'_{s,1},\ldots,c'_{s,N}\}$.

3. A Nelder-Mead optimizer (Nelder and Mead, 1965) as implemented by the NLopt library is used to iteratively evaluate the forward model for different values of $\{\phi,S_w,T,\Psi\}$ to minimize the square root of the sum of squared errors e_r between the observed and calculated wave speeds:

$$e_r=\sqrt{\sum_{k=1}^{N}(c_{s,k}-c'_{s,k})^2} \tag{3.73}$$

The $\{\phi,\theta_w,T,\Psi\}$ are determined by application of the inverse model. This allows for measurement of snow porosity ϕ, density ρ, temperature T and the structure coefficient Ψ from the inverse model output.

Because the UTAM model is not very sensitive to snow temperature T, choosing T as a fixed value exhibits minuscule effect on the solution of density and liquid water content. Therefore, T can be either found from the inversion procedure given above or can be set to an approximate estimate of snow temperature at a field site. The inversion procedure is thus more useful for determining density ρ and temperature T.

3.5. Acoustic Measurement Model

To collect acoustic data from snow for the purposes of (1) obtaining an image from the snowpack and (2) applying the inverse UTAM, a measurement system model is required. The measurement system must send sound waves into the snowpack and receive the sound waves. Implementation details of this system are given in Chapter 4.

The measurement system is situated in the air medium above the surface of the snowpack, and is comprised of a loudspeaker situated at an offset distance of 10.8 cm to six microphones with separation distances of 3.7 mm. Selection of these parameters is discussed in

Chapter 4 of this thesis. The setup is similar to FMCW (Gubler and Hiller, 1984), bistatic sonar (Cox, 1989) and radar (Willis, 1991) systems (Figure 3.9). The loudspeaker produces an acoustic wave in the air medium, the acoustic wave propagates into the snowpack due to acoustic-to-seismic coupling (Albert and Orcutt, 1989), and reflections from the snowpack are sensed in the air medium by the microphone. The acoustic wave is band-limited by the frequency response of the loudspeaker transducer and the sensing system. Because audible sound waves are in the frequency range of 20 Hz to 20 kHz (Raichel, 2006), the sound wave can be heard by human beings. As discussed in later sections of this thesis, the source signal is band-limited to 10 kHz.

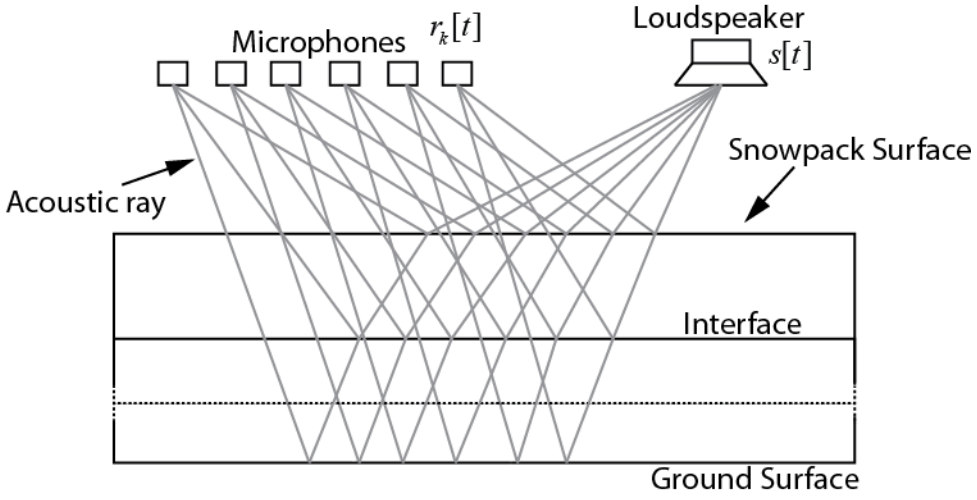

Figure 3.9. Conceptual diagram showing the acoustic measurement model. A loudspeaker is situated at an offset distance from six microphones. The signal sent from the loudspeaker is denoted as $s[t]$ and the signal received by a microphone is $r_k[t]$ for microphone number $k \in \mathbb{Z}$ where $1 \leq k \leq 6$. The measurement arrangement is referred to in this thesis as a "pseudo-CSG."

Reflections from the snow medium will occur due to changes in acoustic impedance. Changes in acoustic impedance do not always coincide with stratigraphic snowpack layers. The interfaces between the layers are taken to be "effective," and can only be detected when there is a reflection. Over a time scale of seconds as the wave passes through the snowpack, these parameters are assumed to not change. This is because snowpack evolution processes operate on time scales of hours to days. This is a reasonable assumption because snowpack evolution models (Pomeroy et al., 2007b) are often run on hourly timesteps. The snowpack is assumed to

be anisotropic, such that the acoustic parameters do not show change over direction within a control volume of the snow medium.

Similar to sonar being reflected from a rough seabed (Lurton, 2002), buried vegetation and rough interfaces between layers will cause acoustic scattering. Acoustic scattering occurs when the sound wave deviates from a straight-line reflection as it passes through the medium. Although acoustic scattering can be modelled using a Rayleigh parameter (Brekhovskikh and Lysanov, 2003), this is not considered due to the need to estimate surface roughness. The theory behind estimation of the Rayleigh parameter for acoustic sensing of snow is discussed by Kinar and Pomeroy (2008). Following Kinar and Pomeroy (2007), Figure 3.9 shows the interface between layers as being modelled by a line that approximates the average position of the rough interface.

Using seismic terminology, the uneven snowpack layers are referred to as "dipping reflectors" (Gadallah and Fisher, 2005). As recognized by Kinar and Pomeroy (2007), the speed of the sound wave may also gradually change over the vertical extent of the layer. Although sophisticated algorithms exist for seismic imaging and speed analysis in dipping layers using traveltime reflection tomography (Biondi, 2007), these algorithms are computationally intensive, and are not addressed in this thesis. The speed of the sound wave is assumed to be the average speed in each layer.

The idea of an acoustic source situated at an offset distance to receiving sensors is widely used in reflection seismology to obtain echoes from a layered earth medium (Burger et al., 2006). The receiving sensors are situated on a line collinear with the source in a survey transect. Because the source and receivers are not moved, the sensing system is similar to a common-shot gather (CSG) in seismic data acquisition, where the receivers sense a reflection from different points on a reflector. Due to spatial offset, there is a time difference between reflections arriving at different receivers (Robinson and Treitel, 2000). The novel idea being presented here is that the measurement system is similar to a CSG, but at a smaller conceptual scale. For seismic data acquisition using geophones, the distance between receivers is on the order of meters, whereas for the measurement model described in this section, the microphones are only situated millimeters apart. In this thesis, the arrangement shown in Figure 3.9 is a "pseudo-CSG."

Most seismic data acquisition surveys use a common midpoint (CMP) gather, where the reflection from a layer is situated at the midpoint between the source and the receiver. This is

accomplished by collecting a series of CSGs where the geophones and microphones have been translated along the survey transect. The CSGs are then subjected to a geophysical procedure referred to as stacking, where the digitized signals from the geophones are added to improve the signal-to-noise ratio (SNR). The disadvantage of using a CSG for data acquisition is that the reflections arriving at the microphones are of small amplitude and are not resilient to noise contamination. Although these effects cannot be completely eliminated, the traces are corrected for attenuation using signal processing and a Maximum Length Sequence (MLS) is used as the source signal to reduce the effects of noise contamination.

Let $s[t]$ be the digital source signal sent from the loudspeaker, and let $r_k[t]$ be the signal received by the six microphones, with $k \in \mathbb{Z}$ and $1 \leq k \leq 6$. The digital source signal $s[t]$ is a Maximum Length Sequence (MLS). The microphone selection and sampling rate is discussed in Chapter 3.

For the snowpack medium, the digital signal received by the microphones $r_k[t]$ is expressible as a convolution (Equation (3.74)). The convolutional model with additive noise $n[t]$ has been used in seismology to describe the effects of a layered seismic medium (Liner, 2004), and is adapted here for use with snow.

$$r_k[t] = \mu_k[t] * \varphi[t] + n[t] \tag{3.74}$$

$$\mu_k[t] = m_k[t] * p[t] * e[t] * d[t] * c[t] * s[t]$$

In the above Equation (3.74), $m_k[t]$ is the time response of each microphone, $p[t]$ is the time response of the loudspeaker, $e[t]$ is the time response of the electronic circuit used to sample the microphones and produce the source signal, $d[t]$ is the direct wave that travels from the loudspeaker to the microphones, $c[t]$ is the effect of the enclosure case on which the loudspeaker and the microphones are mounted, $\varphi[t]$ is the filter kernel of the snowpack medium, and $n[t]$ is environmental noise from wind, animals or anthropogenic sources. The $\mu_k[t]$ signal represents the total measurement response of the system. The loudspeaker as an electromechanical transducer does not have a flat frequency response (Atkinson, 1997).

Equation (3.74) treats the snowpack as a type of digital filter (Oppenheim and Schafer, 2010), with the $\varphi[t]$ as a filter kernel being applied to the measurement system response $\mu_k[t]$. This implies that the snowpack modifies the source signal $s[t]$ by a multiplication in the frequency domain.

Following Rosa and Ulrych (1991), and assuming that the snowpack is similar to a seismic earth medium, the snowpack filter kernel is considered to be minimum-phase. This is reasonable assumption for most seismic media (Pritchett, 1990).

3.6. Maximum Length Sequence (MLS) Measurements

3.6.1. Overview

The signal being sent from the loudspeaker is a Maximum Length Sequence (MLS). As produced by the loudspeaker, the MLS is a binary (two-state) pseudorandom noise signal (Borish and Angell, 1983). A pseudorandom noise signal is a self-repeating sequence that appears to be random, but is completely deterministic (Brown and Hwang, 1996; Golomb and Gong, 2005). Qualitatively, the MLS sounds similar to a burst of white noise sent from the loudspeaker. Due to the MLS similarity to white noise, a filter can be applied to the MLS sequence to produce colored noise (Borish, 1985).

The MLS is used to determine the filter kernel of a system. Treating the snowpack as a digital filter, the MLS allows for determination of the snowpack filter kernel $\varphi[t]$. This can be recognized as a form of deconvolution (Orfanidis, 1988; Smith, 2002): removing the effects of the convolution (Equation (3.74)) to determine $\varphi[t]$.

The MLS is selected for determining the kernel $\varphi[t]$ of the snowpack medium for the following reasons. Measurements of $\varphi[t]$ of a system using transient clicks (Fincham, 1985), frequency sweeps (Clarkson et al., 1985) or tones at a single frequency (Yong-Shen, 1985) have a low Signal-to-Noise Ratio (SNR) relative to the MLS. Although the MLS measurement obtains a similar estimate of $\varphi[t]$, the time-integrated signal energy of the MLS is greater than these other methods due to the length of time that the signal is produced and the greater power of the signal.

The MLS has a longer duration than a transient click so the signal energy is spread over a longer amount of time. The length L_M of the MLS is always $\left(L_M = 2^m - 1\right) \in \mathbb{N} \setminus \{0\}$, with $m \in \mathbb{N} \setminus \{0\}$ as the MLS order (Vanderkooy, 1994). For a DAC sampling rate f_{ds} the duration t_{mls} of the MLS sequence is (Rife and Vanderkooy, 1989):

$$t_{mls} = \frac{L}{f_{ds}} \tag{3.75}$$

For f_{ds} in the audible frequency range of $20\ \text{Hz} \le f_{ds} \le 20\ \text{kHz}$, the duration of the MLS is t_{mls}. The duration t_{mls} is on the order of seconds, making the MLS have greater time-integrated signal energy than a click lasting for less than one second.

Let P_s be the power of a periodic non-MLS sequence. The signal power P_{MLS} of the MLS is related to the power P_s of the periodic sequence by (Rife and Vanderkooy, 1989):

$$P_{\text{MLS}} = \left(L + 1\right) P_s = 2^m P_s \tag{3.76}$$

Equation (3.76) shows that the signal power P_{MLS} is orders of magnitude greater than the power of a frequency sweep or a tone as $m \to \infty$.

When the MLS is used to determine the kernel $\varphi[t]$ of a system, an assumption is being made that the system is Linear Time Invariant (LTI) (Rife and Vanderkooy, 1989; Vanderkooy, 1994). An LTI system is a system where (1) the input is related to the output by a linear map, and (2) the system is assumed to not change over the duration of the measurement (Schetzen, 2002). The first assumption is satisfied by a mathematical property of convolution (Oppenheim and Schafer, 2010), whereas the second assumption is satisfied by the property that the snowpack will not change over the time of the measurement.

Although the loudspeaker may not be a perfect LTI system due to distortion (Vanderkooy, 1994) non-linearity in the electromechanical system (Dunn and Hawksford, 1993), start-up transients (Rife and Vanderkooy, 1989) or temperature changes due to environmental or self-heating, it is considered to approximate an LTI system. Some of these effects are removed by empirically determining the MLS sent from the loudspeaker and the system response $\mu_k[t]$. Moreover, the audio amplifier used in the sensing system described in

this thesis had a built-in filter at the audio amplifier input. This helped to reduce the distortion of the MLS sent into the amplifier by limiting the slew rate of the MLS signal (Vanderkooy, 1994)

Although SineSweep source signals can be used to remove the LTI assumption (Farina, 2000), this source signal shows a lowered immunity to noise and is more appropriate for measurements made in quiet environments (Stan et al., 2002). Signal pre-emphasis techniques can correct for distortion artifacts by modifying the MLS before the signal is sent to the loudspeaker (Cobo et al., 2007; Kovitz, 1994; Niedrist, 1993), but this application is not considered here and is suitable for future research. Immunity of the MLS to distortion is discussed by Dunn and Hawksford (1993) and Vanderkooy (1994), and effects of pre-filtering the MLS is discussed by Godfrey (1975) and Vanderkooy (1994).

The bandwidth of the MLS signal is given by (Rife and Vanderkooy, 1989):

$$B = \left(\frac{f_{ds}}{L_M} \right) \left(\frac{L_M - 1}{2} \right) \approx \frac{f_{ds}}{2} \tag{3.77}$$

Because the MLS bandwidth is maximally-flat (Rife and Vanderkooy, 1989) up to the frequency $B \approx f_{ds} / 2$, this makes the MLS suitable for wideband measurements. The Biot theory model in previous sections have shown that the response of the snowpack is frequency-dependent, as would be expected for a porous medium (Allard and Atalla, 2009), and the MLS as a source signal is able to measure some of this frequency dependence.

3.6.2. Measurement of Snowpack Filter Kernel

From the signal $r_k[t]$ detected by the microphones and the $\mu_k[t]$ system response, the kernel $\varphi[t]$ of the snowpack as sensed by a microphone k is determined by cross-correlation (Borish and Angell, 1983):

$$\varphi_k[t] = \mu_k[t] \star r_k[t] \tag{3.78}$$

Although efficient algorithms have been devised to recompose $\varphi_k[t]$ given the mathematical sequence of the MLS (Borish and Angell, 1983; Jeffery Borish, 1985; Cohn and Lempel, 1977; Fino and Algazi, 1976), these algorithms cannot be applied here because the system response $\mu_k[t]$ is measured in an anechoic chamber (cf. Chapter 4.4).

Treating Equation (3.78) as a convolution between two signals, with one of the signals reversed (Smith, 2002), Equation (3.78) is re-written as Equation (3.79). Let the discrete signal $\mu_k[t]$ have M elements, and the discrete signal $r_k[t]$ have N elements. Expressing the correlation as a convolution that is of length $M+N-1$ to avoid the effects of circular convolution:

$$\varphi_k[t] = \sum_{\substack{j=0 \\ (i-j)\not<0 \\ (i-j)\not>(N-1)}}^{M-1} \mu_k[j] r_k[N-1-(i-j)], \quad \forall\ 0 \le i \le (M+N-1) \tag{3.79}$$

Equation (3.79) shows that the deconvolution operation to obtain $\varphi_k[t]$ is a form of matched filtering, which is known to be optimal in the rejection of noise $n[t]$ uncorrelated with the source signal (Rife and Vanderkooy, 1989). The $\{i, j\} \in \mathbb{Z}$ elements are indices.

However, because Equation (3.79) is slow to calculate in the time domain due to the repeated summation of terms, the correlation process can be done more efficiently in the Fourier domain. Using Fourier transform properties (Bracewell, 1978; Hansen, 2002; Jansson, 1996), Equation (3.79) is re-written in the frequency domain as:

$$\mathrm{F}(\varphi_k[t]) = \mathrm{FFT}\left(\mu_k[t]\right) \odot \mathrm{Rev}\left(\mathrm{FFT}\left(r_k[t]\right)\right) \tag{3.80}$$

In Equation (3.80), $\mathrm{F}(\,)$ represents the discrete Fourier transform operator (numerically implemented as the FFT), $\odot$ represents the Hadamard (point-by-point) multiplication between the complex signals in the frequency domain, and $\mathrm{Rev}(\,)$ is an operator that reverses the discrete signal so that the first element is the last and the last element is the first. Equation (3.80) is well-suited for small signals, but since the cross-correlation between signals $\mu_k[t]$ and $r_k[t]$ cannot fit into processor memory, a more efficient algorithm must be used based on Equation (3.80). The algorithm is similar to the Overlap-Add (OA) signal processing procedure of convolution (Smith, 2002), and is implementable in programmable logic (Blahut, 2010).

Using terminology from sonar and radar signal processing, the maximum number of samples required of $\varphi_k[t]$ is referred to as a "lag" (Nielsen, 1991). Because the kernel $\varphi_k[t]$ is truncated at the end of the signal to remove unwanted reflections at arrival times greater than needed for acoustic imaging of snow, selection of the lag L_{lag} must be greater than the time

sample t corresponding to the maximum time of travel of the sound wave in the snowpack, and $L << M + N - 1$.

Before running the efficient algorithm for cross-correlation, $\mu_k[t]$ and $r_k[t]$ are padded with zeros to ensure that both signals are the same size and that a sequence of size $2L_{lag}$ can evenly fit into the padded sequences. Let $x_w[t]$ be a discrete signal buffer extracted from $\mu_k[t]$, and $y_w[t]$ be a discrete signal buffer extracted from $r_k[t]$. Let w represent a sub-sequence of the $\mu_k[t]$ and $r_k[t]$ signals that is the same size as the buffers. Let $\varphi_k^*[f]$ represent the truncated kernel in the Fourier domain. The $\varphi_k^*[f]$ array is also the same size as the buffers and can hold complex numbers. Then for each sub-sequence w, the following signal processing procedure is applied (Nielsen, 1991):

$$x_w[t] = \begin{cases} \mu_k[t + (w-1)L_{lag}] & \text{for } t = 0, \ldots, L_{lag} - 1 \\ 0 & \text{for } t = \mathrm{L}_{lag}, \ldots, 2L_{lag} - 1 \end{cases}$$

$$y_w[t] = y[t + (w-1)L_{lag}] \qquad \text{for } t = 0, \ldots, 2L_{lag} - 1$$

$$\varphi_k^*[t] = \varphi_k^*[t] + \mathrm{conj}\left(\mathrm{F}\left(x_w[t]\right)\right) \odot \mathrm{F}\left(y_w[t]\right)$$

Once the summation process is performed for all of the buffers, the inverse Fourier transform (numerically implemented as the IFFT) is performed on $\varphi_k^*[t]$ to obtain $\varphi_k[t] = \mathrm{IF}\left(\varphi_k^*[t]\right)$. The calculated $\varphi_k[t]$ is then truncated to have the same number of elements as L_{lag}.

3.6.3. Production of the MLS

The mathematical MLS sequence is produced using a linear feedback shift register (LFSR). The LFSR is a signal processing procedure where bits in a datatype are successively added and shifted (Davies, 1966; Lüke, 1986; MacWilliams and Sloane, 1976; Stahnke, 1973; Vanderkooy, 1994). Figure 3.10a shows a shift register corresponding to the MLS polynomial $x^4 + x + 1$. The binary MLS output of this polynomial is shown in Figure 3.10b. The shift register can be considered as being similar to a queue datatype where elements are ordered according to a FIFO (First-in First-out) property (Cormen et al., 2009).

Figure 3.10c shows the optimal flatness of an MLS magnitude in the frequency domain. The corresponding phase of the MLS is shown as Figure 3.10d. Because the MLS magnitude is flat, it is the phase that is most important in the cross-correlation operation of Equation (3.78).

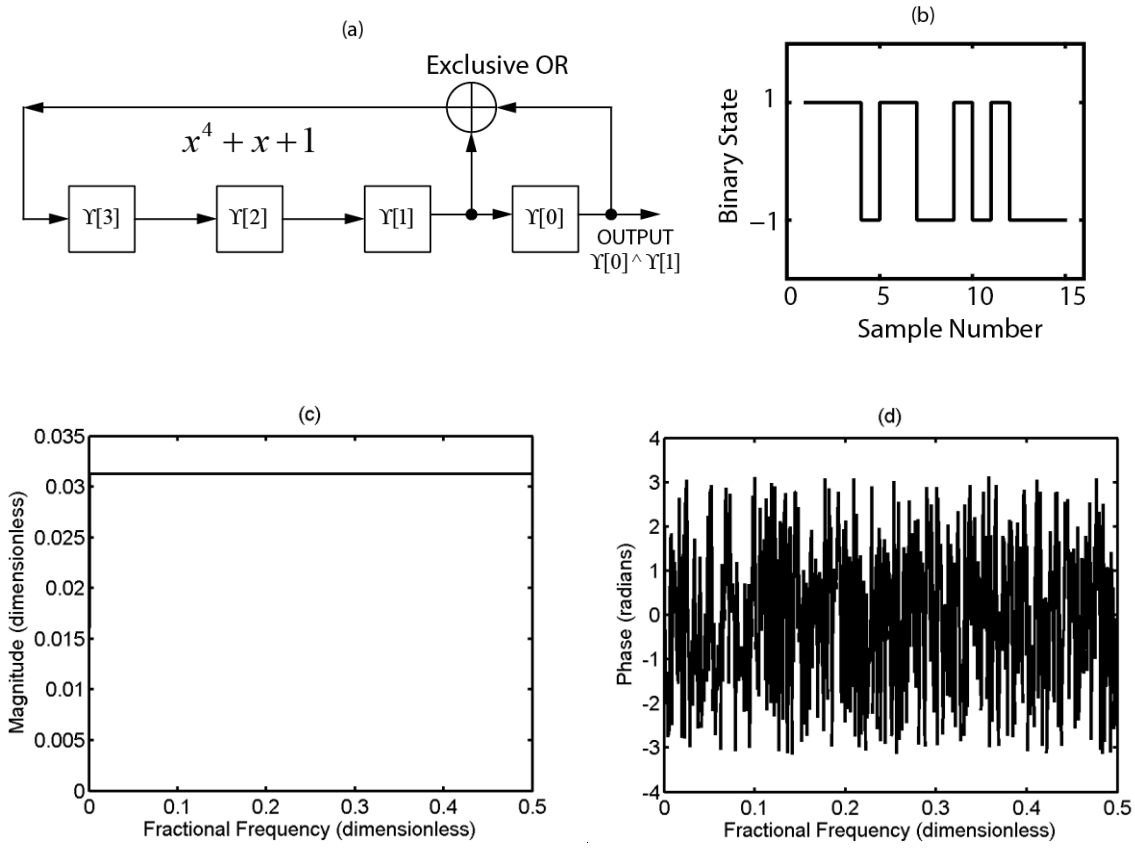

Figure 3.10. Diagram showing the Linear Feedback Shift Register (LFSR) as (a) and the output MLS as (b). The example LFSR is shown corresponding to the MLS polynomial $x^4 + x + 1$ for an MLS order of $m = 4$. The $\{\Upsilon[0], \Upsilon[1], \Upsilon[2], \Upsilon[3]\}$ are the elements of the LFSR. The exclusive OR operation is represented by the $\oplus$ symbol. Dots on subfigure (a) represent connections similar to electrical schematics. Subfigure (c) shows the magnitude response of a MLS with $m = 10$, whereas subfigure (d) shows the phase of the MLS.

The shift register is stored in a datatype or a container Υ that is at least the same length as the order m of the MLS. The shift register is filled with a known initial state: each element of the container is set to binary 1. Randomization of initial state is not required because the MLS is not being used for cryptographic purposes (Paar and Pelzl, 2010). However, randomization of initial state may be useful if more than one acoustic sensing system is deployed per field site.

Because MLS sequences with randomized state are uncorrelated (Golomb and Gong, 2005), more than one system may be able to take measurements at the same time due to the ability for the cross-correlation operation (Equation (3.78)) to reject uncorrelated noise.

Using a loop to execute $L_M = 2^m - 1$ times, the elements in the shift register corresponding to terms in the MLS polynomial are extracted and summed using a mod-2 adder (MacWilliams and Sloane, 1976). In the C/C++ and Verilog programing languages, mod-2 addition is represented by the exclusive-OR ^ operator. This is also referred to as a bitwise XOR operator.

Using the shift register shown in Figure 3.10a as an example, the term of the MLS polynomial (x^4) with the highest degree is the length of the shift register $m = 4$ and the second and first elements of the shift register are used in the exclusive-OR operation. Accessing the container using C programming language notation, the binary output of the shift register is $\Upsilon[0] \wedge \Upsilon[1]$. The output is then placed as the leftmost element in the shift register, whereas the first element is removed. The loop then repeats for the next iteration.

For different orders of m, the table given by Stahnke (1973) is used to obtain MLS polynomials for $m = 1$ to $m = 168$. Since the output of the LFSR is binary $\{0,1\}$, the output is mapped by changing $0 \to 1$ and $1 \to -1$ for a voltage output (Dunn and Hawksford, 1993).

3.6.4. Reconstruction of PDM Sound Wave

The signal $r_k[t]$ from each measurement microphone is recomposed from a Pulse Density Modulated (PDM) bitstream. As discussed in Chapter 4, this bitstream is produced by an oversampling 1-bit Delta-Sigma ADC situated inside of each microphone. The PDM bitstream is similar to an MLS in that it has only two binary states $\{0,1\}$. A greater number of pulses per unit time represent a higher amplitude sound wave than a smaller number of pulses per unit time. Lowpass filtering of the bitstream will recompose the $r_k[t]$ sensed waveform (Candy and Temes, 1991).

Let $B_k^*[t]$ be the raw bitstream from microphone number k. For a 16-bit output, the raw bitstream is scaled by mapping $0 \to 0$ and $1 \to \left(2^{16} - 1 = 65535\right)$. This produces binary signal $B_k[t]$ with range $[0, 65535]$. The $B_k[t]$ signal was then passed through four lowpass

Butterworth filters designed as series Second-Order Sections (SOS) using integer arithmetic. Integer math was used to ensure filter stability and increase the speed of the computations (Smith, 2002).

The lowpass Butterworth filter was chosen in lieu of any other digital filter due to its maximally-flat passband and minimum-phase property (Smith, 2007). Because the snowpack medium is assumed to be a minimum-phase filter, convolution of the lowpass Butterworth filter with the $B_k[t]$ signal will produce an output that is minimum-phase. If the lowpass filter is zero-phase, then the convolution will produce an output that is mixed-phase (Misra and Chopra, 2011). For a microphone sampling rate of $f_s = 2.1\,\text{MHz}$ (as discussed in Chapter 3), the lowpass cutoff of the Butterworth filter was selected as $f_c = 44\,\text{kHz}$. The cutoff frequency is greater than the bandwidth of the acoustic source signal being sent from the loudspeaker.

The SOS filter design is necessary to ensure stability (Smith, 2007) since the Butterworth filter is designed with an Infinite Impulse Response (IIR) topology. The IIR filter uses feedback, and has the potential to become unstable unlike Finite Impulse Response (FIR) filters (Smith, 2002).

The SOS was implemented as three cascaded Direct II Form Digital Biquad Filters (Smith, 2007). A signal processing flow diagram (Figure 3.11) shows the difference equation calculations (Equation (3.81)).

In Equation (3.81), the filter coefficients are b_k with $0 \le k \le 8$ and a_k with $1 \le k \le 6$, the $B_k[t]$ is the raw data input from microphone number k and $r_k[t]$ is the microphone output signal. These filter coefficients are for a 7$^{\text{th}}$ order filter.

Figure 3.12 shows the cutoff frequency response of the filter. Since all of the poles and zeros are inside or on the unit circle (Figure 3.13), the filter is stable (Lyons, 2010).

$$\begin{aligned} y_1[t] &= b_0 h_1[t] + b_1 h_1[t-1] + b_2 h_1[t-2] \\ h_1[t] &= B_k[t] - a_1 h_1[t-1] - a_2 h[t-2] \end{aligned} \qquad (3.81)$$

$$\begin{aligned} y_2[t] &= b_3 h_2[t] + b_4 h_2[t-1] + b_5 h_2[t-2] \\ h_2[t] &= y_1[t] - a_3 h_2[t-1] - a_4 h_2[t-2] \end{aligned}$$

$$r_k[t] = b_6 h_3[t] + b_7 h_3[t-1] + b_8 h_3[t-2]$$
$$h_3[t] = y_2[t] - a_5 h_3[t-1] - a_6 h_3[t-2]$$

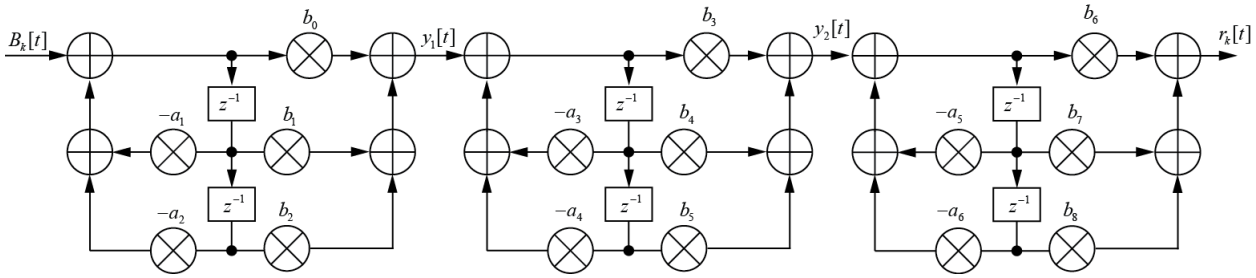

Figure 3.11. Signal processing flow diagram for the lowpass Butterworth filter. The input signal is $B_k[t]$ and the output is $r_k[t]$. Additions are represented by $\oplus$ and multiplications by $\otimes$. All other coefficients are the filter coefficients in Equation (3.81).

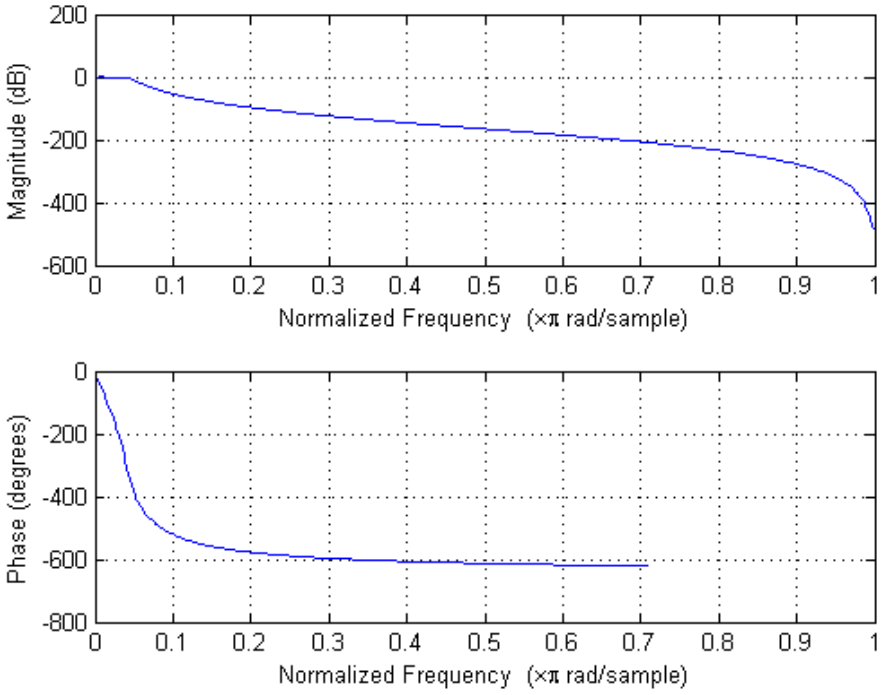

Figure 3.12. Frequency response of the lowpass Butterworth filter.

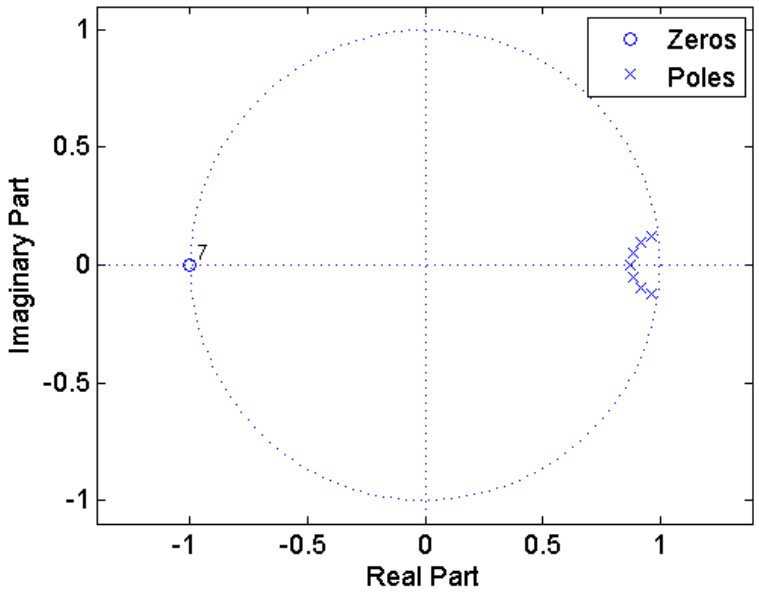

Figure 3.13. Zeros and poles for the Butterworth digital filter. The circles on the plot are the zeros and the x-markers are the poles. The zero-pole plot shows that the filter is stable.

3.7. Attenuation Analysis

3.7.1. Introduction

The attenuation of a sound wave passing through a medium such as snow is expressed as a dimensionless value Q that relates the energy loss ΔW of the medium to the energy W stored in the medium during application of energy to the medium by a sound wave (Wang, 2008):

$$Q = \frac{2\pi W}{\Delta W} \tag{3.82}$$

From Equation (3.82), the attenuation coefficient a as used by the Biot theory is related to the Q value by angular frequency ω and sound speed c_s in a layer of the snowpack for the zero-offset Q_0 value:

$$a = \frac{\omega}{2c_s Q_0} \tag{3.83}$$

The loss tangent δ is related to Q_0 by the following expression (Stoll, 1985):

$$\delta = \frac{\pi}{Q_0} \tag{3.84}$$

As shown by the model of Equation (3.83), attenuation of the sound wave changes with respect to frequency and speed. For a broadband pulse such as a Maximum Length Sequence (MLS), attenuation of the sound wave in the medium will be different for each instantaneous frequency.

Estimation of Q is used to correct for the effects of attenuation on a seismic trace. This enhances seismic resolution, and in a similar fashion to radar or sonar system processing, is a form of automatic gain control (Yilmaz, 2001) that strengthens reflections from successive depths beneath the surface of the earth medium. Correcting for attenuation allows for better interpretation of stratigraphy from reflections (Wang, 2008), and in the context of acoustic imaging of snow, enables an estimate of the distance from the top surface of the snowpack to the ground. Without correction for attenuation, reflections from greater depth beneath the surface of the snowpack appear smaller than reflections near the snowpack surface, making it difficult to detect the ground surface or snowpack stratigraphy. An extensive review on the geophysics of Q is given by Barton (2007).

A forward-Q filter is a signal processing procedure that attenuates an acoustic wave. The purpose of the forward-Q filter is to test Q-analysis algorithms. An inverse-Q filter is a filter that takes an attenuated acoustic wave and attempts to find a non-attenuated reconstruction of the waveform. An inverse-Q filter requires estimates of Q values using Q-analysis techniques (Wang, 2008). In lieu of knowing Q values, a reconstruction of the original waveform can be estimated by smoothing in the time-frequency domain (Margrave et al., 2011).

3.7.2. Q-Analysis Techniques

Determination of Q directly from seismic data has been performed by a number of methods. Vertical seismic profiling (VSP) techniques of Q-analysis involve a spectral ratio method. Recorded signals from a string of geophones inserted down a borehole are subjected to spectral analysis (Stainsby and Worthington, 1985). Ratios between signal spectra at successive depth beneath the surface are used to estimate the Q-value (Raikes and White, 1984). In signal

processing, this is equivalent to determining a transfer function between each geophone as the seismic wavefield propagates from the surface into the medium (Gadallah and Fisher, 2005). Transfer function determination of snow has been performed by Moore et al. (1991), but this requires the placement of microphones beneath the snow surface in a similar fashion to VSP.

A similar spectral-ratio technique is also used for estimating Q from seismic reflection data collected from geophones placed near the surface of a seismic medium (Spencer et al., 1982). However, since reflection data is of geophysical waves that have passed through the medium, the acoustic response is not determined in the same fashion as VSP surveying and it is impossible to directly compute a transfer function. The spectral ratio is therefore computed using a source signal such as the first reflection from a sea bed (Dasgupta and Clark, 1998).

Assuming that $A[t,\omega]$ is the attenuated signal spectrum at an instantaneous time t and angular frequency ω, $A_0[t,\omega]$ is the spectrum of the source signal, and $M_Q[t,\omega]$ is a function that is used to model the relationship between the Q, ω and c variables, the equation used for determining Q from seismic reflection data using the spectral ratio method is of the following form:

$$A[t,\omega] / A_0[t,\omega] = M_Q[t,\omega] \tag{3.85}$$

Because the ratio $A[t,\omega]/A_0[t,\omega]$ is computed over a moving time window, an inaccurate source signal spectrum will also lead to spurious estimates of Q values. Although some implementations of Q-analysis algorithms assume that the source spectrum is flat, such that $A_0[t,\omega]=1$ for all t and ω (Crider and Gutowski, 1995), this is an approximation that may not hold when sound sources such as loudspeakers are used. The time window length for spectral analysis will also influence the determined Q values. Moreover, automated picking of the source signal spectrum $A_0[t,\omega]$ from the reflection data can be challenging to automate, and is better suited for offline processing with a human seismic interpreter (Dasgupta and Clark, 1998).

Equation (3.85) can be recognized as a form of deconvolution by division in the frequency domain (Smith, 2002). It is apparent that $A_0[t,\omega]\neq 0$ and small errors in $A_0[t,\omega]$ will cause the deconvolution to be inaccurate. Although regularization algorithms can be used to ensure smoothness of the deconvolution (Hansen, 2002), this does not eliminate the need to estimate the source spectrum.

Elapavuluri and Bancroft (2004) describe a technique to determine Q values from synthetic seismic traces passed through a forward filter with a constant value of Q. The traces were cross-correlated with a number of synthetic wavelets. Each synthetic wavelet had a known Q-value. The highest cross-correlation between a given trace and wavelet was used to determine the constant Q-value of the synthetic seismic trace. This method has not been tested on real seismic data and can only be used when the seismic trace has a constant Q-value. Moreover, the signal processing is quite intensive due to the generation of a large number of synthetic wavelets. These wavelets may not model actual wavelets that propagate through an earth medium.

Wang (2008) determined Q by collapsing a 2D Gabor Transform spectrum into a 1D spectrum. Non-linear curve fitting was then used to determine Q over the support of the 1D spectrum. However, the model being used to estimate Q via this technique is not the same as the model used by Wang (2008) to correct for attenuation. A similar procedure was used by Margrave et al. (2011) to automatically correct for Q using the Gabor transform of a seismic trace. The procedure is similar to Wang (2008), but the spectral collapsing is applied by Margrave et al. (2011) as hyperbolic smoothing of the seismic trace in the time-frequency domain of a Gabor transform. However, attenuation of waves in porous media is best modelled by an exponential loss function (Allard and Atalla, 2009; Meyer and Neumann, 1972; Wang, 2008), and so the hyperbolic smoothing is only an approximation of attenuation.

3.7.3. Forward and Inverse Gabor Transforms

Following Wang (2008), the forward and inverse Gabor transforms are required for application of forward and inverse Q filters. In a later section of this thesis, these transforms are also used to apply the vanishing constant filter (VCF).

The Gabor transform $G[t,\omega]$ is a Short-Time Fourier Transform (Allen and Rabiner, 1977) with a window $w[t]$. The STFT produces a time-frequency representation of frequency changes in a signal over time (Burrus et al., 1997). The window $w[t]$ is a sub-sequence of a time-domain input signal $h[t]$. For acoustic sensing of snow, $h_k[t]=r_k[t]$ is one of the microphone signals.

The Gabor transform is used here in lieu of wavelet-transform signal processing methods (Burrus et al., 1997) due to historical purposes. This is because the STFT mathematics is reasonably well-established (Allen and Rabiner, 1977) and the STFT has been used for similar Q-analysis and filtering operations (Wang, 2008). The filtering operation discussed in the following sections could potentially be adapted for use with wavelet-transform signal processing. Wavelet transforms are more accurate at representing fast changes in the signal with respect to time. This is a potential improvement.

The $G[t,\omega]$ is a $m \times n$ matrix with complex elements, where the number of columns is the same length n of the discrete time-domain signal. For each signal timestep t_k, where $0 \le k < n$, the Gabor transform is computed using an odd-numbered window size of w_s so there is an even number of points on either side of the window. The t_k element is situated at the center of the window. To compute elements at the beginning and end of the signal vector $h[t]$, the time window is padded with zeros so that the number of rows in the Gabor-transformed matrix is the same length n as the signal vector $x[t]$.

Following Quatieri (2001), the Short-Time Fourier Transform (STFT) is computed by extracting each time domain window $w[t]$ from $h[t]$, multiplying the window $w[t]$ by a Gaussian windowing function $w_f[t]$ (for the Gabor transform), taking each window into the frequency domain using the complex FFT as $W[f] = \mathrm{F}(w[t])$, and arranging elements of the $W[f]$ along the columns of the Gabor matrix $G[t,\omega]$. Because the complex FFT of a real signal in the time domain is symmetric in the frequency domain (Lyons, 2010), each column of the transform is symmetric around the $(w_s / 2 + 1)$ element, for a total number of $w_s = m$ elements. The frequency-domain variable is f and is the dual of the t variable.

The Gaussian window function $w_f[t]$ with length of n is given by (Wang, 2008):

$$w_f[t] = \frac{2}{T_h\sqrt{\pi}} \exp\left[-\left(\frac{2t_w}{T_h} \right)^2 \right] \tag{3.86}$$

In the above Equation (3.86), T_h is the total time on either side of the center of the window and the time at the center of the window is $t_w = 0$ s. To evaluate Equation (3.86) the range of t_w is $-T_h \le t_w \le T_h$ and the timestep $\Delta t = 1/f_s$ is related to the sampling rate f_s of the signal.

The inverse Gabor transform reconstructs an estimate of a time domain signal $x'[t]$ from the time-frequency representation $G[t,\omega]$. This is an Inverse Short-Time Fourier Transform (ISTFT) that is referred to as a synthesis operation. There are two methods for recomposing the input signal. The Overlap-Add (OLA) method takes the IFFT of each column of $G[t,\omega]$ and adds the columns together. The Filter-Bank Summation (FBS) method (Portnoff, 1976) considers each row of $G[t,\omega]$ as a filter bank. The rows are heterodyned and then added together to recompose an estimate of $x'[t]$ as a time-domain signal (Quatieri, 2001).

If modifications are made in the frequency domain by $\Delta[t,\omega] \odot G[t,\omega]$ where $\Delta[t,\omega]$ is a filter kernel, then the time domain signal $\mathrm{IFT}(\Delta[t_0,\omega])$ as the inverse FFT of a column of $\Delta[t,\omega]$ must have a time-domain response that is less than $2m-1$ points to prevent spectral aliasing when using the OLA method of synthesis. This is because $\Delta[t,\omega] \odot G[t,\omega]$ is a multiplication in the frequency domain (Rabiner and Schafer, 1978). Modifications made before FBS does not result in an actual convolution (Allen and Rabiner, 1977), so the OLA method is used instead of FBS.

However, because the ISTFT may not produce a signal that is mathematically valid after the modification $\Delta[t,\omega] \odot G[t,\omega]$, the OLA procedure is implemented (Quatieri, 2001) so that the signal $h_k[t]$ is estimated in a least-squares sense (Griffin and Lim, 1984):

$$h_k[t] = \frac{\sum_{y=-\infty}^{\infty} w_f[y-t]\, g[y,t']}{\sum_{y=-\infty}^{\infty} \left(w_f[y-t]\right)^2} \tag{3.87}$$

In Equation (3.87), the IFFT of each column of $G[t,\omega]$ is $g[t,t']$, where t is the time element corresponding to a column of $G[t,\omega]$ and the time element corresponding to a row of $G[t,\omega]$ is t'.

3.7.4. Forward and Inverse Q Filters

Forward Q filtering is applied in the frequency domain by determining a filter kernel $\Delta[t,\omega]$ that will attenuate $G[t,\omega]$ by the scaling operation $\Delta[t,\omega]\odot G[t,\omega]$. An inverse Q filter is applied by dividing $G[t,\omega]$ by $\Delta[t,\omega]$ so that $G[t,\omega]\odot(1/\Delta[t,\omega])$. This is a form of simple deconvolution with $\Delta[t,\omega]\neq 0$. Although Tikhonov regularization and matrix-based methods of deconvolution (Hansen, 2010) were tried when developing these algorithms, a smooth method of deconvolution (Claerbout, 1992) with a small number $\varepsilon_s = 1.0\times10^{-7}$ was used. This is due to the processing time required to run the matrix inversion and the good performance of the smooth method. The addition of a small number is similar to a form of regularization (Hansen, 2002), and is given by (Claerbout, 1992):

$$G'[t,\omega] = G[t,\omega]\odot\frac{\text{conj}\left(\Delta[t,\omega]\right)}{\Delta[t,\omega]\text{conj}\left(\Delta[t,\omega]\right)+\varepsilon_s^2} \tag{3.88}$$

In Equation (3.88), $\text{conj}(\ )$ is the complex conjugate of the kernel function matrix $\Delta[t,\omega]$.

Most inverse-Q filters use a form of downward wave continuation that is an integration over time (Bickel and Natarajan, 1985; Hale, 1981; Hargreaves and Calvert, 1991; Hargreaves, 1992). This method for forward and inverse-Q filtering is re-written as the kernel $\Delta[t,\omega]$ using theory given in the monograph by Wang (2008):

$$\sigma_p = \exp\left[-\left(0.23G_{\text{lim}}+1.63\right)\right]$$

$$\Phi[t,\omega] = \exp\left[-\int_0^t \frac{\omega}{2Q[t']}\left(\frac{\omega}{\omega_h}\right)^{-\frac{1}{\pi Q[t']}}dt'\right]$$

$$\Lambda_1[t,\omega] = \frac{\Phi^2(t,\omega)+\sigma_p}{\Phi(t,\omega)+\sigma_p}$$

$$\Lambda_2[t,\omega] = \exp\left[i\omega\int_0^t\left(\left(\frac{\omega}{\omega_h}\right)^{\frac{1}{\pi Q[t']}}-1\right)dt'\right]$$

$$\Delta[t,\omega] = \Lambda_1[t,\omega]\Lambda_2[t,\omega] \tag{3.89}$$

In Equation (3.89), σ_p is a dimensionless semi-empirical stabilization parameter used to prevent numerical instability, G_{lim} is a gain limit (dB), ω is the angular frequency in radians corresponding to the rows of $G[t,\omega]$ from the first to the $(w_s/2+1)$ element, ω_h is a highcut frequency taken in this thesis to be the maximum frequency $f_s/2$ at the Nyquist sampling rate corresponding to the $(w_s/2+1)$ element, $i=\sqrt{-1}$ as an imaginary number, $Q[t]$ as a discrete vector of elements with n columns to correspond with the n columns of the $G[t,\omega]$, and the integration is a continuous integration, not a discrete integration as found in signal processing (Oppenheim and Schafer, 2010). The continuous integration is numerically implemented using the trapezoidal rule.

Taking the real part of Equation (3.89) and assuming that $Q[t]=Q$ is constant (or approximately constant) over time, it is apparent that:

$$\Phi[t,\omega] \approx \exp\left[-\frac{\omega}{2Q}\right] \approx \Lambda_1[t,\omega] \tag{3.90}$$

Equation (3.90) supports the idea identified by Margrave et al. (2011) that deconvolution using a constant Q value is suitable for seismic signals with approximately constant Q.

Before the scaling operation $\Delta[t,\omega]\odot G[t,\omega]$ is applied, the kernel $\Delta[t,\omega]$ must be symmetrical around the $(w_s/2+1)$ element. The first half of the kernel is computed using Equation (3.89) or (3.90), whereas the second half is the complex conjugate of the first half. This is done to ensure that the kernel is similar to a FFT (Lyons, 2010).

The scaling operation $\Delta[t,\omega]\odot G[t,\omega]$ must result in a minimum-phase signal $x'[t]$ due to the assumption that the attenuating medium acts as a minimum-phase filter (Hale, 1981). This is also an assumption made for the snowpack model. Before the scaling operation $\Delta[t,\omega]\odot G[t,\omega]$ is applied, each column of the kernel $\Delta[t,\omega]$ is passed through a homomorphic filter that computes the minimum phase equivalent (Smith, 2007).

3.7.5. The Vanishing Constant Filter (VCF)

As discussed in the previous sections, methods of Q analysis use spectral ratios, cross-correlation of wavelets, or spectral collapsing. This implies that two different models are being used: one model to estimate Q values from an input signal $h[t]$, and another model to correct the input signal $h[t]$ for attenuation. The Vanishing Constant Filter (VCF) presented in this section uses the same model to estimate and correct for attenuation. This makes the filtering procedure more robust. Similar to Margrave et al. (2011), the filter automatically corrects for attenuation without measuring the value of Q. The basic idea behind the VCF is that the term with the Q variable is made to disappear by mathematical transformations. This is a blind deconvolution algorithm that does not involve smoothing of the waveforms using spectral collapsing or averaging. Robinson-Weiner deconvolution (Margrave et al., 2011) is another way of accomplishing this type of signal processing operation.

Using the relationship given by Equation (3.90), take $\beta_1[t,\omega]$ as the Gabor transform $G[t,\omega]$ of an attenuated signal $\varphi_k[t]$ that has passed through a porous medium, let $A_a[t,\omega]$ be the Gabor transform of the un-attenuated signal, and let $\Theta[t,\omega]$ be a function that models the phase in a similar fashion to $\Lambda_2[t,\omega]$:

$$\beta_1[t,\omega] = A_a[t,\omega]\exp\left(\frac{-\omega t}{2Q}\right)\exp\left(i\Theta[t,\omega]\right) \tag{3.91}$$

Taking the absolute value of Equation (3.91) eliminates the exponential function with an imaginary argument. This is due to the multiplicative property of the absolute value and the property $\text{abs}\left(\exp(ix)\right)=1$ with $x\in\mathbb{R}$. Equation (3.91) becomes Equation (3.92), where it is assumed that $\exp\left(-\omega t/\left(2Q\right)\right)>0$. Also let $A[t,\omega]=\left|A_a[t,\omega]\right|$. Equation (3.92) takes on only real values.

$$\beta_2[t,\omega] = \left|A_a[t,\omega]\right|\exp\left(\frac{-\omega t}{2Q}\right) = A[t,\omega]\exp\left(\frac{-\omega t}{2Q}\right) \tag{3.92}$$

Homomorphic filtering is a signal processing procedure that attempts to separate two signals multiplied together (Lim, 1990). Homomorphic filtering can be considered as a type of

blind deconvolution (Kundur and Hatzinakos, 1996), where the signals are separated without knowledge of the filter kernel. Homomorphic filtering has been used to remove multiplicative noise kernels from images (Lim, 1990); to remove the source signature and noise from seismic traces (Buhl et al., 1974; Stoffa et al., 1974); to improve the resolution of ultrasound images (Taxt, 1997, 1995); to obtain a minimum-phase signal from a mixed-phase signal (Oppenheim et al., 1976); and to separate components of speech for speech analysis and speaker recognition (Quatieri, 2001). A review of homomorphic signal processing is given by Childers et al. (1977).

The basic idea behind homomorphic filtering is that the mathematical property of logarithms is used to transform a multiplied pair of signals into an additive pair (Oppenheim et al., 1976). Linear filtering techniques are then used to suppress the unwanted noise (Lim, 1990). The VCF takes this idea further by using the differentiation and integration operations as digital filters to remove attenuation.

For expository purposes, the Vanishing Constant Filter (VCF) is described in a series of steps. Each of these steps corresponding with an equation is implemented as a signal processing procedure. The derivatives and cumulative integrals in the section below are computed using FFT methods, as discussed in the next section.

The Vanishing Constant Filter (VCF) is aptly named since the Q is removed from a term in Equation (3.93). The Q is said to "vanish."

Taking the logarithm of both sides of Equation (3.92),

$$\gamma_1[t,\omega] = \log\left(A[t,\omega]\right) - \frac{\omega t}{2Q} \tag{3.93}$$

Taking the partial derivative of Equation (3.93) with respect to t,

$$\gamma_2[t,\omega] = \frac{\partial}{\partial t}\log\left(A[t,\omega]\right) - \frac{\omega}{2Q} \tag{3.94}$$

Taking the partial derivative with respect to t again,

$$\gamma_3[t,\omega] = \frac{\partial^2}{\partial t^2}\log\left(A[t,\omega]\right) \tag{3.95}$$

Equation (3.95) shows that the term with the Q has been removed. Integrating Equation (3.95) over time yields:

$$\gamma_4[t,\omega] = \int_0^t \gamma_3[t',\omega]\partial t' = \frac{\partial}{\partial t}\log\left(A[t,\omega]\right) + C_1[\omega] \tag{3.96}$$

The time integration shown in Equation (3.96) is cumulative, and the $C_1[\omega] \in \mathbb{R}$ sequence is a constant of integration as a function of ω. Taking the difference,

$$\gamma_5[t,\omega] = \gamma_4[t,\omega] - \gamma_2[t,\omega] = C_1[\omega] + \frac{\omega}{2Q} \tag{3.97}$$

If $C_1[\omega]$ is constant for all ω, then by taking the partial derivative of Equation (3.97) with respect to ω will produce $1/(2Q)$, and it is trivial to solve for Q. However, for signals that have passed through an attenuating medium, $C_1[\omega]$ is not constant and varies with ω.

Taking the partial derivative with respect to ω of $\gamma_5[t,\omega]$ yields:

$$\gamma_6[t,\omega] = \frac{\partial}{\partial\omega}C_1[\omega] + \frac{1}{2Q} \tag{3.98}$$

Taking the integral of $\gamma_6[t,\omega]$ yields:

$$\gamma_7[t,\omega] = C_1[\omega] + C_2 + \frac{\omega}{2Q} \tag{3.99}$$

In Equation (3.99), the constant of integration is $C_2 \in \mathbb{R}$. From Equations (3.97) and (3.99), it is apparent that:

$$C_2 = \text{mean}\left(\gamma_7[t,\omega] - \gamma_5[t,\omega]\right) \tag{3.100}$$

In Equation (3.100), the mean value of all elements in the matrix is denoted by $\text{mean}(\,)$, and the subtraction is performed in a point-by-point fashion.

Taking the second derivative of $\gamma_6[t,\omega]$ removes the term with the Q variable:

$$\gamma_8[t,\omega] = \frac{\partial^2}{\partial\omega^2} C_1[\omega] \tag{3.101}$$

Integrating Equation (3.101) over ω,

$$\gamma_9[t,\omega] = \int_0^{\omega} \gamma_8[t,\omega']\partial\omega' = \frac{\partial}{\partial\omega} C_1[\omega] + C_3 \tag{3.102}$$

In Equation (3.102), C_3 is a constant of integration. When the cumulative integration is computed using FFTs using the signal processing procedure given in the next section, the C_3 is given by the first point in the $\partial C_1[\omega]/\partial\omega$ signal. The $\partial C_1[\omega]/\partial\omega$ signal is one element less than the number of rows in $\gamma_5[t,\omega]$ due to the truncation created by the signal processing procedure that computes the derivatives using FFTs. For ω_k with $1 \le k \le m$,

$$C_3 = -\frac{\partial}{\partial\omega} C_1[\omega_2] \tag{3.103}$$

The $C_1[\omega_2]$ element is the first element in $\partial C_1[\omega]/\partial\omega$. Assuming "smoothness" between the first and second derivatives of $C_1[\omega_2]$ near the first point, the C_3 constant is chosen as a value that is sufficiently "close" to C_3 by Equation (3.104).

$$C_3 = -\frac{\partial}{\partial\omega} C_1[\omega_2] \approx -\Delta\omega\left[\frac{\partial^2}{\partial\omega^2} C_1[\omega_3]\right] \tag{3.104}$$

In Equation (3.104), $\Delta\omega$ is the frequency step set by the length of the FFT used to compute the STFT and $C_1[\omega_3]$ is the first point of the column.

Integrating $\gamma_9[t,\omega]$ over ω again,

$$\gamma_{10}[t,\omega] = \int_0^{\omega} \gamma_9[t,\omega']\partial\omega' = C_1[\omega] + C_2 + \omega C_3 \tag{3.105}$$

Since C_2 and C_3 have been estimated, both can be successively removed from Equation (3.105):

$$\gamma_{11}[t,\omega] = C_1[\omega] + \omega C_3$$

$$\gamma_{12}[t,\omega] = C_1[\omega]$$

The $C_1[\omega]$ is removed from $\gamma_4[t,\omega]$:

$$\gamma_{13}[t,\omega] = \gamma_4[t,\omega] - \gamma_{12}[t,\omega] = \frac{\partial}{\partial t}\log\left(A[t,\omega]\right) \tag{3.106}$$

Integrating Equation (3.106) over t,

$$\gamma_{14}[t,\omega] = \int_0^t \gamma_{13}[t,\omega']\partial t' = \log\left(A[t,\omega]\right) + C_4 \tag{3.107}$$

The $C_4 \in \mathbb{R}$ is a constant of integration. To find C_4, Equation (3.94) is integrated over t and C_4 is calculated as Equation (3.109).

$$\gamma_{15}[t,\omega] = \int_0^t \gamma_2[t,\omega']\partial t' = \log\left(A[t,\omega]\right) - \frac{\omega t}{2Q} + C_4 \tag{3.108}$$

$$C_4 = \gamma_{15}[t,\omega] - \gamma_1[t,\omega] \tag{3.109}$$

Removing the constant from $\gamma_{14}[t,\omega]$,

$$\gamma_{16}[t,\omega] = \log\left(A[t,\omega]\right) \tag{3.110}$$

Equation (3.110) is an estimate of the un-attenuated signal in the log domain. An estimate of the kernel in the log domain is:

$$\gamma_{17}[t,\omega] = \gamma_1[t,\omega] - \gamma_{16}[t,\omega] \approx \frac{-\omega t}{2Q} \tag{3.111}$$

For acoustic signals that have passed through a snowpack, the cross-correlation operation (Section 2.8.2) will remove the negative sign in Equation (3.111). The negative sign is restored by a simple multiplication. Homomorphic filtering (Smith, 2007) is then applied to $\gamma_{17}[t,\omega]$ so that a minimum-phase approximation of the kernel $\Delta[t,\omega]$ is reconstructed. This is necessary

since the phase function $\Theta[t,\omega]$ has been removed and Equation (3.111) does not have a complex part. The un-attenuated time domain signal $h_k[t]$ is then reconstructed using the deconvolution given by Equation (3.88) and the inverse STFT.

To estimate Q, Equation (3.111) is normalized to the interval $[0,1]$. This is required since Equation (3.111) is an approximation of the kernel that attenuates the signal and numerical values slightly greater than 1.0 are not physically reasonable. A matrix $\hat{Q}[t,\omega]$ is calculated for each element of the $\gamma_{18}[t,\omega]$ matrix using the $-\omega t/\left(2\hat{Q}[t,\omega]\right)$ model. The values of $\hat{Q}[t,\omega]$ are then spatially averaged to obtain Q.

3.7.6. Differentiation and Integration Using FFTs

A high-accuracy method for computing the derivative and cumulative integral of a discrete signal is required for implementation of the Vanishing Constant Filter (VCF). Although the derivative can be computed using finite-differencing (Fletcher, 1991), this method will cause non-smooth discontinuities in the signals. Lanczos differentiators (Savitzky and Golay, 1964) are used to reduce noise when taking the derivative of a signal. However, the derivative computed using a Lanczos differentiator is only an approximation of a smoothed derivative.

To compute high-accuracy derivatives and cumulative intergrals, FFT methods were used. These methods are similar to computational procedures used for pseudospectral solutions of computational fluid mechanics problems (Fornberg, 1998) or for optical sensing applications (Yaroslavsky, 2003; Yaroslavsky et al., 2005).

Let $y[z]$ be a real-valued discrete signal that is a row or column of a matrix $M[t,\omega]$, where z is an element number of the signal. Let Δy be the spacing between discrete samples, so that $\Delta y = \Delta t$ for the timestep and $\Delta y = \Delta\omega$ for the step in angular frequency. Using linear differential operator theory from Oppenheim et al. (1997) and Hörmander (1983), the derivative of $y[z]$ is computed by the convolution:

$$\frac{\partial y[z]}{\partial \Delta y} = \frac{y[z] * u_1[z]}{\Delta y} \tag{3.112}$$

$$u_1[z] = \begin{cases} 1 & \text{for } z = \text{floor}\left(N_k / 2 + 1\right) \\ -1 & \text{for } z = \text{floor}\left(N_k / 2 + 1\right) + 1 \\ 0 & \text{otherwise} \end{cases}$$

In Equation (3.112), the number of elements in the kernel $u_1[z]$ is N_k and $u_1[z]$ is a discrete version of the unit doublet function that is a discrete approximation of the Dirac delta function derivative. For the Vanishing Constant Filter (VCF), $N_k = 1024$ was selected as an adequate kernel length. The kernel length N_k is the same as commonly used for most signal processing applications (Smith, 2002). Computation of the derivative by a linear convolution using Equation (3.112) requires that one point is lost at the beginning of the signal. The output of the convolution is situated between the $N_k / 2 + 2$ and $N_k / 2 + 2 + N - 1$ points of the padded convolution, where N is the length of the signal $y[z]$.

The cumulative integral is computed using a discrete version of the Heaviside function $U[z]$. Once again using theory from Oppenheim et al. (1997) and Hörmander (1983):

$$\int y[z'] \partial z' = \left(y[z] * U[z]\right) \Delta y \tag{3.113}$$

$$U[z] = \begin{cases} 1 & \text{for } z = \text{floor}\left(N_k / 2 + 1\right) \text{ to } N \\ 0 & \text{otherwise} \end{cases}$$

For the VCF, the length of the kernel N_k used for integration was taken as $N_k = 2N$ to ensure that the integration filter operated over all frequencies in the input signal $y[z]$. Because no points are lost during integration, the output is situated between the $N_k / 2 + 1$ and $N_k / 2 + 2 + N - 1$ points of the convolution output. The convolution of Equation (3.113) is scaled by Δy.

3.7.7. Zero-offset Q

The numerical value of Q found using the VCF is the Q value for a particular microphone signal $r_k[t]$. This value of Q is not the zero-offset value of Q_0 required for finding the loss tangent δ due to spherical spreading. Because the value of Q will vary in a similar fashion to the slope of the spectral ratio with the square of the offset distance (Dasgupta and Clark, 1998), non-linear curve-fitting is used to determine Q.

Let x be the offset distance of the microphone k to the loudspeaker. These offsets are contained in the vector $\mathbf{x_{os}}$. The value of Q_0 is computed for each $r_k[t]$ over $1 \le k \le 6$, forming the vector $\hat{\mathbf{Q}}_\mathrm{y}$. Then the following model is used to find Q_0 by curve-fitting:

$$\hat{\mathbf{Q}}_\mathbf{y} = m_s \mathbf{x}_\mathbf{os}^2 + Q_0 \tag{3.114}$$

In Equation (3.114), $\hat{\mathbf{Q}}_\mathrm{y}$ is the dependent variable, the $\mathbf{x_{os}}$ is the vector of microphone offsets, and Q_0 is the value of Q at zero-offset that is determined from Equation (3.114).

3.8. FBS Analysis

To apply the UTAM model, $c_s[t,x]$ is required as a function of angular frequency ω. To determine $c_s[t,\omega,x]$, the attenuation-corrected traces $h_k[t]$ for $1 \le k \le 6$ are taken into time-frequency space by the Gabor transform, yielding $H_k[t,\omega]$. The absolute value of each column $\left|H_k[t,\omega]\right|$ is treated as a filtered version of the signal, using the bandpass filter view of the STFT (Quatieri, 2001). The Gabor transform computed m different frequencies with $1 \le \ell \le m$. This idea is similar to the group velocity analysis of Stoll (2002).

3.9. Speed Analysis

The speed c_s of the P-wave in the pore spaces of the snowpack is found by creating a matrix $\Gamma[t, x, \omega_\ell]$ where each column of the matrix is a vector $\left|H_k[t, \omega_\ell]\right|$ of filtered signals for a microphone k at a frequency ω_ℓ. Each microphone signal is of length n, and since there are six microphones in total per row, the matrix $\Gamma[t, x, \omega_\ell]$ has n rows and six columns. Velocity analysis algorithms from seismology are applied to obtain the speed $c_s[t, x, \omega_\ell]$ as a function of time t, offset x and frequency ω_ℓ. The speed $c_s[t, x, \omega_\ell]$ is used as an input to the UTAM model and also for imaging of snow.

Toldi (1985, 1989) was perhaps the first investigator to automate the determination of velocity from a seismic dataset. The idea proposed by Toldi was to compute semblance plots of the seismic dataset and then use numerical optimization to fit a model of velocity to the dataset. Before the work of Toldi, velocity had to be "picked" by human interpretaton. This was accomplished by drawing a line on the semblance plot. Semblance is a 2D plot of velocity versus travel time, with the semblance plotted on the third axis. Higher values of semblance at a certain velocity imply that the wave is moving at that velocity through the seismic earth medium (Luo and Hale, 2012). Constrained versions of velocity estimation was later introduced by Clapp et al. (1998), and Fomel (2009) used a fast-marching eikonal equation solver (Alkhalifah and Fomel, 2001) to pick velocity. The difficulty with such methods is that the picking procedure can be inaccurate. Using plane-wave destructor filters (Claerbout, 1992; Fomel, 2002), Fomel (2007) showed that velocity could be estimated directly from a seismic dataset without the picking operation.

The plane-wave destructor filter used for finding the speed of sound in snow was implemented from Chen et al. (2013). Given a dataset of $\Gamma[t, x]$ with time t and offset x, let $u[t, x]$ be the wavefield. Then given an appropriate choice of parameter Ω, the plane wave destructor filter is the following partial differential equation that removes plane waves from the dataset (Claerbout, 1992):

$$\frac{\partial u[t, x]}{\partial x} + \Omega \frac{\partial u[t, x]}{\partial t} = 0 \tag{3.115}$$

The Z-transform of $u[t,x]$ is $U[Z_t, Z_x]$, and $\{Z_t, Z_x\}$ are the discrete time-shift and spatial shift operators. Let $C(\Omega)$ be an operator. Then using a three-point finite-difference approximation, the plane wave destructor filter is given by (Chen et al., 2013):

$$\left(1 - Z_x Z_t^{\Omega}\right) U\left(Z_t, Z_x\right) = 0$$

$$C(\Omega) = B\left(Z_t\right) - Z_x B\left(1/Z_t\right)$$

$$B\left(Z_t\right) = \frac{(1+\Omega)(2+\Omega)}{12} Z_t^{-1} + \frac{(2+\Omega)(2-\Omega)}{6} + \frac{(1-\Omega)(2-\Omega)}{12} Z_t$$

$$C\left(\Omega, Z_x, Z_t\right) U\left(Z_x, Z_t\right) \approx 0 \tag{3.116}$$

Using Equation (3.116), Newton iteration (Chen et al., 2013) is used to find Ω as a constant value for the entire signal that has passed through the snowpack. The Ω parameter is found as a constant value to ensure stability of the Newton iteration when applied to SAS2 acoustic data. Smoothness of the solution is ensured by the use of shaping regularization (Fomel, 2007b), which is similar to a constraint when solving inverse problems (Hansen, 2010). Ill-posedness of the solution for the acoustic waves passed through snow did not allow for "layered" estimates of the speed of sound in snow. This means that the snowpack is assumed to be an effective "one-layer" model.

Assuming that $\Omega \neq 0$, the moveout velocity $v[t,x]$ is computed using the Ottolini equation (Fomel, 2007a; Ottolini, 1983):

$$v[t,x] = \left(\frac{x}{\Omega}\right)^{1/2} \tag{3.117}$$

In Equation (3.117), the offset distance between the loudspeaker and a microphone is x. The moveout velocity is used in NMO (Normal Moveout). This is a geometrical correction of the acoustic data so that acoustic reflections are not curved due to spherical spreading (Claerbout, 1992). The NMO as applied by the Ottolini equation is (Fomel, 2007a):

$$t_0 = \left(t^2 - \Omega t x\right)^{1/2} \tag{3.118}$$

In Equation (3.118), t_0 is the offset time that is remapped from the signal time at which the signals $\Gamma[t,x]$ are recorded. The time-remapping is accomplished by inverse B-spline interpolation (Fomel, 2000). The time-remapped $\Gamma[t,x]$ is $\Gamma_M[t,x]$.

The interval velocity c_s was obtained from Ω by:

$$\vartheta = \Delta t\Omega + t\frac{\partial\Omega}{\partial t} = \Delta t\Omega \text{, since } \frac{\partial\Omega}{\partial t} = 0 \text{ and } \Omega \text{ is constant}$$

$$c_s[t,x] = \frac{x^2\Delta x\Delta t\vartheta[t,x] - 2\Omega t^2\Delta x}{\Omega^2 t\left(2t\Delta x - x\vartheta[t,x]\right) + \varepsilon_s} \tag{3.119}$$

In Equation (3.119), Δx is the offset distance step between the microphones, Δt is the timestep, ε_s is a small number that prevents division by zero, and all other variables are as previously defined. Once $c_s[t,x]$ is known, averaging over the entire matrix is used to obtain c_s as a constant speed over the entire signal. The snow depth $\bar{y}$ is measured using a depth rod or SR50 ultrasonic depth gauge and simple kinematics is used to select the maximum cutoff time $t_{\max}$.

There is a need to select a maximum cutoff time $t_{\max}$ from a cutoff depth $\bar{y}$ to identify when the sound wave has reached the bottom of the snowpack. This is because attenuation of the sound wave in snow does not always permit the bottom of the snowpack to be clearly identified. This maximum cutoff time could be assumed. If the cutoff time $t_{\max}$ is assumed instead of measuring snow depth $\bar{y}$, late-time reflections from elements other than the snowpack will have a greater contribution to the error in determination of snow density, liquid water content and temperature using the UTAM model. Future work could use physics of reflections from the ice or soil at the base of the snowpack to identify a cutoff time using signal processing.

3.10. Signal Processing Flow

Figure 3.14 shows the signal processing flow. The diagram synthesizes all of the information given in this chapter, showing how the calculations proceed.

An MLS is generated using a LFSR (Section 3.6.3). The MLS is sent into the snowpack by a loudspeaker. As described in Section 3.5, six microphones at an offset distance from the

loudspeaker sense the reflections and output Pulse Density Modulated bitstreams $B_k^*[t]$. The bitstreams are scaled to produce $B_k[t]$. An IIR Butterworth lowpass filter with a cutoff frequency $f_c = 44$ kHz is used to obtain $r_k[t]$. The kernel $\varphi_k[t]$ is computed by a cross-correlation operation (Section 3.6.2). The cross-correlation operation was performed by the FPGA in the system (cf. Chapter 4). The Vanishing Constant Filter (VCF) is applied to $\varphi_k[t]$ so that an un-attenuated trace $h_k[t]$ is obtained (Section 3.7.5). Zero-offset Q is obtained (Section 3.7.7). A Gabor transform is applied to calculate $|H_k[t,\omega]|$ for each microphone. Rows of $|H_k[t,\omega]|$ are extracted for velocity analysis. Each extracted row is $|H_k[t,\omega_\ell]|$. Velocity analysis for a number of ω_ℓ is used to find c_{sh} and the speeds at a number of different frequencies for input into the UTAM. A snowpack image is obtained from $\Gamma[t,x,\omega_m]$.

3.11. Computation of Parameters

The speed c_s is found at a frequency ω_ℓ and Ω is constant over time. There is only one value of c_s over the entire time of the signal for a frequency ω_ℓ. This means that the UTAM model will output depth-averaged values of density $\bar{\rho}$, liquid water content $\bar{\theta}_w$, and temperature $\bar{T}$. The liquid water content is reported as a percentage. The measurements of $\bar{\rho}$ are similar to the depth-averaged values of density that are determined using an SR50 snow tube.

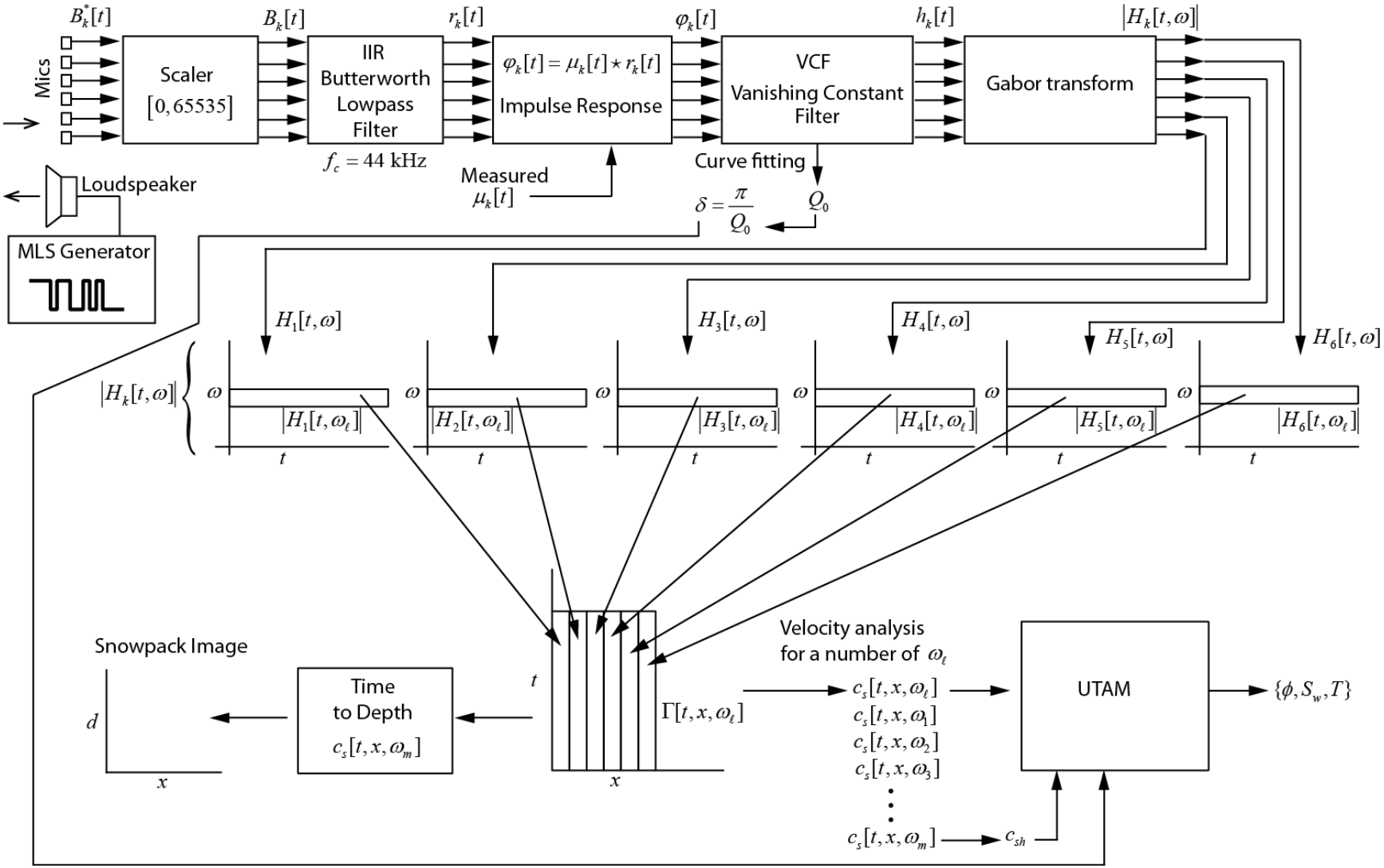

Figure 3.14. Signal processing flowchart. Details are given in the text.

CHAPTER 4
APPARATUS

4.1. Introduction

To collect acoustic data suitable for use with models of sound propagation through snow, prototype electronic systems were designed and constructed. The following sections describe the systems created and discuss engineering choices made during development. The apparatus is identified by the acronym SAS2 as a "System for the Acoustic Sensing of Snow." As a system, the apparatus is comprised of hardware and software components used to collect data as inputs for acoustic models. The penultimate development goal was to create a device suitable for collecting acoustic data to apply the Unified Thermoacoustic Model (UTAM) presented in Chapter 3. Although this development goal was the objective of the paper, three initial prototypes were created before the objective was achieved with a fourth prototype system. The sampling system design is related to the physics of sound propagation in porous media.

4.2. Initial Prototype Systems

Two prototypes of the SAS2 were initially created and deployed at field sites in the Wolf Creek Research Basin near Whitehorse, Yukon Territory, and also at field sites in the Rocky Mountains of Alberta. Figure 4.1 shows these two prototype systems. Both systems were portable and transported to each field site in a backpack.

Each system was comprised of a single loudspeaker and electret microphone situated on the front of an enclosure case. A semiconductor temperature sensor placed inside of a PVC Tee pipe superglued to the side of each case served as a shielded thermometer to measure air temperature. Inside of each enclosure case was an electronic circuit responsible for driving the loudspeaker and collecting acoustic data from the microphone. As shown in Figure 4.1a, the

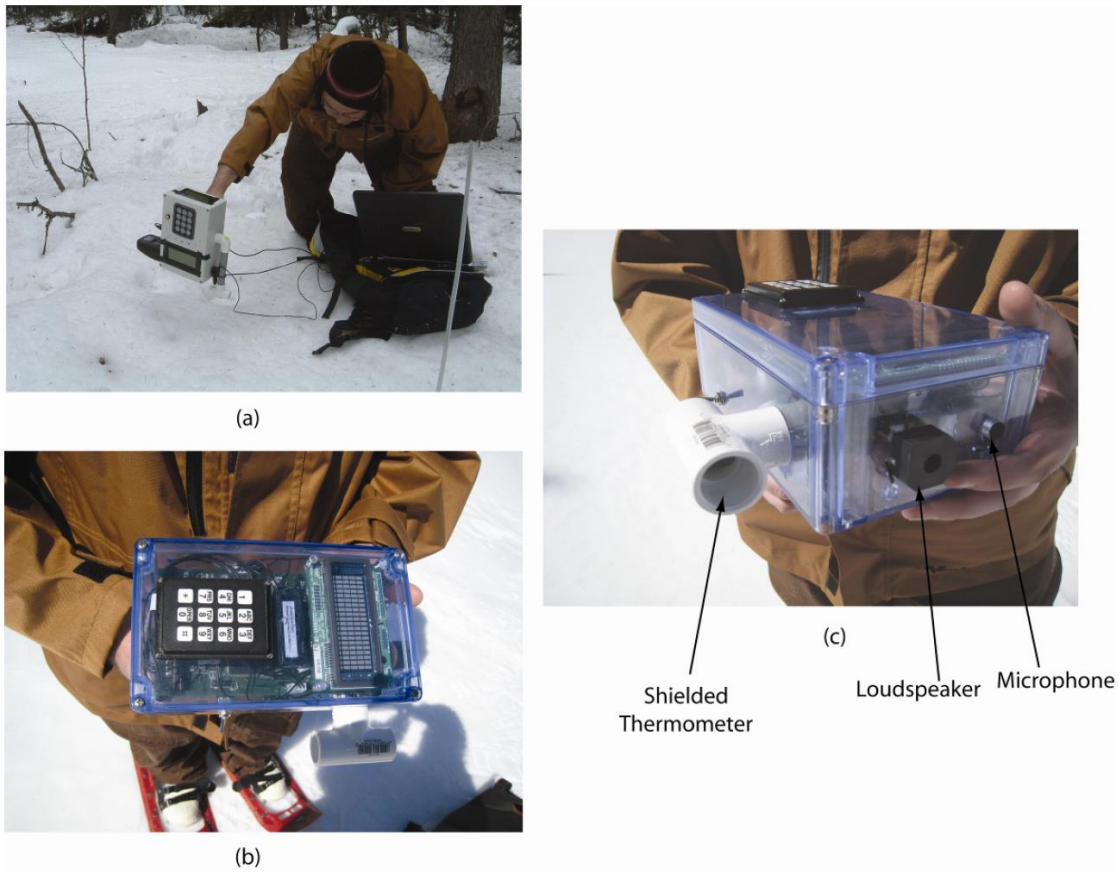

Figure 4.1. Pictures of the two initial prototype devices. The first prototype is shown as (a), whereas the second prototype is shown as (b). A front view of the second prototype shows the positioning of the thermometer, loudspeaker and microphone.

system was positioned above the surface of the snowpack using a pistol-grip handle and the loudspeaker sent a Maximum Length Sequence (MLS) into snow. At the same time that the MLS was produced, the microphone detected the reflection response from the snowpack. An operational amplifier (op-amp) circuit and Analog-to-Digital Converter (ADC) was used to digitize the voltage output from the microphone. The voltage output was related to the instantaneous sound pressure incident at the microphone surface. A time series of sound pressure measurements from the microphone was used as an input for an acoustic model that determined depth-integrated SWE and density of snow. With only one microphone, the acoustic model was recursive, with successive reflections being used to estimate cumulative changes in porosity beneath the surface of the snowpack. The idea is similar to recursive seismic layer-stripping models. Because the model is recursive, errors in previous measurements are

cumulative (Aki and Richards, 2002). Further details related to the sampling system and snow acoustic models are given by Kinar and Pomeroy (2008a, 2008b, 2009).

An initial prototype of a stationary version of the acoustic sensing system was deployed at the Upper Clearing site in the Marmot Creek Research Basin, situated in the Rocky Mountains. As shown in Figure 4.2, a metal mounting stand was used to suspend the acoustic gauge above the surface of the snowpack. For this prototype, six electret microphones were attached to the outside of an enclosure case at an offset distance from a loudspeaker situated inside of another enclosure case. Wires from the loudspeaker and microphones were passed back into a third enclosure case, on the side of which was a PVC Tee pipe set up in a similar configuration to the temperature sensor used for the two initial prototypes. The third enclosure case contained an electronic circuit that was triggered each hour by a datalogger. This electronic circuit was responsible for sending an MLS from the loudspeaker and sampling voltage data from each of the microphones. Three enclosure cases were required to provide space for the loudspeaker, microphones, and processing circuitry, demonstrating that the physical size of the sampling system will increase with a larger number of microphones. This was due to physical size of the microphones and the associated sampling circuitry.

A Campbell Scientific SR50 snow depth sensor was situated next to the prototype. A heat flux plate was buried under the snowpack near the ground surface to provide measurements of heat exchange at the snow-ground interface. An infrared thermometer was used to measure snow surface temperature, and a thermocouple array recorded temperatures throughout the snowpack.

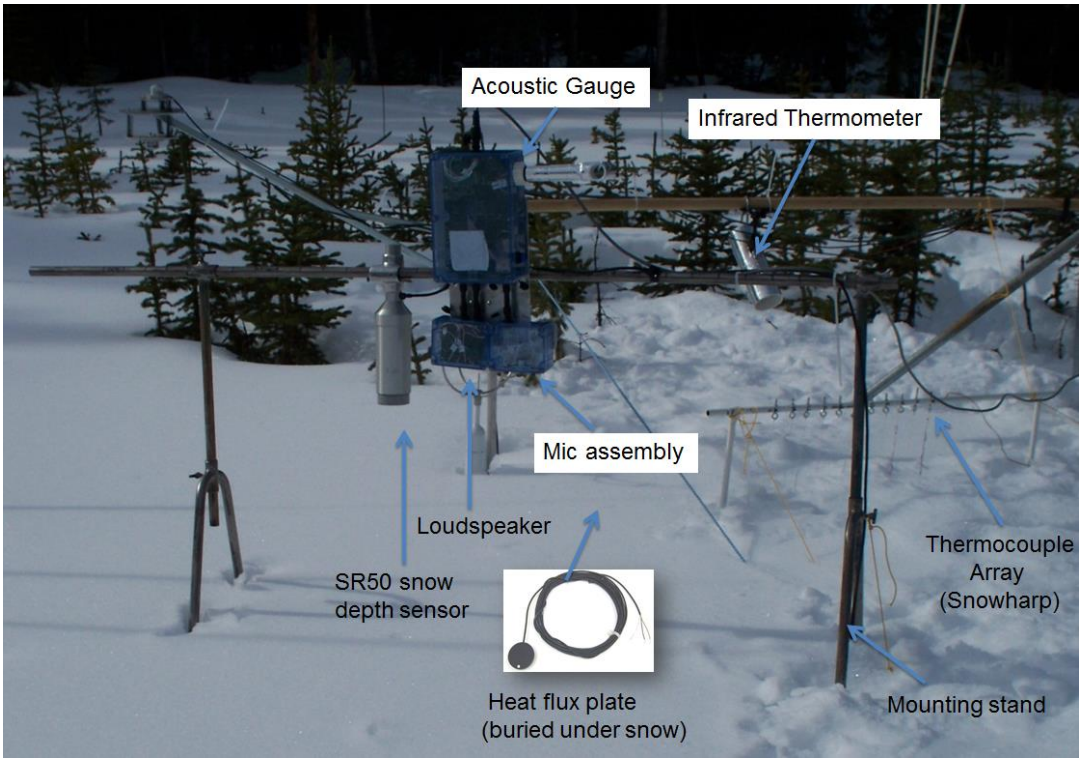

Figure 4.2. Picture of the first stationary prototype device deployed at the Upper Clearing site in the Marmot Creek Research Basin, Rocky Mountains of Alberta.

4.3. Final Prototype Systems

Building on the ideas embodied in the three initial prototype systems, the fourth version of the SAS2 was designed to be used in both portable and stationary configurations. Two copies of the same system were created, one for each configuration. The data collected from this system was sufficient to provide inputs for the UTAM model so that measurements of snow thermal and physical parameters could be obtained. This is because the microphone array consisted of a larger number of sensitive microphones that were used to sample the reflected sound pressure wave; the microphones used for this system had a high sensitivity relative to the other sampling systems; and the sampling system geometry and electronic circuit permitted the detection of small-amplitude reflections from beneath the surface of the snowpack.

4.3.1. Hardware

The sensing system was comprised of a loudspeaker situated at an offset distance from a planar array of 24 microphones on a small printed circuit board (PCB), along with another PCB mounted in an enclosure case. The enclosure case was Bud Industries NBF-32424 with outside

dimensions of approximately 38.5 cm by 28 cm. Figure 4.3 shows a side view of the device, whereas Figure 4.4 shows the front sensing part. Due to the similarity of the two devices, pictures of the SAS2 used for the portable configuration are shown.

The loudspeaker was mounted in the enclosure case by first creating a hole with a circular saw, and then bolting the loudspeaker in place with flat-head machine screws inserted through holes created in the case with a drill. A countersink was used to ensure that the machine screws were flush with the front of the enclosure case. Rubber washers placed on the machine screw threads inside of the enclosure case prevented ingress from water and moisture. A design choice was made to not install a grille on the front of the loudspeaker since this would have changed the acoustic response of the loudspeaker (Newell and Holland, 2006). However, the grille would have protected the loudspeaker from mechanical damage.

The microphone circuit board was also mounted in a similar fashion to the loudspeaker assembly. Holes were created to mount the microphone PCB flush with the side of the enclosure case using flat-head machine screws. Once again, a countersink was used to ensure that the machine screws did not protrude from the front of the enclosure case. Creating a flat sensing surface helped to reduce spurious reflections received by the microphones.

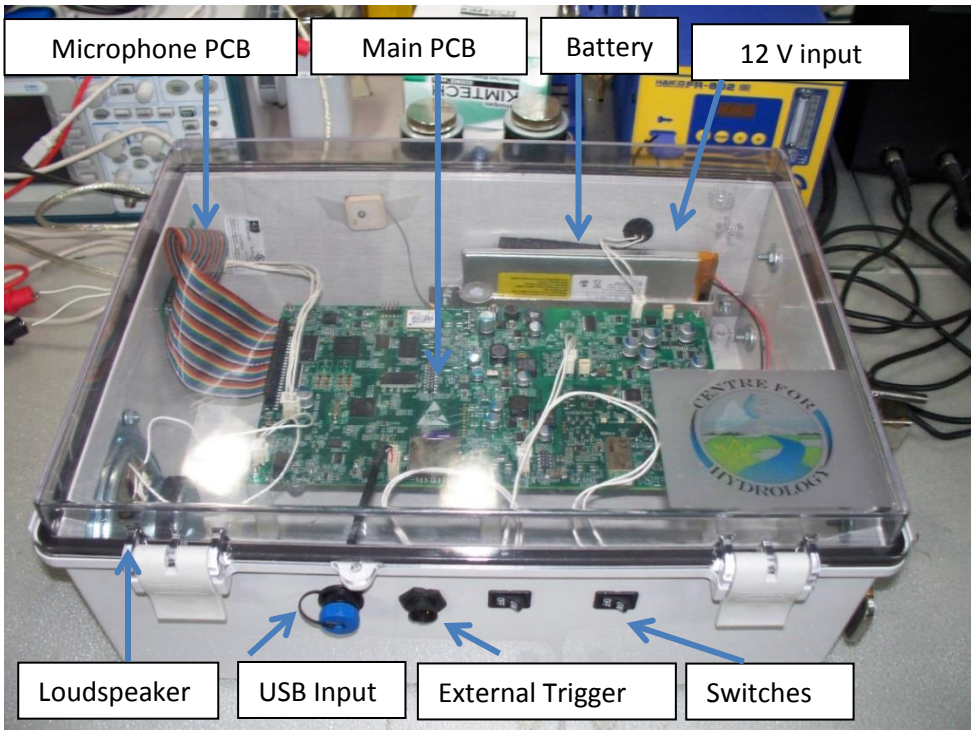

Figure 4.3. Side view of SAS2 in an enclosure box.

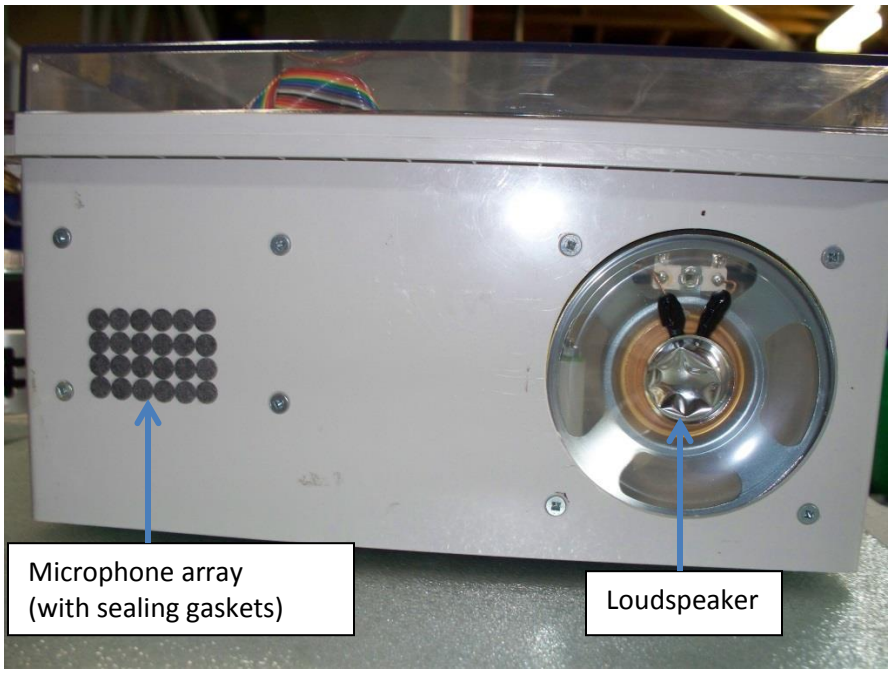

Figure 4.4. Front view of SAS2. The microphone array and loudspeaker is identified on the diagram.

To allow the microphones to sense acoustic pressure waves, 24 holes with a diameter of ~1 mm were created in the front of the enclosure case using a Dremmel tool and a drilling template. The holes acted as waveguides (Blackstock, 2000) for the received reflections, rejecting some sound pressure wave arrivals from angles away from the normal of each microphone.

When the microphone PCB was bolted to the inside wall of the enclosure case, each hole in the case was aligned with a microphone hole on the PCB. Adhesive acoustic vents (GORE part number GAW1020308 from Sealing Devices Inc., Lancaster NY) were applied to the outside of the enclosure case over the top of each microphone hole. The acoustic vent protected the microphones from water and moisture while permitting an acoustic pressure wave to be sensed by each microphone. Acoustic vents were applied to the outside of the enclosure case to prevent the possible formation of a Helmholtz resonator (Rossing and Fletcher, 1995). This may be created if a sealing gasket is placed inside of the case at the back of the microphone PCB (Khenkin and Lewis, 2012).

Holes were created on the sides of the enclosure case for waterproof connectors and switches. The switches were used to turn the system on/off, trigger the system, and turn on/off the onboard battery chargers. A USB input allowed for data to be offloaded from the system. An external trigger input allowed for the system to take a sample using an external switch. A 12 V input allowed for the system to be powered with a battery. Sealing gaskets were inserted between the enclosure case wall and each connector to protect the system from environmental ingress (Figure 4.3).

4.3.2. Mounting Platforms

For the portable system, a mounting attachment was created out of metal using a welding machine and an Oxy-Acetylene Torch. The mounting attachment was bolted on the top of the enclosure case (Figure 4.5). A child chariot carrier (Chariot Carriers Inc., Calgary, Alberta) was modified with a metal stand that mated with the mounting attachment (Figure 4.6). A hole was cut in the bottom of the child chariot carrier and a ski attachment kit replaced the child chariot carrier wheels. The mounting attachment held the SAS2 system above the surface of the snowpack at a distance of no more than 10 cm from the snowpack whilst an operator pushed the chariot carrier over the snow surface. A pushbutton connected via wires to a connector on the side of the enclosure case was used to trigger measurements when the portable mounting platform was not moving.

For the stationary system, a mounting plate was created out of stainless steel and bolted to the back of the enclosure case. The mounting attachment allowed for the acoustic device to be deployed on a boom arm above the snow surface. This deployment strategy is similar to the deployment of electronic devices on a met station (Figure 4.7).

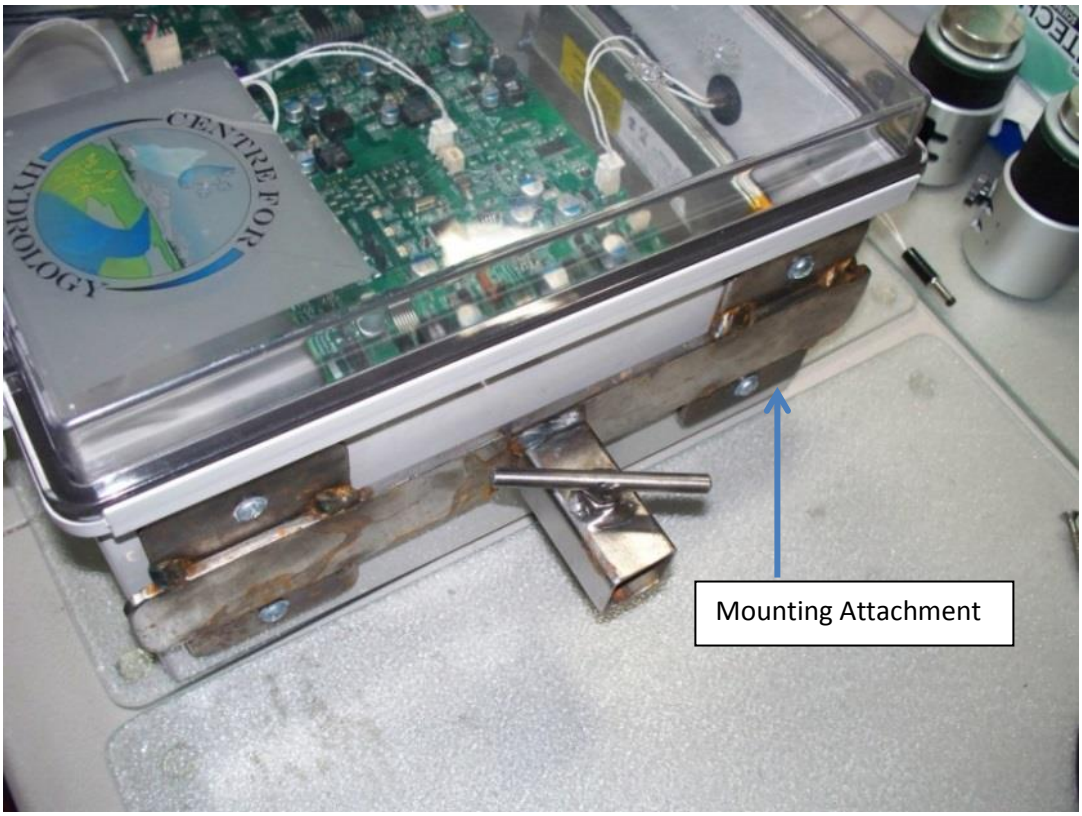

Figure 4.5. Mounting attachment situated on the top side of the portable SAS2.

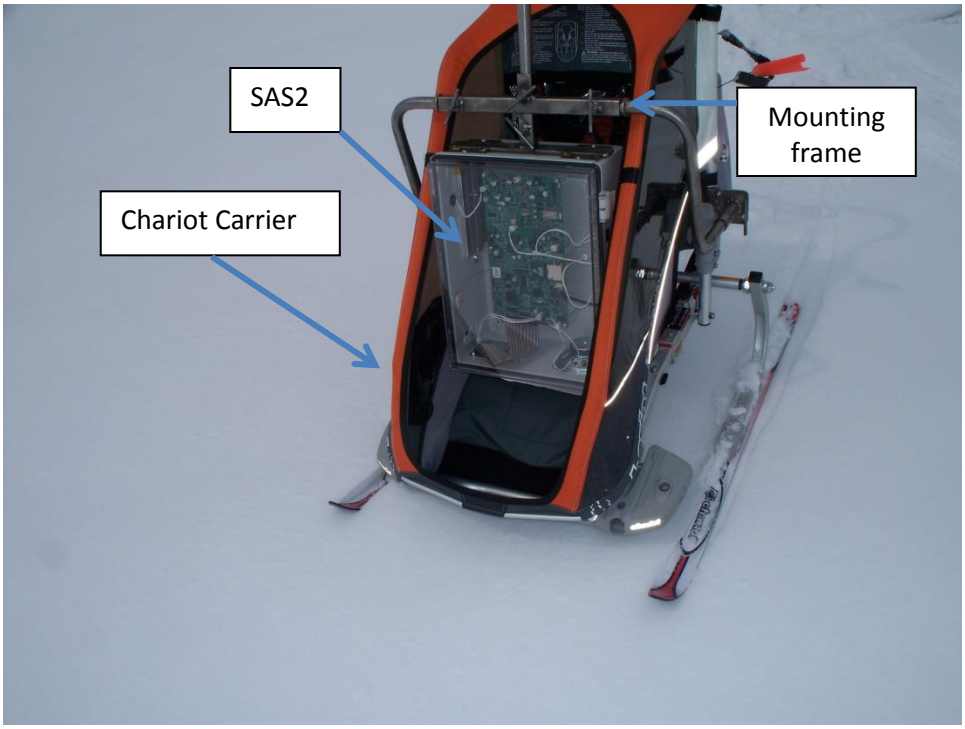

Figure 4.6. Portable version of the SAS2 mounted in a child chariot carrier.

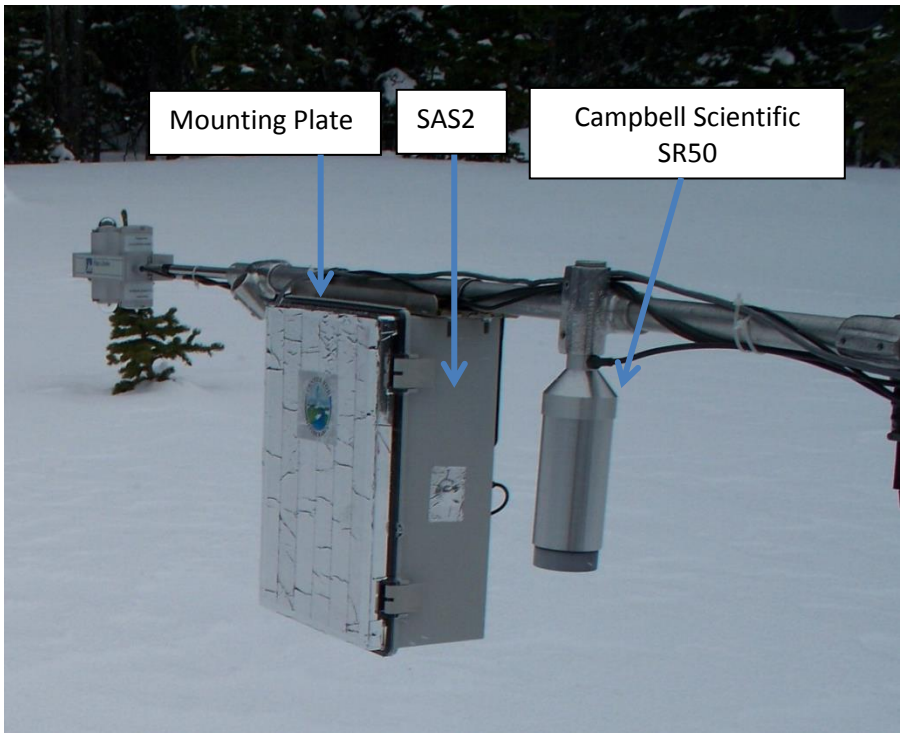

Figure 4.7. Stationary version of the SAS2 mounted on a boom arm.

4.3.3. Electronic Circuits

Figure 4.8a is a picture of the two printed circuit boards (PCB) designed for the SAS2 system. A block diagram of the system is given as Figure 4.8b. The microphone PCB was a 4-layer circuit board, whereas the main PCB was an 8-layer circuit board. Due to the similarity of the two circuit boards, Figure 4.8a only shows the version of PCB created for the portable configuration device. All electronic components used on the circuit board were specified for operation down to -40 °C, the minimum temperature of the industrial operating range. Appendix A provides a complete schematic for the SAS2 system. Parts of the schematic are described below with the appendix page numbers given in brackets (i.e. A.1 for the first page of the Appendix A).

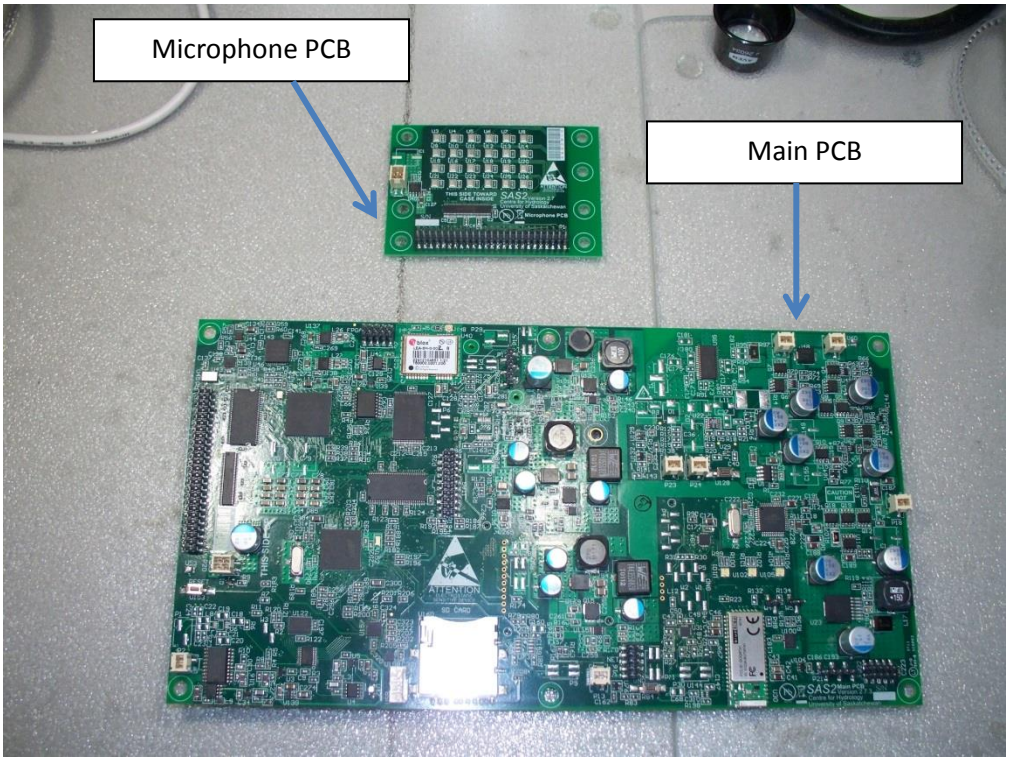

Figure 4.8a. Two printed circuit boards (PCBs) designed for the SAS2 system. The main PCB and microphone PCBs are shown.

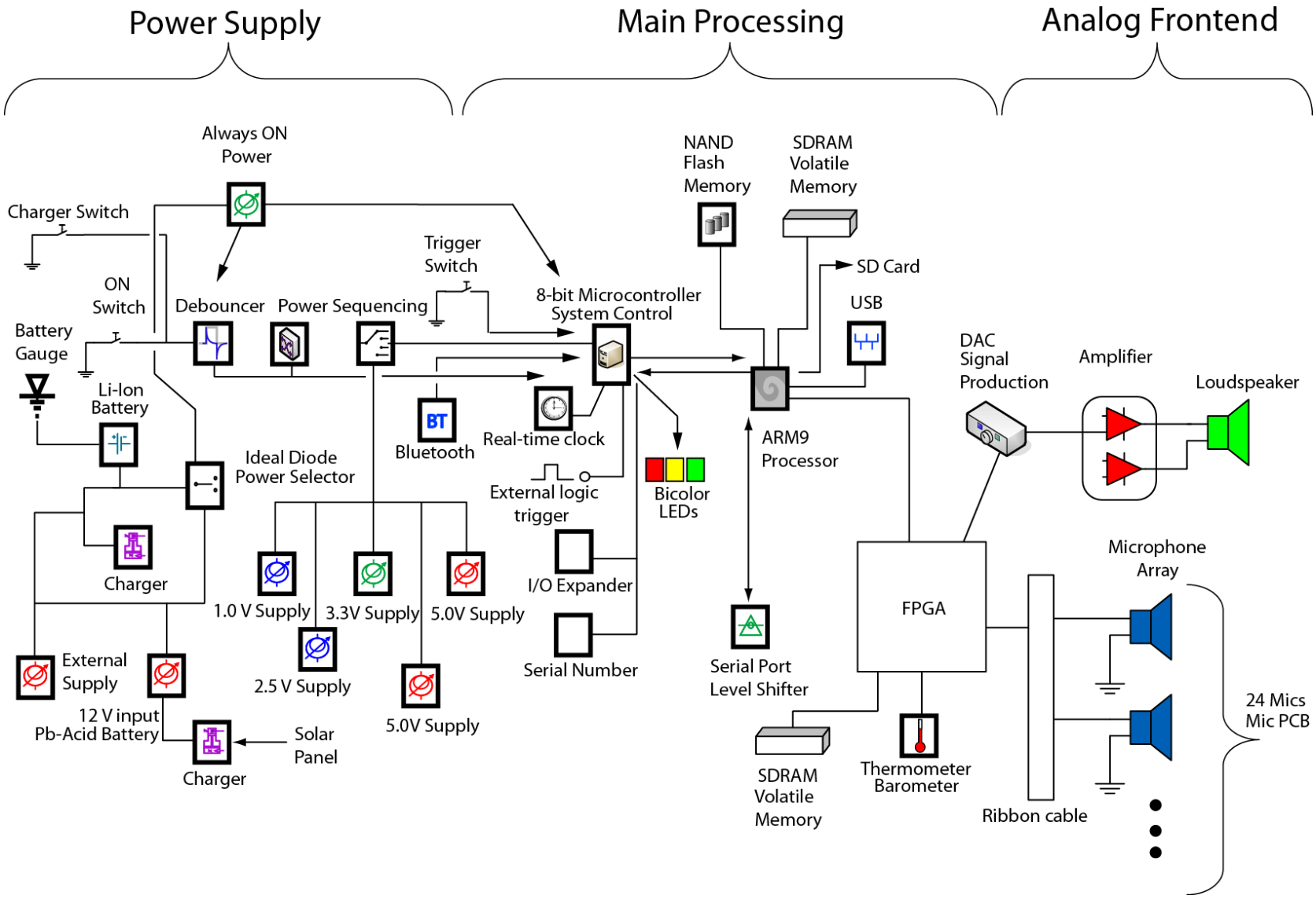

Figure 4.8b. Block diagram of the system, showing the power supply, main processing and analog frontend block.

As shown on pages A.1 to A.2 of Appendix A, and in Figure 4.8b, the SAS2 main circuit board had the ability to be powered by three different power supplies. A 12 V input allowed a lead-acid battery to provide power for the system. Three FETs and an ideal diode controller enabled automatic switching of system load between a regulated DC input from an external supply, the 12 V input, and a 3.7 V Lithium-ion battery with a 12.6 Amp·hr capacity. The ideal diode controller automatically selected the input with the highest voltage. An overvoltage protection controller switched off either the 12 V or DC input if the applied voltage exceeded 19 V or if the inputs were of the wrong polarity. This protected the system from overvoltage due to improper connection to the wrong power supply. A battery charger (page A.9) with a maximum 1 A output current was powered via a connected solar panel input cable. The battery charger circuit was responsible for charging the connected 12 V lead-acid battery. This allowed the SAS2 system to dynamically manage power when used in a stationary configuration above the surface of the snowpack. ESD diodes on each power input protected the system from electrostatic discharge. Since the electric field strength in blowing snow has been recorded as high as $30\ \mathrm{kV\ m^{-1}}$ (Schmidt et al., 1999), ESD protection is necessary to ensure that the circuit will continue operation during the snow accumulation season.

An 8-bit microcontroller (pages A.4) powered with an always-on low-dropout 3.3 V linear regulator (page A.3) was used to control system operation. The signals from rocker switches on the side of the enclosure case were debounced using a hardware circuit before being input into microcontroller port pins. The rocker switches were responsible for signalling the microcontroller to either turn on/off the system, trigger a sample measurement, or to turn on a battery charger. The microcontroller program could selectively re-assign or disable the rocker switches. This allowed for two different configurations of the system, and also helped to prevent the system from being inadvertently switched on or triggered when deployed in a stationary configuration. A 5V-tolerant buffer and inverter implemented an auxiliary logic input to a port pin of the 8-bit microcontroller so an external device (such as a datalogger) could be used to turn on/off the system. A battery-backed real-time clock (page A.5) and I/O expander (page A.7) was connected via I2C bus to the 8-bit microcontroller. This clock was used to obtain a timestamp for every acoustic measurement collected by the SAS2. Also interfaced with the I2C bus was a serial number IC, giving each SAS2 a unique identifier that could be determined by the 8-bit microcontroller.

Port pins of the 8-bit microcontroller were connected to three bicolour LEDs to provide a visual indication of battery charger status and system operation (page A.5). The LEDs were bright enough to be semi-visible in sunlight. When the Lithium-ion battery charger (page A.10) or the Lead-Acid solar panel battery charger was switched on, the 8-bit microcontroller also turned on one of the LEDs. In a similar fashion to the rocker switches, the microcontroller software allowed for any of the LEDs to be disabled or re-assigned to another function. This saved power when the SAS2 system was configured in the stationary application.

The 8-bit microcontroller software was written in the C programming language. The software implemented a user interface with a command-prompt over two serial ports (0 V to 3.3 V levels) at 115200 baud. One serial port was connected to a Bluetooth transceiver (page A.6), allowing the SAS2 system to be remotely controlled by a device such as a laptop. The other serial port was connected to a header for debugging. Removable jumpers on the circuit board also connected this serial port to a serial port of a 32-bit microcontroller by crossing RX/TX lines.

The 8-bit microcontroller communicated with the 32-bit microcontroller during system operation. The user interface implemented by the 8-bit microcontroller enabled setting and reading of the system real-time clock, re-assignment of the LEDs and switches, and for checking voltage inputs and enabling battery chargers. The 8-bit microcontroller also set up a real-time clock interrupt so that the system could be autonomously turned on once every hour to take a measurement. Once the measurement was complete, the 32-bit microcontroller would send a command to the 8-bit microcontroller, instructing that the system was to be turned off. A 15-minute “kill switch” was programmed in the 8-bit microcontroller software to turn the main system power off is the system malfunctioned.

A 5 V-tolerant buffer and inverter were used to sense a USB plug event when a 5 V-powered USB cable was plugged into the SAS2. The output of the buffer and inverter pair was debounced using a hardware circuit. The debounced output was connected to a port pin of the 8-bit microcontroller. The microcontroller software registered an interrupt for the port pin so that a change in voltage level associated with a USB plug event would turn on the SAS2 system. This enabled data to be transferred between the SAS2 and a computer.

To turn on the system, the 8-bit microcontroller used a port pin connected to an FET gate driver IC that provided enough current to saturate an N-Channel FET acting as a switch for main

system power. For maximum power efficiency, three DC/DC buck-boost switcher circuits with inductors (pages A.11 to A.13) were used to provide one 3.3 V and two 5 V power rails current-limited to 2 A. The converters followed the design proposed by Ćuk and Middlebrook (1976), permitting the input voltage to be greater or less than the output voltage. The 3.3 V supply powered most of the ICs on the circuit board, including the microcontroller I/O ports. One 5 V supply powered the loudspeaker audio amplifier, whereas the other 5 V supply provided power for the microphone PCB. Power for the main microcontroller core and the FPGA core were provided by three step-down DC/DC switcher circuits with 1 V and 2.5 V outputs (pages A.14 to A.15). All analog power circuits were designed using SPICE simulations to ensure proper operation under operating loads and environmental temperatures. A switched-capacitor inverter circuit (page A.15) provided a -5 V power supply rail for the Digital-to-Analog Converter (DAC) and op-amp signal chain use to produce the acoustic waveform.

The main microcontroller (page A.16) of the system was a 32-bit ARM9 processor (Atmel AT91SAM9G20B) running the GNU/Linux operating system. The operating frequency of the processor was 400 MHz. GNU/Linux was chosen as the OS for the SAS2 since the Free and Open Source (FOSS) kernel could be easily modified, and there were pre-existing device drivers already available for serial ports and the SD card. All other device drivers for the SAS2 hardware were custom-written for the SAS2 in the C programming language. The userspace program running on the embedded system was written in a mixture of C/C++, with low-level program code written exclusively in C for easy interfacing with the GNU/Linux system (file I/O, device driver accessing and sysfs support). Startup scripts were also written for the embedded system shell. Further information on device drivers and embedded Linux system development is given by Yaghmour et al. (2008) and Venkateswaran (2008).

When the system was turned on, the 8-bit microcontroller power-sequenced the processor core DC/DC switchers. The processor core switchers were enabled 50 milliseconds after the 3.3 V power rail to ensure that transient inrush current at startup did not damage the processor. At startup, the AT91SAM9G20B embedded SAM-BA bootloader checked an SPI flash memory chip (page A.17) for a secondary bootloader (AT9Bootstrap), modified specifically for the SAS2 system. The secondary bootloader set up system clocks, enabled processor communication buses, and then loaded the U-Boot tertiary bootloader. As of the time of writing, the U-boot bootloader is widely used for booting Linux kernels on embedded systems, and it provides a user

interface with a command prompt over a serial port link (Yaghmour et al., 2008). The U-boot bootloader was responsible for loading the Linux kernel into volatile SDRAM memory from a UBIFS partition on the NAND flash IC. The total amount of SDRAM memory on the circuit board was 128 MB and the capacity of the NAND flash was 500 MB. The root file system of the NAND flash was stored on a separate UBIFS partition.

An unused I2C master connected to the main processor via I2C buffers allowed for external interfacing of add-on circuits via a male pin-head connector (page A.18). Moreover, a serial port level-shifter (page A.21) ensured that -5/+5V levels were present on a header intended for interfacing either a datalogger or a modem. This allowed the SAS2 system to communicate with other embedded systems or for communications via a satellite or cellular phone modem. SDIO WiFi interfaces and radio modem interfaces were also built into the system. These features were intended for future application and were not used during deployment of the SAS2.

A full-speed (12 Mbit/s) USB transceiver on the main processor was connected to a waterproof Mini-B connector on the side of the enclosure case via a header and an IC with an integrated USB bus switch and SD card switch (page A.20). The IC was capable of disconnecting the USB bus and the SD card bus from the main processor and emulating a mass storage device as the SD card. This allowed for a USB cable to be plugged into a laptop computer, and for data to be transferred from the embedded system at USB High Speed (480 Mbit/s) rates. A 5 V-tolerant buffer IC connected to a processor port pin enabled the userspace program to determine if a USB plug event occurred. This was accomplished by the main userspace program registering an interrupt with the Linux kernel using the sysfs kernel subsystem.

Data was sampled from each of the microphones on the microphone PCB by an FPGA (pages A.25 to A.30), a reconfigurable logic device situated on the main PCB. The FPGA logic design was created using the Verilog hardware description language (HDL). Because FPGA devices cannot be debugged over JTAG, testbenches were created to model system operation before the design was synthesized in hardware.

An FPGA had to be used to sample the microphones due to the 2.1 MHz sampling rate. The high sampling rate did not permit a single microcontroller to be used due to latency involved in collecting and processing the data. The FPGA was also responsible for the cross-correlation operation required in MLS signal processing.

The digital data from the microphone PCB was streamed to the FPGA over a ribbon cable (page A.30). To ensure signal integrity, each digital bus line on the ribbon cable was paired with a ground wire acting as a shield. This entailed that data was transferred using every second wire on the ribbon cable. On the main PCB, a bus buffer with rail-to-rail switching further ensured signal integrity of the logic signals from the microphones.

The FPGA was responsible for producing a Maximum Length Sequence (MLS) signal using a Digital-to-Analog Converter (DAC) and at the same time sampling acoustic data from each of the microphones (page A.31). The analog design of the DAC and associated op-amp output buffer was conducted with reference to Terrell (1996), and the books edited by Jung (2005) and Kester (2005). The sampling rate of the DAC was 10 kHz, whereas the sampling rate of each microphone was 2.1 MHz. The acoustic data from the microphones was initially cached in a 64 MB SDRAM attached to the FPGA. Volatile SDRAM memory was chosen in lieu of simpler solutions such as SRAM due to the large memory density of the SDRAM. Although this increased the complexity of the logic design expressed in Verilog, it enabled larger amounts of acoustic data to be cached during sampling. Pages A.32 to A.34 are the schematics for the Microphone PCB.

The output of the audio DAC was connected to the input of a 3.5 W audio amplifier (page A.31). A loudspeaker with $8\,\Omega$ impedance was connected to the output of the audio amplifier. The loudspeaker as an electromagnetic transducer was responsible for producing the audible MLS sequence. Because the diaphragm of the loudspeaker was exposed to the outside of the enclosure case, a waterproof loudspeaker was chosen.

The FPGA was interfaced with the main processor via an SRAM bus. The SRAM bus allowed for the microphone data to be quickly transferred to the main processor by having the FPGA act similar to an SRAM integrated circuit. The FPGA state machine also served as an I2C slave, allowing the main processor I2C master to send the FPGA state machine various commands over the I2C bus.

An acoustic measurement was triggered by the 8-bit microcontroller communicating with the main processor over the serial port connection. The 8-bit microcontroller software permitted acoustic measurements to be requested “on demand” using the Bluetooth interface, or on a set time schedule ranging from minutes to hours. On startup, the userspace program running on the main processor registered an interrupt with the serial port connected to the 8-bit microcontroller.

The userspace program then waited in a while loop until the 8-bit microcontroller sent a command over the serial port. After a command was sent and a serial port interrupt occurred, the command string was then read from the serial port char device and matched to a list of possible commands.

After receiving a serial port command requesting an acoustic measurement, the main processor would send an I2C command to the FPGA state machine. The FPGA state machine logic would produce the MLS using the DAC and audio amplifier, and at the same time samples of digital data would be taken from the microphone bus. This is a well-suited operation for an FPGA because unlike most microcontrollers, there can be no sampling latency associated with FPGA logic devices (Maxfield, 2004). Moreover, this eliminates the latency inherent by design in GNU/Linux, despite the availability of various patches and techniques to make this OS a "real –time" operating system (Abbott, 2012; Yaghmour et al., 2008). Once the full MLS sequence had been produced, the FPGA logic would stop sampling microphone data.

During the sampling operation, the microphone data was stored in the SDRAM connected to the FPGA. The main processor polled an I2C slave register exposed by the FPGA state machine to determine when microphone data was available for reading from the SRAM bus. Once the sampling operation was complete and data was available for reading, the userspace program would send another command via sysfs and the I2C bus to switch the FPGA state machine over to SRAM emulation mode. The SRAM emulation mode permitted the main microcontroller to read acoustic data from the SDRAM attached to the FPGA as if the SDRAM was an SRAM.

Reading of acoustic data from the FPGA SRAM interface was accomplished using a custom char device driver written for the GNU/Linux OS. The userspace program would then store the acoustic data in an array. The array was cached in local SDRAM memory attached to the main processor so it could be passed to a function responsible for running an acoustic model to extract snowpack parameters.

Since the SD card was mounted as a directory on system startup, the GNU/Linux userspace program utilized ordinary file I/O operations to write the acoustic data to SD card along with a timestamp requested from the real-time clock interfaced with the 8-bit microcontroller. To provide visual indication of the end of the sampling process, the main processor instructed the 8-bit microcontroller to toggle one of the bicolour LEDs. Alternately, if

the 8-bit microcontroller had turned the system on for acoustic measurements taken autonomously on a time schedule (i.e. once an hour), power to the main processor would be turned off after the SD card and other file systems had been un-mounted. Un-mounting of file systems is necessary before shut-down to make the SAS2 power off in a known state, and to ensure that the non-volatile UBIFS on the NAND flash is not inadvertently corrupted, despite the resilience of this file system to power cuts.

4.3.4. Microphone Selection

The microphones used for the SAS2 are classified as Microelectromechanical systems (MEMS) technology (Lyshevski, 2005), where the sensor is a mechanical device with physical dimensions measuring in the micrometer to millimeter range. The microphone selected was the omnidirectional ADMP421 from Analog Devices (Norwood, Massachusetts, USA). This microphone was initially selected for its small size (3 mm by 4 mm by 1 mm), enabling an array of microphones to be created on a PCB. Since the microphone is small relative to the acoustic wavelengths of sound being measured by the SAS2 system, it is suitable for measuring lower frequencies of sound. When the wavelength of the incident sound pressure wave approaches the size of the microphone, acoustic measurements will be inaccurate due to reflections from the microphone itself (Raichel, 2006).

Moreover, since the microphone contains an Application-Specific Integrated Circuit (ASIC) (Barr, 2006) with an oversampling 1-bit Delta-Sigma ADC (Candy and Temes, 1991), there is no need to digitize voltages from each microphone. The digitized acoustic data is available as a Pulse-Density Modulated (PDM) bitstream sent over the ribbon cable to the FPGA on the main circuit board. This eliminates the need for an op-amp and ADC front-end for each microphone and simplifies signal processing, as discussed in Chapter 2.

The digital microphone sensitivity was specified in the datasheet as typically -26 dB full-scale, measured by the manufacturer using a nominal 1 kHz source at 94 dB SPL. The input noise level for the digital microphone is $L_n = 32$ dB SPL (Lewis, 2011). This represents the smallest SPL that can be measured by the microphone, since once a signal amplitude is less than the inherent noise level of the sensing system, it cannot be measured (Smith, 2002). Since the microphone is an electromechanical measuring device (Kinsler and Frey, 1962), there may be changes in the noise level with changes in temperature, air pressure, and relative humidity. A

measurement of changes in microphone noise level is outside of the scope of this thesis since it would require an anechoic chamber with adjustable environmental parameters.

For purposes of assessing the suitability of the ADMP421 for the SAS2 acoustic sensing application a sensitivity analysis was conducted. As shown in Figure 4.9, assume that the SAS2 is situated above a snowpack at a maximum distance of y_a. The microphone assembly and loudspeaker are situated in a bistatic sonar configuration above the surface of the snowpack. As an approximation, the snowpack is taken to be an effective acoustic medium. This is similar to the notion of lumped models in hydrology (Ponce, 1989). Furthermore, assume that under the snowpack is a frozen ground surface that reflects the sound wave.

Assume that an MLS is sent from the loudspeaker into the snow. The sound wave travels through the snowpack, is reflected by the ground surface, and is detected in the air medium by an ADMP421 microphone situated in the microphone assembly.

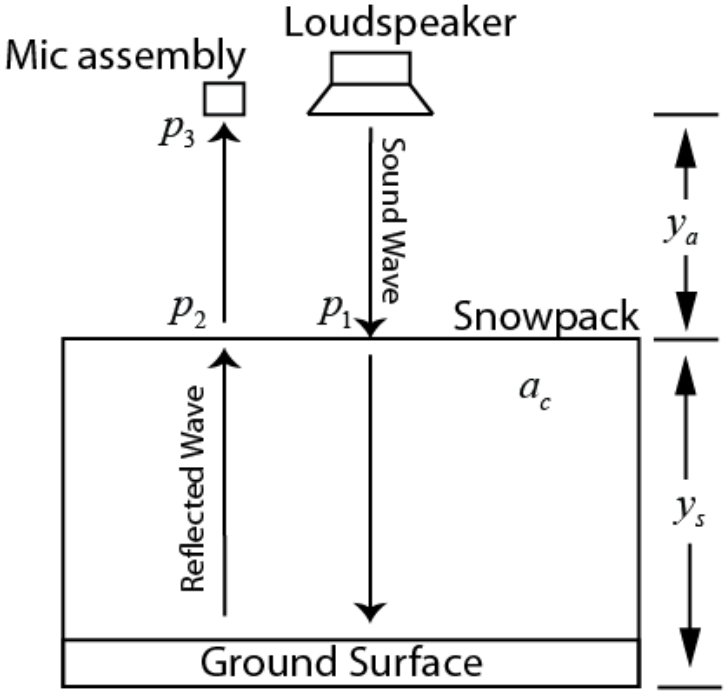

Figure 4.9. Physical system used for conducting a sensitivity analysis used for microphone selection. A loudspeaker and microphone assembly are situated at a distance of y_a above the surface of the snowpack in a bistatic sonar arrangement. The snow depth is y_s, and the "lumped" attenuation coefficient of the snowpack is a_c. The RMS wave pressure at the

surface of the snowpack is p_1, whereas the RMS pressure of the reflected wave exiting the snowpack is p_2. The RMS pressure of the sound wave at the microphone assembly is p_3.

The attenuation coefficient of snow at the maximum MLS bandwidth frequency is given by a_c. Taking the snowpack as an effective acoustic medium a_c is the mean attenuation coefficient for the snowpack. Since, in a similar fashion to most porous media (Allard and Atalla, 2009; Stoll, 1989), the attenuation of sound in snow is greater at higher frequencies, this a_c value represents the maximum attenuation coefficient that can be expected for snow. The attenuation of sound in air is negligible for audible frequencies of sound less than 20 kHz (Rossing and Fletcher, 1995).

The loudspeaker is assumed to be a point source situated on a reflective surface half-space that is the SAS2 enclosure case. As measured in the preceding section, the SPL of the loudspeaker source is taken to be $L_s = 120$ dB at a distance of $y = 5$ cm from the dust cap of the loudspeaker source.

Although sound pressure and sound power are not the same physical quantities, the sound power of the source is estimated in Watts as P using Equations (4.1) and (4.2) below. Assuming hemispherical propagation of a point source, Equation (4.1) is given by Chadderton (2013), whereas Equation (4.2) is given by Crocker (1998), with a reference pressure P_0. Both equations are presented in re-arranged versions. The directionality factor $S_0 = 2\ \text{m}^2$ is for a sound source on a reflective surface half-space.

$$L_{\text{W}} \approx L_s - 10\log_{10}\left(\frac{S_0}{4\pi y^2}\right) \approx 102\ \text{dB} \tag{4.1}$$

$$P = P_0 10^{L_W/10} = 0.0158\ \text{W} \tag{4.2}$$

$$P_0 = 1.0\times10^{-12}\ \text{W}$$

For hemispherical propagation of the wave in the air medium, the RMS pressure p_1 of the sound wave from the loudspeaker at the snow surface is (Raichel, 2006):

$$p_1 = \left(\frac{\rho_a c_a P}{2\pi y_a^2} \right)^{1/2} \tag{4.3}$$

$$\rho_a = \frac{p_a}{RT} \tag{4.4}$$

$$c_a = \left(\chi_g R_g T \right)^{1/2} \tag{4.5}$$

In the above Equation (4.3) to Equation (4.5), ρ_a is the density of the air in the medium above the surface of the snowpack, c_a is the speed of sound in the air, y_a is the distance from the SAS2 to the surface of the snowpack, p_a is the barometric air pressure, $\gamma = 1.4$ is the adiabatic index for air, the gas constant for air is $R_g = 287.058$ J kg^{-1} K^{-1}, and the temperature T (Kelvin). Equation (4.4) is the ideal gas law, and Equation (4.5) is given by Raichel (2006). After acoustic-to-seismic coupling of the sound wave to the snow medium (Albert and Hole, 2001; Albert, 2001; Boeckx et al., 2004), the round-trip attenuation of the sound wave through the snowpack as a porous medium is modelled as the incident pressure p_1 scaled by an exponential function (Meyer and Neumann, 1972). Sound pressure transmission coefficients (Blackstock, 2000; Ingard, 1988) represent the fractional amount of sound pressure energy transmitted through the air-snow and snow-air interfaces. The transmission coefficients are Λ_1 and Λ_2. The pressure reflection coefficient (Bjørndal and Frøysa, 2008; Blackstock, 2000) at the ground surface is taken to be the dimensionless value Γ_r. For the pressure wave exiting the snowpack medium, the RMS pressure is expressed as:

$$p_2 = p_1 \exp\left(-2a_c y_s\right) \varsigma \tag{4.6}$$

$$\varsigma = \left|\Lambda_1\right| \left|\Lambda_2\right| \left|\Gamma_r\right| \tag{4.7}$$

In Equation (4.6), a_c is the dimensionless attenuation coefficient at its maximum value and y_s is the snow depth. Assuming that the wave exiting the snowpack has spherical spreading in the air medium, the RMS pressure of the sound wave arriving at the microphone is given by (Smith, 2010):

$$p_3 \approx \frac{p_2}{(y_a)(m^{-1})} \tag{4.8}$$

The pressure p_3 is related to the SPL in decibels by (Raichel, 2006):

$$L_3 = 20\log_{10}\left(\frac{p_4}{p_{ref}}\right) \tag{4.9}$$

$$p_{ref} = 20\times10^{-6}\ \text{Pa}$$

For the sensitivity analysis, assume that the model parameters are within the following ranges, with a baseline parameter being situated near the center of each range. The baseline parameter is the parameter that is held constant in one-at-a-time (OAT) sensitivity analysis designs (Saltelli et al., 2009). The parameter ranges used for the sensitivity analysis are:

- $-40\ °\text{C} \le T \le 0\ °\text{C}$ for the temperature range, with the lowest temperature coincident with the minimum operating temperature of the SAS2 device. The baseline temperature is -20 °C.

- $30\ \text{kPa} \le p_a \le 120\ \text{kPa}$ as the normal range of barometric air pressures. This range includes most barometric air pressures at locations in Canada and on mountain tops. The baseline air pressure is 100 kPa.

- $0\ \text{Np m}^{-1} \le a_c \le 2.0\ \text{Np m}^{-1}$ as the range of maximum snow attenuation coefficients. This range was selected to show the threshold value of $L_n = 32\ \text{dB SPL}$ for the microphone sensitivity, and also to be coincident with the nominal range of snow attenuation coefficients measured by the experiments reported in this thesis. Similar snowpack attenuation coefficients have also been reported by Ishida (1965). The baseline attenuation coefficient is 1.0, in the center of this range.

- $0 \le \varsigma \le 1.0$ as the range of transmission and reflection coefficients. This range includes the complete transfer of sound waves through the snowpack ($\varsigma = 1.0$) and the complete loss of reflected sound waves due to transmission and reflection ($\varsigma = 0$). The complete loss of reflected sound waves will occur if there is a large difference in magnitude between the effective acoustic impedances of the porous medium and the air. Although it is possible for transmission coefficients to be greater than unity, particularly for ocean waves breaking near the shore (Claerbout, 1985),

this phenomenon is not addressed within the context of this model. The baseline parameter is $\varsigma = 0.5$.

- $5\text{ cm} \leq y_a \leq 3\text{ m}$ as the distance from the loudspeaker and microphone array to the snow surface. The minimum value of the range is selected as being coincident with the closest distance that the microphones are placed to the snow surface using the portable configuration, whereas the maximum range is selected as being the maximum distance above the snow surface that the SAS2 would be mounted in a stationary configuration on a met station. The baseline value for this parameter is 1.5 m.

- $5\text{ cm} \leq y_a \leq 5\text{ m}$ as the depth of snow. This includes the range of snow depth found on the prairies (Pomeroy and Gray, 1995) and in some areas of the Rocky Mountains (Erxleben et al., 2002). Although snow depth in the mountains can greatly exceed 5 m (Hood and Hayashi, 2010), particularly for snow accumulation in glaciated areas (Martini et al., 2001), and for Arctic snowpacks that have accumulated in gullies (Woo and Sauriol, 1980), this sensitivity range is chosen to demonstrate the limitations of the acoustic sensing method relative to the microphone technology. The baseline value for this range is 2.5 m.

Figure 4.10 shows a sensitivity analysis of the model parameters. Changes in temperature (Figure 4.10a) cause an approximately linear drop in SPL received at the microphone. Since the change in temperature is associated with a reduction of SPL less than 1 dB, the ability for the microphone to resolve acoustic reflections is only weakly dependent on temperature, given that the noise level does not appreciably change over the temperature range. Alternately, changes in air pressure (Figure 4.10b) demonstrate an approximately linear increase in SPL as well, but the sensitivity of this parameter is similar to that of temperature.

The attenuation coefficient for the snowpack exhibits high sensitivity (Figure 4.10c), with an 80 dB drop in received SPL as a_c varies over the range $0\text{ Np m}^{-1} \leq a_c \leq 2.0\text{ Np m}^{-1}$. The dashed line on the plot of Figure 4.10c is the input noise level of the microphone at $L_n = 32$ dB SPL, showing that when $a_c \geq 1$, the SPL of the reflection at the microphone is under the input noise level and cannot be detected. The reduction in SPL is approximately linear with an increase in a_c.

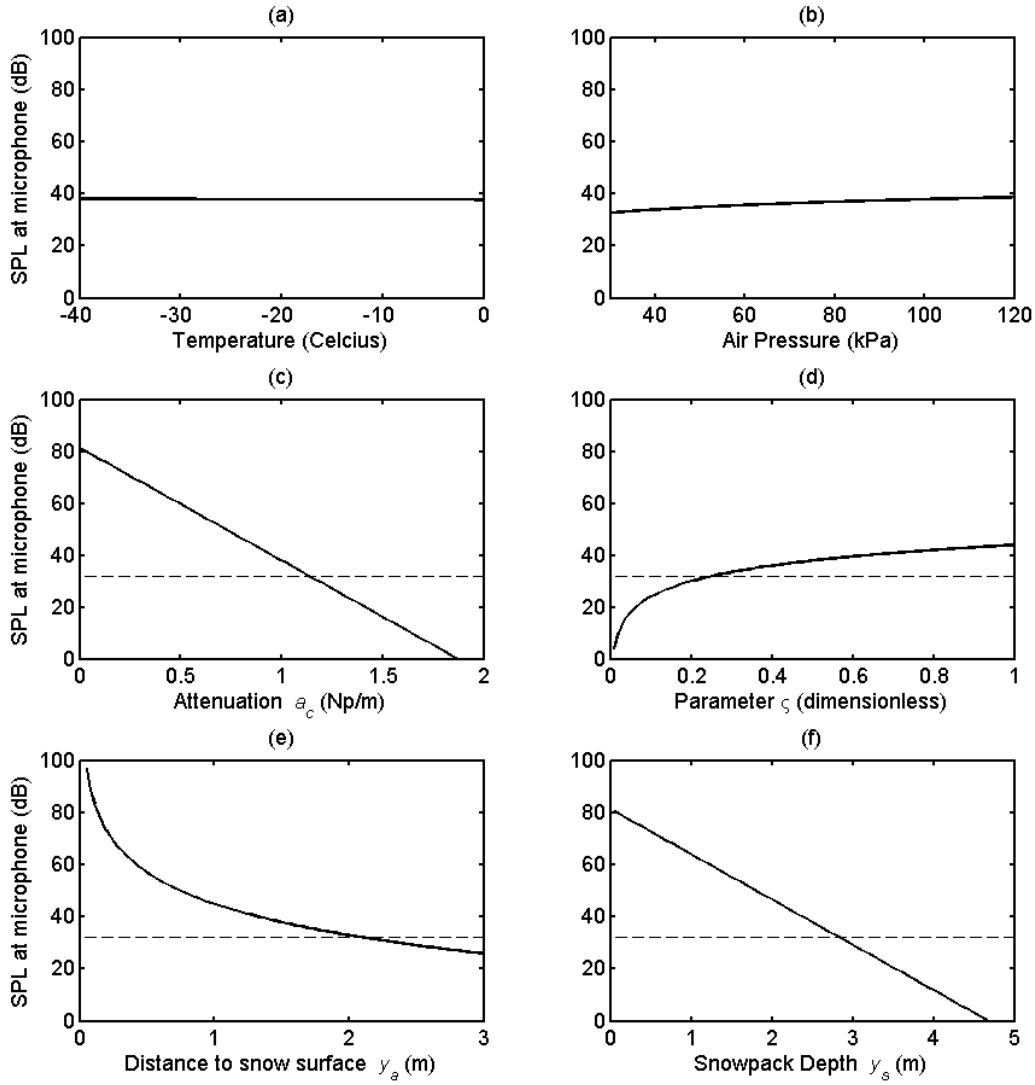

Figure 4.10. Sensitivity analysis of model parameters. The dashed line on the plots represents the $L_n = 32$ dB SPL noise level of the microphone. If the SPL level of the reflection is smaller than the noise level it cannot be detected.

The reflection/transmission coefficient parameter ς exhibits an approximately hyperbolic increase over its range (Figure 4.10d), with the received SPL exceeding the input noise level for $\varsigma > 0.25$. This suggests that at least 25% of the RMS sound pressure energy must be transmitted and reflected through the snowpack for the ADMP421 microphone to detect a pressure wave and make an acoustic measurement.

Figure 4.10e shows that as the loudspeaker and microphone assembly moves further away from the snow surface, the SPL at the microphone exhibits an approximately hyperbolic decrease in SPL. When the distance to the snow surface exceeds 2 m, and the snowpack depth is 1.5 m with $\varsigma = 0.5$ and $a_c = 1.0$, the reflection from the snowpack is under the noise level of the microphone and cannot be detected.

Figure 4.10f shows that as the snowpack depth increases, the received sound pressure at the microphone exhibits an approximately linear decrease. The received SPL is lower than the microphone noise level for snow depths approximately greater than 3 m, demonstrating that the snow depth is also a limiting factor for the detection of reflections from the snowpack.

This sensitivity analysis demonstrated that the ADMP421 microphone is a good choice for the SAS2 system due to the low noise level of $L_n = 32$ dB SPL. Given a range of parameters for snow, a microphone with this sensitivity level is able to detect reflections from the snowpack.

4.3.5. Microphone Sampling Rate

The sampling rate of each ADMP421 microphone was $f_s = 2.1\,\text{MHz}$. Although this sampling rate is within the range of recommended sampling rates specified by the manufacturer, it is customary to use a Cascaded-Integrator-Comb filter (Lyons, 2004; Meyer-Baese, 2007) to downsample the microphone data to a professional audio rate of 96 kHz (Hegde, 2010).

Data was sampled from the microphones at a rate of $f_s = 2.1\,\text{MHz}$ and not decimated until later in the signal processing chain, as discussed in Chapter 3. This was done for three reasons: (1) The MLS reference waveform was measured in an anechoic chamber at the same sampling rate, and the cross-correlation operation to obtain the snowpack filter kernel required that the signals be sampled at the same rate . (2) The sampling rate had to be high enough to resolve spatial differences in time of arrival of a reflected sound pressure wave in order to perform sound speed analysis using seismic algorithms (Claerbout, 1992; Fomel, 2007a). The $f_s = 2.1\,\text{MHz}$ sampling rate was found to be sufficient for this application with the SAS2 system. (3) To prevent temporal aliasing, the sampling rate $f_s > 2 f_{\max}$ must be greater than the

maximum frequency component f_{max} in the received signal. This is the Nyquist criterion (Lyons, 2004; Smith, 2002). Since $f_s = 2.1\,\text{MHz}$ is much greater than audible frequencies of sound, $f_{max} = 20\,\text{kHz}$ and $f_s >> 2 f_{max}$.

4.3.6. DAC Output and MLS Signal Amplitude

Using a DAC voltage of maximum 2.0 V to generate the MLS and a maximum total voltage gain of 36 dB at the audio amplifier results in an MLS being produced by an $8\,\Omega$ loudspeaker at an A-weighted Sound Pressure Level (SPL) of ~120 dB, measured at a distance of ~5 cm from the dust cap of the loudspeaker source in an anechoic chamber with an SPL meter.

The DAC voltage was selected to ensure that the DAC could produce an MLS without large amounts of distortion at the slew rate of the DAC op-amp output buffer. The slew rate is the maximum rate of change of the output voltage (Terrell, 1996). In addition, selection of a 2.0 V input to the audio amplifier ensured that "clipping" did not occur, where the audio amplifier is driven to produce a voltage output greater than its maximum rating (Cordell, 2010). The maximum DAC voltage was fixed and not changed over the entire time of operation of the SAS2 system. Some small changes in the output voltage level with temperature will occur due to tolerances of the electronic components (Kester, 2005). This was mitigated by sensitivity analysis of component changes with temperature during the design phase of the SAS2, and by using higher-precision tolerance of components (i.e 0.1% tolerances).

The input to the audio amplifier was band-limited by a built-in filter at the audio amplifier input. This helped to reduce the distortion (Vanderkooy, 1994) caused by the binary MLS. For future designs, an RC input filter could also be used as a low-pass input filter to the audio amplifier, or the MLS signal could be passed through a digital Butterworth filter before being produced by the ADC. The MLS signal could also be produced by the port pin of an FPGA.

4.3.7. Sound Pressure Level

Ideally, the higher the SPL of the sound wave near the source, the greater the penetration depth of snow and sound wave reflections will arrive back at the microphone array with SPL levels above the input noise level. Due to the fixed maximum voltage output of the DAC, the

maximum SPL of the loudspeaker was close to 120 dB and not changed for any of the experiments conducted with the SAS2 system.

The SPL near the loudspeaker cone is not high enough to cause permanent modification of the snowpack, as occurs when explosives are used for clearing minefields in snow-covered areas (Albert, 1983; Brown, 1979; Johnson, 1990). Since the RMS pressure of a 120 dB source signal is 20 Pa, this value is orders of magnitude lower than the Megapascal range of applied pressures that permanently deform the porous ice skeleton of snow (Johnson et al., 1993). However, additional testing could be done to determine the safety of acoustic system use for human beings with respect to daily noise doses (Raichel, 2006) or the effect of the noise on animals (West et al., 2007), particularly those living in the subnivian layer (Aitchison, 2001).

4.3.8. Length and Sampling Rate of MLS

For MLS testing applications, the duration of the MLS produced by the loudspeaker must exceed the response time of the physical system being tested (Schneider and Jamieson, 1993). Because of this criterion, the duration of the MLS for the SAS2 was selected to ensure that the temporal truncation of the snowpack response did not occur. Let the reflection from the snowpack have a duration t_m, and let $\left(L_M = 2^m - 1\right) \in \mathbb{N} \setminus \{0\}$ be the length of the MLS sequence, with $m \in \mathbb{N} \setminus \{0\}$. For a DAC sampling rate f_{ds} the duration t_{mls} of the MLS sequence is:

$$t_{mls} = \frac{L}{f_{ds}}$$

The MLS duration t_{mls} must exceed the maximum time taken for the sound wave to propagate through the snowpack. Moreover, the bandwidth B of the MLS signal has to be low enough to permit acoustic wave penetration of the snowpack. The bandwidth of the MLS signal is given by (Rife and Vanderkooy, 1989):

$$B = \left(\frac{f_{ds}}{L}\right)\left(\frac{L-1}{2}\right)$$

To ensure that the DAC can produce an MLS sequence without large amounts of distortion, the DAC sampling rate was chosen as $f_{ds} = 20$ kHz. Then, the mathematical analysis below was used to select the MLS length L.

Using the same physical system as shown in Figure 4.9 above and Equations (4.5) and (3.75), simple kinematics was used to calculate the minimum value of $L_{\min}$ required for a sound wave to travel from the loudspeaker through the air and snow mediums:

$$L_{\min} \geq \left\lceil f_{ds} \left(\frac{2y_a}{\left(\chi_g R_g T\right)^{1/2}} + \frac{2y_s}{c_s} \right) \right\rceil \tag{4.10}$$

In the above Equation (4.10), c_s is the speed of the Biot slow wave in the pore spaces of the effective snowpack medium, $\text{ceil}(x) = \lceil x \rceil$ represents the ceiling function, and all other parameters are the same as those previously defined.

The air temperature T, distance to the snowpack surface y_a and snow depth y_s are taken as having the same ranges as parameters used for the sensitivity analysis in Chapter 3. The range of the slow wave speed in snow is taken as $10\ \text{m s}^{-1} \leq c_s \leq 331\ \text{m s}^{-1}$ with recourse to the observations made in this paper and the observations made by Ishida (1965) and Johnson (1982).

The value for L_M is maximized when $y_a = 3\ \text{m}$, $y_s = 5\ \text{m}$, $T = -40\ ^\circ\text{C}$, and $c_s = 10\ \text{m s}^{-1}$. When Equation (4.10) is evaluated using these parameters, $L_M \geq 20393$. Using Equation (3.75), this value for L_M coincides with $t_{mls} = 1\ \text{s}$. To increase the noise immunity of the MLS measurement, the length of the MLS sequence was increased to $L_M = 32767$, corresponding to a total measurement time of $t_{mls} = 1.6\ \text{s}$. Increasing the length of the MLS increases the signal-to-noise ratio (SNR) of the signal by spreading the signal energy over a longer time (Dunn and Hawksford, 1993). In addition, the choice of L_M must also be made to ensure that sampled data from the microphones is small enough to be stored in SDRAM memory by the FPGA.

With $L_M = 32767$ and $f_{ds} = 20\ \text{kHz}$, the MLS bandwidth is $B = 10\ \text{kHz}$. This is the maximum effective bandwidth of sound propagation through snow identified by Lang (1976). Previous experiments sending MLS sound waves through snow have also demonstrated the applicability of frequencies in the range of 20 Hz to 20 kHz for acoustic sensing of snow (Kinar and Pomeroy, 2009).

4.3.9. Loudspeaker

The loudspeaker used for the SAS2 system was the GF1004M from CUI Inc (Tualatin, OR). The frequency response curve of the loudspeaker had a low frequency limit of ~20 Hz. The response varied over 10 dB between 200 Hz and 10 kHz. This makes the loudspeaker suitable for sending the MLS with a maximum bandwidth of 10 kHz into snow. The cone of the loudspeaker was made of waterproof plastic, allowing it to be used in outdoor applications. The diameter of the loudspeaker was $d = 9$ cm.

In a similar fashion to sonar transducers, the diameter of the loudspeaker relative to the size of the enclosure case was chosen to be as large as possible to maximize the acoustic power output of the source and maximize the emitted low frequencies (Wilson, 1989). Since lower frequencies have less attenuation in porous media than higher frequencies (Allard and Atalla, 2009), a large loudspeaker will ensure that low frequencies will be generated and sent into snow, thereby ensuring maximum propagation depth of the sound wave for frequencies in the MLS bandwidth.

4.3.10. Loudspeaker and Microphone Array Separation

The microphone array was situated at an offset distance of 10.8 cm from the loudspeaker. In a similar fashion to bistatic sonar (Cox, 1989) or radar (Willis, 1991), this offset distance was selected to ensure that the maximum input SPL of the microphones was not exceeded during production of the MLS by the loudspeaker. This also ensured that the direct wave (Burger et al., 2006) from the emitted source signal did not mask reflections from the snowpack. In the context of the SAS2 system, the direct wave is the acoustic wave that travels between the loudspeaker and microphones in the air medium and inside the enclosure case without propagating through the snowpack. This offset distance also separated the loudspeaker and the microphones so that the sampling system is similar to a common shot-gather in seismic data collection (Liner, 2004).

Increasing the distance between the loudspeaker and micropone array would increase the relative time of arrival of the sound wave between adjacent microphones, thereby allowing for a smaller microphone sampling rate to be used and potentially increasing the amount of information that can be used in the UTAM model. However, this would not permit the sampling system to be placed into a single enclosure case.

4.3.11. Array Design and Footprint

As shown in Figure 4.11, the microphones were situated in a rectangular grid comprised of 6 rows by 4 columns. For signal processing only using array elements along rows or columns, the planar array becomes a linear array of elements arranged along a line (Skolnik, 2001).

The planar rectangular array (Milligan, 2005) is normally used for beam-scanning, a digital signal processing procedure where the array can be effectively turned to any angle in a hemisphere to eliminate unwanted reflections from a particular direction. Wideband beam-scanning (Liu and Weiss, 2010) is appropriate for use with a microphone array due to the large bandwidth of acoustic transducers.

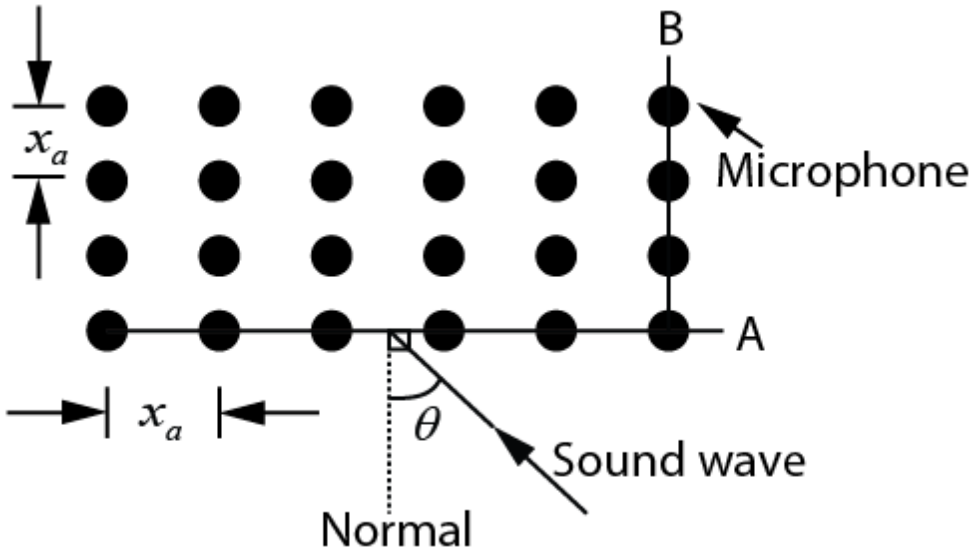

Figure 4.11. Planar microphone array. The spacing between microphones is x_a and θ is the incidence angle of the sound wave relative to the front of the array. There are 6 rows by 4 columns of microphones. Each horizontal row is a linear array "A" and each column is a linear array "B" as marked on the figure.

However, because the microphone holes in the enclosure case acted similar to waveguides for the received acoustic pressure wave, thereby rejecting some spurious reflections from directions other than the snowpack beneath the sensor assembly, beam-scanning was not used for the experiments reported in this paper. This is suitable when the sensing array is situated close to the surface of the snowpack. Only linear arrays in the directions A and B shown in Figure 4.11 were used. This idea is justified below.

To ensure that spatial aliasing of waves received by the microphone array did not occur, the inter-element spacing x_a of the array elements was chosen as (Barger, 1998):

$$x_a < \lambda / 2 \tag{4.11}$$

$$\lambda = c_a / f_a \tag{4.12}$$

In Equation (4.11) and (4.12), λ is the wavelength of the sound pressure wave incident on the array, c_a is the speed of the sound wave, and f_a is the frequency. For $-40\ ^\circ\text{C} \le T \le 0\ ^\circ\text{C}$, the speed of sound in air is $306\ \text{m s}^{-1} \le c_a \le 331\ \text{m s}^{-1}$. Taking the effective range of frequencies for the array as $20\ \text{Hz} \le f_a \le 10\ \text{kHz}$, the minimum value of x_a is such that $x_a < 1.5\ \text{cm}$. Given this constraint, the microphone separation was chosen as $x_a = 7.5\ \text{mm}$. This constraint was also affected by the spacing and layout of the microphones on the PCB.

Assuming an unshaded array, the magnitude of the beam pattern $D_{dB}(\theta)$ as a function of sound wave incidence angle θ of the "A" linear array marked on Figure 4.11 was calculated using Equations (4.13) to (4.15) from Barger (1998). Equation (4.16) is defined by Liu and Weiss (2010).

$$D(\theta) = \left(\frac{\sin(NX)}{\sin(X)} \right)^2 \tag{4.13}$$

$$X = \frac{1}{2} k x_a \sin(\theta) \tag{4.14}$$

$$k = \frac{2\pi f_a}{c_a} \tag{4.15}$$

$$D_{dB}(\theta) = 20 \log_{10} \frac{|D(\theta)|}{\max|D(\theta)|} \tag{4.16}$$

In the above Equations (4.13) to (4.15), N is the number of microphones in the linear array, and k is the wavenumber. For speeds of sound in air ranging between $306\ \text{m s}^{-1} \le c_a \le 331\ \text{m s}^{-1}$ and for frequencies $20\ \text{Hz} \le f_a \le 10\ \text{kHz}$, Figure 4.12 shows how the beam pattern of the array

changes for $N = 6$ microphones over sound wave incidence angles of $\pm 90°$. The $N = 4$ case is similar to Figure 4.12, but with a smaller number of side lobes and a main lobe of slightly greater width. The main lobe is the maximum magnitude response of the array, whereas the side lobes represent smaller magnitude responses (Milligan, 2005).

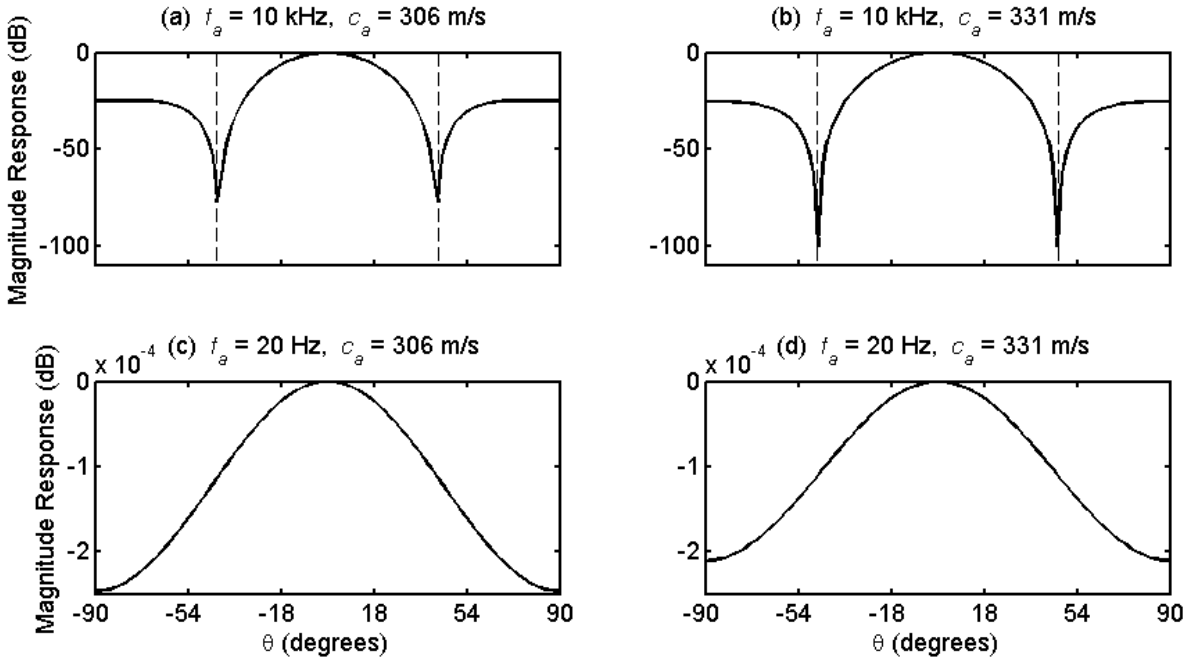

Figure 4.12. Beam pattern of the array for $N = 6$ microphones as a function of the angle of incidence θ of the sound wave. The dashed lines represent the width of the main lobe. For Figures 3.12c and 3.12d, the main lobe width is situated close to $\theta = \pm 90°$.

For an incident wave frequency of 10 kHz and a sound speed in the air medium of 306 m s^{-1} coinciding with a temperature of -40 °C, the central beam lobe is between incidence angles of $\theta = \pm 43°$ (Figure 4.12a). When the speed of sound in air rises with temperature to $c_a = 331 \text{ m s}^{-1}$ but the incident frequency of the sound wave remains the same, the main lobe widens to $\theta = \pm 47°$, with notches of low magnitude (nulls) becoming smaller (Figure 4.12b). For an incident wave at frequency 20 Hz, the nulls are near the broadside extremes of the array at $\theta = \pm 90°$, and the magnitude is mostly constant for sound waves incident to the array at all angles (Figure 4.12c and Figure 4.12d).

This analysis shows that the response of the linear microphone array is most directional for higher reflected frequencies of sound, with low reflected frequencies having the least

directional response. The smallest lobe width of $\theta = \pm 43°$ establishes an upper limit to the effective footprint of the sensing device on the snowpack surface.

In a similar fashion to radar (Yankielun et al., 2004), the footprint in the context of the SAS2 design is the approximate area on the surface of the snowpack that is sensed by the microphone array. Assume that the minimum half-width of the central lobe given in radians is θ_m. For a lobe width of $\theta = \pm 43°$, the half-width is $\theta_m = 43°$. Then the effective sensing footprint x_s of the array on the snow surface is approximated by:

$$x_s \approx 2 y_a \tan(\theta_m) \tag{4.17}$$

For $5\text{ cm} \leq y_a \leq 3\text{ m}$, evaluation of Equation (4.17) gives $9\text{ cm} \leq x_s \leq 5.6\text{ m}$ as the effective footprint on the snowpack surface. The 9 cm effective footprint on the snowpack surface is slightly larger than the theoretical inner diameter of 7.1 cm for the Canadian MSC snow sampler (Goodison et al., 1981), but 5.6 m is large enough for shrubs and vegetation buried beneath the snowpack to cause significant amounts of acoustic scattering in a similar fashion to objects on a seabed (Lurton, 2002). This suggests that wideband beamforming algorithms (Liu and Weiss, 2010) could be applied to reduce the effective footprint area of the imaging sensor. However, the microphone holes in the front of the enclosure case may function as waveguides for the received sound wave.

4.3.12. Snowpack Layer Resolution

Similar to seismic imaging, the smallest resolution of the acoustic measurement in the snowpack is related to the wavelength of the source signal. Assume that the source signal is comprised of a wavelet that propagates through the porous snowpack medium (Aki and Richards, 2002). This is true for an MLS after the cross-correlation signal processing operation has recovered the filter kernel (Borish and Angell, 1983). Then, destructive interference between wavelets reflected from successive acoustic "layers" in the snowpack establishes an imaging resolution (Widess, 1973):

$$\Delta y > \lambda_s / 4 \tag{4.18}$$

$$\lambda_s = c_s / f_a \tag{4.19}$$

For $10\ \text{m s}^{-1} \leq c_s \leq 331\ \text{m s}^{-1}$ and $20\ \text{Hz} \leq f_a \leq 10\ \text{kHz}$ for the MLS bandwidth, the minimum acoustic layer width Δy that can be resolved is $\Delta y > 2.5 \times 10^{-4}\ \text{m}$. This is a theoretical minimum and Δy is dependent on the speed of the sound wave in the porous snowpack medium.

4.4 Anechoic Chamber Measurements

To empirically determine the MLS source signal sent from the loudspeaker as a system response $\mu_k[t]$, the SAS2 system was taken into an anechoic chamber at the University of Saskatchewan (Room 2C96.1, Department of Electrical and Computer Engineering). The anechoic chamber is a room designed specifically for acoustic measurements (Raichel, 2006). Sound-absorbing material and wedges mounted on the walls, ceiling and floor of the room reduce the ambient SPL to a minimum. The dimensions of the room are $6.9\ \text{m} \times 4.5\ \text{m} \times 4\ \text{m}$. Figure 4.14 is a picture of the measurement being made in the anechoic chamber.

The SAS2 system was placed on a specially constructed metal table stand situated at a height of 73 cm ± 5 cm above the metal grating floor. A loudspeaker was situated at a distance of 1.25 m from the microphone assembly on the end of a musician's microphone stand. A cable connected the loudspeaker to the SAS2 audio amplifier. The loudspeaker mounted on the front of the SAS2 enclosure case remained in place during the tests.

The room was closed before measurements commenced and the inside pressure was allowed to equilibrate for 15 minutes. The ambient temperature was ~22 °C. The Bluetooth interface was used to trigger the SAS2 from outside of the chamber, sending acoustic waves from the loudspeaker into the microphone assembly. Twenty measurements in total were taken and one measurement was selected for operational use in the SAS2 system.

Assuming that the room is a cuboid, $a_s = 7\ \text{cm}$ is the dimension of the sound source relative to the longest room dimension $d_r = 6.9\ \text{m}$, and $l_w = 1\ \text{m}$ is the length of the sound-absorbing wedges, the largest wavelength λ_{sr} that can be measured in the room is given by (Ressl and Wundes, 2010):

$$\lambda_{sr} = 2\left[d_r - \left(5a_s + 2l_w\right)\right] = 9.1\ \text{m} \tag{4.20}$$

At a temperature of 22 °C, this corresponds to a cutoff frequency of 37.8 Hz. This is the lowest assumed MLS cutoff frequency for the reference MLS measurement of system response.

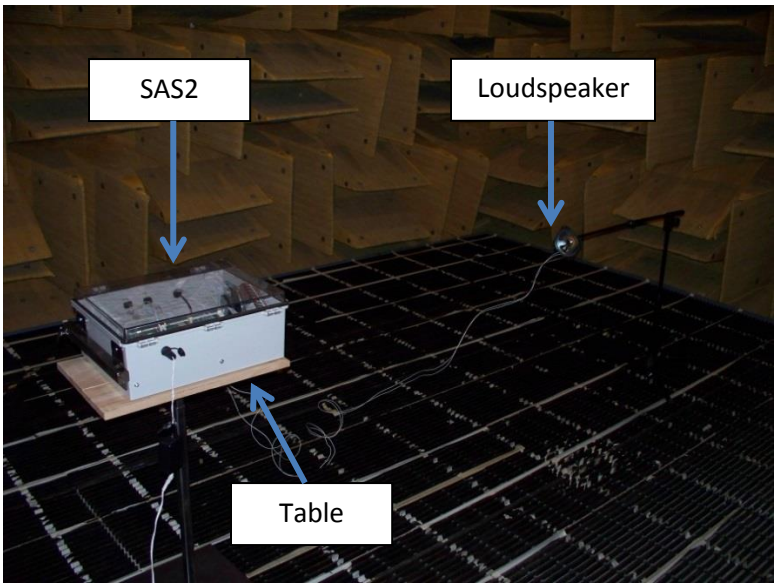

Figure 4.13. Picture of the SAS2 measurement setup in the anechoic chamber.

Figure 4.14 shows a plot of the sound wave detected by one of the microphones in the anechoic chamber for the 5th test, out of 22 tests in total. Signals collected from this test were used as the reference waveforms. Each microphone in the 24 microphone array had a reference signal similar to the one shown. The 5th test was chosen because the amplitude of the signal envelope was more evenly distributed over the time that the signal was produced. Small movements of the loudspeaker on the end of the microphone stand did not always permit the amplitude to be as evenly distributed as the 5th test signal.

Figure 4.15 shows the magnitude and phase of a signal (Figure 4.14) from the 5th test, whereas Figure 4.16 shows the magnitude and phase from each of the 22 tests. The detected waveform frequency response is not flat (i.e. similar to Figure 3.10c) due to the frequency response of the loudspeaker convolved with the frequency response of the MLS. Signal averaging of all the test signals was not used due to small differences in the phase of the waveform resulting due to vibrations of the loudspeaker on the end of the microphone stand

(Figure 4.16b). This was a disadvantage of the measurement setup and necessitated the selection of a single reference waveform. Although a metal retaining stand for the loudspeaker was used in preliminary tests, this retaining stand modified the loudspeaker frequency response so that it could not be used as a reference signal in the signal processing inversion.

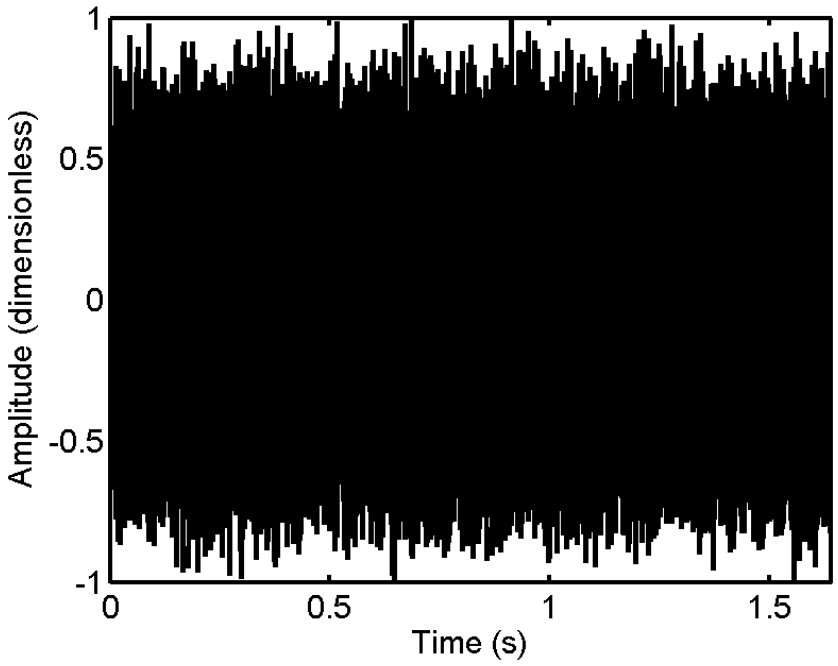

Figure 4.14. Plot of the sound wave detected by one of the microphones in the array for use as the reference signal. The sound wave was detected in the anechoic chamber.

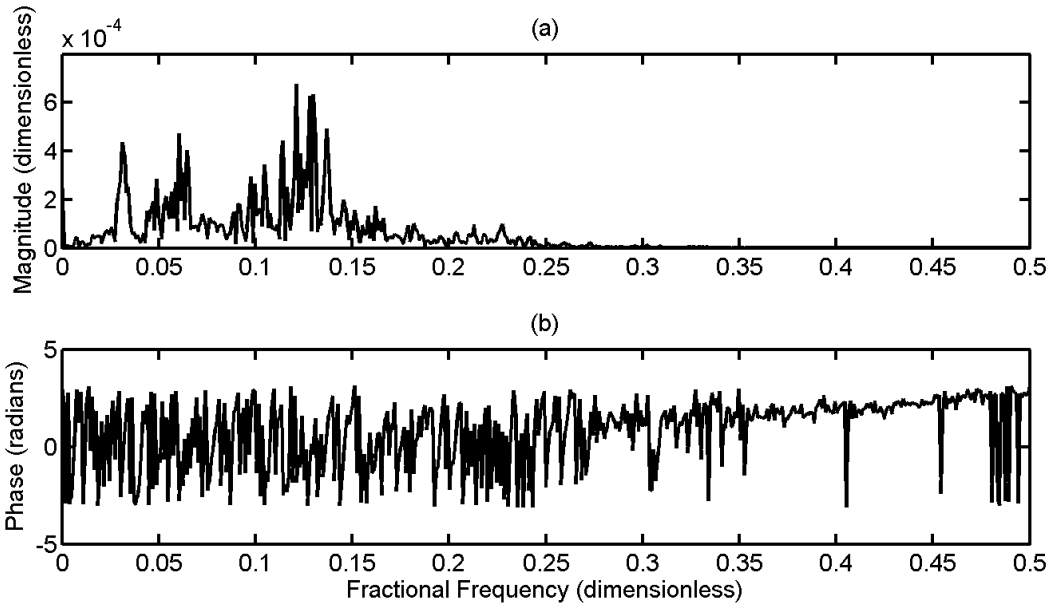

Figure 4.15. Plots of the magnitude and phase of the reference signal. The phase is constrained to the interval $[-\pi, \pi]$.

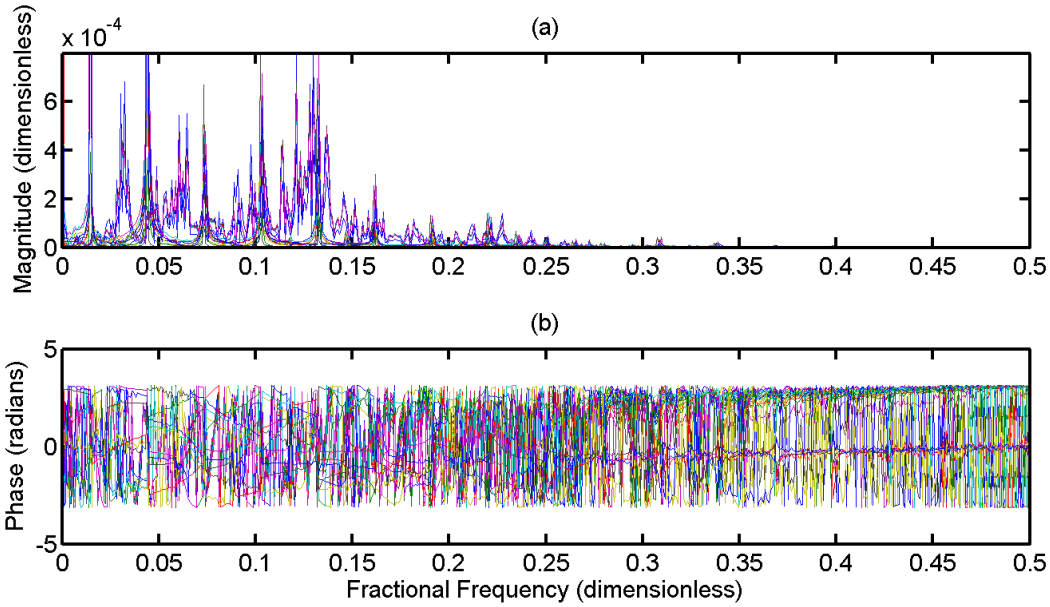

Figure 4.16. Plots of the magnitude and phase of all signals collected in the anechoic chamber. Differences in color represent the different signals collected. This shows differences between the test signals collected in the anechoic chamber. The phase is constrained to the interval $[-\pi, \pi]$.

CHAPTER 5
FIELD LOCATIONS AND DATA COLLECTION

5.1. Introduction

To test the SAS2 on snow, ten field sites were selected in the Canadian Rocky Mountains of Alberta, in western Canada. The geographic area of the Canadian Rockies was used for these acoustic experiments for the following reasons.

(1) The Canadian Rockies are a natural laboratory with a wide range of vegetation types (Chinnappa and Hallworth, 1997; Habeck, 1987; Moss, 1955; Scotter and Zoltai, 1982), ecotones (Howell and Harris, 1978; Kernaghan and Harper, 2001; Macdonald, 1987) and mass and energy balances (Ellis et al., 2013, 2011; Helgason and Pomeroy, 2012a, 2012b; Pomeroy et al., 2012). Due to changes in elevation, uneven topography, forest type and canopy cover, snowpacks develop with large variability in depth, density, temperature and wetness. These factors provide a number of ideal locations for testing the SAS2 system developed in this thesis.

(2) Snowpacks in the Canadian Rockies provide water in the form of snowmelt to the Bow River, the City of Calgary, and the South Saskatchewan River (Pomeroy et al., 2007a). Moreover, mass and energy exchanges between the atmosphere and snowpacks in the Rockies influence local climatology (Helgason and Pomeroy, 2012b). Tests of the SAS2 in this environment validates the use of acoustic technologies for a future snow observation network that studies the availability and change in water resources to ensure adequate human use and consumption as well as a better understanding of the relationships between snow, water availability and climate.

(3) Locations with large changes in environmental conditions can be easily accessed by road or by a brief hike and sites with widely-varying changes in snowpack properties are situated close together, thereby simplifying the ability for data collection.

(4) The Marmot Creek Research Basin is an experimental site in the Rockies currently operated by the Centre for Hydrology. Because the watershed has been used extensively in the past and present for hydrological research (Forsythe, 1997; Golding and Swanson, 1986; Harlan, 1969; Storr, 1972, 1967), it provides a location where instrumentation can be set up and periodically checked by field personnel.

(5) The Centre for Hydrology has an office and laboratory facility situated at the University of Calgary's Barrier Lake Field Station located in the Kananaskis Valley. This simplifies the logistics of accessing the field sites and deploying instrumentation.

The geographic locations, site elevations and change in elevation at each field site are listed in Table 5.1. The sites span a large geographic area of the Canadian Rockies. The largest north-south line distance between sites is 160 km. The sites range in elevation from 1523.9 MASL to 2102.7 MASL. Descriptions of the sites are given in the next section.

5.2. Sites and Deployment

5.2.1. Upper Clearing Stationary (UCS) Site

The Upper Clearing (UCS) site was situated in the Marmot Creek Research Basin (MCRB). MCRB elevation ranges from 1600 MASL to 2825 MASL, placing the UCS site near the lower reach of the basin. The MCRB is near to the Nakiska Ski Resort, and the UCS site was accessed during the winter months by hiking up a snowmobile path that services this resort. The UCS site was situated 400 m from the snowmobile path.

#	Name	Acronym	Latitude (°N)	Longitude (°W)	Minimum Elevation (MASL)	Maximum Elevation (MASL)	Max Change (MASL)
1	Upper Clearing Stationary	UCS	50.956524833000004	115.17526599999999	1846	1846	0
3	Boulton Campground	BC	50.637631167000002	115.107010333	1687.2	1722.8	35.6
6	Bow Summit	BS	51.715226999999994	116.4957945	2063.5	2102.7	39.2
2	Upper Clearing Portable	UCP	50.9564405	115.17563699999999	1837	1853.9	16.9
4	Sawmill Creek	SC	50.747676167000002	115.245452	1825.6	1857.1	31.5
7	Bow Meadow	BM	51.703477332999998	116.476415833	1995.7	2057	61.3
8	Bow Lake	BL	51.673902832999998	116.451093667	1934.4	1941.1	6.6
9	Nakiska Ski Hills	NSH	50.9427005	115.153063667	1523.9	1544.7	20.9
5	Black Prince Cirque	BPC	50.704814832999998	115.197102	1720.8	1751.2	30.4
10	Icefields Parkway Forest Site	IPFS	51.722083166999996	116.492946	2066.2	2089.7	23.5

Table 5.1. Names, acronyms, geographic locations and minimum and maximum elevations of acoustic sampling points at each site. The elevations are given in Meters Above Sea Level (MASL). The maximum change in elevation at each site is also given.

Figure 5.1 shows the stationary SAS2 setup at the UCS site, next to a meteorological tower near the centre of the clearing. Guy wires used to support the permanent meteorological tower are visible in the background. Surrounding the clearing is a forest of subalpine fir (*Abies lasiocarpa*) and Engelmann spruce (*Picea engelmanni*). Young spruce trees, small shrubs and sparse grass were buried under the snow in the clearing. Some of these trees are visible in the background of the picture.

The SAS2 was located on a boom arm suspended over the snow surface. An external solar panel provided auxiliary power to the SAS2 so that a 12 V lead acid battery could be charged. Next to the SAS2 was a Campbell Scientific SR50 ultrasonic snow depth sensor. On the end of the boom arm was a Kipp & Zonen CNR1 net radiometer to measure the incoming and outgoing shortwave and longwave radiation. A cup anemometer measured wind speed. A Vaisala HMP45CF hygrothermometer in a radiation shield measured air temperature and relative humidity near to the datalogger enclosure box. A shielded narrow beam Exergen IRTC infrared (IR) thermometer measured snow surface temperature near the met station. At the bottom of the snowpack was a heat flux plate (HFP01) to measure heat transport between the ground and snow surface.

A Type E thermocouple array developed by Helgason and Pomeroy (2012) and controlled by a multiplexer was buried under the snow surface at the position indicated in Figure 5.1. This is referred to as a "snow harp." The thermocouple array installation is shown as Figure 5.2, and dimensions of the thermocouple array are shown in Figure 5.3. The thermocouple array was composed of 11 vertical wires situated parallel to the ground surface. Each wire was suspended from a metal frame approximately 60 cm high. The distance between each wire was 3 cm. The array was located close to the datalogger box (Figure 5.2) since the wires connecting the thermocouples to the datalogger were short.

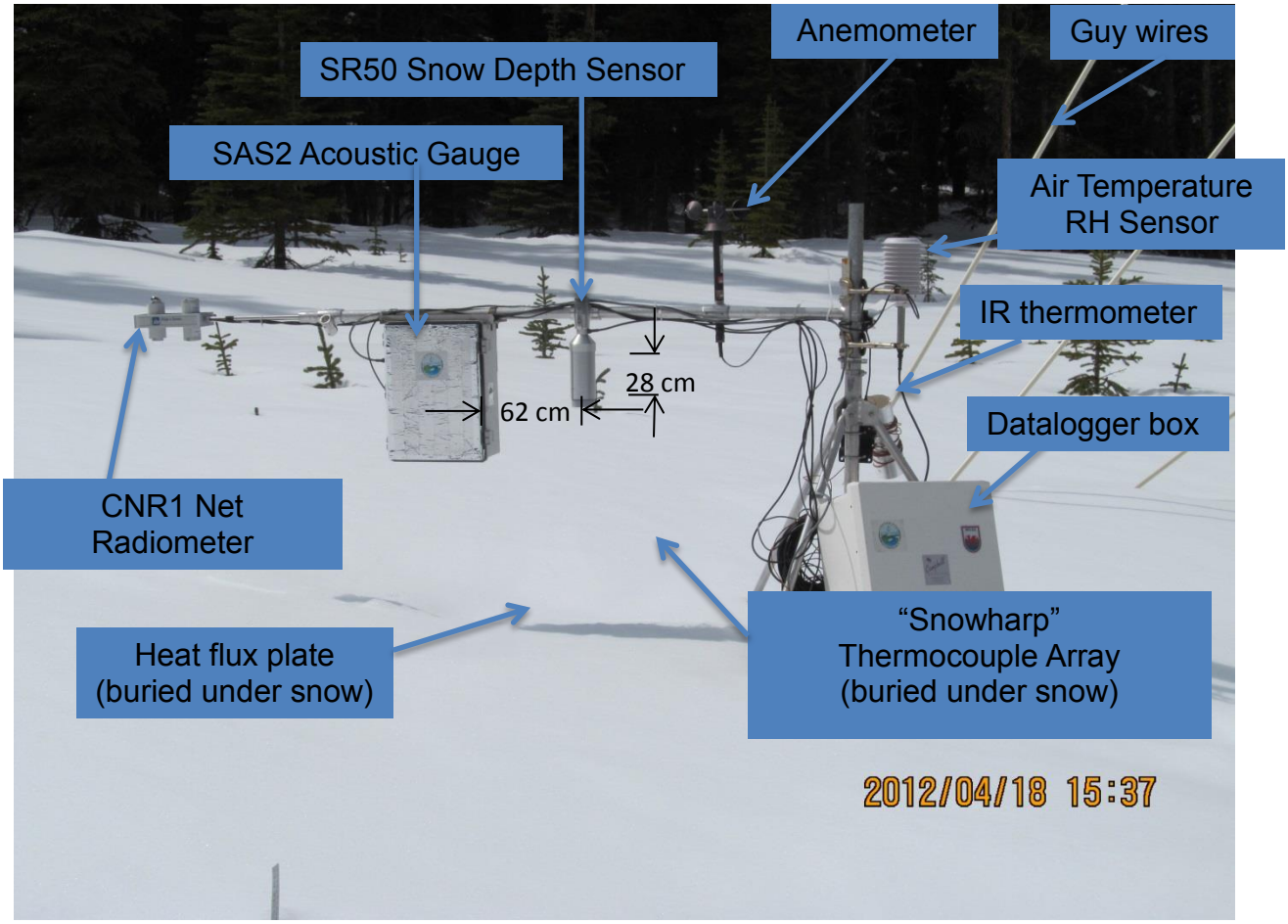

Figure 5.1. Stationary SAS2 setup at the UC site. Equipment deployed at the UC site is listed on the diagram as well as the distances between the ultrasonic SR50 and the SAS2.

Figure 5.2. Stationary SAS2 setup at the UC site showing the position of the snowharp thermocouple array relative to the met station setup.

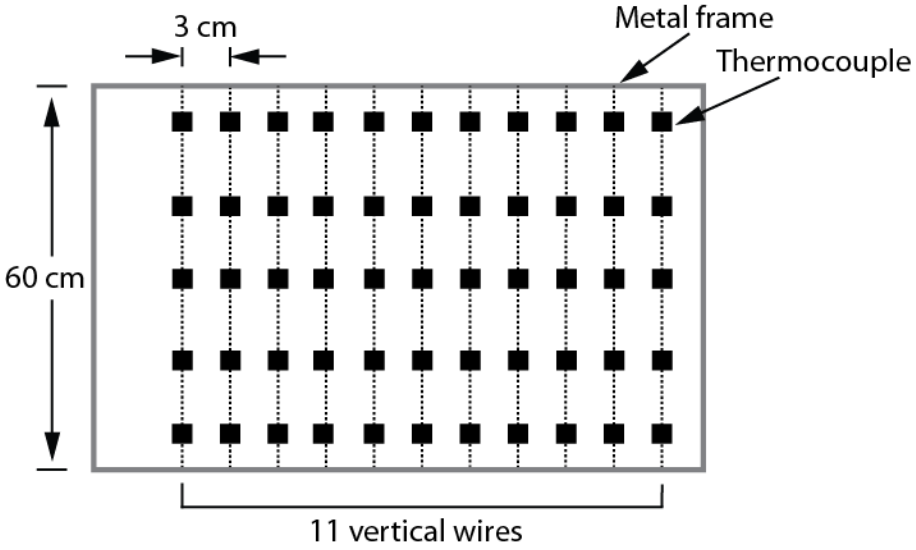

Figure 5.3. Frame with thermocouples referred to as a "snowharp."

The SAS2 was programmed to take one acoustic sample per hour. The system automatically turned itself on, produced the sound wave, and then switched itself off. The one hour sampling rate was selected for two reasons. Snowpack evolution models and cold region hydrological process models are run using timesteps of at least one hour (Pomeroy et al., 2007b). These models have been validated using field observations of snow. This strongly implies that sampling of snowpack properties on a one hour time scale is likely suitable for acoustic observations. The second reason for the one hour sampling rate is due to battery capacity and system power consumption. To ensure that the system could be powered by a 12 V battery with finite capacity throughout the winter, the sampling rate had to be chosen to minimize power consumption.

From instruments deployed at the UCS site, a datalogger was used to sample: (1) snow depth; (2) incoming and outgoing solar radiation; (3) windspeed; (4) air temperature; (5) relative humidity; (6) snow surface temperature; (7) heat flux; and (8) snowharp temperatures once every 15 minutes. This is the same thermocouple sampling rate used by Brandt and Warren (1997), which was suitable for validation of an implicit finite-difference model of heat conduction in snow. Because the values sampled were logged to internal datalogger memory, the sampling rate was chosen to minimize the amount of time between samples and maximize the number of samples that could be stored. The thermocouple array was sampled once every minute and temperature measurements averaged by the datalogger to record one temperature per thermocouple once every 15 minutes. This sampling rate is four times greater than the sampling rate of the SAS2 to provide indication of changes in parameters between SAS2 samples.

The site was periodically visited at monthly intervals and a snowpit was dug near the stationary measurement device at a distance of ~2 m from the SAS2. Because snowpit creation is an invasive process, the snowpit could not be dug directly under the SAS2 device. Snowpack stratigraphy was recorded and measurements of snow density were made with a triangular scoop (RIP) sampler. Measurements of snowpack wetness with a Denoth meter were made when the device was available. Because the Denoth meter electronics did not utilize a microcontroller, the twin-T bridge had to be balanced by turning a potentiometer. This added a very small human source of error to measurements of snow wetness made with the Denoth meter. The same Denoth meter was used for measurements taken at other field locations where data was collected.

5.2.2. Upper Clearing Portable (UCP) Site

The portable version of the SAS2 was taken to the UC site and used to collect acoustic measurements of snow in the clearing and nearby forest. For measurements taken in the clearing, the SAS2 was placed on the child chariot carrier and pushed along the snow surface (Figure 5.4). Acoustic measurements were made at sample points by pressing a button mounted on the handle-bars of the child chariot carrier. Acoustic "miss-firings" where the sensor was not pointed at the snow surface were excluded from the dataset. After the acoustic samples were taken, an ESC30 snow sampling tube (cf. Section 1.3.2) was used to measure depth-integrated SWE and density near each sampling point. Snow depth was measured using a rod. The procedure of taking the acoustic sample first and the invasive sample after was repeated at all other field sites. This was done to prevent refraction of the sound wave through the hole created in the snow surface by the extraction of the invasive sample.

The chariot carrier could not be pushed into this forest due to the presence of undergrowth. For all measurements made in the forest the SAS2 was taken off the child chariot carrier and placed on a mounting rod. The mounting rod was held in the hand of the investigator and the SAS2 was suspended over the snow surface when an acoustic sample was taken. When mounted on the child chariot carrier or held above the snow surface, the SAS2 was suspended at no more than a maximum of ~15 cm from the snow surface. Figure 5.14 shows this method of sampling. At all other field sites, the SAS was also suspended at a distance of no more than ~15 cm from the snow surface.

Two snowpits were created in the clearing. One of these snowpits (situated on the NE side of the clearing) is shown in Figure 5.5. The first snowpit was created near the stationary SAS2, and the second snowpit was created at the NE side of the clearing. Stratigraphy and density measurements were made in each snowpit using human observations and a scoop sampler. Snow wetness was also determined by inserting the Denoth meter into the snowpit wall. When the snowpit and SAS2 measurements were collected, the sky was overcast and light snow was falling.

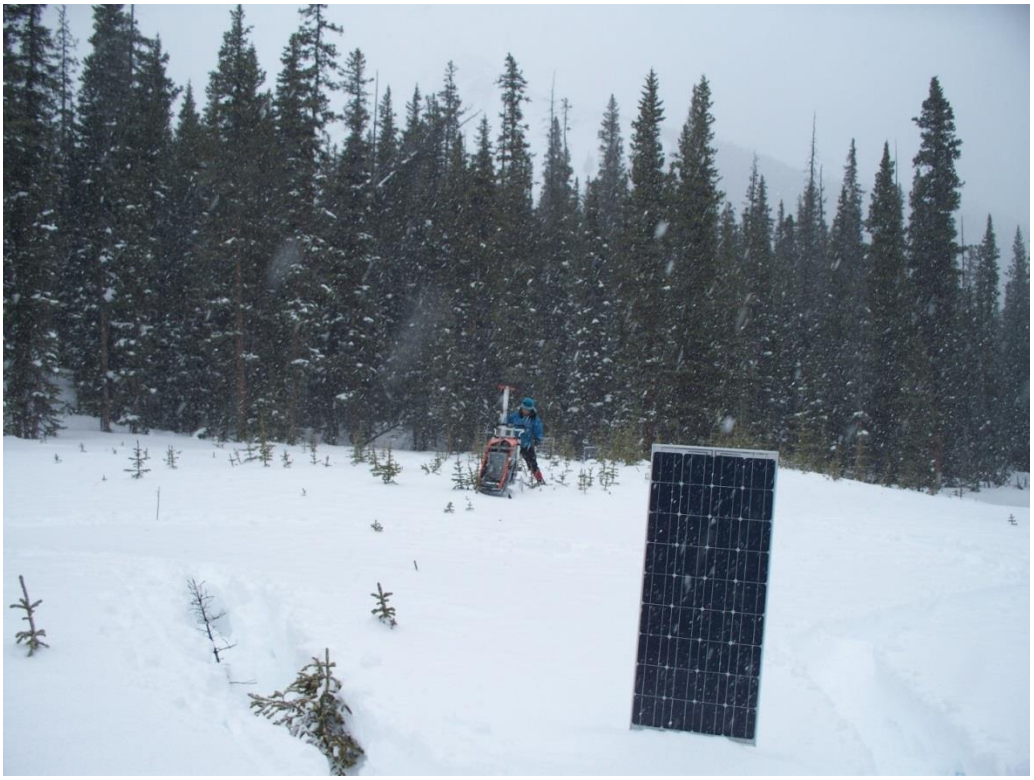

Figure 5.4. Portable measurements being made at the UC with the SAS2 placed on the child chariot carrier. A solar panel is visible in the foreground.

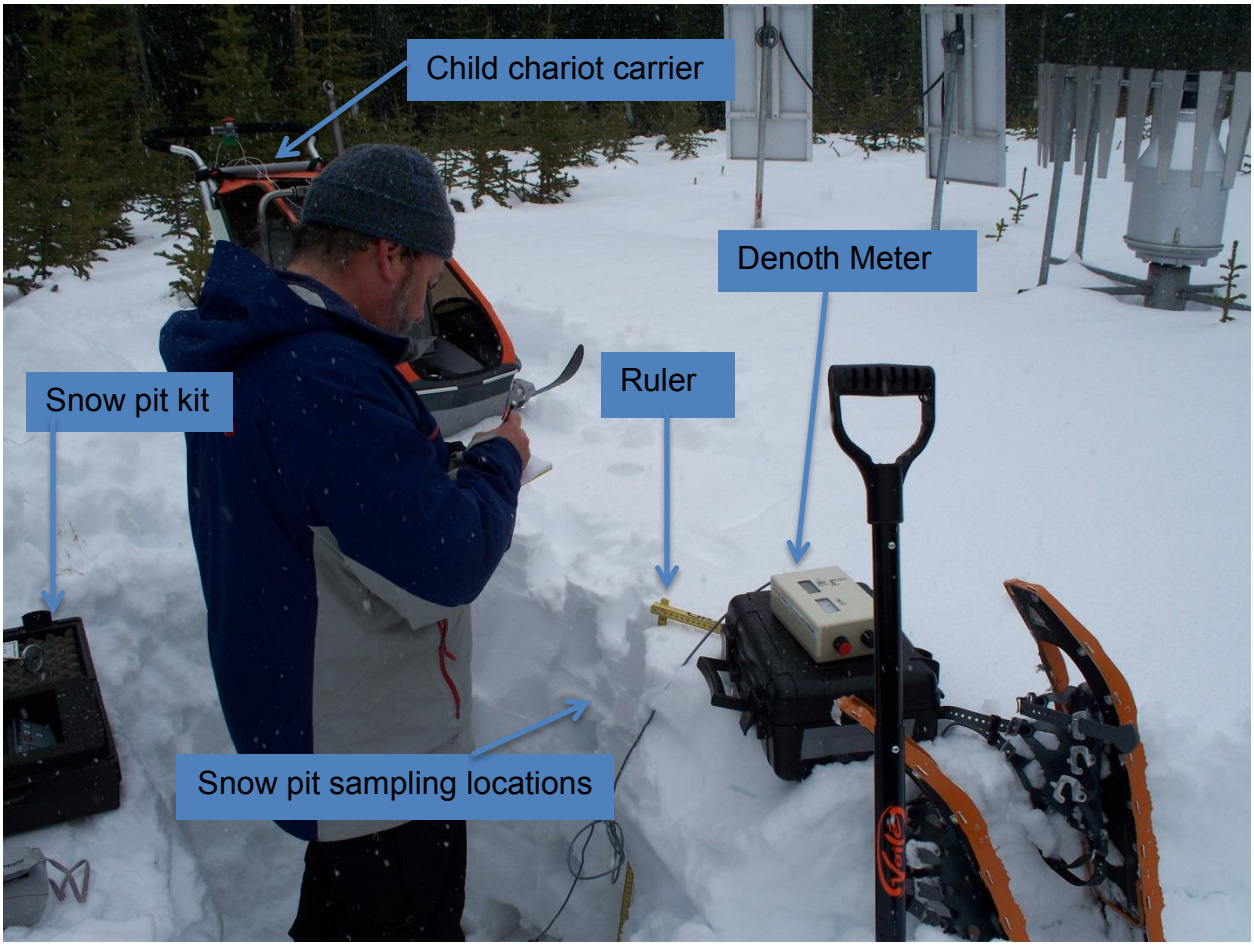

Figure 5.5. Snowpit being sampled at UC site. The Denoth meter is visible in the foreground. A shovel was used to dig the snowpit, and gravimetric samples were extracted from the snowpit wall using a snow pit kit. A collapsible ruler was used to record snow depth, and a thermometer was inserted into the snowpack wall to measure temperature. The snow stratigraphy, density, Denoth meter measurements, and snow temperatures were recorded in a lab book. Visible in the background is the child chariot carrier on which the SAS2 was mounted.

4.2.3. Boulton Campground (BC) Site

The BCS was situated in Peter Lougheed Provincial Park within the Kananaskis Valley, 1 km east of the Lower Kananaskis Lake. The site was accessed via the Kananaskis Lakes Road and the Whiskey Jack Trail.

The portable version of the SAS2 was placed on the child chariot carrier and acoustic measurements were made in a clearing and nearby dense forest (Figure 5.6). The SAS2 remained mounted on the child chariot carrier for all sample points. An ESC snow sampler was used to measure depth-integrated SWE and density, and snow depth measurements were made

using a rod. Dielectric measurements of liquid water content were not made at this site because measurement equipment was not available.

Two snowpits were created at this site. One snowpit was dug in the clearing, whereas the other snowpit was dug in the forest underneath a tree. Light snow was falling when the snowpit and acoustic measurements were collected. This deposited a layer of low-density snow on top of the snow surface. For some acoustic measurements, the loudspeaker and microphones on the front of the enclosure case were inserted directly into the snowpack when the child chariot carrier inadvertently dipped into the snow. These measurements were later excluded from the dataset.

Figure 5.6. Picture of the BC site, showing the open clearing and nearby dense forest.

5.2.4 Sawmill Creek (SC) Site

The SC site was accessed via the Spray Lakes Road situated in the Peter Lougheed Provincial Park. The site was situated on a small plateau near Mount Inflexible.

Acoustic samples and gravimetric samples were made on a ridge situated next to the access road and in the nearby forest (Figure 5.7). The forest had undulating snow surface topography and uneven snow accumulation due to snow unloading (Figure 5.8). Detritus was observed on the snow surface within the forest. At some of the sampling points in the forest, the SAS2 was removed from the child chariot carrier and suspended above the snow surface via a mounting rod. This was done because the skis on the child chariot carrier were too big for maneuverability in the forest.

At the ecotone between the forest and the open ridge (Figure 5.9), small shrubs were buried beneath the snow surface whereas large shrubs were observed above the snow surface. At sampling points near the shrubs, water and detritus from the duff layer was observed at the bottom of the ESC tube. The sound of running water was heard near the shrubs. This implies that a small stream may have been situated under the snow near the shrubs. Five snowpits in total were made at the SC site, two on the ridge and two in the forest.

Figure 5.7. Picture of the SC site on the ridge looking toward Mount Inflexible.

Figure 5.8. Picture of the SC site taken in the forest. Undulating snow topography and detritus is visible on the snow surface.

Figure 5.9. Ecotone between the forest and the open ridge for the SC site. Water and detrius from the duff layer was found at the bottom of the ESC tube after a snow sample had been extracted, implying that a stream may have been located under the snowpack.

5.2.5 Black Prince Cirque (BPC)

The BPC site was accessed via the Spray Lakes Road in Peter Lougheed Provincial Park. The site was situated close to Smith-Dorrien Creek. The SAS2 was held in the hand of the investigator and suspended above the snow surface using the mounting rod. Once again, the SAS2 was suspended no more than ~15 cm above the snow surface. Acoustic samples were taken along a transect starting in a clearing and ending in a forest 6 m from the bank of the Smith-Dorrien Creek (Figure 5.10). Measurements of snow depth were made along the transect, as well as depth-integrated SWE and density with an ESC30 sampler. Two snowpits were created, one in the clearing and the other in the forest. Buried shrubs approximately 60 cm high were found under the snow surface in the clearing.

Figure 5.10. Picture of the BPC site showing the clearing and the forest.

5.2.6 Bow Summit (BS)

The BS was situated in Banff National Park. The site was accessed via the Icefields Parkway (Highway 93 north). The site was situated 1 km east of Peyto Lake near the lower slopes of Mount Jimmy Simpson, and 4.4 km north of Bow Lake. The truck conveying the child chariot carrier and SAS2 was parked near the highway and the child chariot carrier was pulled up a scenic access road closed during the winter season. The site was situated 150 m from the access road. Fresh low-density snow had been deposited on the snowpack the previous night.

The SAS2 was placed on the child chariot carrier and acoustic samples were taken in a clearing and nearby forest (Figure 5.11). ESC snow sampler and snow depth measurements were made. Three snowpits were dug in the clearing. Measurements of snow stratigraphy, density and water content were made in the snowpits using gravimetric samplers and the Denoth meter.

Figure 5.11. Picture of the Bow Summit (BS) site, showing the clearing and nearby forest. Also shown is the child chariot carrier and a sled carrying shovels and gravimetric measurement instrumentation.

5.2.7 Bow Meadow (BM) Site

The BM site was situated in Banff National Park, 50 m to the west of the Icefields Parkway and 2 km south of the BSS. At lower elevations near the road, the site is characterized by an alluvial outwash plain with a meandering stream channel situated under the snowpack. At higher elevations, a forest is situated on the slopes of Mount Jimmy Simpson (Figure 5.12).

The SAS2 was placed on the child chariot carrier and acoustic samples were taken along a transect starting near the road and ending near the treeline of the forest. The elevation at the first point in the transect was 1855 MASL, and the elevation at the last point in the transect was 2057 MASL, with a total change in elevation of 202 m over the transect. The transect crossed the meandering stream, and acoustic samples of snow were taken on top of a snow bridge situated over the running water. Snow tube and snow depth measurements were made after acoustic measurements had been taken (Figure 5.13).

Four snowpits in total were created at this site. The first snowpit was created just west of the road, whereas the second snowpit was created west of the stream channel. The third snowpit was created on the mountain slope, and the fourth snowpit was created in the forest under a tree. The snow in this snowpit was observed to be unloaded snow. At higher elevations in the forest, the child chariot carrier could not be successfully maneuvered, and the SAS2 had to be held in the investigator's hand over the snow surface so that acoustic measurements could be taken. Figure 5.14 shows an example of this sampling configuration. The SAS2 was suspended no more than ~15 cm above the snow surface.

Figure 5.12. Picture of the BM site, showing an alluvial outwash plain and a forest on the slopes of Mount Jimmy Simpson. A sampling transect crossed the plain and went up into the forest.

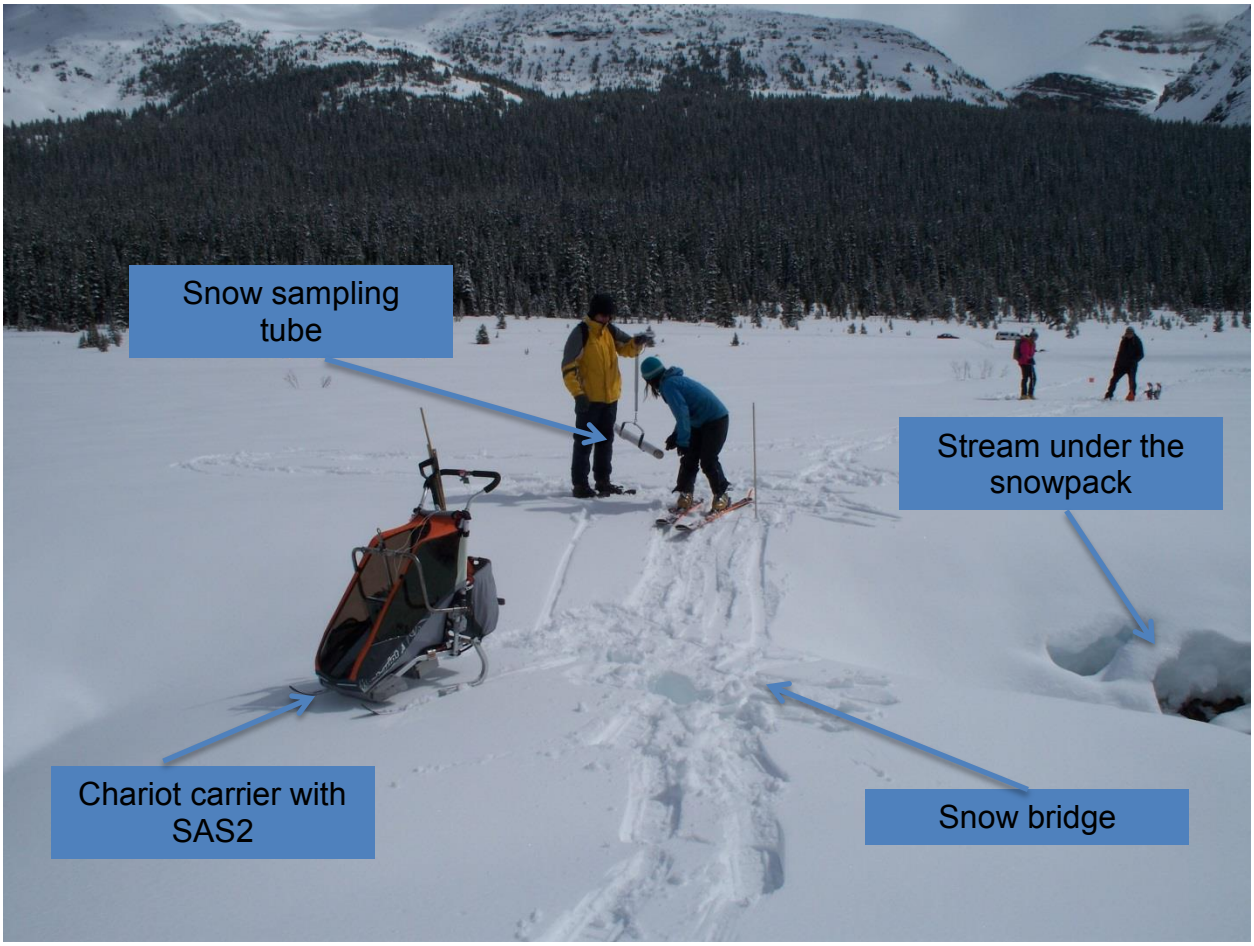

Figure 5.13. Acoustic and gravimetric samples being taken along the tranect. The child chariot carrier is visible in the foreground, and an ESC snow sampling tube is being weighed on a scale to determine depth-integrated SWE and density. The snow bridge situated over the stream is also visible.

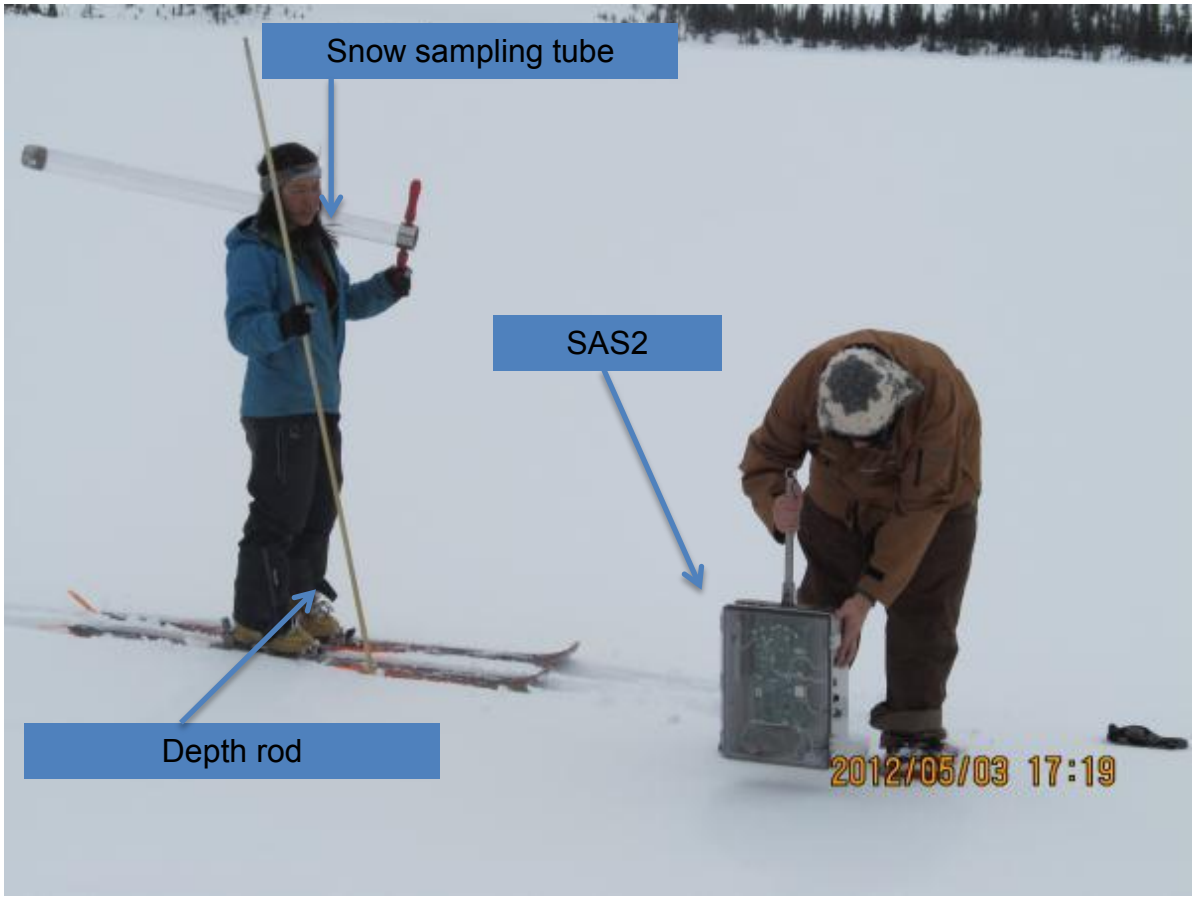

Figure 5.14. Acoustic and gravimetric samples being taken along the transect with the SAS2 being held in the hand of the investigator. An acoustic wave is being sent into the snow. An ESC snow sampling tube and depth measurement rod is also visible.

4.2.8 Bow Lake (BL) Site

The BL site was situated 4 km south of the BMS site on the frozen ice of Bow Lake, a glacial lake originating from the Bow Glacier. The SAS2 was removed from the child chariot carrier and held over snow that had accumulated on top of the ice so that acoustic measurements could be made. Snow depth was measured using a rod, as well as depth-integrated SWE and density using an ESC snow sampler. The snow in the ESC snow sampler was observed to be wet due to water from the lake on top of the ice. No snowpits were dug at this site. The purpose of collecting data at the BLS was to observe the effects of water and ice on the acoustic sampling procedure.

Figure 5.15. Picture of the Bow Lake site situated on the frozen ice of Bow Lake.

5.2.9 Nakiska Ski Hill (NSH) Site

The NSH site was situated in the Nakiska Ski Resort Area close to the chairlift and administrative areas. The purpose of selecting this site was to determine if the acoustic sampling procedure could be used on late-season snow that was artificially-made. Acoustic samples were taken and sampling of snow with a snow tube and depth rod was used for comparison. In a similar fashion to the BLS, acoustic samples of snow were made with the SAS2 held over the snow surface. Sampling of snow also occurred on a steep ski hill. Snow at this site had undergone ablation. The snowcover was patchy and the surface had uneven melt topography. No snowpits were dug at this site due to the shallow snow depth.

Figure 5.16. Picture of the NSH site showing the slope with artificial old-season snow.

5.2.10 Icefields Parkway Forest (IFPF) Site

The IFPF was situated on a road and in a forest located near the Icefields Parkway (Figure 5.17). The snow at this site was late-season and had undergone heavy ablation and melt. To collect acoustic samples from the road and nearby forest, the child chariot carrier was not used and the acoustic gauge was held over the snow surface. Snow tube and depth rod samples were taken at each acoustic sampling point. Light rain and fog occurred when the data was collected. The snow was visibly wet. Once again, no snowpits were dug at this site due to the shallow snow depth.

Figure 5.17. Picture of the IPFS, showing the road and the nearby forest.

CHAPTER 6
RESULTS

6.1. Introduction

The following sections of this thesis present the results determined from acoustic data collected using stationary and portable versions of the SAS2 deployed at field sites described in Chapter 5. Observations made at the UCS site with the SAS2 and met station instrumentation is discussed. The portable version of the SAS2 was deployed and tested at different field sites.

6.2. Snowpack Measurements

6.2.1. Ultrasonic

At the UCS site, snow depth measurements were made over the time of observation using the ultrasonic SR50 sensor situated next to the stationary version of the SAS2. At all of the sites where the SAS2 was deployed, depth measurements were also made using a depth rod.

The ultrasonic SR50 snow depth measurements $\bar{y}$ (Figure 6.1a) corresponded reasonably well with nearby depth rod data measurements, exhibiting an RMSD of 9.0 cm and a MB of -8 cm for a maximum snow depth of 1 m. This indicated that the SR50 under-predicted measurements of snow depth, similar to the observations of Goodison (1985). The under-prediction of snow depth $\bar{y}$ may have occurred due to partial penetration of the ultrasonic wave at the air-snow interface, as suggested by Goodison et al. (1984). Moreover, because snow depth measurements with the depth rod were not made directly under the SR50 sensor, variations in snow surface topography observed at the UC site may also be responsible for this error, given that the SR50 has a specified range resolution of 0.1 mm and a beam acceptance (half-width) of 22°. Some interception of snow on the mast arm and on the deployed SAS2 device may have caused less snow to accumulate under the SR50 and SAS2. This is due to the size of the SAS2 enclosure box.

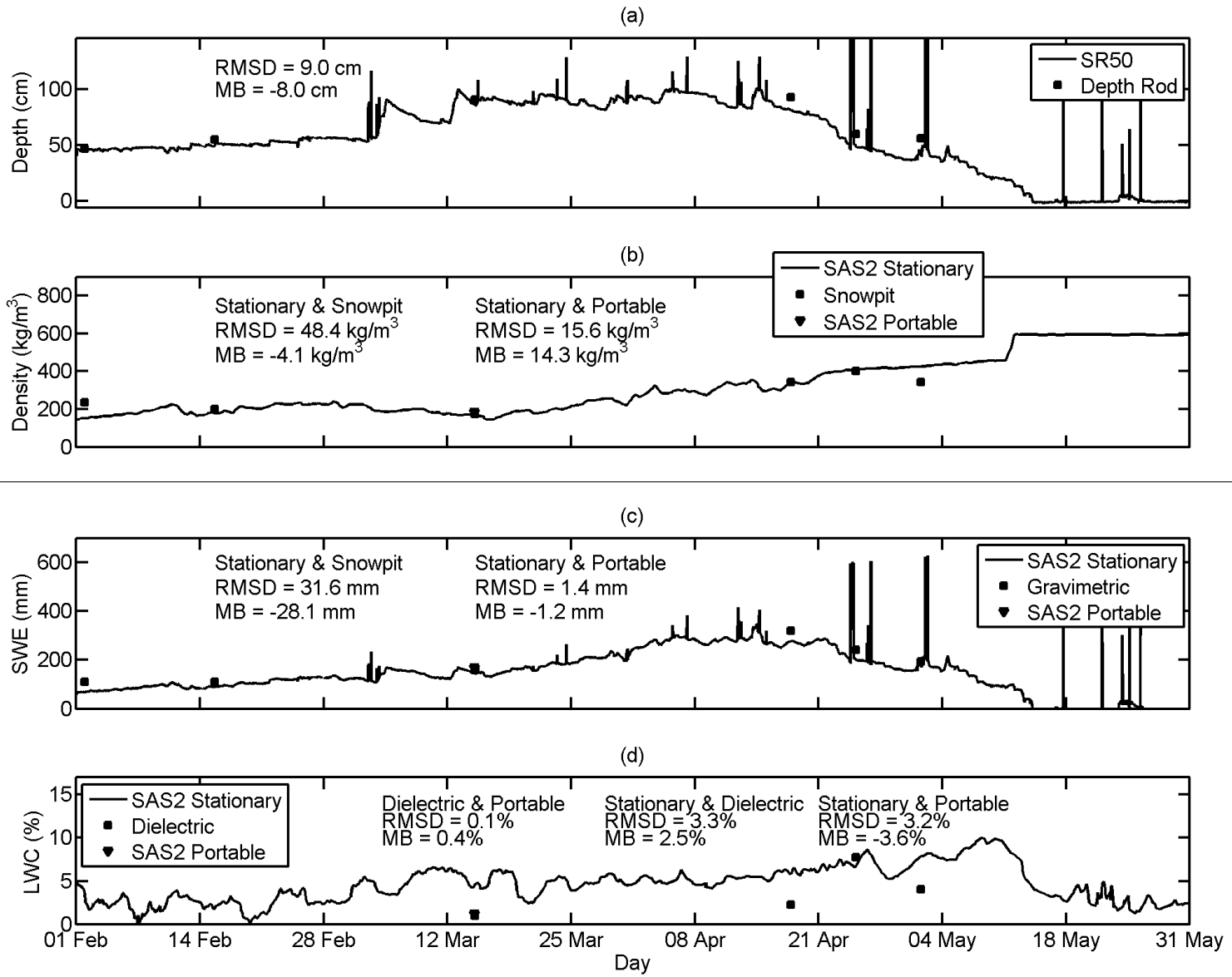

Figure 6.1. Upper Clearing Stationary (UCS) site time-series data showing (a) SR50 snow depth $\bar{y}$, (b) average density $\bar{\rho}$, (c) SWE, and (d) liquid water content $\bar{\theta}_w$ as LWC.

Using Equation (4.17), and given that the SR50 was situated at a distance of $0.5\,\text{m} \leq y_a \leq 1.5\,\text{m}$ above the snow surface due to changes in snow depth, the theoretical SR50 beam footprint ranged between $0.40\,\text{m}$ at a distance of $0.5\,\text{m}$ from the snow surface, and a distance of $1.2\,\text{m}$ when the SR50 was situated at a distance of $1.5\,\text{m}$. The error in depth measurement was greatest when the footprint was largest due to acoustic scattering of the sound wave by exposed vegetation at low snow depths and spurious reflections from vegetation and the met station mounting hardware situated at a distance of less than $1.2\,\text{m}$ from the SR50. Moreover, because the horizontal separation distance between the SR50 and the SAS2 was 62 cm, this distance is greater than the SR50 footprint size of $x_s / 2 = 23\,\text{cm}$ at a distance of $28\,\text{cm}$ between the bottom of the SAS2 enclosure case and the bottom of the SR50 facing the snow surface. This implies that SR50 acoustic measurements were not adversely affected by the close proximity of the SAS2 enclosure case and reflections of the ultrasonic wave from the SAS2 enclosure case were of small magnitude.

Errors in snow depth measured using the SR50 occurred due to acoustic scattering of the sound wave during high wind and snowfall events. This effect is similar to scattering of sonar pulses in the ocean by suspended sediment (Richards et al., 1997). Large "spikes" corresponding to over-prediction errors in ultrasonic measurements of snow depth are visible in the time series plot of snow depth (Figure 6.1a). Before 15 April, the spikes occurred during snow deposition events when snow depth increased (Figure 6.5a). After 15 April, a general decrease in snow depth occurred due to ablation. The spikes of largest magnitude occurred during the time of ablation, suggesting that uneven surface topography or water on the snow surface during melt may have caused additional scattering of the acoustic pulse. Acoustic scattering from an uneven snow surface is similar to scattering of sonar from a rough seabed (Kinar and Pomeroy, 2008a, 2008b). After 15 May, the acoustic pulse from the SR50 contacted the ground surface. Residual amounts of snow on the ground may have been responsible for large over-prediction errors after 15 May, particularly on 23 May when ~5.8 cm of snowfall occurred. The residual amounts of snow do not provide a horizontal surface for reflection of the ultrasonic wave. Snow ablation processes removed all of the snow from the UCS site by 26 May.

6.2.2. Ultrasonic and SAS2

The SR50 is an ultrasonic pulse-based measurement system that operates on principles similar to monopulse sonar and radar systems. Because the duration of the pulse is in the millisecond time range, the time-integrated energy of the sound wave produced by the SR50 is less than the time-integrated energy of the MLS sound wave sent from the SAS2 suspended over the surface of the snowpack. Unlike the SR50, time series of parameters measured by the SAS2 (Figure 6.1b,d; Figure 6.5a; Figure 6.9) do not show spurious measurement spikes of large magnitude, indicating the noise robustness of the MLS signal relative to pulse-based measurement systems. The time of the MLS signal was $t_{mls} = 1.6$ s. Moreover, unlike the ultrasonic SR50 sound waves that are reflected from the snow surface, the audible sound wave produced by the SAS2 will penetrate the snowpack, creating reflections from the snow and the ground surface.

Given the smallest half-width of the SAS2 sensor array as $\theta_m = 43°$ at 10 kHz (Section 4.3) and taking the vertical distance between the bottom of the SAS2 enclosure case and the bottom of the SR50 as 28 cm, evaluation of Equation (4.17) shows that the SAS2 footprint size of $x_s / 2 = 26$ cm was less than 31 cm, implying that close proximity of the SR50 to the SAS2 did not interfere with the SAS2 acoustic measurement for higher frequencies received by the microphone array. However, design calculations given in Section 4.3 show that for low frequencies approaching 20 kHz, the main lobe width is $\theta = \pm 90°$. Low-frequency reflections from the met station apparatus and vegetation at the UC site may have affected the SAS2 measurement for frequencies approaching 20 Hz. Because the SAS2 was situated at a distance of $0.22 \text{ m} \leq y_a \leq 1.22 \text{ m}$ from the snow surface due to changes in snow depth, the theoretical SAS2 device footprint ranged from 41 cm to 2.3 m for a half-width of $\theta_m = 43°$. This is larger than the device footprint of the SR50. Since the microphone holes on the SAS2 enclosure case acted as waveguides, these effects may have been considerably lessened.

6.2.3. Density

At the UCS site, the RMSD between stationary SAS2 and snowpit measurements of depth-averaged density $\bar{\rho}$ was 48.4 kg m^{-3}, with a MB of -4.1 kg m^{-3}, indicating that the SAS2 installed at the UC site under-predicted density measurements (Figure 6.1b). The RMSD value

had the same order of magnitude as the RMSD values determined by comparing gravimetric and acoustic methods of snow density collected using the portable version of the SAS2 (Table 6.3). The SWE values at the UCS site were under-predicted as well (Figure 6.1c), with an RMSD of 48.5 mm and a MB of -28.1 mm. This is because SWE is the numerical product of snow depth and density and the SR50 was being used to measure snow depth at the UCS site. Figure 6.1b shows that a general rise in snow density was apparent over the time of the observation season due to snowpack metamorphism and compaction.

Because the portable version of the SAS2 deployed at the field sites listed in Table 6.3 was situated at distances of no more than ~15 cm from the snow surface, the footprint at a half-width of $\theta_m = 43°$ for the portable device was ~30 cm at this distance. Since the footprint of the stationary SAS2 device had a greater range at the UCS site relative to the maximum footprint range of the portable SAS2 device, there was an increased possibility for spurious reflections and acoustic scattering to affect the measurement during sampling of snow using the stationary version of the SAS2.

Although some variation in results can be explained by hardware differences between the stationary and portable versions of the SAS2, an observation made on 15 March by the portable version of the SAS2 situated close (~2 m) to the stationary version of the SAS2 had an RMSD of 15.6 kg m^{-3} and a MB of 14.3 kg m^{-3}. This suggests that the stationary and portable versions of the acoustic gauge can obtain similar measurement results.

At the time of installation of the SAS2 on 1 February, the acoustic snow density $\bar{\rho}$ was measured as 145 kg m^{-3}. The density $\bar{\rho}$ gradually increased between 1 February and 11 February to 225 kg m^{-3}. The small amounts of snow deposited from 1 February and 11 February were not enough to offset larger increases in depth-integrated density $\bar{\rho}$ occurring due to mechanical compaction and metamorphic processes. This caused a corresponding rise in SWE as well due to small increases in snow depth $\bar{y}$ over this period. The rise in SWE occurred due to snowfall that increased snow depth.

During the first major snow deposition event lasting from 4 March to 6 March, the snow density $\bar{\rho}$ dropped from 205 kg m^{-3} to 160 kg m^{-3}, showing that fresh low-density snow had been added to the snowpack, decreasing the depth-averaged density. From 6 March to 11 March, the snow density rose to 201 kg m^{-3}. With a concomitant decrease in snow depth, this indicated

compaction of the snowpack and metamorphic processes that increased snow density. By 15 March, the snow density dropped to 170 kg m^{-3}, once again indicating the addition of fresh low-density snow. The snow density continued to increase from 15 March to 30 March, due to slight compaction of the snowpack and metamorphic processes, reaching 256 kg m^{-3} by 30 March. Small drops in snow density were apparent during this time due to the addition of fresh snow to the snowpack.

On 31 March the snow density $\bar{\rho}$ was 221 kg m^{-3}. On 3 April the snow density peaked at 323 kg m^{-3} showing that $\bar{\rho}$ increased a total of 102 kg m^{-3} over 4 days due to higher levels of liquid water content. A snow deposition event from 4 to 5 April caused an increase in snow depth of 10 cm from a depth of 88 cm to 99 cm and a decrease in snow density from 323 kg m^{-3} to 283 kg m^{-3}. Decreases in density during snowfall events were also apparent during the 12 April and 14 April snowfall events.

A gradual increase in snow density from 17 March to 14 April due to compaction and metamorphic processes was apparent. On 17 March the snow density was 180 kg m^{-3}, and this increased to 351 kg m^{-3} on 14 April. The last major snowfall before ablation occurred on 14 April, with a drop in snow density $\bar{\rho}$ to 294 kg m^{-3} indicating the addition of fresh snow to the snowpack.

The snow depth was 101 cm on 14 April, and all of the snow had undergone ablation by 14 May. The first major drop in snow depth occurred between 14 April and 21 April, when the snow depth decreased from 99 cm to 78 cm, a total of 21 cm. During this time rapid cycles in liquid water content occurred due to the production of meltwater during ablation. The density increased to 379 kg m^{-3} by 21 April. The second major drop in snow depth occurred between 21 April and 26 April, when the snow depth decreased from 76 cm to 48 cm, a total of 28 cm.

On 26 April, the snow depth was 48 cm, and the snow density $\bar{\rho}$ was 411 kg m^{-3}, a measurement in the range of snow densities recorded at the NSH site (Table 6.4) for late-season old snow. The snow depth continued to decrease during ablation until 1 May, when a brief snowfall event increased snow depth to 50 cm. On 1 May, the snow density was 422 kg m^{-3}, showing that despite the deposition of freshly-fallen snow at air temperatures exceeding 0 °C, the density $\bar{\rho}$ did not decrease. The density continued to increase due to rapid metamorphism at higher air temperatures and snow surface temperatures near 0 °C as the snowpack continued to warm.

Due to compaction and metamorphism of the snow during ablation, the snow depth reached 39 cm by 4 May, with the density increasing to 429 kg m^{-3}. Another brief snowfall event on 5 May increased snow depth to 50 cm, but the snow density continued to increase to 429 kg m^{-3}, indicating rapid metamorphism, compaction of the snowpack, and higher levels of liquid water content. By 11 May, the snow density $\bar{\rho}$ was within the range of mean snow densities observed at both the BL and NSH sites (Table 6.4), indicating that the snowpack was wet and comprised of old-season snow.

On 12 May, the acoustic snow density rose to 595 kg m^{-3} and remained at this density until the end of the observation season. The snow depth measured by the SR5 was 12.8 cm on 12 May, and all snow had ablated by 14 May. Despite a small drop in the acoustic measurement of density to 592 kg m^{-3} on 23 May when ~5.8 cm of snowfall occurred, the nearly-constant acoustic snow density may represent a limitation of the acoustic method to measure wet, old-season snow that had undergone extensive metamorphism over the snow accumulation and ablation season.

Figures 6.2 to 6.4 and Tables 6.1 and 6.2 show the RMSD and MB between ESC30 snowtube, snowpit and SAS2 acoustic measurements of density and SWE. The low MB magnitude between these quantities indicated that although the acoustic density $\bar{\rho}$ was slightly under-predicted, the SAS2 was able to obtain measurements similar to the ESC30 snowtube. The SAS2 can therefore be used as a replacement technology for non-invasively determining depth-averaged density $\bar{\rho}$ in lieu of a snowtube. The RMSD between ESC30 snowtube measurements of SWE and acoustic measurements of SWE showed slight over-prediction of SWE due to error in snow depth measurements collected using a rod. The maximum snow depth observed at all of the 10 observation sites was 2 m.

Table 6.1 shows that that acoustic measurements of $\bar{\rho}$ were under-predicted relative to gravimetric snowpit measurements due to a negative MB. The acoustic SWE measurements also showed this under-prediction error as well. The RMSD for comparisons between snowpit and acoustic measurements of $\bar{\rho}$ was less than the RMSD between snowpit and snowtube density, suggesting that the SAS2 is more accurate than ESC30 measurements and most similar to snowpit measurements of $\bar{\rho}$. Similar results were also found for comparisons between snowpit measurements and ESC30 measurements of SWE. Snowtube measurements were less

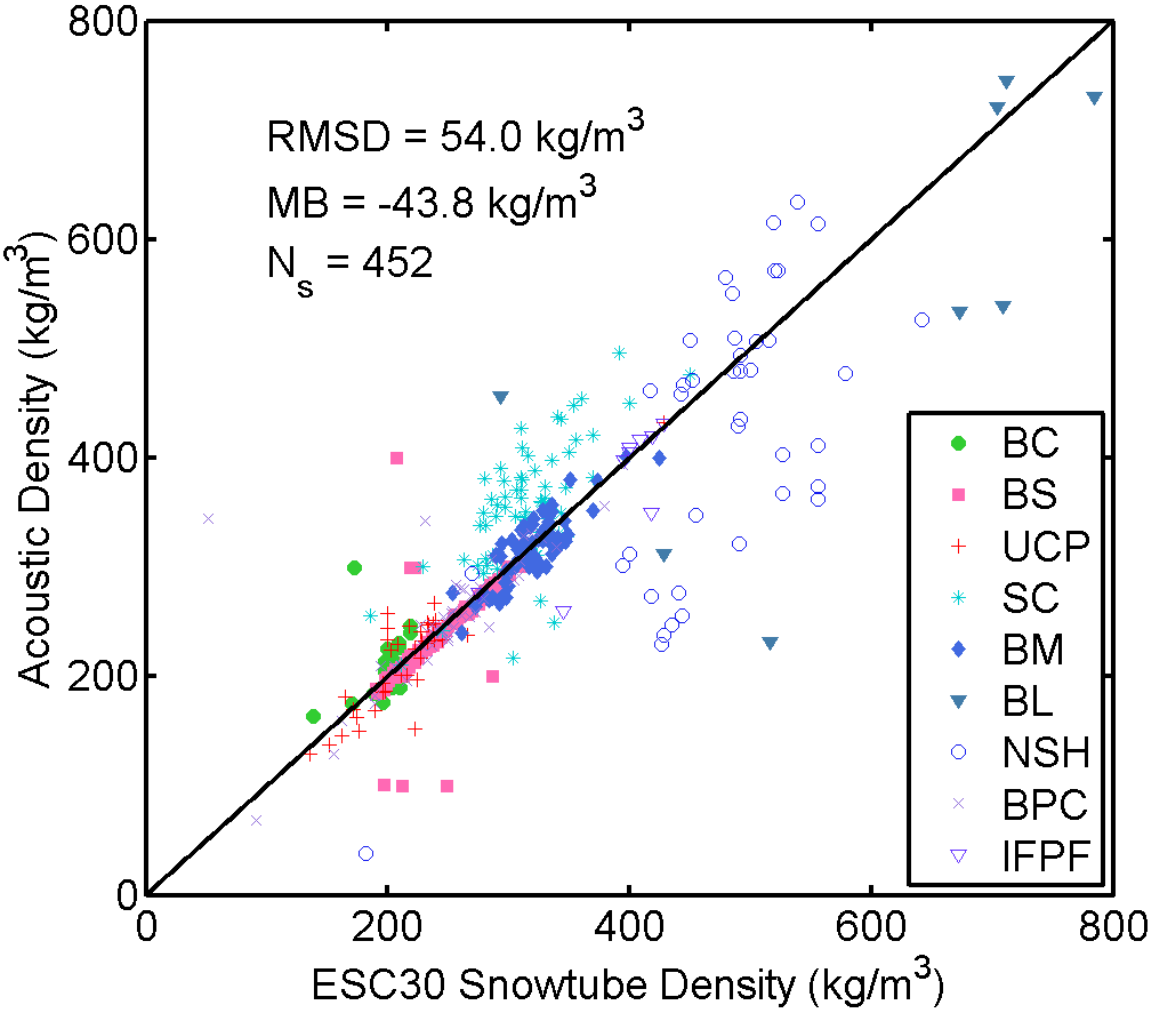

Figure 6.2. Comparison between depth-averaged density measured using an ESC30 snow tube and depth-averaged acoustic density measured using the portable version of the SAS2 at nine field sites. The black line on the plot is the 1:1 line. The Boulton Campground (BC), Bow Summit (BS), Upper Clearing Portable (UCP), Sawmill Creek (SC), Bow Meadows (BM), Bow Lake (BL), Nakiska Ski Hills (NSH), Black Prince Cirque (BPC), and Icefields Parkway Forest (IFPF) sites are listed in the legend. The number of samples is given as N_s.

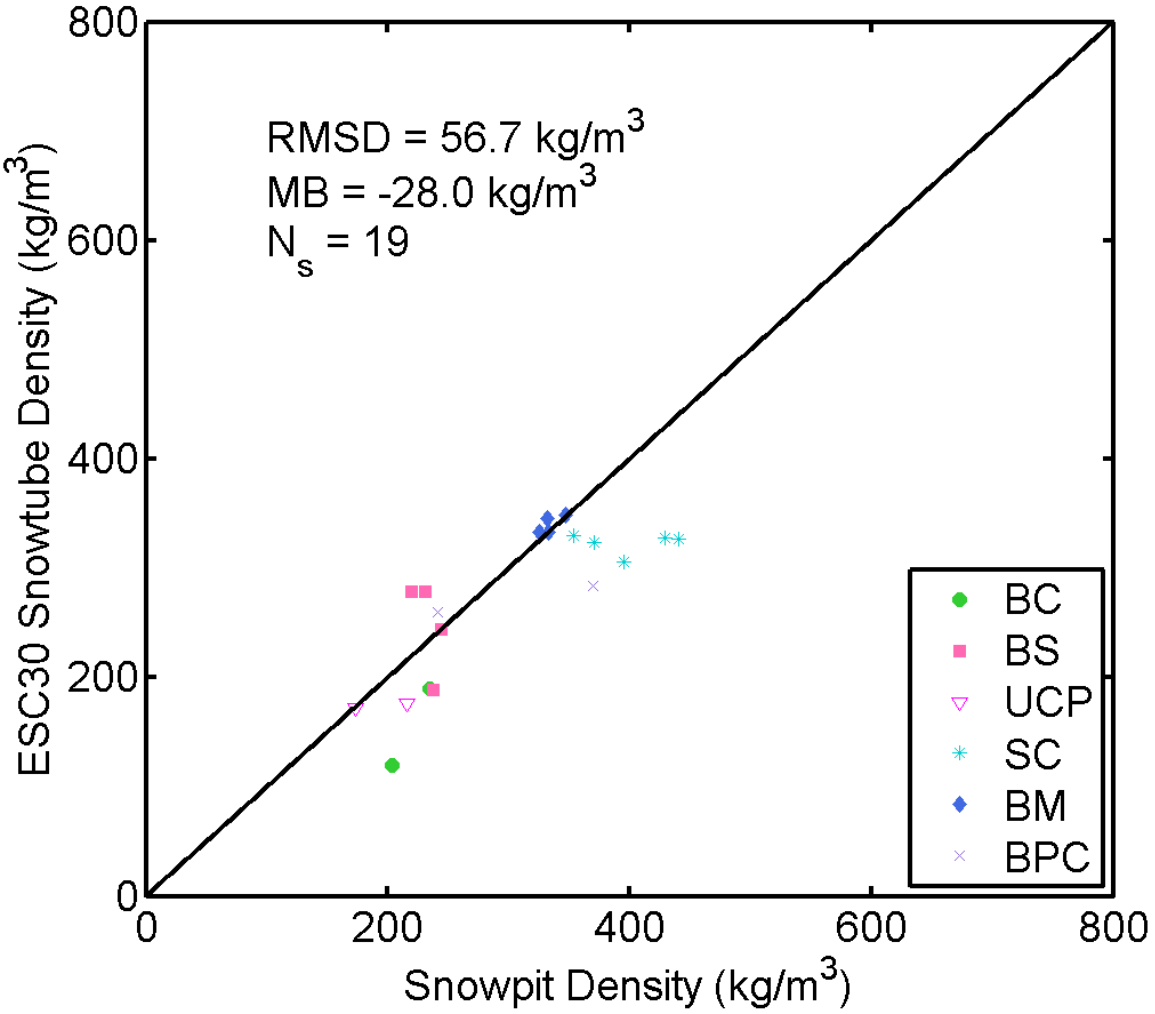

Figure 6.3. Comparison between average density measured using an ESC30 snow tube and depth-averaged snowpit density measured at six field sites. The black line on the plot is the 1:1 line. The Boulton Campground (BC), Bow Summit (BS), Upper Clearing Portable (UCP), Sawmill Creek (SC), Bow Meadow (BM), and Black Prince Cirque (BPC) sites are listed in the legend. The number of samples is given as N_s.

$\bar{\rho}$ comparison	RMSD (kg m^{-3})	MB (kg m^{-3})	N_s
ESC30 & SAS2	54.0	-8	452
Snowpit & Snowtube	56.7	-28.0	19
Snowpit & SAS2	24.2	-4.9	19

Table 6.1. Overall comparisons between gravimetric and acoustic measurements of density $\bar{\rho}$.

SWE comparison	RMSD (mm)	MB (mm)	N_s
ESC30 & SAS2	47.3	9.00	452
Snowpit & Snowtube	112.4	-10.11	19
Snowpit & SAS2	29.5	-2.30	19

Table 6.2. Overall comparisons between gravimetric and acoustic measurements of SWE.

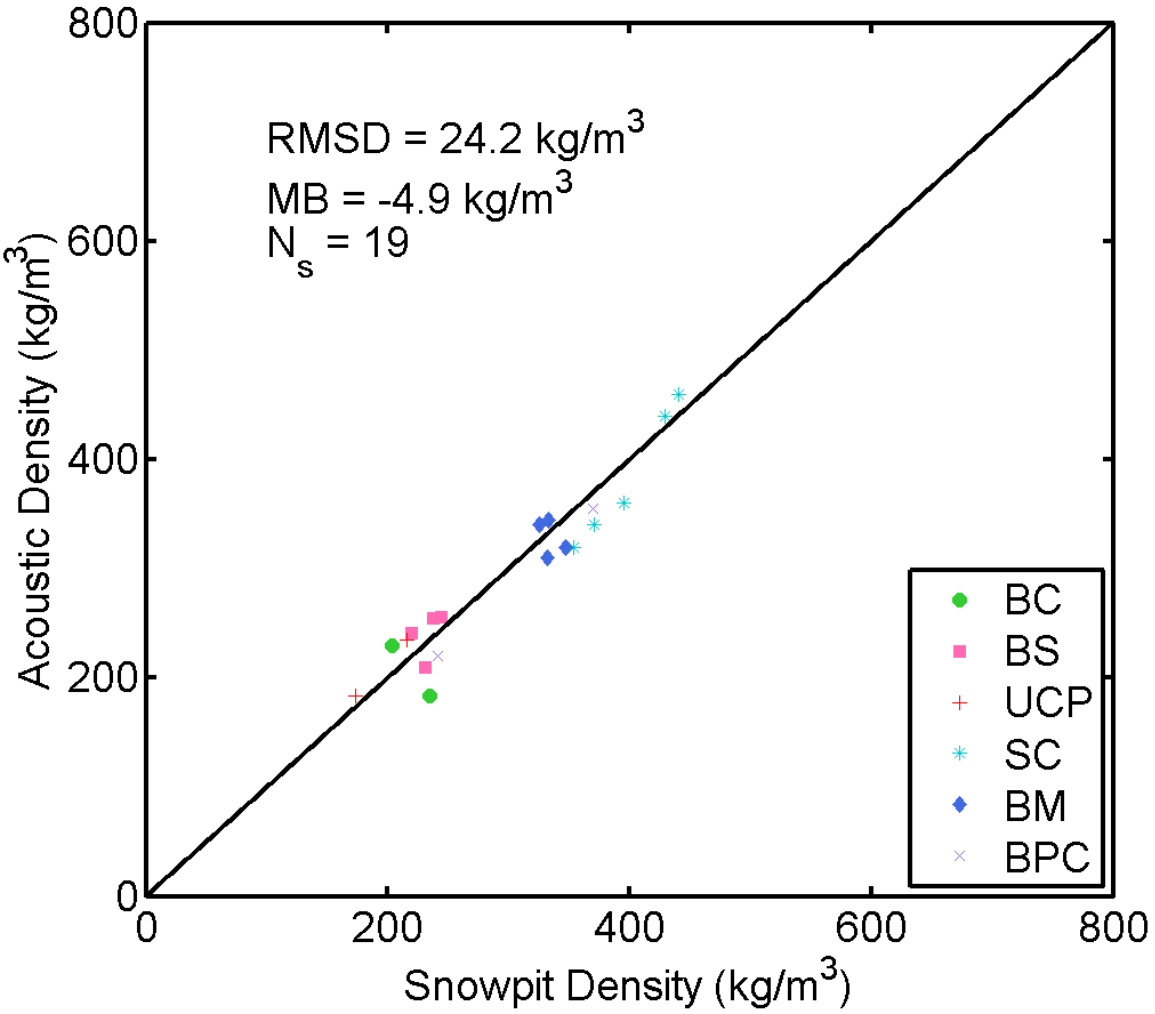

Figure 6.4. Comparison between depth-averaged gravimetric snowpit density and depth-averaged acoustic density measured using the portable version of the SAS2 at six field sites. The black line on the plot is the 1:1 line. The Boulton Campground (BC), Bow Summit (BS), Upper Clearing Portable (UCP), Sawmill Creek (SC), Bow Meadow (BM), and Black Prince Cirque (BPC) sites are listed in the legend.

accurate than snowpit measurements due to the error effects discussed in Section 1.3.2 of this thesis.

Table 6.3 aggregates data comparisons for the sites, showing that the RMSD values for site comparisons between snowpit and acoustic measurements of $\overline{\rho}$ were less than the RMSD values between snowpit and snowtube density. The Boulton Campground (BC) site data was the earliest dataset collected with the SAS2. The data points collected at the BS site had lower RMSD and MB magnitudes than the data points at the BC site, indicating that the BS site showed a better correspondence between acoustic and gravimetric density $\overline{\rho}$ due to smaller amounts of buried vegetation and less acoustic scattering. The Upper Clearing Portable (UCP) site data points showed more scatter than the previous BC and BS sites (Figure 6.2) and a higher range of acoustic densities (Table 6.4) due to error introduced by acoustic scattering caused by buried vegetation (small trees) in the clearing and in the forest.

The Sawmill Creek (SC) site data, collected later in the snow observation season, had higher densities than the previous sites due to snowpack metamorphism and higher levels of liquid water content (Table 6.4). This increased the scatter in the acoustic data points (Figure 6.2). The acoustic densities at the SC site showed greater error than the UCP and BS sites due to refraction of sound in the vicinity of tree wells, scattering of sound by buried vegetation in the clearing, forest and ecotone, as well as possible scattering and mode conversion of sound waves. Compared to all of the sites in Table 6.3, the Bow Meadows (BM) site had the lower RMSD values due to snowpacks with small amounts of buried vegetation that reduced acoustic scattering and snowpack stratigraphy with layer boundaries that best approximated horizontal lines. The horizontal line approximation was most similar to the acoustic model described in Section 3.5 of this thesis as a basis for operation of the SAS2.

The Bow Lake (BL) site dataset showed the highest error between gravimetric and acoustic measurements of $\overline{\rho}$, possibly owing to acoustic scattering and mode conversion of sound waves due to ponded water completely filling the pore spaces of the snow. This increased the scatter in the data points (Figure 6.2). The mean liquid water content determined using acoustics at the BL site was the second-highest of all of the field sites (Table 6.10), with higher levels of liquid water content only observed at the IFPF site on 1 June.

Site	Dates	$\bar{\rho}$ comparison	RMSD ($kg\ m^{-3}$)	MB ($kg\ m^{-3}$)	N_s
UCS	1 February to 31 May	ESC30 & SAS2	NA	NA	NA
		Snowpit & Snowtube	NA	NA	NA
		Snowpit & SAS2	48.4	-4.10	6
BC	13 March	ESC30 & SAS2	47.1	19.5	12
		Snowpit & Snowtube	67.4	64.5	2
		Snowpit & SAS2	40.5	-12.5	2
BS	14 March	ESC30 & SAS2	29.0	3.2	117
		Snowpit & Snowtube	45.0	-14.3	4
		Snowpit & SAS2	18.1	7.3	4
UCP	15 March	ESC30 & SAS2	25.2	3.8	35
		Snowpit & Snowtube	28.0	20.4	2
		Snowpit & SAS2	15.5	15.0	2
SC	1 May	ESC30 & SAS2	62.3	43.5	65
		Snowpit & Snowtube	82.6	75.2	5
		Snowpit & SAS2	27.7	-14.0	5
BM	3 May	ESC30 & SAS2	17.9	-2.8	63
		Snowpit & Snowtube	19.9	-5.5	4
		Snowpit & SAS2	8.2	-6.2	4
BL	3 May	ESC30 & SAS2	147.4	-68.9	8
		Snowpit & Snowtube	NA	NA	NA
		Snowpit & SAS2	NA	NA	NA
NSH	4 May	ESC30 & SAS2	109.5	-53.5	40
		Snowpit & Snowtube	NA	NA	NA
		Snowpit & SAS2	NA	NA	NA
BPC	4 May	ESC30 & SAS2	50.1	7.3	45
		Snowpit & Snowtube	62.6	33.7	2
		Snowpit & SAS2	18.2	-18.0	2
IFPF	1 June	ESC30 & SAS2	36.7	-13.5	9
		Snowpit & Snowtube	NA	NA	NA
		Snowpit & SAS2	NA	NA	NA

Table 6.3. Comparisons between gravimetric and acoustic measurements of density $\bar{\rho}$ at individual field sites. Observations that are not available are marked with "NA." The RMSD, MB and number of samples N_s are listed. The site locations are Upper Clearing Stationary (UCS), Boulton Campground (BC), Bow Summit (BS), Upper Clearing Portable (UCP), Sawmill Creek (SC), Bow Meadows (BM), Bow Lake (BL), Nakiska Ski Hills (NSH), Black Prince Cirque (BPC), and Icefields Parkway Forest Site (IFPF). The same site location names are used in the following tables. There were 10 sites in total.

Site	Dates	Mean ($kg\ m^{-3}$)	Median ($kg\ m^{-3}$)	Min ($kg\ m^{-3}$)	Max ($kg\ m^{-3}$)	Range ($kg\ m^{-3}$)
UCS	1 Feb to 31 May	291	241	145	597	452
BC	13 March	202	195	154	261	107
BS	14 March	242	239	190	312	122
UCP	15 March	250	234	130	456	327
SC	1 May	364	358	210	600	390
BM	3 May	317	320	240	401	161
BL	3 May	534	537	231	745	514
NSH	4 May	420	459	38	635	597
BPC	4 May	258	255	69	394	325
IFPF	1 June	374	405	260	431	171

Table 6.4. Descriptive statistics of density $\bar{\rho}$ ($kg\ m^{-3}$) measured using the SAS2.

The artificial snow at the NSH site showed an under-prediction of acoustic snow density $\bar{\rho}$ but a higher accuracy than the BL site (Table 6.3) due to a lack of ponded water. The BPC site transect data, collected on same day as the NSH site transect data, showed lower RMSD error than the dataset collected at the NSH site (Table 6.3). Despite the presence of a few outliers (Figure 6.2), the IFPF site sample points had a lower RMSD error than the BL or NSH dataset. This suggested that although the snowpack was observed to be very wet at this field site, ponding of meltwater did not occur and water did not accumulate in the pore spaces of the snowpack. Because the snowpack was well-drained at the IFPF site, this reduced acoustic scattering and mode conversion occurring due to the ponded water. This reduced scatter in the data points shown in Figure 6.2.

Because time series data of snow density and SWE is not available at locations where the portable version of the SAS2 was deployed, more than one measurement cannot be used to show that error in the acoustically-determined data relative to gravimetric samples has a relationship with time. An increase in the scatter shown by Figure 6.2 may have occurred due to the inherent inaccuracies of the ESC30 snow sampler associated with loss of snow and water from the tube or due to mechanical modification of the snow sample during the invasive ESC30 sampling process. This suggests the inherent inaccuracies of the ESC30 sampler with respect to the SAS2.

6.2.4. Thermal

For most of the time of observation, the snowharp and depth-averaged snowharp temperature $\bar{T}$ observations at the UCS site (Figure 6.5a, b) show results that are physically reasonable. The snowharp measurements were constrained to ≤ 0 ℃, allowing for comparison with the acoustic SAS2 measurements that were constrained to ≤ 0 ℃ by the UTAM model. The SR50 ultrasonic snow depth measurements are also shown on Figure 6.5b, indicating that there are four periods of observation. The averaged snowharp temperatures (Figure 6.5a) only use thermocouples that are completely covered by snow. These are the thermocouples situated at distances from the ground less than the snow depth measured by the SR50.

The first period coincided with the beginning of the observation season when the snowharp was not completely covered by snow; the second period coincided with the time when the snowharp was completely covered by snow; the third period coincided with the time of ablation, when there was a reduction in snow depth and uneven snow topography around the snowharp; and the fourth period coincided with the time when most of the snow had ablated. The RMSD and MB between snowharp and SAS2 measurements for each period is given by Table 6.5, whereas overall comparisons between snowpit and SAS2 and snowpit and snowharp measurements are given by Table 6.6.

Measurement	First Period	Second Period	Third Period	Fourth Period
RMSD (℃)	3.0	1.1	1.2	0.32
MB (℃)	-2.9	-0.76	-0.051	-0.27

Table 6.5. Comparisons between snowharp and SAS2 measurements over observation periods.

Measurement	Snowpit & Acoustic	Snowpit & Snowharp	Snowharp & Acoustic
RMSD (℃)	3.9	2.6	1.8
MB (℃)	-2.6	1.4	-1.1

Table 6.6. Overall comparisons of snowharp temperature over the entire time of observation.

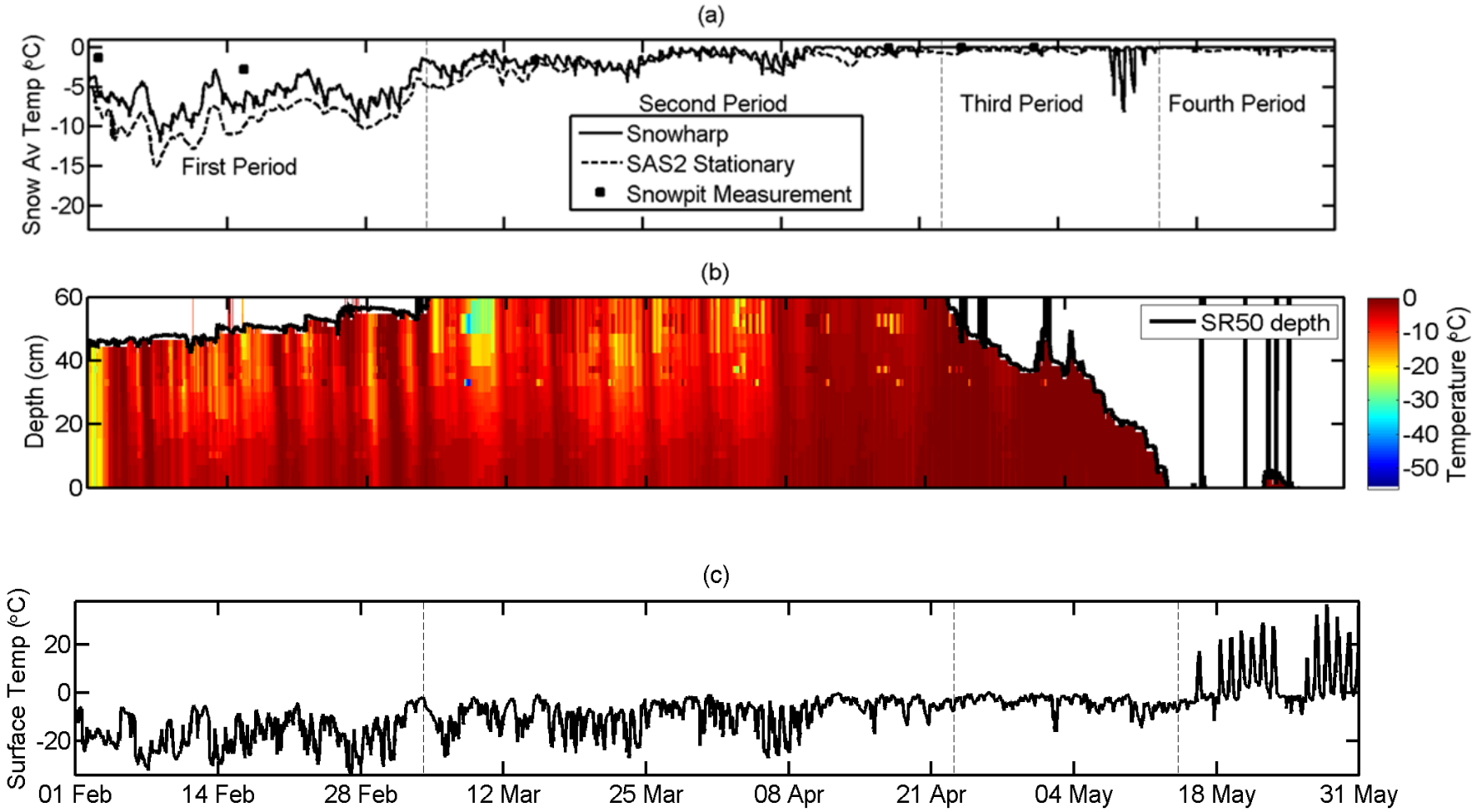

Figure 6.5. Upper Clearing Stationary (UCS) site time-series data showing (a) depth-averaged snowharp temperature and depth-averaged acoustic temperature $\overline{T}$, (b) spatial distribution of temperature observed using the snowharp, and (c) temperature at the snow surface measured using the IR thermometer.

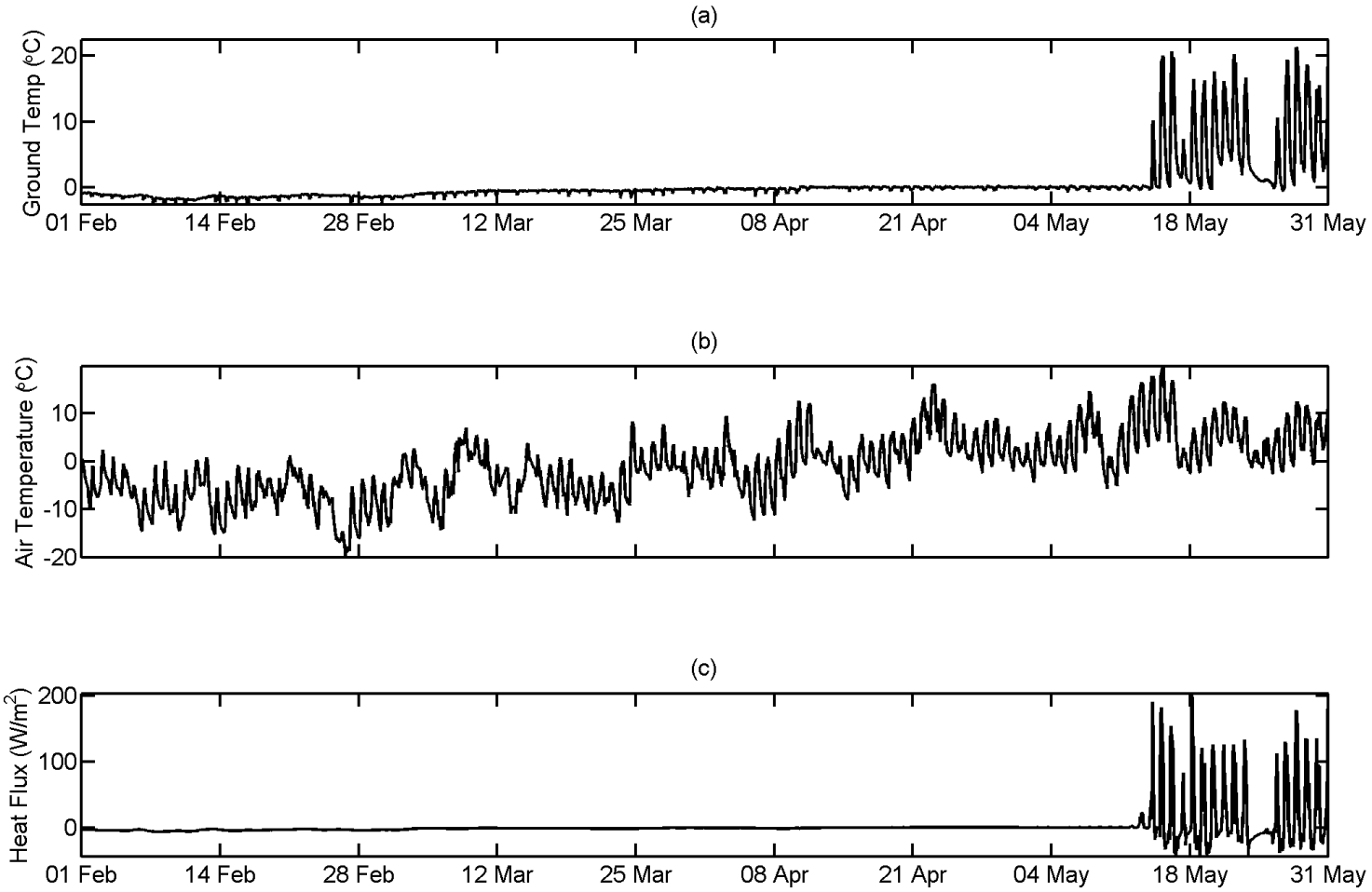

Figure 6.6. Upper Clearing Stationary (UCS) site time-series data showing (a) ground temperature, (b) air temperature, and (c) heat flux at the bottom of the snowpack.

Tables 6.5 and 6.6 show that acoustic measurements of temperature $\bar{T}$ have the same order of magnitude as snowharp and snowpit measurements. The acoustic measurements made by the SAS2 are under-predicted relative to other measurements. Compared to the second and third observation periods (Table 6.5), the RMSD between snowharp and SAS2 measurements was highest during the first period of observation. Although thermocouples not covered with snow were excluded from the analysis, this may indicate that heat conduction along the thermocouple wires increased the temperature sensed by the thermocouples. The RMSD and MB magnitudes were lower during the second period of observation when the snowharp structure was completely covered with snow. By the third period when snow ablation occurred, the snow temperature $\bar{T}$ was close to 0 °C. Since both the snowharp and acoustic measurements are constrained to ≤ 0 °C, both the RMSD and MB magnitudes remained low during the third period. Constraining the measurements also caused the RMSD to remain low during the fourth period. However, the MB magnitude during the fourth period was higher than the other periods of observation.

Over the entire observation period (Table 6.6) the snowharp and acoustic measurements had the lowest RMSD and MB magnitudes. The snowpit and acoustic measurements had the highest RMSD and MB magnitudes due to spatial differences in snow temperature between the snowpit and SAS2 sampling locations. The snowpit and snowharp RMSD and MBs showed values that were intermediate between the RMSD and MB values used to compare the other measurements.

Despite a temperature anomaly apparent at the beginning of the observation period from 1 February to 4 February on the snowharp plot (Figure 6.5b) and possible inaccuracies of the invasive snowharp measurement method occurring due to heat conduction along the wires, the snowharp data showed that temperatures near the top of the snowpack were colder than temperatures near the ground surface. The difference in temperature between the top and bottom of the snowpack established a temperature gradient, resulting in depth hoar formation near the snowpack bottom as water vapour was transferred across pore spaces from warmer to colder surfaces. These processes are discussed in Section 2.2 of this thesis.

Diurnal heating and cooling cycles were apparent, with the snowpack gradually warming during the day due to a positive net shortwave radiation K^* balance (Figure B.4a, Appendix B). The IR surface temperature of the snowpack (Figure 6.5c) was colder than the temperature at the

bottom of the snowpack (Figure 6.6a) due to longwave radiative cooling near the snow surface, evaporative cooling and a small but persistent negative heat flux ($\sim -3\ \mathrm{W\,m^{-2}}$) from the ground into the snow during the snow accumulation season (Figure 6.6c). This observed heat flux had the same order of magnitude as the heat flux values listed in Table 2.1 of Chapter 2. Wet soil fed by groundwater exfiltration at the UC site where the ground was slow to freeze may have contributed to this heat flux.

After 16 April, the heat flux (Figure 6.6c) was small and positive ($\sim 0.2\ \mathrm{W\,m^{-2}}$), indicating that the snowpack was transferring energy into the ground during the time of ablation due to rising temperatures and the production of meltwater after the snowpack reached $0\ ^{\circ}\mathrm{C}$. The ground temperature (Figure 6.6a) and heat flux plots (Figure 6.6c) were similar, with diurnal cycling of temperature most apparent on the plot of ground temperature (Figure 6.6a). The heat flux (Figure 6.6c) continued to increase until it exceeded $1.0\ \mathrm{W\,m^{-2}}$ on 13 May. After ablation of all snow at the UCS site by 14 May, the heat flux rose to $\sim 200\ \mathrm{W\,m^{-2}}$, indicating heating and cooling of the ground surface by direct radiative fluxes. A snow deposition event of short temporal duration lasting from 24-25 May depressed ground temperature and suppressed the heat flux associated with diurnal warming and cooling of the ground surface.

Comparisons between temperatures measured in snowpits using a thermometer and the acoustic temperature $\bar{T}$ measured using the SAS2 (Figure 6.7) showed an RMSD of $1.6\ ^{\circ}\mathrm{C}$ and a MB of $-1.1\ ^{\circ}\mathrm{C}$ for $N_s = 19$ samples. The RMSD and MB indicated that the acoustic temperature measurements are the same order of magnitude as the snowpit measurements of temperature. This strongly suggested that the SAS2 was able to measure snow temperature. Snow temperature $\bar{T}$ measured by the SAS2 increased over the winter season (Table 6.8 and Figure 6.5a), with higher mean temperatures apparent at the BM, BL, and NSH sites.

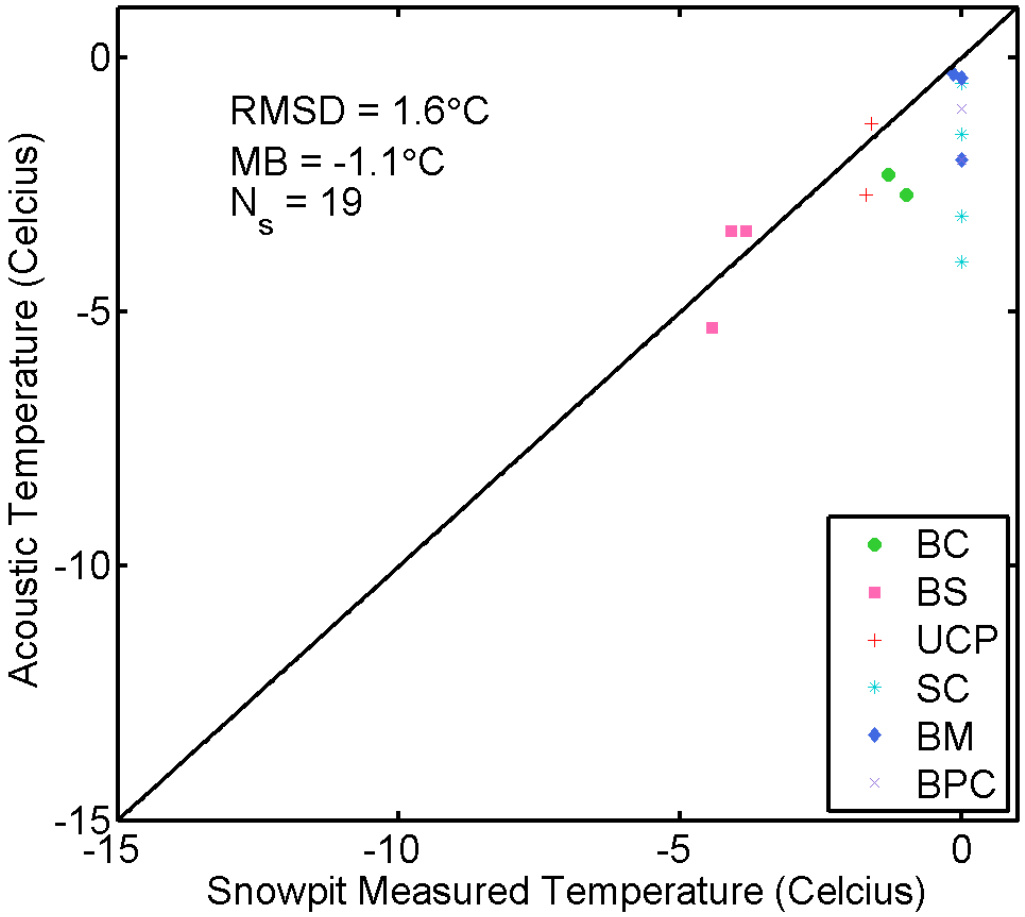

Figure 6.7. Comparison between depth-averaged temperature measured using snowpits and depth-averaged acoustic temperature measured using the portable and stationary versions of the SAS2 at ten field sites. The black line on the plot is the 1:1 line. The Upper Clearing Portable (UCP), Upper Clearing Stationary (UCS), Boulton Campground (BC), Sawmill Creek (SC), Black Prince Cirque (BPC), Bow Summit (BS), and Bow Meadows (BM) sites are listed in the legend.

Site	Dates	$\bar{T}$ RMSD (°C)	$\bar{T}$ MB (°C)	N_s
UCS	1 Feb to 31 May	3.9	-2.6	6
BC	13 March	1.4	-1.4	2
BS	14 March	0.7	0.1	4
UCP	15 March	0.7	-0.4	2
SC	1 May	2.5	-2.2	5
BM	3 May	1.0	-0.7	4
BL	3 May	NA	NA	NA
NSH	4 May	NA	NA	NA
BPC	4 May	0.2	-1.5	2
IFPF	1 June	NA	NA	NA

Table 6.7. Comparisons between snowpit and acoustic measurements of temperature $\bar{T}$.

Site	Dates	Mean (°C)	Median (°C)	Min (°C)	Max (°C)	Range (°C)
UCS	1 Feb to 31 May	-3.4	-1.5	-15.0	0.0	15.0
BC	13 March	-4.9	-4.5	-9.0	-2.0	7.0
BS	14 March	-6.0	-5.6	-8.6	-3.1	5.5
UCP	15 March	-4.8	-5.4	-6.5	-1.0	5.3
SC	1 May	-1.3	-1.0	-4.0	0.0	4.0
BM	3 May	-0.9	-0.9	-2.0	-0.1	1.9
BL	3 May	-0.3	-0.3	-0.5	-0.1	0.4
NSH	4 May	-1.4	-1.0	-4.0	-0.5	3.5
BPC	4 May	-2.5	-2.0	-5.0	-0.9	4.1
IFPF	1 June	-0.1	-0.1	-0.3	0.0	0.3

Table 6.8. Descriptive statistics of snow temperature $\bar{T}$ measured using the SAS2.

6.2.5. Liquid Water Content

Over the entire period of observation at the UCS site, there was an RMSD of 3.3% and a MB of 2.5% between the stationary SAS2 and dielectric measurements of liquid water content $\bar{\theta}_w$, indicating that dielectric measurements were under-predicted relative to the acoustic measurements (Figure 6.1d). An RMSD of 3.2% and a MB of -3.6% occurred between liquid water contents $\bar{\theta}_w$ measured using the stationary and portable versions of the SAS2, indicating spatial differences in liquid water content between measurement locations. The dielectric liquid water content and portable version of the SAS2 showed an RMSD of only 0.1% and a MB of 0.4%, demonstrating the ability of the SAS2 to measure $\bar{\theta}_w$ within a 0.5% RMSD difference,

similar to the ±0.5% liquid water content measurement error associated with dielectric measurements (Techel and Pielmeier, 2011).

Because the RMSD and MB magnitudes used to compare the dielectric and portable measurements of liquid water content was lower than the RMSD and MB magnitudes of the other $\bar{\theta}_w$ comparisons (Figure 6.1d), this suggested that $\bar{\theta}_w$ varied spatially between the stationary SAS2 sampling location and the portable sampling location situated close (~2 m) to the stationary device. The finding is supported by the literature reviewed in Section 2.2.9 of this thesis, showing that liquid water content is highly variable over distances spanning only 50 cm.

Some observations of liquid water content $\bar{\theta}_w$ are < 1.3% by volume within the dry region classified using the Techel and Pielmeier (2011) scheme, and most observations are < 8% by volume as found by Kattelmann and Dozier (1999) for natural snowpacks. For wet snow during the time of ablation, the acoustic observations of liquid water content $\bar{\theta}_w$ approach 10%. This is apparent for the stationary SAS2 observations made at the UCS site (Figure 6.1d) as well as for measurements of LWC made at other sites (Figure 6.8 and Table 6.10). The liquid water content values do not reach levels of ~0% due to the presence of irreducible water content in the snowpack resulting due to the presence of a quasi-liquid layer surrounding the snow particles.

The liquid water content increased over the observation season as the snowpack warmed due to higher levels of net radiation and increasing air temperatures. This is apparent at the UCS site and at the portable sites visited later in the observation season (Table 6.10). All observations of liquid water content made using the SAS2 are within the range of liquid water contents given by the Martinec classification scheme and the Fierz et al. (1999) scheme. Because the acoustic values of water content observed at the UCS site are in the same range of liquid water contents observed by other investigators (Section 2.29), this strongly implies that the acoustic sensor measurements are physically reasonable, though it is not possible to exactly confirm the readings.

At the UCS site, the liquid water content $\bar{\theta}_w$ was lowest on 8 February at 1%, indicating a very dry snowpack (Figure 6.1d). This is in agreement with the Fierz et al. (1999) classification of liquid water content being close to 0% for dry snow and irreducible liquid water contents θ_e of 1% to 2% (Marsh, 1991). The liquid water content never dropped as low as 0% due to the presence of irreducible liquid water held in the pore spaces of the snowpack.

After 8 February at the UCS site, higher levels of depth-averaged temperature $\overline{T}$ measured by the snowharp was apparent, and this is coincident with higher levels of liquid water content $\overline{\theta}_w$. Diurnal cycles of $\overline{\theta}_w$ were also present at this time, with a slight rise in liquid water content during the afternoon following peaks in shortwave radiation $K\downarrow$, indicating that energy was being transferred to the snowpack due to positive net shortwave radiation K^*.

Cycles of $\overline{\theta}_w$ were apparent, with the period of an average cycle (peak to trough of the waveform) lasting over the time period of ~1 day, indicating diurnal changes in $\overline{\theta}_w$ associated with warming of the snowpack during the day and cooling of the snowpack during the night. Because the cold content of the snowpack will increase due to a negative energy balance during the night, the cold content will only decrease when the net energy balance becomes positive and the snowpack warms. The cycles in depth-averaged water content $\overline{\theta}_w$ are created due to the heat capacity of the snowpack, which creates a time lag between the application of a positive energy balance and a rise in water content $\overline{\theta}_w$. Over the time of observation, the $\overline{\theta}_w$ values continued to increase due to increases in K^* and air temperature. A gradual increase in snow average temperature $\overline{T}$ (Figure 6.5a) showed that the snowpack continued to warm over the observation season.

The water content once again reached a low level of 1% on 20 February (Figure 6.1d). This was the last time during the observation period when the liquid water content was as low as 1% due to gradually-increasing values of downward shortwave radiation $K\downarrow$, net shortwave radiation K^*, and air temperature occurring due to seasonal changes.

The first major drop in snow depth occurred between 14 April and 21 April, when the snow depth decreased from 99 cm to 78 cm due to ablation. The liquid water content $\overline{\theta}_w$ increased from 5.4% to 6% during this time (Figure 6.1d), continuing the upward trend apparent over the observation period. The second drop in snow depth occurred between 21 April and 26 April, when the snow depth decreased from 76 cm to 48 cm, a total of 28 cm. The water content was at 8.6% on 26 April, increasing a total of 2.6% from the observed 6% on 21 April.

After 10 May, a decrease in liquid water content $\overline{\theta}_w$ indicated that the snowpack was at the end of the ripening phase and had entered the output phase, as the snowpack was unable to

hold any more water. Beyond this point, water drained from the snowpack and the liquid water content did not increase.

The error between dielectric measurements and acoustic measurements of water content $\bar{\theta}_w$ collected at all of the field sites was small (Figure 6.8), as suggested by an RMSD of 0.5% and a MB of -0.7% for $N_s = 19$ samples. These results indicated that the RMSD was the same as the 0.5% measurement error associated with dielectric measurements, despite some small errors occurring due to manual balancing of the Denoth meter bridge. This demonstrated that the SAS2 was able to obtain measurements of liquid water content similar to dielectric measurements. The SAS2 can therefore be used in lieu of invasive dielectric measurements of liquid water content. Higher levels of liquid water content $\bar{\theta}_w$ were measured at sites visited later in the winter season than at sites visited at an earlier time (Table 6.10).

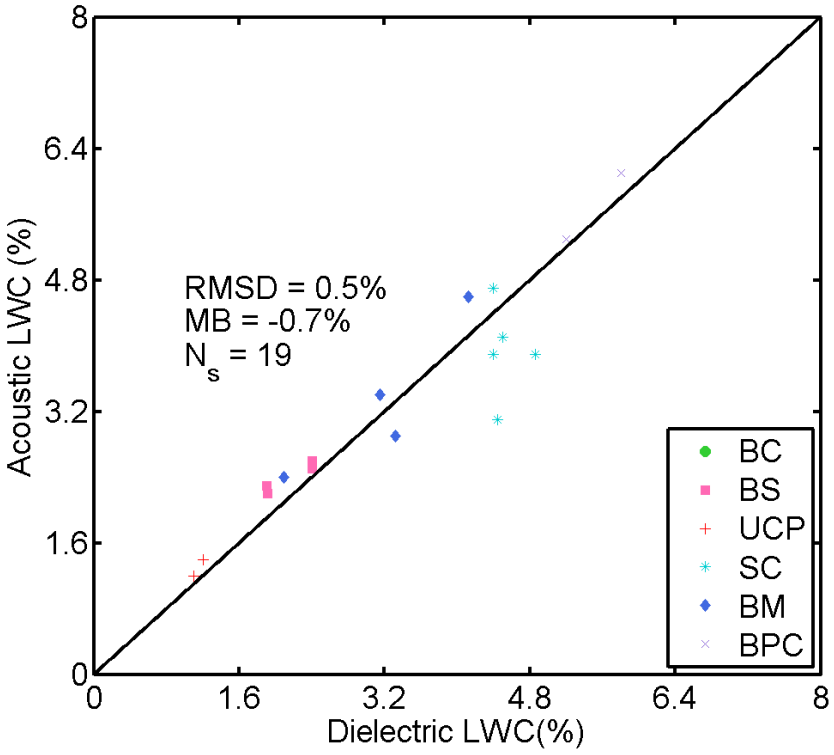

Figure 6.8. Comparison between depth-averaged liquid water content measured using dielectric methods and liquid water content measured using the SAS2 at field sites. The black line on the plot is the 1:1 line. The Boulton Campground (BC), Bow Summit (BS), Upper Clearing Portable (UCP), Sawmill Creek (SC), Bow Meadows (BM) and Black Prince Cirque (BPC) sites are listed in the legend.

Site	Dates	$\bar{\theta}_w$ RMSD (%)	$\bar{\theta}_w$ MB (%)	N_s
UCS	1 Feb to 31 May	3.3	2.5	6
BC	13 March	NA	NA	NA
BS	14 March	0.3	0.2	4
UCP	15 March	0.2	0.1	2
SC	1 May	0.8	-0.6	5
BM	3 May	0.4	0.2	4
BL	3 May	NA	NA	NA
NSH	4 May	NA	NA	NA
BPC	4 May	0.2	0.2	2
IFPF	1 June	NA	NA	NA

Table 6.9. Comparisons between dielectric and acoustic measurements of liquid water content $\bar{\theta}_w$.

Site	Dates	Mean (%)	Median (%)	Min (%)	Max (%)	Range (%)
UCS	1 Feb to 31 May	4.2	4.1	1.0	10	9
BC	13 March	1.8	1.7	1.1	2.5	1.4
BS	14 March	2.0	2.1	1.1	3.1	2.0
UCP	15 March	0.9	0.9	1.0	1.4	1.3
SC	1 May	4.4	4.0	2.0	9.0	7.0
BM	3 May	3.1	3.2	1.9	4.6	2.7
BL	3 May	7.9	8.0	5.0	9.0	4.0
NSH	4 May	6.8	7.0	4.0	9.0	5.0
BPC	4 May	3.8	3.0	1.0	8.0	7.0
IFPF	1 June	8.4	8.5	7.0	9.1	2.1

Table 6.10. Descriptive statistics of liquid water content $\bar{\theta}_w$ measured using the SAS2.

6.2.6. Acoustic

Figure 6.9a shows that at the UCS site, the speed of sound in snow, frequency-averaged from DC to the lowpass filter cutoff frequency ($f_c = 44$ KHz), was less than the speed of sound in air. The speed of sound in air was computed using the air temperature (Figure 6.6b). Table 6.11 shows descriptive statistics of the speed of sound in snow at the field sites. The mean, minimum and maximum values of the speed of sound in snow at the field sites were less than the minimum speed of sound in air.

These findings suggest that the sound wave propagating through the snowpack is the Biot second P-wave that travels through the pore spaces of the snow medium. The physics of sound wave propagation in porous media shows that the Biot second P-wave may travel at a speed less than the speed of sound in air (Allard and Atalla, 2009; Johnson and Plona, 1980; Johnson et al., 1982).

Figure 6.9b shows that the frequency-averaged attenuation a_c was not constant over the snow accumulation and ablation season at the UCS site due to snowpack metamorphism and an increase in snow depth. Coincident with a rise in snow depth after the first large snow deposition event occurring on 4-5 March, the attenuation for the sound wave passing through the snowpack gradually increased during the time of snow accumulation and then decreased during the time of ablation after 16 April. For observations made at all of the field sites (Table 6.12), the mean, minimum and maximum attenuation values were in the range of $0 \text{ Np m}^{-1} \leq a_c \leq 2.0 \text{ Np m}^{-1}$. This range was used in the sensitivity analysis of Section 4.3.4, which showed that the theoretical maximum depth of snow over which an acoustic wave from the SAS2 could propagate was ~3 m.

The maximum snow depth at the UCS site was ~1 m, whereas the maximum snow depth at all of the sites (Table 6.13) was ~2 m. Because the SAS2 was deployed at these field sites, this indicates that the SAS2 could obtain acoustic measurements of snow up to this maximum depth.

The Ψ coefficient (Figure 6.9c) represents differences between the elastic constants of ice and the elastic constants of the snow particles (Section 3.2.3). For most of the snow accumulation and ablation season, Figure 6.16c shows that $\Psi > 1$. This suggests that the elastic constants of snow particles comprising the snowpack were less than the elastic constants of ice. During the time of ablation after 16 May, the Ψ coefficient was $\Psi \leq 1$, thereby suggesting that the elastic constants of the snow particles were either the same or similar to the elastic constants of ice. Descriptive statistics (Table 6.14) showed that for most of the field sites, the mean, minimum and maximum values of Ψ were $\Psi > 1$. However, for the BL and IFPF field sites, the mean Ψ coefficient was $\Psi \leq 1$, suggesting the presence of grain-coarsening of snow particles that occurred due to high liquid water contents and old, metamorphosed snow. Wet snow metamorphism that occurred due to the ponded water at the BL site may have been responsible for making the elastic constants of snow similar to the elastic constants of ice.

Site	Dates	Min Air ($m\ s^{-1}$)	Mean ($m\ s^{-1}$)	Median ($m\ s^{-1}$)	Min ($m\ s^{-1}$)	Max ($m\ s^{-1}$)	Range ($m\ s^{-1}$)
UCS	1 Feb to 31 May	319	257	258	190	318	128
BC	13 March	329	307	308	292	311	19
BS	14 March	329	302	302	292	309	17
UCP	15 March	328	301	303	268	315	47
SC	1 May	330	287	288	236	309	73
BM	3 May	331	294	294	281	305	24
BL	3 May	331	251	254	210	306	96
NSH	4 May	335	274	270	227	327	100
BPC	4 May	333	301	302	280	324	44
IFPF	1 June	336	285	281	276	303	27

Table 6.11. Descriptive statistics of the speed of sound in snow c_s ($m\ s^{-1}$) measured using the SAS2. The minimum speed of sound in air at each of the field sites is given in the column with the "Min Air" heading. The speed of sound in snow is less than the minimum speed of sound in air at each of the field sites.

Site	Dates	Mean	Median	Min	Max	Range
UCS	1 Feb to 31 May	1.3	1.4	0.0	2.0	2.0
BC	13 March	0.5	0.4	0.2	1.0	0.8
BS	14 March	0.3	0.2	0.0	1.3	1.3
UCP	15 March	1.2	1.2	0.5	1.8	1.3
SC	1 May	0.6	0.5	0.1	1.9	1.8
BM	3 May	1.2	1.2	0.1	1.7	1.6
BL	3 May	1.9	1.9	1.8	2.0	0.2
NSH	4 May	1.2	1.3	0.1	1.6	1.5
BPC	4 May	0.5	0.4	0.1	1.4	1.3
IFPF	1 June	1.7	1.7	1.5	1.8	0.3

Table 6.12. Descriptive statistics of sound attenuation a_c measured using the SAS2.

Site	Dates	Mean (cm)	Median (cm)	Min (cm)	Max (cm)	Range (cm)
UCS	1 Feb to 31 May	56	53	0	100	100
BC	13 March	97	100	59	110	51
BS	14 March	175	178	119	201	82
UCP	15 March	78	75	26	123	97
SC	1 May	98	97	18	160	142
BM	3 May	125	125	65	162	97
BL	3 May	58	53	51	70	19
NSH	4 May	49	44	3	1.6	113
BPC	4 May	57	56	22	92	70
IFPF	1 June	43	42	30	55	25

Table 6.13. Descriptive statistics of snow depth $\bar{y}$ measured using a depth rod.

Site	Dates	Mean	Median	Min	Max	Range
UCS	1 Feb to 31 May	1.4	1.5	0.0	2.0	2.0
BC	13 March	1.2	1.3	0.5	1.6	1.1
BS	14 March	1.3	1.3	1.0	1.9	0.9
UCP	15 March	1.3	1.3	1.1	1.5	0.5
SC	1 May	1.5	10.5	0.9	2.0	1.1
BM	3 May	1.3	1.3	1.0	1.8	0.8
BL	3 May	0.7	0.6	0.5	1.1	0.6
NSH	4 May	1.1	1.2	0.1	1.8	1.7
BPC	4 May	1.5	1.5	1.1	2.0	0.9
IFPF	1 June	0.8	0.8	0.5	1.2	0.7

Table 6.14. Descriptive statistics of Ψ coefficient measured using the SAS2.

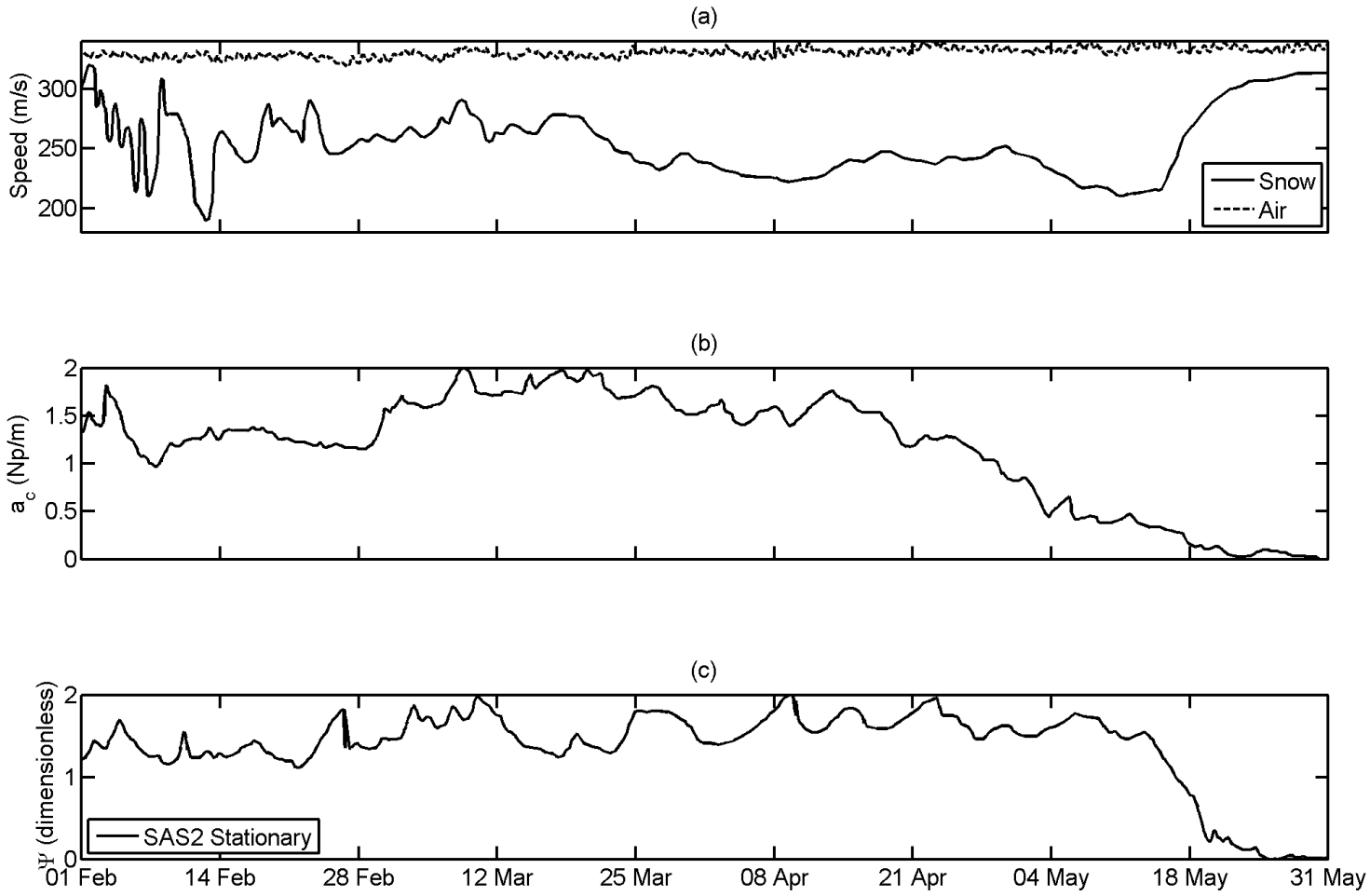

Figure 6.9. Upper Clearing Stationary (UCS) site time-series data showing (a) frequency-averaged speed of sound in snow and in air, (b) frequency-averaged attenuation, and (c) Ψ coefficient.

6.3. Acoustic Imaging Example

Figure 6.10 shows an example of an acoustic image created using the SAS2 at the UC stationary site on 15 March. The figure consists of processed signals arranged at cumulative microphone offset distances from the loudspeaker. The processing required to form this image is discussed in Chapter 3. The elements of the image matrix have been scaled to amplitudes of $[0,1]$ for visual display. The observation was made on 15 March shortly before a snowpit was created next to the acoustic sensor. The snowpit was created at a distance of ~2 m from the acoustic sensor. The total snow depth was 91 cm. As shown by Figure 6.10, the snowpit stratigraphy was comprised of a wind-crusted surface layer with clumps and hard snow overlying a layer with rounded dendric particles; under this layer was a layer of snow particles with rounded columns; and at the bottom of the snowpack was a layer of depth hoar with facetted particles.

As shown by Figure 6.10, the snow density near the surface of the snowpack remained close to 130 kg m^{-3} with an increase in snow density to 220 kg m^{-3} and a slight drop in snow density to 214 kg m^{-3} in the bottom layers of the snowpack due to the presence of facetted depth hoar with unconsolidated crystals. The RMSD between the snowpit and acoustic measurements of $\bar{\rho}$ was 4.46 kg m^{-3}, indicating that for this measurement, the SAS2 under-predicted depth-averaged snow density $\bar{\rho}$. The SWE was similarly under-predicted due to under-prediction of the density. The depth-averaged snowpit temperature $\bar{T}$ was $-1.6^{\circ}\mathrm{C}$, slightly greater than the acoustic measurement of temperature at $-2.5^{\circ}\mathrm{C}$. The RMSD between temperature measurements was $0.91^{\circ}\mathrm{C}$, indicating that there was $\sim 1^{\circ}\mathrm{C}$ difference between temperature measurements made from the side of a snowpit and acoustic measurements.

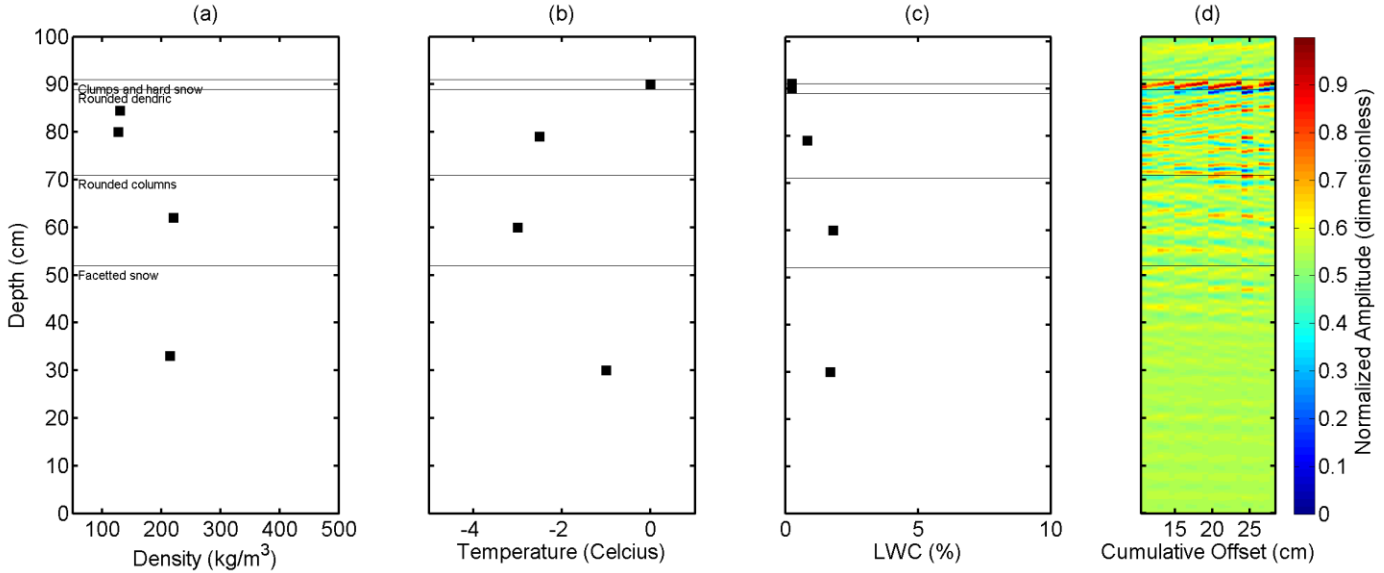

235

Measurement	Gravimetric/Thermal/Dielectic	Acoustic	RMSD	MB
$\bar{\rho}$ (kg m^{-3})	173	168	4.46	-4.46
SWE (mm)	157	142	15.6	-15.6
$\bar{T}$ (°C)	-1.60	-2.50	0.910	-0.910
$\bar{\theta}_w$	0.960	4.70	3.70	3.70

Figure 6.10. Snowpit stratigraphy at Upper Clearing Stationary (UCS) site observed on 15 March. The snowpit was situated close to the SAS2 sensor; subplots are: (a) gravimetric density measurements; (b) temperature measured from the snowpit wall using a thermometer; (c) liquid water content; and (d) acoustic image of snowpit with cumulative offset. A table shows a comparison between the snowpit and acoustic measurements.

The acoustic image (Figure 6.10d) showed reflections from the snowpack. The resolution is qualitatively similar to a sonar image sensed using a sediment-profiling sonar system (Lurton, 2002) or a medical ultrasonography image (Ng and Swanevelder, 2011). Owing to the empirical measurement of the system response $\mu_k[t]$ (Section 4.4), there may be a loss of resolution and the creation of some spurious reflections in the SAS2 image. The resolution may be lower (i.e. the minimum resolvable width $\Delta y >> 2.5\times10^{-4}$ m) then the minimum resolution given by design calculations in Section 4.3.12.

Because the sound wave from the SAS2 is reflected due to changes in the acoustic impedance of snow, reflections shown by Figure 6.10d do not always coincide with snowpack layers observed by an experienced snow surveyor. This is a limitation of the acoustic method occurring due to the physics of sound propagation in snow and is similar to limitations of sonar and medical ultrasonography. The finding reported here is similar to the finding reported by Harper and Bradford (2003), who found that radar images do not always coincide with snowpit measurements due to small changes in the dielectric constant of snow. This implies that small-scale variability in snow acoustic properties may be a reason for differences between snowpits and the SAS2. Moreover, because time-to-depth conversion was accomplished using the average speeds of sound in snow, reflections may not exactly coincide with the depths of measured snowpack layers. The time-to-depth conversion in the air medium above the surface of the snowpack was accomplished by using the speed of the sound wave in air, calculated using air temperature.

Near the snow surface at 91 cm, the acoustic image from the SAS2 shows a high-amplitude reflection associated with the sound wave crossing the air-snow interface. The high-amplitude reflection occurred due to differences in acoustic impedance between the air and snow mediums. Above the air-snow interface, reflections of small amplitude are visible. These reflections may be multiple reflections from the snowpack, or could represent changes in the speed and attenuation of the sound wave in the boundary layer above the snow surface due to changes in temperature. A low-amplitude reflection was visible at 89 cm depth after the sound wave exited the wind-crusted layer and moved to a greater depth beneath the snow surface. Within the second snowpack layer from 89 cm to 71 cm, acoustic scattering of the sound wave and internal reflections caused a series of linear features to appear in the image. These linear features disappear after 71 cm, indicating the start of another layer in the snowpack. The linear

features are of higher amplitude than the features in the preceding layer from 71 cm to 52 cm. From 52 cm to the ground surface, there was a loss of resolution and an increase in attenuation as the sound wave propagated into the depth hoar layer. This attenuation occurs since the sound wave has propagated through a porous medium comprised of coarse particles (Stoll, 1989).

6.4. Seasonal Snowpack Changes

Figures 6.11 to 6.18 show snowpits and acoustic images observed at the UCS site. The first snowpit observed on 2 February showed a layer of fresh snow overlying a layer of loosely-packed soft snow with extensive depth hoar formation at the bottom. An increase in snow density occurred with depth due to overburden compaction by overlying snow layers and depth hoar particles with large mass. The temperature continued to increase with depth beneath the snow surface, indicating the presence of a temperature gradient due to a ground heat flux. A temperature gradient was also apparent in the snowharp and heat flux plate data (Figure 6.5 and 6.6).

The layer of soft snow deposited on the top of the snowpack was visible on the acoustic image as a large amplitude reflection. Some internal reflections were caused due to acoustic scattering by the fresh snow. The layer of soft snow under the fresh snow layer was barely visible on the acoustic image. There was a loss of resolution and an increase in attenuation in the depth hoar layer. The RMSD and MB indicate good agreement between the measured and acoustic parameters.

By 16 February, the layer of fresh snow observed on 2 February had been compacted, and a small layer of fresh snow near the snow surface was also present. The density and temperature increased with depth. The acoustic image showed the top of the snowpack as a reflection with large amplitude. Some reduction in acoustic scattering was apparent in the second packed layer, with a change in the acoustic image apparent at less than 30 cm depth from the bottom of the snowpack, showing a change in density within the depth hoar layer.

The snowpit shown for 15 March has already been discussed in the previous section of this thesis (Figure 6.10). By 18 April the snowpit showed lower density at distances closer to the bottom of the snowpack due to the presence of wet layers near the snow surface. The snow temperature was near $0^{\circ}C$, indicating that the snowpack was close to isothermal. The liquid

water content $\bar{\theta}_w$ decreased with depth due to warming of the snowpack near the snow surface. Acoustic imaging of the snowpack showed more spatial variability in the layers at this time.

By 25 April, the snowpack showed extensive metamorphism. A layer of wet snow on the top of the snowpack was observed above a slightly denser layer. Near the bottom of the snowpack was a layer of wet columns and wet depth hoar. The snowpack was isothermal at $0\ ^\circ\mathrm{C}$, indicating that the snow was melting. The first two snow layers are visible on the acoustic image, with some internal reflections visible in the denser layer and a loss of resolution as well as an increase in attenuation for layers near the bottom of the snowpack.

On 2 May, the snowpack was once again isothermal at $0\ ^\circ\mathrm{C}$. Wet snow metamorphism resulted in the destruction of snowpack layers observed earlier in the observation season. The water content was greatest near the snow surface due to warming by radiative fluxes. A decrease in water content was apparent for fresh snow, whereas the water content was slightly greater for the underlying layer of hard-packed crystals. The acoustic image shows the top layer as a high-amplitude reflection, followed by internal reflections within the underlying snowpack layers.

By 10 May, the snowpack had a temperature near $0\ ^\circ\mathrm{C}$ shortly before the drop in water content observed after this date (Figure 6.1d). This is when the snowpack exited the ripening phase and the water content decreased during the output phase. The acoustic image showed a loss of resolution at a distance of less than 5 cm from the snow surface, indicating the presence of meltwater ponded between the bottom of the snowpack and the frozen ground surface. By 14 May, there was a rapid decrease in snow depth and water content. The snowpack was in the output phase where the production of meltwater occurred. Few reflections from the snowpack are visible on the acoustic image and the water content $\bar{\theta}_w$ was lower than the liquid water content $\bar{\theta}_w$ on 10 May.

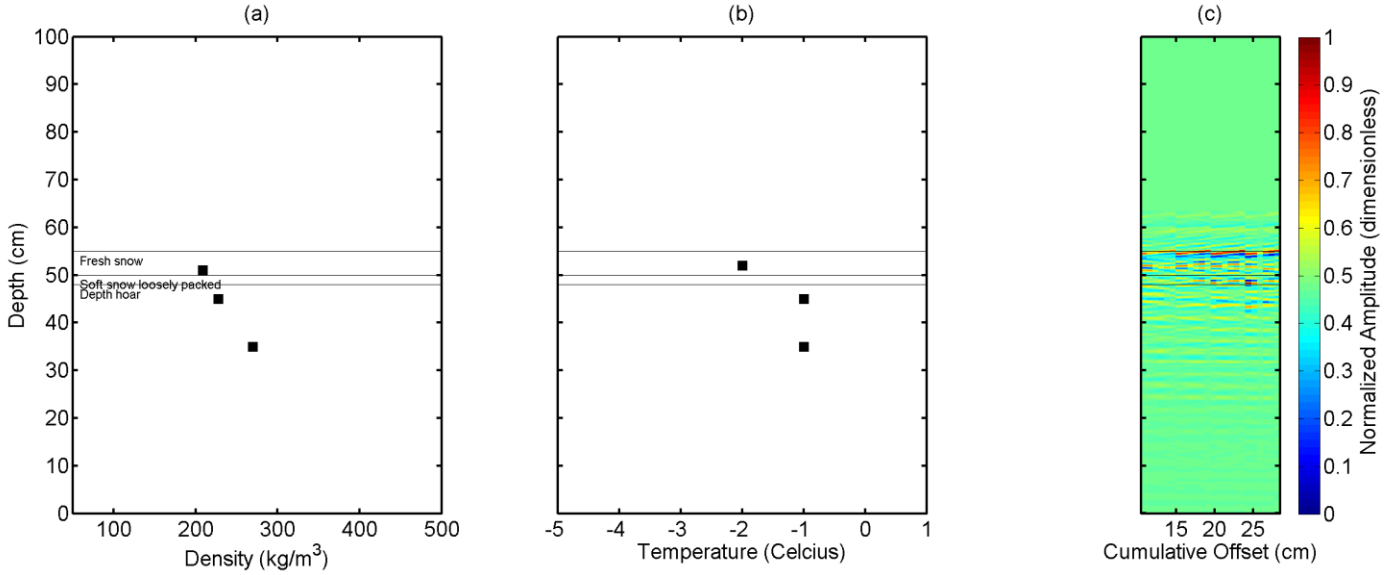

Measurement	Gravimetric/Thermal/Dielectric	Acoustic	RMSD	MB
$\bar{\rho}$ (kg m^{-3})	235	153	82.7	-82.7
SWE (mm)	129	67.5	61.9	-61.9
$\bar{T}$ (°C)	-1.30	-7.70	6.40	6.40

Figure 6.11. Snowpit stratigraphy at Upper Clearing Stationary (UCS) site observed on 2 February. The snowpit was situated close to the SAS2 sensor; subplots are: (a) gravimetric density measurements; (b) temperature measured from the snowpit wall using a thermometer; and (c) acoustic image of snowpit with cumulative offset. A table shows a comparison between the snowpit and acoustic measurements.

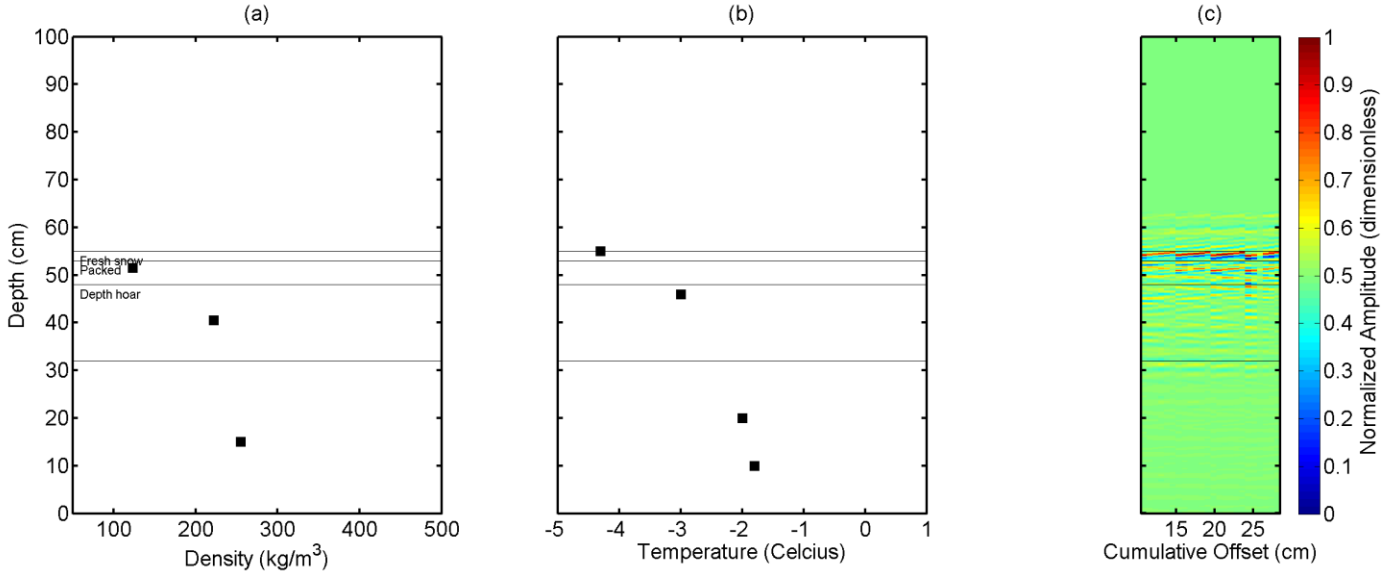

Measurement	Gravimetric/Thermal/Dielectric	Acoustic	RMSD	MB
$\bar{\rho}$ (kg m^{-3})	200	177	22.2	-22.2
SWE (mm)	110	89.8	20.2	-20.2
$\bar{T}$ (°C)	-2.80	-9.90	7.10	7.10

Figure 6.12. Snowpit stratigraphy at Upper Clearing Stationary (UCS) site observed on 16 February. The snowpit was situated close to the SAS2 sensor; subplots are: (a) gravimetric density measurements; (b) temperature measured from the snowpit wall using a thermometer; and (c) acoustic image of snowpit with cumulative offset. A table shows a comparison between the snowpit and acoustic measurements.

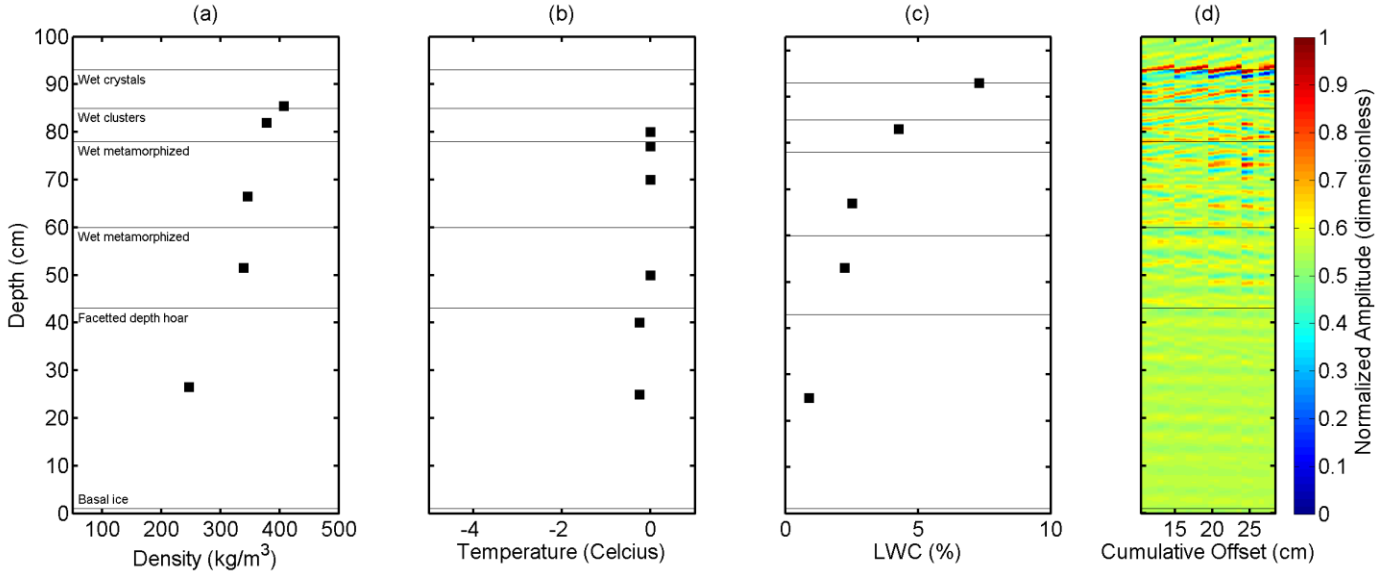

241

Measurement	Gravimetric/Thermal/Dielectric	Acoustic	RMSD	MB
$\bar{\rho}$ (kg m^{-3})	343	339	4.24	-4.24
SWE (mm)	319	280	39.2	-39.2
$\bar{T}$ (°C)	-0.01	-0.67	0.600	0.6
$\bar{\theta}_w$ (%)	2.22	5.83	3.60	3.60

Figure 6.13. Snowpit stratigraphy at Upper Clearing Stationary (UCS) site observed on 18 April. The snowpit was situated close to the SAS2 sensor; subplots are: (a) gravimetric density measurements; (b) temperature measured from the snowpit wall using a thermometer; (c) liquid water content; and (d) acoustic image of snowpit with cumulative offset. A table shows a comparison between the snowpit and acoustic measurements.

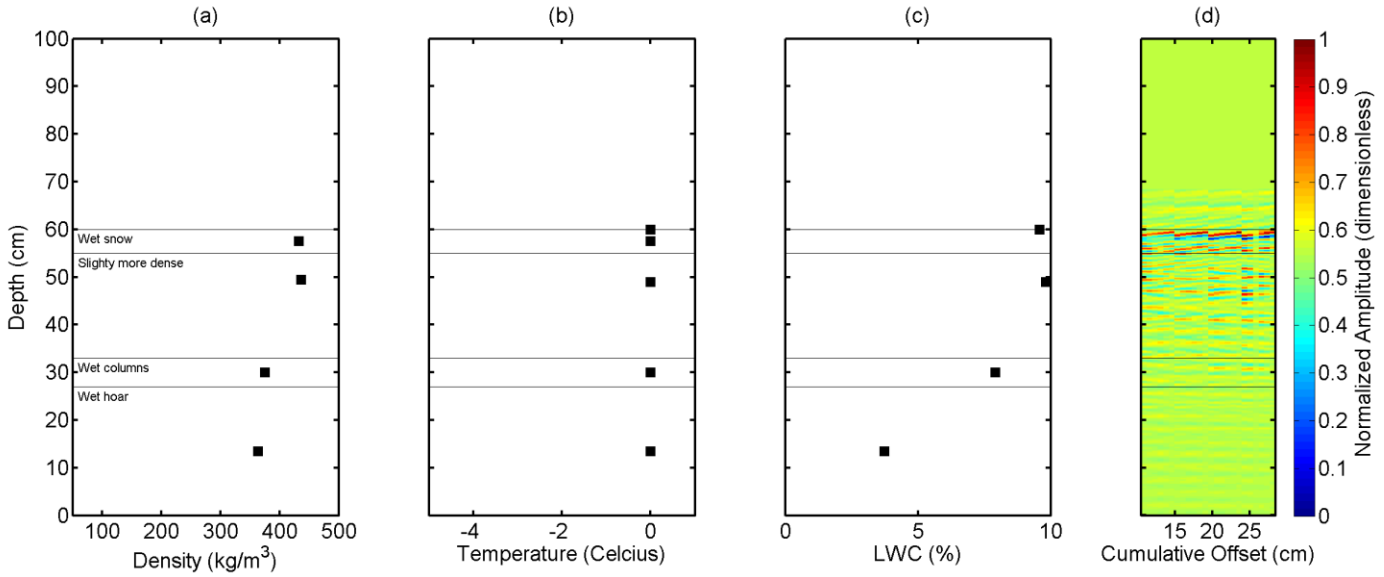

Measurement	Gravimetric/Thermal/Dielectric	Acoustic	RMSD	MB
$\bar{\rho}$ (kg m^{-3})	402	409	7.74	7.74
SWE (mm)	241	160	80.7	-80.7
$\bar{T}$ (°C)	0.500	-0.500	1.00	1.00
$\bar{\theta}_w$ (%)	7.76	6.70	1.06	1.06

Figure 6.14. Snowpit stratigraphy at Upper Clearing Stationary (UCS) site observed on 25 April. The snowpit was situated close to the SAS2 sensor; subplots are: (a) gravimetric density measurements; (b) temperature measured from the snowpit wall using a thermometer; (c) liquid water content; and (d) acoustic image of snowpit with cumulative offset. A table shows a comparison between the snowpit and acoustic measurements.

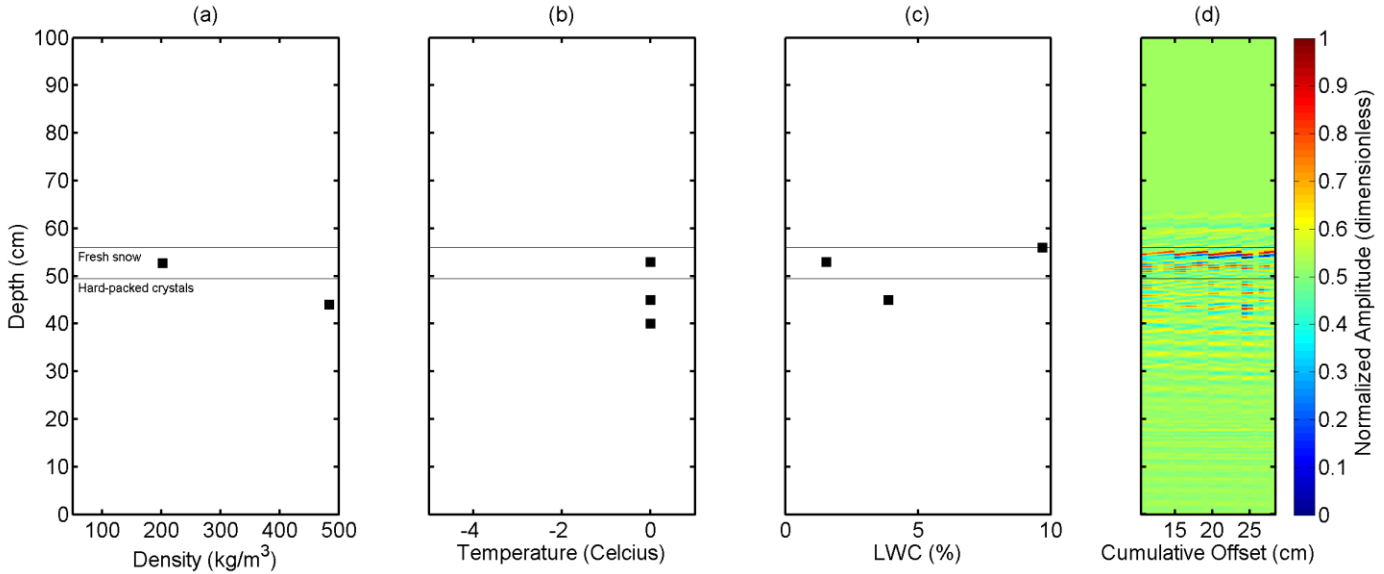

Measurement	Gravimetric/Thermal/Dielectric	Acoustic	RMSD	MB
$\bar{\rho}$ (kg m^{-3})	343	424	81.3	81.3
SWE (mm)	192	132	59.6	-59.6
$\bar{T}$ (°C)	0.500	-0.366	0.866	-0.866
$\bar{S}_w$ (%)	5.10	7.90	2.80	2.80

Figure 6.15. Snowpit stratigraphy at Upper Clearing Stationary (UCS) site observed on 2 May. The snowpit was situated close to the SAS2 sensor; subplots are: (a) gravimetric density measurements; (b) temperature measured from the snowpit wall using a thermometer; (c) liquid water content; and (d) acoustic image of snowpit with cumulative offset. A table shows a comparison between the snowpit and acoustic measurements.

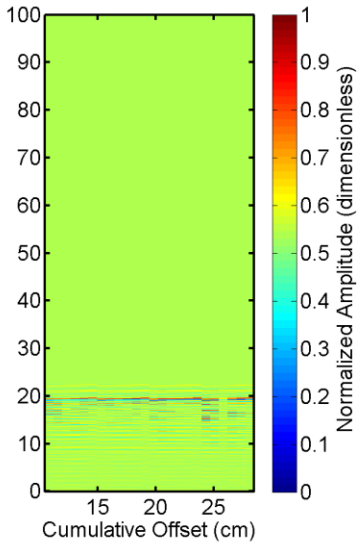

Measurement	Acoustic
$\bar{\rho}$ (kg m^{-3})	334
SWE (mm)	67.0
$\bar{T}$ (°C)	-0.340
$\bar{\theta}_w$ (%)	9.80

Figure 6.16. Acoustic image at Upper Clearing Stationary (UCS) site observed on 10 May at 12:00 hrs. The snowpit was situated close to the SAS2 sensor. A table shows the acoustic measurements observed by the SAS2. The snow depth was 20 cm (measured by the SR50).

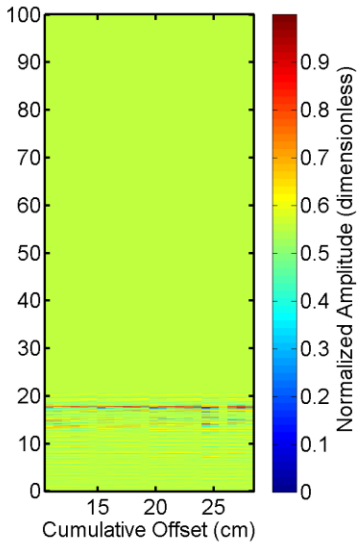

Measurement	Acoustic
$\bar{\rho}$ (kg m^{-3})	366
SWE (mm)	66.0
$\bar{T}$ (°C)	0.00
$\bar{\theta}_w$ (%)	8.10

Figure 6.17. Acoustic image at Upper Clearing Stationary (UCS) site observed on 12 May at 12:00 hrs. The snowpit was situated close to the SAS2 sensor. A table shows the acoustic measurements observed by the SAS2. The snow depth was 18 cm (measured by the SR50).

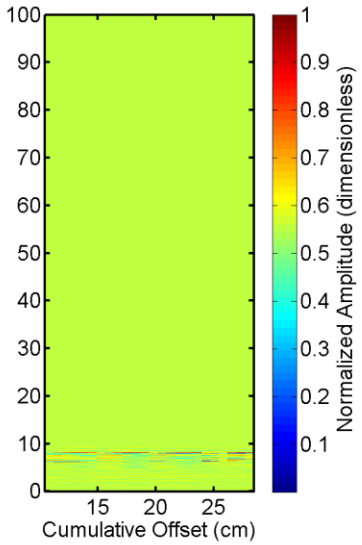

Measurement	Acoustic
$\bar{\rho}$ (kg m^{-3})	310
SWE (mm)	16.0
$\bar{T}$ (°C)	0.00
$\bar{\theta}_w$ (%)	4.50

Figure 6.18. Acoustic image at Upper Clearing Stationary (UCS) site observed on 14 May at 12:00 hrs. The snowpit was situated close to the SAS2 sensor. A table shows the acoustic measurements observed by the SAS2. The snow depth was 5.1 cm (measured by the SR50)

6.5. Repeatability of Successive Measurements

Tables 6.15 to 6.17 and Figure 6.19 show the results of an experiment conducted on 2 February shortly before the digging of the first snowpit observation made at the UCS site. The stationary version of the SAS2 was repeatedly used to take 30 acoustic observations over a time period of 6 minutes. The duration of each acoustic sample was $t_{mls} = 1.6$ s. The purpose of this experiment was to test differences between repeated acoustic samples. The snow depth was 47 cm at this time and the SAS2 was situated at a distance of 75 cm above the snow surface. The experiment could not be conducted for every acoustic sample taken using the SAS2 due to the lack of capacity for storage of acoustic data on the SD card.

For depth-averaged density $\bar{\rho}$ the measures of central tendency (mean, median and mode) are in close agreement and the maximum and minimum values have a range of only 1.25 kg m^{-3}, indicating that differences between 30 successive measurements are small. An RMSD of 0.34 kg m^{-3} and a MB of 0.10 kg m^{-3} also demonstrated the ability for the SAS2 to take successive measurements of density with values that are numerically similar. The negative skewness value of -0.03 indicated that the distribution was slightly skewed with more values greater than the mean. The kurtosis value of 2.16 showed that the distribution of $\bar{\rho}$ was platykurtic. This suggests that the histogram distribution is "flat" and the error between measurements was widely distributed over the range due to small variations in acoustic scattering between acoustic samples and small changes in wind speed under the SAS2 sensor assembly over the duration of the experiment.

The mean, median and mode were similar for depth-averaged temperature $\bar{T}$ with a range of only 0.19 °C. Small values of RMSD and MB for the $\bar{T}$ parameter also demonstrate the ability for successive measurements of snow temperature to be numerically close to the measured values. The positive skewness value of 0.14 indicates that most values in the histogram distribution are less than the mean. The kurtosis value of 1.45 suggests that similar to successive measurements of $\bar{\rho}$, the distribution is platykurtic and the error between measurements is distributed over the range of $\bar{T}$ values.

Similar to the measurements of $\bar{\rho}$ and $\bar{\theta}_w$ the range of liquid water content values was small with low RMSD and MB values. The skewness of 0.61 for the dataset was higher than the

skewness values for the $\bar{\rho}$ and $\bar{\theta}_w$ datasets. The positive skewness value of 0.61 indicated that more values in the histogram distribution were less than the mean. The kurtosis value of 2.71 indicates that the distribution of depth-integrated liquid water content values $\bar{\theta}_w$ was not as "flat" as the histogram distributions of $\bar{\rho}$ and $\bar{T}$ parameters, with more values situated closer to the mean. These results strongly suggest that successive measurements taken by the SAS2 system are repeatable.

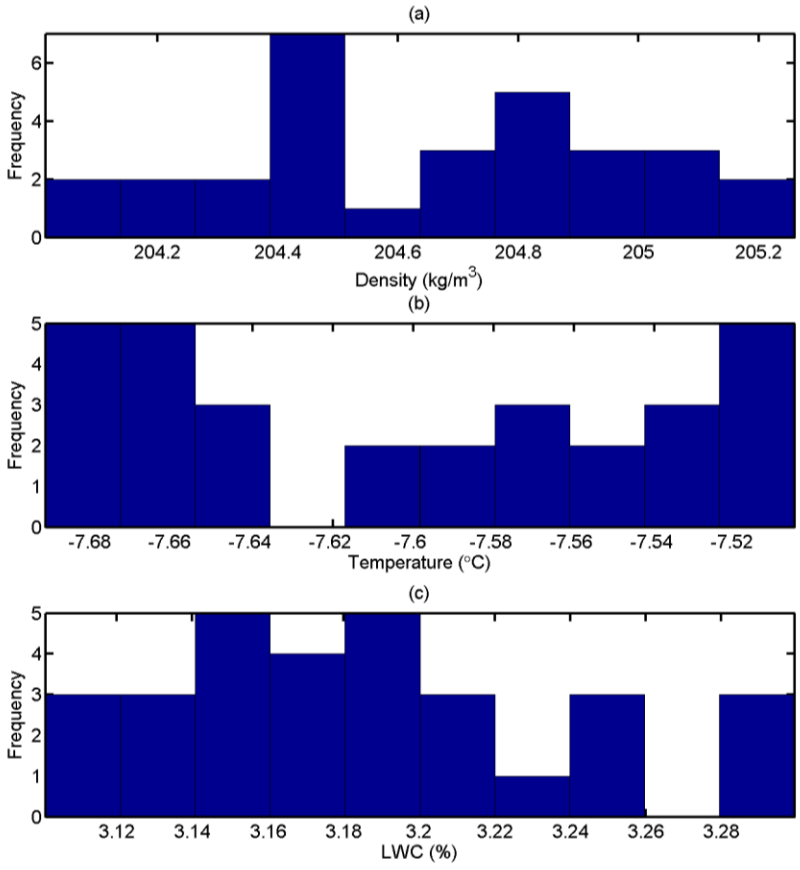

Figure 6.19. Experiment conducted on 2 February at the UCS site using the stationary version of the SAS2. The stationary version of the SAS2 was used to repeatedly take 30 acoustic observations over a time period of 10 minutes. (a) Histogram of repeated measurements for depth-integrated snow density $\bar{\rho}$. (b) Histogram of repeated measurements for depth-integrated temperature $\bar{T}$. (c) Histogram of repeated measurements for depth-integrated liquid water content $\bar{\theta}_w$.

Statistic	$\bar{\rho}$ (kg m^{-3}) or %
Mean	204.64
median	204.67
mode	204.01
max	205.26
min	204.01
range	1.25
RMSD	0.34
MB	0.10
skewness	-0.03
kurtosis	2.16

Table 6.15. Descriptive statistics for the experiment of repeated measurements conducted on 2 February at the UCS site using the stationary version of the SAS2. The depth-integrated density is $\bar{\rho}$. The RMSD and MB are used to compare each of the 30 measurements to the mean of the 30 measurements. The mean of the 30 measurements is taken as the observed value.

Statistic	$\bar{T}$ (°C) or %
mean	-7.60
median	-7.60
mode	-7.69
max	-7.69
min	-7.69
range	0.19
RMSD	0.06
MB	-0.10
skewness	0.14
kurtosis	1.45

Table 6.16. Descriptive statistics for the experiment of repeated measurements conducted on 2 February at the UCS site using the stationary version of the SAS2. The depth-integrated temperature is $\bar{T}$. The RMSD and MB are calculated in the same manner as Table 5.1.

Statistic	$\bar{\theta}_w$ (dimensionless) or %
mean	3.19
median	3.18
mode	3.10
max	3.30
min	3.10
range	0.20
RMSD	0.05
MB	0.12
skewness	0.61
kurtosis	2.71

Table 6.17. Descriptive statistics for the experiment of repeated measurements conducted on 2 February at the UCS site using the stationary version of the SAS2. The depth-integrated liquid water content is $\bar{\theta}_w$. The RMSD and MB are calculated in the same manner as Table 5.1.

6.6. Influence of Wind on SAS2 Measurements

To assess the error introduced by wind on acoustic observations made using the SAS2, Figure 6.20 shows the anemometer-measured windspeed (Figure B.1a, Appendix B) plotted against the absolute temperature error $|\varepsilon_T|$. The $|\varepsilon_T|$ is the absolute difference between the depth-averaged measurements of temperature made using the snowharp and the depth-averaged measurements of $\bar{T}$ made using the SAS2. The temperature measurements were chosen because this is the most complete SAS2 dataset collected at the Upper Clearing Stationary (UCS) site over the snow accumulation and ablation season with $N_s = 2390$ measurements.

A significant correlation between windspeed and $|\varepsilon_T|$ will imply that wind movement of the SAS2 sensor above the surface of the snowpack or wind diffraction of sound waves influenced the acoustic measurements. The Spearman rank correlation coefficient was chosen as a measure of correlation because it is non-parametric and unlike the nominal Pearson rank correlation coefficient, the data does not have to be normally distributed. Moreover, the Spearman rank correlation coefficient tests for a possible non-linear relationship between the windspeed and the error $|\varepsilon_T|$.

Choosing a 95% significance level and using a null hypothesis rejection test (Ebdon, 1991), the Spearman rank correlation coefficient of $r_s = 0.03$ indicated that the null hypothesis cannot be rejected at the 95% level and there is no correlation between windspeed and $|\varepsilon_T|$. This implies that small movements of the SAS2 on the met station boom and wind transport of sound waves did not influence acoustic measurements. This was likely due to the signal power and length of the Maximum Length Sequence (MLS). The errors in the acoustic measurements were therefore spread over the entire time that the MLS was produced, unlike the ultrasonic depth sensor with its monopulse source signal.

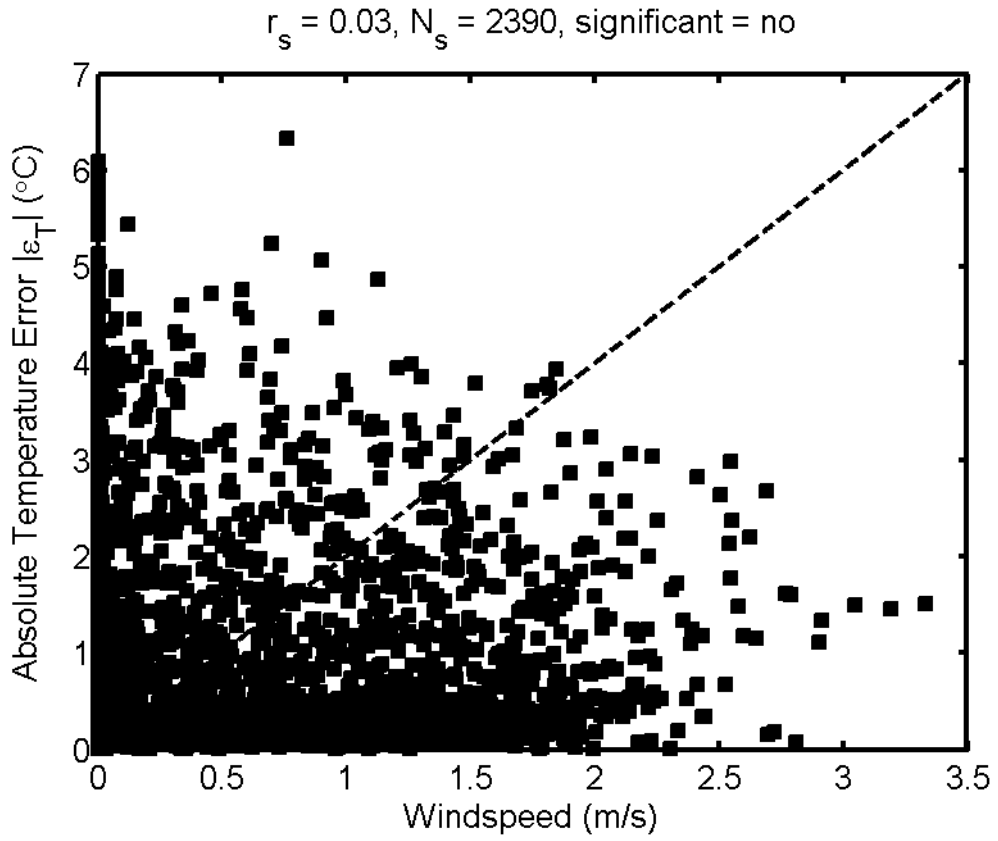

Figure 6.20. Correlations between the absolute temperature error $|\varepsilon_T|$ and the anemometer-measured windspeed at the UCS site. The absolute temperature error $|\varepsilon_T|$ is the absolute value of the difference between the depth-averaged snowharp and acoustic measurements of $\bar{T}$. The correlation r_s is the non-parametric Spearman rank correlation coefficient and the number of samples is N_s. The dashed line is provided for visual reference.

6.7. Example of Portable SAS2 Observation Site

This section presents an example of observations made using the portable version of the SAS2. Observations made at the other field sites are given in Appendix B of this thesis.

The Sawmill Creek (SC) site was chosen because it is most demonstrative of acoustic observations made using the SAS2. The SC site transect started in a clearing on the ridge, headed into an avenue of trees in a gully, crossed an ecotone between the clearing and the forest, and then finished in the forest (Figure 6.21 and 6.22, Table 6.18). Similar to the other field sites (Table 6.3) the RMSD and MB magnitudes at the SC site were highest for the ESC30 and snowpit measurements and lowest for the snowpit and acoustic measurements, indicating that the acoustic device had a higher overall accuracy than the ESC30 sampler and could also be used in lieu of the ESC30 sampler.

The RMSD comparing dielectric to acoustic measurements of liquid water content $\overline{\theta}_w$ was 0.8% at the SC site, slightly higher than the 0.5% error in liquid water content nominally associated with dielectric methods. However, the error between acoustic and dielectric measurements still remained close to 0.5%, similar to other site data shown in Table 6.9 and Appendix B.

In the same manner as the other sites, the error between gravimetric and acoustic measurements of $\overline{\rho}$ was greatest at sample points where vegetation was buried beneath the snowpack, demonstrating the effects of acoustic scattering. Larger differences in acoustic snow density relative to ESC30 density were apparent in the clearing situated on a ridge before a gully due to the presence of shrubs and small trees buried beneath the snow surface. These larger differences were not as apparent between snowpit and acoustic measurements, indicating that the ESC30 snowtube measurements were affected by the presence of vegetation.

The depth-averaged liquid water content $\overline{\theta}_w$ was lower on the ridge and in the avenue of trees than near the clearing and the ecotones, where a rise in liquid water content measured by the SAS2 was concomitant with observations of water at the bottom of the ESC30 tube used to extract snow samples. This also implied that a stream was situated under the snowpack, as suggested by the sound of running water near the shrubs. The liquid water content along the transect showed lower values in the forest than in the clearing or in the ecotone, indicating the presence of drier snow resulting due to lower levels of solar radiation occurring due to extinction of light by the forest canopy.

The acoustic SAS2 measurements showed a small drop in snow temperature on the ridge near the buried tree, suggesting the presence of the "chimney" effect identified by Sturm (1992), where temperatures are colder in the area surrounding the tree due to the rising of warm air through the void space surrounding the tree. The snow temperature remained approximately constant over the avenue of trees and clearing sections of the transect. The snow temperature $\overline{T}$ was higher in the clearing and approached 0 °C, coincident with higher measurements of $\overline{\theta}_w$ and visual observations of liquid water within the snowpack. The drop in temperature in the forest indicated a reduction in shortwave radiation from the sun and lower values of $\overline{\theta}_w$. The temperature showed an increase in variability within the forest section of the transect due to transfer of heat from vegetation to the snowpack and spatial variability in canopy cover.

The speed of sound in snow (Figure 6.22) had a similar order of magnitude as the sound speeds observed at the UCS site (Figure 6.9a), once again suggesting that a P-wave propagated in the pore spaces of the medium. The air temperature at this site was ~0 °C, corresponding with a speed of sound of ~331 m s^{-1}. The observed speed of sound in snow was << 331 m s^{-1}, indicating that the speed of sound in snow was less than the speed of sound in air.

The attenuation a of sound in snow was spatially variable along the transect. The Ψ coefficient showed that the elastic constants of the snow particles were less than the elastic constants of ice along the transect since $\Psi \geq 1$ (Figure 6.22).

Figures 6.23 to 6.27 show acoustic images corresponding with snowpits created at five locations along the transect. Most of the snowpits showed gradual increases in snow density with depth due to compression and metamorphic processes, with a slight decrease in density within layers near the bottom of the snowpack due to the presence of depth hoar. Reflections from the snow surface and a loss of resolution at the bottom of the snowpack due to the presence of depth hoar are visible on the image. Although buried shrubs were present at the bottom of the snowpack, the loss of resolution did not allow for visual identification of these elements.

Snowpit #1 (Figure 6.23) in the clearing shows a reflection from an ice crust at the snow surface. The ice crust had a high enough permeability to permit propagation of the acoustic wave through the ice crust and into the snowpack. Compared to snowpit #1, changes in snowpack stratigraphy are visible in the acoustic image of snowpit #2 (Figure 6.24), which was sampled in the avenue of trees within the clearing. The acoustic image of snowpit #2 showed that the snow surface did not generate as large as a reflection as the reflection from an ice crust

visible on the acoustic image of snowpit #1. Fine layers are noticeable in the acoustic image of snowpit #2 immediately below the surface showing changes in the acoustic properties of snow that do not immediately coincide with visually-observed snowpack stratigraphy.

The acoustic image of snowpit #3 (Figure 6.25) shows a change in reflections near the top of the snowpack when the acoustic wave passed through a layer of loose and wet snow. Smaller reflections are apparent on both sides of the buried ice layer. A few multiple reflections appear in a dense layer near the bottom of the snowpack.

For snowpit #4 (Figure 6.26) observed in the forest, a loose layer of unloaded snow from the canopy created multiple reflections at the top of the acoustic image. Some multiple reflections were also apparent in the loose layer of depth hoar near the bottom of the snowpack. The unloaded snow was also observed in the acoustic image of snowpit #5 (Figure 6.27), where the fine structure of the unloaded snow also created multiple reflections. These reflections were not present after the sound wave passed through a hard layer of snow.

Figure 6.28 shows an example of an acoustic image with a buried conifer tree situated under the snowpack. This point is marked on the transect (Figure 6.21). Reflections occurring due to the buried tree are marked on the image. Unlike the other snowpits, where there is a loss of resolution at the bottom of the snowpack due to buried depth hoar, the void space created by the conifer tree is clearly visible. The additional reflections caused acoustic snow density $\bar{\rho}$ measured by the SAS2 to be over-predicted relative to measurements made by the ESC30 snowtube. However, despite the over-prediction of density, the acoustic snow density $\bar{\rho}$ is within the same order of magnitude as the densities collected using the ESC30 snowtube.

In the avenue of trees situated within the gully, acoustic scattering and diffraction of sound occurred for SAS2 samples taken near tree wells, resulting in over-prediction of density $\bar{\rho}$. For an acoustic sample taken near a tree well, propagation of the sound wave through the snow into the air within the tree well occurred, increasing the error in the acoustic measurement. Reflections from the tree trunk may have also contributed to this error.

Figure 6.29 shows an acoustic image taken near a tree well at a sample point marked on the transect (Figure 6.21). A loss of amplitude of the reflected sound wave at greater offset distances from the loudspeaker is indicative of diffraction of the sound wave by the tree well.

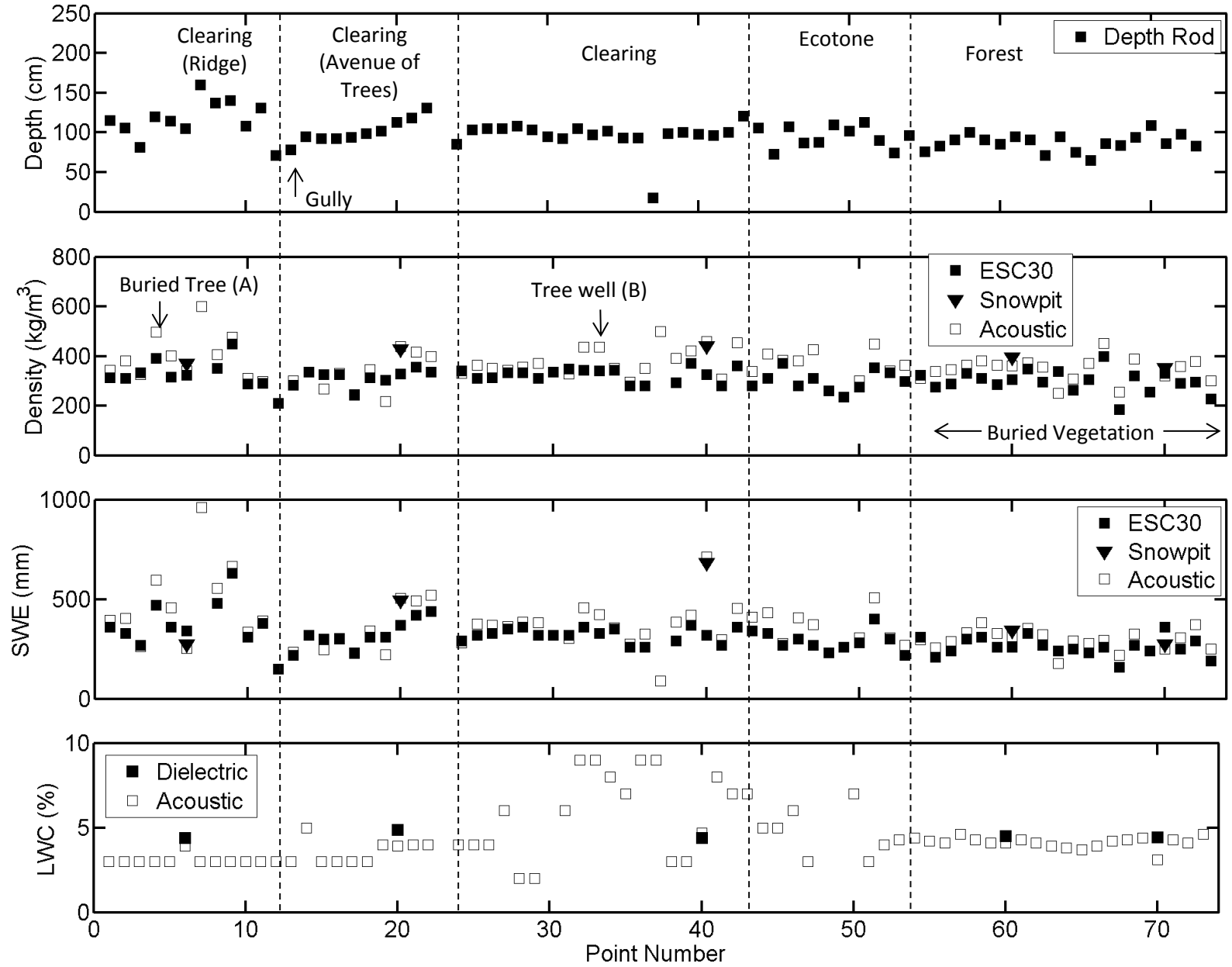

Figure 6.21. Sawmill Creek (SC) Site transects showing depth, average density $\bar{\rho}$, SWE, and depth-averaged liquid water content.

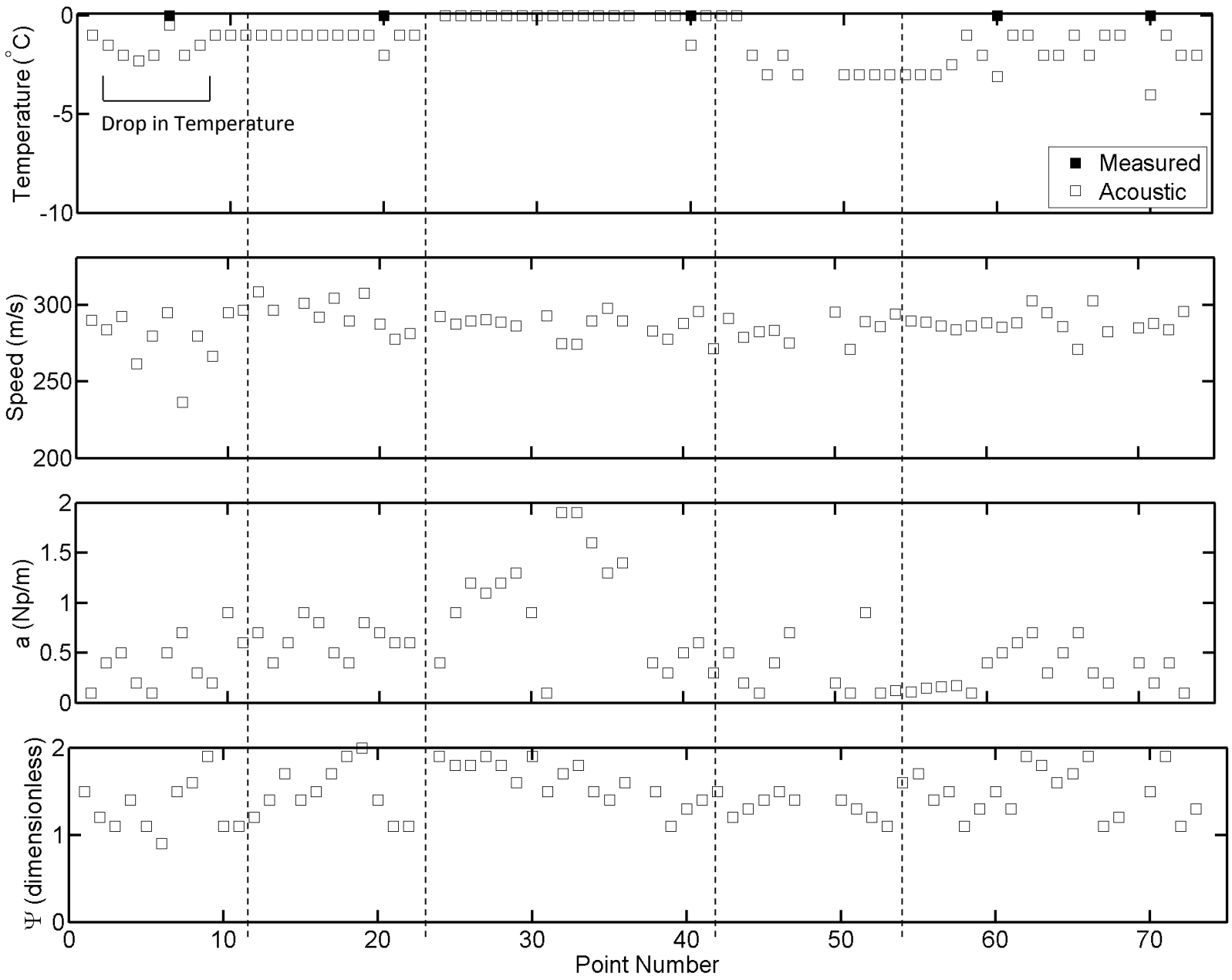

Figure 6.22. Sawmill Creek (SC) Site transects showing average temperature, frequency-averaged speed and attenuation, and Ψ coefficient.

$\bar{\rho}$ **Comparison**	**Snowpit & Snowtube**	**ESC30 & SAS2**	**Snowpit & SAS2**
RMSD ($kg\ m^{-3}$)	82.6	62.3	27.7
MB ($kg\ m^{-3}$)	75.2	43.5	-14.0

SWE **Comparison**	**Snowpit & Snowtube**	**ESC30 & SAS2**	**Snowpit & SAS2**
RMSD (mm)	182.4	79.7	24.9
MB (mm)	84.4	44.9	-7.6

$\bar{\theta}_w$ **Comparison**	**Dielectic & SAS2**
RMSD (%)	0.8
MB (%)	-0.6

$\bar{T}$ **Comparison**	**Thermometer & SAS**
RMSD (°C)	2.5
MB (°C)	-2.2

Table 6.18. Comparisons between snowpit, ESC30, and acoustic measurements of $\bar{\rho}$, SWE, $\bar{\theta}_w$ and $\bar{T}$ for the SC site.

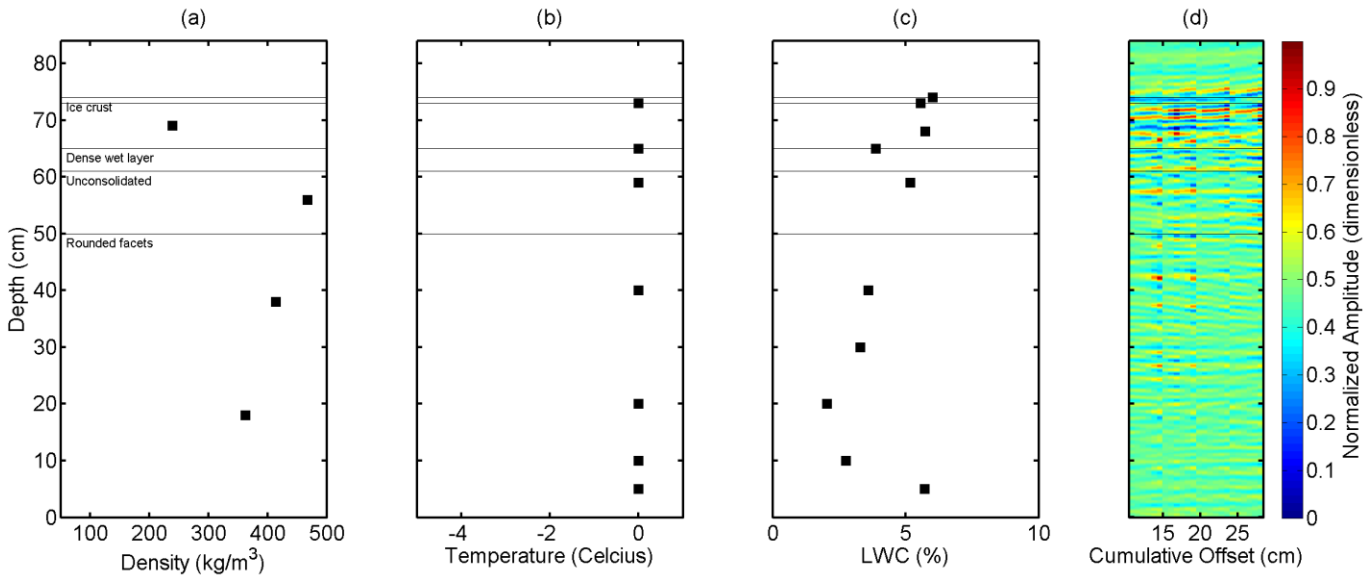

Measurement	Gravimetric/Thermal/Dielectric	Acoustic	RMSD	MB
$\bar{\rho}$ (kg m^{-3})	371	340	31.0	-31.0
SWE (mm)	274	252	22.0	-22.0
T (°C)	0.000	-0.500	0.500	-0.500
$\bar{\theta}_w$ (%)	4.40	3.91	0.490	-0.490

Figure 6.23. Snowpit #1 stratigraphy at SC site. The snowpit was situated on the ridge; subplots are: (a) depth-averaged gravimetric density measurements; (b) depth-averaged temperature measured from the snowpit wall using a thermometer; (c) depth-averaged liquid water content (LWC) measured with Denoth meter; and (d) depth-averaged acoustic image of snowpit with cumulative offset. A table shows a comparison between the gravimetric, dielectric and acoustic measurements

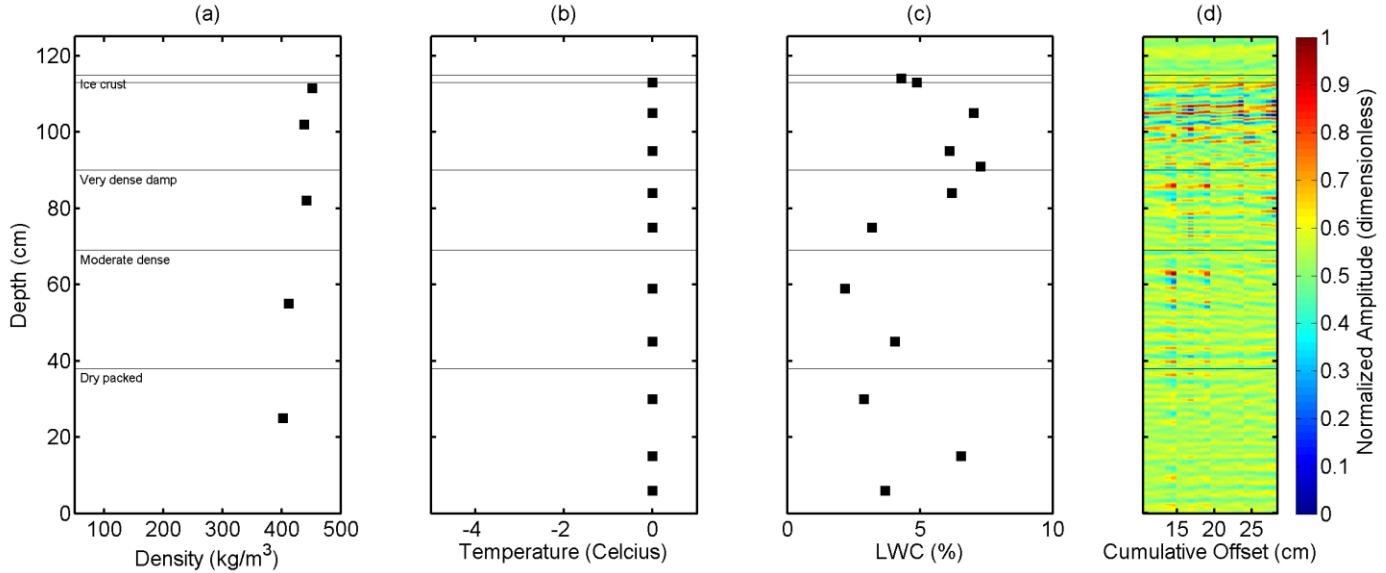

Measurement	Gravimetric/Thermal/Dielectric	Acoustic	RMSD	MB
$\bar{\rho}$ (kg m^{-3})	429	440	10.8	10.8
SWE (mm)	494	506	12.4	12.4
$\bar{T}$ (°C)	0.000	-2.000	1.900	1.900
$\bar{\theta}_w$ (%)	4.86	3.90	0.96	-0.96

Figure 6.24. Snowpit #2 stratigraphy at SC site. The second snowpit was situated in a clearing on the ridge; subplots are: (a) snowpit measurements; (b) temperature measured from the snowpit wall using a thermometer; (c) depth-averaged liquid water content (LWC) measured with Denoth meter; and (d) acoustic image of snowpit with cumulative offset. A table shows a comparison between the gravimetric, dielectric and acoustic measurements.

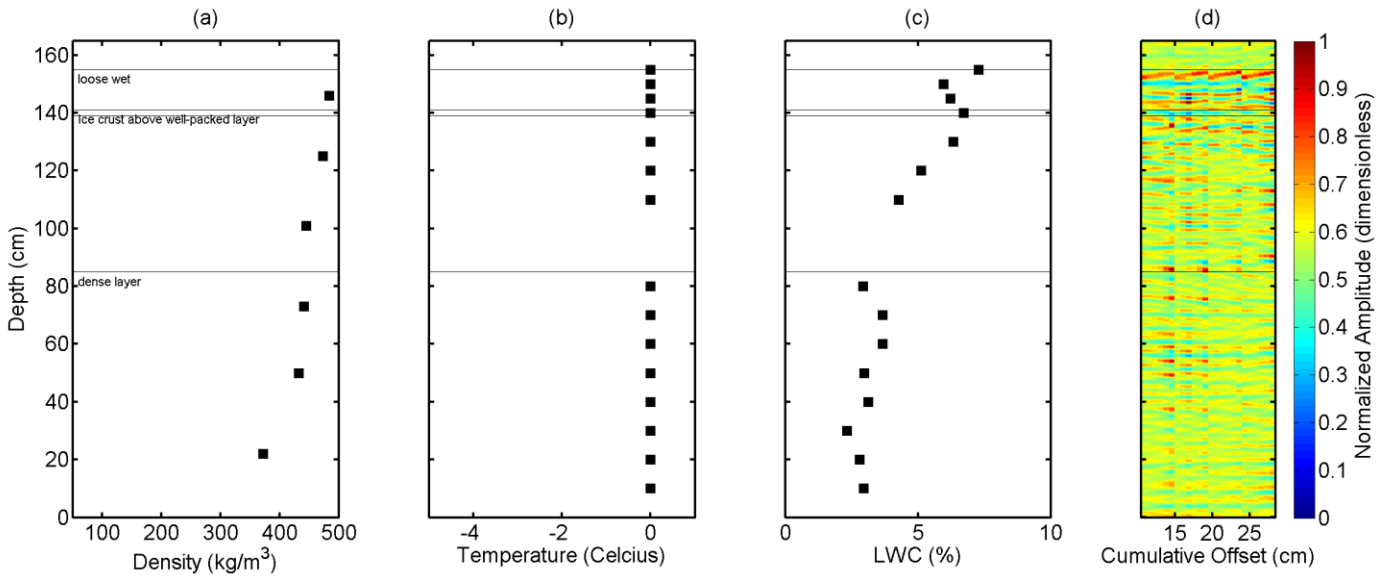

Measurement	Gravimetric/Thermal/Dielectric	Acoustic	RMSD	MB
$\bar{\rho}$ (kg m^{-3})	441	460	18.8	18.8
SWE (mm)	684	713	29.2	29.2
$\bar{T}$ (°C)	0.00	-1.50	1.50	1.50
$\bar{\theta}_w$ (%)	4.40	4.70	0.280	0.280

Figure 6.25. Snowpit #3 stratigraphy at SC site. The third snowpit was also situated in a clearing on the ridge; subplots are: (a) snowpit measurements; (b) temperature measured from the snowpit wall using a thermometer; (c) depth-averaged liquid water content (LWC) measured with Denoth meter; and (d) acoustic image of snowpit with cumulative offset. A table shows a comparison between the gravimetric, dielectric and acoustic measurements.

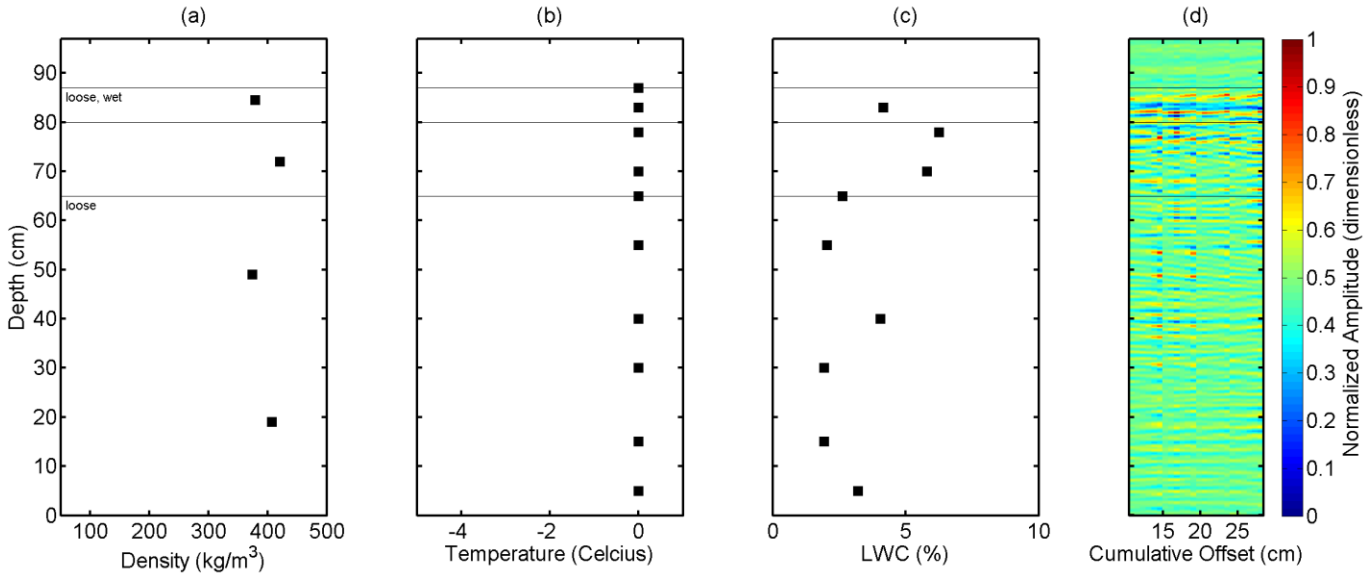

Measurement	Gravimetric/Thermal/Dielectric	Acoustic	RMSD	MB
$\bar{\rho}$ (kg m^{-3})	395	360	35.1	-35.1
SWE (mm)	344	313	30.6	-30.6
$\bar{T}$ (°C)	0.00	-3.10	2.90	2.90
$\bar{\theta}_w$ (%)	4.50	4.10	0.350	-0.350

Figure 6.26. Snowpit #4 stratigraphy at SC site. The fourth snowpit was situated in the forest nearby the ridge; subplots are: (a) gravimetric density measurements; (b) temperature measured from the snowpit wall using a thermometer; (c) depth-averaged liquid water content (LWC) measured with Denoth meter; and (d) acoustic image of snowpit with cumulative offset. A table shows a comparison between the gravimetric, dielectric and acoustic measurements.

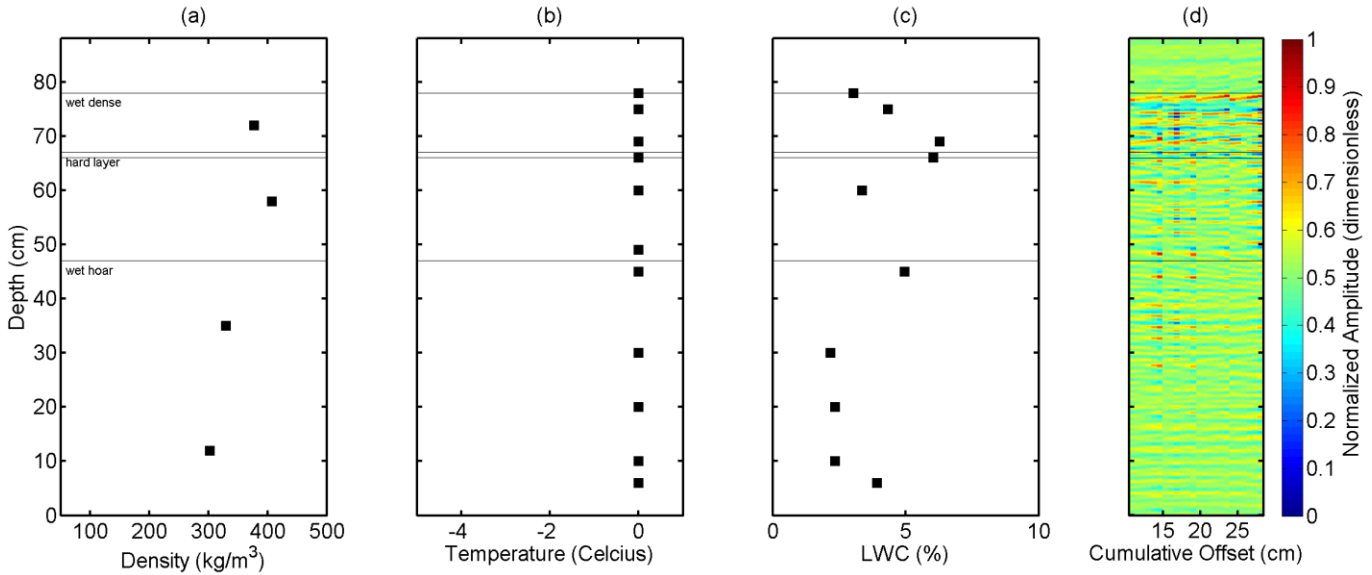

Measurement	Gravimetric/Thermal/Dielectric	Acoustic	RMSD	MB
$\bar{\rho}$ (kg m^{-3})	354	320	33.8	-33.8
SWE (mm)	276	250	26.3	-26.3
$\bar{T}$ (°C)	0.00	-4.00	3.900	3.900
$\bar{S}_w$ (%)	4.44	3.10	1.33	-1.33

Figure 6.27. Snowpit #5 stratigraphy at SC site. The fifth snowpit was situated in the forest nearby the ridge; subplots are: (a) gravimetric density measurements; (b) temperature measured from the snowpit wall using a thermometer; (c) depth-averaged liquid water content (LWC) measured with Denoth meter; and (d) acoustic image of snowpit with cumulative offset. A table shows a comparison between the gravimetric, dielectric and acoustic measurements.

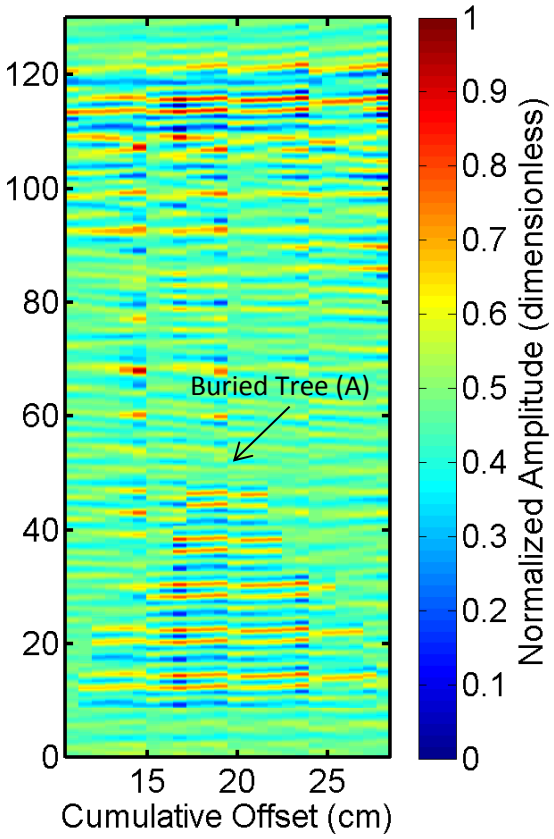

Measurement	SR50 Gravimetric	Acoustic	RMSD	MB
$\bar{\rho}$ (kg m^{-3})	392	496	104	104
SWE (mm)	470	595	125	125
$\bar{T}$ (°C)	NA	-2.3	NA	NA
S_w (%)	NA	3	NA	NA

Figure 6.28. Example of acoustic scattering due to buried conifer tree at the SC site. The position of the buried tree is marked on the image above and the sampling point location is indicated on the transect (Figure 6.21). A table presents comparisons between measurements made with the SR50 snowtube and SAS2 acoustic gauge. Comparisons that cannot be made due to a lack of observations are marked as "NA" in the table. The snow depth at this observation point was measured using a depth rod as 120 cm.

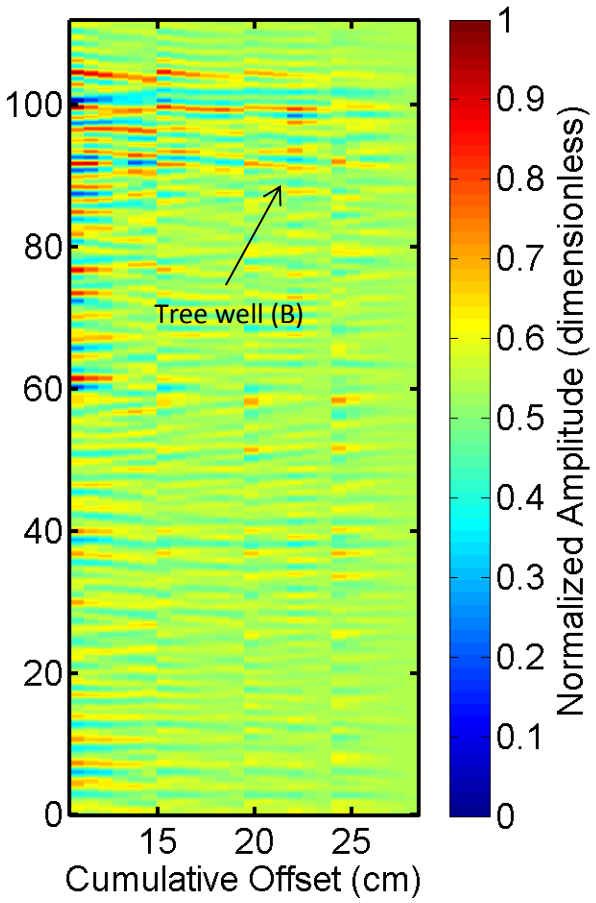

Measurement	SR50 Gravimetric	Acoustic	RMSD	MB
$\bar{\rho}$ (kg m^{-3})	343	436	93	93
SWE (mm)	360	458	98	98
$\bar{T}$ (°C)	NA	0	NA	NA
S_w (%)	NA	9	NA	NA

Figure 6.29. Example of acoustic image taken at a sample point near a tree well at the SC site, showing a loss of amplitude with increasing offset distance due to diffraction of the sound wave by the tree well. The position of the tree well is marked on the image above and the sampling point location is indicated on the transect (Figure 6.21). A table presents comparisons between measurements made with the SR50 snowtube and SAS2 acoustic gauge. Comparisons that cannot be made due to a lack of observations are marked as "NA" in the table. The snow depth at this observation point was 105 cm.

6.8. Error Comparisons

Figures 6.30 and 6.31 were used to determine if a relationship existed between the magnitude and the absolute error between variables measured using acoustic and non-acoustic methods. The variable measured using a non-acoustic method was plotted on the x-axis of each plot, and the absolute error between the acoustic and non-acoustic method was plotted on the y-axis. In the same manner as Section 6.5 of this thesis, the Spearman rank correlation coefficient was used to check for a non-linear relationship. The dashed lines on the plots are provided for visual reference.

Figure 6.30a shows that there is a significant relationship between ESC30 snowtube measurements of density $\bar{\rho}$ and the error between acoustic and non-acoustic measurements of density. Points with higher SAS2 snowtube densities had a higher acoustic density error. However, despite the smaller number of snowpit samples relative to ESC30 samples, there was not a significant relationship between the depth-averaged snowpit density and the error in the determination of density using the SAS2 (Figure 6.30b). This suggests that the density error between ESC30 snowtube and acoustic measurements may have been influenced by error in ESC30 measurements such as a bias associated with snow samples of greater mass due to spring scale or snowtube inaccuracies. This suggestion is supported by the significant relationship shown by Figure 6.30c, which compares snowpit to snowtube measurement errors.

There is a significant relationship between snowpit and snowharp measurements and the error in acoustic measurement of temperature $\bar{T}$ (Figure 6.30d). The error is greatest for lower temperatures, indicating the presence of temperature shifts in the SAS2 measurement apparatus (circuit, loudspeaker and microphones) or error in the UTAM model at lower temperatures.

Despite larger errors in acoustic parameters at the BL field site due to ponded liquid water in the snowpack, Figure 6.30e shows that there is not a significant relationship between dielectric measurements of liquid water content and the absolute error in acoustic measurement of liquid water content. Neither is there a significant relationship between liquid water content and the absolute error in acoustic density (Figure 6.30f). These results suggest that the SAS2 and UTAM model are able to determine liquid water content $\bar{\theta}_w$ and density $\bar{\rho}$ without being affected by the $\bar{\theta}_w$ magnitude, provided that a P-wave can propagate in the pore spaces of the snowpack.

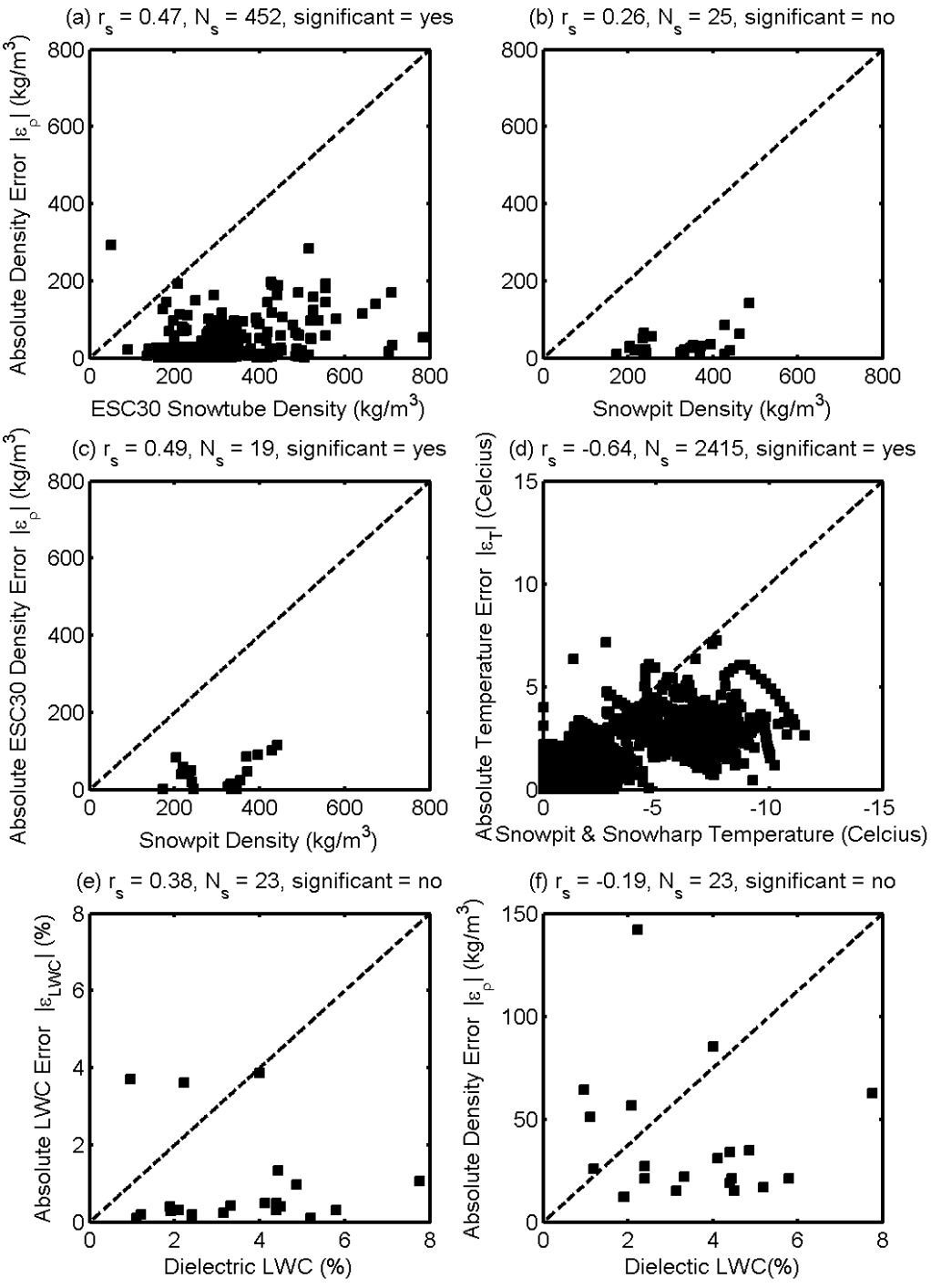

Figure 6.30. Error comparisons between acoustic and non-acoustic parameters. The Spearman rank correlation coefficient is given by r_s and the number of samples used in the analysis is N_s.

Figure 6.31 shows that there is no significant relationship between the measured snowpit density $\bar{\rho}$ and the error in determining acoustic temperature $\bar{T}$. Neither is there a relationship between dielectric measurements of LWC and acoustic measurements of temperature (Figure 6.31b). As the snow density $\bar{\rho}$ increases, the error in determination of acoustic liquid water content does not increase significantly (Figure 6.31c). There is also no significant relationship between snowpit temperature $\bar{T}$ and the error in acoustic determination of liquid water content (Figure 6.31d). These results show that the SAS2 measurements and UTAM model outputs are not biased by increases in magnitude of these measurement parameters.

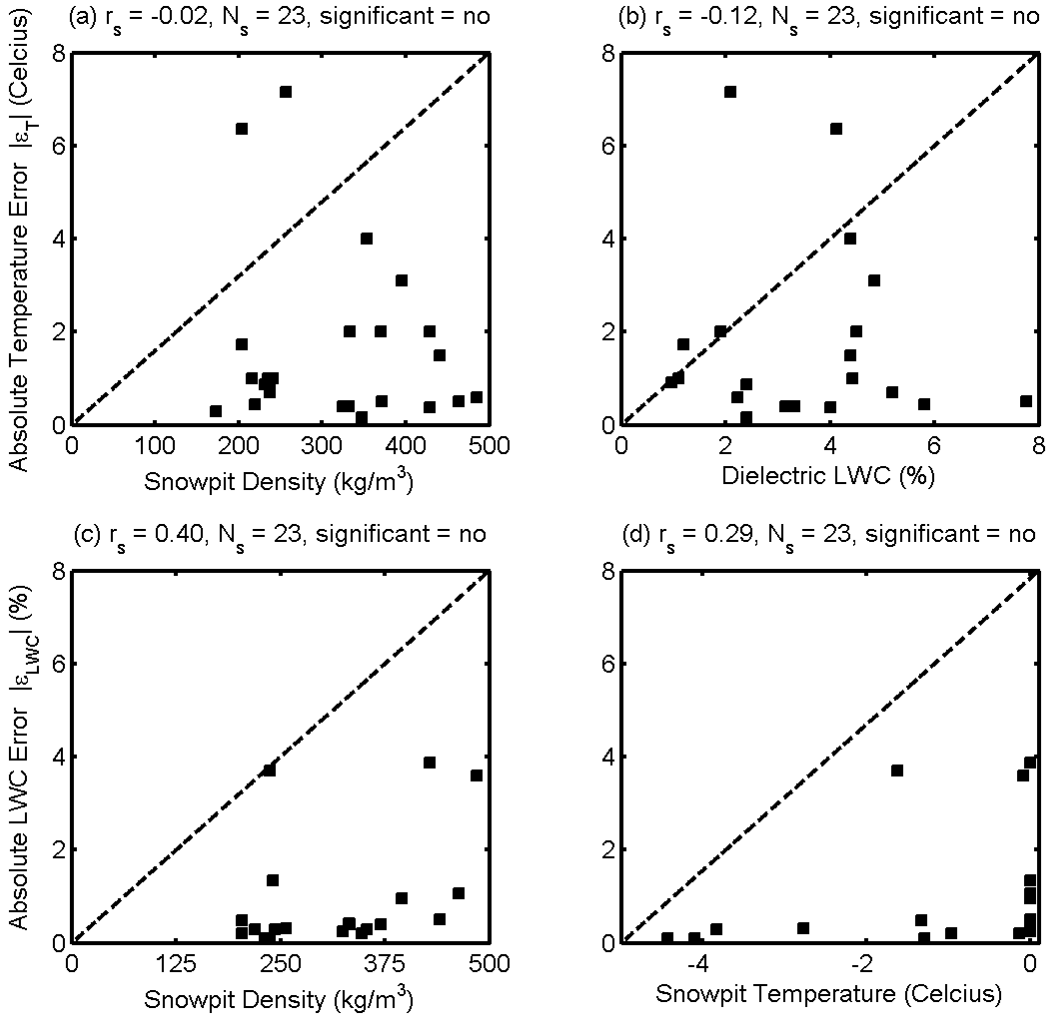

Figure 6.31. Error comparisons between acoustic and non-acoustic parameters. The Spearman rank correlation coefficient is given by r_s and the number of samples is N_s.

6.9. Effect of Signal Cutoff Time on Inverse UTAM Model Results

A maximum signal cutoff time $t_{\max}$ was determined from measured snow depth $\bar{y}$ and the frequency-averaged speed of sound in snow. This signal cutoff time was used to truncate the signal so that the inverse UTAM model was only applied to part of the signal representative of the sound wave that had propagated through the snowpack. Reflections at time $t > t_{\max}$ were not used in the analysis. However, if snow depth measurements are not available then a reasonable assumption of the maximum cutoff time is required.

To assess the effect of $t_{\max}$ on the error associated with measuring snowpack variables using the SAS2 and the inverse UTAM model, an error analysis (Figure 6.32) was performed using data collected at all of the field sites using the stationary and portable versions of the SAS2. The error analysis was conducted by progressively increasing the cutoff time up to $t_{\max} = t_{\mathrm{mls}} = 1.6\ \mathrm{s}$. The error analysis series was treated similar to a time-domain signal and low-pass filtered using a Butterworth filter with a cutoff frequency of 50 Hz to suppress the effects of higher-frequency oscillations. A moving-average filter was then applied to further suppress noise.

Figure 6.32a shows that as the cutoff time increases, the mean absolute error between ESC30 density and acoustic density increases by $\sim 8\ \mathrm{kg\ m^{-3}}$, indicating that the error is relatively insensitive to cutoff time. Figure 6.32b shows a similar increase and insensitivity to cutoff time for the mean absolute error between gravimetric snowpit density and acoustic density, with a density error range of $\sim 2\ \mathrm{kg\ m^{-3}}$. Figure 6.32b shows a lower error range than Figure 6.32a due to the inherent error in samples collected using the ESC30 snow sampler. The error in temperature (Figure 6.32c) is also relatively insensitive to cutoff time. This to be expected since the UTAM model sensitivity analysis showed relative insensitivity to snow temperature. Furthermore, the mean absolute error between dielectric and acoustic measurements of LWC (Figure 6.32d) has a range of <0.2%, which is within the 0.5% range of errors associated with two different dielectric measurement techniques. The insensitivity of the inverse UTAM model to the cutoff time $t_{\max}$ is due to reflections of relatively low amplitude that occurred at times after the sound wave propagated through the snowpack. These reflections contributed relatively little error to the inputs of the inverse UTAM model.

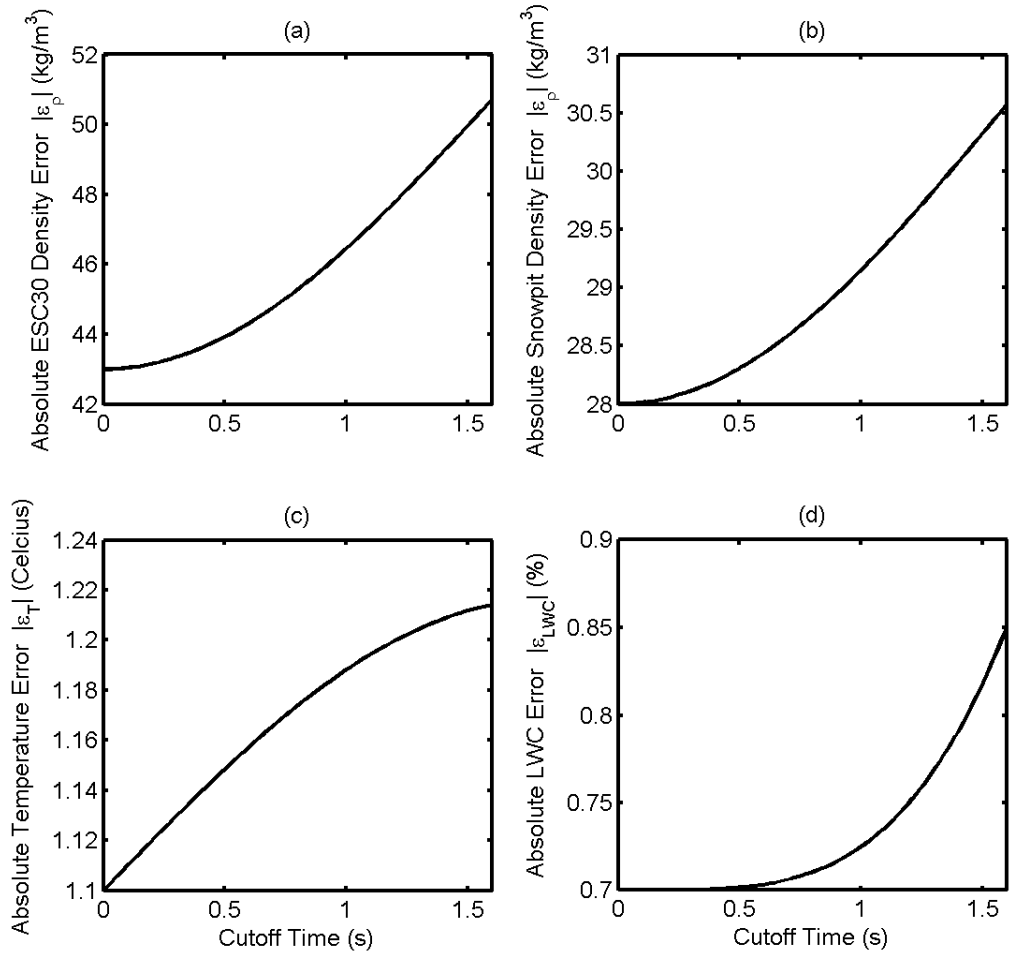

Figure 6.32. Error comparisons showing the effect of an assumed $t_{\max}$ on the mean absolute error between acoustic SAS2 measurements and measurements made using ESC30, gravimetric, thermometer and dielectric instruments.

CHAPTER 7
CONCLUSIONS

This thesis described the theory, design and testing results of the System for the Acoustic Sensing of Snow (SAS2), an electronic device used to obtain acoustic samples of sound waves passed into and reflected from snowpacks at field sites in the Rocky Mountains of Alberta, Canada. The research reported in this thesis suggested the following conclusions and opportunities for future investigation.

7.1. Non-invasive Measurement of Snowpack Variables

The SAS2 obtained non-invasive observations of depth-averaged density $\bar{\rho}$, temperature $\bar{T}$ and liquid water content $\bar{\theta}_w$ similar to measurements made with invasive ESC30 snowtube, snowpits, thermometers, thermocouples and dielectric measurement devices. The invasive methods of observation disrupted the snowpack, modifying it when an observation was made. The SAS2 used a sound wave that did not modify the snowpack. This permitted multiple measurements of snowpack variables to be made at the same location (Upper Clearing Stationary site) and measurements to be made at field sites without having to extract snow samples. Although snow depth or an assumption of a maximum signal cutoff time was required, it is generally easier to measure snow depth than snow density, temperature and liquid water content, particularly for stationary met station applications.

The measurement of snow density and liquid water content by the SAS2 could be used to provide an estimate of the dielectric constant (relative permittivity) and speed of propagation of electromagnetic waves in snow. Paired with a FMCW radar system, the SAS2 could provide information that would allow for the FMCW radar system to determine the depth to reflectors without the use of assumed or gravimetric snow densities.

Because the UTAM model is relatively insensitive to temperature, and given the differences between thermometer and acoustically-determined snow temperatures shown by the results, it is apparent that the SAS2 is a system with a primary purpose of determining snow density and liquid water content. An assumed ground temperature and a measured air temperature would obtain a reasonable estimate of snow temperature in lieu of acoustic measurements.

7.2. Unified Thermoacoustic Model (UTAM)

The Biot-Stoll constitutive equations modelling sound wave propagation through porous media were modified using a mixture theory approach to describe snow comprised of ice, air and water constituents. This was the UTAM model described in Chapter 2. A scaling coefficient modelled differences between the elastic constants of snow particles and ice.

The UTAM model allowed for the determination of the density, liquid water content and temperature of snow. Future updates of this model could restrict the solution for temperature or density based on the liquid water content.

Percolation theory (PT) was used to relate shear modulus and bulk modulus variables used in the Biot-Stoll model to snow porosity. The Consolidation Theory (CT) Model presented in this thesis provided an estimate of the porosity at which the snowpack ceased to act as a cellular solid and becomes an equivalent fluid. Mechanical parameters used as inputs for the Biot-Stoll constitutive equations were calculated using a mixture theory model and empirical equations were used to estimate mechanical and thermal parameters. Sensitivity analyses investigated changes in the model outputs to input parameters. Numerical methods were presented to evaluate these models.

Dielectric measurements of snowpack properties usually rely on empirical relationships between variables to make measurements. Unlike these dielectric measurements, the UTAM model did not require empirical calibration. Despite the use of empirical equations to estimate mechanical and thermal variables in the UTAM model, no relationships were utilized that directly related sound wave reflections to snowpack variables.

Because the Consolidation Theory (CT) model presented in this thesis predicts when the snowpack loses cohesion and becomes an equivalent fluid, the potential exists for future research to use this model for avalanche predictions.

Future work could be done to quantify uncertainty in the results of the inverse UTAM model. This would allow error bar estimates to be placed on the plots. A Monte Carlo method would be useful in this endeavor where the inputs are randomly varied and changes in the model outputs observed.

7.3. Signal Processing Techniques

A Maximum Length Sequence (MLS) was used as the source signal sent from the loudspeaker into the snowpack. The MLS was selected as a source signal due to its high noise immunity and time-integrated signal energy. The results presented in this thesis showed that an MLS source signal could be used for acoustic sampling of snow. Use of an MLS assumes that the snowpack is a Linear Time Invariant (LTI) system and does not change over the time of measurement ($t_{mls} = 1.6$ s). Although another source signal without the LTI assumption such as the SineSweep (Farina, 2000) could be used in lieu of the MLS, further experimentation is required to determine if alternate source signals are usable for acoustic sampling of snow.

The SAS2 system response (source signal and microphones) was experimentally determined in an anechoic chamber. Future work could eliminate the need to measure this system response by a mathematical model of the SAS2 enclosure case and microphone assembly. Finite-difference or finite-element models of sound wave propagation through the enclosure case would be used to construct this model.

The Vanishing Constant Filter (VCF) was proposed to be able to measure and remove attenuation from a signal. This is a method of blind deconvolution. Future research could apply the VCF to seismic data, LIDAR data, or spectrometer data to measure attenuation of waves passing through rocks or sediment, the canopy of a forest, or light transmission through snow.

A maximum cutoff time $t_{\max}$ was selected from a cutoff depth $\bar{y}$ to identify when the sound wave had reached the bottom of the snowpack due to attenuiation of the sound wave in snow. Attenuation did not always permit the bottom of the snowpack to be clearly identified using acoustics.

If the cutoff time $t_{\max}$ is assumed instead of measuring snow depth $\bar{y}$, late-time reflections from elements other than the snowpack have small contributions to the error in determination of snow density, liquid water content and temperature using the inverse UTAM model. Because the inversion procedure is relatively insensitive to cutoff time $t_{\max} \le t_{\mathrm{mls}}$, an average or maximum cutoff time could be used if snow depth is not known. This eliminates the need to measure snow depth.

7.4. System for the Acoustic Sensing of Snow (SAS2)

In a similar fashion to FMCW or bistatic radar and sonar, the SAS2 sensing system utilized a loudspeaker situated at an offset distance to a microphone assembly. The loudspeaker produced an audible sound wave in the frequency range from 20 Hz to 10 kHz at an SPL of 120 dB. Unlike the pulse from the ultrasonic SR50, the sound wave produced by the SAS2 entered the snowpack and was reflected from the snow due to changes in acoustic impedance. The sound wave was sensed in the air medium by the microphone assembly and processed using a custom-designed circuit.

The relative size of the SAS2 packaged in an enclosure case with dimensions of 38.5 cm by 28 cm reduced the portability of the device. Mounted on the chariot carrier, the portable SAS2 setup was difficult to transport to field sites with greater than ~2 m of snow accumulation in the Rocky Mountains due to time and logistical constraints.

Further research could be conducted to reduce the size of the SAS2 and therefore increase the portability of the system. This entails the use of experimentation to find: an optimal separation distance between the loudspeaker and microphone assembly; the sampling rate of the microphones; and the maximum SPL of the loudspeaker required for acoustic sampling of snow. The possibility exists for an acoustic snow sampling system to be constructed that will fit in the pocket of a snow surveyor, similar to the size of a mobile phone device at the time of writing.

Further experimentation is also required to: validate whether the microphone holes created in the front of the enclosure case acted as waveguides, rejecting sound wave arrivals from angles away from the normal of each microphone hole; and to determine how error in the acoustic measurement is related to footprint size and response of the acoustic array.

An updated version of the sensing system could be created with a larger separation distance between the microphones and loudspeaker. This would still allow for the system to be portable, but would also permit a smaller microphone sampling rate and potentially allow for more information to be available for application of the UTAM or an updated model based on similar principles.

As shown in Chapter 4 and by the results of Chapter 6, the footprint size and system response may have ramifications associated with the accuracy and sampling size of each acoustic snow sample, particularly for stationary deployments of the SAS2 when the distance from the

snow surface to the SAS2 microphone assembly changes over time. This effect was most prevalent for the stationary version of the SAS2 system and also affected ultrasonic measurements made with the SR50 sensor. The stationary version of the SAS2 was situated at a distance of $0.22\ \text{m} \leq y_a \leq 1.22\ \text{m}$ from the snow surface, whereas the portable version of the SAS2 was situated at no more than a maximum distance of 15 cm from the snow surface. Nevertheless, despite the changing distance to the snow surface, both the SR50 and SAS2 were able to adequately obtain acoustic samples of snow depth (for the SR50) and acoustic samples of snow properties (for the SAS2).

Hardware modification of the SAS2 circuit board is required to add accelerometer and gyroscope integrated circuits so that accurate measurements of SAS2 gauge movement during the time of acoustic measurement can be determined. Movement of the SAS2 during sampling occurred when the SAS2 was placed on the child chariot carrier and when the SAS2 was held in the investigator's hand over the snow surface. The accelerometer and gyroscope measurements, as well as careful modelling of sound wave propagation through snow, would quantify the effects of movement on the acoustic sampling procedure.

Movement of the acoustic gauge during the time of acoustic sampling on the child chariot carrier or in the hand of the investigator may have contributed to error in acoustic measurements made at these site locations. Further experimentation is required to quantify this error. However, because the SAS2 could collect physically-reasonable data that corresponded well with gravimetric, dielectic and snow pit measurements, this implies that minuscule movements during sampling have a small effect on the operational use of the acoustic gauge. Placing the SAS2 at large (glancing) angles to the snow surface may induce mode conversion resulting in a P-wave changing into am S-wave and vice versa.

To measure snow depth so that a cutoff time for the signal can be provided, an ultrasonic depth gauge (i.e. SR50) could be incorporated into the SAS2 system. For stationary deployment of the SAS2 on a met station, the ultrasonic depth gauge could communicate with the SAS2 using the SDI-12 protocol. Communication would occur by placing a connector on the side of the SAS2 case so that the system can autonomously "talk with" and provide power for an ultrasonic depth gauge. Alternately, the connector could be used to provide a serial port with ±5 V levels so that the SAS2 can communicate with a commercially-available datalogger. The

datalogger would provide snow depth information to the SAS2 obtained from an ultrasonic depth gauge attatched to the datalogger.

7.5. Deployment of SAS2

The results of experiments conducted using the SAS2 suggested that by using the apparatus described in this thesis the audible sound wave was able to make measurements of snow at 10 field sites in the Rocky Mountains.

Acoustic observations of snow were taken once every hour at the Upper Clearing Stationary (UCS) site. An experiment conducted at the UCS site showed that successive measurements taken by the acoustic system were repeatable. This experiment could not be conducted once every hour over the entire snow observation season due to the lack of storage capacity of data on the SD card. Repeating the experiment once every hour would allow for examination of footprint size changes on the repeatability of successive measurements as the snow depth changed. However, an updated hardware version of the SAS2 could be made in the future with more storage space (i.e. a greater number of SD card slots) for collecting a larger amount of acoustic data.

The wind speed and wind transport of sound waves did not appear to influence acoustic SAS2 measurements at the UCS site over the observation season. Measurements of blowing snow using the particle detector described by Brown and Pomeroy (1989) could also be used in future experiments to determine the influence of blowing snow events on the SAS2 signal. Because the SAS2 signal was longer in time ($t_{mls} = 1.6$ s) and had greater time-integrated signal energy than the short pulse sent from the SR50, "spikes" in the acoustic SAS2 data were not present. These spikes occurred in the SR50 data during snow deposition events and ablation due to acoustic scattering of the ultrasonic SR50 pulse by snow particles passing under the sensor assembly and uneven snow surface topography during snowmelt.

7.6. Snowpack Measurements

Comparisons between snowpit and snowtube measurements of $\bar{\rho}$ were less accurate than comparisons between snowpit and SAS2 measurements, suggesting that the SAS2 has an accuracy most comparable to snowpit measurements of $\bar{\rho}$. The ESC30 snowtube was not as accurate as SAS2 and snowpit measurements. However, the SAS2 could be used in lieu of an ESC30 snowtube to determine depth-integrated measurements of density $\bar{\rho}$.

The Upper Clearing Stationary (UCS) site observations showed an increase in density over the time of the observation season, indicating compaction of the snowpack and metamorphic processes acting over the snow observation season. A decrease in density was observed to occur with the addition of fresh snow to the snowpack.

SAS2 measurements of liquid water content were similar to dielectric measurements and were within a nominal 0.5% error associated with dielectric measurements. This indicated that the SAS2 was able to function similar to a dielectric device used to measure liquid water content.

Measurements of depth-averaged liquid water content $\bar{\theta}_w$ at the Upper Clearing Stationary (UCS) site showed cycles coincident with inputs of net shortwave radiation that warmed the snowpack and reduced its cold content. Rising temperatures and an increase in the magnitude of the net shortwave radiation over the observation season increased the liquid water content $\bar{\theta}_w$ as the snowpack passed through the warming, ripening and output phases. The water output phase was observed as a reduction in liquid water content near the end of the ablation season when the snowpack could not hold any more melt water.

Observations at the UCS site showed that liquid water content $\bar{\theta}_w$ increased over the snow accumulation and ablation season. The $\bar{\theta}_w$ was higher later in the observation season than sites visited at an earlier time due to a greater magnitude of net shortwave radiation and higher air temperatures that warmed the snowpack and reduced its cold content.

For sites with higher levels of liquid water content and ponded water beneath the snowpack, acoustic scattering and mode conversion of sound waves may have occurred, increasing the error between SAS2 measurements relative to gravimetric measurements. This was most apparent at the Bow Lake (BL) site. Despite the presence of late-season snow at the Icefields Parkway Forest Site (IFPF), the RMSD and MB comparing gravimetric to acoustic densities $\bar{\rho}$ remained lower than the BL site, indicating that the snow may have been well-drained and ponding of water did not occur at the IFPF site. This indicated that acoustic measurement of snow using the SAS2 and UTAM required the propagation of an air-coupled sound wave through the pore spaces of the snowpack. The pore spaces of the snowpack could not be completely filled with ponded water.

The frequency-integrated speed of sound in snow was observed to be less than the speed of sound in air. This is similar to the observations made by other investigators of the speed of sound in snow (Section 2.5). The UTAM model and the Biot-Stoll model of sound propagation suggests that the air-coupled sound wave propagating in the pore spaces of the snowpack was a P-wave.

The Ψ coefficient indicated that the elastic coefficients of the snow particles comprising the snowpack were different than the elastic coefficients of ice. There is a need to use experimental techniques to measure the elastic coefficients of snow particles to verify the values of the Ψ coefficient determined using acoustics.

Although the sound wave produced by the ultrasonic SR50 gauge will be completely reflected from or may partially penetrate the snow surface (Goodison et al., 1984), complete attenuation measurements of sound in snow from frequencies approaching DC (~0 Hz) to the ultrasonic range (> ~20 kHz) have not been reported in the literature. The experiments described in this paper showed that the frequency-averaged attenuation of sound in snow was in the range of $0 \text{ Np m}^{-1} \leq a \leq 2 \text{ Np m}^{-1}$ for a band-limited source signal in the range of 20 Hz to 10 kHz.

Over this range of attenuation coefficients, the sensitivity analysis given in Section 3.4 suggested that the maximum depth of snow that can be measured using the SAS2 system is 3 m. This is ~1 m greater than the ~2 m maximum depth of snow observed at the 10 field sites. The results showed that acoustic sampling of snow using the SAS2 was successful for snowpacks of ~2 m depth. More sensitive microphones could be used to extend this range. However, microphones with a higher sensitivity may experience clipping due to close proximity of the loudspeaker to the microphone assembly.

Field sites with greater than ~2 m of snow accumulation can be found in the Rocky Mountains and elsewhere in the world (i.e. the Alps). Although the logistics of visiting these sites and deploying instrumentation increases the complexity of field work, future research can be used to validate SAS2 measurements of the attenuation of sound in snow and the ability for the SAS2 system to measure snowpacks with greater than ~2 m depth.

Infrasound (sound with frequencies less than 20 Hz) could be used to ensure greater penetration of the snowpack for deep snowpacks. As predicted by the Biot theory, lower frequency sound waves will penetrate to greater depth beneath the snow surface due to lower levels of attenuation, whereas higher frequencies will have greater attenuation and will not travel

as far. However, the production of infrasound requires a sound source of greater dimension than the loudspeaker used in the SAS2 sensing system. Moreover, the physical size of the microphones and the microphone sensitivity will affect the ability to detect infrasound.

Reflections from the snowpack occurred due to changes in acoustic impedance. Images of these reflections did not necessarily coincide with snowpack layers as obtained by stratigraphy determination with a trained observer. The acoustic images were shown in this thesis. Further research is required to develop signal processing algorithms to extract snow stratigraphy information from the acoustic data. A possible way to do this would be to use neural networks (Smith, 2002) on the acoustic image data using a training dataset derived from snowpit observations of snow stratigraphy. The idea is similar to the use of algorithms to identify snowpack layers (Marshall et al., 2007; Tape et al., 2010).

Ice layers and crusts in the snowpack reflect sound waves. Ice layers that are semi-permeable allow for sound waves to still propagate through the snowpack. Further research is required to quantify the permeability for which sound waves cannot propagate through ice layers in the snowpack.

For sampling points near tree wells, an error in the acoustic measurement occurred due to propagation of the sound wave through the snow into the air space within the tree well. Reflections from the tree trunk may have also contributed to this error.

Although a loss of resolution occurred at the bottom of the snowpack due to sound wave propagation through the depth hoar layer, an acoustic observation of the void space created due to a buried tree demonstrated that sound wave reflections from vegetation were sometimes visible. Further research could involve the mathematical modelling of sound waves in tree wells and the interaction of sound waves with vegetation using finite-difference or finite-element methods.

An increase in the error between gravimetric and acoustic measurements of density occurred when vegetation was buried beneath the snowpack. Because this vegetation could not always be detected due to a loss of resolution in the depth hoar layer, it was impossible to determine completely by the use of acoustics whether vegetation was buried beneath the snow surface.

Future work could be done to determine the effect of ground cover on the propagation of the acoustic wave through shallow snow. The vegetation under the shallow snowpack may cause attenuation or scattering of the acoustic wave.

The loss of resolution in the depth hoar layer occurred due to viscous damping caused by the sound wave travelling through a porous medium comprised of coarse particles (Stoll, 1989). In areas such as the Arctic, where extensive depth hoar formation occurs throughout the entire snowpack, it is possible that the SAS2 may not be able to perform acoustic sampling of snow. This may represent a limitation of the acoustic measurement technique presented in this thesis.

The SAS2 shows great promise for a number of potential applications. For continuous monitoring of snow, variables measured by the SAS2 could be used as internal state parameters in mathematical models of snowpack evolution. Rather than estimating the state parameters of the snowpack from mass and energy fluxes, the acoustic estimates could be used directly in the model. This suggests the way forward for a new generation of snowpack evolution models.

The SAS2 has the potential for reducing the time and effort taken to make observations of snow. Since the SAS2 is non-invasive when deployed in a stationary met station configuration, more than one sample can be taken at the same location, enabling continuous monitoring of snowpack parameters. Deployed at a location that is dangerous or impossible to visit during the winter season, the SAS2 enables the measurement of these parameters without human intervention. Deployed over a large geographic area, a network of SAS2 gauges may entail greater availability of data for global water security assessments or more accurate models for assessing the potential for drought or flooding.

The SAS2 could be used to non-invasively measure density and liquid water content on a slope or in an area where it is difficult or impossible to take samples. The SAS2 would be mounted on a small gantry crane or on a telescopic crane and moved over the snow surface under computer control. Such cranes are often used on movie sets for camera movement. Moreover, a small toy helicopter could be used to suspend the SAS2 over the snow surface.

There is a need to validate, test, and deploy a network of SAS2 gauges at a number of field sites situated at different locations in the Rocky Mountains, and in different mountain chains, countries and landscapes so that the models and instrumentation described in this paper can be verified, additionally tested in a number of cold environments, and potentially improved. A collaborative effort is required for this global undertaking.

LIST OF REFERENCES

Abbott, D., 2012. Linux for Embedded and Real-time Applications, 3rd ed. Newnes.

Abramovich, R., 2007. Uses of natural resources conservation service snow survey data and products. Proceedings of the Western Snow Conference 75, 103–113.

Abramowitz, M., Stegun, I.A., 1964. Handbook of mathematical functions with formulas, graphs, and mathematical tables. Courier Dover Publications.

Adam, L., Batzle, M., Brevik, I., 2006. Gassmann's fluid substitution and shear modulus variability in carbonates at laboratory seismic and ultrasonic frequencies. Geophysics 71, F173–F183.

Adams, E.E., Brown, R.L., 1982. Further results on studies of temperature-gradient metamorphism. Journal of Glaciology 28, 205–210.

Adams, E.E., Sato, A., 1993. Model for effective thermal conductivity of a dry snow cover composed of uniform ice spheres. Annals of Glaciology 18, 300–304.

Adams, W.P., 1981. Snow and ice on lakes, in: Handbook of Snow: Principles, Processes, Management and Use. Pergamon Press Canada, pp. 437–474.

Adams, W.P., 1982. Spatial variability of snow and ice on lakes and a strategy for measurement based on three years' data from Elizabeth Lake, Labrador. Proceedings of the Western Snow Conference 50, 49–62.

Adams, W.P., Lasenby, D.C., 1982. Lake ice growth and conductivity. Proceedings of the Western Snow Conference 50, 184–185.

Aitchison, C.W., 2001. The effect of snow cover on small animals, in: Snow Ecology: An Interdisciplinary Examination of Snow-Covered Ecosystems. Cambridge University Press, Cambridge, pp. 229–265.

Aki, K., Richards, P.G., 2002. Quantitative seismology, 2nd ed. University Science Books, Sausalito, CA.

Akitaya, E., 1985. A calorimeter for measuring free water content of wet snow. Annals of Glaciology 6, 246–247.

Albert, D.G., 1983. Review of the propagation of inelastic pressure waves in snow. CRREL, Hanover, New Hampshire.

Albert, D.G., 1987. The effect of snow on vehicle-generated seismic signatures. The Journal of the Acoustical Society of America 81, 881–887.

Albert, D.G., 1993a. A comparison between wave propagation in water-saturated and air-saturated porous materials. Journal of Applied Physics 73, 28–36.

Albert, D.G., 1993. Attenuation of outdoor sound propagation levels by a snow cover (CRREL Report No. 93-20). U.S. Army Corps of Engineers, Hanover, New Hampshire.

Albert, D.G., 1993b. Attenuation of outdoor sound propagation levels by a snow cover, CRREL Report 93-20. Cold Regions Research and Engineering Laboratory, Hanover, New Hampshire.

Albert, D.G., 1998. Snow cover effects on impulsive noise propagation in a forest. Noise Control Engineering Journal 46, 208–214.

Albert, D.G., 2001. Acoustic waveform inversion with application to seasonal snow. Journal of the Acoustical Society of America 109, 91–101.

Albert, D.G., 2003. Observations of acoustic surface waves in outdoor sound propagation. Journal of the Acoustical Society of America 113, 2495–2500.

Albert, D.G., Hole, L.R., 2001. Blast wave propagation above a snow cover. Journal of the Acoustical Society of America 109, 2675–2681.

Albert, D.G., Orcutt, J.A., 1989. Observations of low-frequency acoustic-to-seismic coupling in the summer and winter. The Journal of the Acoustical Society of America 86, 352–359.

Albert, D.G., Orcutt, J.A., 1990. Acoustic pulse propagation above grassland and snow: Comparison of theoretical and experimental waveforms. The Journal of the Acoustical Society of America 87, 93–100.

Albert, M.R., 1993. Some numerical experiments on firn ventilation with heat transfer. Annals of Glaciology 18, 161–165.

Albert, M.R., 2002. Effects of snow and firn ventilation on sublimation rates. Annals of Glaciology 35, 52–56.

Albert, M.R., McGilvary, W.R., 1991. Multidimensional obsevation of snow temperature on windy days. Proceedings of the Eastern Snow Conference 48, 189–200.

Albert, M.R., McGilvary, W.R., 1992a. Induced flow channels in a natural snowpack. Proceedings of the Eastern Snow Conference 49, 55–60.

Albert, M.R., McGilvary, W.R., 1992b. Thermal effects due to air flow and vapor transport in dry snow. Journal of Glaciology 38, 273–281.

Alkhalifah, T., Fomel, S., 2001. Implementing the fast marching eikonal solver: spherical versus Cartesian coordinates. Geophysical Prospecting 49, 165–178.

Allard, J., Atalla, N., 2009. Propagation of Sound in Porous Media: Modelling Sound Absorbing Materials, 2nd ed. Wiley.

Allard, J., Castagnede, B., Henry, M., 1994. Evaluation of tortuosity in acousic porous materials saturated by air. Review of Scientific Instruments 65, 754–755.

Allen, J.B., Rabiner, L.R., 1977. A unified approach to short-time Fourier analysis and synthesis. Proceedings of the IEEE 65, 1558 – 1564.

Anderson, D.L., Benson, C.S., 1963. The densification and diagenesis of snow, in: Ice and Snow: Properties, Processes, and Applications. M.I.T. Press, Cambridge, Massachusetts, pp. 391–411.

Anderson, E., Larson, L., 1996. The role of snowmelt in the January 1996 floods in the Northwestern United States. Proceedings of the Eastern Snow Conference 53, 141–149.

Anderson, H.W., McDonald, P.M., Gay, L.W., 1965. Use of radioactive sources in measuring characteristics of snowpacks, U.S. Forest Service Research Note PSW-11. Pacific Southwest Forest and Range Experimental Station, Berkeley, California.

Anderson, J., Wirt, J., 2008. Utrasonic snow depth sensor accuracy, reliability and performance. Proceedings of the Western Snow Conference 76, 99–105.

Anderson, J.D., 1991. Fundamentals of aerodynamics, 2nd ed, McGraw-Hill series in aeronautical and aerospace engineering. McGraw-Hill, New York.

Armstrong, B.R., 1981. A quantitative analysis of avalanche hazard on U.S. Highway 550, Southwestern Colorado. Proceedings of the Western Snow Conference 49, 95–104.

Armstrong, R.L., 1973. Avalanche studies in the San Juan Mountains of Southwestern Colorado. Proceedings of the Western Snow Conference 41, 44–51.

Armstrong, R.L., 1976. The application of isotopic profiling snow gauge data to avalanche research. Proceedings of the Western Snow Conference 44, 606–676.

Armstrong, R.L., 1980. An analysis of compressive strain in adjacent temperature-gradient and equi-temperature layers in a natural snow cover. Journal of Glaciology 26, 283–289.

Arons, E.M., Colbeck, S.C., 1995. Geometry of heat and mass transfer in dry snow: a review of theory and experiment. Reviews of Geophysics 33, 463–493.

Arons, E.M., Colbeck, S.C., Gray, J.M.N.T., 1998. Depth-hoar growth rates near a rocky outcrop. Journal of Glaciology 44, 477–484.

Ashton, G.D., 1986. River and lake ice engineering. Water Resources Publications, Littleton, Colo., U.S.A.

Assaf, H., Loukas, A., Quick, M.C., 1995. Updating seasonal snowmelt estimates using snowcourse measurements. Proceedings of the Western Snow Conference 63, 21–28.

Atkinson, J., 1997. Loudspeakers: What Measurements Can Tell Us-and What They Can't Tell Us! AES Convention Proceedings 103, 4608.
Attenborough, K., 1983. Acoustical characteristics of rigid fibrous absorbents and granular materials. The Journal of the Acoustical Society of America 73, 785–799.
Attenborough, K., 1987. On the acoustic slow wave in air-filled granular media. The Journal of the Acoustical Society of America 81, 93–102.
Attenborough, K., Buser, O., 1988. On the application of rigid-porous models to impedance data for snow. Journal of Sound and Vibration 124, 315–327.
Bader, H., 1950. Note on the liquid water content of wet snow. Journal of Glaciology 1, 466–467.
Banfield, C.E., 1991. Snow accumulation and climate over the Grand Lake Catchment, Newfoundland. Proceedings of the Eastern Snow Conference 48, 133–148.
Bardsley, T., Julander, R., 2005. The documentation of extreme events: two case studies in Utah, water year 2005. Proceedings of the Western Snow Conference 73, 33–42.
Barger, J.E., 1998. Sonar Systems, in: Handbook of Acoustics. John Wiley & Sons, pp. 435–455.
Barnaby, I.E., 1980. Snowmelt observations in Alberta. Proceedings of the Western Snow Conference 48, 128–137.
Barnett, T.P., Adam, J.C., Lettenmaier, D.P., 2005. Potential impacts of a warming climate on water availability in snow-dominated regions. Nature 438, 303–309.
Barnett, T.P., Pierce, D.W., Hidalgo, H.G., Bonfils, C., Santer, B.D., Das, T., Bala, G., Wood, A.W., Nozawa, T., Mirin, A.A., Cayan, D.R., Dettinger, M.D., 2008. Human-Induced Changes in the Hydrology of the Western United States. Science 319, 1080–1083.
Barr, K., 2006. ASIC Design in the Silicon Sandbox: A Complete Guide to Building Mixed-Signal Integrated Circuits, 1st ed. McGraw-Hill Professional.
Bartelt, P., Lehning, M., 2002. A physical SNOWPACK model for the Swiss avalanche warning Part I: numerical model. Cold Regions Science and Technology 35, 123–145.
Bartlett, P.A., MacKay, M.D., Verseghy, D.L., 2006. Modified Snow Algorithms in the Canadian Land Surface Scheme: Model Runs and Sensitivity Analysis at Three Boreal Forest Stands. Atmosphere-Ocean 44, 207–222.
Barton, N., 2007. Rock Quality, Seismic Velocity, Attenuation and Anisotropy, Balkema-proceedings and monographs in engineering, water, and earth sciences. Taylor & Francis, London ; New York.
Bates, R.E., Gerard, S., 1989. Snow surface temperature analysis. Proceedings of the Eastern Snow Conference 46, 109–116.
Bear, J., 1972. Dynamics of fluids in porous media, Environmental science series. New York, American Elsevier Pub. Co.
Beaumont, P., 1998. Restructuring of water usage in the Tigris-Euphrates basin: the impact of modern water management policies, in: Transformations of Middle Eastern Natural Environments: Legacies and Lessons, Bulletin Series No. 103. Yale School of Forestry and Environmental Studies, New Haven, Connecticut, USA, pp. 168–186.
Beaumont, R.T., 1965. Mt. Hood pressure pillow snow gauge. Proceedings of the Western Snow Conference 29–35.
Beaumont, R.T., 1966. Snow accumulation. Proceedings of the Western Snow Conference 34, 3–6.
Beloe, W., 1812. Herodotus: translated from the Greek with notes and life of the author. L. Hansard & Sons, Jones & Company, Temple of the Muses, London, UK.
Bengtsson, L., 1982. Percolation of meltwater through a snowpack. Cold Regions Science and Technology 6, 73–81.
Bergman, J.A., 1989. An evaluation of the acoustic snow depth sensor in a deep Sierra Nevada snowpack. Proceedings of the Western Snow Conference 57, 126–129.

Bernier, P.Y., Swanson, R.H., 1986. A watershed mangement pilot project in Alberta. Proceedings of the Western Snow Conference 54, 87–92.
Berryman, J.G., 1980. Confirmation of Biot's Theory. Applied Physics Letters 37, 382–384.
Berryman, J.G., 1983. Effective conductivity by fluid analogy for a porous insulator filled with a conductor. Phys. Rev. B 27, 7789–7792.
Bickel, S.H., Natarajan, R.R., 1985. Plane-wave Q deconvolution. Geophysics 50, 1426–1439.
Bilaniuk, N., Wong, G.S.K., 1993. Speed of sound in pure water as a function of temperature. Journal of the Acoustical Society of America 93, 1609–1612.
Bilaniuk, N., Wong, G.S.K., 1996. Erratum: Speed of sound in pure water as a function of temperature. Journal of the Acoustical Society of America 99, 3257.
Billings, W.D., Bliss, L.C., 1959. An Alpine Snowbank Environment and Its Effects on Vegetation, Plant Development, and Productivity. Ecology 40, 388–397.
Biondi, B., 2007. Concepts and Applications in 3D Seismic Imaging. Society of Exploration Geophysicists (SEG), Tulsa, Oklahoma.
Biot, M.A., 1956a. Theory of elastic waves in a fluid-saturated porous solid. II. Higher frequency range. Journal of the Acoustical Society of America 28, 179–191.
Biot, M.A., 1956b. Theory of elastic waves in a fluid-saturated porous solid. I. Low Frequency Range. Journal of the Acoustical Society of America 28, 168–178.
Biot, M.A., 1956c. Mechanics of deformation and acoustic propagation in porous dissipative media. Journal of Applied Physics 33, 1482–1498.
Biot, M.A., 1962. Generalized theory of acoustic propagation in porous dissipative media. Journal of the Acoustical Society of America 44, 1254–1264.
Birkeland, K.W., 1996. The effect of ski run cutting and artificial snowmaking on snow water accumulation at Bigg Sky Ski Area, Montana. Proceedings of the Western Snow Conference 64, 137–148.
Bissell, V.C., Peck, E.L., 1973. Monitoring snow water equivalent by using natural soil radioactivity. Water Resour. Res. 9, 885.
Bjørndal, E., Frøysa, K.-E., 2008. Acoustic methods for obtaining the pressure reflection coefficient from a buffer rod based measurement cell. IEEE Trans Ultrason Ferroelectr Freq Control 55, 1781–1793.
Blackstock, D.T., 2000. Fundamentals of physical acoustics. Wiley, New York.
Blahut, R.E., 2010. Fast Algorithms for Signal Processing. Cambridge University Press.
Blincow, D.W., Dominey, S.C., 1974. A portable profiling snow gauge. Proceedings of the Western Snow Conference 42, 53–57.
Blyth, K., Cooper, M. a. R., Lindsey, N.E., Painter, R.B., 1974. Snow depth measurement with terrestrial photos. Photogrammetric Engineering 40, 937–942.
Boeckx, L., Jansens, G., Lauriks, W., 2004. Modelling acoustic surface waves above a snow layer. Acta Acustica United With Acustica 90, 246–250.
Bogorodskii, V.V., Dobrotin, D.D., 1963. Results of an investigation of the physiomechanical properties of the snow cover on ice floes. Soviet Physics, Acoustics 9, 89–90.
Bogorodskii, V.V., Gavrilo, V.P., Niktin, V.A., 1974. Characteristics of sound propagation in snow. Soviet Physics, Acoustics 20, 121–122.
Bonan, G.B., Oleson, K.W., Vertenstein, M., Levis, S., Zeng, X., Dai, Y., Dickinson, R.E., Yang, Z.-L., 2002. The Land Surface Climatology of the Community Land Model Coupled to the NCAR Community Climate Model. Journal of Climate 15, 3123–3149.
Bonsal, B.R., Prowse, T.D., Pietroniro, A., 2003. An assessment of global climate model-simulated climate for the western cordillera of Canada (1961–90). Hydrological Processes 17, 3703–3716.

Booth, A.D., Mercer, A., Clark, R., Murray, T., Jansson, P., Axtell, C., 2013. A comparison of seismic and radar methods to establish the thickness and density of glacier snow cover. Annals of Glaciology 54, 73–82.

Borden, C., Ying, Q., Kobor, J., Guy, B., 2010. A modeling approach to evaluating the impacts of climate change and mountain pine beetle infestation on water resouces in the Okanagan Basin, British Columbia. Proceedings of the Western Snow Conference 78, 31–42.

Borish, J., 1985. An efficient algorithm for generating colored noise using a pseudorandom sequence. Journal of the Audio Engineering Society 33, 141–144.

Borish, J., 1985. Self-Contained Crosscorrelation Program for Maximum-Length Sequences. Journal of the Audio Engineering Society 33, 888–891.

Borish, J., Angell, J.B., 1983. An efficient algorithm for measuring the impulse response using pseudorandom noise. Journal of the Audio Engineering Society 31, 478–487.

Bowles, D., 1967. Bridger data system multipoint snowpack thermometry. Proceedings of the Western Snow Conference 35, 29–34.

Box, M.J., 1965. A New Method of Constrained Optimization and a Comparison With Other Methods. The Computer Journal 8, 42–52.

Boyne, H.S., Fisk, D., 1987. A comparison of snow cover liquid water measurement techniques. Water Resources Research 23, 1833–1836.

Boyne, H.S., Fisk, D.J., 1990. A laboratory comparison of field techniques for measurement of the liquid water fraction of snow, CRREL Report 90-3. Cold Regions Research and Engineering Laboratory, Hanover, New Hampshire.

Bracewell, R.N., 1978. The Fourier transform and its applications, 2nd ed, McGraw-Hill electrical and electronic engineering series. McGraw-Hill, New York.

Bradley, J.S., 1996. Optimizing the decay range in room acoustics measurements using Maximum-Length Sequence Techniques. Journal of the Audio Engineering Society 44, 266–273.

Brandt, R.E., Warren, S.G., 1993. Solar-heating rates and temperature profiles in Antarctic snow and ice. Journal of Glaciology 39, 99–110.

Brandt, R.E., Warren, S.G., 1997. Temperature measurements and heat transfer in near-surface snow at the South Pole. Journal of Glaciology 43, 339–351.

Brekhovskikh, L.M., Lysanov, Y.P., 2003. Fundamentals of ocean acoustics, 3rd ed, AIP series in modern acoustics and signal processing. Springer, New York.

Brooks, P.D., Schmidt, S.K., Sommerfeld, R., Musselman, R., 1993. Distribution and abundance of microbial biomass in Rocky Mountain spring snowpacks. Proceedings of the Western Snow Conference 61, 301–306.

Brown, A.J., 1978. The California two year drought. Proceedings of the Western Snow Conference 46, 85–91.

Brown, R.D., 1995. Spatial and temporal variability of North American snow cover, 1971-1992. Proceedings of the Eastern Snow Conference 52, 69–78.

Brown, R.D., Tapsoba, D., 2007. Improved mapping of Snow Water Equivalent over Quebec. Proceedings of the Eastern Snow Conference 64, 3–7.

Brown, R.G., Hwang, P.Y.C., 1996. Introduction to Random Signals and Applied Kalman Filtering with Matlab Exercises and Solutions, 3rd ed. Wiley.

Brown, R.L., 1979. An analysis of plastic shock waves in snow. CRREL, Hanover, New Hampshire.

Brown, R.L., 1980. A volumetric constitutive law for snow based on a neck growth model. Journal of Applied Physics 51, 161–165.

Brown, R.L., Edens, M.Q., 1991. On the relationship between neck length and bond radius during compression of snow. Journal of Glaciology 37, 203–208.

Brown, R.L., Hansen, A., 1987. Field studies on stress waves in natural snow cover, in: Snow Property Measurement Workshop : April 1-3, 1985, Chateau Lake Louise, Alberta, Canada. National Research Council of Canada, Ottawa, pp. 89–110.

Brown, T., Pomeroy, J.W., 1989. A blowing snow particle detector. Cold Regions Science and Technology 16, 167–174.

Bruce, J.P., 1962. Snowmelt contributions to maximum floods. Proceedings of the Eastern Snow Conference 18-19, 85–103.

Bruin, C.G.M. de, Wapenaar, C.P.A., Berkhout, A.J., 1990. Angle-dependent reflectivity by means of prestack migration. Geophysics 55, 1223–1234.

Brun, 1989. Investigation on wet-snow metamorphism in respect of liquid water content. Annals of Glaciology 13, 22–26.

Brun, E., David, P., Sudul, M., Brunot, G., 1992. A numerical model to simulate snow-cover stratigraphy for operational avalanche forecasting. Journal of Glaciology 38, 13–22.

Brun, E., Martin, E., Simon, V., Gendre, C., Coleou, C., 1989. An energy and mass balance model of snow cover suitable for operationa avalanche forcasting. Journal of Glaciology 35, 333–342.

Brunengo, M.J., 2007. A monte carlo model for simulation of rain-on-snow events in the Pacific northwest. Proceedings of the Western Snow Conference 75, 89–102.

Bryant, A.C., Painter, T.H., 2010. Radiative forcing by dust in snowmelt-dominated hydrologic systems using coupled satellite and in situ measurements. Proceedings of the Western Snow Conference 78, 43–47.

Buhl, P., Stoffa, P.L., Bryan, G.M., 1974. The application of homomorphic deconvolution to shallow-water marine seismology; Part II; Real data. Geophysics 39, 417–426.

Burger, H.R., Sheehan, A.F., Jones, C.H., 2006. Introduction to applied geophysics: exploring the shallow subsurface. W.W. Norton, New York.

Burrus, C.S., Gopinath, R.A., Guo, H., 1997. Introduction to Wavelets and Wavelet Transforms: A Primer, 1st ed. Prentice Hall.

Buser, O., 1986. A rigid frame model of porous media for the acoustic impedance of snow. Journal of Sound and Vibration 111, 71–92.

Buser, O., Good, W., 1986. Acoustic, geometric and mechanical parameters of snow. Avalanche Formation, Movement and Effects, Proceedings of the Davos Symposium, IAHS Publication 162, 61–71.

Byrne, J., Kienzle, S., Johnson, D., Duke, G., Gannon, V., Selinger, B., Thomas, J., 2006. Current and future water issues in the Oldman River Basin of Alberta, Canada. Water Sci. Technol. 53, 327–334.

Caillet, A., D'Aillon, F.G., Zawadzki, I., 1979. An ultrasound low-power sonar for snow thickness measurements. Proceedings of the Eastern Snow Conference 36, 108–116.

Callaghan, T.V., Johansson, M., Brown, R.D., Groisman, P.Y., Labba, N., Radionov, V., Bradley, R.S., Blangy, S., Bulygina, O.N., Christensen, T.R., Colman, J.E., Essery, R.L.H., Forbes, B.C., Forchhammer, M.C., Golubev, V.N., Honrath, R.E., Juday, G.P., Meshcherskaya, A.V., Phoenix, G.K., Pomeroy, J., Rautio, A., Robinson, D.A., Schmidt, N.M., Serreze, M.C., Shevchenko, V.P., Shiklomanov, A.I., Shmakin, A.B., Sköld, P., Sturm, M., Woo, M., Wood, E.F., 2011. Multiple Effects of Changes in Arctic Snow Cover. AMBIO 40, 32–45.

Calonne, N., Flin, F., Morin, S., Lesaffre, B., Rolland du Roscoat, S., Geindreau, C., 2011. Numerical and experimental investigations of the effective thermal conductivity of snow. Geophysical Research Letters 38, L23501.

Camp, P.R., LaBrecque, D.R., 1992. Determination of the water content of snow by dielectric measurements, CRREL report 91-18. CRREL, Hanover, New Hampshire.

Campisi, P., Egiazarian, K., 2007. Blind image deconvolution: theory and applications. CRC Press, Boca Raton.

Candy, J.C., Temes, G.C., 1991. Oversampling Delta-Sigma Data Converters: Theory, Design, and Simulation, 1st ed. Wiley-IEEE Press.

Carcione, J.M., Cavallini, F., Santos, J.E., Ravazzoli, C.L., Gauzellino, P.M., 2004. Wave propagation in partially saturated porous media: simulation of a second slow wave. Wave Motion 39, 227–240.

Carslaw, H.S., Jaeger, J.C., 1959. Conduction of heat in solids, 2nd ed. Clarendon Press, Oxford.

CBC, 2008. Avalanche death toll hits 24 across Western Canada, U.S. [WWW Document]. URL http://www.cbc.ca/canada/calgary/story/2008/01/08/bc-avalanchedeathtollhits23.html?ref=rss

CBC, 2013. Flood-ravaged Alberta continues to rebuild a month later - Calgary - CBC News [WWW Document]. URL http://www.cbc.ca/news/canada/calgary/story/2013/07/18/calgary-flood-month-after-w.html (accessed 7.22.13).

Chadderton, D.V., 2013. Building Services Engineering. Routledge.

Charvat, G.L., Williams, J.H., Fenn, A.J., Kogon, S., Herd, J.S., 2013. Build a Small Radar System Capable of Sensing Range, Doppler, and Synthetic Aperture Radar Imaging, RES.LL-003, Massachusetts Institute of Technology: MIT OpenCourseWare. MIT, Massachusetts.

Chavent, G., 2009. Nonlinear Least Squares for Inverse Problems: Theoretical Foundations and Step-by-Step Guide for Applications. Springer.

Chen, W., Xia, T., Sun, M., Zhai, C., 2012. Transverse wave at a plane interface between isotropic elastic and unsaturated porous elastic solid half-spaces. Transp Porous Med 94, 417–436.

Chen, Z., Fomel, S., Lu, W., 2013. Accelerated plane wave destruction. Geophysics 78, V1–V9.

Cheng, J.D., 1987. Assessing landslide occurence with snow data and other site information. Proceedings of the Western Snow Conference 55, 53–60.

Chevalier, F.L., 2002. Principles of Radar and Sonar Signal Processing. Artech House.

Childers, D.G., Skinner, D.P., Kemerait, R.C., 1977. The cepstrum: A guide to processing. Proceedings of the IEEE 65, 1428–1443.

Chinnappa, C.C., Hallworth, B., 1997. Plants of Kananaskis Country in the Rocky Mountains of Alberta. University of Alberta Press, Edmonton.

Christner, J., Harr, R.D., 1982. Peak streamflows from the transient snow zone, western Cascades, Oregon. Proceedings of the Western Snow Conference 50, 27–38.

Chu, W.T., 1984. Architectural acoustic measurements using periodic pseudorandom sequences and FFT. The Journal of the Acoustical Society of America 76, 475–478.

Church, J.E., 1933. Snow Surveying: Its Principles and Possibilities. Geographical Review 23, 529–563.

Claerbout, J.F., 1985. Fundamentals of geophysical data processing: with applications to petroleum prospecting. Blackwell Scientific Publications, Palo Alto, CA.

Claerbout, J.F., 1992. Earth Soundings Analysis: Processing Versus Inversion. Blackwell Scientific Publications, Boston.

Clagett, G., McClure, R., 1994. Northern latitude snow pilow installation procedures. Proceedings of the Western Snow Conference 62, 143–146.

Clagett, G.P., 1978. Surveying snow in Arctic Alaska to determine its effects on reindeer herding. Proceedings of the Western Snow Conference 46, 63–68.

Clapp, R.L., Sava, P., Claerbout, J.F., 1998. Interval velocity estimation with a null-space, Stanford Exploration Project Report 97. Stanford Exploration Project.

Clarke, G.K.C., Waddington, E.D., 1991. A three-dimensional theory of wind pumping. Journal of Glaciology 37, 89–96.

Clarkson, P.M., Mourjopoulos, J., Hammond, J.K., 1985. Spectral, phase and transient equalization for audio systems. Journal of the Audio Engineering Society 33.

Claus, B.R., Russell, S.O., Schaerer, P., 1984. Variation of ground snow loads with elevation in Southern British Columbia. Candian Journal of Civil Engineering 11, 480–493.

Cline, D., Elder, K., Bales, R., 1997. Scale effects in a distributed SWE and snowmelt model for mountain basins. Proceedings of the Western Snow Conference 317–328.
Cline, D.W., 1993. Measuring alpine snow depths by digital photogrammetry. Part 1. Conjugate point identification. Proceedings of the Western Snow Conference 61, 265–271.
Cobo, P., Fernández, A., Cuesta, M., 2007. Measuring short impulse responses with inverse filtered maximum-length sequences. Applied Acoustics 68, 820–830.
Cohn, M., Lempel, A., 1977. On fast M-sequence transforms (Corresp.). IEEE Transactions on Information Theory 23, 135–137.
Colbeck, S.C., 1972. A theory of water percolation in snow. Journal of Glaciology 11, 369–385.
Colbeck, S.C., 1974a. Water flow through snow overlying an impermeable boundary. Water Resources Research 10, 119–123.
Colbeck, S.C., 1974b. The capillary effects of water percolation in homogeneous snow. Journal of Glaciology 13, 85–97.
Colbeck, S.C., 1976a. An analysis of water flow in dry snow. Water Resources Research 12, 523–527.
Colbeck, S.C., 1976b. On the use of tensiometers in snow hydrology. Journal of Glaciology 17, 135–140.
Colbeck, S.C., 1978. The difficulties of measuring the water saturation and porosity of snow. Journal of Glaciology 20, 189–201.
Colbeck, S.C., 1982a. An overview of seasonal snow metamorphism. Reviews of Geophysics and Space Physics 20, 45–61.
Colbeck, S.C., 1982b. The geometry and permittivity of snow at high frequencies. Journal of Applied Physics 53, 4495–4500.
Colbeck, S.C., 1986a. Classification of seasonal snow cover crystals. Water Resources Research 22, 59S–70S (Supplement).
Colbeck, S.C., 1986b. Snow Metamorphism and Classification, in: Seasonal Snowcovers: Physics, Chemistry, Hydrology. D. Reidel Publishing Company, pp. 1–35.
Colbeck, S.C., 1989a. Snow-crystal growth with varying surface temperatures and radiation penetration. Journal of Glaciology 35, 23–29.
Colbeck, S.C., 1989b. Air movement in snow due to windpumping. Journal of Glaciology 35, 209–213.
Colbeck, S.C., 1991. The layered character of snow covers. Reviews of Geophysics 29, 81–96.
Colbeck, S.C., 1993. The vapor diffusion coefficient for snow. Water Resources Research 29, 109–115.
Colbeck, S.C., 1997. Model of wind pumping for layered snow. Journal of Glaciology 43, 60–65.
Colbeck, S.C., 1997. A review of sintering in seasonal snow, CRREL report 97-10. Cold Regions Research and Engineering Laboratory, Hanover, New Hampshire.
Colbeck, S.C., Anderson, E.A., 1982. The permeability of a melting snow cover. Water Resources Research 18, 904–908.
Colbeck, S.C., Parssinen, N., 1978. Regelation and the deformation of wet snow. Journal of Glaciology 21, 639–650.
Coléou, C., Lesaffre, B., 1998. Irreducible water saturation in snow: experimental results in a cold laboratory. Annals of Glaciology 26, 64–68.
Collins, D.N., 1988. Outburst and rainfall-induced peak runoff events in glacierised alpine basins. Proceedings of the Eastern Snow Conference 55, 27–36.
Conway, H., Benedict, R., 1994. Infiltration of water into snow. Water Resources Research 30, 641–649.
Conway, H., Gades, A., Raymond, C.F., 1996. Albedo of dirty snow during conditions of melt. Water Resources Research 32, 1713–1718.
Cooley, K.R., Huber, A.L., Robertson, D.C., Zuzel, J.F., 1981. Effects of snowdrift management on rangeland runoff. Proceedings of the Western Snow Conference 49, 55–63.
Cooley, K.R., Palmer, P., 1997. Characteristics of snowmelt from NCRS SNOTEL (SNOwTELemetry) sites. Proceedings of the Western Snow Conference 65, 1–11.

Corapcioglu, M.Y., Tuncay, K., 1996. Propgation of waves in porous media, in: Advances in Porous Media, Volume 3. Elsevier, Amsterdam, The Netherlands, pp. 361–440.
Cordell, B., 2010. Designing Audio Power Amplifiers, 1st ed. McGraw-Hill/TAB Electronics.
Cormen, T.H., Leiserson, C.E., Rivest, R.L., Stein, C., 2009. Introduction to Algorithms, 3rd ed. The MIT Press.
Corripio, J.G., 2004. Snow surface albedo estimation using terrestrial photography. International Journal of Remote Sensing 25, 5705–5729.
Cox, H., 1989. Fundamentals of bistatic active sonar, edited by Y.T. Chan, in: Underwater Acoustic Data Processing. Springer, pp. 3–24.
Cox, L.M., Bartree, L.D., Crook, A.G., Farnes, P.E., Smith, J.L., 1978. The care and feeding of snow pillows. Proceedings of the Western Snow Conference 46, 40–47.
Cox, P.M., Betts, R.A., Bunton, C.B., Essery, R.L.H., Rowntree, P.R., Smith, J., 1999. The impact of land surface physics on the GCM simulation of climate and climate sensitivity. Climate Dynamics 15, 183–203.
CRC, 1981. CRC Handbook of Chemistry and Physics. CRC Press, Cleveland, Ohio.
Crider, R., Gutowski, P., 1995. Seismic Q estimation, BP America unpublished report. BP America.
Crocker, M.J., 1998. Introduction, in: Handbook of Acoustics. John Wiley & Sons, New York, pp. 3–19.
Crook, A.G., Davis, R.T., Moreland, R.E., 1981. Snow surveys and Mount St. Helens. Proceedings of the Western Snow Conference 49, 77–84.
Crook, A.G., Freeman, T.G., 1973. A comparison of techniques of sampling the arctic-subarctic snowpack in Alaska. Proceedings of the Western Snow Conference 41, 62–68.
Crowe, R.B., Baker, W.M., 1983. A preliminary investigation of snow cover patterns and risk implications for Canadian winter resort operators. Proceedings of the Eastern Snow Conference 40, 53–63.
Ćuk, S., Middlebrook, R.D., 1976. A general unified approach to modelling switching-converter power stages. Proceedings of the IEEE Power Electronics Specialists Conference 73–86.
Cullen, R.M., Marshall, S.J., 2011. Mesoscale temperature patterns in the Rocky Mountains and Foothills region of Southern Alberta. Atmosphere-Ocean 49, 189–205.
Cummings, W.C., Holliday, D.V., 1983. Preliminary measurements of sound attenuation by snow over a model seal lair. Journal of the Acoustical Society of America 74, S55.
Curry, G.E., Mann, A.S., 1965. Estimating Precipitation on a remote headwater area of Western Alberta. Proceedings of the Western Snow Conference 33, 58–66.
Daly, S.F., Davis, R., Ochs, E., Pangburn, T., 2000. An approach to spatially distributed snow modelling of the Sacramento and San Joaquin basins, California. Hydrological Processes 14, 3257–3271.
Dandekar, B.W., Brown, R.L., 1986. A numerical evaluation of flexible footing settlement into uniform snowcover. Cold Regions Science and Technology 12, 131–138.
Dantl, G., 1968. Die elastischen Moduln von Eis-Einkristallen. Physik der Kondensierten Materie 7, 390–397.
Darmesteter, J., 1880. The Zend Avesta, part 1: The Vendidad. Clarendon Press, Oxford.
Das, S.B., Alley, R.B., 2005. Characterization and formation of melt layers in polar snow: observations and experiments from West Antarctica. Journal of Glaciology 51, 307–312.
Dasgupta, R., Clark, R.A., 1998. Estimation of Q from surface seismic reflection data. Geophysics 63, 2120–2128.
Daugharty, D.A., Dickison, R.B.B., 1982. Snow cover distribution in forested and deforested landscapes in New Brunswick, Canada. Proceedings of the Western Snow Conference 50, 10–19.
Davies, W.D.T., 1966. Generation and Properties of Maximum-Length Sequences. Control 302–304, 364–365, 431–433.
Davis, R., Pangburn, T., Daly, S., Ochs, E., Hardy, J.P., Bryant, E., Pugner, P., 1999. Can satellite snow maps, ground measurements and modeling improve water management and control in the

Kings River Basin, California? Efforts toward finding the answer. Proceedings of the Western Snow Conference 67, 54–61.
Davis, R.E., Dozier, J., 1984. Snow wetness measurement by fluorescent dye dilution. Journal of Glaciology 30, 362–363.
Davis, R.E., Dozier, J., LaChapelle, E.R., Perla, R., 1985. Field and laboratory measurements of snow liquid water by dilution. Water Resources Research 21, 1415–1420.
Davis, R.T., 1973. Operational snow sensors. Proceedings of the Eastern Snow Conference 30, 57–70.
Davison, J., Powers, L., 2013. Why Alberta's floods hit so hard and fast - Calgary - CBC News [WWW Document]. URL http://www.cbc.ca/news/canada/calgary/story/2013/06/21/f-alberta-floods.html (accessed 7.19.13).
De Scally, F.A., 1995. Delaying seasonal snowmelt with avalanche activity: some results from the Cascade Mountains, Southern British Columbia. Proceedings of the Western Snow Conference 63, 38–48.
De Scally, F.A., 1996. Hydrologic roles of snow avalanches in high-mountain environments: a review. Proceedings of the Western Snow Conference 69–80.
Debeer, C.M., Pomeroy, J.W., 2009. Modelling snow melt and snowcover depletion in a small alpine cirque, Canadian Rocky Mountains. Hydrological Processes 23, 2584–2599.
Delany, M.E., Bazley, E.N., 1970. Acoustical properties of fibrous absorbent materials. Applied Acoustics 3, 105–116.
Denoth, A., 1980. The pendular-funicular liquid transition in snow. Journal of Glaciology 25, 93–97.
Denoth, A., 1982. The pendular-funicular liquid transition and snow metamorphism. Journal of Glaciology 28, 357–364.
Denoth, A., 1989. Snow dielectric measurements. Advances in Space Research 9, 233–243.
Denoth, A., 1994. An electronic device for long-term snow wetness recording. Annals of Glaciology 19, 104–106.
Denoth, A., 1999. Wet snow pendular regime: the amount of water in ring-shaped configurations. Cold Regions Science and Technology 30, 13–18.
Denoth, A., Foglar, A., Weiland, P., Mätzler, C., Aebischer, H., Tiuri, M., Sihvola, A., 1984. A comparative study of instruments for measuring the liquid water content of snow. Journal of Applied Physics 56, 2154–2160.
Denoth, A., Wilhelmy, I., 1988. Snow dielectric devices and field applications. Proceedings: 1988 International Snow Science Workshop, Whistler, October 12-15 203–206.
Dent, J.D., 1993. The dynamic friction characteristics of a rapidly sheared granular material applied to the motion of snow avalanches. Annals of Glaciology 18, 215–220.
Desrochers, D.T., Granberg, H.B., 1986. An investigation of woodland snow thermal regime in the Schefferville area, Northern Quebec. Proceedings of the Eastern Snow Conference 43, 204–210.
Diaz, H.F., 2007. Rapid climate change in the west: snowpacks and forests at risk. Proceedings of the Western Snow Conference 75, 53–56.
Dietrich, T., Rieman, R., 2001. Water resources forecasting in the north platte basin. Proceedings of the Western Snow Conference 69, 92–94.
Dingman, S.L., 2002. Physical Hydrology, 2nd ed. Prentice Hall, Upper Saddle River, NJ.
Douville, H., Royer, J.F., Mahfouf, J.F., 1995. A new snow parameterization for the Meteo-France Climate Model. I. Validation in Stand-Alone Experiments. Climate Dynamics 12, 21–35.
Drake, E., DeSisto, C., McDonald, S., Evans, S., Barry, D., Baccus, B., 2008. Untangling climate and wildfire influenes from snow water equivalent measurements on the Deer Park, WA, snow course. Proceedings of the Western Snow Conference 2008, 107–110.

Duband, D., Lallement, C., 1992. 40 years snow cover measurements in France: Network evaluation, forecast interest (application of historical and realtime data to the multipurpose of water management). Proceedings of the Western Snow Conference 60, 18–27.
Dunn, C., Hawksford, M.O., 1993. Distortion immunity of MLS-derived impulse response measurments. Journal of the Audio Engineering Society 41, 314–335.
Dutta, N.C., Odé, H., 1979. Attenuation and dispersion of compressional waves in fluid-filled porous rocks with partial gas saturation (White model)—Part I: Biot theory. Geophysics 44, 1777–1788.
Earl, W.M., Grey, G.R., Conway, H., Abrahamson, J., 1985. Remote sensing of snow accumulation. Cold Regions Science and Technology 11, 199–202.
Ebdon, D., 1991. Statistics in Geography: A Practical Approach - Revised with 17 Programs, 2nd ed. Wiley-Blackwell.
Edens, M.Q., Brown, R.L., 1991. Changes in the microstructure of snow under large deformations. Journal of Glaciology 37, 193–202.
Edey, S.N., 1985. Remote monitoring of depth of snow on ground with a micrologger. Proceedings of the Snow Property Measurements Workshop, 1-3 April 1985 207–214.
Elapavuluri, P., Bancroft, J., 2004. Estimation of Q. 2004 CSEG National Convention 1–4.
Elder, K., Gray, M., Major, P., Nyberg, C., 1999. Measuring and monitoring snow depth using the global positioning system. Proceedings of the Western Snow Conference 67, 104–113.
Ellerbruch, D.A., Boyne, H.S., 1980. Snow stratigraphy and water equivalence measured with an active microwave system. Journal of Glaciology 26, 225–233.
Ellis, C.R., Pomeroy, J.W., 2007. Estimating sub-canopy shortwave irradiance to melting snow on forested slopes. Hydrological Processes 21, 2581–2593.
Ellis, C.R., Pomeroy, J.W., Essery, R.L.H., Link, T.E., 2011. Effects of needleleaf forest cover on radiation and snowmelt dynamics in the Canadian Rocky Mountains. Canadian Journal of Forest Research 41, 608–620.
Ellis, C.R., Pomeroy, J.W., Link, T.E., 2013. Modeling increases in snowmelt yield and desynchronization resulting from forest gap-thinning treatments in a northern mountain headwater basin. Water Resources Research 49, 936–949.
Erxleben, J., Elder, K., Davis, R., 2002. Comparison of spatial interpolation methods for estimating snow distribution in the Colorado Rocky Mountains. Hydrological Processes 16, 3627–3649.
Essery, R., Pomeroy, J., Ellis, C., Link, T., 2008. Modelling longwave radiation to snow beneath forest canopies using hemispherical photography or linear regression. Hydrological Processes 22, 2788–2800.
Ewing, J., Ewing, M., Aitken, T., Ludwig, W.J., 2013. North Pacific Sediment Layers Measured by Seismic Profiling, in: Knopoff, L., Drake, C.L., Hart, P.J. (Eds.), Geophysical Monograph Series. American Geophysical Union, Washington, D. C., pp. 147–173.
Fang, X., Pomeroy, J.W., 2008. Drought impacts on Canadian prairie wetland snow hydrology. Hydrological Processes 22, 2858–2873.
Fang, X., Pomeroy, J.W., Ellis, C.R., MacDonald, M.K., DeBeer, C.M., Brown, T., 2013. Multi-variable evaluation of hydrological model predictions for a headwater basin in the Canadian Rocky Mountains. Hydrology and Earth System Sciences 17, 1635–1659.
Faraday, M., 1859. Note on Regelation. Proceedings of the Royal Society of London 10, 440–450.
Farina, A., 1998. MLS impulse response measurements for underwater bottom profiling. The European Conference on Underwater Acoustics 1998 (ECUA ’98), Rome, Italy 108, n.p.
Farina, A., 2000. Simultaneous Measurement of Impulse Response and Distortion with a Swept-Sine Technique. Presented at the Audio Engineering Society Convention 108, Audio Engineering Society.

Farnes, P.E., 1967. Criteria for determining mountain snow pillow sites. Proceedings of the Western Snow Conference 35, 59–62.
Farnes, P.E., Goodison, B.E., Peterson, N.R., Richards, R.P., 1980. Proposed metric snow samplers. Proceedings of the Western Snow Conference 48, 107–119.
Farnes, P.E., Peterson, N.R., Goodison, B.E., Richards, R.P., 1982. Metrification of manual snow sampling equipment. Proceedings of the Western Snow Conference 50, 120–132.
Farnes, P.E., Romme, W.H., 1993. Estimating localized SWE on the Yellowstone Northern Range. Proceedings of the Western Snow Conference 61, 59–65.
Farnes, P.E., Rompel, J., 1969. Montana telemetry system. Proceedings of the Western Snow Conference 37, 102–107.
Fassnacht, S.R., Helfrich, S.R., Lampkin, D.J., Dressler, K.A., Bales, R.C., Halper, E.B., Reigle, D., Imam, B., 2001. Snowpack modelling of the salt basin with water management implications. Proceedings of the Western Snow Conference 69, 65–76.
Fassnacht, S.R., Heun, C.M., López-Moreno, J.I., Latron, J., 2010. Variability of snow density measurements in the Rio Esera Valley, Pyrenees Mountains, Spain. Cuadernos de Investigación Geográfica 36, 59–72.
Fassnacht, S.R., Stednick, J.D., Deems, J.S., Corrao, M.V., 2009. Metrics for assessing snow surface roughness from digital imagery. Water Resources Research 45, W00D31.
Ffolliott, P.F., Gottfried, G.J., 2003. Contributions of snow reasearch to forest watershed management in the southwestern United States. Proceedings of the Western Snow Conference 71, 29–38.
Fierz, C., Armstrong, R.L., Durand, Y., Etchevers, P., Greene, E., McClung, D.M., Nishimura, K., Satyawali, P.K., Sokratov, S.A., 1999. The International Classification for Seasonal Snow on the Ground. IHP-VII Technical Documents in Hydrology N°83, IACS Contribution N°1, UNESCO-IHP, Paris. UNESCO, Paris, France.
Fierz, C., Fohn, P.M.B., 1994. Long-term observation of the water content of an Alpine snowpack. Proceedings of the 1994 International Snow Science Workshop, Snowbird, Utah 117–131.
Fierz, C., Lehning, M., 2001. Assessment of the microstructure-based snow-cover model SNOWPACK: thermal and mechanical properties. Cold Regions Science and Technology 33, 123–131.
Fincham, L.R., 1985. Refinements in the impulse testing of loudspeakers. Journal of the Audio Engineering Society 33, 133–140.
Fino, B.J., Algazi, V., 1976. Unified Matrix Treatment of the Fast Walsh-Hadamard Transform. IEEE Transactions on Computers C-25, 1142–1146.
Fisk, D., 1986a. Method of measuring liquid water mass fraction of snow by alcohol solution. Journal of Glaciology 32, 538–539.
Fisk, D., 1986b. Method of measuring liquid water mass fraction of snow by alcohol solution. Journal of Glaciology 32, 538–539.
Fitzharris, B.B., 1987. A climatology of major avalanche winters in Western Canada. Atmosphere-Ocean 25, 115–136.
Fletcher, C.A.J., 1991. Computational techniques for fluid dynamics, 2nd ed, Springer series in computational physics. Springer-Verlag, Berlin ; New York.
Fletcher, J.E., 1967. Atmospheric water resources of the Wasatch Front, Utah. Proceedings of the Western Snow Conference 35, 94–98.
Fomel, S., 2000. Inverse B-Spline Interpolation SEP report 105. Stanford Exploration Project, Stanford.
Fomel, S., 2002. Applications of plane-wave destruction filters. Geophysics 67, 1946–1960.
Fomel, S., 2007a. Velocity-independent time-domain seismic imaging using local event slopes. Geophysics 72, S139–S147.
Fomel, S., 2007b. Shaping regularization in geophysical-estimation problems. Geophysics 72, R29–R36.
Fomel, S., 2009. Velocity analysis using AB semblance. Geophysical Prospecting 57, 311–321.

Fornberg, B., 1998. A Practical Guide to Pseudospectral Methods. Cambridge University Press.
Forsythe, K.W., 1997. Stepwise multiple regression snow models: GIS applications in the Marmot Creek Research Basin (Kananaskis Country, Alberta) Canada and the National Park Berchtesgaden, (Bayern) Germany. Proceedings of the Eastern Snow Conference 54, 238–247.
Fortin, G., Jones, G.H., Bernier, M., Schneebeli, M., 2002. Changes in the structure and permeability of artificial ice layers containing florescent tracer in cold and wet snow cover. Proceedings of the Eastern Snow Conference 59, 257–266.
Fortin, R., Fortier, R., 2001. Tomographic imaging of a snowpack. Eastern Snow Conference 58.
Fourtier, R., 2009. Towards a geographical information system of snow cover in Eastern townships (Canada). Proceedings of the Eastern Snow Conference 66, 73–80.
Fowler, W.B., 1974. Thermal conductivity - basis of a potential method for determining in situ snow density. Proceedings of the Western Snow Conference 42, 46–52.
Freeman, G.J., 1997. Hydrofuels, Maintenance and Pricing Risk Assessment - Changing Times in Snow Zone Water Management. Proceedings of the Western Snow Conference 65, 12–19.
Freeman, G.J., 2009. Diminishing Snowfall in Central and Northern California's Mixed Rain and Snow Elevation Zone 77, 25–35.
Frei, A., Tedesco, M., Lee, S., Foster, J., Hall, D.K., Kelly, R., Robinson, D.A., 2012. A review of global satellite-derived snow products. Advances in Space Research 50, 1007–1029.
Fukusako, S., 1990. Thermophysical properties of ice, snow, and sea ice. Int J Thermophys 11, 353–372.
Fukuzawa, T., Akitaya, E., 1993. Depth-hoar crystal growth in the surface under high temperature gradient. Annals of Glaciology 18, 39–45.
Furukawa, T., Date, K., 1995. Ray-Modeling for Computer Simulation of Ultrasonic Testing, in: Thompson, D.O., Chimenti, D.E. (Eds.), Review of Progress in Quantitative Nondestructive Evaluation. Springer US, Boston, MA, pp. 1111–1118.
Gadallah, M.R., Fisher, R.L., 2005. Applied Seismology: A Comprehensive Guide to Seismic Theory and Application. PennWell, Tulsa, Okla.
Gammon, P., Kiefte, H., Clouter, M., Denner, W., 1983. Elastic Constants of Artificial and Natural Ice Samples by Brillouin Spectroscopy. Journal of Glaciology 29, 433–460.
Gan, T.W., Singh, P.R., Seneka, M., 1997. Impact of climate warming to the droughts of Canadian Prairies. Proceedings of the Western Snow Conference 65, 260–269.
Gan, T.Y., 2000. Reducing Vulnerability of Water Resources of Canadian Prairies to Potential Droughts and Possible Climatic Warming. Water Resources Management 14, 111–135.
Gary, H.L., 1967. Density variation in a snowpack of Northern New Mexico. Proceedings of the Western Snow Conference 35, 6–10.
Gawad, S., Sun, T., Green, N.G., Morgan, H., 2007. Impedance spectroscopy using maximum length sequences: application to single cell analysis. Rev Sci Instrum 78, 054301.
Gay, L.W., 1962. Measuring snowpack properties with radioactive sources. Proceedings of the Western Snow Conference 30, 14–19.
Gay, M., Fily, M., Genthon, C., Frezzotti, M., Oerter, H., Winther, J.-C., 2002. Snow grain-size measurements in Antarctica. Journal of Glaciology 48, 527–535.
Geiger, R., Aron, R.H., Todhunter, P., 2003. The Climate Near the Ground. Rowman & Littlefield.
Gerdel, R.W., 1952. The development of the radioactive snow gauge. Proceedings of the Eastern Snow Conference 9, 1–12.
Gerdel, R.W., 1954. The storage and transmission of water in snow. Proceedings of the Eastern Snow Conference 10-11, 18–21.
Gerdel, R.W., Hansen, B.L., Cassidy, W.C., 1950. The use of radioisotopes for the measurement of the water equivalent of a snow pack. Transactions, American Geophysical Union 31, 449–453.

Gerland, S., Oerter, H., Kipfstuhl, J., Wilhelms, F., Miller, H., Miners, W.D., 1999. Density log of a 181 m long ice core from Berkner Island, Antarctica. Annals of Glaciology 29, 215–219.
Gluns, D.R., Rose, G., 1992. An improved carrying case for snow tubes. Proceedings of the Western Snow Conference 60, 146–149.
Godbout, S.A., Chenard, L., Marquis, A., 2000. Instantaneous Young's Modulus of ice from liquid manure. Canadian Agricultural Engineering 42, 6.1–6.14.
Godfrey, K.R., 1975. Filtered binary sequences with no skewing. Electronics Letters 11, 456–457.
Gold, L.W., 1957. The influence of snow cover on heat flow from the ground, in: Snow and Ice, IAHS Publication No. 46. IAHS Press, Wallingford, Oxfordshire, UK.
Golding, D.L., Swanson, R.H., 1978. Snow accumulation and melt in small forest openings in Alberta. Canadian Journal of Forest Research 8, 380–388.
Golding, D.L., Swanson, R.H., 1986. Snow distribution patterns in clearings and adjacent forest. Water Resources Research 22, 1931–1940.
Golomb, S.W., Gong, G., 2005. Signal Design for Good Correlation: For Wireless Communication, Cryptography, and Radar, 1st ed. Cambridge University Press.
Good, W., 1986. Thin sections, serial cuts and 3D analysis of snow. Avalanche Formation, Movement and Effects, Proceedings of the Davos Symposium, IAHS Publication 35–48.
Goodison, B., Wilson, B., Wu, K., Metcalfe, J., 1984. An inexpensive remote snow-depth gauge: an assessment. Proceedings of the Western Snow Conference 52, 188–191.
Goodison, B.E., 1975. Standardization of snow course data: reporting and publishing. Proceedings of the Eastern Snow Conference 32, 12–23.
Goodison, B.E., 1978. Accuracy of snow samplers for measuring shallow snowpacks: an update. Proceedings of the Eastern Snow Conference 35, 36–49.
Goodison, B.E., 1985. The impact of automation on winter precipitaiton measurement, Proceedings of the Snow Property Measurments Workshop, Lake Louise, Alberta. pp. 471–490.
Goodison, B.E., Ferguson, H.L., McKay, G.A., 1981. Measurement and Data Analysis, in: Handbook of Snow: Principles, Processes, Management and Use. Pergamon Press Canada, Toronto, pp. 191–274.
Goodison, B.E., Metcalf, R.A., Wilson, R.A., Jones, K., 1988. The Canadian automatic snow depth sensor: a performance update. Proceedings of the Western Snow Conference 56, 178–181.
Granger, R.J., Gray, D.M., 1990. A net radiation model for calculating daily snowmelt in open environments. Nordic Hydrology 21, 217–234.
Granger, R.J., Male, D.H., 1978. Melting of a prairie snowpack. Journal of Applied Meteorology 17, 1833–1842.
Granger, R.J., Male, D.H., Gray, D.M., 1978. Prairie snowmelt. Proceedings of the Applied Prairie Hydrology Symposium, 7th Symposium of the Water Studies Institute 7, 1–10.
Granlund, N., Gustafson, D., Feiccabrino, J., Lundberg, A., 2007. Laboratory test of snow wetness influence on impulse radar amplitude damping. Proceedings of the Westsern Snow Conference 75, 151–155.
Gray, C.H., 1967. Current Corps of Engineers Radio System Developments. Proceedings of the Western Snow Conference 35, 35–42.
Gray, C.H., 1968. Alaska telemetering network for the Corps of Engineers and the U.S. Weather bureau. Proceedings of the Western Snow Conference 84–88.
Gray, D.M., 1972. Preliminary Progress Report on Development of a Portable System for Point Measurements of Radiation, Temperature and Humidity. Arctic Land Use Research Program (Canada).
Gray, D.M., Landine, P.G., 1988. An energy-budget snowmelt model for the Canadian Prairies. Canadian Journal of Earth Sciences 25, 1292–1303.

Gray, D.M., Landine, P.G., Granger, R.J., 1985. Simulating infiltration into frozen Prairie soils in streamflow models. Canadian Journal of Earth Sciences 22, 464–472.
Gray, D.M., Norum, D.I., Dyck, G.E., 1970. Snow measurement in the Prairie environment. Canadian Agricultural Engineering 12, 38–41.
Gray, D.M., Norum, D.I., Dyck, G.E., 1970. Densities of prairie snowpacks, Research paper no. 2, Division of Hydrology, University of Saskatchewan. Division of Hydrology, University of Saskatchewan, Saskatoon.
Griffin, D.W., Lim, J.S., 1984. Signal estimation from modified short-time Fourier transform. IEEE Transactions on Acoustics Speech and Signal Processing 32, 236–242.
Grimmett, G., 1999. Percolation, 2nd ed. ed, Grundlehren der mathematischen Wissenschaften. Springer, Berlin ; New York.
Gubler, H., 1978. Determination of the mean number of bonds per snow grain and of the dependence of the tensile strength of snow on stereological parameters. Journal of Glaciology 20, 329–341.
Gubler, H., 1981. An inexpensive remote snow-depth gauge based on ultrasonic wave reflection from the snow surface. Journal of Glaciology 27, 157–163.
Gubler, H., Hiller, M., 1984. The use of microwave FMCW radar in snow and avalanche research. Cold Regions Science and Technology 9, 109–119.
Gustafsson, D., Stähli, M., Jansson, P.-E., 2001. The surface energy balance of a snow cover: comparing measurements to two differentsimulation models. Theoretical and Applied Climatology 70, 81–96.
Habeck, J.R., 1987. Present-Day Vegetation in the Northern Rocky Mountains. Annals of the Missouri Botanical Garden 74, 804–840.
Hale, D., 1981. An inverse-Q Filter, Stanford Exploration Project Note SEP-26. Stanford Exploration Project, Stanford.
Halliday, I.G., 1950. The liquid water content of snow measurement in the field. Journal of Glaciology 1, 357–361.
Hallikainen, M., Ulaby, F., Abdelrazik, M., 1986. Dielectric properties of snow in the 3 to 37 GHz range. IEEE Transactions on Antennas and Propagation 34, 1329–1340.
Hannaford, J., Howard, C.H., 1979. Operational and technical considerations regarding recent forecast seasons in California. Proceedings of the Western Snow Conference 47, 80–90.
Hansen, P.C., 2002. Deconvolution and Regularization with Toeplitz Matrices. Numerical Algorithms 29, 323–378.
Hansen, P.C., 2010. Discrete inverse problems: insight and algorithms, Fundamentals of algorithms. Society for Industrial and Applied Mathematics, Philadelphia.
Hardy, J.P., Albert, M.R., 1995. Snow-induced thermal variations around a single conifer tree. Hydrological Processes 9, 923–933.
Hardy, J.P., Melloh, R., Robinson, P., Jordan, R., 2000. Incorporating effects of forest litter in a snow process model. Hydrological Processes 14, 3227–3237.
Hare, F.K., Thomas, M.K., 1979. Climate Canada, 2d ed. ed. J. Wiley & Sons Canada, Toronto.
Hargreaves, N.D., 1992. Similarity and the inverse Q filter: some simple algorithms for inverse Q filtering. Geophysics 57, 944–947.
Hargreaves, N.D., Calvert, A.J., 1991. Inverse Q filtering by Fourier transform. Geophysics 56, 519–527.
Harlan, R.L., 1969. Soil-water freezing, snow accumulation and ablation in Marmot Creek Experimental Watershed, Alberta, Canada. Proceedings of the Western Snow Conference 37, 29–33.
Harper, J.T., Bradford, J.H., 2003. Snow stratigraphy over a uniform depositional surface: spatial variability and measurement tools. Cold Regions Science and Technology 37, 289–298.
Harr, R.D., 1981. Some characteristics and consequences of snowmelt during rainfall in western Oregon. Journal of Hydrology 277–304.

Harrington, A.W., 1953. Snow surveys in the northeast and uses of data. Proceedings of the Western Snow Conference 21, 1–2.
Harrison, R., Kinnaird, V., McBoyle, G.R., Quinlan, C., Wall, G., 1986. The resiliency and sensitivity of downhill skiing in Ontario to climate change. Proceedings of the Eastern Snow Conference 43, 94–105.
Harshburger, B.J., Blandford, T.R., Humes, K.S., Walden, V.., Moore, B.C., 2005. Evaluation of enhancements to the snowmelt runoff model. Proceedings of the Western Snow Conference 2005, 57–63.
Hawley, R.L., Morris, E.M., 2006. Borehole optical stratigraphy and neutron-scattering density measurements at Summit, Greenland. Journal of Glaciology 52, 491–496.
Hegde, N., 2010. Seamlessly interfacing MEMS microphones with Blackfin Processors, Application Note EE-350. Analog Devices, Norwood, MA.
Helgason, W., Pomeroy, J., 2012a. Problems Closing the Energy Balance over a Homogeneous Snow Cover during Midwinter. Journal of Hydrometeorology 13, 557–572.
Helgason, W., Pomeroy, J.W., 2012b. Characteristics of the Near-Surface Boundary Layer within a Mountain Valley during Winter. Journal of Applied Meteorology and Climatology 51, 583–597.
Helgason, W.D., Pomeroy, J.W., 2005. Uncertainties in Estimating Turbulent Fluxes to Melting Snow in a Mountain Clearing. Proceedings of the Eastern Snow Conference 62, 129–142.
Hellström, R.A., Mark, B.G., 2006. An embedded sensor network for measuring hydrometeorological variability within an Alpine valley. Proceedings of the Eastern Snow Conference 63, 263–279.
Henderson, T.J., 1953. The use of aerial photographs of snow depth markers in water supply forecasting. Proceedings of the Western Snow Conference 21, 44–47.
Hennon, P.E., 2007. The vital role of snow in protecting yellow-cedar from an extensive forest decline in Alaska. Proceedings of the Western Snow Conference 75, 77–88.
Hess, H.M., Attenborough, K., Heap, N.W., 1990. Ground characterization by short-range propagation measurements. The Journal of the Acoustical Society of America 87, 1975–1986.
Hobbs, P.V., 1974. Ice physics. Clarendon Press, Oxford.
Hodge, A.J., Huxley, H.E., Spiro, D., 1954. A simple new microtome for ultrathin sectioning. Journal of Histochemistry & Cytochemistry 2, 54–61.
Hoham, R.W., 1989. Snow microorganisms and their interaction with the environment. Proceedings of the Western Snow Conference 57, 31–35.
Hoham, R.W., Laursen, A.E., Clive, S.O., Duval, B., 1993. Snow algae and other microbes in several alpine sites in New England. Proceedings of the Western Snow Conference 61, 165–173.
Holland, C.W., Brunson, B.A., 1988. The Biot–Stoll sediment model: An experimental assessment. The Journal of the Acoustical Society of America 84, 1437–1443.
Holmgren, J., Sturm, M., Yankielun, N.E., Koh, G., 1998. Extensive measurements of snow depth using FM-CW radar. Cold Regions Science and Technology 27, 17–30.
Hood, J.L., Hayashi, M., 2010. Assessing the application of a laser rangefinder for determining snow depth in inaccessible alpine terrain. Hydrol. Earth Syst. Sci. 14, 901–910.
Hopkinson, C., 1997. The net volumetric loss of glacier cover within the Bow Valley above Banff, 1951-1993. Proceedings of the Western Snow Conference 65, 270–278.
Hopkinson, C., Young, G., 1997. The impact of glacier rescession upon the discharge of the Bow River above Banff, Alberta, 1951-1993. Proceedings of the Western Snow Conference 65, 91–102.
Hörmander, L., 1983. The analysis of linear partial differential operators, Grundlehren der mathematischen Wissenschaften. Springer-Verlag, Berlin ; New York.
Howe, C.C., Houghton, R.J., 1968. The twin-probe snow density gage. Proceedings of the Eastern Snow Conference 25, 61–72.

Howell, J.D., Harris, S.A., 1978. Soil-Forming Factors in the Rocky Mountains of Southwestern Alberta, Canada. Arctic and Alpine Research 10, 313–324.

Hubbart, J., Link, T., Campbell, C., Cobos, D., 2005. Evaluation of a low-cost temperature measurement system for environmental applications. Hydrological Processes 19, 1517–1523.

Huber, M.L., Perkins, R.A., Laesecke, A., Friend, D.G., Sengers, J.V., Assael, M.J., Metaxa, I.N., Vogel, E., Mareš, R., Miyagawa, K., 2009. New International Formulation for the Viscosity of H2O. Journal of Physical and Chemical Reference Data 38, 101–125.

IEC, CIE, 1987. CIE International lighting vocabulary: IEC international electrotechnical vocabulary = Vocabulaire international de l'éclairage : vocabulaire electrotechnique international. CIE, Geneve.

Ingard, K.U., 1988. Fundamentals of Waves and Oscillations. Cambridge University Press.

Ingersoll, G.P., Mast, M.A., Campbell, D.H., Clow, D.W., Nanus, L., 2009. Declining Snowpack Depths and Snow Water Equivalent at Snowpack Monitoring Sites in the Rocky Mountain Region, USA, 1993-200. Proceedings of the Western Snow Conference 77, 145–148.

Insana, M.F., Wood, J.G., Hall, T.J., 1992. Identifying acoustic scattering sources in normal renal parenchyma in vitro by varying arterial and ureteral pressures. Ultrasound in Medicine & Biology 18, 587–599.

Intihar, M.R., Stewart, R.E., 2005. Extratropical cyclones and precipitation within the Canadian Archipelago during the Cold Season. Arctic 58, 162–174.

Ishida, T., 1965. Acoustic properties of snow. Contributions of the Institute of Low Temperature Science, Series A 20, 23–63.

Ishizaka, M., 1993. An accurate measurement of densities of snowflakes using 3-D microphotographs. Annals of Glaciology 18, 92–96.

Iwase, T., Sakuma, T., Yoshihisa, K., 2001a. Measurements on sound propagation characteristics in snow layer. ICA Proceedings.

Iwase, T., Sakuma, T., Yoshihisa, K., 2001b. Measurements and simulations on sound propagation above snow field. ICA Proceedings.

Jaafar, H., Picot, J.J.C., 1970. Thermal conductivity of snow by a transient state probe method. Water Resources Research 6, 333–335.

Jairell, R.L., Schmidt, R.A., 1992. Harvesting snow when water levels are low. Proceedings of the Western Snow Conference 60, 121–124.

Jairell, R.L., Schmidt, R.A., 1995. Tree rows for snow accumulation in stock ponds. Proceedings of the Western Snow Conference 63, 152–155.

Jamieson, J.B., Schweizer, J., 2000. Texture and strength changes of buried surface-hoar layers with implications for dry snow-slab avalanche release. Journal of Glaciology 46, 151–160.

Janowicz, J.R., Ford, G., 1994. Impact of climate change on water supply in the Upper Yukon River. Proceedings of the Western Snow Conference 62, 171–174.

Jansson, P.A., 1996. Deconvolution of Images and Spectra, Second Edition, 2nd ed. Academic Press.

Jarosch, A.H., Denoth, A., 2004. Alpine and maritime snow covers: similarities and differences in water distribution. Proceedings of the 2004 International Snow Science Workshop, Jackson Hole, Wyoming 51–55.

Jin, J., Gao, X., Sorooshian, S., Yang, Z.-L., Bales, R., Dickinson, R.E., Sun, S.-F., Guo-Xiong Wu, 1999. One-dimensional snow water and energy balance model for vegetated surfaces. Hydrological Processes 13, 2467–2482.

Johnson, D.L., Plona, T.J., 1980. Acoustic slow waves and the consolidation transition. Journal of the Acoustical Society of America 72, 556–565.

Johnson, D.L., Plona, T.J., Scala, C., Pasierb, F., Kojima, H., 1982. Tortuosity and acoustic slow waves. Physical Review Letters 49, 1840–1844.

Johnson, J.B., 1982. On the application of Biot's theory to acoustic wave propagation in snow. Cold Regions Science and Technology 6, 49–60.
Johnson, J.B., 1985. Audibility within and outside deposited snow. Journal of Glaciology 31, 136–142.
Johnson, J.B., 1990. Estimates of shock wave attenuation in snow, CRREL Report 90-8. CRREL, Hanover, New Hampshire.
Johnson, J.B., 2004. A theory of pressure sensor performance in snow. Hydrological Processes 18, 53–64.
Johnson, J.B., Gelvin, A., Schaefer, G.L., 2007. An engineering design study of electronic Snow Water Equivalent sensor performance. Proceedings of the Western Snow Conference 75, 23–30.
Johnson, J.B., Hopkins, M.A., 2005. Identifying microstructural deformation mechanisms in snow using discrete-element modeling. Journal of Glaciology 51, 432–442.
Johnson, J.B., Marks, D., 2004. The detection and correction of snow water equivalent pressure sensor errors. Hydrological Processes 18, 3513–3525.
Johnson, J.B., Schaefer, G.L., 2002. The influence of thermal, hydrologic, and snow deformation mechanisms on Snow Water Equivalent pressure sensor accuracy. Proceedings of the Western Snow Conference 70, 111–121.
Johnson, J.B., Solie, D.J., Brown, J.A., Gaffney, E.S., 1993. Shock response of snow. Journal of Applied Physics 73, 4852–4861.
Johnson, T., Dozier, J., Michaelson, J., Foel, P., 1997. River basin variations in Sierra Nevada snowpack accumulation trends. Proceedings of the Western Snow Conference 65, 310–316.
Jones, E.B., Rango, A., Howell, S.M., 1983. Snowpack liquid water determinations using freezing calorimetry. Nordic Hydrology 14, 113–126.
Jones, H.G., Pomeroy, J.W., Davies, T.D., Tranter, M., Marsh, P., 1999. CO2 in Arctic snow cover: landscape form, in-pack gas concentration gradients, and the implications for the estimation of gaseous fluxes. Hydrological Processes 13, 2977–2989.
Jones, S.B., Wraith, J.M., Or, D., 2002. Time domain reflectometry measurement principles and applications. Hydrological Processes 16, 141–153.
Jordan, R., 1991. A one-dimensional temperature model for a snow cover: Technical documentation for SNTHERM.89. Cold Regions Research and Engineering Laboratory, Hanover, New Hampshire.
Judson, A., 1977. The avalanche warning program in Colorado. Proceedings of the Western Snow Conference 45, 19–27.
Judson, A., Doesken, N., 2000. Density of Freshly Fallen Snow in the Central Rocky Mountains. Bull. Amer. Meteor. Soc. 81, 1577–1587.
Julander, R., Vaughn, K., Bricco, M., Uriona, B., Nault, B., 2011. The Mill Flat Fire hydrologic and flood potential evaluation. Proceedings of the Western Snow Conference 2011, 15–23.
Julander, R.P., 2007. Soil surface temperature differences between steel and hypalon pillows. Proceedings of the Western Snow Conference 75, 165–169.
Jung, W.G., 2005. Op Amp Applications Handbook. Newnes; Elsevier, Burlington, MA.
Kaempfer, T.U., Schneebeli, M., Sokratov, S.A., 2005. A microstructural approach to model heat transfer in snow. Geophysical Research Letters 32, L21503.
Kalliomaki, N.M., Courtin, G.M., Clulow, F.V., 1984. Thermal index and thermal conductivity of snow and their relationship to winter survival of the Meadow Vole, Microtus Pennsylvanicus. Proceedings of the Eastern Snow Conference 41, 153–164.
Kattelmann, R., 1986. Snow compaction effects on nighttime freezing. Proceedings of the Western Snow Conferenc 54, 168–171.
Kattelmann, R., 1989. Spatial variability of snow-pack outflow at a site in Sierra Nevada, U.S.A. Annals of Glaciology 13, 124–128.
Kattelmann, R., 1990. Variability of liquid water content in an alpine snowpack. Proceedings of the International Snow Science Workshop 1990 261–265.

Kattelmann, R., 1996. Snowmelt contributions to flooding in the American River Basin. Proceedings of the Western Snow Conference 145–148.
Kattelmann, R., 1997. Very warm storms and Sierra Nevada snowpacks. Proceedings of the Western Snow Conference 65, 125–128.
Kattelmann, R., 1999. Snowmelt contributions to flooding in the Lake Tahoe Basin. Proceedings of the Western Snow Conference 64, 167–170.
Kattelmann, R., Dozier, J., 1999. Observations of snowpack ripening in the Sierra Nevada, California, U.S.A. Journal of Glaciology 45, 409–416.
Kattelmann, R.C., McGurk, B.J., Berg, N.H., 1983. The isotope profiling snow gauge: twenty years of experience. Proceedings of the Western Snow Conference 1983, 1–8.
Kaufmann, B., 2013. Cost of flood damage in Calgary could reach $1B [WWW Document]. Toronto Sun. URL http://www.torontosun.com/2013/07/02/cost-of-flood-damage-in-calgary-could-reach-1b?utm_source=facebook&utm_medium=recommend-button&utm_campaign=Cost of flood damage in Calgary could reach $1B (accessed 7.22.13).
Kawashima, K., Yamada, T., Wakahama, G., 1993. Investigations of internal structure and transformational processes from firn to ice in a perennial snow patch. Annals of Glaciology 18, 117–122.
Kaye, G.W.C., Evans, E.J., 1940. The sound-absorbing properties of some common out-door materials. Proc. Phys. Soc. 52, 371.
Keeler, C., 1969. The growth of bonds and the increase of mechanical strength in a dry seasonal snow cover. Journal of Glaciology 8, 441–450.
Kendra, J., Ulaby, F.T., Sarabandi, K., 1994. Snow probe for in-situ determination of wetness and density. IEEE Journal of Geoscience and Remote Sensing 32, 1152–1159.
Kernaghan, G., Harper, K.A., 2001. Community Structure of Ectomycorrhizal Fungi across an Alpine/Subalpine Ecotone. Ecography 24, 181–188.
Kester, W.A., 2005. Data Conversion Handbook. Newnes; Elsevier, Burlington, MA.
Khenkin, A., Lewis, J., 2012. Recommendations for mounting and connecting the Analog Devices, Inc., Bottom-Ported MEMS Microphones, Application Note AN-1003. Analog Devices, Norwood, MA.
Kinar, N.J., Pomeroy, J.W., 2007. Determining snow water equivalent by acoustic sounding. Hydrological Processes 21, 2623–2640.
Kinar, N.J., Pomeroy, J.W., 2008a. Operational techniques for determining SWE by sound propagation through snow: I. General Theory. Proceedings of the Eastern Snow Conference 309–323.
Kinar, N.J., Pomeroy, J.W., 2008b. Operational techniques for determining SWE by sound propagation through snow: II. Instrumentation and testing. Proceedings of the Eastern Snow Conference 65, 19–33.
Kinar, N.J., Pomeroy, J.W., 2009. Automated Determination of Snow Water Equivalent by Acoustic Reflectometry. Geoscience and Remote Sensing, IEEE Transactions on 47, 3161–3167.
Kind, R.J., 1981. Snow drifting, in: Hanbook of Snow: Principles, Processes, Management and Use. Pergamon Press Canada, pp. 338–359.
King, J.C., Pomeroy, J.W., Gray, D.M., Fierz, C., Fohn, P.M.B., Harding, R.J., Jordan, R.E., Martin, E., Pluss, C., 2008. Snow-atmosphere energy and mass balance, in: Snow and Climate: Physical Processes, Surface Energy Exchange and Modeling. Cambridge University Press, Cambridge, pp. 70–124.
Kingery, W.D., 1960. Regelation, Surface Diffusion, and Ice Sintering. Journal of Applied Physics 31, 833–838.
Kinsler, L.E., Frey, A.R., 1962. Fundamentals of acoustics, 2nd ed. ed. Wiley, New York.
Klauder, J.R., Price, A.C., Darlington, S., Albersheim, W.J., 1960. The theory and design of chirp radars. The Bell System Technical Journal 39, 745–808.

Kluitenberg, G.J., Ham, J.M., Bristow, K.L., 1993. Error analysis of the heat pulse method for measuring soil volumetric heat capacity. Soil Science Society of America Journal 57, 1444–1451.
Koch, R.W., Fisher, A.W., 2000. Effects of inter-annual and decadal-scale climate variability on winter and spring streamflow in western Oregon and Washington. Proceedings of the Western Snow Conference 68, 1–11.
Koh, G., Jordan, R., 1995. Sub-surface melting in a seasonal snow cover. Journal of Glaciology 41, 474–482.
Koh, G., Lever, J.H., Arcone, S.A., Marshall, H., Ray, L.E., 2010. Autonomous FMCW radar survey of Antarctic shear zone, in: 2010 13th International Conference on Ground Penetrating Radar (GPR). Presented at the 2010 13th International Conference on Ground Penetrating Radar (GPR), pp. 1–5.
Koh, G., Mulherin, N.D., Hardy, J.P., Davis, R.E., Twombly, A., 2002. Microwave interaction with snowpack observed at the Cold Land Processes Field Experiment. Proceedings of the Eastern Snow Conference 59, 251–254.
König, M., Winther, J.-G., Isaksson, E., 2001. Measuring snow and glacier ice properties from satellite. Reviews of Geophysics 39, 1–27.
Kováčik, J., 2001. Correlation between shear modulus and porosity in porous materials. Journal of Materials Science Letters 20.
Kováčik, J., Emmer, š., 2013. Correlation between Shear Wave Velocity and Porosity in Porous Solids and Rocks. Journal of Powder Technology 2013, 1–3.
Kovitz, P.S., 1994. Removing Distortion Artifacts from Maximum-Length Sequence Impulse-Response Measurements. Presented at the Audio Engineering Society Convention 97, Audio Engineering Society.
Krimmel, R.M., Tangborn, W.V., 1974. South Cascade Glacier: The Moderating Effect of Glaciers on Runoff. Proceedings of the Western Snow Conference 42, 9–13.
Kundur, D., Hatzinakos, D., 1996. Blind image deconvolution. IEEE Signal Processing Magazine 13, 43–64.
Kuroiwa, D., 1961. A Study of Ice Sintering. Tellus 13, 252–259.
Kuz'min, P.P., 1957. Physical properties of snow covers. Gidrometizdat.
LaChapelle, E.R., 1977. Field guide to snow crystals. J. J. Douglas, Vancouver.
Lacroix, P., Grasso, J.-R., Roulle, J., Giraud, G., Goetz, D., Morin, S., Helmstetter, A., 2012. Monitoring of snow avalanches using a seismic array: Location, speed estimation and relationships to meteorological variables. Journal of Geophysical Research 117, F01034.
Lahtinen, P., 2011. Brief communication "Snow profile associated measurements (SPAM); a new instrument for quick snow profile measurements". The Cryosphere Discussions 5, 1737–1748.
Lang, T.E., 1976a. Measurements of acoustic properties of hard-pack snow. Journal of Glaciology 17, 269–276.
Lang, T.E., 1976b. Measurements of the acoustic propertiues of hard-pack snow. Journal of Glaciology 17, 269–276.
Langham, E.J., 1981. Physics and Properties of Snowcover, in: Hanbook of Snow: Principles, Processes, Management and Use. Pergamon Press Canada, Toronto, pp. 275–337.
Lapp, S., Byrne, J., Townshend, I., Kienzle, S., 2005. Climate warming impacts on snowpack accumulation in an alpine watershed. International Journal of Climatology 25, 521–536.
Lazar, B., Smith, J., Williams, M., 2006. Estimating changes in climate and snow quantity at the Aspen Ski Area for the years 2030 and 2100. Proceedings of the Western Snow Conference 74, 109–120.
Le, L.H., Zhang, C., Ta, D., Lou, E., 2010. Measurement of tortuosity in aluminum foams using airborne ultrasound. Ultrasonics 50, 1–5.
Lea, J., 2007. The NOHRSC SNODAS Snow Water Equivalent Determination on Mount St. Helens, Washington. Proceedings of the Western Snow Conference 75, 175–178.

Lea, J., Reid, I., 2006. An evaluation of SNODAS for determining Snow Water Equivalent on Mount St. Helens, Washington. Proceedings of the Western Snow Conference 74, 165–169.
LeBlanc, L.R., Schock, S.G., Panda, S., 1991. Pulse and Aperture Design Considerations For A Marine Sediment of Classification Chirp Sonar. OCEANS "91. 'Ocean Technologies and Opportunities in the Pacific for the 90's". Proceedings. 2, 1027.
Lee, S., Rogers, J.C., 1985. Characterization of snow by acoustic sounding: a feasibility study. Journal of Sound and Vibration 99, 247–266.
Lee, T.M., 1961. Note on Young's modulus and Poisson's ratio of naturally compacted snow and processed snow, USA CRREL Technical Note. Cold Regions Research and Engineering Laboratory, Hanover, New Hampshire.
Lee, T.-M., 1963. Method of determining dynamic properties of viscoelastic solids employing forced vibration. Journal of Applied Physics 34, 1524–1529.
Lehning, M., Bartelt, P., Brown, B., Fierz, C., 2002a. A physical SNOWPACK model for the Swiss Avalanche warning Part III: meteorological forcing, thin layer formation and evaluation. Cold Regions Science and Technology 35, 169–184.
Lehning, M., Bartelt, P., Brown, B., Fierz, C., Satyawali, P., 2002b. A physical SNOWPACK model for the Swiss avalanche warning Part II. Snow microstructure. Cold Regions Science and Technology 35, 147–167.
Lehning, M., Bartelt, P., Brown, B., Russi, T., Stökli, U., Zimmerli, M., 1999. SNOWPACK model calculations for avalanche warning based upon a new network of weather and snow stations. Cold Regions Science and Technology 30, 145–157.
Lehning, M., Fierz, C., Lundy, C., 2001. An objective snow profile comparison method and its application to SNOWPACK. Cold Regions Science and Technology 33, 253–261.
Leonard, K.C., Cullather, R.I., 2008. Snowfall measurements in the Amundsen and Bellingshausen Seas, Antarctica. Proceedings of the Eastern Snow Conference 65, 87–98.
Lewis, J., 2011. Microphone specifications explained. Analog Devices Application Note AN-1112. Analog Devices, Norwood, MA.
Libbrecht, K.G., 2005. The physics of snow crystals. Rep. Prog. Phys. 68, 855.
Lim, J.S., 1990. Two-dimensional signal and image processing, Prentice-Hall signal processing series. Prentice Hall, Englewood Cliffs, N.J.
Liner, C.L., 2004. Elements of 3D Seismology. PennWell Books.
Link, T.E., Marks, D., 1999. Point simulation of seasonal snow cover dynamics beneath boreal forest canopies. Journal of Geophysical Research: Atmospheres 104, 27841–27857.
Liu, G., Si, B.C., 2008. Dual-probe heat pulse method for snow density and thermal properties measurement. Geophysical Research Letters 35, 1–5.
Liu, G., Si, B.C., 2010. Error analysis of heat pulse probe methods: experiments and simulations. Soil Science Society of America Journal 74, 797–803.
Liu, W., Weiss, S., 2010. Wideband Beamforming: Concepts and Techniques. John Wiley and Sons.
Louge, M.Y., Foster, R.L., Jensen, N., Patterson, R., 1998. A portable capacitance snow sounding instrument. Cold Regions Science and Technology 28, 73–81.
Lucas, R.M., Harrison, A.R., 1990. Snow observation by satellite: A review. Remote Sensing Reviews 4, 285–348.
Luce, C.H., Tarboton, D.G., 2001. A modified force-restore approach to modelling snow-surface heat fluxes. Proceedings of the Western Snow Conference 69, 103–114.
Lüke, H.D., 1986. Folgen mit perfekten periodischen Auto-und Kreuzkorrelationsfunktionen. Frequenz 40.
Lundberg, A., Richardson-Näslund, C., Andersson, C., 2006. Snow density variations: consequences for ground-penetrating radar. Hydrological Processes 20, 1483–1495.

Lundquist, J., Rochford, C., 2007. Distributed temperatures in the snow zone: spatial patterns and innovative measurement techniques. Proceedings of the Western Snow Conference 75, 43–51.
Lundquist, J.D., Cayan, D.R., Dettinger, M.D., 2003. Meterology and Hydrology in Yosemite National Park: A Sensor Network Application. Proceedings of the IPSEN Conference 518–528.
Luo, S., Hale, D., 2012. Velocity analysis using weighted semblance. Geophysics 77, U15–U22.
Lurton, X., 2002. An Introduction to Underwater Acoustics: Principles and Applications. Springer, New York.
Lyons, R.G., 2004. Understanding Digital Signal Processing, 2nd ed. Prentice Hall.
Lyons, R.G., 2010. Understanding Digital Signal Processing, 3rd ed. Pearson Education.
Lyshevski, S.E., 2005. Nano- and Micro-Electromechanical Systems: Fundamentals of Nano- and Microengineering, Second Edition, 2nd ed. CRC Press.
Macdonald, G.M., 1987. Postglacial Development of the Subalpine-Boreal Transition Forest of Western Canada. Journal of Ecology 75, 303–320.
MacWilliams, F.J., Sloane, N.J.A., 1976. Pseudo-random sequences and arrays. Proceedings of the IEEE 64, 1715–1729.
Magnanimo, V., La Ragione, L., Jenkins, J.T., Wang, P., Makse, H.A., 2008. Characterizing the shear and bulk moduli of an idealized granular material. EPL Journal 81, 34006–1 to 34006–6.
Mahajan, P., Brown, R.L., 1993. A microstructure-based constitutive law for snow. Annals of Glaciology 18, 287–294.
Male, D.H., Granger, R.J., 1979. Energy and mass fluxes at the snow surface in a prairie environment, in: Proceedings of the Modelling of Snow Cover Runoff. Cold Regions Research and Engineering Laboratory, Hanover, New Hampshire, pp. 101–124.
Male, D.H., Granger, R.J., 1981. Snow surface energy exchange. Water Resources Research 17, 609–627.
Male, D.H., Gray, D.M., 1975. Problems in developing a physically based snowmelt model. Canadian Journal of Civil Engineering 2, 474–488.
Marbouty, D., 1980. An experimental study of temperature-gradient metamorphism. Journal of Glaciology 26, 303–312.
Marco, O., Buser, O., Villemain, P., 1996. Analysis of a rigid frame model of porous media for the acoustic properties of dense snow. Journal of Sound and Vibration 196, 439–451.
Marco, O., Buser, O., Villemain, P., Touvier, F., Revol, H.P., 1998. Acoustic impedance measurement of snow density. Annals of Glaciology 26, 92–96.
Margrave, G.F., Lamoureux, M.P., Henley, D.C., 2011. Gabor deconvolution: Estimating reflectivity by nonstationary deconvolution of seismic data. Geophysics 76, W15–W30.
Mariner, T., 1961. Critique of the Reverberant Room Method of Measuring Air-Borne Sound Transmission Loss. The Journal of the Acoustical Society of America 33, 1131–1139.
Marks, D., Cooley, K., Robertson, D., Winstral, A., 2001. Long-Term Snow Database, Reynolds Creek Experimental Watershed, Idaho, United States. Water Resour. Res. 37, 2835–2838.
Marks, D., Winstral, A., Flerchinger, G., Reba, M., Pomeroy, J., Link, T., Elder, K., 2008. Comparing Simulated and Measured Sensible and Latent Heat Fluxes over Snow under a Pine Canopy to Improve an Energy Balance Snowmelt Model. Journal of Hydrometeorology 9, 1506–1522.
Marsh, C.B., Pomeroy, J.W., Spiteri, R.J., 2012. Implications of mountain shading on calculating energy for snowmelt using unstructured triangular meshes. Hydrological Processes 26, 1767–1778.
Marsh, P., 1990. Snow Hydrology, in: Northern Hydrology: Canadian Perspectives. NHRI Science Report No. 1. National Water Research Institute, Saskatoon, pp. 37–61.
Marsh, P., 1991. Water flux in melting snow covers, in: Advances in Porous Media, Volume 1. Elsevier Science Publishers, Amsterdam, The Netherlands, pp. 61–124.
Marsh, P., Pomeroy, J.W., 1996. Meltwater fluxes at an arctic forest-tundra site. Hydrological Processes 10, 1383–1400.

Marsh, P., Woo, M.-K., 1984a. Wetting front advance and freezing of meltwater within a snow cover. 1. Observations in the Canadian Arctic. Water Resources Research 20, 1853–1864.

Marsh, P., Woo, M.-K., 1984b. Wetting front advance and freezing of meltwater within a snow cover. 2. A simulation model. Water Resources Research 20, 1865–1874.

Marsh, P., Woo, M.-K., 1985. Meltwater movement in natural heterogeneous snow covers. Water Resources Research 21, 1710–1716.

Marshall, H.-P., Koh, G., 2008. FMCW radars for snow research. Cold Regions Science and Technology 52, 118–131.

Marshall, H.-P., Koh, G., Forster, R.R., 2004. Ground-based frequency-modulated continuous wave radar measurements in wet and dry snowpacks, Colorado, USA: an analysis and summary of the 2002–03 NASA CLPX data. Hydrological Processes 18, 3609–3622.

Marshall, H.-P., Koh, G., Forster, R.R., 2005. Estimating alpine snowpack properties using FMCW radar. Annals of Glaciology 40, 157–162.

Marshall, H.-P., Schneebeli, M., Koh, G., 2007. Snow stratigraphy measurements with high-frequency FMCW radar: Comparison with snow micro-penetrometer. Cold Regions Science and Technology 47, 108–117.

Martel, L., 2013. Canmore flood surprises province [WWW Document]. Pique Magazine. URL http://www.piquenewsmagazine.com/whistler/canmore-flood-surprises-province/Content?oid=2462735 (accessed 7.19.13).

Martinec, J., Rango, A., 1995. Seaonal runoff forecasts for hydropower based on remote sensing. Proceedings of the Western Snow Conference 63, 10–20.

Martini, I.P., Brookfield, M.E., Sadura, S., 2001. Principles of Glacial Geomorphology and Geology, 1st ed. Prentice Hall.

Massman, W.J., Sommerfeld, R., Zeller, K., Hehn, T., Hudnell, L., Rochelle, S., 1995. CO2 flux through a Wyoming seasonal snowpack: diffusional and pressure pumping effects, in: Biogeochemistry of Seasonally Snow-Covered Catchments, IAHS Publication No. 228. IAHS Press, pp. 71–79.

Mast, M.A., Wickland, K.P., Striegl, R.T., Clow, D.W., 1998. Winter fluxes of CO2 and CH4 from subalpine soils in Rocky Mountain National Park, Colorado. Global Biogeochemical Cycles 12, 607–620.

Matonse, A.H., Pierson, D.C., Frei, A., Zion, M.S., Schneiderman, E.M., Anandhi, A., Mukundan, R., Pradhanang, S.M., 2010. Effects of changes in snow pattern and the timing of runoff on NYC water supply. Proceedings of the Eastern Snow Conference 67, 61–71.

Maxfield, C. “Max,” 2004. The Design Warrior’s Guide to FPGAs: Devices, Tools and Flows, 1st ed. Newnes.

Maxwell, L.M., Warnick, C.C., Beattie, L.A., Hespelt, G.G., 1960. Automatic measurement of hydrologic parameters at remote locations. Proceedings of the Western Snow Conference 28, 25–31.

Mazurkiewicz, A., McGurk, B., Tsang, M., 2011. Effect of snow covered area and delayed snowmelt on water quality and reservoir management: 2010 Turbidity event in Hetchy Hetchy reservoir. Proceedings of the Western Snow Conference 79, 47–62.

McClung, D., Schaerer, P., 2006. The Avalanche Handbook, 3rd ed. Mountaineers Books.

McGrath, K.E., Dawley, E.M., Geist, D.R., 2006. Total dissolved gas effects on fishes of the Lower Columbia River, PNNL-15525 Total Dissolved Gas Effects on Fishes of the Lower Columbia River, Final Report, March 2006 Prepared for the U.S. Army Corps of Engineers, Portland District, Portland, Oregon, Under a Related Services Agreement with the U.S. Department of Energy, Contract DE-AC05-76RL01830. Pacific Nprthwest National Laboratory.

McGurk, B.J., 1983. Snow temperature profiles in the Central Sierra Nevada. Proceedings of the Western Snow Conference 51, 9–18.

McGurk, B.J., 1992. Propylene glycol and ethanol as a replacement antifreeze for precipitation gauges: dilution, disposal and safety. Proceedings of the Western Snow Conference 60, 56–65.

McGurk, B.J., Berg, N.H., Kattelman, R.C., 1993. Identification and regional/spatial extent of rain-domainated winter storms in California's Sierra Nevada. Proceedings of the Western Snow Conference 61, 67–74.
McGurk, B.J., Kattelmann, R.C., 1988. Evidence of liquid water flow through snow from thick-section photography. Proceedings of the 1988 International Snow Science Workshop 137–139.
McGurk, B.J., Marsh, P., 1995. Flow-finger continuity in serial thick-sections in a melting Sierran snowpack, in: Biogeochemistry of Seasonally Snow-Covered Catchments, IAHS Publication No. 228. IAHS Press, Wallingford, Oxfordshire, UK, pp. 81–88.
McKay, G.A., Adams, W.P., 1981. Snow and Living Things, in: Handbook of Snow: Principles, Processes, Management and Use. Pergamon Press Canada, pp. 3–31.
McKay, G.A., Blackwell, S.R., 1961. Plains snowpack water equivalent from climatological records. Proceedings of the Western Snow Conference 29, 27–43.
McKay, G.A., Findlay, B.F., 1971. Variation of snow resources with climate and vegetation in Canada. Proceedings of the Western Snow Conference 39, 17–26.
McNeill, J.R., 1992. The mountains of the Mediterranean world: an environmental history, Studies in environment and history. Cambridge University Press, Cambridge ; New York.
Meikle, H., 2008. Modern radar systems. Artech House.
Mellor, M., 1974. A review of basic snow mechanics, in: Snow Mechanics, Proceedings of the Grindelwald Symposium, International Association of Hydrological Sciences Publication No. 114. pp. 251–291.
Mellor, M., 1977. Engineering properties of snow. Journal of Glaciology 19, 15–66.
Ménard, P., Duguay, C.R., Flato, G.M., Rouse, W.R., 2002. Simulation of ice phenology on a large lake in the Mackenzie River Basin (1960-2000). Proceedings of the Eastern Snow Conference 59, 3–12.
Metcalfe, R.A., Buttle, J.M., 1998. A statistical model of spatially distributed snowmelt rates in a boreal forest basin. Hydrological Processes 12, 1701–1722.
Metcalfe, R.A., Wilson, R.A., Goodison, B.E., 1987. The use of acoustic ranging devices as snow depth sensors: an assessment. Proceedings of the Eastern Snow Conference 44, 203–207.
Meuler, A.J., Smith, J.D., Varanasi, K.K., Mabry, J.M., McKinley, G.H., Cohen, R.E., 2010. Relationships between Water Wettability and Ice Adhesion. ACS Appl. Mater. Interfaces 2, 3100–3110.
Meyer, E., Neumann, E.-G., 1972. Physical and applied acoustics; an introduction [by] Erwin Meyer [and] Ernst-Georg Neumann. Translated by John M. Taylor, Jr. New York, Academic Press.
Meyer-Baese, U., 2007. Digital Signal Processing with Field Programmable Gate Arrays, 3rd Printing. ed. Springer.
Mikhail, E.M., Bethel, J.S., McGlone, J.C., 2001. Introduction to modern photogrammetry. Wiley, New York : Chichester.
Miller, D.H., 1964. Interception processes during snowstorms, U.S. Forest Service Research Paper PSW-18. Pacific Southwest Forest and Range Experimental Station.
Milligan, T.A., 2005. Modern antenna design, 2nd ed. ed. Wiley-Interscience : IEEE Press, Hoboken, N.J.
Millington, R.J., 1959. Gas diffusion in porous media. Science 130, 100–120.
Mims, F.M., 2000. Mims Circuit Scrapbook. Newnes.
Misra, S., Chopra, S., 2011. Mixed-phase wavelet estimation - a case study. CSEG Recorder February 2011.
Mitterer, C., Heilig, A., Schweizer, J., Eisen, O., 2011. Upward-looking ground-penetrating radar for measuring wet-snow properties. Cold Regions Science and Technology 69, 129–138.
Mocko, D.M., Sud, Y.C., 2001. Refinements to SSiB with an emphasis on snow physics: evaluation and validation using GSWP and Valdai data. Earth Interactions 5, 1–31.

Mocko, D.M., Walker, G.K., Sud, Y.C., 1999. New snow-physics to complement SSiB. Part II: Effects on soil moisture initialization and simulated particle fluxes, precipitation, and hydrology of GEOS II GCM. Journal of the Meteorological Society of Japan 77, 49–366.

Moeser, C.D., Walker, M.J., Skalka, C., Frolik, J., 2011. Application of a wireless sensor network for distributed snow water equivalence estimation. Proceedings of the Western Snow Conference 79, 83–90.

Moffitt, J.A., 1995. Snow plates: preliminary results. Proceedings of the Western Snow Conference 63, 156–159.

Moldestad, D.A., 2005. Characteristics of liquid water content and snow density in a cross-country race ski track. Bulletin of Glaciological Research 22, 39–49.

Molnau, M., 1971. Comparison of runoff from a catchment snow pillow and a small forested watershed. Proceedings of the Western Snow Conference 39, 39–43.

Moore, H.M., Attenborough, K., Rogers, J., Lee, S., 1991. In-situ acoustical investigations of deep snow. Applied Acoustics 33, 281–301.

Moran, M.L., Albert, D.G., 1996. Source location and tracking capability of a small array, CRREL Report 96-8. Cold Regions Research and Engineering Laboratory, Hanover, New Hampshire.

Morgan, P.A., Watts, G.R., 2003. A novel approach to the acoustic characterisation of porous road surfaces. Applied Acoustics 64, 1171–1186.

Mori, Y., Hopmans, J.W., Mortensen, A.P., Kluitenberg, G.J., 2003. Multi-Functional Heat Pulse Probe for the Simultaneous Measurement of Soil Water Content, Solute Concentration, and Heat Transport Parameters. Vadose Zone Journal 2, 561–571.

Morin, S., Domine, F., Arnaud, L., Picard, G., 2010. In-situ monitoring of the time evolution of the effective thermal conductivity of snow. Cold Regions Science and Technology 64, 73–80.

Morland, L.W., Kelly, R.J., Morris, R.M., 1990. A mixture theory for a phase-changing snowpack. Cold Regions Science and Technology 17, 271–285.

Morris, E.M., 1981. Field measurement of the liquid water content of snow. Journal of Glaciology 27, 175–178.

Morris, E.M., 2008a. A theoretical analysis of the neutron scattering method of measuring snow and ice density. Journal of Geophysical Research: Earth Surface 113, F0319.

Morris, E.M., 2008b. Correction to ``A theoretical analysis of the neutron scattering method of measuring snow and ice density''. Journal of Geophysical Research (Earth Surface) 113, F4099.

Morris, E.M., Cooper, J.D., 2003. Density measurements in ice boreholes using neutron scattering. Journal of Glaciology 49, 599–604.

Morris, E.M., Kelly, R.J., 1990. A theotetical determination of the characteristic equation of snow in the pendular regime. Journal of Glaciology 36, 179–187.

Morrison, R.G., 1976. Nuclear techniques applied to hydrology. Proceedings of the Western Snow Conference 44, 1–6.

Moss, E.H., 1955. The Vegetation of Alberta. Botanical Review 21, 493–567.

Mote, P.W., Casson, J., Hamlet, A., Reading, D., 2007. Sensitivity of northwest ski areas to warming. Proceedings of the Western Snow Conference 75, 63–67.

Mote, P.W., Hamlet, A.F., 2009. Anthropogenic climate change and snow in the Pacific Northwest. Proceedings of the Western Snow Conference 69, 51–52.

Mott, R., Schirmer, M., Bavay, M., Grünewald, T., Lehning, M., 2010. Understanding snow-transport processes shaping the mountain snow-cover. The Cryosphere 4, 545–559.

Mount, J.F., 1995. California rivers and streams: the conflict between fluvial process and land use. University of California Press, Berkeley.

Nachlinger, J.L., Berg, N.H., 1988. Snowpack-vegetation dynamics: mountain hemlocks in the Lake Tahoe area. Proceedings of the Western Snow Conference 56, 23–34.

Nakaya, U., 1959. Visco-elastic properties of snow and ice in the Greenland Ice Cap, U.S. Army Snow, Ice and Permafrost Research Establishment (USA SIPRE) Research Report 46. U.S. Army, Hanover, New Hampshire.

Needham, J., 1959. Science and Civilisation in China, Volume 3: Mathematics and the Sciences of the Heavens and the Earth. Cambridge University Press.

Nelder, J.A., Mead, R., 1965. A Simplex Method for Function Minimization. The Computer Journal 7, 308–313.

New York Times, 1906. First Egyptian record of snow is discovered: word found by Prof. Breasted in the Temple of Abu Simbel. New York Times 9.

Newell, P., Holland, K., 2006. Loudspeakers: For music recording and reproduction, 1st ed. Focal Press.

Ng, A., Swanevelder, J., 2011. Resolution in ultrasound imaging. Contin Educ Anaesth Crit Care Pain 11, 186–192.

Niang, M., Bernier, M., Gauthier, Y., Fortin, G., Van Bochove, E., Stacheder, M., Brandelik, A., 2003. On the validation of snow densities derived from SNOWPOWER probes in a temperate snow cover in Eastern Canada: first results. Proceedings of the Eastern Snow Conference 60, 175–187.

Niedrist, G., 1993. Echo Suppression for Loudspeaker-Microphone System Measurements. JAES 41, 143–153.

Nielsen, R.O., 1991. Sonar Signal Processing, The Artech House acoustics library. Artech House, Boston.

Nikolaevskaya, E., Khimich, A., Chistyakova, T., 2012. Programming with Multiple Precision, 2012th ed. Springer.

Noilhan, J., Mahfouf, J.-F., 1996. The ISBA land surface parameterization scheme. Global and Planetary Change 13, 145–159.

Nolin, A.W., Phillippe, J., 2008. Glacier melt makes a significant contribution to summertime streamflow in the Upper Middle Fork Hood River. Proceedings of the Western Snow Conference 76, 131–134.

O'Neel, S., Marshall, H.P., McNamara, D.E., Pfeffer, W.T., 2007. Seismic detection and analysis of icequakes at Columbia Glacier, Alaska. Journal of Geophysical Research 112, F03S23.

O'Neill, A.D.J., Gray, D.M., 1973a. Solar radiation penetraion through snow. Proceedings of UNESCO-WMO-IAHS Symposium on the Role of Snow and Ice in Hydrology 1, 229–249.

O'Neill, A.D.J., Gray, D.M., 1973b. Spatial and temporal variations of the albedo of a prairie snowpack, in: The Role of Snow and Ice in Hydrology, Proceedings of the Banff Symposium. pp. 176–186.

Oke, T.R., 1992. Boundary Layer Climates, 2nd ed. ed. Routledge, London.

Oleson, K.W., Dai, Y., Bonan, G.B., Bosilovich, M., Dirmeyer, P., Hoffman, F., Houser, P., Lewis, S., Niu, G.-Y., Thornton, P., Yang, Z.-L., Zeng, X., 2004. Technical Description of the Community Land Model (CLM). NCAR, Boulder, Colorado.

Olfert, E., 1970. Modification of a gamma attenuation snow density gauge, Internal Report, Division of Hydrology, College of Engineering, University of Saskatchewan. University of Saskatchewan.

Oppenheim, A., Kopec, G., Tribolet, J., 1976. Signal analysis by homomorphic prediction. IEEE Transactions on Acoustics, Speech and Signal Processing 24, 327–332.

Oppenheim, A.V., Schafer, R.W., 2010. Discrete-time signal processing, 3rd ed. ed, Prentice-Hall signal processing series. Prentice Hall : imprint of Pearson, Upper Saddle River [N.J.].

Oppenheim, A.V., Willsky, A.S., Nawab, S.H., 1997. Signals & systems, 2nd ed, Prentice-Hall signal processing series. Prentice Hall, Upper Saddle River, N.J.

Ord, M.J., 1968. Some comparisons from the use of radio reporting isotope snow gauges and the snow pressure pillows. Proceedings of the Western Snow Conference 36, 89–94.

Orfanidis, S.J., 1988. Optimum Signal Processing: An Introduction, 2nd ed. ed. McGraw-Hill, New York.

Osterhuber, R., 1999. Precipitation intensity during rain-on-snow. Proceedings of the Western Snow Conference 67, 153–155.

Osterhuber, R., Edens, T., McGurk, B.J., 1994. Snow depth measurement using ultrasonic sensors and temperature correction. Proceedings of the Western Snow Conference 62, 159–162.
Osterhuber, R., Hogan, M., Grismer, M., Drake, K., 2007. Delaying snowpack ablation. Proceedings of the Western Snow Conference 75, 133–136.
Osterhuber, R., Howle, J., Bawden, G., 2008. Snow measurement using ground-based tripod laser. Proceedings of the Western Snow Conference 2008, 135–138.
Ottolini, R., 1983. Velocity Independent Seismic Imaging. SEP Reports 37, 59–68.
Oura, H., 1952a. Sound velocity in the snow cover. Low Temperature Science Series A, Physical Sciences 9, 171–178.
Oura, H., 1952b. Reflection of sound at snow surface and mechanisms of sound propagation in snow. Low Temperature Science Series A, Physical Sciences 9, 179–186.
Özdoğan, M., 2011. Climate change impacts on snow water availability in the Euphrates-Tigris basin. Hydrol. Earth Syst. Sci. 15, 2789–2803.
Paar, C., Pelzl, J., 2010. Understanding Cryptography: A Textbook for Students and Practitioners. Springer.
Painter, T.., Dozier, J., 2002. Measurements of the bidirectional reflectance of snow at fine spectral and angular resolution. Proceedings of the Western Snow Conference 70, 37–48.
Painter, T.H., Barrett, A.P., Landry, C.C., Neff, J.C., Cassidy, M.P., Lawrence, C.R., McBride, K.E., Farmer, G.L., 2007. Impact of disturbed desert soils on duration of mountain snow cover. Geophysical Research Letters 34, L12502.
Painter, T.H., Molotch, N.P., Cassidy, M., Flanner, M., Steffen, K., 2007. Contact spectroscopy for determination of stratigraphy of snow optical grain size. Journal of Glaciology 53, 121–127.
Painter, T.H., Paden, B.E., Dozier, J., 2000. Automated spectro-goniometer: a robotic arm for the measurement of snow bi-directional reflectance distribution function. Proceedings of the Western Snow Conference 2000, 12–21.
Patil, B.M., Joshi, R.C., Toshniwal, D., 2010. Impact of K-means on the performance of classifiers for labelled data, in: Contemporary Computing: Communications in Computer and Information Science, Volume 94. Springer-Verlag, Berlin; Heidelberg, pp. 423–434.
Paulin, G., 1978. Developments in snow measurements with gamma radiation. Proceedings of the Eastern Snow Conference 35, 56–62.
Peck, E.L., 1972. Snow measurement predicament. Water Resources Research 8, 244–248.
Peitzsch, E., Birkeland, K.W., Hansen, K.J., 2008. Water movement and capillary barriers in a stratified and inclined snowpack. Proceedings of the 2008 International Snow Science Workshop 179–187.
Pelto, M., 2004. Temperature-ablation relationships on glaciers and in Alpine areas, North Cascades, Washington. Proceedings of the Eastern Snow Conference 61, 135–145.
Pelto, M., Brown, C., 2011. Mass balance loss of Mount Baker, Washington, glaciers 1990-2010. Proceedings of the Eastern Snow Conference 68, 55–64.
Perla, R., 1985. Snow in strong or weak temperature gradients. Part II: Section plane analysis. Cold Regions Science and Technology 11, 181–186.
Perla, R., 1991. Real permittivity of snow at 1 MHz and 0° C. Cold Regions Science and Technology 19, 215–219.
Perla, R., Banner, J., 1988. Calibration of capacitive cells for measuring water in snow. Cold Regions Science and Technology 15, 225–231.
Perla, R., Beck, T.M.H., Cheng, T.T., 1982. The shear strength index of alpine snow. Cold Regions Science and Technology 6, 11–20.
Perla, R., LaChapelle, E.R., 1984. Dilution method for measuring liquid water in snow. Proceedings of the Western Snow Conference 52, 80–85.

Perla, R., Ommanney, C.S.L., 1985. Snow in strong or weak temperature gradients. Part I: Experiments and quantitative observations. Cold Regions Science and Technology 11, 23–35.
Perla, R.I., 1981. Avalanche release, motion, and impact, in: Dynamics of Snow and Ice Masses. Academic Press, New York, pp. 397–462.
Perla, R.I., 1982. Preparation of section planes in snow specimens. Journal of Glaciology 28, 199–210.
Peterson, N.R., Brown, A.J., 1975. Accuracy of snow measurements. Proceedings of the Western Snow Conference 43, 1–9.
Petrenko, V.F., Whitworth, R.W., 2002. Physics of ice. Oxford University Press, Oxford ; New York.
Petrovic, J.J., 2003. Mechanical properties of ice and snow. Journal of Materials Science 38, 1–6.
Petty, G.W., 2006. A first course in atmospheric radiation. Sundog Pub., Madison, Wis.
Pfeffer, W.T., Mrugala, R., 2002. Temperature gradient and initial snow density as controlling factors in the formation and structure of hard depth hoar. Journal of Glaciology 48, 485–494.
Phani, K.K., Niyogi, S.K., 1987. Young's modulus of porous brittle solids. Journal of Materials Science 22, 257–263.
Pierson, D., Kick, J.W., 1995. Use of a GIS to develop a stratified snow survey in a moutainous agricultral landscape. Proceedings of the Eastern Snow Conference 52, 59–68.
Pintelon, R., Schoukens, J., 2012. System Identification: A Frequency Domain Approach, 2nd ed. Wiley-IEEE Press.
Pomeroy, J., Fang, X., Ellis, C., 2012. Sensitivity of snowmelt hydrology in Marmot Creek, Alberta, to forest cover disturbance. Hydrological Processes 26, 1891–1904.
Pomeroy, J., Hedstrom, N., Parviainen, J., 1999. The snow mass balance of Wolf Creek, Yukon: Effects of Snow Sublimation and Redistribution, in: Wolf Creek Research Basin: Proceedings of a Workshop Held in Whitehorse, Yukon, 5-7 March 1998. National Water Research Institute, Saskatoon, pp. 15–30.
Pomeroy, J., McDonald, M., DeBeer, C., Brown, T., 2009. Modelling alpine snow hydrology in the Canadian Rocky Mountains. Proceedings of the Western Snow Conference 77, 3–11.
Pomeroy, J.W., 1988. Wind transport of snow, PhD Thesis. Department of Agricultural Engineering, University of Saskatchewan.
Pomeroy, J.W., Bewley, D.S., Essery, R.L.H., Hedstrom, N.R., Link, T., Granger, R.J., Sicart, J.E., Ellis, C.R., Janowicz, J.R., 2006. Shrub tundra snowmelt. Hydrological Processes 20, 923–941.
Pomeroy, J.W., de Boer, D., Martz, L.W., 2007a. Hydrology and Water Resources, in: Saskatchewan: Geographic Perspectives. Canadian Plains Research Center, Regina, pp. 63–80.
Pomeroy, J.W., Essery, R.L.H., 1999. Turbulent fluxes during blowing snow: field tests of model sublimation predictions. Hydrological Processes 13, 2963–2975.
Pomeroy, J.W., Goodison, B.E., 1997. Winter and Snow, in: The Surface Climates of Canada. McGill-Queen's University Press, Montreal; Kingston; London; Buffalo, NY, pp. 68–100.
Pomeroy, J.W., Gray, D.M., 1995. Snowcover accumulation, relocation, and management, National Hydrology Research Institute Science Report No. 7. National Water Research Institute, Saskatoon, Canada.
Pomeroy, J.W., Gray, D.M., Brown, T., Hedstrom, N.R., Quinton, W.L., Granger, R.J., Carey, S.K., 2007b. The cold regions hydrological model: a platform for basing process representation and model structure on physical evidence. Hydrological Processes 21, 2650–2667.
Pomeroy, J.W., Gray, D.M., Hedstrom, N.R., Janowicz, J.R., 2002. Prediction of seasonal snow accumulation in cold climate forests. Hydrological Processes 16, 3543–3558.
Pomeroy, J.W., Gray, D.M., Landine, P.G., 1993. The Prairie Blowing Snow Model: characteristics, validation, operation. Journal of Hydrology 144, 165–192.

Pomeroy, J.W., Gray, D.M., Shook, K.R., Toth, B., Essery, R.L.H., Pietroniro, A., Hedstrom, N., 1998. An evaluation of snow accumulation and ablation processes for land surface modelling. Hydrological Processes 12, 2339–2367.

Pomeroy, J.W., Jones, H.G., 1996. Y Cymry 'N Erbyn Yr Eira: The influence of snow on the Welsh settlements of North America. Proceedings of the Eastern Snow Conference 53, 181–188.

Pomeroy, J.W., Marks, D., Link, T., Ellis, C., Hardy, J., Rowlands, A., Granger, R., 2009. The impact of coniferous forest temperature on incoming longwave radiation to melting snow. Hydrological Processes 23, 2513–2525.

Pomeroy, J.W., McDonald, M., DeBeer, C., Brown, T., 2009. Modeling Alpine snow hydrology in the Canadian Rocky Mountains. Proceedings of the Western Snow Conference 3–11.

Pomeroy, J.W., Parviainen, J., Hedstrom, N., Gray, D.M., 1998. Coupled modelling of forest snow interception and sublimation. Hydrological Processes 12, 2317–2337.

Pomeroy, J.W., Pietroniro, A., Fang, X., Shaw, D., Armstrong, R.L., Shook, K., Comeau, L., Toth, B., Martz, L.W., Westbrook, C., 2011. Canadian prairie drought hydrology, in: The 1999-2005 Canadian Prairies Drought: Science, Impacts, and Lessons. Drought Research Initiative, Winnipeg, pp. 59–62.

Pomeroy, J.W., Schmidt, R.A., 1993. The Use of Fractal Geometry in Modelling Intercepted Snow Accumulation and Sublimation. Proceedings of the Eastern Snow Conference 50, 1–10.

Pomeroy, J.W., Toth, B., Granger, R.J., Hedstrom, N.R., Essery, R.L.H., 2003. Variation in surface energetics during snowmelt in a subarctic mountain catchment. Journal of Hydrometeorology 4, 702–719.

Ponce, V.M., 1989. Engineering Hydrology: Principles and Practices. Prentice Hall.

Porter, J.H., Horton, G.D., 2010. Application of snow core and automated remote data collection to monitor SWE in NYC's water supply watershed. Proceedings of the Eastern Snow Conference 67, 87–91.

Portnoff, M.R., 1976. Implementation of the digital phase vocoder using the fast Fourier transform. IEEE Transactions on Acoustics, Speech and Signal Processing 24, 243–248.

Potter, M.C., 2002. Mechanics of fluids, 3rd ed. ed. Brooks Cole/Thompson Learning, Pacific Grove, CA.

Powell, D.R., 1987. Observations on consistency and reliability of field data in snow survey measurements. Proceedings of the Western Snow Conference 55, 69–77.

Powers, D., O'Neill, K., Colbeck, S.C., 1985. Theory of natural convection in snow. Journal of Geophysical Research 90, 10641.

Pritchett, W.C., 1990. Acquiring Better Seismic Data. Springer.

Prowse, T.D., 1990. Northern Hydrology: An Overview, in: Northern Hydrology: Canadian Perspectives. NHRI Science Report No. 1. pp. 1–36.

Pruppacher, H.R., Klett, J.D., 2010. Microphysics of clouds and precipitation[. Springer.

Pyper, G.R., 1962. A progress report on radioactive snow gage use. Proceedings of the Eastern Snow Conference 18-19, 52–66.

Quatieri, T.F., 2001. Discrete-Time Speech Signal Processing: Principles and Practice, 1st ed. Prentice Hall.

Rabiner, L.R., Schafer, R.W., 1978. Digital processing of speech signals, Prentice-Hall signal processing series. Prentice-Hall, Englewood Cliffs, N.J.

Raichel, D.R., 2006. The Science and Applications of Acoustics, 2nd ed. Springer Science+Business Media, New York.

Raikes, S.A., White, R.E., 1984. Measurements of Earth Attenuation from Downhole and Surface Seismic Recordings. Geophysical Prospecting 32, 892–919.

Rango, A., Steele, C., DeMouche, L., 2010. Infrastructure improvements for snowmelt runoff assessments of climate change impacts on water supplies in the Rio Grande basin. Proceedings of the Western Snow Conference 78, 83–90.

Rau, G., Chaney, R.C., 1988. Triaxial testing of marine sediments with high gas contents, in: Advanced Triaxial Testing of Soil and Rock, Issue 977. American Society for Testing and Materials, pp. 338–352.

Raymond, C.F., Tusima, K., 1979. Grain coarsening of water-saturated snow. Journal of Glaciology 22, 83–105.

Reba, M.L., Pomeroy, J., Marks, D., Link, T.E., 2012. Estimating surface sublimation losses from snowpacks in a mountain catchment using eddy covariance and turbulent transfer calculations. Hydrological Processes 26, 3699–3711.

Rees, G., 2006. Remote Sensing of Snow and Ice. Taylor and Francis, Boca Raton.

Rees, W.G., 1998. A rapid method for measuring snow surface profiles. Journal of Glaciology 44, 674–675.

Ressl, M.S., Wundes, P.E., 2010. Design of an acoustic anechoic chamber for application in hearing aid research. AMTA'10 Proceedings of the 11th WSEAS International Conference on Acoustics & Music: Theory & Applications 11, 18–23.

Reynolds, O., 1873. On the Refraction of Sound by the Atmosphere. Proceedings of the Royal Society of London 22, 531–548.

Rice, R., Bales, R., 2008. Embedded sensor network design for spatial snowcover. Proceedings of the Western Snow Conference 76, 35–46.

Rice, R., Painter, T., Dozier, J., 2007. Snowcover along elevation gradients in the upper Merced and Tuolumne River Basins of the Sierra Nevada of California from MODIS and blended ground data. Proceedings of the Western Snow Conference 75, 3–12.

Richards, S.D., Hewitt, R.N., Heathershaw, A.D., 1997. The effect of sediment plumes on sonar performance, in: , Seventh International Conference on Electronic Engineering in Oceanography, 1997. Technology Transfer from Research to Industry. Presented at the , Seventh International Conference on Electronic Engineering in Oceanography, 1997. Technology Transfer from Research to Industry, pp. 67–72.

Riche, F., Schneebeli, M., 2013. Thermal conductivity of snow measured by three independent methods and anisotropy considerations. The Cryosphere 7, 217–227.

Rife, D.D., Vanderkooy, J., 1989. Transfer-function measurement with maximum-length sequences. Journal of the Audio Engineering Society 37, 419–444.

Rittger, K., Kahl, A., Dozier, J., 2011. Topographic distribution of Snow Water Equivalent in the Sierra Nevada. Proceedings of the Western Snow Conference 2011, 37–46.

Robinson, E.A., Treitel, S., 2000. Geophysical signal analysis, Prentice-Hall signal processing series. Prentice-Hall, Englewood Cliffs, N.J.

Ronda, R.J., Bosveld, F.C., 2009. Deriving the Surface Soil Heat Flux from Observed Soil Temperature and Soil Heat Flux Profiles Using a Variational Data Assimilation Approach. Journal of Applied Meteorology and Climatology 48, 644–656.

Roos, M., 1991. A trend of decreasing snowmelt runoff in Northern California. Proceedings of the Western Snow Conference 59, 29–36.

Roos, M., 1995. The recent California drought. Proceedings of the Western Snow Conference 63, 124–134.

Roos, M., 2006. Monitoring monthly snowmelt runoff in the Sierra Nevada to detect climate change. Proceedings of the Western Snow Conference 74, 197–203.

Rosa, A.L.R., Ulrych, T.J., 1991. Processing via spectral modeling. Geophysics 56, 1244–1251.

Rosenthal, W., Dozier, J., 1996. Automated mapping of montane snow cover at subpixel resolution from the Landsat Thematic Mapper. Water Resources Research 32, 115–130.
Ross, A.A., Picot, J.J.C., 1975. Convective heat transfer to a snowpack. Proceedings of the Eastern Snow Conference 32, 36–50.
Rossing, T.D., Fletcher, N.H., 1995. Principles of vibration and sound. Springer-Verlag, New York.
Rowlands, A., Pomeroy, J., Hardy, J., Marks, D., Elder, K., Melloh, R., 2002. Small-scale spatial variability of radiant energy for snowmelt in a mid-latitude sub-alpine forest. Proceedings of the Eastern Snow Conference 59, 109–117.
Rudnick, I., 1947. The propagation of an acoustic wave along a boundary. Journal of the Acoustical Society of America 19, 348–356.
Ryan, W.A., Doesken, N.J., Fassnacht, S.R., 2008. Preliminary results of ultrasonic snow depth sensor testing for National Weather Service (NWS) snow measurements in the US. Hydrological Processes 22, 2748–2757.
Sachse, F.B., 2004. Computational Cardiology: Modeling of Anatomy, Electrophysiology, and Mechanics. Springer.
Sahimi, M., 1994. Applications of percolation theory. CRC Press.
Saltelli, A., Chan, K., Scott, E.M., 2009. Sensitivity Analysis. Wiley.
Sampson, F., 1961. Peace River project with specific reference to reservoir filling and runoff forecasts. Proceedings of the Western Snow Conference 20–24.
Sato, T., Kimura, T., Ishimaru, T., Maruyama, T., 1993. Field test of a new snow-particle counter (SPC) system. Annals of Glaciology 18, 149–154.
Sauter, K.A., Tanner, B.D., 1992. Minimizing measurment errors in automated snowpack profile temperature measurements. Proceedings of the Western Snow Conference 60, 36–45.
Savelyev, S.A., Gordon, M., Hanesiak, J., Papakyriakou, T., Taylor, P.A., 2006. Blowing snow studies in the Canadian Arctic Shelf Exchange Study, 2003–04. Hydrological Processes 20, 817–827.
Savitzky, A., Golay, M.J.E., 1964. Smoothing and Differentiation of Data by Simplified Least Squares Procedures. Anal. Chem. 36, 1627–1639.
Scheler, K., Hood, E., Carter, P., Glude, B., 2003. Near-surface facetted crystal growth and snow stability in a high-latitude Maritime snow climate. Proceedings of the Eastern Snow Conference 71, 127–132.
Schetzen, M., 2002. Linear Time-Invariant Systems, 1st ed. Wiley-IEEE Press.
Schmidt, D.S., Schmidt, R.A., Dent, J.D., 1999. Electrostatic Force in Blowing Snow. Boundary-Layer Meteorology 93, 29–45.
Schneider, T., Jamieson, D.G., 1993. A dual-channel MLS-based test system for hearing-aid characterization. Journal of the Audio Engineering Society 41, 583–594.
Schreiber, E., Anderson, O.L., Soga, N., 1974. Elastic constants and their measurement. McGraw-Hill.
Schweizer, J., Camponovo, C., 2002. The temperature dependence of the effective elastic modulus of snow. Cold Regions Science and Technology 35, 55–64.
Schytt, V., Danfors, E., Fleetwood, Å., 1962. Notes on Glaciological Activities in Kebnekajse, Sweden. 1962. Geografiska Annaler 44, 407–412.
Scotter, G.W., Zoltai, S.C., 1982. Earth Hummocks in the Sunshine Area of the Rocky Mountains, Alberta and British Columbia. Arctic 35, 411–416.
Şensoy, A., Şorman, A.A., Tekeli, A., Şorman, A.Ü., Garen, D.C., 2005. Temporal and spatial distribution of physically-based point snowmelt model applications in Turkey. Proceedings of the Western Snow Conference 73.
Shannon, W.G., 1968. Snow surveying by electonic telemetry. Proceedings of the Western Snow Conference 36, 568–98.

Shea, C., Jamieson, B., Birkeland, K.W., 2012. Use of a thermal imager for snow pit temperatures. The Cryosphere 6, 287–299.
Shook, K., Gray, D.M., Pomeroy, J.W., 1993. Geometry of patchy snowcovers. Proceedings of the Eastern Snow Conference 50, 89–96.
Shook, K., Pomeroy, J., 2012. Changes in the hydrological character of rainfall on the Canadian prairies. Hydrological Processes 26, 1752–1766.
Sicart, J.E., Pomeroy, J.W., Essery, R.L.H., Bewley, D., 2006. Incoming longwave radiation to melting snow: observations, sensitivity and estimation in Northern environments. Hydrological Processes 20, 3697–3708.
Sicart, J.E., Pomeroy, J.W., Essery, R.L.H., Hardy, J., Link, T., Marks, D., 2004. A sensitivity study to daytime net radiation during snowmelt to forest canopy and atmospheric conditions. Journal of Hydrometeorology--Special Section 5, 774–784.
Sihvola, A., Tiuri, M., 1986. Snow fork for field determination of the density and wetness profiles of a snow pack. IEEE Transactions on Geoscience and Remote Sensing GE-24, 717–721.
Singh, A.K., 1999. An investigation of the themal conductivity of snow. Journal of Glaciology 45, 356–351.
Skalka, C., Frolik, J., Walker, M.J., Moeser, C.D., 2009. Development of a Distributed In Situ Instrument for Snowpack Monitoring. AGU Fall Meeting Abstracts 23, 1074.
Skaloud, J., Vallet, J., Veyssière, G., Kölbl, O., Keller, K., 2005. HELIMAP: Rapid Large Scale Mapping Using Handheld LiDAR/CCD/GPS/INS Sensors on Helicopters. Proceedings of the ION GNSS Conference.
Skidmore, P., Hansen, K., Quimby, W., 1994. Snow accumulation and ablation under fire-altered lodgepole pine forest canopies. Proceedings of the Western Snow Conference 62, 43–52.
Skolnik, M.I., 2001. Introduction to radar systems, 3rd ed. McGraw Hill, Boston.
Sloan, V.F., 1986. Relationships between glacier terminus melt processes and climatic conditions, Boundary Glacier, Alaska. Proceedings of the Eastern Snow Conference 43, 222–227.
Smith, C.D., 2009. The Relationship Between Monthly Precipitation and Elevation in the Canadian Rocky Mountain Foothills, in: Cold Region Atmospheric and Hydrologic Studies. The Mackenzie GEWEX Experience, Volume 1: Atmospheric Dynamics. Springer, pp. 167–186.
Smith, F.M., Cooper, C.F., Chapman, E.G., 1967. Measuring snow depth by aerial photogrammetry. Proceedings of the Western Snow Conference 35, 66–72.
Smith, F.W., Boyne, H.S., 1981. Snow pillow behavior under controlled laboratory conditions. Proceedings of the Western Snow Conference 49, 13–22.
Smith, J.., 2007. Introduction to Digital Filters with Audio Applications. W3K Publishing, California.
Smith, J.L., 1965. The elastic constants, strength and density of Greenland snow as determined from measurements of sonic wave velocity, CRREL Technical Report 167. Cold Regions Research and Engineering Laboratory, Hanover, New Hampshire.
Smith, J.L., Halverson, H.., 1969. Hydrology of snow profiles obtained with the profiling snow gauge. Proceedings of the Western Snow Conference 37, 41–48.
Smith, J.L., Willen, D.W., 1966. Gamma-transmission profiling radioisotope snow density and depth gauge. Proceedings of the Western Snow Conference 34, 69–77.
Smith, J.L., Willen, D.W., Owens, M.S., 1965. Measurement of snowpack profiles with radioactive isotopes. Weatherwise 18, 246–251.
Smith, J.L., Willen, D.W., Owens, M.S., 1967. Isotope snow gages for determining hyrologic characteristics of snowpacks, in: Isotope Techniques in the Hydrologic Cycle: Papers Presented at a Symposium at the University of Illinois, November 10-12, 1965. American Geophysical Union, Washington, D.C., pp. 11–21.
Smith, J.O., 2010. Physical Audio Signal Processing. W3K Publishing, California.

Smith, N., 1969. Determining the dynamic properties of snow and ice by forced vibration, CRREL Technical Report 216. Cold Regions Research and Engineering Laboratory, Hanover, New Hampshire.

Smith, S., 2002. Digital Signal Processing: A Practical Guide for Engineers and Scientists, 1st ed. Newnes.

Solano, C., 2008. Forecasting Coquitlam River Basin, British Columbia. Proceedings of the Western Snow Conference 76, 147–151.

Solheim, H., 1995. Early stages of blue-stain fungus invasion of lodgepole pine sapwood following mountain pine beetle attack. Canadian Journal of Botany 73, 70–74.

Sommerfeld, R.A., 1982. A Review of Snow Acoustics. Rev. Geophys. 20, 62–66.

Sommerfeld, R.A., LaChapelle, E., 1970. The classification of snow metamorphism. Journal of Glaciology 9, 3–17.

Sommerfeld, R.A., Massman, W.J., Musselman, R.C., Mosier, A.R., 1996. Diffusional flux of CO2 through snow: Spatial and temporal variability among alpine-subalpine sites. Global Biogeochemical Cycles 10, 473–482.

Spanier, J., Oldham, K.B., 1987. An Atlas of functions. Hemisphere Pub. Corp, Washington.

Speers, D.D., 1972. The application of snowmelt forecasting to combat Columbia River Nitrogen supersaturation problems. Proceedings of the Western Snow Conference 40, 17–22.

Speers, D.D., Versteg, J.D., 1982. Runoff forecasting for reservoir operations - the past and the future. Proceedings of the Western Snow Conference 50, 149–156.

Spencer, T.W., Sonnad, J.R., Butler, T.M., 1982. Seismic Q; stratigraphy or dissipation. Geophysics 47, 17–25.

St. Jacques, J.-M., Sauchyn, D.J., Zhao, Y., 2010. Northern Rocky Mountain streamflow records: Global warming trends, human impacts or natural variability? Geophys. Res. Lett. 37, L06407.

Stahnke, W., 1973. Primitive Binary Polynomials. Mathematics of Computation 27, 977–980.

Stainsby, S.D., Worthington, M.H., 1985. Q estimation from vertical seismic profile data and anomalous variations in the central North Sea. Geophysics 50, 615–626.

Stan, G.-B., Embrechts, J.-J., Archambeau, D., 2002. Comparison of Different Impulse Response Measurement Techniques. JAES 50, 249–262.

Star Phoenix, 2013. Sask., North Dakota officials begin border flood talks. Saskatoon Star Phoenix A9.

Stepphun, H., 1975. Accuracy in estimating snow cover water equivalents. Canadian Hydrology Symposium 1–5.

Stepphun, H., 1980. Snow management for crop production on the Canadian Prairies. Proceedings of the Western Snow Conference 48, 50–61.

Stepphun, H., 2005. Salinity, snow and salvation. Proceedings of the Western Snow Conference 73, 3–12.

Stepphun, H., Nicholaichuk, W., 1986. Managing snow to extend the areal range of winter wheat production. Proceedings of the Western Snow Conference 54, 30–40.

Stepphun, H., Wall, K.G., 1996. Can livestock producers manage snow to grow more alfalfa in dryland watersheds? Proceedings of the Western Snow Conference 64, 1–12.

Steppuhn, H., Cutforth, H.W., Judiesch, D., Wall, K.G., 2003. Are snow resources on the northern Plains and Prairies Dwindling? Proceedings of the Western Snow Conference 71, 113–124.

Steppuhn, H., Cutforth, H.W., Judiesch, D., Wall, K.G., 2003. Are snow resources on the northern Plains and Prairies dwindling? Proceedings of the Western Snow Conference 71, 113–124.

Steppuhn, H., Miller, M., 1998. Managing snow to abate salinity. Proceedings of the Western Snow Conference 66, 1–8.

Steppuhn, H., Stumborg, M., Lafond, G., McConkey, B., 2009. Managing Snowcovers in Grain Fields Harvested for Straw Fiber. Proceedings of the Western Snow Conference 77, 103–114.

Stewart, R., Pomeroy, J., Lawford, R., 2011. The Drought Research Initiative: A Comprehensive Examination of Drought over the Canadian Prairies. Atmosphere-Ocean 49, 298–302.
Stoffa, P.L., Buhl, P., Bryan, G.M., 1974. The application of homomorphic deconvolution to shallow-water marine seismology; Part I, Models. Geophysics 39, 401–416.
Stoll, R.D., 1979. Experimental studies of attenuation in sediments. The Journal of the Acoustical Society of America 66, 1152–1160.
Stoll, R.D., 1980. Theoretical aspects of sound transmission in sediments. The Journal of the Acoustical Society of America 68, 1341–1350.
Stoll, R.D., 1985. Marine sediment acoustics. The Journal of the Acoustical Society of America 77, 1789–1799.
Stoll, R.D., 1989. Sediment Acoustics. Springer-Verlag, New York; Berlin; Heidelberg.
Stoll, R.D., 2002. Velocity dispersion in water-saturated granular sediment. The Journal of the Acoustical Society of America 111, 785–793.
Stoll, R.D., Bryan, G.M., 1970. Wave Attenuation in Saturated Sediments. The Journal of the Acoustical Society of America 47, 1440–1447.
Stoll, R.D., Kan, T.-K., 1981. Reflection of acoustic waves at a water–sediment interface. The Journal of the Acoustical Society of America 70, 149–156.
Storr, D., 1967. Precipitation variations in a small forested watershed. Proceedings of the Western Snow Conference 35, 11–17.
Storr, D., 1972. Estimating effective net radiation for a mountainous Watershed. Boundary-Layer Meteorology 3, 3–14.
Stove, A.G., 1992. Linear FMCW radar techniques. Radar and Signal Processing, IEE Proceedings F 139, 343–350.
Sturges, D.L., 1989. Evaporation and seepage from a livestock resevoir equipped with a snow fence for water recharge. Proceedings of the Western Snow Conference 57, 9–20.
Sturm, M., 1992. Snow distribution and heat flow in the taiga. Arctic and Alpine Research 24, 145–152.
Sturm, M., 1999. Self-recording snow depth probe, CRREL Factsheet. Cold Regions Research and Engineering Laboratory, Hanover, New Hampshire.
Sturm, M., Benson, C.S., 1997. Vapor transport, grain growth and depth-hoar development in the subarctic snow. Journal of Glaciology 43, 42–59.
Sturm, M., Holmgren, J., König, M., Morris, K., 1997. The thermal conductivity of seasonal snow. Journal of Glaciology 43, 26–41.
Sturm, M., Johnson, J.B., 1991. Natural convection in the subarctic snow cover. Journal of Geophysical Research 96, 11657–11671.
Sturm, M., Johnson, J.B., 1992. Thermal conductivity measurements of depth hoar. Journal of Geophysical Research 97, 2129–2139.
Sud, Y.C., Mocko, D.M., 1999. New snow-physics to complement SSiB. Part I: Design and Evaluation with ISLSCP Initiative I Datasets. Journal of the Meteorological Society of Japan 77, 335–348.
Sundström, N., Gustafsson, D., Kruglyak, A., Lundberg, A., 2013. Field evaluation of a new method for estimation of liquid water content and snow water equivalent of wet snowpacks with GPR. Hydrology Research 44, 600.
Swanson, R.H., 1968. A system for making remote and undistubed measurements of snow settlement and temperature. Proceedings of the Western Snow Conference 36, 1–5.
Swanson, R.H., 1980. Surface wind structure in forest clearings during a Chinook. Proceedings of the Eastern Snow Conference 48, 26–30.
Swanson, R.H., Golding, D.L., 1982. Snowpack management on Marmot watershed to increase late-season streamflow. Proceedings of the Western Snow Conference 50, 215–218.

Swanson, R.H., Stevenson, D.R., 1971. Managing snow accumulation and melt under leafless Aspen to enhance watershed value. Proceedings of the Western Snow Conference 39, 63–69.
Tabler, R.D., 1971. Design of a watershed snow fence system, and first-year snow accumulation. Proceedings of the Western Snow Conference 39, 50–55.
Tabler, R.D., 1982. Frequency distibution of annual peak water-equivalent on Wyoming snow courses. Proceedings of the Western Snow Conference 50, 139–148.
Tabler, R.D., Jairell, R.L., 1980. Studying snowdrift problems with small-scale models outdoors. Proceedings of the Western Snow Conference 48, 1–13.
Takada, M., Ohkhochi, S., Nasu, N., 1954. On the absorption coefficient of snow and the propagation of sound along snow surface. Journal of the Acoustical Society of Japan 10, 23–27.
Takata, K., Emori, S., Watanabe, T., 2003. Development of the minimal advanced treatments of surface interaction and runoff. Global and Planetary Change 38, 209–222.
Takeuchi, N., 2001. The altitudinal distribution of snow algae on an Alaska glacier (Gulkana Glacier in the Alaska Range). Proceedings of the Eastern Snow Conference 58, 107–116.
Tanaka, M., Girard, G., Davis, R., Peuto, A., Bignell, N., 2001. Recommended table for the density of water between 0 °C and 40 °C based on recent experimental reports. Metrologia 38, 301.
Tangborn, W.V., Lettenmaier, D.P., 1981. The impact of Mount St. Helens ash deposition on snowmelt. Proceedings of the Western Snow Conference 49, 85–93.
Tanner, B.D., Gaza, B., 1990. Automated snow depth and snowpack temperature measurements. Proceedings of the Western Snow Conference 58, 73–78.
Tape, K.D., Rutter, N., Marshall, H.-P., Essery, R., Sturm, M., 2010. Recording microscale variations in snowpack layering using near-infrared photography. Journal of Glaciology 56, 75–80.
Tas, N., Sonnenberg, T., Jansen, H., Legtenberg, R., Elwenspoek, M., 1996. Stiction in surface micromachining. J. Micromech. Microeng. 6, 385.
Taxt, T., 1995. Restoration of medical ultrasound images using two-dimensional homomorphic deconvolution. IEEE Transactions on Ultrasonics, Ferroelectrics and Frequency Control 42, 543–554.
Taxt, T., 1997. Comparison of cepstrum-based methods for radial blind deconvolution of ultrasound images. IEEE Transactions on Ultrasonics, Ferroelectrics and Frequency Control 44, 666–674.
Techel, F., Pielmeier, C., 2011. Point observations of liquid water content in wet snow – investigating methodical, spatial and temporal aspects. The Cryosphere 5, 405–418.
Terrell, D.L., 1996. Op Amps: design, applications, and troubleshooting, 2nd ed. ed. Butterworth-Heinemann, Boston.
Teti, P., 2009. Effects of Mountain Pine Beetles and Timber Harvesting on Stand Attributes and Snow on the B.C. Interior Plateau. Proceedings of the Western Snow Conference 77, 93–102.
Thorud, D.B., Ffolliott, P.F., 1972. The Labor Day storm of 1970 in Arizona. Proceedings of the Western Snow Conference 40, 37–42.
Tillotson, J.G., 1966. Attenuation of sound over snow-covered fields. Journal of the Acoustical Society of America 39, 171–173.
Tiuri, M., Sihvola, A., 1986. Snow fork for field determination of the density and wetness profiles of a snow pack, in: Hydrologic Applications of Space Technoloy, Proceedings of the Cocoa Beach Workshop, Florida, August 1985, IASH No. 160, 1986. IAHS Press, pp. 225–230.
Tiuri, M.E., Sihvola, A.H., Nyfors, E., Hallikaiken, M., 1984. The complex dielectric constant of snow at microwave frequencies. IEEE Journal of Oceanic Engineering 9, 377–382.
Toews, D.A.A., 1991. Climatic and hydrologic circumstances antecedent to mass wasting events in southeastern British Columbia. Proceedisngs of the Western Snow Conference 59, 91–102.

Toikka, M., 1992. Field tests with the snow fork in determining the density and wetness profiles of a snow pack, Microwave signature-92 conference proceedings. Deutsche Forschungsanstalt fur Luft- und Raumfahrt D-8031 Oberpfaffenhofen.
Toikka, M., 2010. Snow Fork: A portable instrument for measuring the properties of snow. Toikka Oy, Finland.
Toldi, J., 1985. Velocity analysis without picking, PhD thesis. Stanford University Department of Geophysics, California.
Toldi, J.L., 1989. Velocity analysis without picking. Geophysics 54, 191–199.
Torrance, K., Sparrow, E., 1967. Theory for off-specular reflection from rough surfaces. Journal of the Optical Society of America 57, 1105–1112.
Town, M.S., Waddington, E.D., Walden, V.P., Warren, S.G., 2008. Temperatures, heating rates and vapour pressures in near-surface snow at the South Pole. Journal of Glaciology 54, 487–498.
Turčan, J., Loijens, H.S., 1975. Accuracy of snow survey data and errors in snow sampler measurements. Proceedings of the Eastern Snow Conference 32, 2–11.
Usowicz, B., Lipiec, J., Usowicz, J.B., 2008. Thermal conductivity in relation to porosity and hardness of terrestrial porous media. Planetary and Space Science 56, 438–447.
Vallet, J., 2001. Handheld Mobile Mapping system for Helicopter-based Avalanche Monitoring. OEEPE workshop “Integrated sensor Orientation” 17-18 September 2001 1, 1–12.
Van Dam, R., 2002. Kingdom of snow: Roman rule and Greek culture in Cappadocia. University of Pennsylvania Press, Philadelphia.
Van der Kamp, G., Hayashi, M., 1998. The groundwater recharge function of small wetlands in the semi-arid northern Prairies. Great Plains Research 8, 39–56.
Van Oss, C.J., Giese, R.F., Wentzek, R., Norris, J., Chuvilin, E.M., 1992. Surface tension parameters of ice obtained from contact angle data and from positive and negative particle adhesion to advancing freezing fronts. Journal of Adhesion Science and Technology 6, 503–516.
Vanderkooy, J., 1994. Aspects of MLS measuring systems. Journal of the Audio Engineering Society 42, 219–231.
Vargaftik, N.B., Volkov, B.N., Voijak, L.D., 1983. International tables on the surface tension of water. International tables on the surface tension of water 12, 817–820.
Venkateswaran, S., 2008. Essential Linux Device Drivers, 1st ed. Prentice Hall.
Verseghy, D.L., 1991. CLASS - A Canadian land surface scheme for GCMs. I. Soil Model. International Journal of Climatology 11, 111–133.
Verseghy, D.L., 1996. Local climates simulated by two generations of Canadian GCM land surface schemes. Atmosphere-Ocean 34, 435–456.
Verseghy, D.L., 2000. The Canadian Land Surface Scheme (CLASS): Its history and future. Atmosphere-Ocean 38, 1–13.
Verseghy, D.L., McFarlane, N.A., Lazare, M., 1993. CLASS - A Canadian land surface scheme for GCMs. II. Vegetation model and coupled runs. International Journal of Climatology 13, 347–370.
Viviroli, D., Weingartner, R., Messeril, B., 2003. Assessing the hydrological significance of the world’s mountains. Mountain Research and Development 23, 32–40.
Waite, A.D., 2001. Sonar for Practising Engineers, 3rd ed. Wiley.
Wang, Y., 2008. Seismic inverse Q filtering. Blackwell Pub.
Warren, S.G., 1982. Optical properties of snow. Reviews of Geophysics and Space Physics 20, 67–89.
Warren, S.G., Wiscombe, W.J., 1981. A model for the spectral albedo of snow. II: Snow containing atmospheric aerosols. Journal of the Atmospheric Sciences 37, 2737–2745.
Watanabe, Z., 1993. Proposition of a net-like model of snow. Annals of Glaciology 18, 72–78.
Watson, R.B., 1948. On the propgation of sound over snow. Journal of the Acoustical Society of America 20, 846–848.

Weaver, D.K., 1967. The Bridger data aquisition system at Montana State University, Bozeman, Montana. Proceedings of the Western Snow Conference 35, 24–28.
Weber, B., 2013. Alberta Rockies and foothills forever changed by flooding: scientist [WWW Document]. The Edmonton Journal. URL: http://www.edmontonjournal.com/news/Flooding+changed+Rockies+forever+says+scientist/8571558/story.html (accessed 7.19.13).
West, E.W., Dooling, R.J., Popper, A.N., Buehler, D.M., 2007. Noise impacts on birds: Assessing take of endangered species. The Journal of the Acoustical Society of America 122, 3082–3082.
Widess, M.B., 1973. How thin is a thin bed? Geophysics 38, 1176–1180.
Williams, M.W., Clow, D.W., 1990. Hydrologic and biologic consequences of an avalanche striking an ice-covered lake. Proceedings of the Western Snow Conference 58, 51–60.
Williams, M.W., Erickson, T.A., Petrzelka, J., 2010. Visualizing meltwater propagation through snow at the centimeter-to-meter scale using a snow guillotine. Hydrological Processes 24, 2098–2110.
Williams, M.W., Knoll, M., 2002. Measuring material properties of a wet and draining snowpack using crosshole radar tomography. Proceedings of the Western Snow Conference 70, 49–57.
Williams, M.W., Rikkers, M., Pfeffer, W.T., 2000. Ice columns and frozen rills in a warm snowpack, Green Lakes Valley, Colorado, U.S.A. Nordic Hydrology 31, 169–186.
Williams, M.W., Sommerfeld, R., Massman, S., Rikkers, M., 1999. Correlation lengths of meltwater flow through ripe snowpacks, Colorado Front Range, U.S.A. Hydrological Processes 13, 1807–1826.
Willis, N.J., 1991. Bistatic radar, The Artech House radar library. Artech House, Boston.
Wilson, D.K., Brasseur, J.G., Gilbert, K.E., 1999. Acoustic scattering and the spectrum of atmospheric turbulence. Acoustical Society of America Journal 105, 30–34.
Wilson, O.B., 1989. Introduction to the Theory and Design of Sonar Transducers. Peninsula Pub.
Winkler, R., Boon, S., 2009. A Summary of Research into the Effects of Mountain Pine Beetle Related Stand Mortality on Snow Accumulation and Ablation in British Columbia, Canada. Proceedings of the Western Snow Conference 77, 83–91.
Winski, D., Kreutz, K., Osterberg, E., Campbell, S., Wake, C., 2011. Effects of melt on snowpack stratigraphy and chemistry on the Kahiltna Glacier, Central Alaska Range. Proceedings of the Eastern Snow Conference 68, 67–88.
Wiscombe, W.J., Warren, S.G., 1981. A model for the spectral albedo of snow: I: Pure snow. Journal of the Atmospheric Sciences 37, 2712–2733.
Woo, M., 1980. Hydrology of a Small Lake in the Canadian High Arctic. Arctic and Alpine Research 12, 227–235.
Woo, M.-K., 1982a. Snow hydrology of the High Arctic. Proceedings of the Western Snow Conference 50, 63–74.
Woo, M.-K., 1982b. Upward flux of vapor from frozen materials in the High Arctic. Cold Regions Science and Technology 5, 269–274.
Woo, M.-K., 1997. A guide for ground based measurement of the Arctic snow cover. Climate Research Branch, Atmospheric Environment Service.
Woo, M.-K., Heron, R., 1981. Occurrence of ice layers at the base of High Arctic snowpacks. Arctic and Alpine Research 13, 225–230.
Woo, M.-K., Heron, R., Marsh, P., 1982. Basal ice in High Arctic snowpacks. Arctic and Alpine Research 14, 251–260.
Woo, M.-K., Marsh, P., 1978. Analysis of Error in the Determination of Snow Storage for Small High Arctic Basins. Journal of Applied Meteorology 17, 1537–1541.
Woo, M.-K., Sauriol, J., 1980. Channel Development in Snow-Filled Valleys, Resolute, N. W. T., Canada. Geografiska Annaler. Series A, Physical Geography 62, 37–56.

Woo, M.-K., Steer, P., 1986. Monte Carlo simulation of snow depth in a forest. Water Resources Research 22, 864–868.
Wright, M., Kavanaugh, J., Labine, C., 2011. Performance analysis of GMON3 snow water equivalency sensor. Proceedings of the Western Snow Conference 105–108.
Wylen, G.J.V., Sonntag, R.E., Borgnakke, C., 1993. Fundamentals of Classical Thermodynamics, 4th ed. Wiley.
Xia, Z., Woo, M.-K., 1992. Theoretical analysis of snow-dam decay. Journal of Glaciology 38, 191–199.
Xiang, N., Chu, D., 2004. Fast m-sequence transform for quasi-backscatter sonar in fisheries and zooplankton survey applications, in: 2004 7th International Conference on Signal Processing, 2004. Proceedings. ICSP '04. Presented at the 2004 7th International Conference on Signal Processing, 2004. Proceedings. ICSP '04, pp. 2433–2436 vol.3.
Yaghmour, K., Masters, J., Ben-Yossef, G., Gerum, P., 2008. Building Embedded Linux Systems, Second Edition. ed. O'Reilly Media.
Yamamoto, T., Koning, H.L., Sellmeijer, H., Hijum, E.V., 1978. On the response of a poro-elastic bed to water waves. Journal of Fluid Mechanics 87, 193–206.
Yamazaki, T., 2001. A one-dimensional land surface model adaptable to intensely cold regions and its applications in Eastern Siberia. Journal of the Meteorological society of Japan 79, 1107–1118.
Yamazaki, T., Yabuki, H., Ishii, Y., Ohta, T., Ohata, T., 2004. Water and Energy Exchanges at Forests and a Grassland in Eastern Siberia Evaluated Using a One-Dimensional Land Surface Model. Journal of Hydrometeorology 5, 504–515.
Yang, Z.-L., Niu, G.-Y., 2003. The Versatile Integrator of Surface and Atmosphere processes: Part 1. Model description. Global and Planetary Change 38, 175–189.
Yankielun, N., Rosenthal, W., Davis, R.E., 2004. Alpine snow depth measurements from aerial FMCW radar. Cold Regions Science and Technology 40, 123–134.
Yaroslavsky, L., 2003. Digital Holography and Digital Image Processing: Principles, Methods, Algorithms, 2004th ed. Springer.
Yaroslavsky, L., Moreno, A., Campos, J., 2005. Frequency responses and resolving power of numerical integration of sampled data. Opt Express 13, 2892–2905.
Yilmaz, Ö., 2001. Seismic data analysis: processing, inversion, and interpretation of seismic data, 2nd ed. ed, Investigations in geophysics. Society of Exploration Geophysicists, Tulsa, OK.
Yong-Shen, D., 1985. A tone-burst method for measuring loudspeaker harmonic distortion at high power levels. Journal of the Audio Engineering Society 33, 145–146.
Yosida, Z., 1955. Physical studies on deposited snow. I. Thermal properties. Contributions of the Institute of Low Temperature Science, Series A 19–74.
Yosida, Z., 1967. Free water content of wet snow. Proceedings of the International Conference on Low Temperature Science 1, 773–784.
Young, G.J., 1976. A portable profiling snow gauge results of field tests on glaciers. Proceedings of the Western Snow Conference 44, 7–11.
Zarek, J.H.B., 1978. Sound absorption in flexible porous materials. Journal of Sound and Vibration 61, 205–234.
Zwikker, C., Kosten, C.W., 1949. Sound Absorbing Materials. Elsevier Publishing Company.

APPENDIX A
CIRCUIT DIAGRAMS

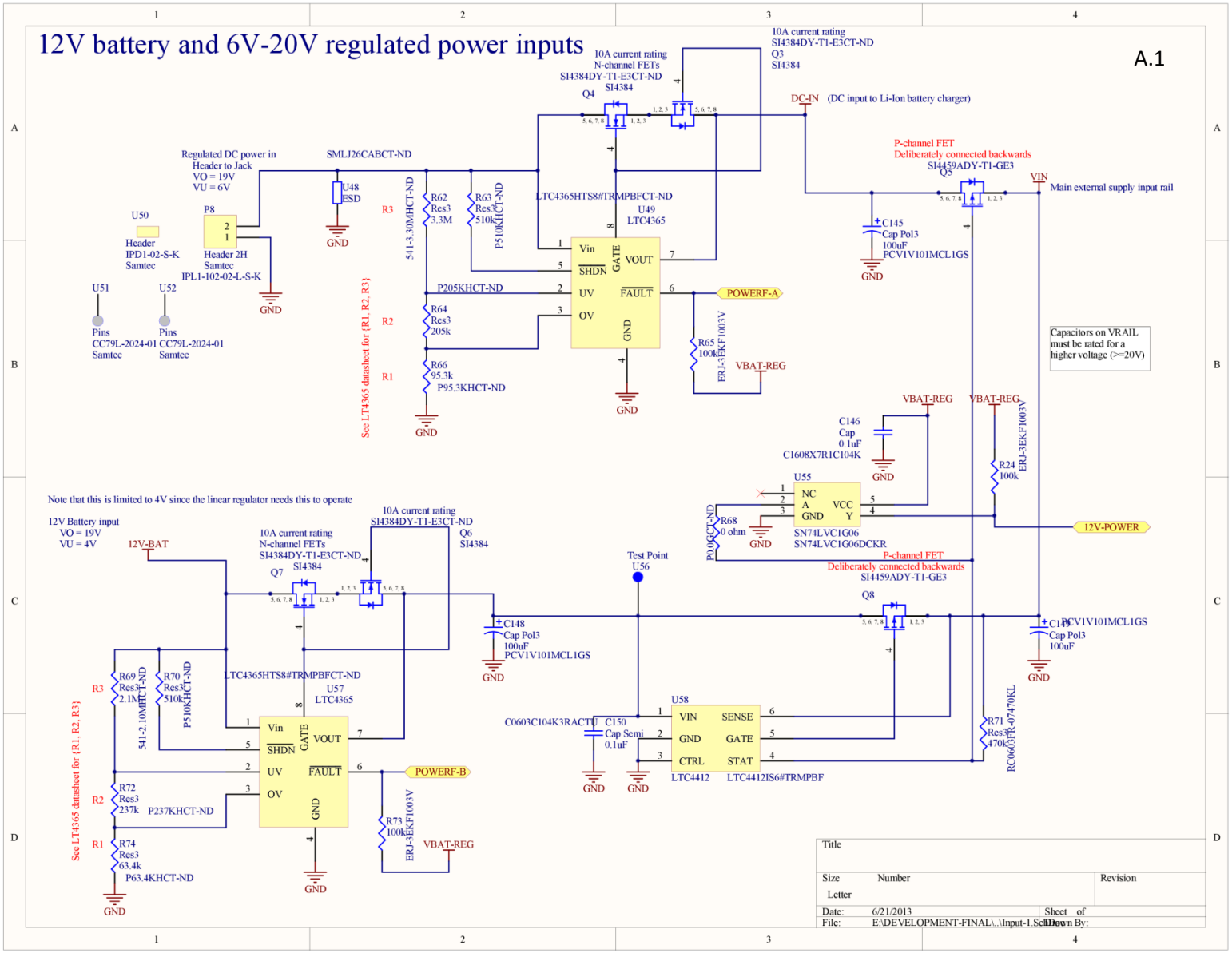
12V battery and 6V-20V regulated power inputs
A.1
10A current rating
SI4384DY-T1-E3CT-ND
Q3
SI4384
10A current rating
N-channel FETs
SI4384DY-T1-E3CT-ND
SI4384
Q4
DC-IN (DC input to Li-Ion battery charger)
P-channel FET
Deliberately connected backwards
SI4459ADY-T1-GE3
Q5
VIN
Main external supply input rail
Regulated DC power in
Header to Jack
VO = 19V
VU = 6V
SMLJ26CABCT-ND
U48
ESD
GND
U50
Header
IPD1-02-S-K
Samtec
P8
Header 2H
Samtec
IPL1-102-02-L-S-K
U51
U52
Pins
CC79L-2024-01
Samtec
R3
541-3.30MHCT-ND
R62
Res3
3.3M
R63
Res3
510K
P510KHCT-ND
LTC4365HTS8#TRMPBFCT-ND
U49
LTC4365
Vin
SHDN
UV
OV
GATE
VOUT
FAULT
GND
P205KHCT-ND
R64
Res3
205k
R66
95.3k
P95.3KHCT-ND
R2
R1
See LT4365 datasheet for {R1, R2, R3}
POWERF-A
R65
100k
ERJ-3EKF1003V
VBAT-REG
C145
Cap Pol3
100uF
PCV1V101MCL1GS
Capacitors on VRAIL must be rated for a higher voltage (>=20V)
C146
Cap
0.1uF
C1608X7R1C104K
R24
100k
U55
NC
A
GND
VCC
Y
SN74LVC1G06
SN74LVC1G06DCKR
P0.0GCT-ND
R68
0 ohm
12V-POWER
Note that this is limited to 4V since the linear regulator needs this to operate
12V Battery input
VO = 19V
VU = 4V
12V-BAT
10A current rating
N-channel FETs
SI4384DY-T1-E3CT-ND
SI4384
Q7
10A current rating
SI4384DY-T1-E3CT-ND
SI4384
Q6
Test Point
U56
P-channel FET
Deliberately connected backwards
SI4459ADY-T1-GE3
Q8
C148
Cap Pol3
100uF
PCV1V101MCL1GS
C149
Cap Pol3
100uF
PCV1V101MCL1GS
R69
Res3
2.1M
541-2.10MHCT-ND
R70
Res3
510K
P510KHCT-ND
LTC4365HTS8#TRMPBFCT-ND
U57
LTC4365
R72
Res3
237k
P237KHCT-ND
R74
Res3
63.4k
P63.4KHCT-ND
POWERF-B
R73
100k
ERJ-3EKF1003V
U58
VIN
GND
CTRL
SENSE
GATE
STAT
LTC4412
LTC4412IS6#TRMPBF
C0603C104K3RACTU
C150
Cap Semi
0.1uF
R71
Res3
470k
RC0603FR-07470KL
Title
Size
Letter
Number
Revision
Date:
6/21/2013
Sheet of
File:
E:\DEVELOPMENT-FINAL\..\Input-1.SchDoc
Drawn By:

Onboard Li-Ion battery input

A.2

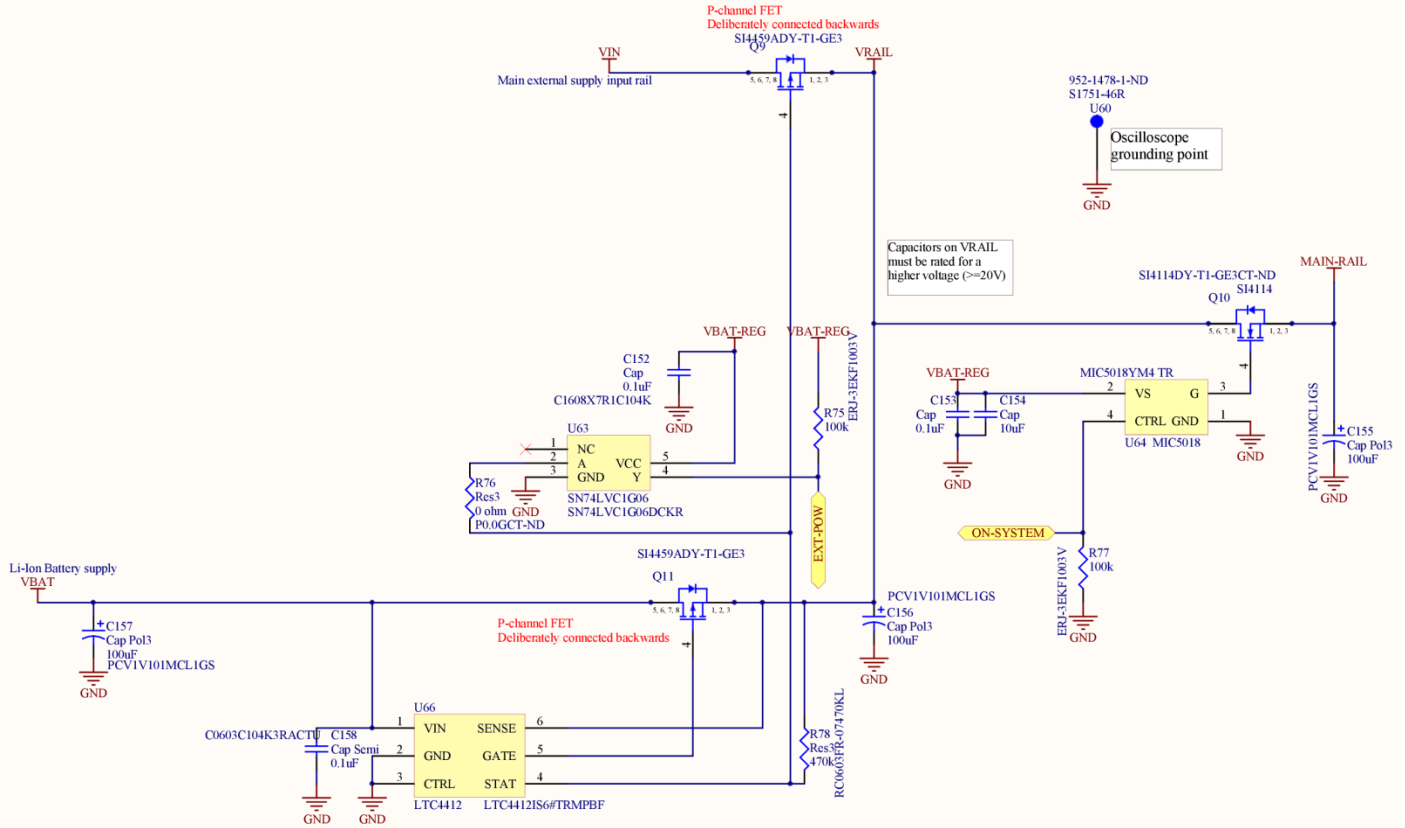

Always-on backup power

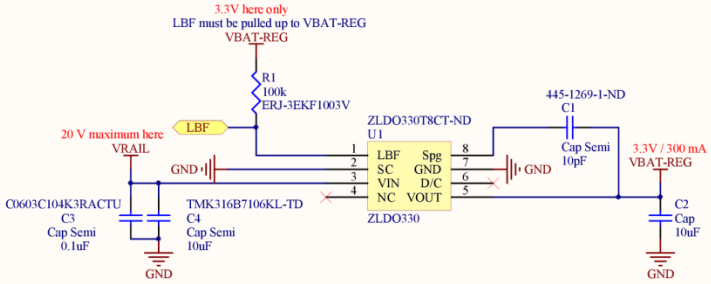

Title		
Size: Letter	Number	Revision
Date: 6/21/2013	Sheet of	
File: E:\DEVELOPMENT-FINAL\..\Always-on Power.SchDoc		

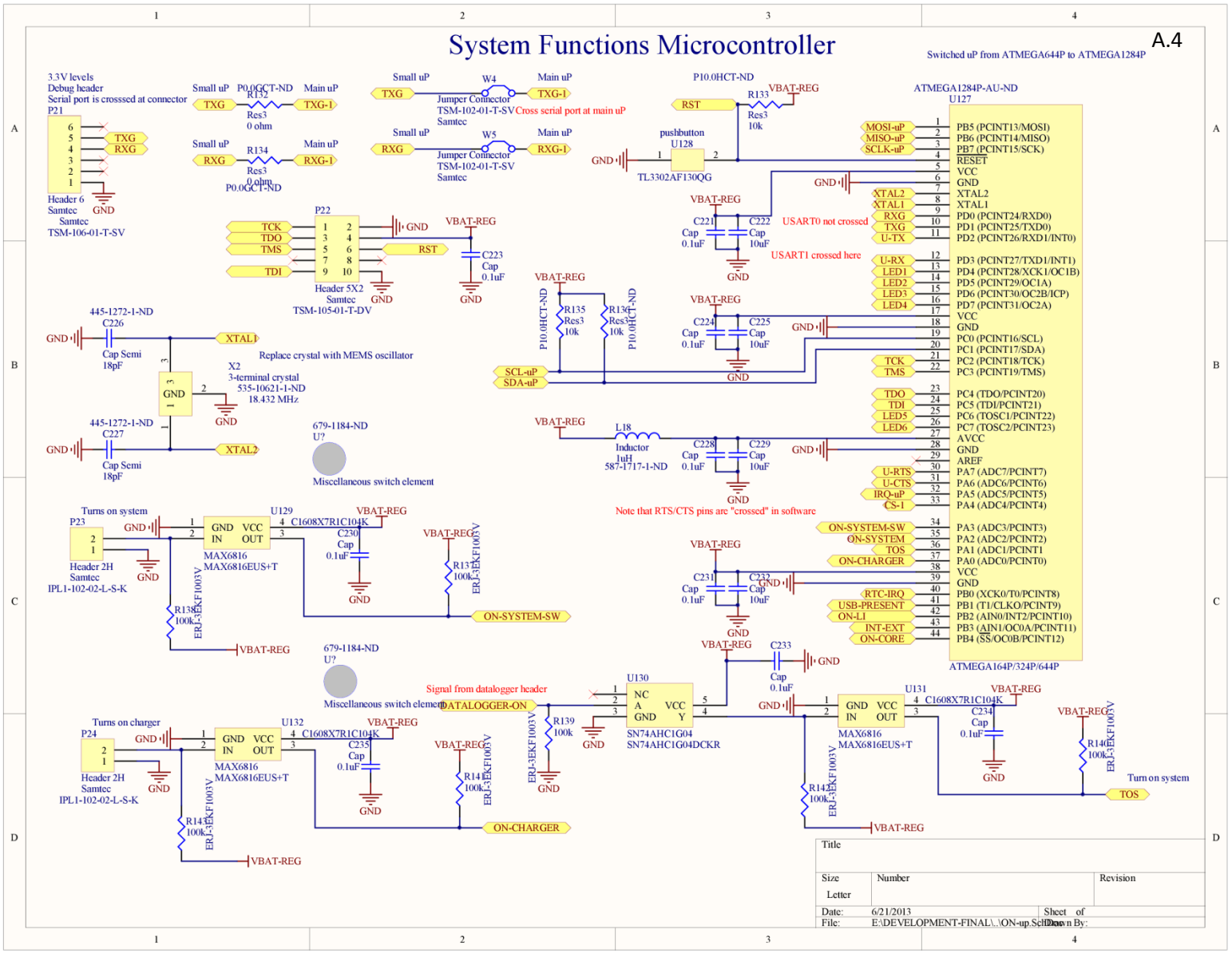
System Functions Microcontroller
A.4
Switched uP from ATMEGA644P to ATMEGA1284P
3.3V levels
Debug header
Serial port is crosssed at connector
P21
Header 6
Samtec
TSM-106-01-T-SV
Small uP
Main uP
TXG
RXG
TXG-1
RXG-1
R132
R134
Res3
0 ohm
P0.0GCT-ND
W4
W5
Jumper Connector
TSM-102-01-T-SV
Samtec
Cross serial port at main uP
P22
Header 5X2
TSM-105-01-T-DV
TCK
TDO
TMS
TDI
RST
GND
VBAT-REG
C223
Cap
0.1uF
445-1272-1-ND
C226
C227
Cap Semi
18pF
X2
3-terminal crystal
535-10621-1-ND
18.432 MHz
XTAL1
XTAL2
Replace crystal with MEMS oscillator
679-1184-ND
U?
Miscellaneous switch element
P10.0HCT-ND
R135
R136
Res3
10k
SCL-uP
SDA-uP
P10.0HCT-ND
R133
pushbutton
U128
TL3302AF130QG
C221
C222
C224
C225
C228
C229
C231
C232
Cap
0.1uF
10uF
USART0 not crossed
USART1 crossed here
L18
Inductor
1uH
587-1717-1-ND
Note that RTS/CTS pins are "crossed" in software
ATMEGA1284P-AU-ND
U127
ATMEGA164P/324P/644P
MOSI-uP
MISO-uP
SCLK-uP
U-TX
U-RX
LED1
LED2
LED3
LED4
U-RTS
U-CTS
IRQ-uP
CS-1
ON-SYSTEM-SW
ON-SYSTEM
TOS
ON-CHARGER
RTC-IRQ
USB-PRESENT
ON-LI
INT-EXT
ON-CORE
PB5 (PCINT13/MOSI)
PB6 (PCINT14/MISO)
PB7 (PCINT15/SCK)
RESET
VCC
GND
XTAL2
XTAL1
PD0 (PCINT24/RXD0)
PD1 (PCINT25/TXD0)
PD2 (PCINT26/RXD1/INT0)
PD3 (PCINT27/TXD1/INT1)
PD4 (PCINT28/XCK1/OC1B)
PD5 (PCINT29/OC1A)
PD6 (PCINT30/OC2B/ICP)
PD7 (PCINT31/OC2A)
PC0 (PCINT16/SCL)
PC1 (PCINT17/SDA)
PC2 (PCINT18/TCK)
PC3 (PCINT19/TMS)
PC4 (TDO/PCINT20)
PC5 (TDI/PCINT21)
PC6 (TOSC1/PCINT22)
PC7 (TOSC2/PCINT23)
AVCC
AREF
PA7 (ADC7/PCINT7)
PA6 (ADC6/PCINT6)
PA5 (ADC5/PCINT5)
PA4 (ADC4/PCINT4)
PA3 (ADC3/PCINT3)
PA2 (ADC2/PCINT2)
PA1 (ADC1/PCINT1)
PA0 (ADC0/PCINT0)
PB0 (XCK0/T0/PCINT8)
PB1 (T1/CLKO/PCINT9)
PB2 (AIN0/INT2/PCINT10)
PB3 (AIN1/OC0A/PCINT11)
PB4 (SS/OC0B/PCINT12)
Turns on system
P23
Header 2H
Samtec
IPL1-102-02-L-S-K
U129
GND VCC
IN OUT
MAX6816
MAX6816EUS+T
C1608X7R1C104K
C230
R137
R138
ERJ-3EKF1003V
100k
ON-SYSTEM-SW
Signal from datalogger header
DATALOGGER-ON
U130
NC
A
GND
VCC
Y
SN74AHC1G04
SN74AHC1G04DCKR
R139
U131
C233
C234
R140
R141
R142
Turns on charger
P24
U132
C235
R143
R144
ON-CHARGER
Turn on system
TOS
Title
Size
Letter
Number
Revision
Date:
6/21/2013
Sheet of
File:
E:\DEVELOPMENT-FINAL\..\ON-up.SchDoc
Drawn By:

Real-Time Clock with Calendar, LEDs, USB Sequencing, and Serial Number

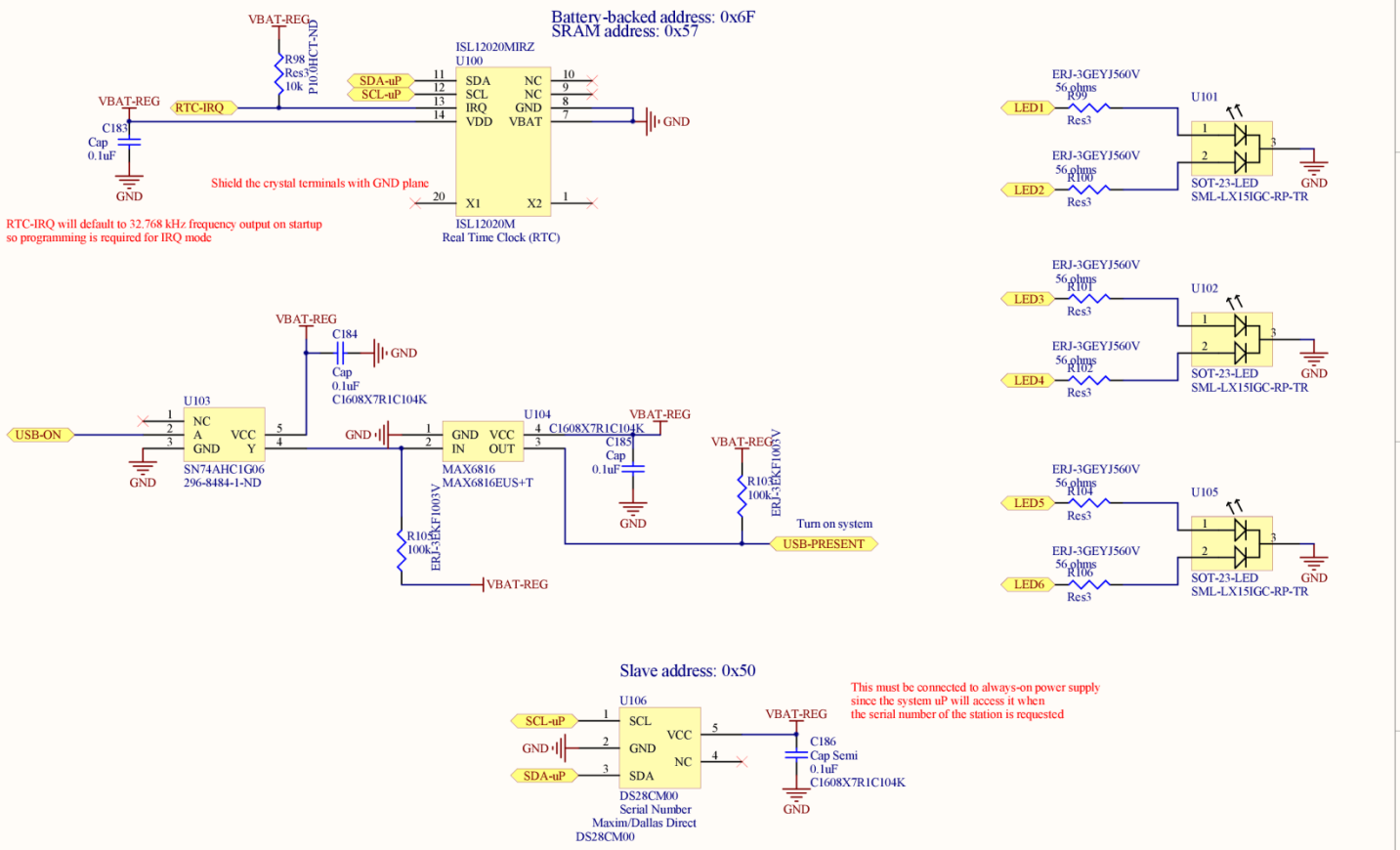

Title		
Size: Letter	Number	Revision
Date: 6/21/2013	Sheet of	
File: E:\DEVELOPMENT-FINAL\..\LEDs.SchDoc	Drawn By:	

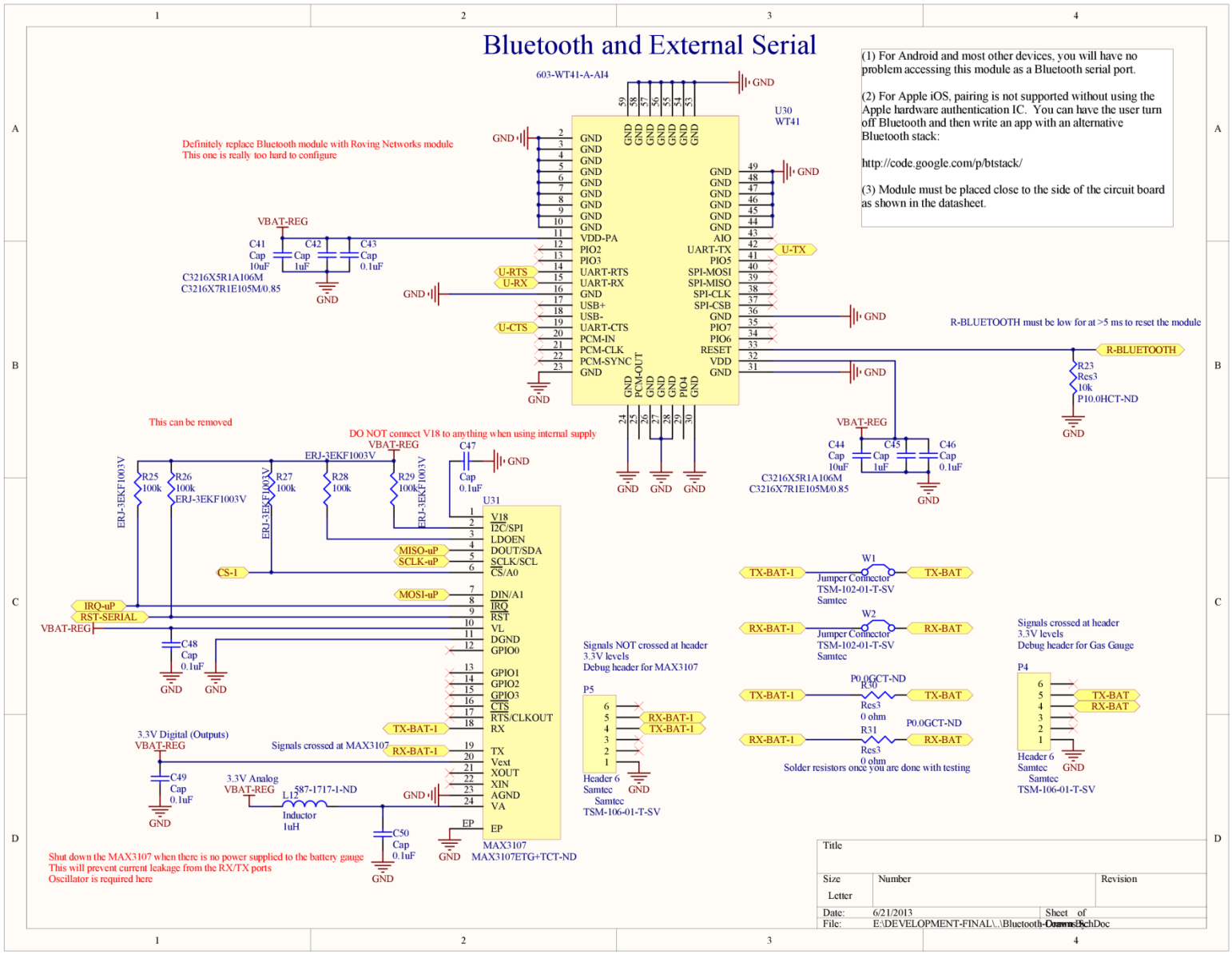
Bluetooth and External Serial
(1) For Android and most other devices, you will have no problem accessing this module as a Bluetooth serial port.
(2) For Apple iOS, pairing is not supported without using the Apple hardware authentication IC. You can have the user turn off Bluetooth and then write an app with an alternative Bluetooth stack:
http://code.google.com/p/btstack/
(3) Module must be placed close to the side of the circuit board as shown in the datasheet.
603-WT41-A-AI4
U30
WT41
Definitely replace Bluetooth module with Roving Networks module
This one is really too hard to configure
R-BLUETOOTH must be low for at >5 ms to reset the module
R-BLUETOOTH
R23
Res3
10k
P10.0HCT-ND
This can be removed
DO NOT connect V18 to anything when using internal supply
U31
MAX3107
MAX3107ETG+TCT-ND
Signals NOT crossed at header
3.3V levels
Debug header for MAX3107
P5
Header 6
Samtec
TSM-106-01-T-SV
Signals crossed at header
3.3V levels
Debug header for Gas Gauge
P4
W1
W2
Jumper Connector
TSM-102-01-T-SV
P0.0GCT-ND
R30
R31
Res3
0 ohm
Solder resistors once you are done with testing
Shut down the MAX3107 when there is no power supplied to the battery gauge
This will prevent current leakage from the RX/TX ports
Oscillator is required here
Title
Size
Letter
Number
Revision
Date: 6/21/2013
Sheet of
File: E:\DEVELOPMENT-FINAL\..\Bluetooth-Comm.SchDoc

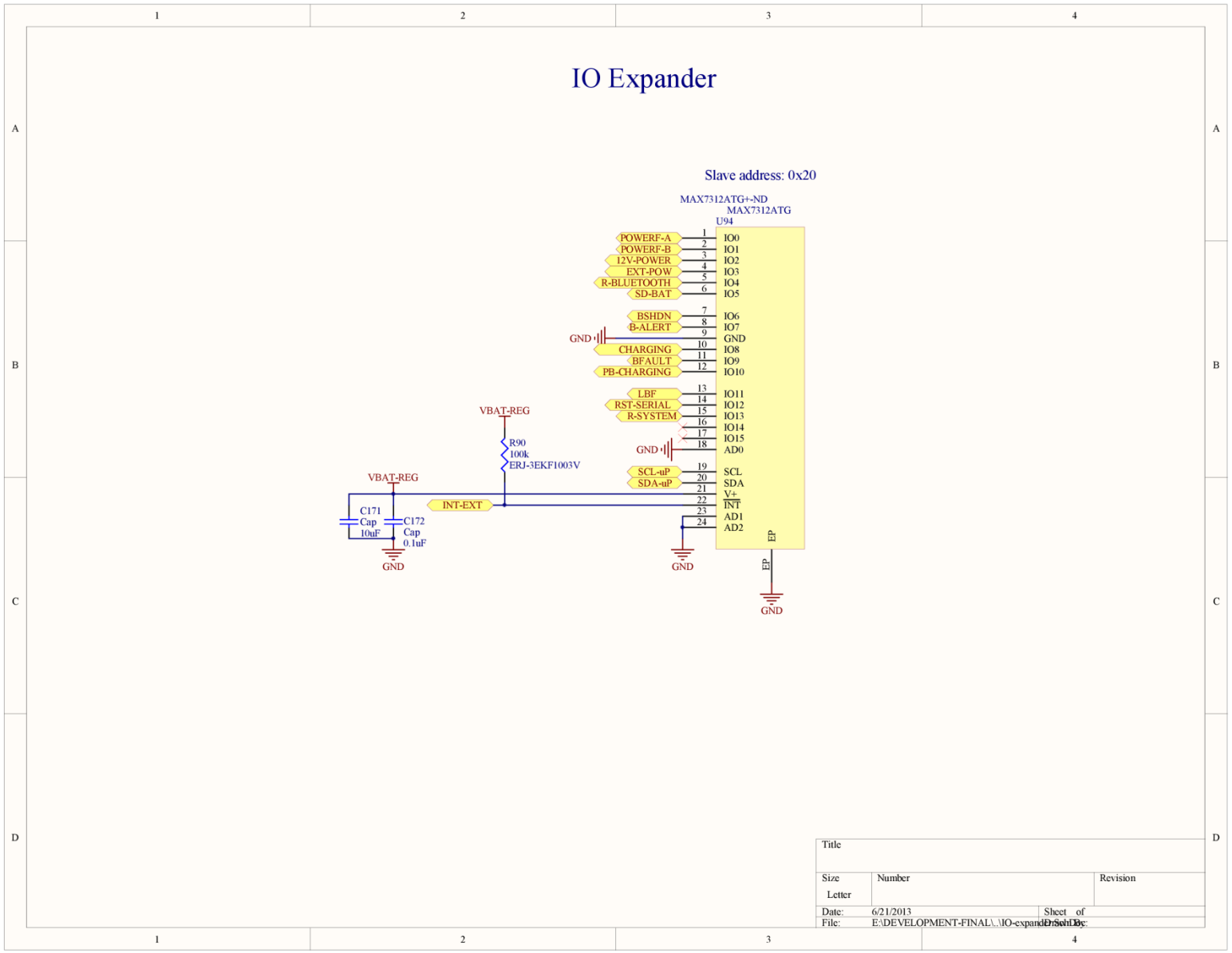
IO Expander
Slave address: 0x20
MAX7312ATG+-ND
MAX7312ATG
U94
POWERF-A
POWERF-B
12V-POWER
EXT-POW
R-BLUETOOTH
SD-BAT
BSHDN
B-ALERT
GND
CHARGING
BFAULT
PB-CHARGING
LBF
RST-SERIAL
R-SYSTEM
GND
SCL-uP
SDA-uP
INT-EXT
GND
IO0
IO1
IO2
IO3
IO4
IO5
IO6
IO7
GND
IO8
IO9
IO10
IO11
IO12
IO13
IO14
IO15
AD0
SCL
SDA
V+
INT
AD1
AD2
EP
EP
GND
VBAT-REG
R90
100k
ERJ-3EKF1003V
VBAT-REG
C171
Cap
10uF
C172
Cap
0.1uF
GND
GND
Title
Size
Letter
Number
Revision
Date:
6/21/2013
Sheet of
File:
E:\DEVELOPMENT-FINAL\..\IO-expander.SchDoc
Drawn By:

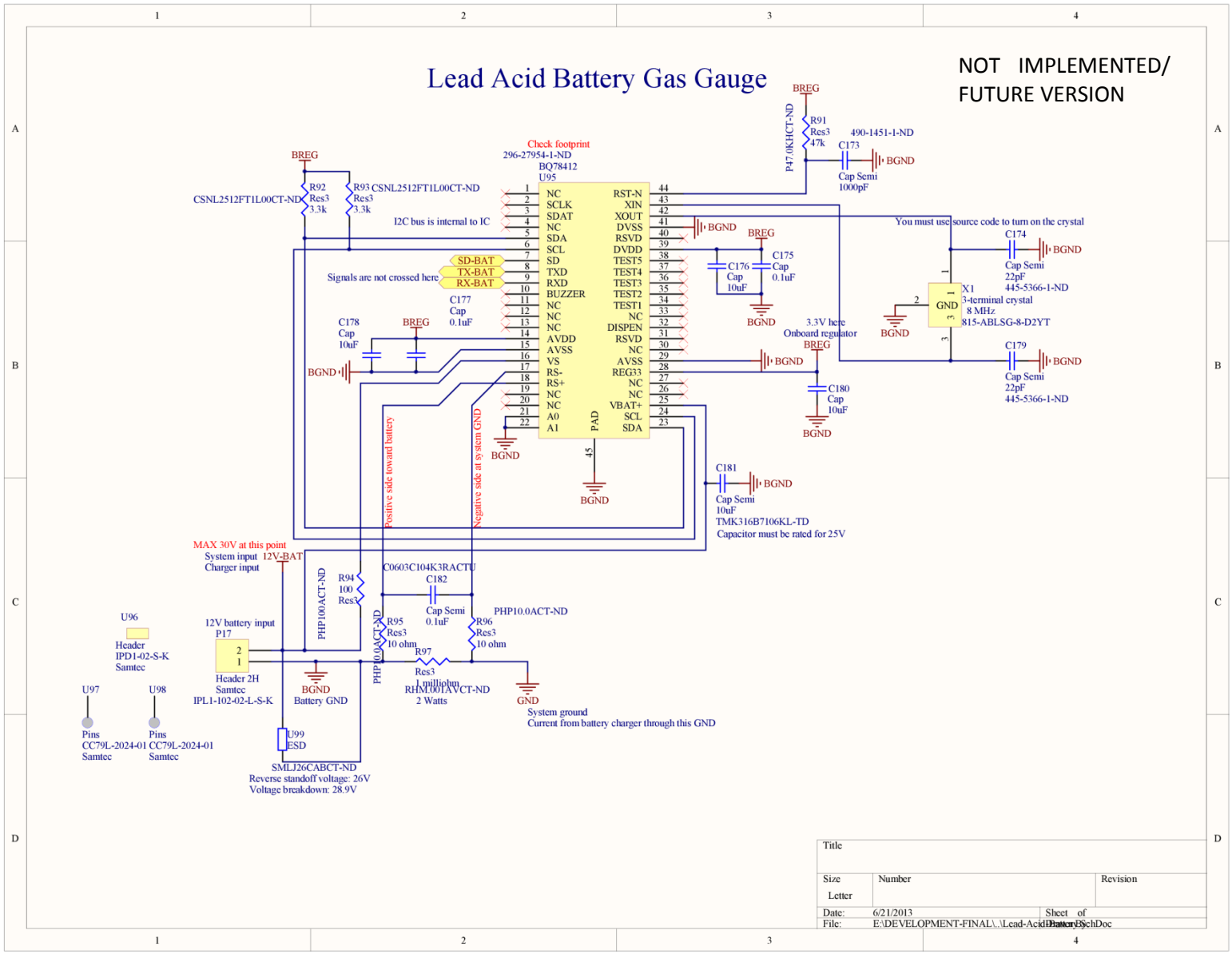
Lead Acid Battery Gas Gauge
NOT IMPLEMENTED/
FUTURE VERSION
BREG
R92
CSNL2512FT1L00CT-ND
Res3
3.3k
R93 CSNL2512FT1L00CT-ND
Res3
3.3k
I2C bus is internal to IC
Check footprint
296-27954-1-ND
BQ78412
U95
NC
SCLK
SDAT
NC
SDA
SCL
SD
TXD
RXD
BUZZER
NC
NC
NC
AVDD
AVSS
VS
RS-
RS+
NC
NC
A0
A1
RST-N
XIN
XOUT
DVSS
RSVD
DVDD
TEST5
TEST4
TEST3
TEST2
TEST1
NC
DISPEN
RSVD
NC
AVSS
REG33
NC
NC
VBAT+
SCL
SDA
PAD
SD-BAT
TX-BAT
RX-BAT
Signals are not crossed here
C177
Cap
0.1uF
C178
Cap
10uF
BGND
P47.0KHCT-ND
R91
Res3
47k
C173
Cap Semi
1000pF
490-1451-1-ND
C176
Cap
10uF
C175
Cap
0.1uF
You must use source code to turn on the crystal
C174
Cap Semi
22pF
445-5366-1-ND
X1
3-terminal crystal
8 MHz
815-ABLSG-8-D2YT
C179
Cap Semi
22pF
445-5366-1-ND
3.3V here
Onboard regulator
C180
Cap
10uF
C181
Cap Semi
10uF
TMK316B7106KL-TD
Capacitor must be rated for 25V
Positive side toward battery
Negative side at system GND
MAX 30V at this point
System input 12V-BAT
Charger input
C0603C104K3RACTU
C182
Cap Semi
0.1uF
R94
100
Res3
PHP100ACT-ND
R95
Res3
10 ohm
R96
Res3
10 ohm
PHP10.0ACT-ND
R97
Res3
1 milliohm
RHM001AVCT-ND
2 Watts
12V battery input
P17
Header 2H
Samtec
IPL1-102-02-L-S-K
Battery GND
System ground
Current from battery charger through this GND
U96
Header
IPD1-02-S-K
Samtec
U97
U98
Pins
CC79L-2024-01
Samtec
U99
ESD
SMLJ26CABCT-ND
Reverse standoff voltage: 26V
Voltage breakdown: 28.9V
Title
Size
Letter
Number
Revision
Date: 6/21/2013
Sheet of
File: E:\DEVELOPMENT-FINAL\..\Lead-Acid-Battery.SchDoc

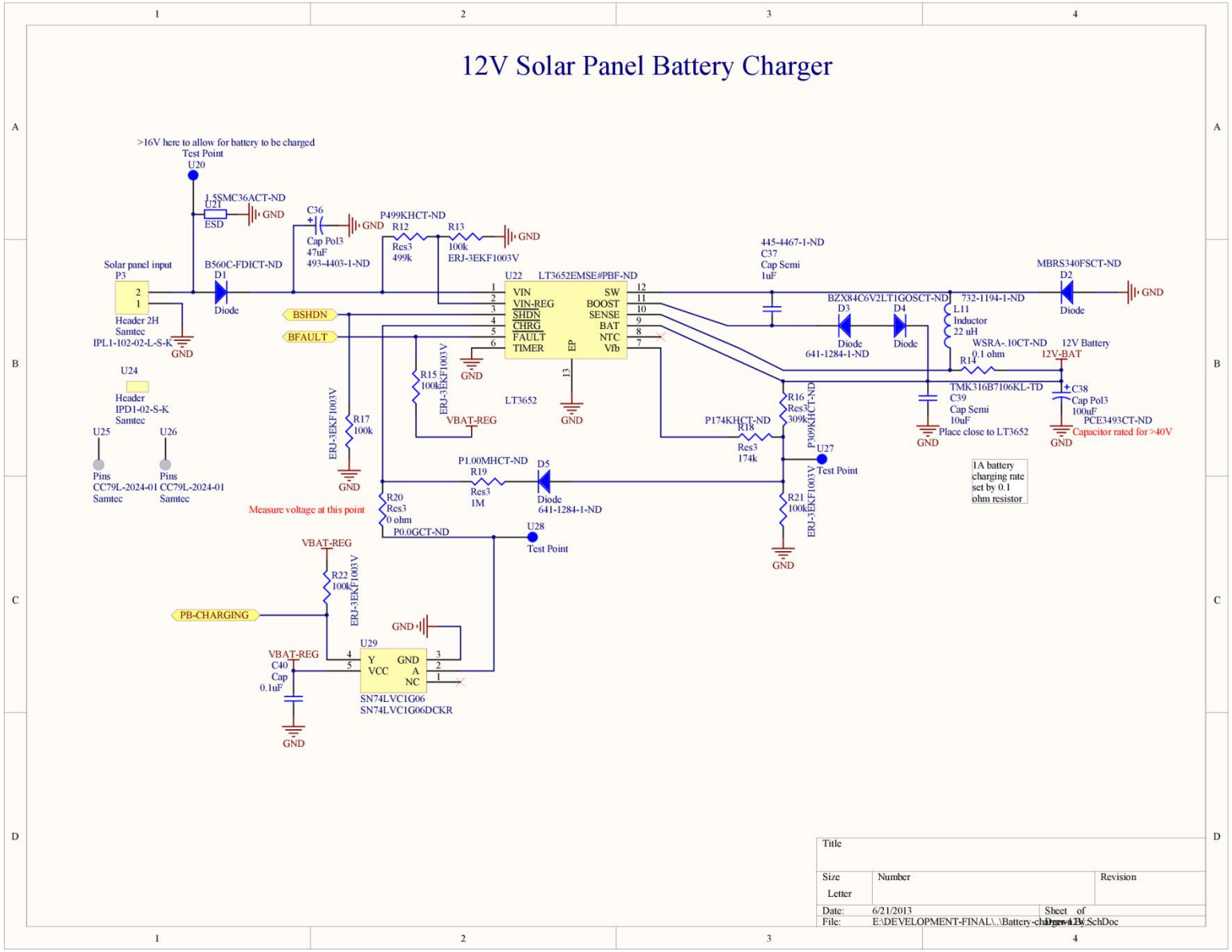
12V Solar Panel Battery Charger
>16V here to allow for battery to be charged
Test Point
U20
1.5SMC36ACT-ND
U21
ESD
GND
C36
Cap Pol3
47uF
493-4403-1-ND
P499KHCT-ND
R12
Res3
499k
R13
100k
ERJ-3EKF1003V
Solar panel input
P3
Header 2H
Samtec
IPL1-102-02-L-S-K
B560C-FDICT-ND
D1
Diode
BSHDN
BFAULT
U22
LT3652EMSE#PBF-ND
VIN
VIN-REG
SHDN
CHRG
FAULT
TIMER
SW
BOOST
SENSE
BAT
NTC
Vfb
EP
445-4467-1-ND
C37
Cap Semi
1uF
BZX84C6V2LT1GOSCT-ND
D3
D4
Diode
641-1284-1-ND
732-1194-1-ND
L11
Inductor
22 uH
WSRA-.10CT-ND
0.1 ohm
R14
MBRS340FSCT-ND
D2
12V Battery
12V-BAT
TMK316B7106KL-TD
C39
Cap Semi
10uF
Place close to LT3652
C38
Cap Pol3
100uF
PCE3493CT-ND
Capacitor rated for >40V
R15
100k
ERJ-3EKF1003V
VBAT-REG
LT3652
R16
Res3
309k
P309KHCT-ND
P174KHCT-ND
R18
Res3
174k
U27
Test Point
1A battery
charging rate
set by 0.1
ohm resistor
U24
Header
IPD1-02-S-K
Samtec
U25
U26
Pins
CC79L-2024-01
Samtec
R17
100k
Measure voltage at this point
P1.00MHCT-ND
R19
Res3
1M
D5
Diode
641-1284-1-ND
R20
Res3
0 ohm
P0.0GCT-ND
U28
Test Point
R21
100k
VBAT-REG
R22
100k
PB-CHARGING
U29
Y
VCC
GND
A
NC
SN74LVC1G06
SN74LVC1G06DCKR
C40
Cap
0.1uF
Title
Size
Letter
Number
Revision
Date:
6/21/2013
Sheet of
File:
E:\DEVELOPMENT-FINAL\..\Battery-charger-12V.SchDoc

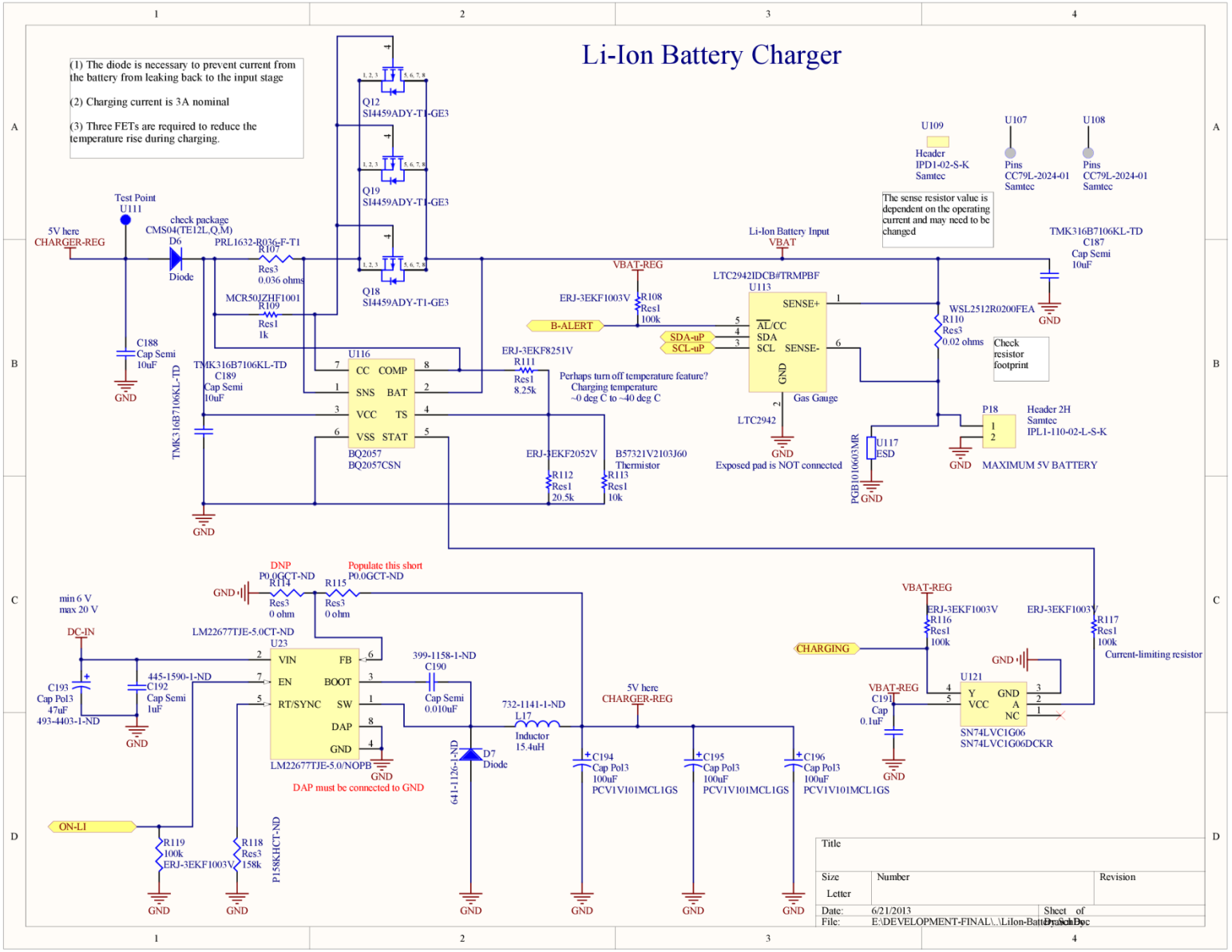
Li-Ion Battery Charger
(1) The diode is necessary to prevent current from the battery from leaking back to the input stage
(2) Charging current is 3A nominal
(3) Three FETs are required to reduce the temperature rise during charging.
Q12 SI4459ADY-T1-GE3
Q19 SI4459ADY-T1-GE3
Q18 SI4459ADY-T1-GE3
U109 Header IPD1-02-S-K Samtec
U107 Pins CC79L-2024-01 Samtec
U108 Pins CC79L-2024-01 Samtec
The sense resistor value is dependent on the operating current and may need to be changed
Test Point U111
5V here CHARGER-REG
check package CMS04(TE12L,Q,M)
D6 Diode
PRL1632-R036-F-T1 R107 Res3 0.036 ohms
MCR50JZHF1001 R109 Res1 1k
C188 Cap Semi 10uF
TMK316B7106KL-TD C189 Cap Semi 10uF
TMK316B7106KL-TD
U116 BQ2057 BQ2057CSN
CC COMP SNS BAT VCC TS VSS STAT
ERJ-3EKF8251V R111 Res1 8.25k
Perhaps turn off temperature feature? Charging temperature ~0 deg C to ~40 deg C
ERJ-3EKF2052V R112 Res1 20.5k
B57321V2103J60 Thermistor R113 Res1 10k
VBAT-REG
ERJ-3EKF1003V R108 Res1 100k
B-ALERT
SDA-uP
SCL-uP
LTC2942IDCB#TRMPBF U113 Gas Gauge
SENSE+ AL/CC SDA SCL SENSE- GND
LTC2942
Exposed pad is NOT connected
Li-Ion Battery Input VBAT
WSL2512R0200FEA R110 Res3 0.02 ohms
Check resistor footprint
TMK316B7106KL-TD C187 Cap Semi 10uF
P18 Header 2H Samtec IPL1-110-02-L-S-K
MAXIMUM 5V BATTERY
U117 ESD PGB1010603MR
DNP P0.0GCT-ND R114 Res3 0 ohm
Populate this short P0.0GCT-ND R115 Res3 0 ohm
min 6 V max 20 V
DC-IN
C193 Cap Pol3 47uF 493-4403-1-ND
445-1590-1-ND C192 Cap Semi 1uF
LM22677TJE-5.0CT-ND
U23 LM22677TJE-5.0/NOPB
VIN FB EN BOOT RT/SYNC SW DAP GND
DAP must be connected to GND
399-1158-1-ND C190 Cap Semi 0.010uF
732-1141-1-ND L17 Inductor 15.4uH
641-1126-1-ND D7 Diode
5V here CHARGER-REG
C194 Cap Pol3 100uF PCV1V101MCL1GS
C195 Cap Pol3 100uF PCV1V101MCL1GS
C196 Cap Pol3 100uF PCV1V101MCL1GS
ON-LI
R119 100k ERJ-3EKF1003V
R118 Res3 158k P158KHCT-ND
CHARGING
VBAT-REG
ERJ-3EKF1003V R116 Res1 100k
ERJ-3EKF1003V R117 Res1 100k Current-limiting resistor
C191 Cap 0.1uF
U121 SN74LVC1G06 SN74LVC1G06DCKR
Y VCC GND A NC
Title
Size Letter
Number
Revision
Date: 6/21/2013
Sheet of
File: E:\DEVELOPMENT-FINAL\..\Lilon-Batt...SchDoc

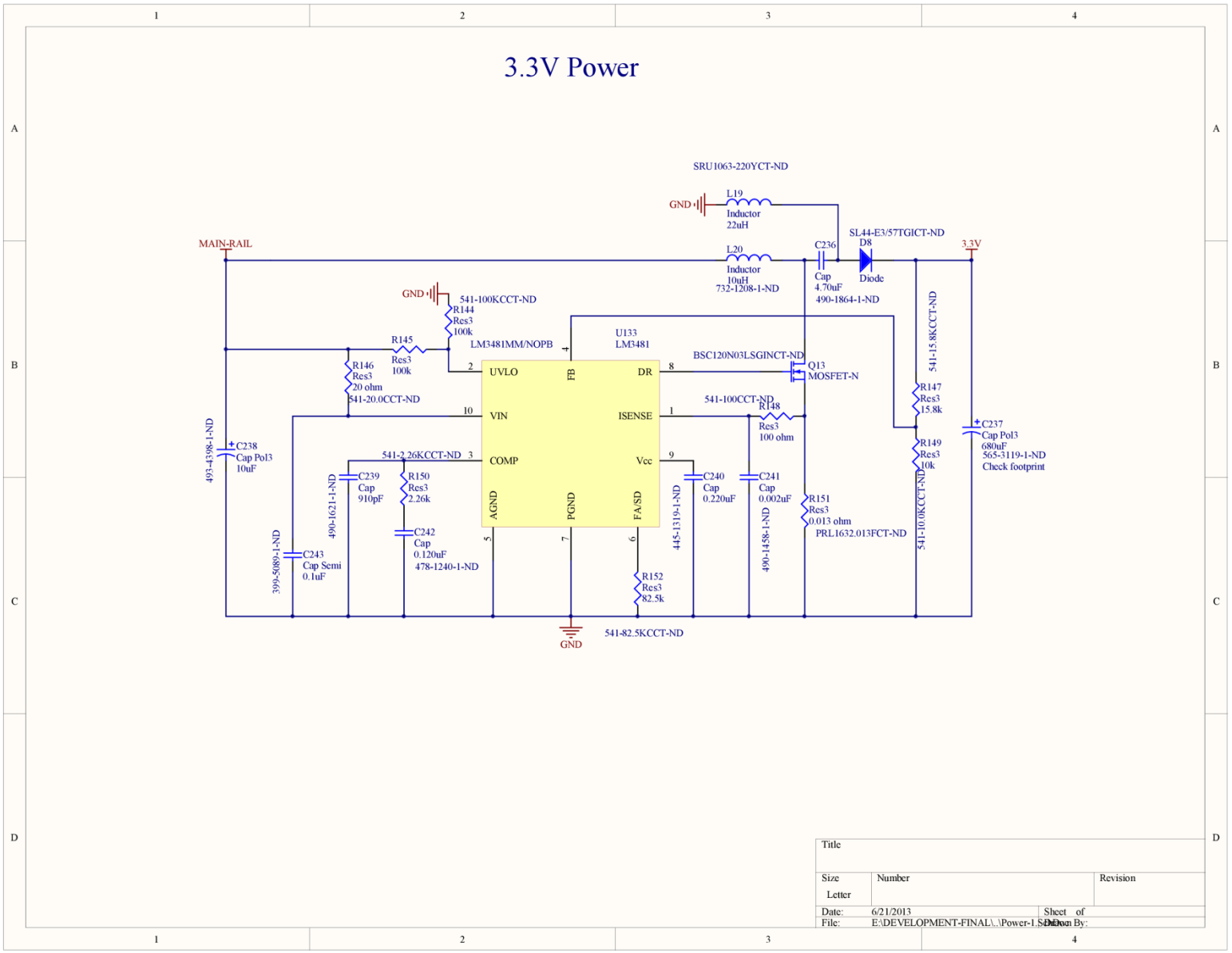
3.3V Power
SRU1063-220YCT-ND
L19
Inductor
22uH
GND
L20
Inductor
10uH
732-1208-1-ND
MAIN-RAIL
C236
Cap
4.70uF
490-1864-1-ND
SL44-E3/57TGICT-ND
D8
Diode
3.3V
541-15.8KCCT-ND
GND
541-100KCCT-ND
R144
Res3
100k
R145
Res3
100k
LM3481MM/NOPB
U133
LM3481
BSC120N03LSGINCT-ND
Q13
MOSFET-N
R146
Res3
20 ohm
541-20.0CCT-ND
UVLO
FB
DR
VIN
ISENSE
COMP
Vcc
AGND
PGND
FA/SD
541-100CCT-ND
R148
Res3
100 ohm
R147
Res3
15.8k
C237
Cap Pol3
680uF
565-3119-1-ND
Check footprint
493-4398-1-ND
C238
Cap Pol3
10uF
541-2.26KCCT-ND
C239
Cap
910pF
490-1621-1-ND
R150
Res3
2.26k
C240
Cap
0.220uF
445-1319-1-ND
C241
Cap
0.002uF
490-1458-1-ND
R149
Res3
10k
541-10.0KCCT-ND
R151
Res3
0.013 ohm
PRL1632.013FCT-ND
399-5089-1-ND
C243
Cap Semi
0.1uF
C242
Cap
0.120uF
478-1240-1-ND
R152
Res3
82.5k
GND
541-82.5KCCT-ND
Title
Size
Letter
Number
Revision
Date:
6/21/2013
Sheet of
File:
E:\DEVELOPMENT-FINAL\..\Power-1.SchDoc
Drawn By:

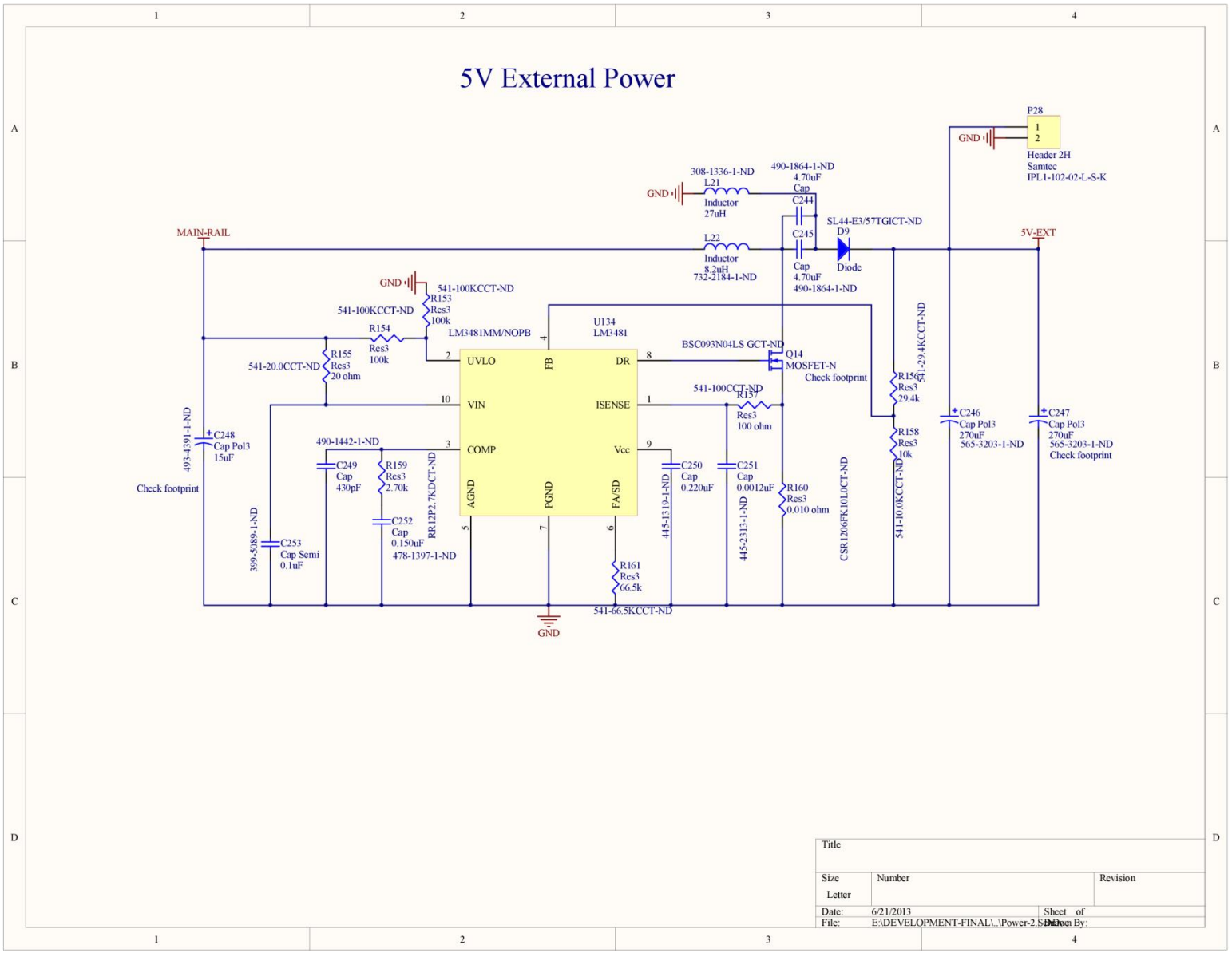
5V External Power
P28
GND
1
2
Header 2H
Samtec
IPL1-102-02-L-S-K
308-1336-1-ND
L21
Inductor
27uH
490-1864-1-ND
4.70uF
Cap
C244
SL44-E3/57TGICT-ND
D9
C245
Cap
4.70uF
490-1864-1-ND
Diode
L22
Inductor
8.2uH
732-2184-1-ND
MAIN-RAIL
5V-EXT
GND
541-100KCCT-ND
R153
Res3
100k
541-100KCCT-ND
R154
Res3
100k
LM3481MM/NOPB
U134
LM3481
541-20.0CCT-ND
R155
Res3
20 ohm
UVLO
FB
DR
BSC093N04LS GCT-ND
Q14
MOSFET-N
Check footprint
VIN
ISENSE
541-100CCT-ND
R157
Res3
100 ohm
541-29.4KCCT-ND
R156
Res3
29.4k
493-4391-1-ND
C248
Cap Pol3
15uF
Check footprint
490-1442-1-ND
COMP
Vcc
C246
Cap Pol3
270uF
565-3203-1-ND
C247
Cap Pol3
270uF
565-3203-1-ND
Check footprint
C249
Cap
430pF
R159
Res3
2.70k
C250
Cap
0.220uF
C251
Cap
0.0012uF
R158
Res3
10k
AGND
PGND
FA/SD
399-5089-1-ND
C253
Cap Semi
0.1uF
C252
Cap
0.150uF
478-1397-1-ND
RR12P2.7KDCT-ND
445-1319-1-ND
445-2313-1-ND
R160
Res3
0.010 ohm
CSR1206FK10L0CT-ND
541-10.0KCCT-ND
R161
Res3
66.5k
541-66.5KCCT-ND
GND
Title
Size
Letter
Number
Revision
Date:
6/21/2013
Sheet of
File:
E:\DEVELOPMENT-FINAL\..\Power-2.SchDoc
Drawn By:

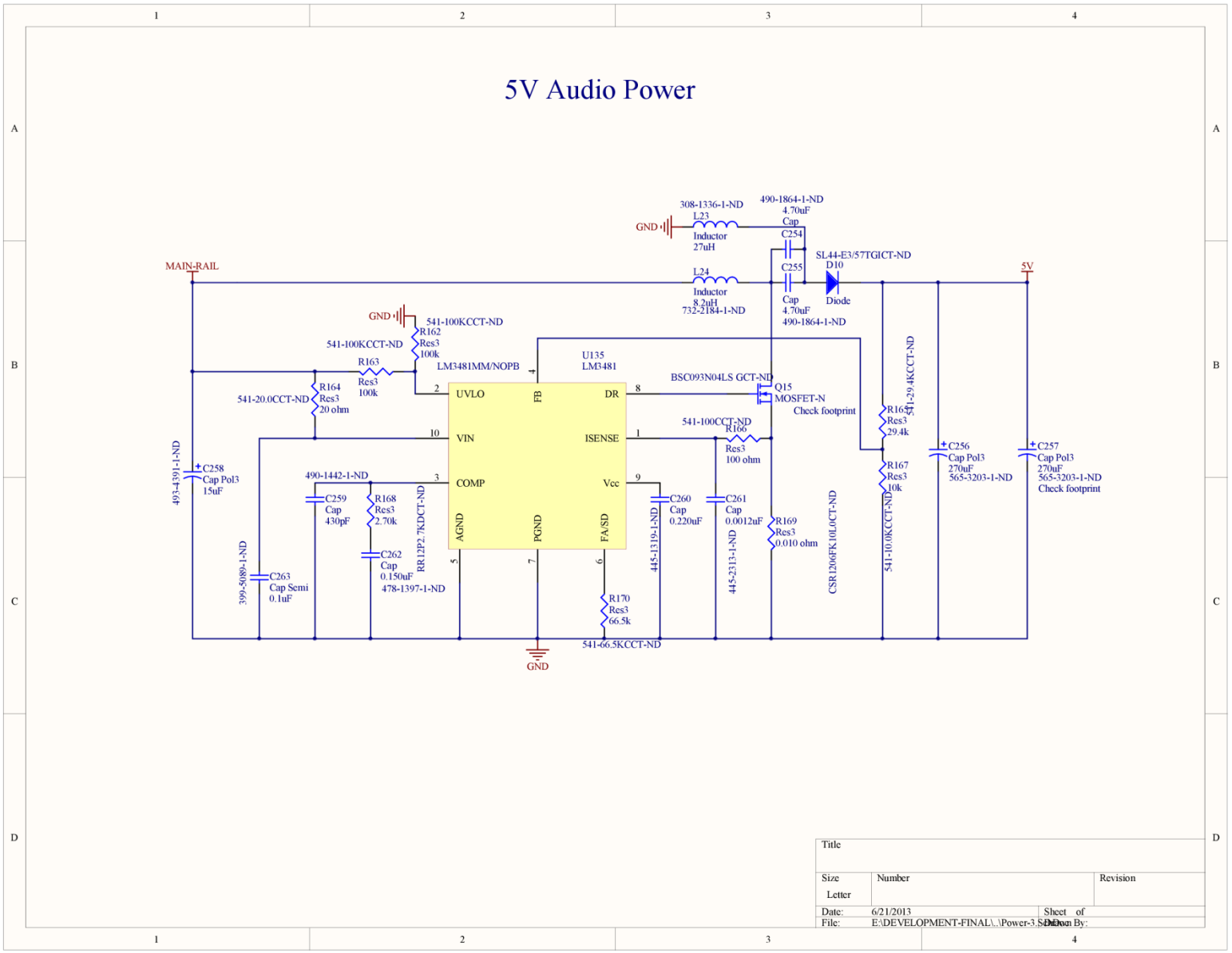
5V Audio Power
MAIN-RAIL
GND
308-1336-1-ND
L23
Inductor
27uH
490-1864-1-ND
4.70uF
Cap
C254
C255
SL44-E3/57TGICT-ND
D10
Diode
5V
L24
Inductor
8.2uH
732-2184-1-ND
Cap
4.70uF
490-1864-1-ND
541-100KCCT-ND
R162
Res3
100k
541-100KCCT-ND
R163
Res3
100k
LM3481MM/NOPB
U135
LM3481
BSC093N04LS GCT-ND
Q15
MOSFET-N
Check footprint
R164
Res3
20 ohm
541-20.0CCT-ND
UVLO
FB
DR
VIN
ISENSE
541-100CCT-ND
R166
Res3
100 ohm
R165
Res3
29.4k
541-29.4KCCT-ND
C256
Cap Pol3
270uF
565-3203-1-ND
C257
Cap Pol3
270uF
565-3203-1-ND
Check footprint
R167
Res3
10k
541-10.0KCCT-ND
493-4391-1-ND
C258
Cap Pol3
15uF
490-1442-1-ND
COMP
Vcc
C259
Cap
430pF
R168
Res3
2.70k
C262
Cap
0.150uF
478-1397-1-ND
RR12P2.7KDCT-ND
C260
Cap
0.220uF
445-1319-1-ND
C261
Cap
0.0012uF
445-2313-1-ND
R169
Res3
0.010 ohm
CSR1206FK10L0CT-ND
AGND
PGND
FA/SD
399-5089-1-ND
C263
Cap Semi
0.1uF
R170
Res3
66.5k
541-66.5KCCT-ND
GND
Title
Size
Letter
Number
Revision
Date:
6/21/2013
Sheet of
File:
E:\DEVELOPMENT-FINAL\..\Power-3.SchDoc
Drawn By:

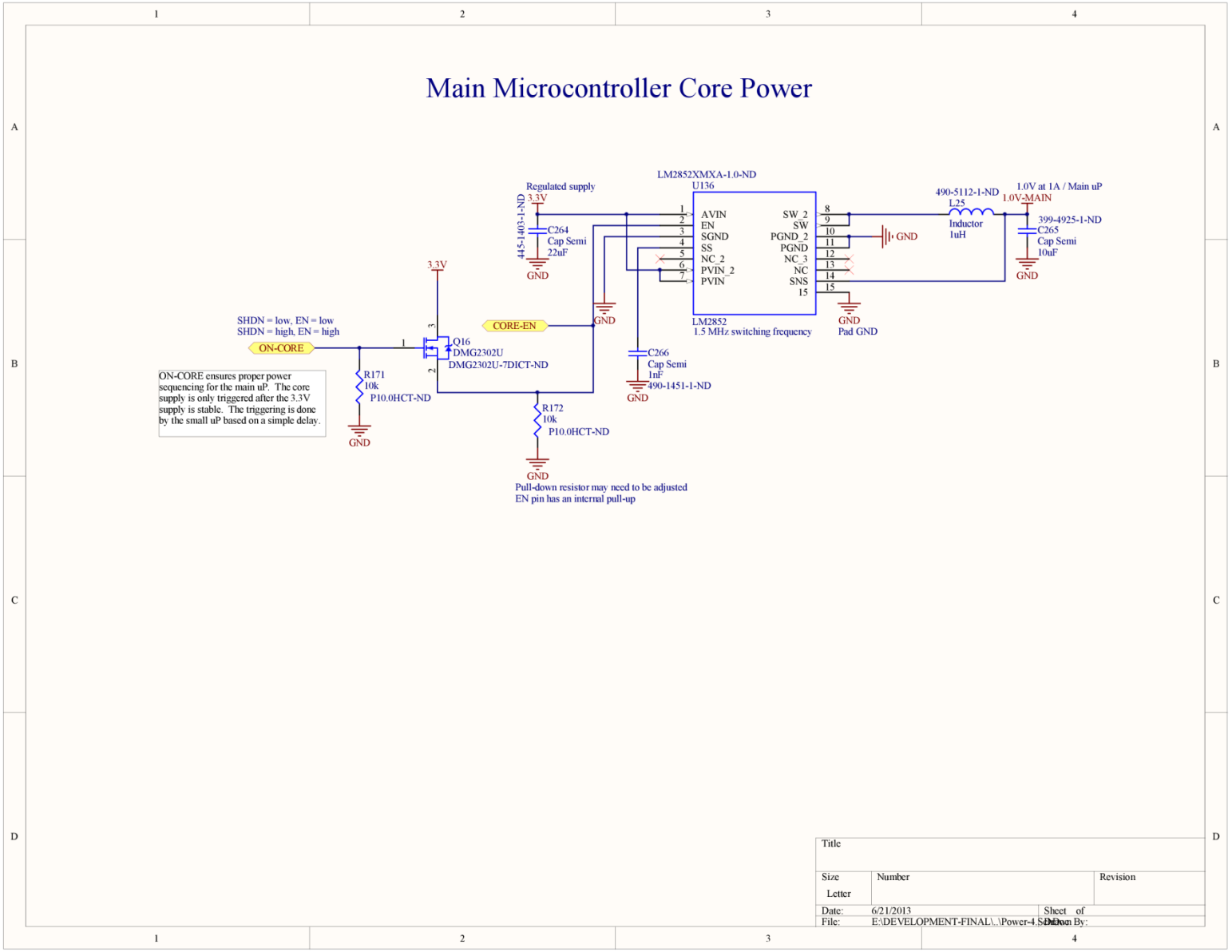
Main Microcontroller Core Power
LM2852XMXA-1.0-ND
U136
Regulated supply
3.3V
445-1403-1-ND
C264
Cap Semi
22uF
GND
AVIN
EN
SGND
SS
NC_2
PVIN_2
PVIN
SW_2
SW
PGND_2
PGND
NC_3
NC
SNS
15
LM2852
1.5 MHz switching frequency
GND
Pad GND
490-5112-1-ND
L25
Inductor
1uH
1.0V at 1A / Main uP
1.0V-MAIN
399-4925-1-ND
C265
Cap Semi
10uF
GND
3.3V
SHDN = low, EN = low
SHDN = high, EN = high
ON-CORE
CORE-EN
Q16
DMG2302U
DMG2302U-7DICT-ND
R171
10k
P10.0HCT-ND
GND
C266
Cap Semi
1nF
490-1451-1-ND
GND
R172
10k
P10.0HCT-ND
GND
Pull-down resistor may need to be adjusted
EN pin has an internal pull-up
ON-CORE ensures proper power sequencing for the main uP. The core supply is only triggered after the 3.3V supply is stable. The triggering is done by the small uP based on a simple delay.
Title
Size
Letter
Number
Revision
Date:
6/21/2013
Sheet of
File:
E:\DEVELOPMENT-FINAL\..\Power-4.SchDoc
Drawn By:

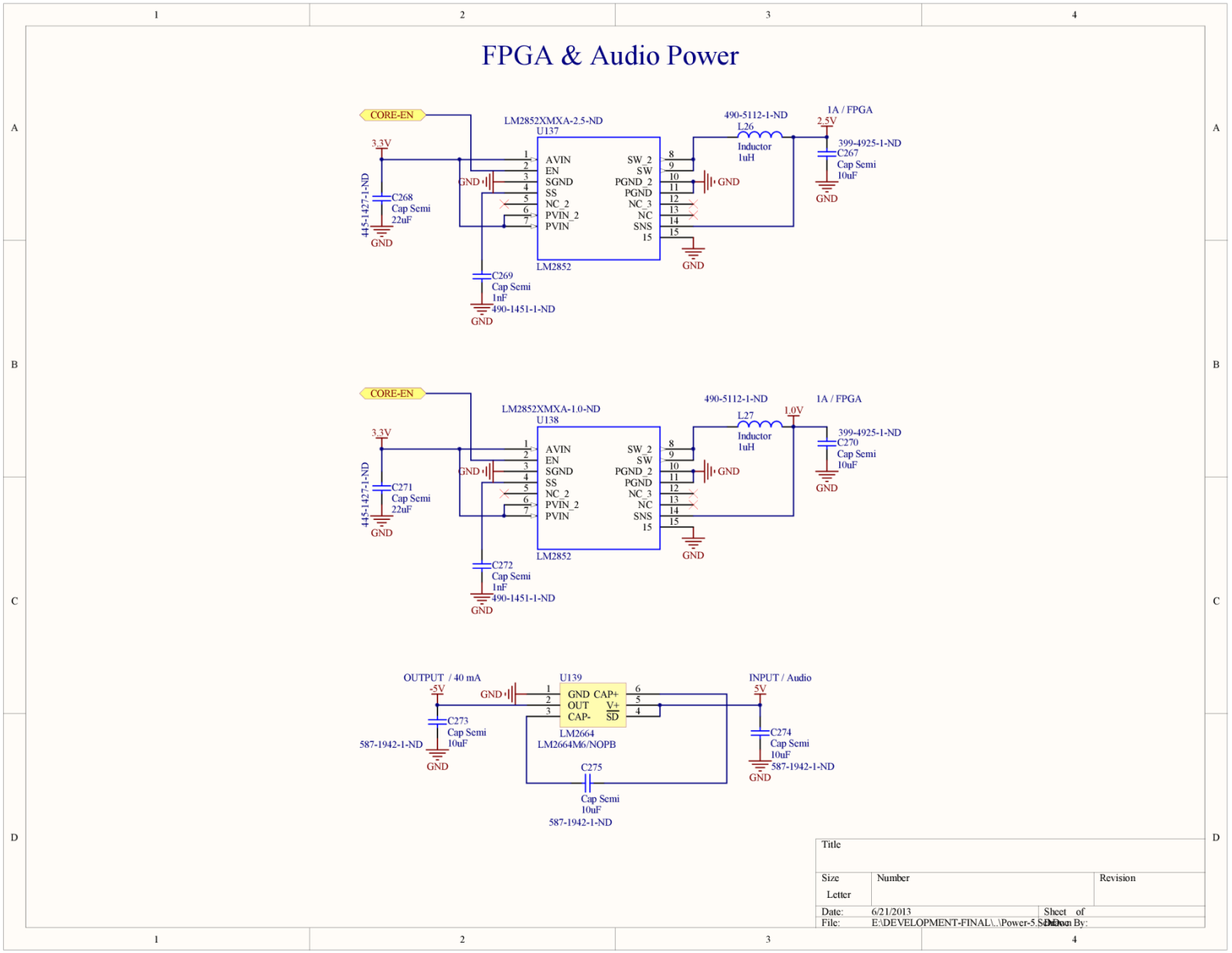
FPGA & Audio Power
CORE-EN
LM2852XMXA-2.5-ND
U137
3.3V
445-1427-1-ND
C268
Cap Semi
22uF
GND
AVIN
EN
SGND
SS
NC_2
PVIN_2
PVIN
SW_2
SW
PGND_2
PGND
NC_3
NC
SNS
15
LM2852
490-5112-1-ND
L26
Inductor
1uH
1A / FPGA
2.5V
399-4925-1-ND
C267
Cap Semi
10uF
C269
Cap Semi
1nF
490-1451-1-ND
CORE-EN
LM2852XMXA-1.0-ND
U138
3.3V
445-1427-1-ND
C271
Cap Semi
22uF
C272
Cap Semi
1nF
490-1451-1-ND
490-5112-1-ND
L27
Inductor
1uH
1.0V
1A / FPGA
399-4925-1-ND
C270
Cap Semi
10uF
OUTPUT / 40 mA
-5V
U139
GND CAP+
OUT V+
CAP- SD
LM2664
LM2664M6/NOPB
C273
Cap Semi
10uF
587-1942-1-ND
C275
Cap Semi
10uF
587-1942-1-ND
INPUT / Audio
5V
C274
Cap Semi
10uF
587-1942-1-ND
Title
Size
Letter
Number
Revision
Date: 6/21/2013
Sheet of
File: E:\DEVELOPMENT-FINAL\..\Power-5.SchDoc
Drawn By:

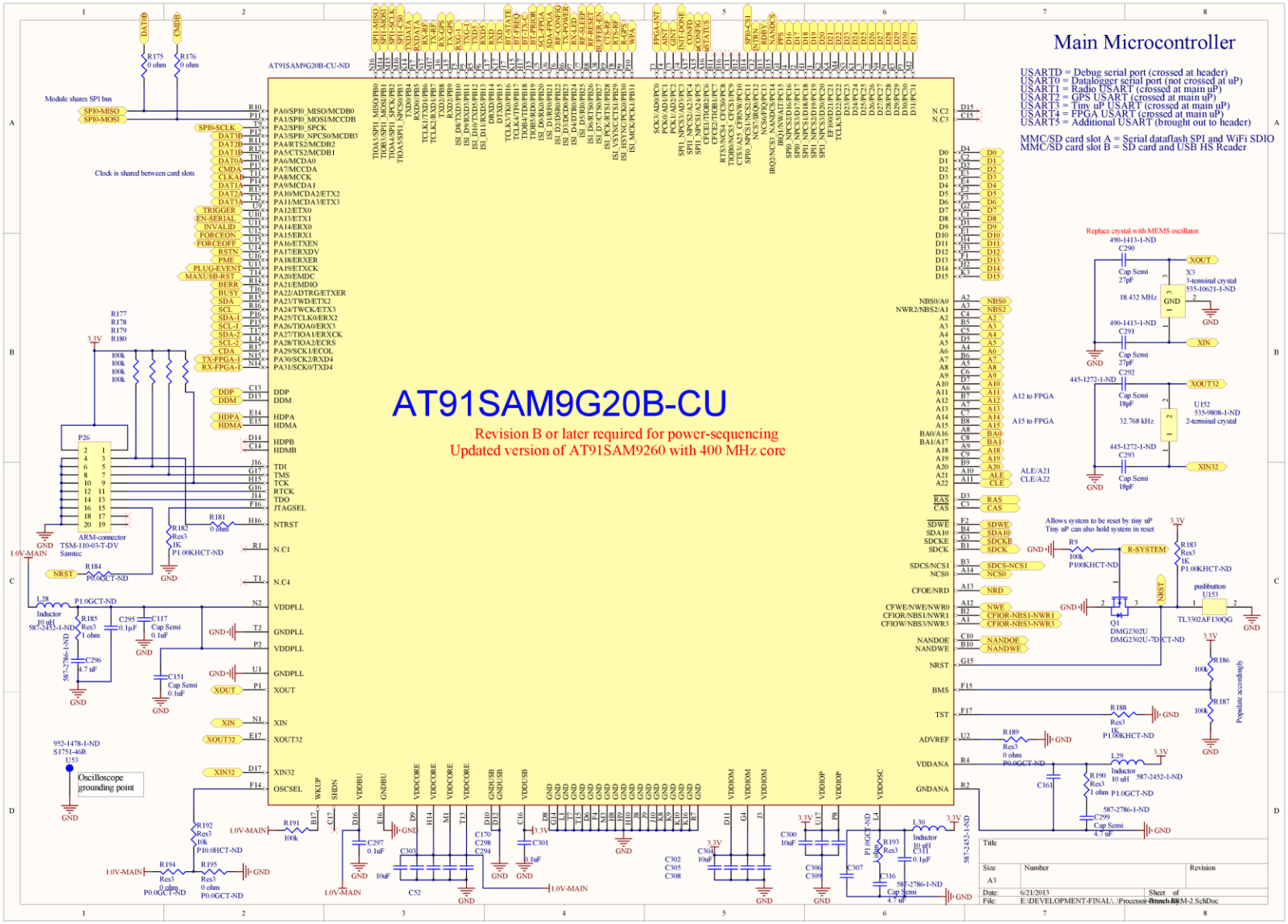
Main Microcontroller
USARTD = Debug serial port (crossed at header)
USART0 = Datalogger serial port (not crossed at uP)
USART1 = Radio USART (crossed at main uP)
USART2 = GPS USART (crossed at main uP)
USART3 = Tiny uP USART (crossed at main uP)
USART4 = FPGA USART (crossed at main uP)
USART5 = Additional USART (brought out to header)
MMC/SD card slot A = Serial dataflash SPI and WiFi SDIO
MMC/SD card slot B = SD card and USB HS Reader
AT91SAM9G20B-CU
Revision B or later required for power-sequencing
Updated version of AT91SAM9260 with 400 MHz core
AT91SAM9G20B-CU-ND
Module shares SPI bus
Clock is shared between card slots
Replace crystal with MEMS oscillator
Allows system to be reset by tiny uP
Tiny uP can also hold system in reset
Oscilloscope grounding point
ARM-connector
TSM-110-03-T-DV
Samtec
Populate accordingly
Title
Size
Number
Revision
Date: 6/21/2013
Sheet of
File: E:\DEVELOPMENT-FINAL\...\Processor-Board-SAM-2.SchDoc

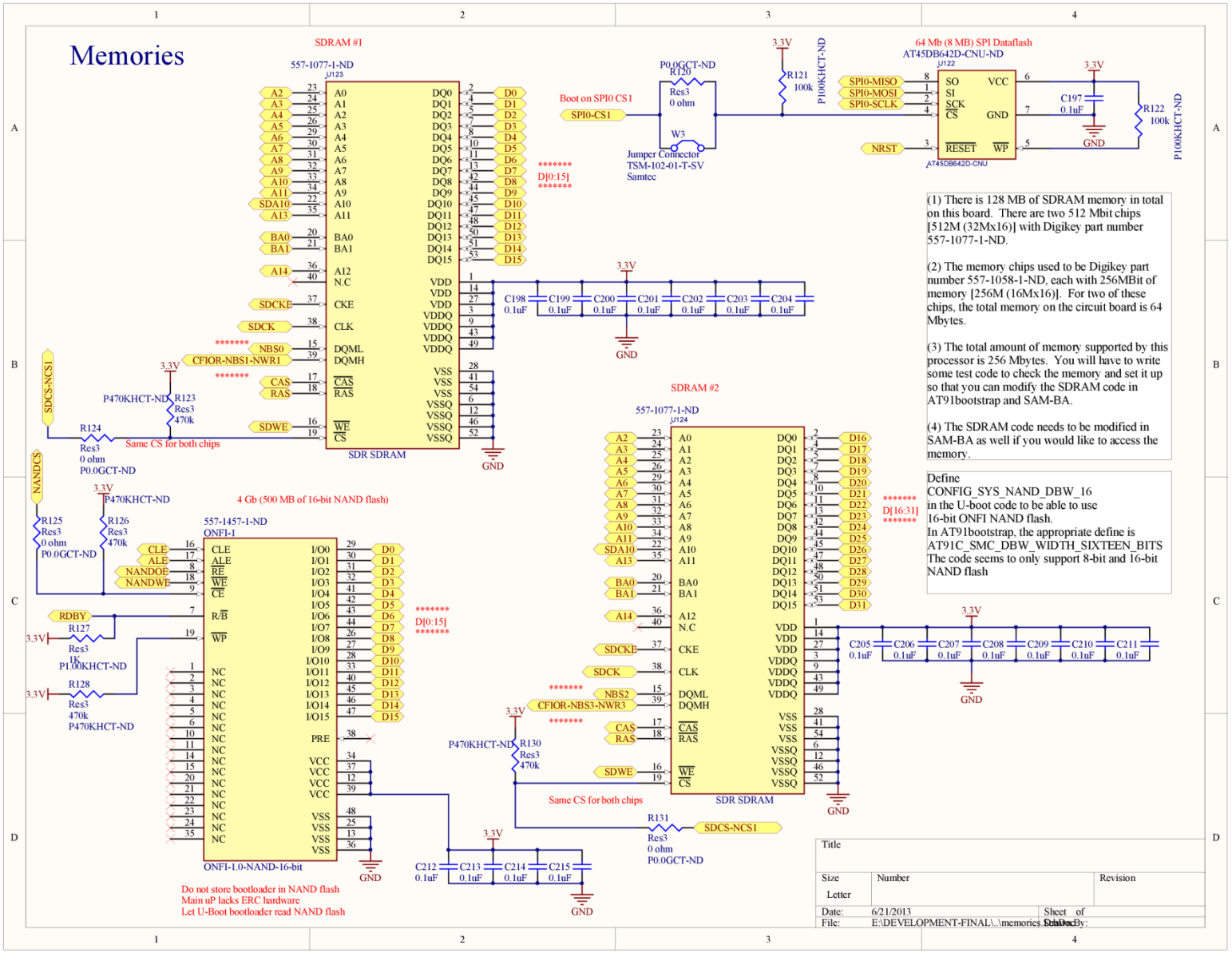
Memories
SDRAM #1
557-1077-1-ND
U123
SDR SDRAM
Boot on SPI0 CS1
SPI0-CS1
P0.0GCT-ND
R120
Res3
0 ohm
Jumper Connector
TSM-102-01-T-SV
Samtec
R121
100k
P100KHCT-ND
64 Mb (8 MB) SPI Dataflash
AT45DB642D-CNU-ND
U122
AT45DB642D-CNU
SPI0-MISO
SPI0-MOSI
SPI0-SCLK
NRST
C197
0.1uF
R122
100k
D[0:15]
SDCKE
SDCK
NBS0
CFIOR-NBS1-NWR1
CAS
RAS
SDWE
SDCS-NCS1
R123
P470KHCT-ND
R124
Same CS for both chips
C198
C199
C200
C201
C202
C203
C204
0.1uF
3.3V
GND
(1) There is 128 MB of SDRAM memory in total on this board. There are two 512 Mbit chips [512M (32Mx16)] with Digikey part number 557-1077-1-ND.
(2) The memory chips used to be Digikey part number 557-1058-1-ND, each with 256MBit of memory [256M (16Mx16)]. For two of these chips, the total memory on the circuit board is 64 Mbytes.
(3) The total amount of memory supported by this processor is 256 Mbytes. You will have to write some test code to check the memory and set it up so that you can modify the SDRAM code in AT91bootstrap and SAM-BA.
(4) The SDRAM code needs to be modified in SAM-BA as well if you would like to access the memory.
SDRAM #2
557-1077-1-ND
U124
D[16:31]
NANDCS
R125
R126
P0.0GCT-ND
4 Gb (500 MB of 16-bit NAND flash)
557-1457-1-ND
ONFI-1
ONFI-1.0-NAND-16-bit
CLE
ALE
NANDOE
NANDWE
RDBY
R127
1K
P100KHCT-ND
R128
470k
P470KHCT-ND
PRE
R/B
WP
Define
CONFIG_SYS_NAND_DBW_16
in the U-boot code to be able to use
16-bit ONFI NAND flash.
In AT91bootstrap, the appropriate define is
AT91C_SMC_DBW_WIDTH_SIXTEEN_BITS
The code seems to only support 8-bit and 16-bit
NAND flash
R130
R131
C205
C206
C207
C208
C209
C210
C211
C212
C213
C214
C215
Do not store bootloader in NAND flash
Main uP lacks ERC hardware
Let U-Boot bootloader read NAND flash
Title
Size
Letter
Number
Revision
Date: 6/21/2013
Sheet of
File: E:\DEVELOPMENT-FINAL\..\memories.SchDoc
Drawn By:

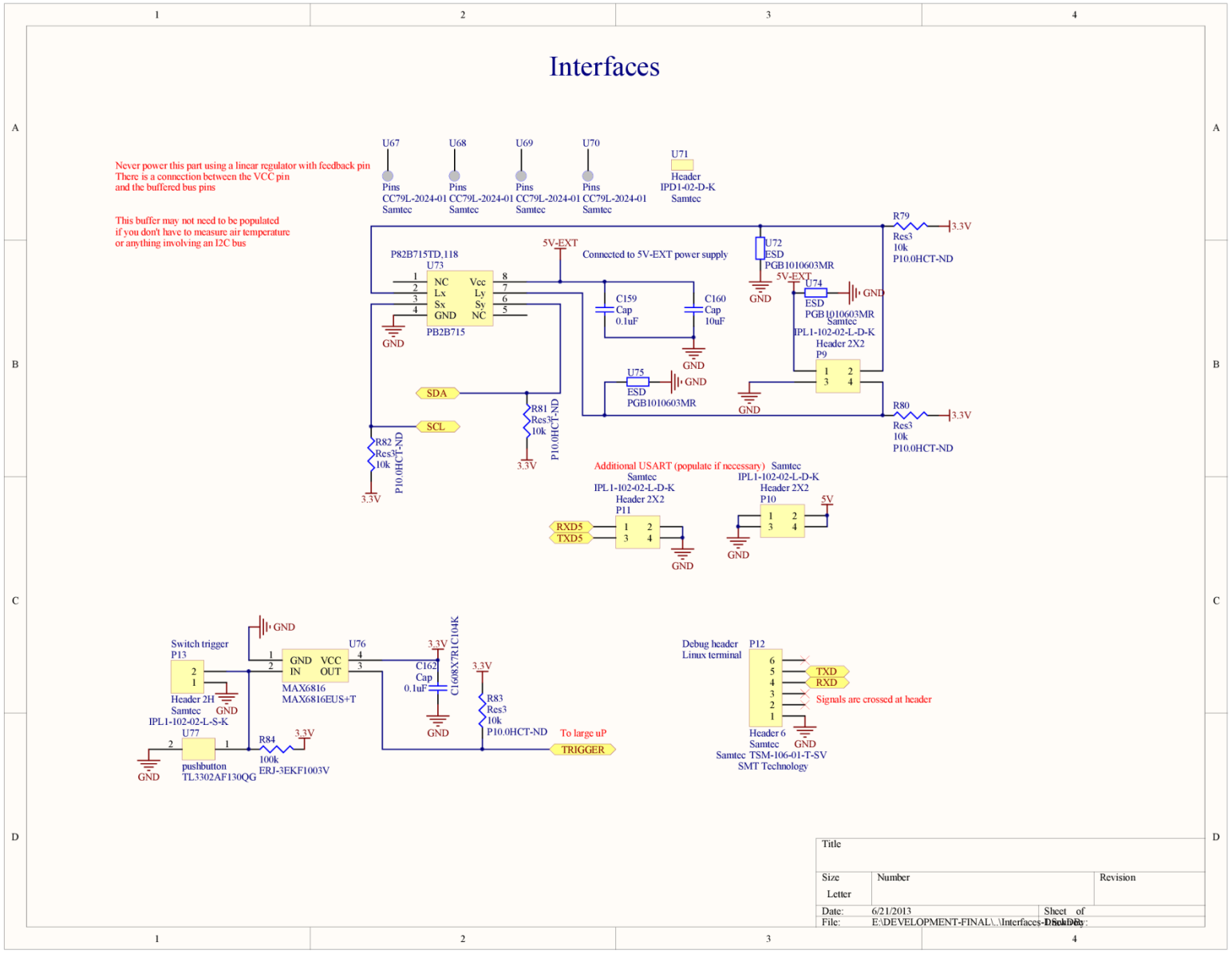
Interfaces
Never power this part using a linear regulator with feedback pin
There is a connection between the VCC pin
and the buffered bus pins
This buffer may not need to be populated
if you don't have to measure air temperature
or anything involving an I2C bus
U67
U68
U69
U70
U71
Pins
CC79L-2024-01
Samtec
Header
IPD1-02-D-K
Samtec
P82B715TD,118
U73
NC
Lx
Sx
GND
Vcc
Ly
Sy
NC
PB2B715
5V-EXT
Connected to 5V-EXT power supply
C159
Cap
0.1uF
C160
Cap
10uF
U72
ESD
PGB1010603MR
U74
U75
R79
Res3
10k
P10.0HCT-ND
3.3V
GND
SDA
SCL
R81
R82
R80
P9
Samtec
IPL1-102-02-L-D-K
Header 2X2
Additional USART (populate if necessary)
P11
P10
RXD5
TXD5
5V
Switch trigger
P13
Header 2H
IPL1-102-02-L-S-K
U76
GND
VCC
IN
OUT
MAX6816
MAX6816EUS+T
C162
Cap
0.1uF
C1608X7R1C104K
R83
Res3
10k
P10.0HCT-ND
To large uP
TRIGGER
U77
pushbutton
TL3302AF130QG
R84
100k
ERJ-3EKF1003V
Debug header
Linux terminal
P12
TXD
RXD
Signals are crossed at header
Header 6
Samtec TSM-106-01-T-SV
SMT Technology
Title
Size
Letter
Number
Revision
Date:
6/21/2013
Sheet of
File:
E:\DEVELOPMENT-FINAL\..\Interfaces-Final.Dd
Drawn By:

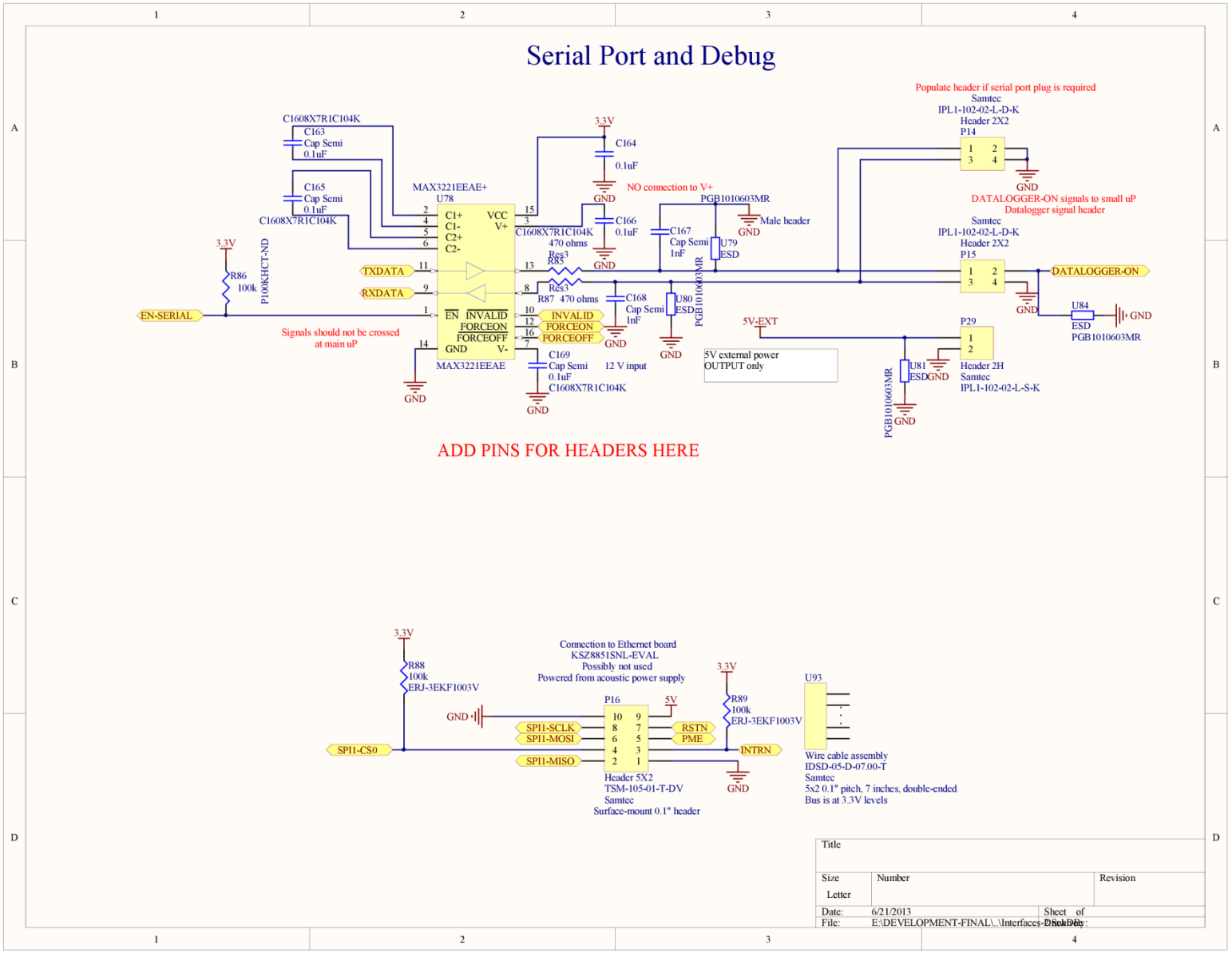
Serial Port and Debug
Populate header if serial port plug is required
Samtec
IPL1-102-02-L-D-K
Header 2X2
P14
C1608X7R1C104K
C163
Cap Semi
0.1uF
C165
Cap Semi
0.1uF
C1608X7R1C104K
3.3V
C164
0.1uF
GND
NO connection to V+
MAX3221IEAE+
U78
C1+
C1-
C2+
C2-
VCC
V+
C1608X7R1C104K
C166
0.1uF
470 ohms
Res3
R85
PGB1010603MR
Male header
C167
Cap Semi
1nF
U79
ESD
DATALOGGER-ON signals to small uP
Datalogger signal header
Samtec
IPL1-102-02-L-D-K
Header 2X2
P15
DATALOGGER-ON
3.3V
R86
100k
P100KHCT-ND
TXDATA
RXDATA
EN-SERIAL
Res3
R87 470 ohms
C168
Cap Semi
1nF
U80
ESD
PGB1010603MR
U84
ESD
PGB1010603MR
EN
INVALID
FORCEON
FORCEOFF
GND
V-
MAX3221IEAE
Signals should not be crossed
at main uP
C169
Cap Semi
0.1uF
C1608X7R1C104K
12 V input
5V-EXT
P29
Header 2H
Samtec
IPL1-102-02-L-S-K
5V external power
OUTPUT only
U81
ESD
PGB1010603MR
ADD PINS FOR HEADERS HERE
3.3V
R88
100k
ERJ-3EKF1003V
Connection to Ethernet board
KSZ8851SNL-EVAL
Possibly not used
Powered from acoustic power supply
P16
5V
SPI1-SCLK
SPI1-MOSI
SPI1-MISO
SPI1-CS0
RSTN
PME
INTRN
R89
100k
ERJ-3EKF1003V
U93
Header 5X2
TSM-105-01-T-DV
Samtec
Surface-mount 0.1" header
Wire cable assembly
IDSD-05-D-07.00-T
Samtec
5x2 0.1" pitch, 7 inches, double-ended
Bus is at 3.3V levels
Title
Size
Letter
Number
Revision
Date:
6/21/2013
Sheet of
File:
E:\DEVELOPMENT-FINAL\..\Interfaces-Debug.DDB
Drawn By:

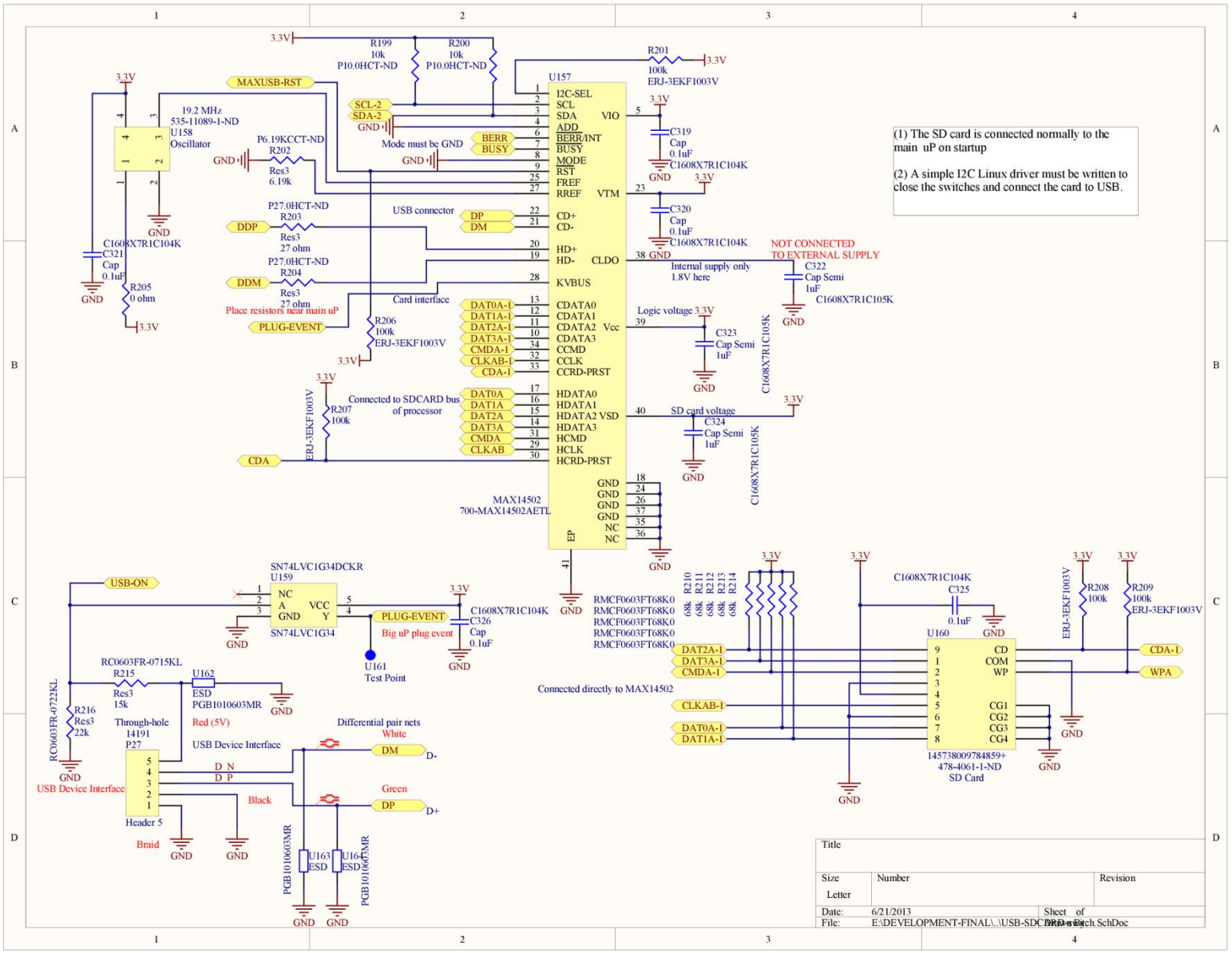
(1) The SD card is connected normally to the main uP on startup
(2) A simple I2C Linux driver must be written to close the switches and connect the card to USB.
MAX14502
700-MAX14502AETL
U157
SN74LVC1G34DCKR
U159
SN74LVC1G34
U160
SD Card
U161
Test Point
U162
U163
U164
U158
Oscillator
19.2 MHz
535-11089-1-ND
Connected directly to MAX14502
Connected to SDCARD bus of processor
Card interface
USB connector
Logic voltage 3.3V
SD card voltage
Internal supply only 1.8V here
NOT CONNECTED TO EXTERNAL SUPPLY
Mode must be GND
Place resistors near main uP
Big uP plug event
USB Device Interface
Differential pair nets
Through-hole 14191
Header 5
Braid
Red (5V)
White
Green
Black
Title
Size Letter
Number
Revision
Date: 6/21/2013
Sheet of
File: E:\DEVELOPMENT-FINAL\..\USB-SDCARD-Rev3.SchDoc

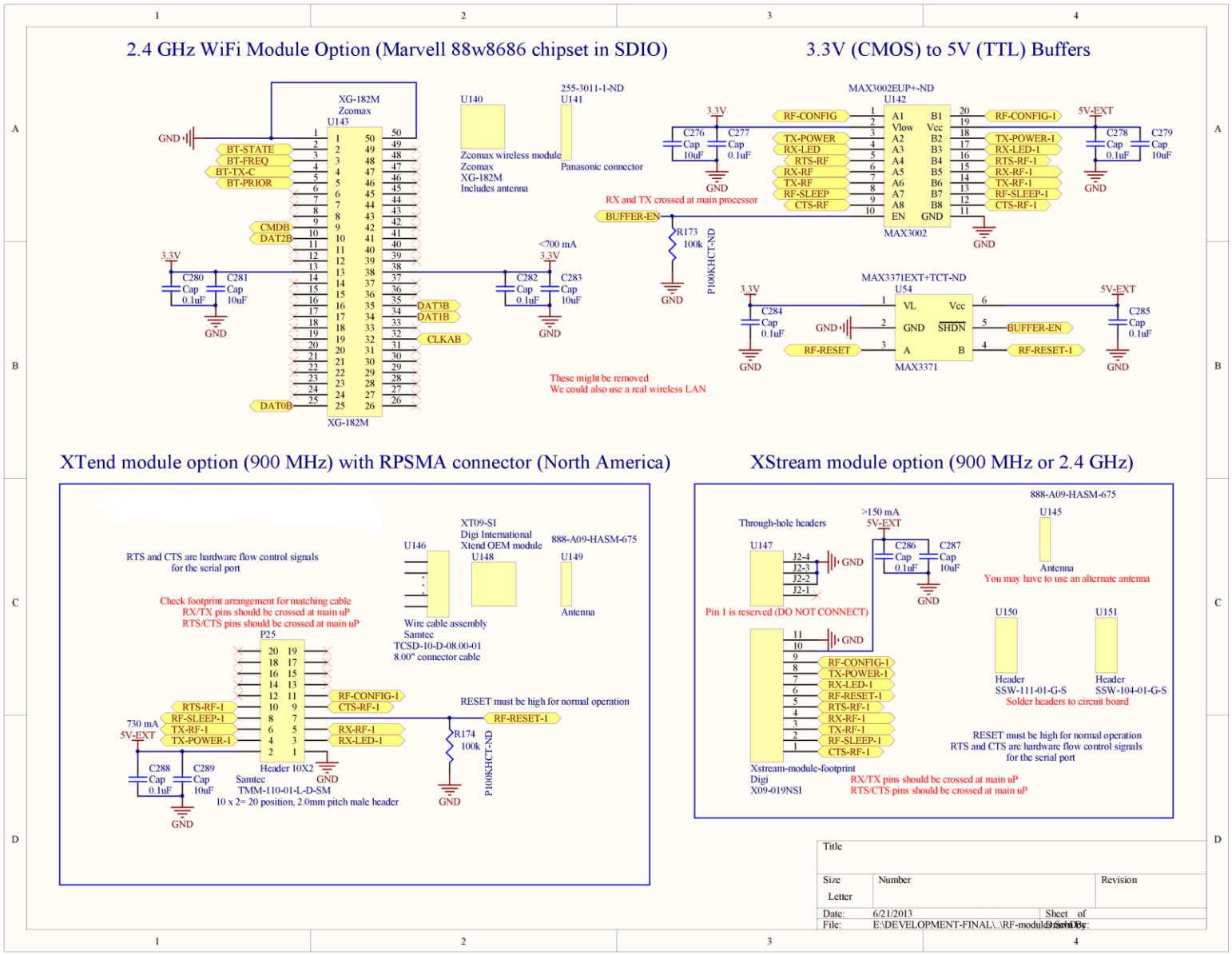
2.4 GHz WiFi Module Option (Marvell 88w8686 chipset in SDIO)
3.3V (CMOS) to 5V (TTL) Buffers
XG-182M
Zcomax
U143
GND
BT-STATE
BT-FREQ
BT-TX-C
BT-PRIOR
CMDB
DAT2B
DAT3B
DAT1B
CLKAB
DAT0B
XG-182M
U140
Zcomax wireless module
Zcomax
XG-182M
Includes antenna
255-3011-1-ND
U141
Panasonic connector
3.3V
C280
Cap
0.1uF
C281
Cap
10uF
<700 mA
C282
Cap
0.1uF
C283
Cap
10uF
MAX3002EUP+-ND
U142
RF-CONFIG
TX-POWER
RX-LED
RX-RF
TX-RF
RF-SLEEP
CTS-RF
RF-CONFIG-1
TX-POWER-1
RX-LED-1
RTS-RF-1
RX-RF-1
TX-RF-1
RF-SLEEP-1
CTS-RF-1
A1
Vlow
A2
A3
A4
A5
A6
A7
A8
EN
B1
Vcc
B2
B3
B4
B5
B6
B7
B8
GND
MAX3002
C276
Cap
10uF
C277
Cap
0.1uF
5V-EXT
C278
Cap
0.1uF
C279
Cap
10uF
RX and TX crossed at main processor
BUFFER-EN
R173
100k
P100KCHCT-ND
MAX3371EXT+TCT-ND
U54
VL
GND
RF-RESET
Vcc
SHDN
A
B
MAX3371
C284
Cap
0.1uF
C285
Cap
0.1uF
BUFFER-EN
RF-RESET-1
These might be removed
We could also use a real wireless LAN
XTend module option (900 MHz) with RPSMA connector (North America)
XStream module option (900 MHz or 2.4 GHz)
RTS and CTS are hardware flow control signals
for the serial port
Check footprint arrangement for matching cable
RX/TX pins should be crossed at main uP
RTS/CTS pins should be crossed at main uP
P25
RTS-RF-1
RF-SLEEP-1
TX-RF-1
TX-POWER-1
RF-CONFIG-1
CTS-RF-1
RX-RF-1
RX-LED-1
730 mA
5V-EXT
C288
Cap
0.1uF
C289
Cap
10uF
Header 10X2
Samtec
TMM-110-01-L-D-SM
10 x 2= 20 position, 2.0mm pitch male header
XT09-SI
Digi International
Xtend OEM module
U146
U148
888-A09-HASM-675
U149
Antenna
Wire cable assembly
Samtec
TCSD-10-D-08.00-01
8.00" connector cable
RESET must be high for normal operation
RF-RESET-1
R174
100k
P100KCHCT-ND
Through-hole headers
>150 mA
5V-EXT
U147
J2-4
J2-3
J2-2
J2-1
C286
Cap
0.1uF
C287
Cap
10uF
888-A09-HASM-675
U145
Antenna
You may have to use an alternate antenna
Pin 1 is reserved (DO NOT CONNECT)
U150
U151
Header
SSW-111-01-G-S
Header
SSW-104-01-G-S
Solder headers to circuit board
RESET must be high for normal operation
RTS and CTS are hardware flow control signals
for the serial port
Xstream-module-footprint
Digi
X09-019NSI
RX/TX pins should be crossed at main uP
RTS/CTS pins should be crossed at main uP
Title
Size
Letter
Number
Revision
Date:
6/21/2013
Sheet of
File:
E:\DEVELOPMENT-FINAL\..\RF-module.SchDoc

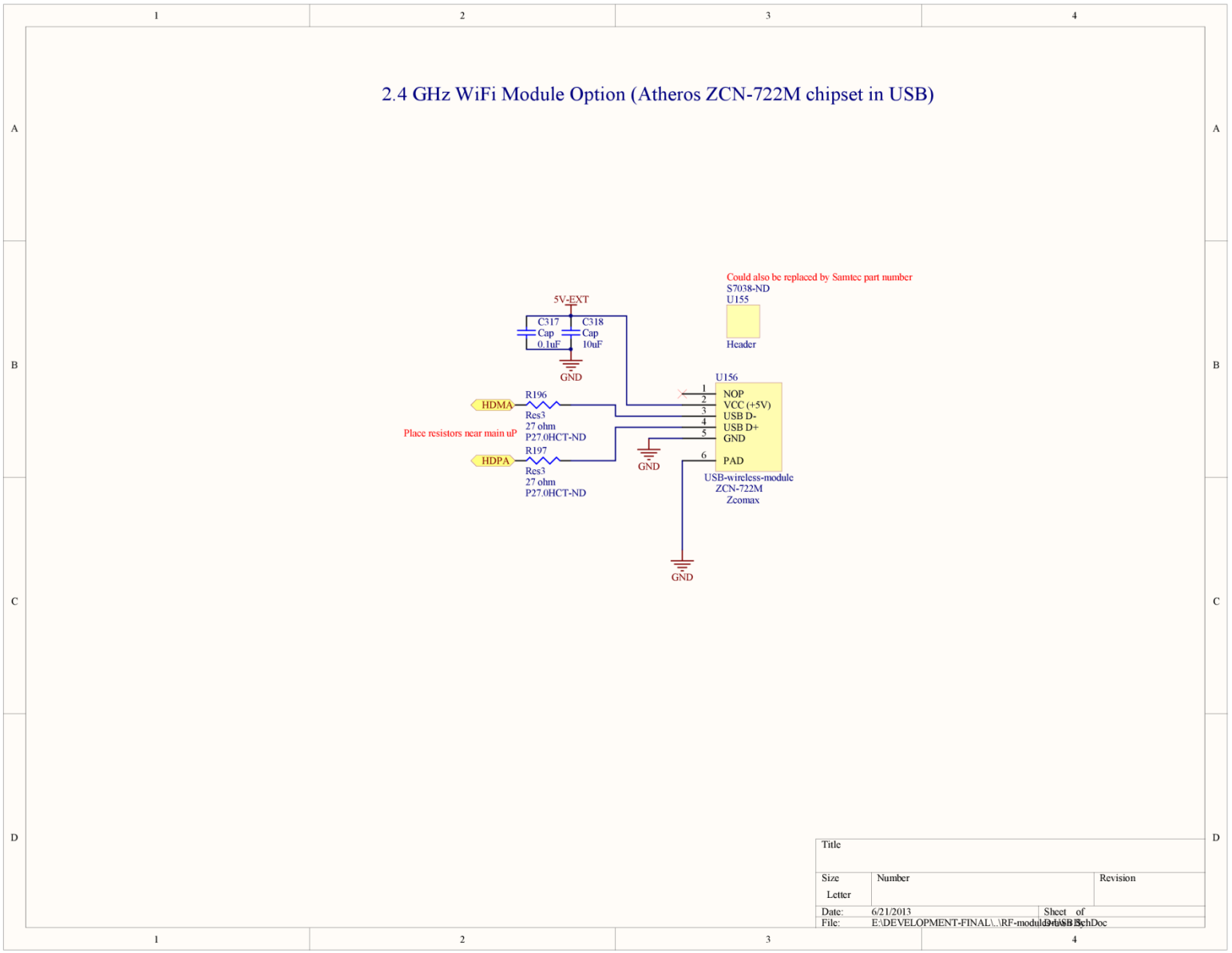
2.4 GHz WiFi Module Option (Atheros ZCN-722M chipset in USB)
Could also be replaced by Samtec part number
S7038-ND
U155
Header
5V-EXT
C317
Cap
0.1uF
C318
Cap
10uF
GND
U156
HDMA
R196
Res3
27 ohm
P27.0HCT-ND
Place resistors near main uP
HDPA
R197
Res3
27 ohm
P27.0HCT-ND
1 NOP
2 VCC (+5V)
3 USB D-
4 USB D+
5 GND
6 PAD
GND
GND
USB-wireless-module
ZCN-722M
Zcomax
Title
Size
Letter
Number
Revision
Date: 6/21/2013
Sheet of
File: E:\DEVELOPMENT-FINAL\..\RF-module-Atheros.SchDoc

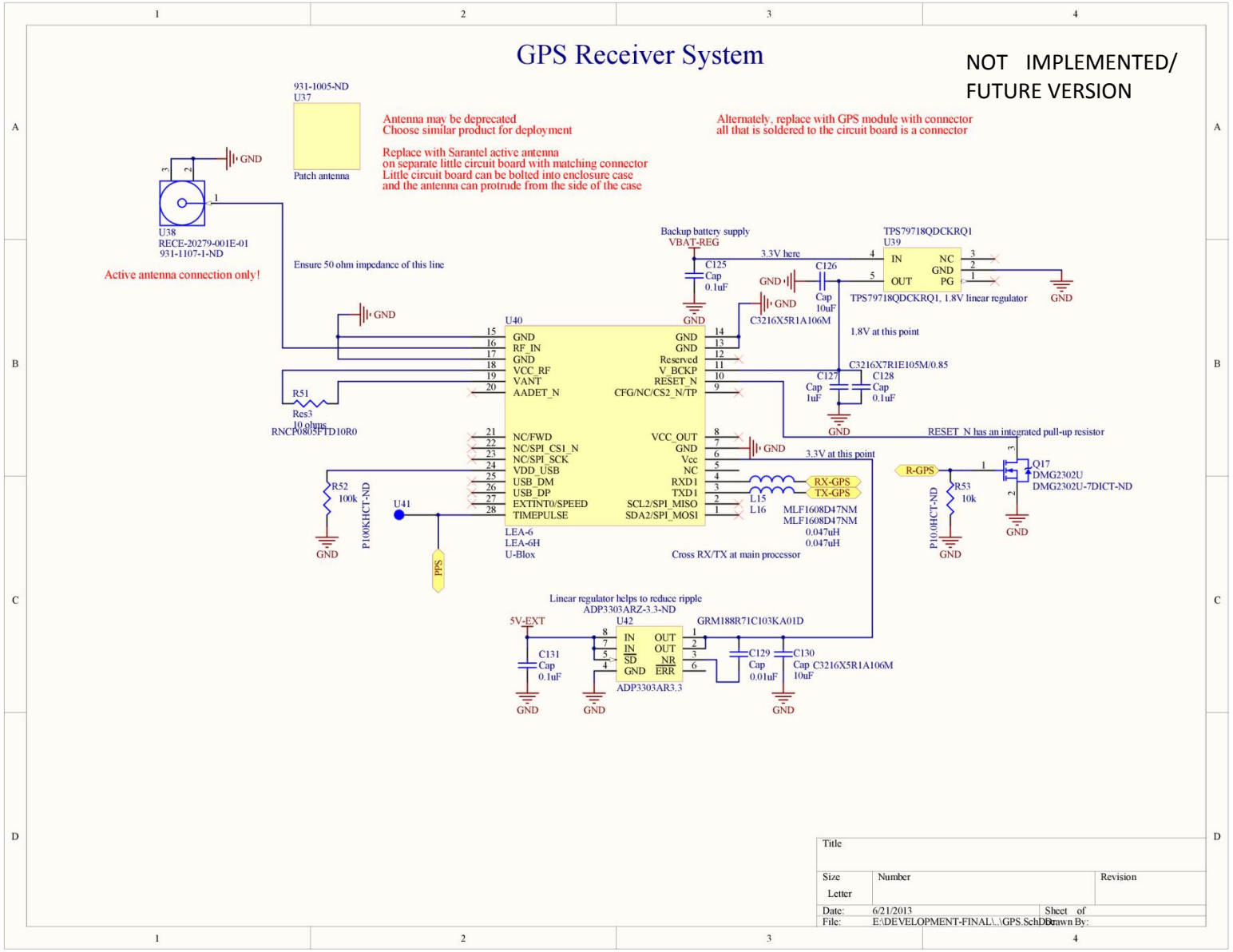
GPS Receiver System
NOT IMPLEMENTED/
FUTURE VERSION
931-1005-ND
U37
Patch antenna
Antenna may be deprecated
Choose similar product for deployment
Replace with Sarantel active antenna
on separate little circuit board with matching connector
Little circuit board can be bolted into enclosure case
and the antenna can protrude from the side of the case
Alternately, replace with GPS module with connector
all that is soldered to the circuit board is a connector
U38
RECE-20279-001E-01
931-1107-1-ND
Active antenna connection only!
Ensure 50 ohm impedance of this line
Backup battery supply
VBAT-REG
TPS79718QDCKRQ1
U39
3.3V here
C125
Cap
0.1uF
C126
Cap
10uF
C3216X5R1A106M
TPS79718QDCKRQ1, 1.8V linear regulator
1.8V at this point
C3216X7R1E105M/0.85
C127
Cap
1uF
C128
Cap
0.1uF
U40
LEA-6
LEA-6H
U-Blox
R51
Res3
10 ohms
RNCP0805FTD10R0
R52
100k
P100KHCT-ND
U41
PPS
RESET_N has an integrated pull-up resistor
3.3V at this point
R-GPS
Q17
DMG2302U
DMG2302U-7DICT-ND
R53
10k
P10.0HCT-ND
RX-GPS
TX-GPS
L15
L16
MLF1608D47NM
MLF1608D47NM
0.047uH
0.047uH
Cross RX/TX at main processor
Linear regulator helps to reduce ripple
ADP3303ARZ-3.3-ND
5V-EXT
U42
ADP3303AR3.3
GRM188R71C103KA01D
C131
Cap
0.1uF
C129
Cap
0.01uF
C130
Cap
10uF
C3216X5R1A106M
Title
Size
Letter
Number
Revision
Date:
6/21/2013
Sheet of
File:
E:\DEVELOPMENT-FINAL\..\GPS.SchDoc
Drawn By:

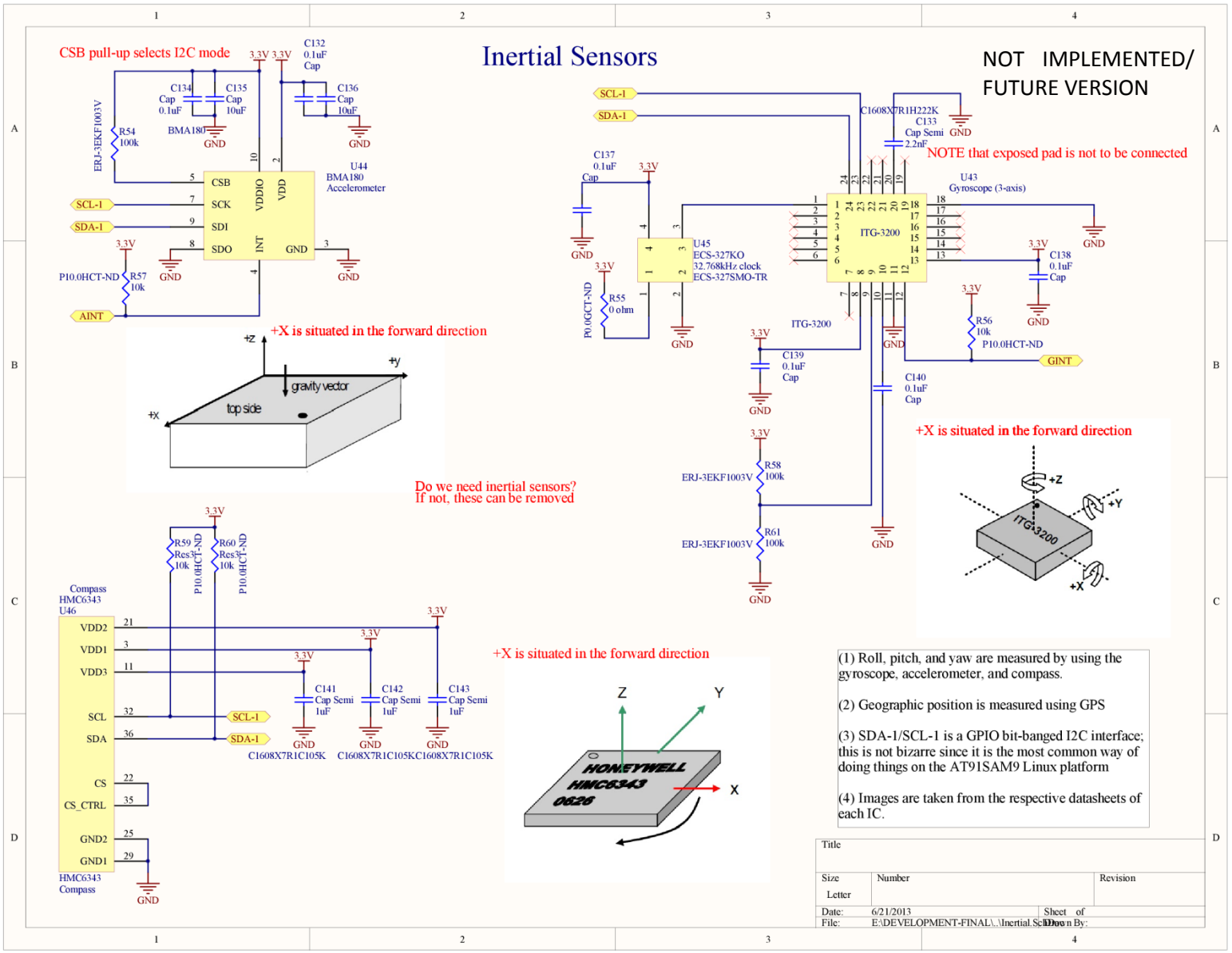
Inertial Sensors
NOT IMPLEMENTED/
FUTURE VERSION
CSB pull-up selects I2C mode
BMA180
Accelerometer
NOTE that exposed pad is not to be connected
ITG-3200
Gyroscope (3-axis)
+X is situated in the forward direction
gravity vector
top side
Do we need inertial sensors?
If not, these can be removed
Compass
HMC6343
HONEYWELL
HMC6343
0628
(1) Roll, pitch, and yaw are measured by using the gyroscope, accelerometer, and compass.
(2) Geographic position is measured using GPS
(3) SDA-1/SCL-1 is a GPIO bit-banged I2C interface; this is not bizarre since it is the most common way of doing things on the AT91SAM9 Linux platform
(4) Images are taken from the respective datasheets of each IC.
Title
Size
Letter
Number
Revision
Date: 6/21/2013
File: E:\DEVELOPMENT-FINAL\..\Inertial.SchDoc
Sheet of
Drawn By:

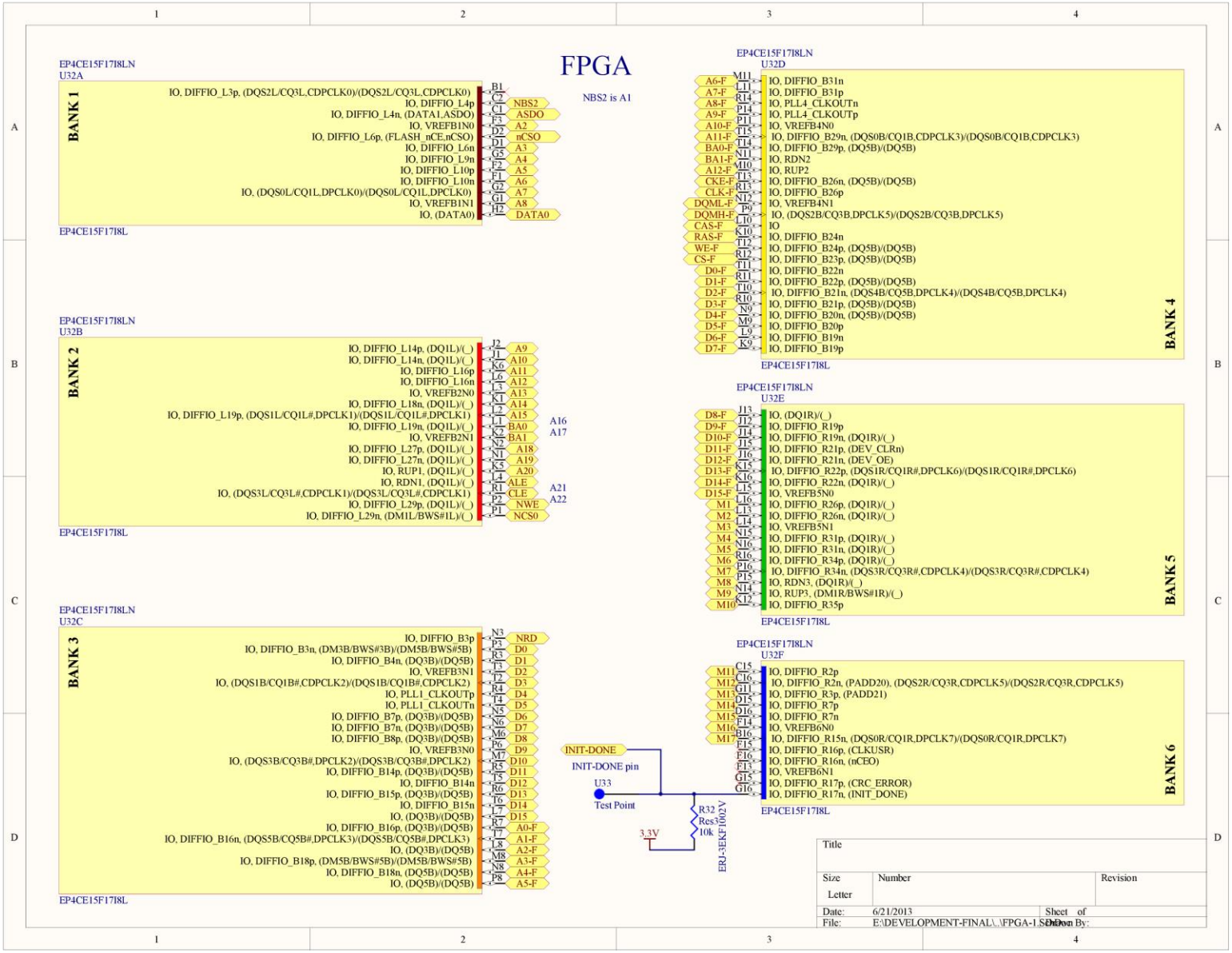
FPGA
NBS2 is A1
EP4CE15F17I8LN
U32A
BANK 1
IO, DIFFIO_L3p, (DQS2L/CQ3L,CDPCLK0)/(DQS2L/CQ3L,CDPCLK0)
IO, DIFFIO_L4p
IO, DIFFIO_L4n, (DATA1,ASDO)
IO, VREFB1N0
IO, DIFFIO_L6p, (FLASH_nCE,nCSO)
IO, DIFFIO_L6n
IO, DIFFIO_L9n
IO, DIFFIO_L10p
IO, DIFFIO_L10n
IO, (DQS0L/CQ1L,DPCLK0)/(DQS0L/CQ1L,DPCLK0)
IO, VREFB1N1
IO, (DATA0)
NBS2
ASDO
A2
nCSO
A3
A4
A5
A6
A7
A8
DATA0
EP4CE15F17I8L
EP4CE15F17I8LN
U32B
BANK 2
IO, DIFFIO_L14p, (DQ1L)/(_)
IO, DIFFIO_L14n, (DQ1L)/(_)
IO, DIFFIO_L16p
IO, DIFFIO_L16n
IO, VREFB2N0
IO, DIFFIO_L18n, (DQ1L)/(_)
IO, DIFFIO_L19p, (DQS1L/CQ1L#,DPCLK1)/(DQS1L/CQ1L#,DPCLK1)
IO, DIFFIO_L19n, (DQ1L)/(_)
IO, VREFB2N1
IO, DIFFIO_L27p, (DQ1L)/(_)
IO, DIFFIO_L27n, (DQ1L)/(_)
IO, RUP1, (DQ1L)/(_)
IO, RDN1, (DQ1L)/(_)
IO, (DQS3L/CQ3L#,CDPCLK1)/(DQS3L/CQ3L#,CDPCLK1)
IO, DIFFIO_L29p, (DQ1L)/(_)
IO, DIFFIO_L29n, (DM1L/BWS#1L)/(_)
A9
A10
A11
A12
A13
A14
A15
A16
A17
A18
A19
A20
A21
A22
NWE
NCS0
EP4CE15F17I8L
EP4CE15F17I8LN
U32C
BANK 3
IO, DIFFIO_B3p
IO, DIFFIO_B3n, (DM3B/BWS#3B)/(DM5B/BWS#5B)
IO, DIFFIO_B4n, (DQ3B)/(DQ5B)
IO, VREFB3N1
IO, (DQS1B/CQ1B#,CDPCLK2)/(DQS1B/CQ1B#,CDPCLK2)
IO, PLL1_CLKOUTp
IO, PLL1_CLKOUTn
IO, DIFFIO_B7p, (DQ3B)/(DQ5B)
IO, DIFFIO_B7n, (DQ3B)/(DQ5B)
IO, DIFFIO_B8p, (DQ3B)/(DQ5B)
IO, VREFB3N0
IO, (DQS3B/CQ3B#,DPCLK2)/(DQS3B/CQ3B#,DPCLK2)
IO, DIFFIO_B14p, (DQ3B)/(DQ5B)
IO, DIFFIO_B14n
IO, DIFFIO_B15p, (DQ3B)/(DQ5B)
IO, DIFFIO_B15n
IO, (DQ3B)/(DQ5B)
IO, DIFFIO_B16p, (DQ3B)/(DQ5B)
IO, DIFFIO_B16n, (DQS5B/CQ5B#,DPCLK3)/(DQS5B/CQ5B#,DPCLK3)
IO, (DQ3B)/(DQ5B)
IO, DIFFIO_B18p, (DM5B/BWS#5B)/(DM5B/BWS#5B)
IO, DIFFIO_B18n, (DQ5B)/(DQ5B)
IO, (DQ5B)/(DQ5B)
NRD
D0
D1
D2
D3
D4
D5
D6
D7
D8
D9
D10
D11
D12
D13
D14
D15
A0-F
A1-F
A2-F
A3-F
A4-F
A5-F
EP4CE15F17I8L
INIT-DONE
INIT-DONE pin
U33
Test Point
3.3V
R32
Res1
10k
ERJ-3EKF1002V
EP4CE15F17I8LN
U32D
BANK 4
A6-F
A7-F
A8-F
A9-F
A10-F
A11-F
BA0-F
BA1-F
A12-F
CKE-F
CLK-F
DQML-F
DQMH-F
CAS-F
RAS-F
WE-F
CS-F
D0-F
D1-F
D2-F
D3-F
D4-F
D5-F
D6-F
D7-F
IO, DIFFIO_B31n
IO, DIFFIO_B31p
IO, PLL4_CLKOUTn
IO, PLL4_CLKOUTp
IO, VREFB4N0
IO, DIFFIO_B29n, (DQS0B/CQ1B,CDPCLK3)/(DQS0B/CQ1B,CDPCLK3)
IO, DIFFIO_B29p, (DQ5B)/(DQ5B)
IO, RDN2
IO, RUP2
IO, DIFFIO_B26n, (DQ5B)/(DQ5B)
IO, DIFFIO_B26p
IO, VREFB4N1
IO, (DQS2B/CQ3B,DPCLK5)/(DQS2B/CQ3B,DPCLK5)
IO
IO, DIFFIO_B24n
IO, DIFFIO_B24p, (DQ5B)/(DQ5B)
IO, DIFFIO_B23p, (DQ5B)/(DQ5B)
IO, DIFFIO_B22n
IO, DIFFIO_B22p, (DQ5B)/(DQ5B)
IO, DIFFIO_B21n, (DQS4B/CQ5B,DPCLK4)/(DQS4B/CQ5B,DPCLK4)
IO, DIFFIO_B21p, (DQ5B)/(DQ5B)
IO, DIFFIO_B20n, (DQ5B)/(DQ5B)
IO, DIFFIO_B20p
IO, DIFFIO_B19n
IO, DIFFIO_B19p
EP4CE15F17I8L
EP4CE15F17I8LN
U32E
BANK 5
D8-F
D9-F
D10-F
D11-F
D12-F
D13-F
D14-F
D15-F
M1
M2
M3
M4
M5
M6
M7
M8
M9
M10
IO, (DQ1R)/(_)
IO, DIFFIO_R19p
IO, DIFFIO_R19n, (DQ1R)/(_)
IO, DIFFIO_R21p, (DEV_CLRn)
IO, DIFFIO_R21n, (DEV_OE)
IO, DIFFIO_R22p, (DQS1R/CQ1R#,DPCLK6)/(DQS1R/CQ1R#,DPCLK6)
IO, DIFFIO_R22n, (DQ1R)/(_)
IO, VREFB5N0
IO, DIFFIO_R26p, (DQ1R)/(_)
IO, DIFFIO_R26n, (DQ1R)/(_)
IO, VREFB5N1
IO, DIFFIO_R31p, (DQ1R)/(_)
IO, DIFFIO_R31n, (DQ1R)/(_)
IO, DIFFIO_R34p, (DQ1R)/(_)
IO, DIFFIO_R34n, (DQS3R/CQ3R#,CDPCLK4)/(DQS3R/CQ3R#,CDPCLK4)
IO, RDN3, (DQ1R)/(_)
IO, RUP3, (DM1R/BWS#1R)/(_)
IO, DIFFIO_R35p
EP4CE15F17I8L
EP4CE15F17I8LN
U32F
BANK 6
M11
M12
M13
M14
M15
M16
M17
IO, DIFFIO_R2p
IO, DIFFIO_R2n, (PADD20), (DQS2R/CQ3R,CDPCLK5)/(DQS2R/CQ3R,CDPCLK5)
IO, DIFFIO_R3p, (PADD21)
IO, DIFFIO_R7p
IO, DIFFIO_R7n
IO, VREFB6N0
IO, DIFFIO_R15n, (DQS0R/CQ1R,DPCLK7)/(DQS0R/CQ1R,DPCLK7)
IO, DIFFIO_R16p, (CLKUSR)
IO, DIFFIO_R16n, (nCEO)
IO, VREFB6N1
IO, DIFFIO_R17p, (CRC_ERROR)
IO, DIFFIO_R17n, (INIT_DONE)
EP4CE15F17I8L
Title
Size
Letter
Number
Revision
Date: 6/21/2013
Sheet of
File: E:\DEVELOPMENT-FINAL\..\FPGA-1.SchDoc
Drawn By:

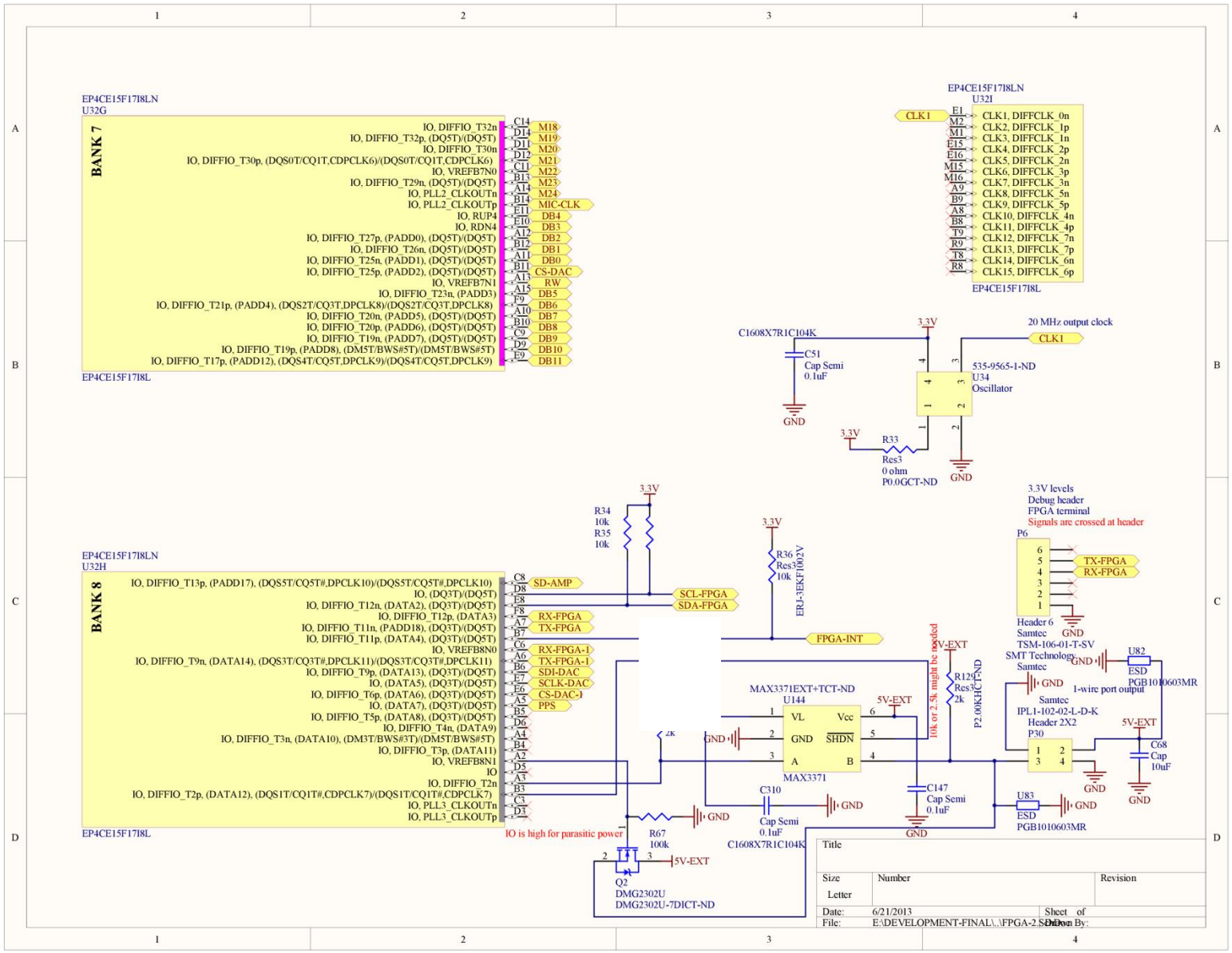
EP4CE15F17I8LN
U32G
BANK 7
IO, DIFFIO_T32n
IO, DIFFIO_T32p, (DQ5T)/(DQ5T)
IO, DIFFIO_T30n
IO, DIFFIO_T30p, (DQS0T/CQ1T,CDPCLK6)/(DQS0T/CQ1T,CDPCLK6)
IO, VREFB7N0
IO, DIFFIO_T29n, (DQ5T)/(DQ5T)
IO, PLL2_CLKOUTn
IO, PLL2_CLKOUTp
IO, RUP4
IO, RDN4
IO, DIFFIO_T27p, (PADD0), (DQ5T)/(DQ5T)
IO, DIFFIO_T26n, (DQ5T)/(DQ5T)
IO, DIFFIO_T25n, (PADD1), (DQ5T)/(DQ5T)
IO, DIFFIO_T25p, (PADD2), (DQ5T)/(DQ5T)
IO, VREFB7N1
IO, DIFFIO_T23n, (PADD3)
IO, DIFFIO_T21p, (PADD4), (DQS2T/CQ3T,DPCLK8)/(DQS2T/CQ3T,DPCLK8)
IO, DIFFIO_T20n, (PADD5), (DQ5T)/(DQ5T)
IO, DIFFIO_T20p, (PADD6), (DQ5T)/(DQ5T)
IO, DIFFIO_T19n, (PADD7), (DQ5T)/(DQ5T)
IO, DIFFIO_T19p, (PADD8), (DM5T/BWS#5T)/(DM5T/BWS#5T)
IO, DIFFIO_T17p, (PADD12), (DQS4T/CQ5T,DPCLK9)/(DQS4T/CQ5T,DPCLK9)
MIC-CLK
DB4
DB3
DB2
DB1
DB0
CS-DAC
RW
DB5
DB6
DB7
DB8
DB9
DB10
DB11
EP4CE15F17I8L
EP4CE15F17I8LN
U32I
CLK1
CLK1, DIFFCLK_0n
CLK2, DIFFCLK_1p
CLK3, DIFFCLK_1n
CLK4, DIFFCLK_2p
CLK5, DIFFCLK_2n
CLK6, DIFFCLK_3p
CLK7, DIFFCLK_3n
CLK8, DIFFCLK_5n
CLK9, DIFFCLK_5p
CLK10, DIFFCLK_4n
CLK11, DIFFCLK_4p
CLK12, DIFFCLK_7n
CLK13, DIFFCLK_7p
CLK14, DIFFCLK_6n
CLK15, DIFFCLK_6p
EP4CE15F17I8L
C1608X7R1C104K
C51
Cap Semi
0.1uF
GND
3.3V
20 MHz output clock
CLK1
535-9565-1-ND
U34
Oscillator
R33
Res3
0 ohm
P0.0GCT-ND
EP4CE15F17I8LN
U32H
BANK 8
IO, DIFFIO_T13p, (PADD17), (DQS5T/CQ5T#,DPCLK10)/(DQS5T/CQ5T#,DPCLK10)
IO, (DQ3T)/(DQ5T)
IO, DIFFIO_T12n, (DATA2), (DQ3T)/(DQ5T)
IO, DIFFIO_T12p, (DATA3)
IO, DIFFIO_T11n, (PADD18), (DQ3T)/(DQ5T)
IO, DIFFIO_T11p, (DATA4), (DQ3T)/(DQ5T)
IO, VREFB8N0
IO, DIFFIO_T9n, (DATA14), (DQS3T/CQ3T#,DPCLK11)/(DQS3T/CQ3T#,DPCLK11)
IO, DIFFIO_T9p, (DATA13), (DQ3T)/(DQ5T)
IO, (DATA5), (DQ3T)/(DQ5T)
IO, DIFFIO_T6p, (DATA6), (DQ3T)/(DQ5T)
IO, (DATA7), (DQ3T)/(DQ5T)
IO, DIFFIO_T5p, (DATA8), (DQ3T)/(DQ5T)
IO, DIFFIO_T4n, (DATA9)
IO, DIFFIO_T3n, (DATA10), (DM3T/BWS#3T)/(DM5T/BWS#5T)
IO, DIFFIO_T3p, (DATA11)
IO, VREFB8N1
IO
IO, DIFFIO_T2n
IO, DIFFIO_T2p, (DATA12), (DQS1T/CQ1T#,CDPCLK7)/(DQS1T/CQ1T#,CDPCLK7)
IO, PLL3_CLKOUTn
IO, PLL3_CLKOUTp
SD-AMP
SCL-FPGA
SDA-FPGA
RX-FPGA
TX-FPGA
RX-FPGA-1
TX-FPGA-1
SDI-DAC
SCLK-DAC
CS-DAC-1
PPS
EP4CE15F17I8L
R34
10k
R35
10k
R36
Res3
10k
ERJ-3EKF1002V
FPGA-INT
3.3V levels
Debug header
FPGA terminal
Signals are crossed at header
P6
TX-FPGA
RX-FPGA
Header 6
Samtec
TSM-106-01-T-SV
SMT Technology
Samtec
U82
ESD
PGB1010603MR
1-wire port output
Samtec
IPL1-102-02-L-D-K
Header 2X2
P30
C68
Cap
10uF
5V-EXT
MAX3371EXT+TCT-ND
U144
VL
Vcc
GND
SHDN
A
B
MAX3371
10k or 2.5k might be needed
R125
Res3
2k
P2.00KHCT-ND
C310
Cap Semi
0.1uF
C147
Cap Semi
0.1uF
C1608X7R1C104K
U83
ESD
PGB1010603MR
IO is high for parasitic power
R67
100k
Q2
DMG2302U
DMG2302U-7DICT-ND
Title
Size
Letter
Number
Revision
Date:
6/21/2013
Sheet of
File:
E:\DEVELOPMENT-FINAL\..\FPGA-2.SchDoc
Drawn By:

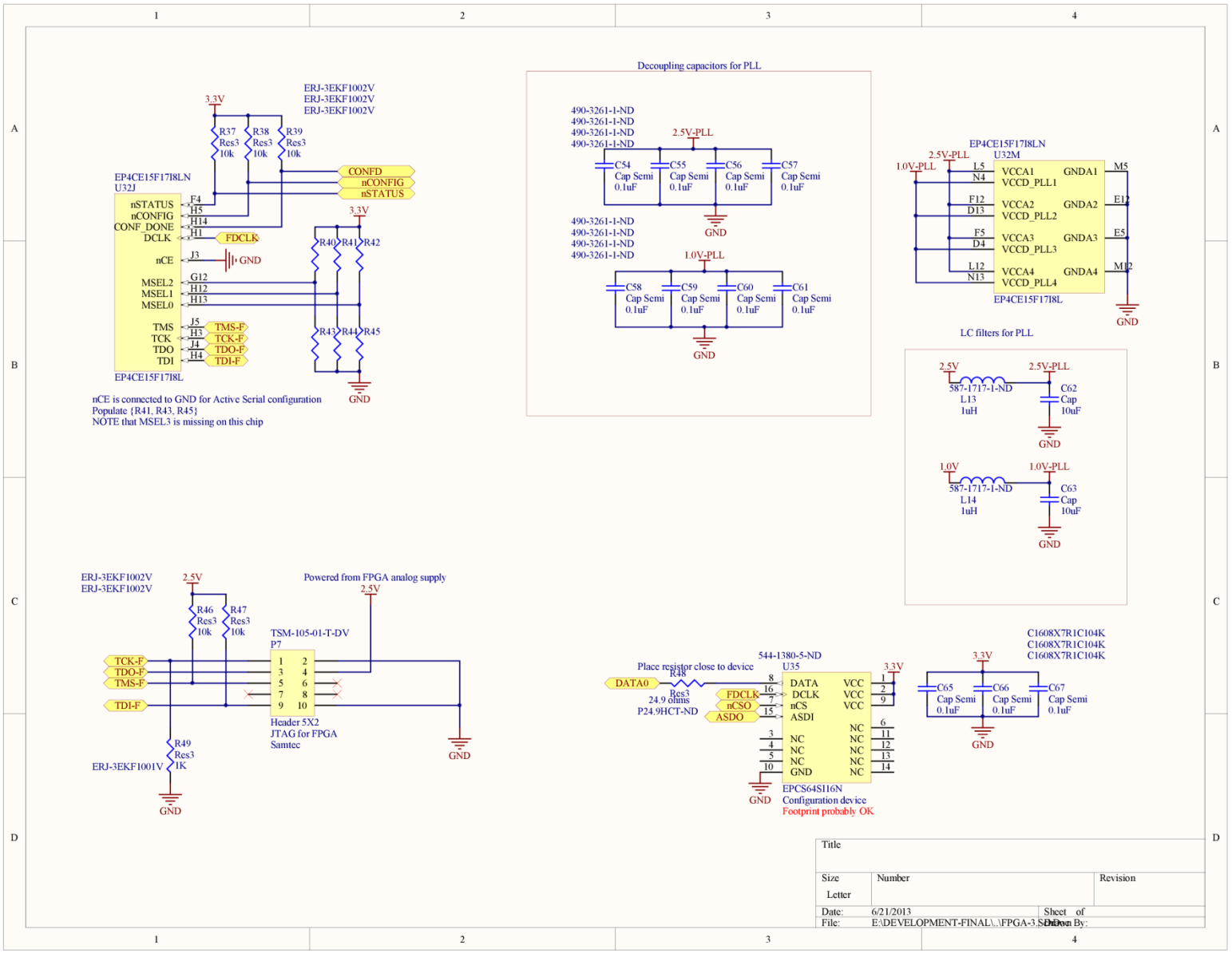
ERJ-3EKF1002V
ERJ-3EKF1002V
ERJ-3EKF1002V
3.3V
R37 Res3 10k
R38 Res3 10k
R39 Res3 10k
EP4CE15F17I8LN
U32J
nSTATUS
nCONFIG
CONF_DONE
DCLK
nCE
MSEL2
MSEL1
MSEL0
TMS
TCK
TDO
TDI
CONFD
nCONFIG
nSTATUS
FDCLK
GND
TMS-F
TCK-F
TDO-F
TDI-F
R40 R41 R42
R43 R44 R45
EP4CE15F17I8L
nCE is connected to GND for Active Serial configuration
Populate {R41, R43, R45}
NOTE that MSEL3 is missing on this chip
Decoupling capacitors for PLL
490-3261-1-ND
2.5V-PLL
C54 Cap Semi 0.1uF
C55 Cap Semi 0.1uF
C56 Cap Semi 0.1uF
C57 Cap Semi 0.1uF
1.0V-PLL
C58 Cap Semi 0.1uF
C59 Cap Semi 0.1uF
C60 Cap Semi 0.1uF
C61 Cap Semi 0.1uF
EP4CE15F17I8LN
U32M
VCCA1 VCCA2 VCCA3 VCCA4
VCCD_PLL1 VCCD_PLL2 VCCD_PLL3 VCCD_PLL4
GNDA1 GNDA2 GNDA3 GNDA4
EP4CE15F17I8L
LC filters for PLL
2.5V
587-1717-1-ND
L13 1uH
C62 Cap 10uF
1.0V
L14 1uH
C63 Cap 10uF
ERJ-3EKF1002V
ERJ-3EKF1002V
2.5V
R46 Res3 10k
R47 Res3 10k
TSM-105-01-T-DV
P7
Header 5X2
JTAG for FPGA
Samtec
ERJ-3EKF1001V
R49 Res3 1K
Powered from FPGA analog supply
544-1380-5-ND
U35
Place resistor close to device
R48
24.9 ohms
P24.9HCT-ND
DATA0
FDCLK
nCSO
ASDO
DATA DCLK nCS ASDI
VCC
NC
GND
EPCS64SI16N
Configuration device
Footprint probably OK
C1608X7R1C104K
C65 Cap Semi 0.1uF
C66 Cap Semi 0.1uF
C67 Cap Semi 0.1uF
Title
Size
Letter
Number
Revision
Date: 6/21/2013
File: E:\DEVELOPMENT-FINAL\..\FPGA-3.SchDoc
Drawn By:

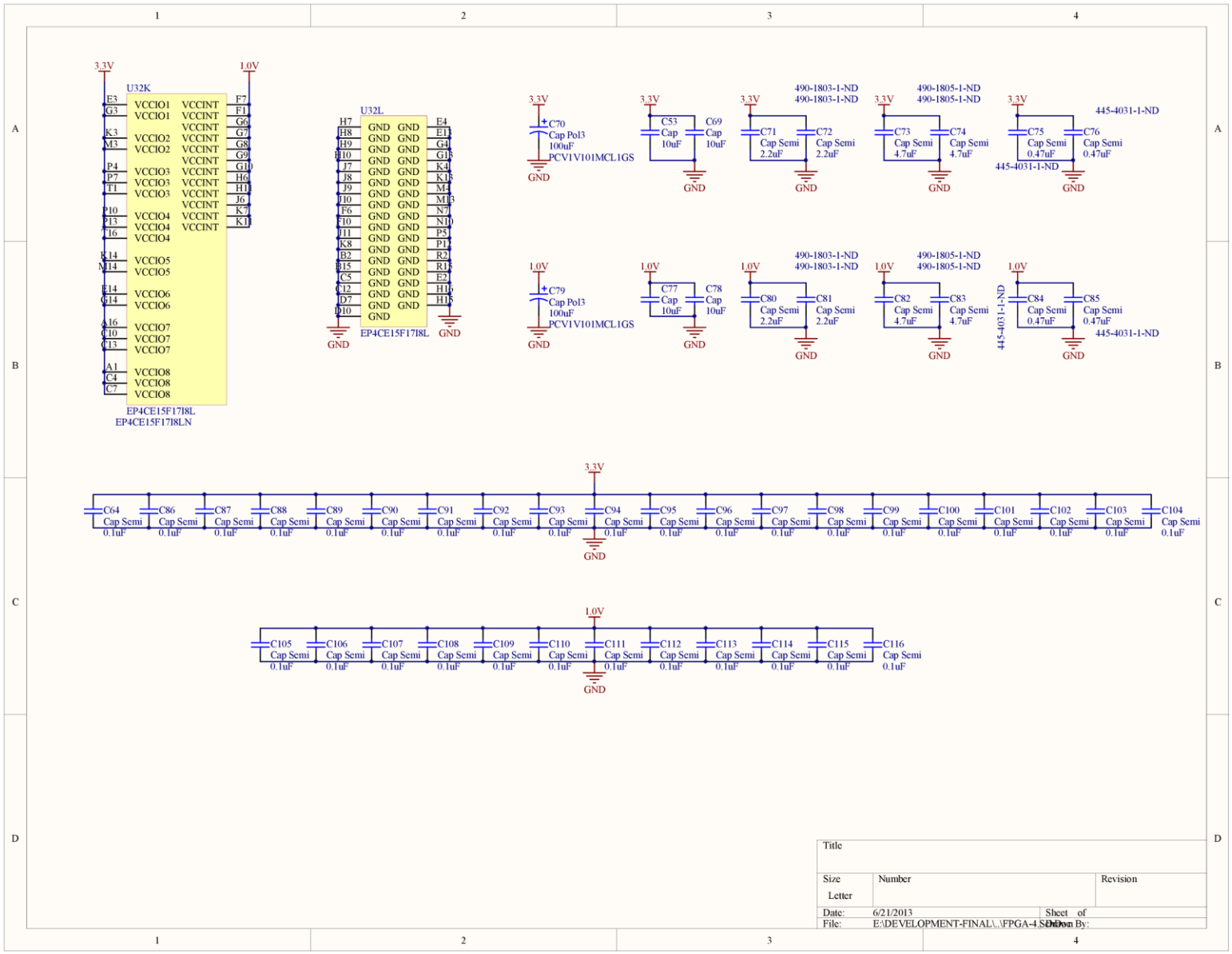
U32K
EP4CE15F17I8L
EP4CE15F17I8LN
U32L
EP4CE15F17I8L
3.3V
1.0V
GND
C70 Cap Pol3 100uF PCV1V101MCL1GS
C53 Cap 10uF
C69 Cap 10uF
C71 Cap Semi 2.2uF
C72 Cap Semi 2.2uF
C73 Cap Semi 4.7uF
C74 Cap Semi 4.7uF
C75 Cap Semi 0.47uF
C76 Cap Semi 0.47uF
490-1803-1-ND
490-1805-1-ND
445-4031-1-ND
C79 Cap Pol3 100uF PCV1V101MCL1GS
C77 Cap 10uF
C78 Cap 10uF
C80 Cap Semi 2.2uF
C81 Cap Semi 2.2uF
C82 Cap Semi 4.7uF
C83 Cap Semi 4.7uF
C84 Cap Semi 0.47uF
C85 Cap Semi 0.47uF
C64 C86 C87 C88 C89 C90 C91 C92 C93 C94 C95 C96 C97 C98 C99 C100 C101 C102 C103 C104
Cap Semi 0.1uF
C105 C106 C107 C108 C109 C110 C111 C112 C113 C114 C115 C116
Cap Semi 0.1uF
Title
Size Letter
Number
Revision
Date: 6/21/2013
Sheet of
File: E:\DEVELOPMENT-FINAL\..\FPGA-4.SchDoc
Drawn By:

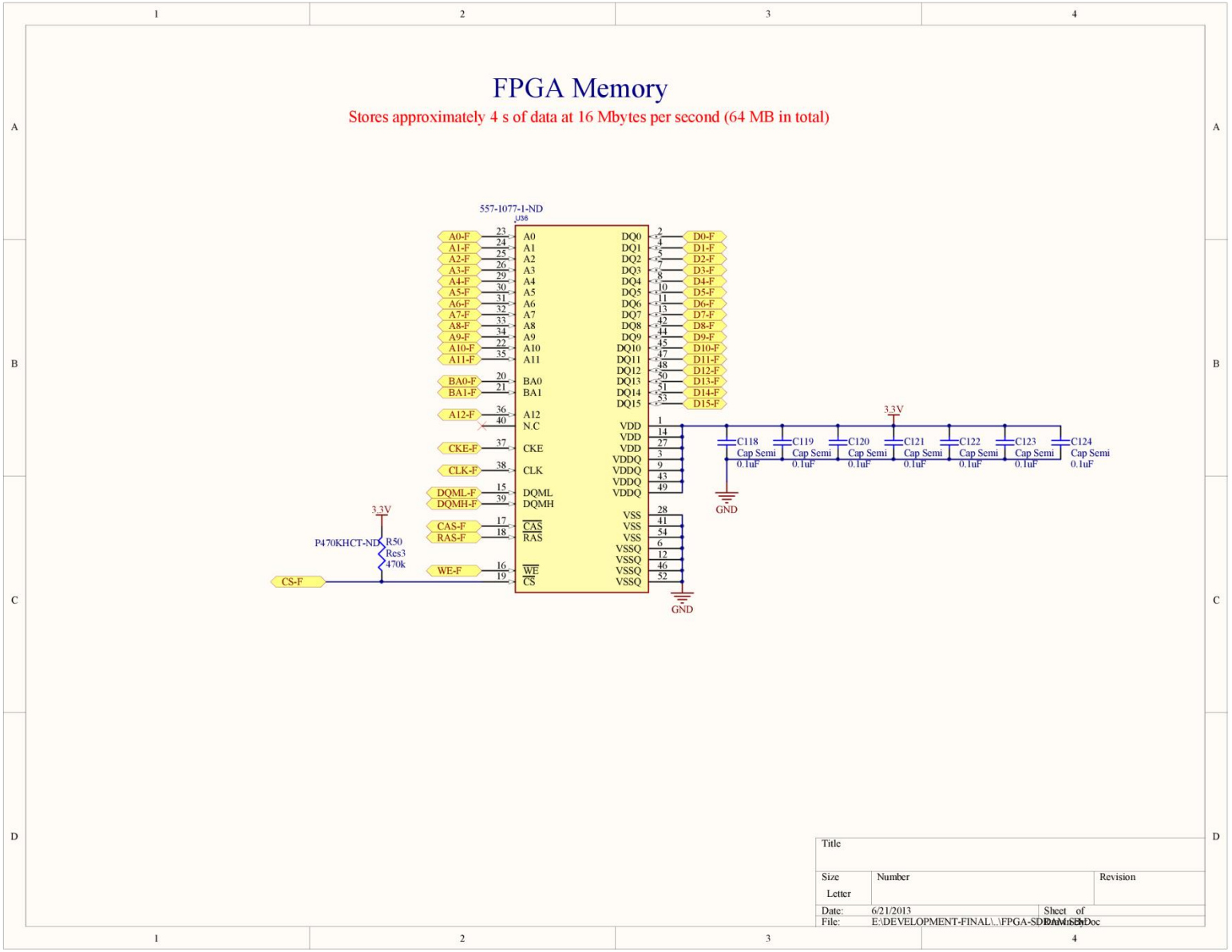
FPGA Memory
Stores approximately 4 s of data at 16 Mbytes per second (64 MB in total)
557-1077-1-ND
U36
A0-F
A1-F
A2-F
A3-F
A4-F
A5-F
A6-F
A7-F
A8-F
A9-F
A10-F
A11-F
BA0-F
BA1-F
A12-F
CKE-F
CLK-F
DQML-F
DQMH-F
CAS-F
RAS-F
WE-F
CS-F
A0
A1
A2
A3
A4
A5
A6
A7
A8
A9
A10
A11
BA0
BA1
A12
N.C
CKE
CLK
DQML
DQMH
CAS
RAS
WE
CS
DQ0
DQ1
DQ2
DQ3
DQ4
DQ5
DQ6
DQ7
DQ8
DQ9
DQ10
DQ11
DQ12
DQ13
DQ14
DQ15
VDD
VDD
VDD
VDDQ
VDDQ
VDDQ
VDDQ
VSS
VSS
VSS
VSSQ
VSSQ
VSSQ
VSSQ
D0-F
D1-F
D2-F
D3-F
D4-F
D5-F
D6-F
D7-F
D8-F
D9-F
D10-F
D11-F
D12-F
D13-F
D14-F
D15-F
3.3V
GND
C118
C119
C120
C121
C122
C123
C124
Cap Semi
0.1uF
P470KHCT-ND
R50
Res3
470k
Title
Size
Letter
Number
Revision
Date:
6/21/2013
Sheet of
File:
E:\DEVELOPMENT-FINAL\..\FPGA-SDRAM.SchDoc

347

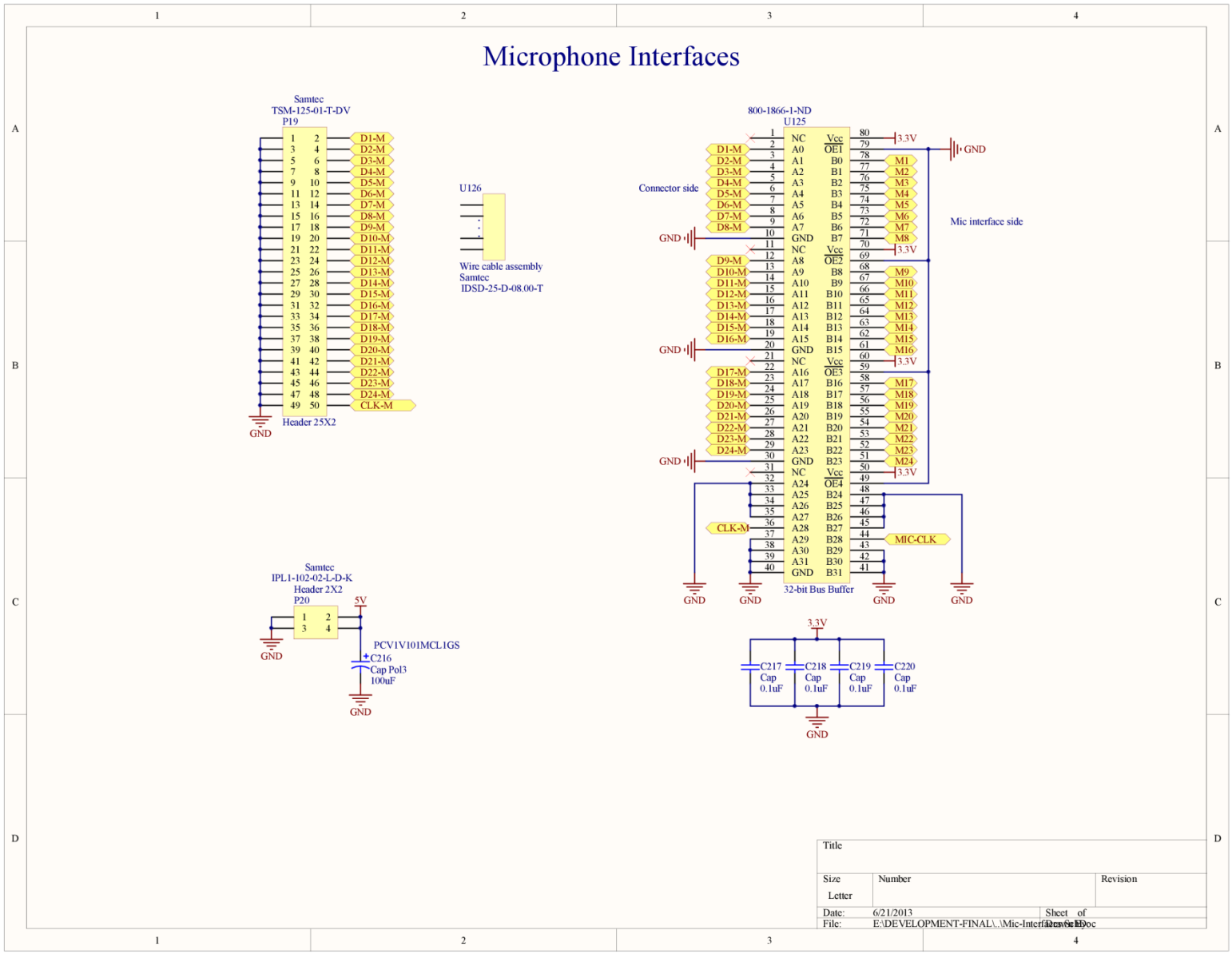
Microphone Interfaces
Samtec
TSM-125-01-T-DV
P19
Header 25X2
U126
Wire cable assembly
Samtec
IDSD-25-D-08.00-T
800-1866-1-ND
U125
Connector side
Mic interface side
32-bit Bus Buffer
Samtec
IPL1-102-02-L-D-K
Header 2X2
P20
PCV1V101MCL1GS
C216
Cap Pol3
100uF
C217
C218
C219
C220
Cap
0.1uF
3.3V
5V
GND
MIC-CLK
Title
Size
Letter
Number
Revision
Date:
6/21/2013
Sheet of
File:
E:\DEVELOPMENT-FINAL\..\Mic-Interface.SchDoc

348

1) Note that instead of using an audio ADC here, you could simply use a single-bit I/O port and use a low-pass filter (op-amp or passive) to create a waveform that could be fed into the audio amp.

2) You could also use a high-speed switch to create a positive and negative voltage at a rate of 2.1 MHz, the same sampling rate as the mics. This would allow you to use the Fast Hadamard Transform as part of the deconvolution process. You would also have to pass the output through a low-pass filter as well.

3) You will have to test this by experimentation to see if there is another amplification stage required beyond low-pass filtering. Maybe create a small test circuit board with a CPLD? You don't want to exceed the slew rate of the audio amplifier!

4) Maybe use a passive filter (RLC) on the output of the ADC ?

5) Instead of using the passive filter, what you could do is digitally low-pass filter the MLS waveform before it is sent out from the system! So you apply the digital filter in Matlab to the MLS waveform, and then the FPGA will only produce the low-pass filtered MLS waveform using the DAC! So you simply store the MLS waveform in the FPGA memory, or write code for a low-pass filter in Verilog and do the filtering on the FPGA!

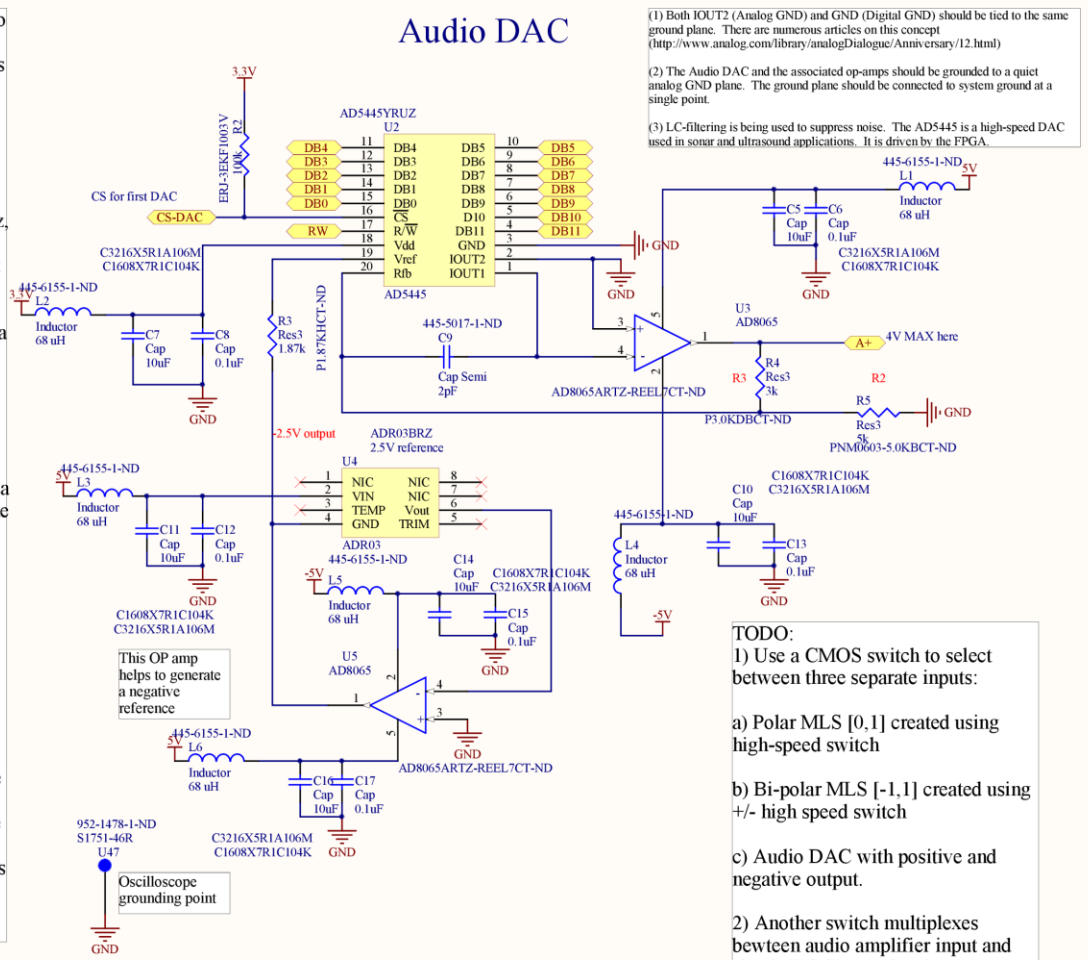

349

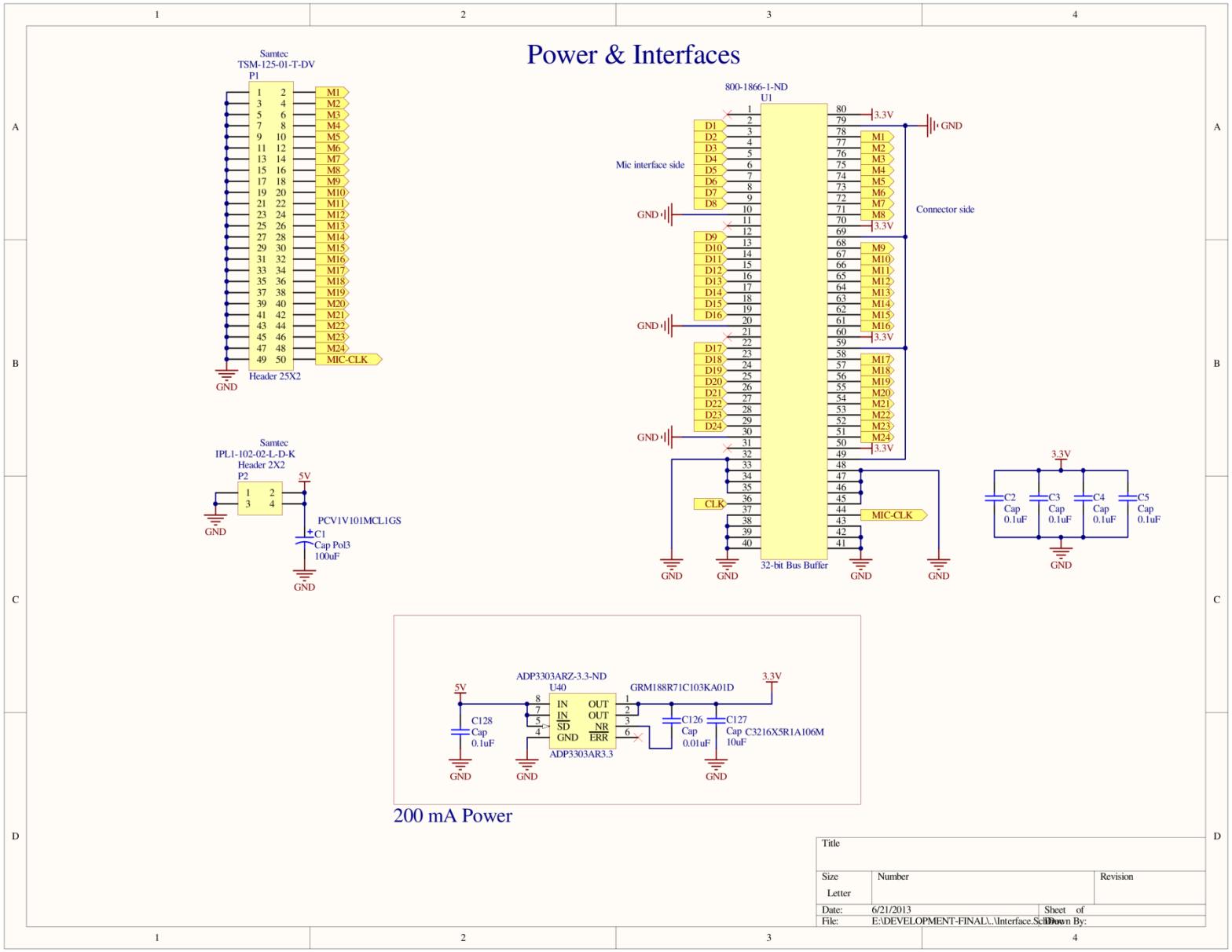
Power & Interfaces
Samtec
TSM-125-01-T-DV
P1
Header 25X2
Samtec
IPL1-102-02-L-D-K
Header 2X2
P2
PCV1V101MCL1GS
Cap Pol3
100uF
800-1866-1-ND
U1
Mic interface side
Connector side
32-bit Bus Buffer
ADP3303ARZ-3.3-ND
U40
ADP3303AR3.3
GRM188R71C103KA01D
C128
Cap
0.1uF
C126
Cap
0.01uF
C127
Cap C3216X5R1A106M
10uF
200 mA Power
Title
Size
Letter
Number
Revision
Date:
6/21/2013
Sheet of
File:
E:\DEVELOPMENT-FINAL\..\Interface.SchDoc
Drawn By:

350

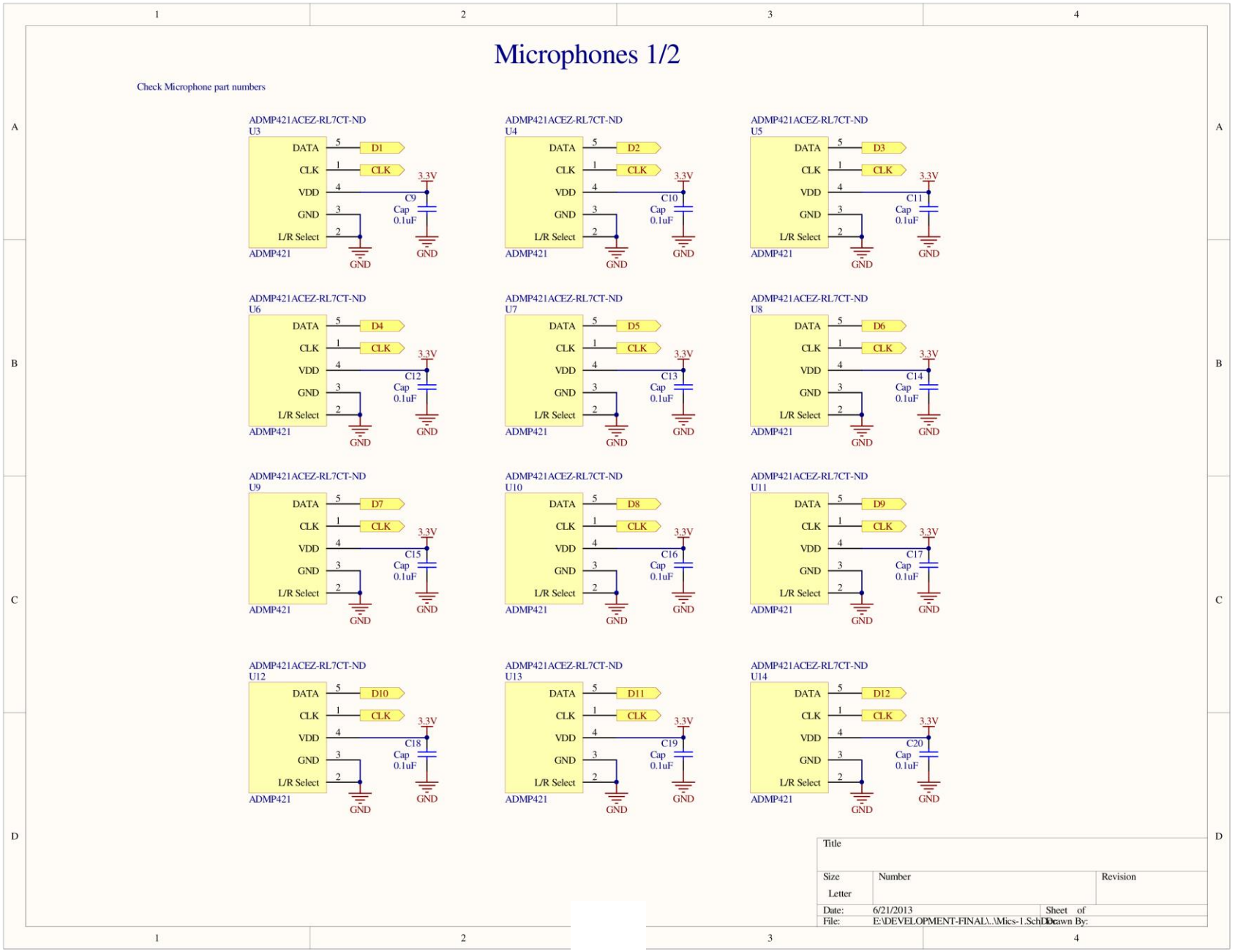
Microphones 1/2
Check Microphone part numbers
ADMP421ACEZ-RL7CT-ND
U3
DATA
CLK
VDD
GND
L/R Select
ADMP421
D1
CLK
3.3V
C9
Cap
0.1uF
GND
ADMP421ACEZ-RL7CT-ND
U4
D2
C10
ADMP421ACEZ-RL7CT-ND
U5
D3
C11
ADMP421ACEZ-RL7CT-ND
U6
D4
C12
ADMP421ACEZ-RL7CT-ND
U7
D5
C13
ADMP421ACEZ-RL7CT-ND
U8
D6
C14
ADMP421ACEZ-RL7CT-ND
U9
D7
C15
ADMP421ACEZ-RL7CT-ND
U10
D8
C16
ADMP421ACEZ-RL7CT-ND
U11
D9
C17
ADMP421ACEZ-RL7CT-ND
U12
D10
C18
ADMP421ACEZ-RL7CT-ND
U13
D11
C19
ADMP421ACEZ-RL7CT-ND
U14
D12
C20
Title
Size
Letter
Number
Revision
Date:
6/21/2013
Sheet of
File:
E:\DEVELOPMENT-FINAL\..\Mics-1.Sch
Drawn By:

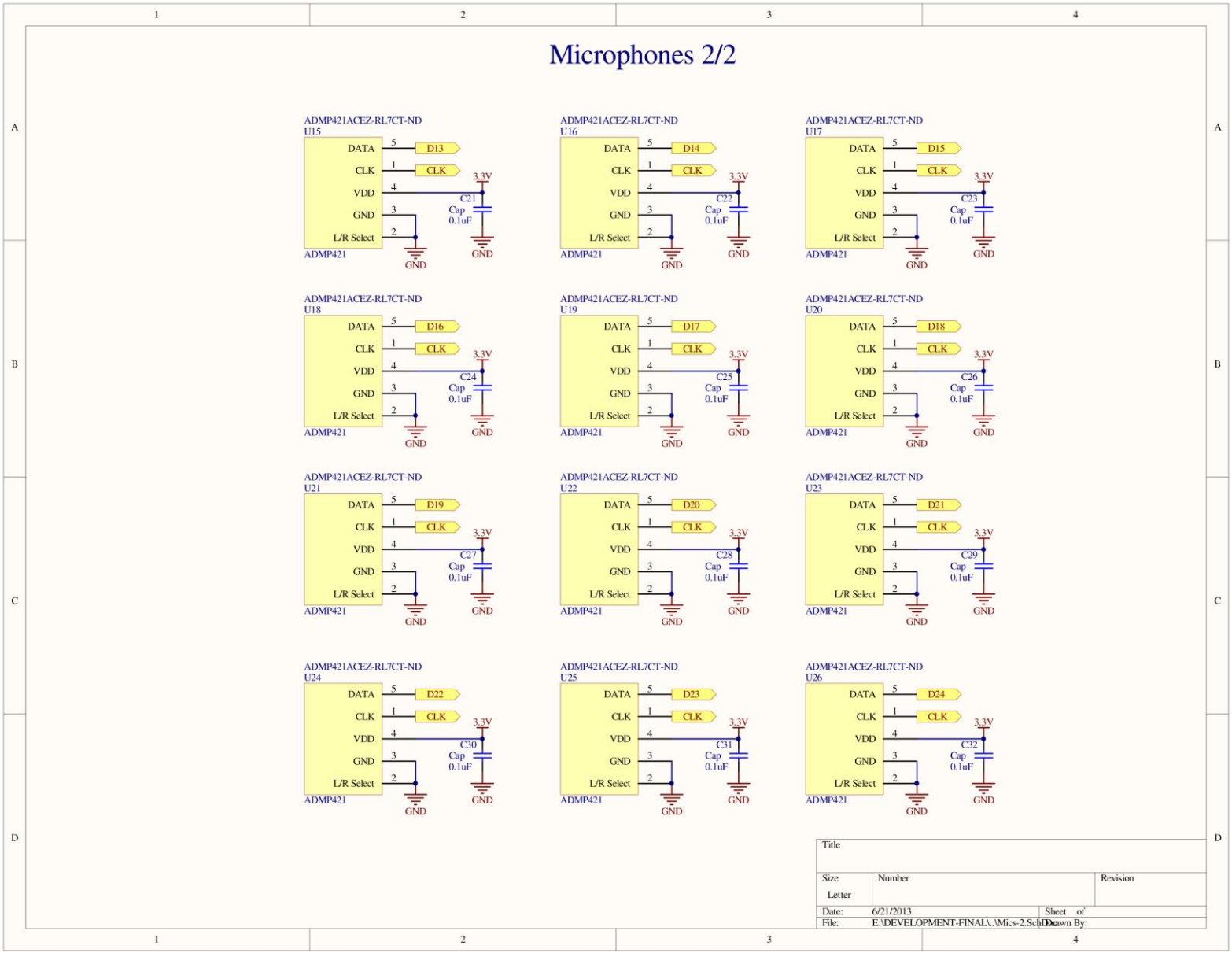
Microphones 2/2
ADMP421ACEZ-RL7CT-ND
U15
DATA
CLK
VDD
GND
L/R Select
ADMP421
D13
CLK
3.3V
C21
Cap
0.1uF
GND
ADMP421ACEZ-RL7CT-ND
U16
D14
C22
ADMP421ACEZ-RL7CT-ND
U17
D15
C23
ADMP421ACEZ-RL7CT-ND
U18
D16
C24
ADMP421ACEZ-RL7CT-ND
U19
D17
C25
ADMP421ACEZ-RL7CT-ND
U20
D18
C26
ADMP421ACEZ-RL7CT-ND
U21
D19
C27
ADMP421ACEZ-RL7CT-ND
U22
D20
C28
ADMP421ACEZ-RL7CT-ND
U23
D21
C29
ADMP421ACEZ-RL7CT-ND
U24
D22
C30
ADMP421ACEZ-RL7CT-ND
U25
D23
C31
ADMP421ACEZ-RL7CT-ND
U26
D24
C32
Title
Size
Letter
Number
Revision
Date:
6/21/2013
Sheet of
File:
E:\DEVELOPMENT-FINAL\..\Mics-2.Sch
Drawn By:

APPENDIX B
ADDITIONAL FIELD SITE OBSERVATIONS

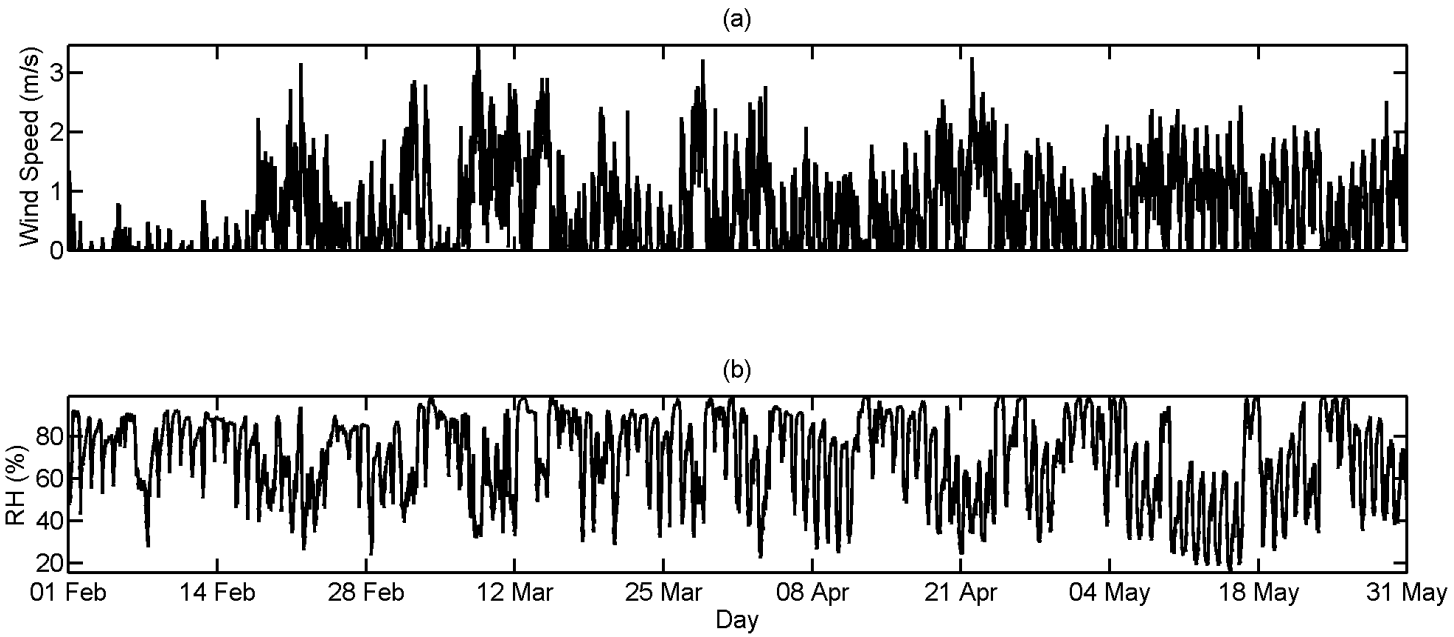

Figure B.1. Upper Clearing Stationary (UCS) site time-series data showing (a) windspeed, and (b) Relative Humidity.

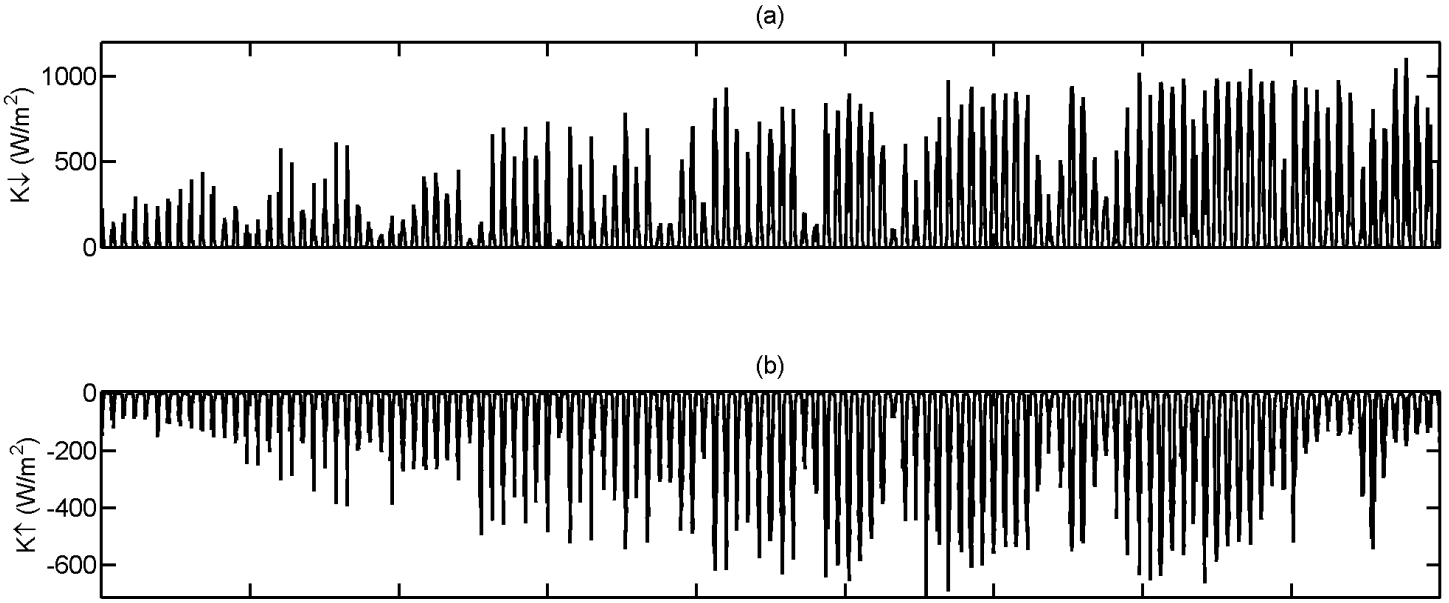

Figure B.2. Upper Clearing Stationary (UCS) site time-series data showing (a) incoming shortwave radiation $K\downarrow$ and (b) outgoing shortwave radiation $K\uparrow$.

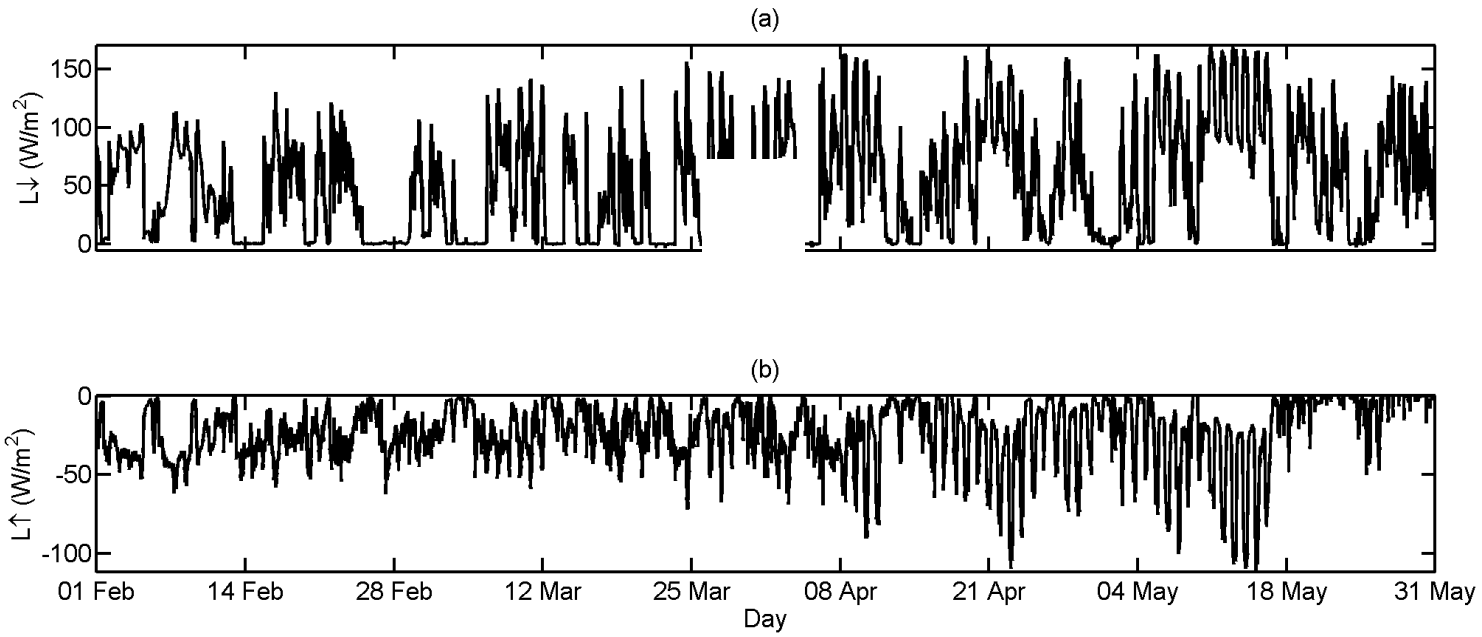

Figure B.3. Upper Clearing Stationary (UCS) site time-series data showing (a) incoming longwave radiation $L\downarrow$, and (b) outgoing longwave radiation $L\uparrow$.

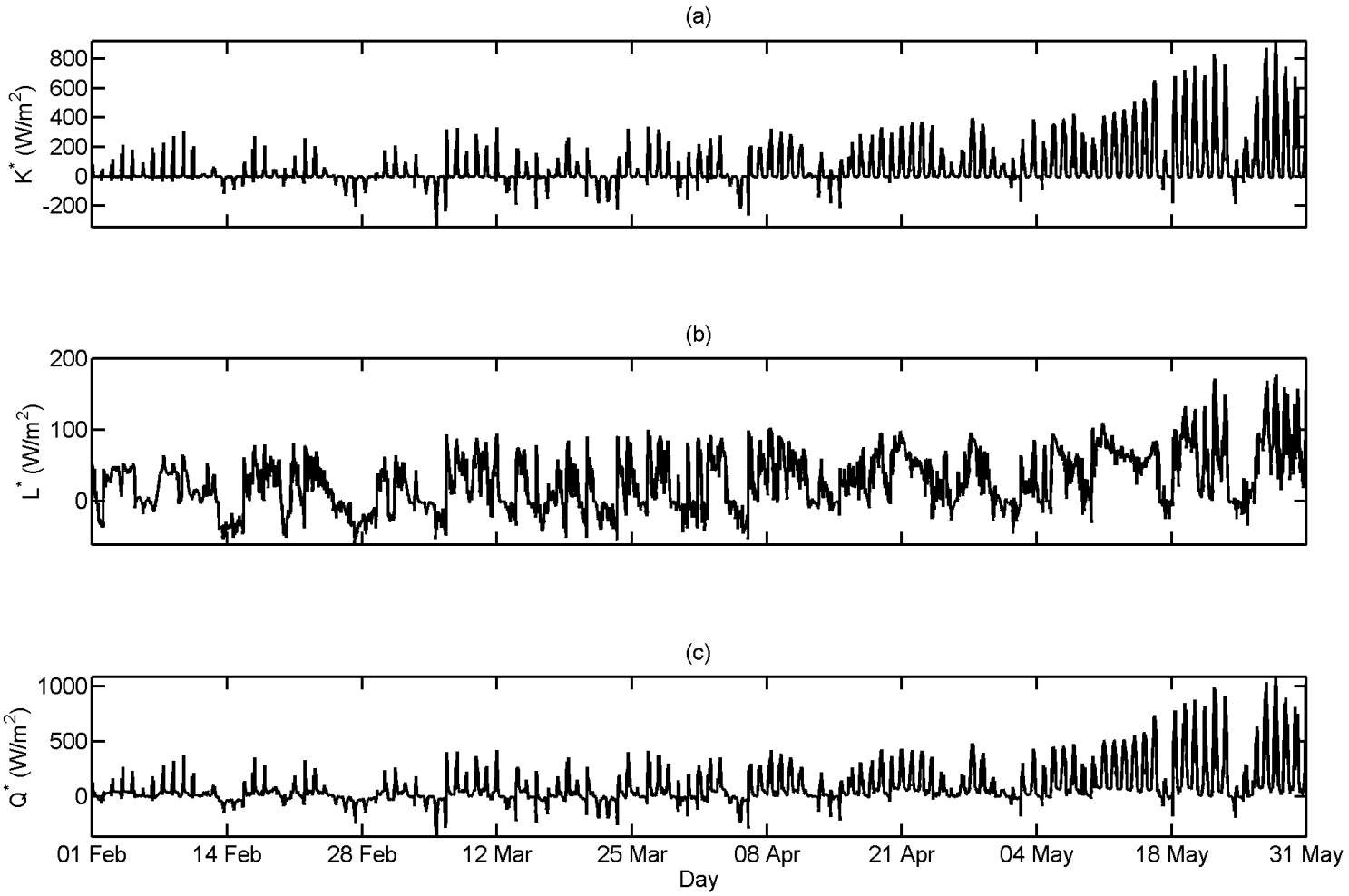

Figure B.4. Upper Clearing Stationary (UCS) site time-series data showing (a) net shortwave radiation K^*, (b) net longwave radiation L^*, and (c) net all-wave radiation Q^*.

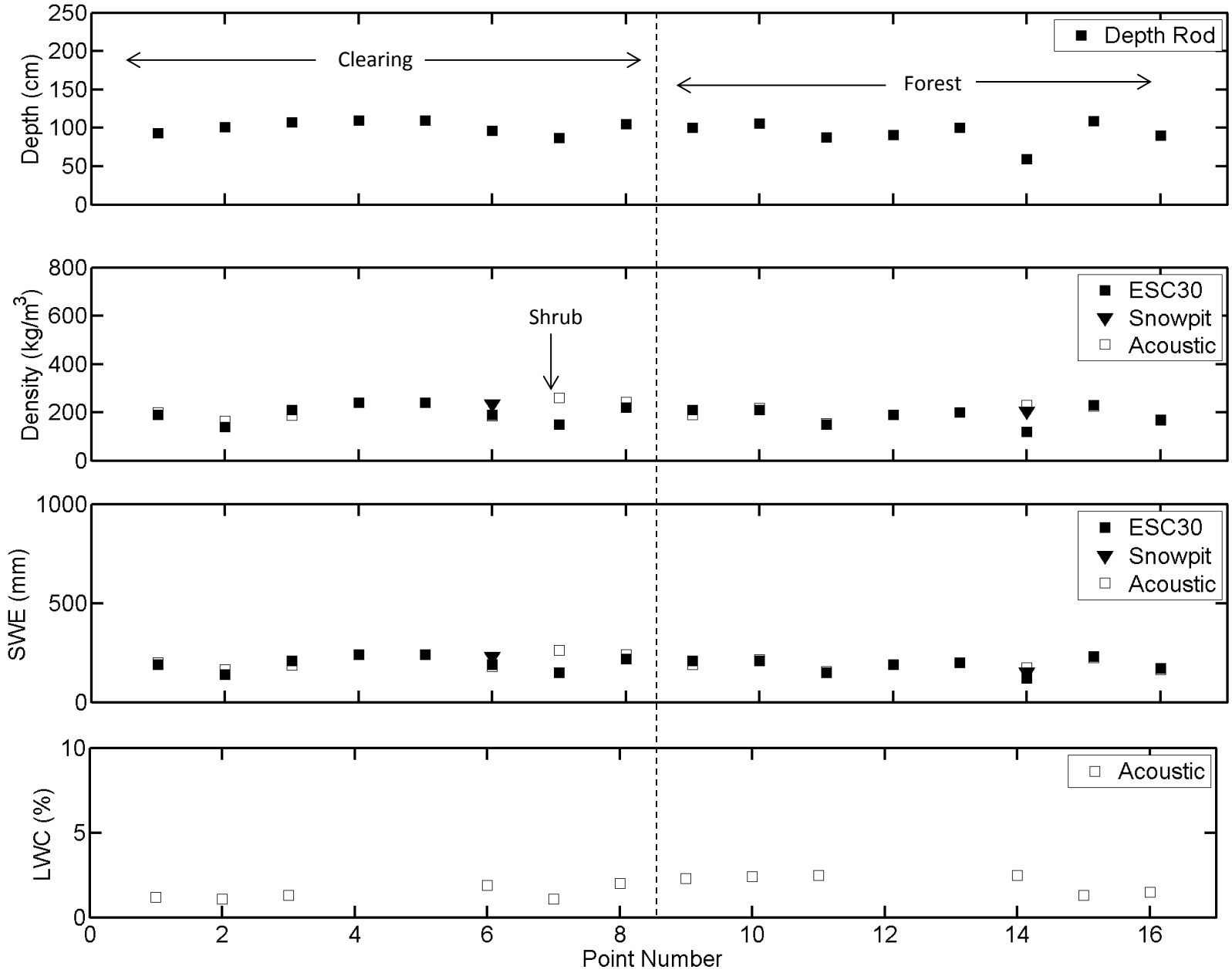

Figure B.5. Boulton Campground (BC) Site transects showing depth, average density $\bar{\rho}$, SWE, and depth-averaged liquid water content.

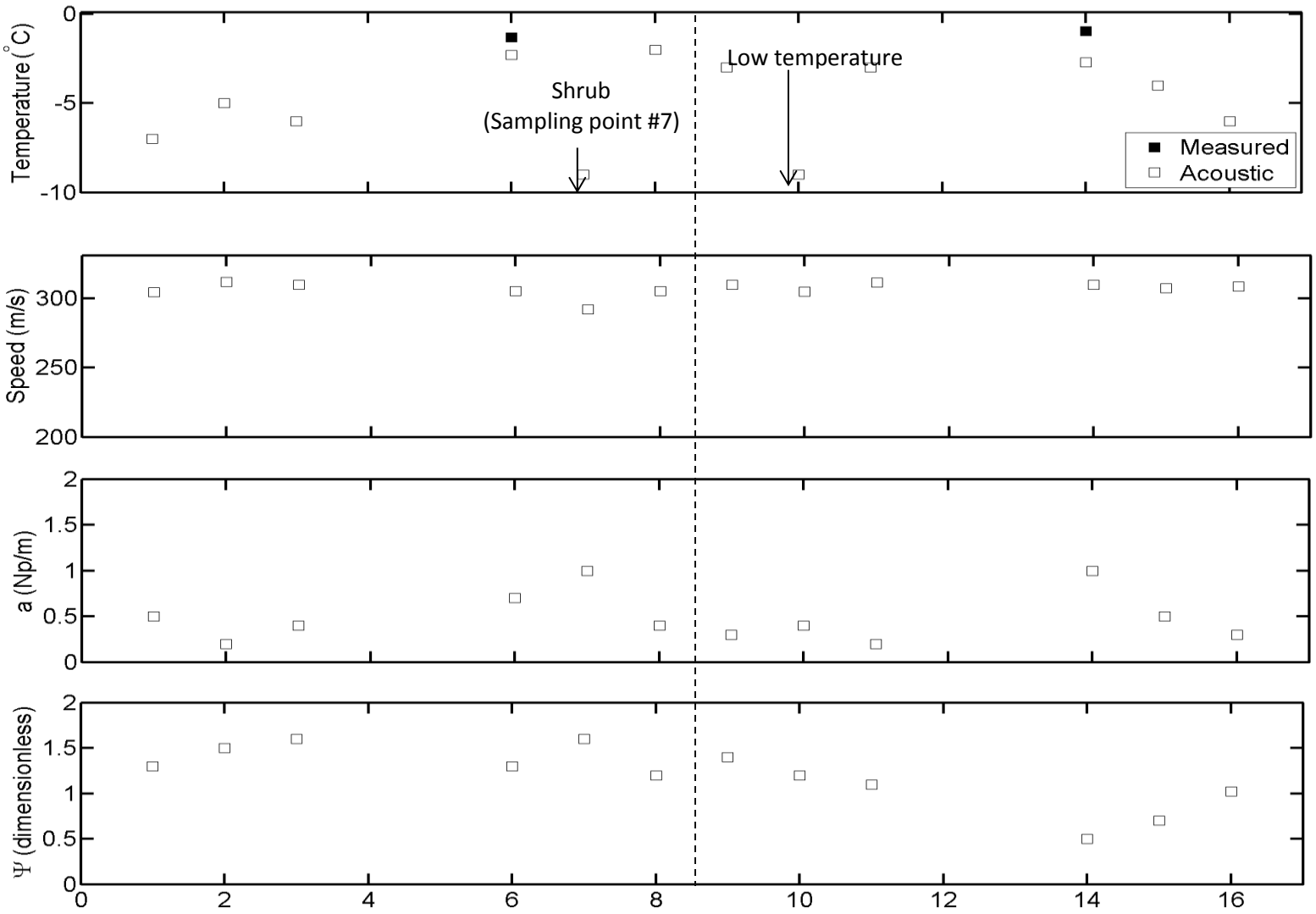

Figure B.6. Boulton Campground (BC) Site transects showing average temperature $\bar{T}$, frequency-averaged speed and attenuation, and Ψ coefficient.

.

$\bar{\rho}$ **Comparison**	**Snowpit & Snowtube**	**ESC30 & SAS2**	**Snowpit & SAS2**
RMSD ($kg\ m^{-3}$)	67.4	47.1	40.5
MB ($kg\ m^{-3}$)	64.5	19.5	-12.5

SWE **Comparison**	**Snowpit & Snowtube**	**ESC30 & SAS2**	**Snowpit & SAS2**
RMSD (mm)	36.7	38.1	34.1
MB (mm)	36.5	14.4	-15.0

$\bar{T}$ **Comparison**	**Thermometer & Acoustic**
RMSD (°C)	1.4
MB (°C)	-1.3

Table B.1. Comparisons between snowpit, ESC30, and acoustic measurements of $\bar{\rho}$, SWE and $\bar{T}$ for the Boulton Campground (BC) site.

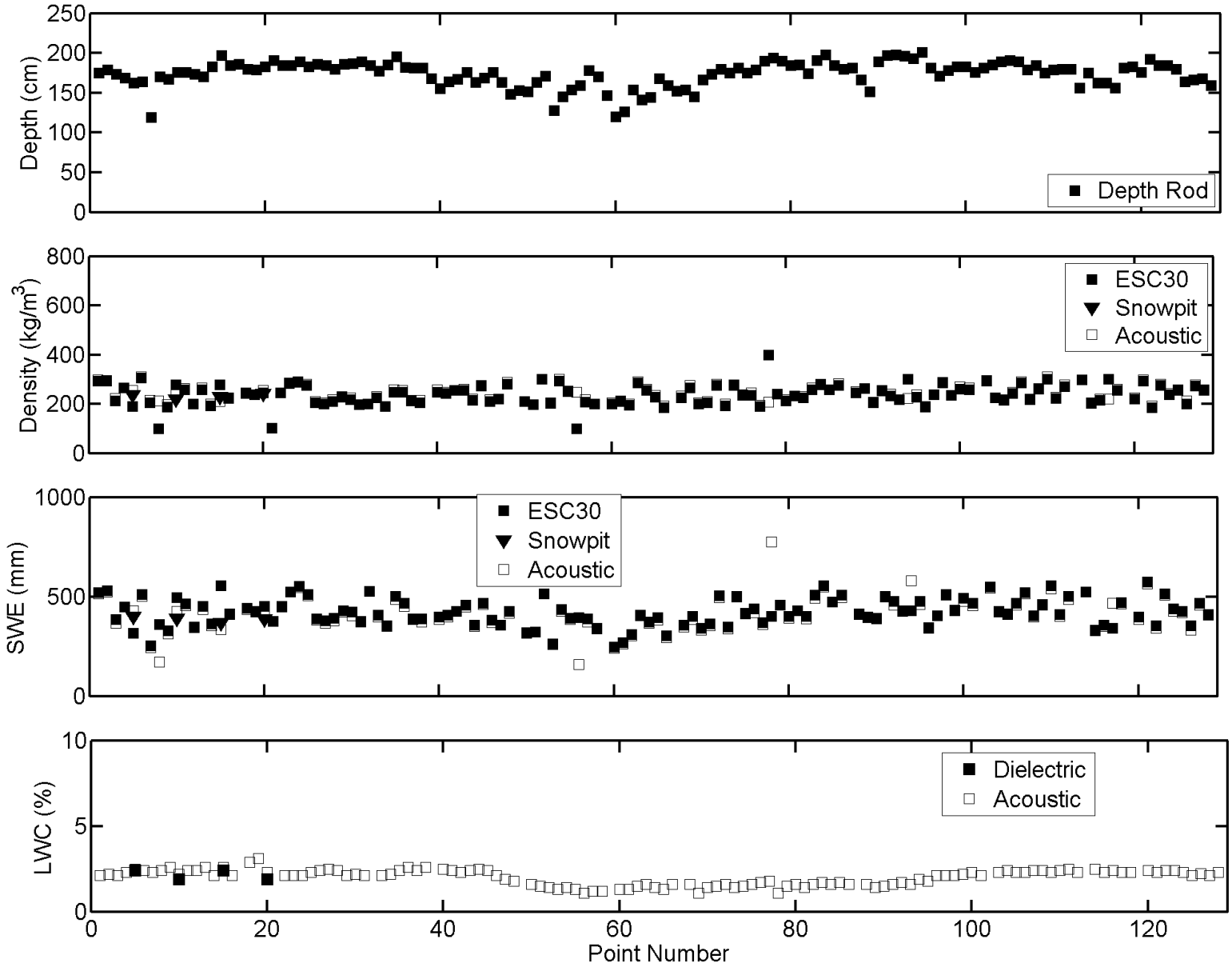

Figure B.7. Bow Summit (BS) Site transects showing depth, average density $\bar{\rho}$, SWE, and depth-averaged liquid water content.

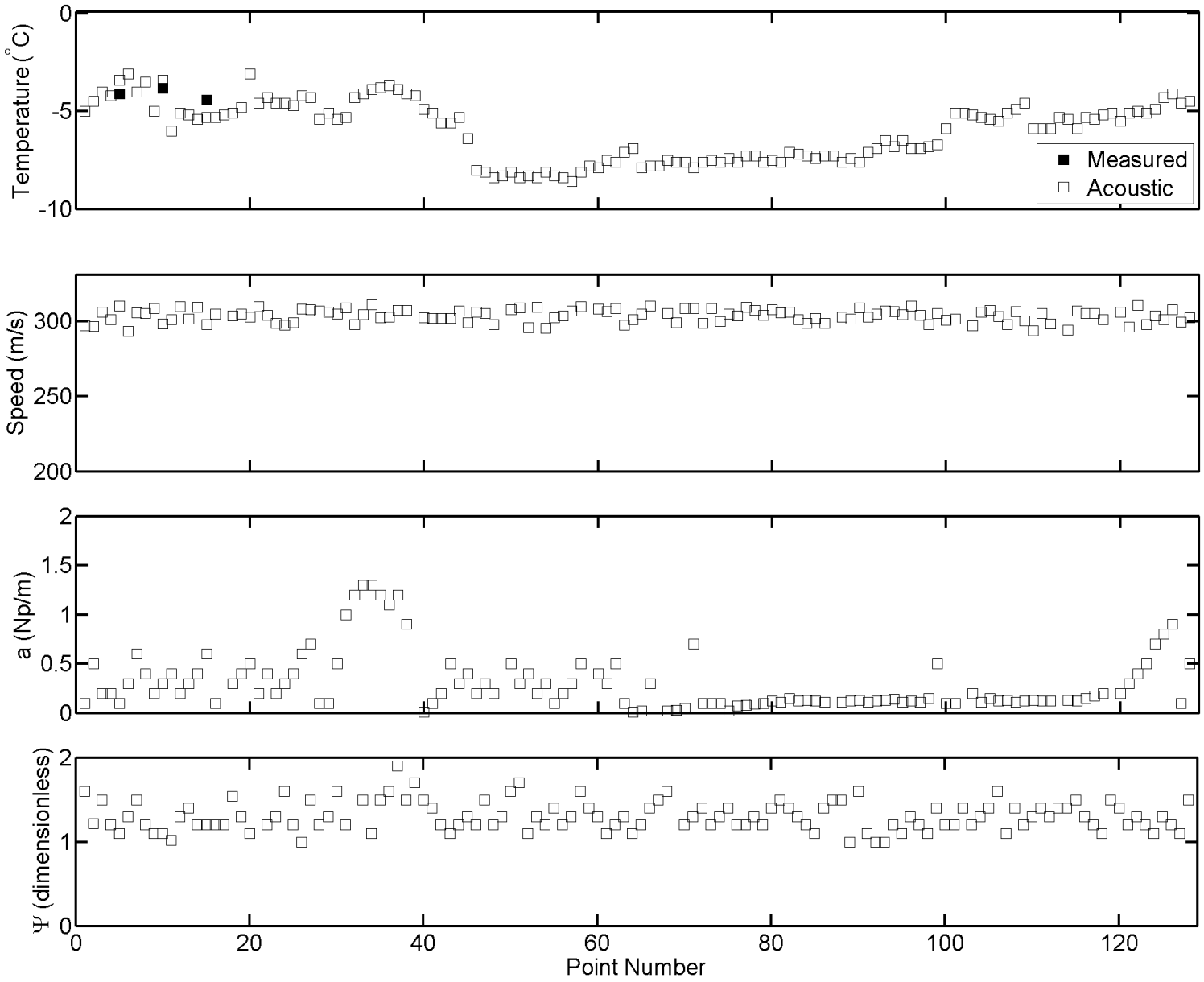

Figure B.8. Bow Summit (BS) Site transects showing average temperature, frequency-averaged speed and attenuation, and Ψ coefficient.

$\bar{\rho}$ **Comparison**	**Snowpit & Snowtube**	**ESC30 & SAS2**	**Snowpit & SAS2**
RMSD ($kg\ m^{-3}$)	45.0	29.0	18.1
MB ($kg\ m^{-3}$)	-14.3	3.2	7.3

SWE **Comparison**	**Snowpit & Snowtube**	**ESC30 & SAS2**	**Snowpit & SAS2**
RMSD (mm)	119.8	54.6	30.3
MB (mm)	-68.2	-7.3	12.5

$\bar{\theta}_w$ **Comparison**	**Dielectric & Acoustic**
RMSD (%)	0.3
MB (%)	0.2

$\bar{T}$ **Comparison**	**Thermometer & Acoustic**
RMSD (°C)	0.7
MB (°C)	0.1

Table B.2. Comparisons between snowpit, ESC30, and acoustic measurements of $\bar{\rho}$, SWE, $\bar{\theta}_w$ and $\bar{T}$ for the Bow Summit (BS) site.

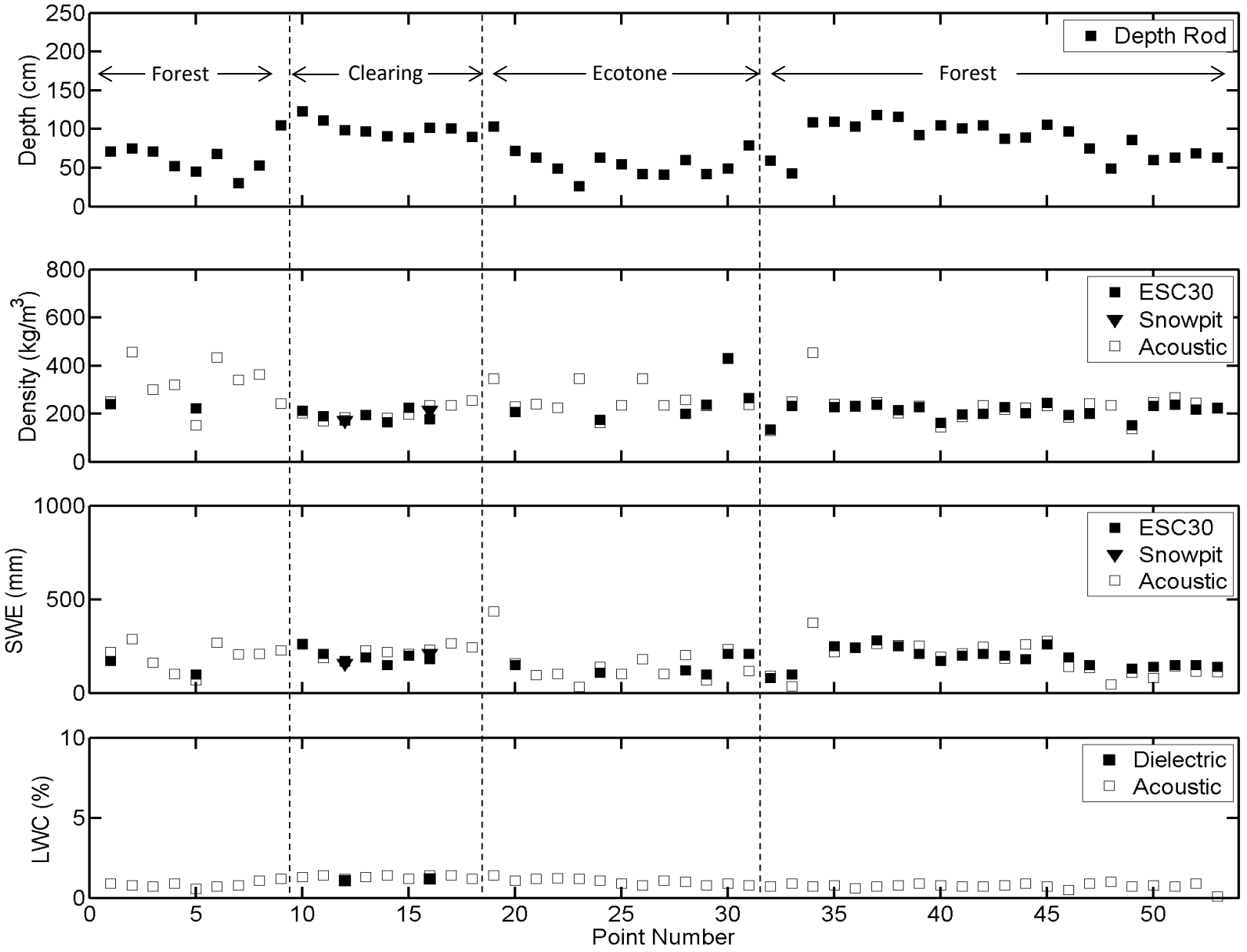

Figure B.9. Upper Clearing Portable (UCP) Site transects showing depth, average density $\bar{\rho}$, SWE, and depth-averaged liquid water content.

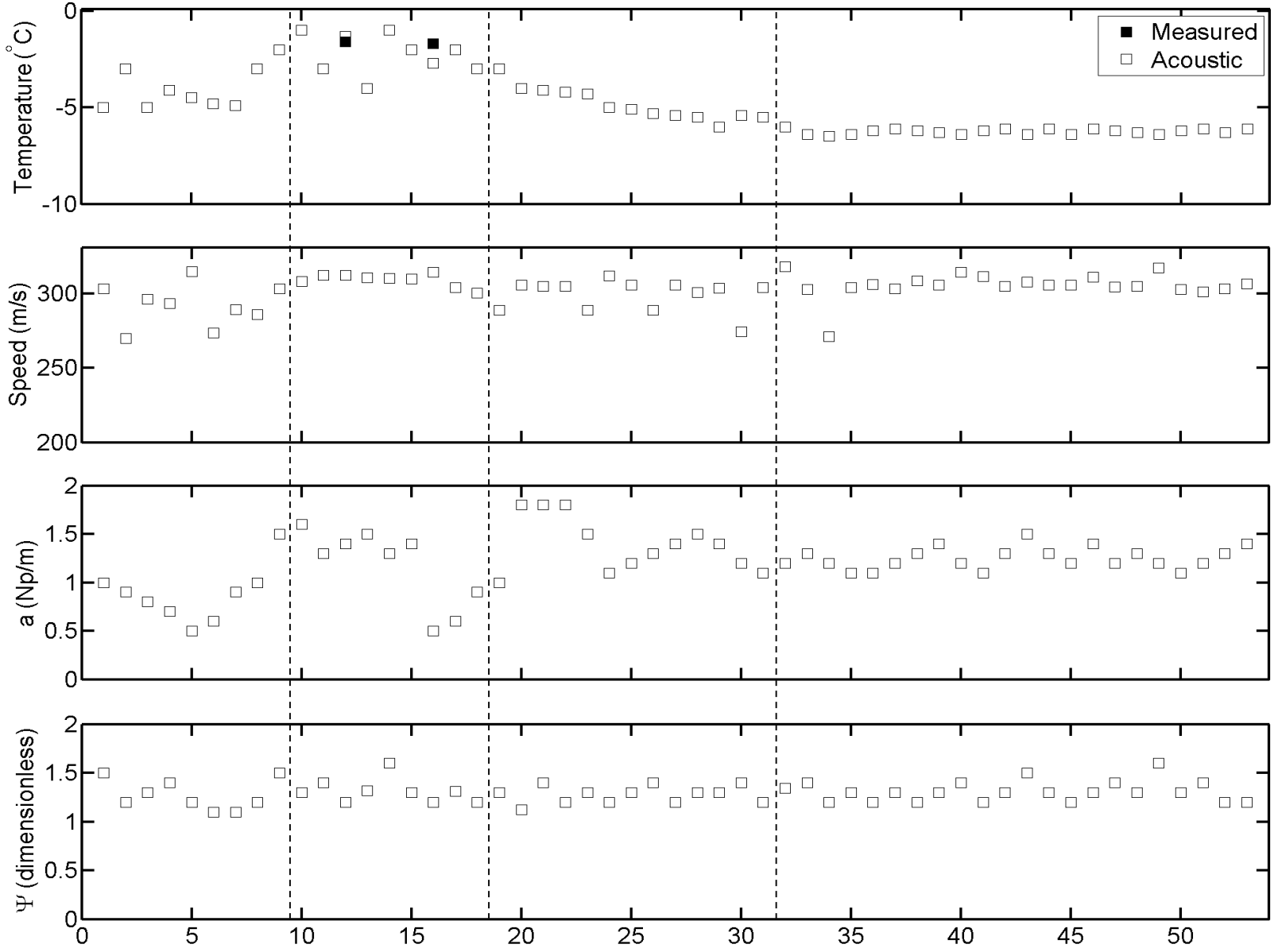

Figure B.10. Upper Clearing (UCP) Site transects showing average temperature $\bar{T}$, frequency-averaged speed and attenuation, and Ψ coefficient.

$\bar{\rho}$ **Comparison**	**Snowpit & Snowtube**	**ESC30 & SAS2**	**Snowpit & SAS2**
RMSD ($kg\ m^{-3}$)	28.0	25.2	15.5
MB ($kg\ m^{-3}$)	20.4	3.8	15.0

SWE **Comparison**	**Snowpit & Snowtube**	**ESC30 & SAS2**	**Snowpit & SAS2**
RMSD (mm)	23.5	18.7	14.9
MB (mm)	9.5	1.6	14.0

$\bar{\theta}_w$ **Comparison**	**Dielectic & Acoustic**
RMSD (%)	0.20
MB (%)	0.10

$\bar{T}$ **Comparison**	**Thermometer & Acoustic**
RMSD (°C)	0.70
MB (°C)	-0.40

Table B.3. Comparisons between snowpit, ESC30, and acoustic measurements of $\bar{\rho}$, SWE, $\bar{\theta}_w$ and $\bar{T}$ for the UCP site.

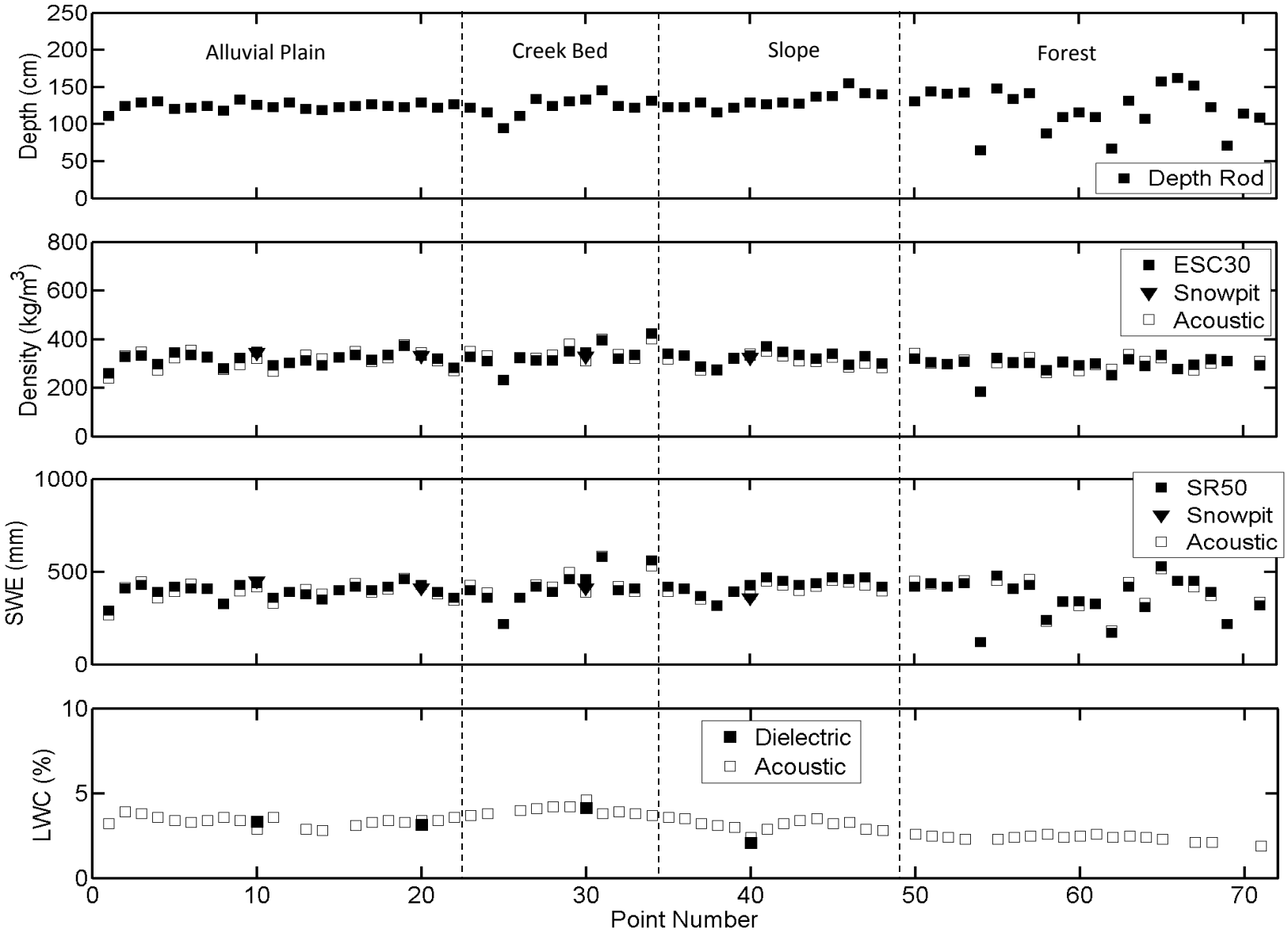

Figure B.11. Bow Meadows (BM) Site transects showing depth, average density $\bar{\rho}$, SWE, and depth-averaged liquid water content.

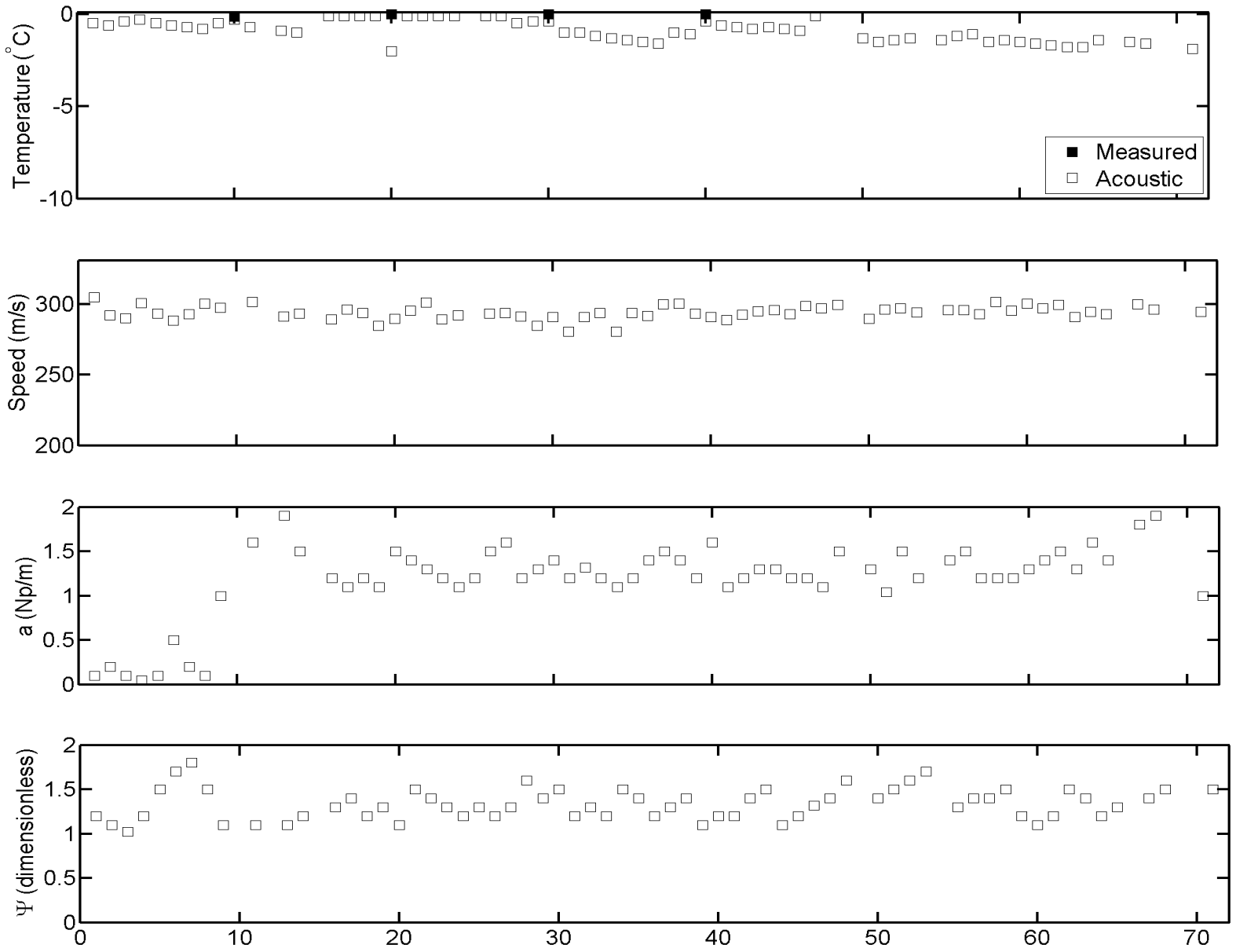

Figure B.12. Bow Meadows (BM) Site transects showing average temperature, frequency-averaged speed and attenuation, and Ψ coefficient.

$\bar{\rho}$ **Comparison**	**Snowpit & Snowtube**	**ESC30 & SAS2**	**Snowpit & SAS2**
RMSD ($kg\ m^{-3}$)	19.9	17.9	8.2
MB ($kg\ m^{-3}$)	-5.5	-2.8	-6.2

SWE **Comparison**	**Snowpit & Snowtube**	**ESC30 & SAS2**	**Snowpit & SAS2**
RMSD (mm)	42.4	24.3	24.7
MB (mm)	-30.0	-5.6	-7.8

$\bar{\theta}_w$ **Comparison**	**Dielectric & Acoustic**
RMSD (%)	0.4
MB (%)	0.2

$\bar{T}$ **Comparison**	**Thermometer & Acoustic**
RMSD (°C)	1.0
MB (°C)	-0.7

Table B.4. Comparisons between snowpit, ESC30, and acoustic measurements of $\bar{\rho}$, SWE, $\bar{\theta}_w$ and $\bar{T}$ for the BM site.

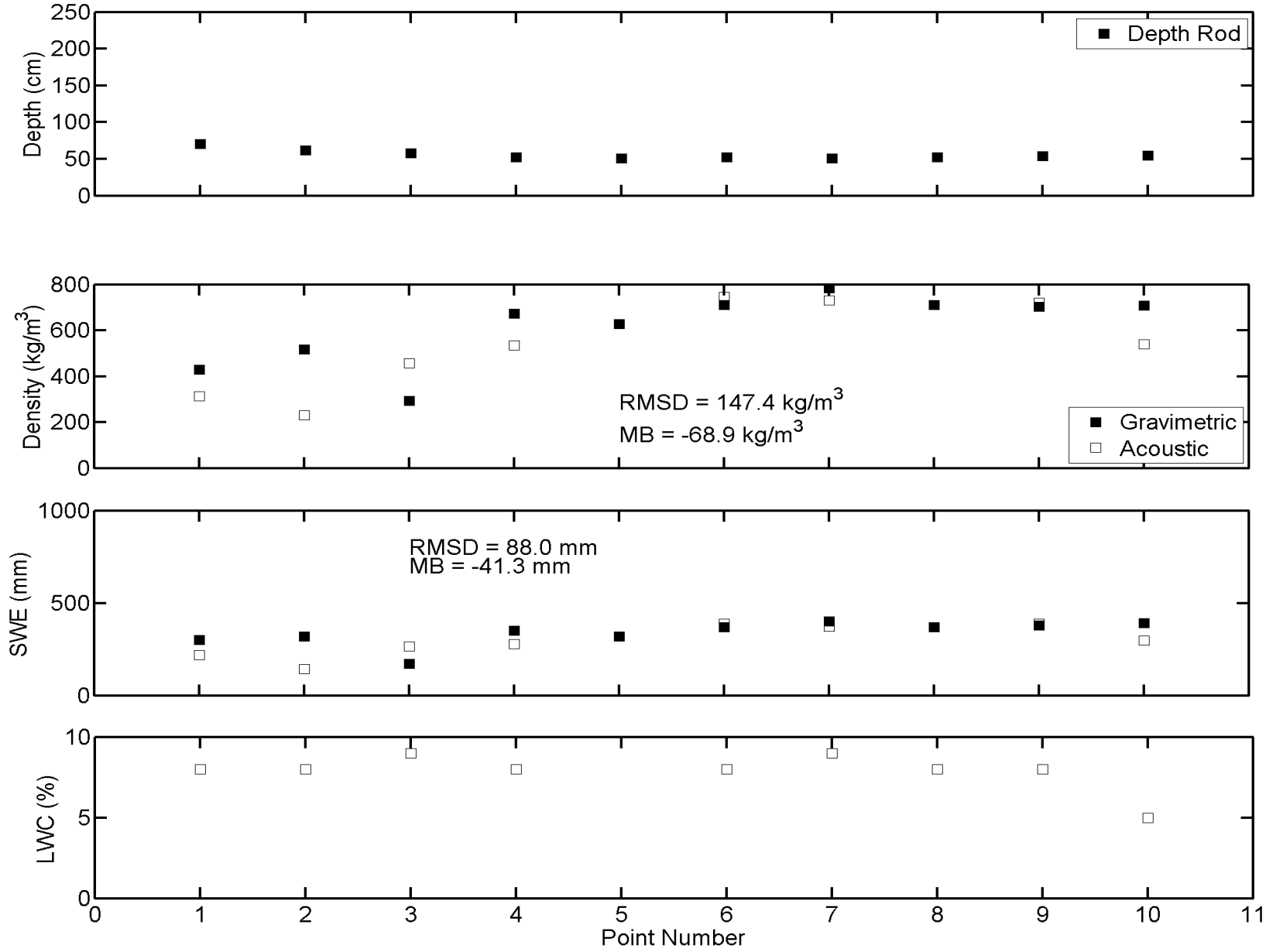

Figure B.13. Bow Lake (BL) Site transects showing depth, average density, SWE, and depth-averaged liquid water content.

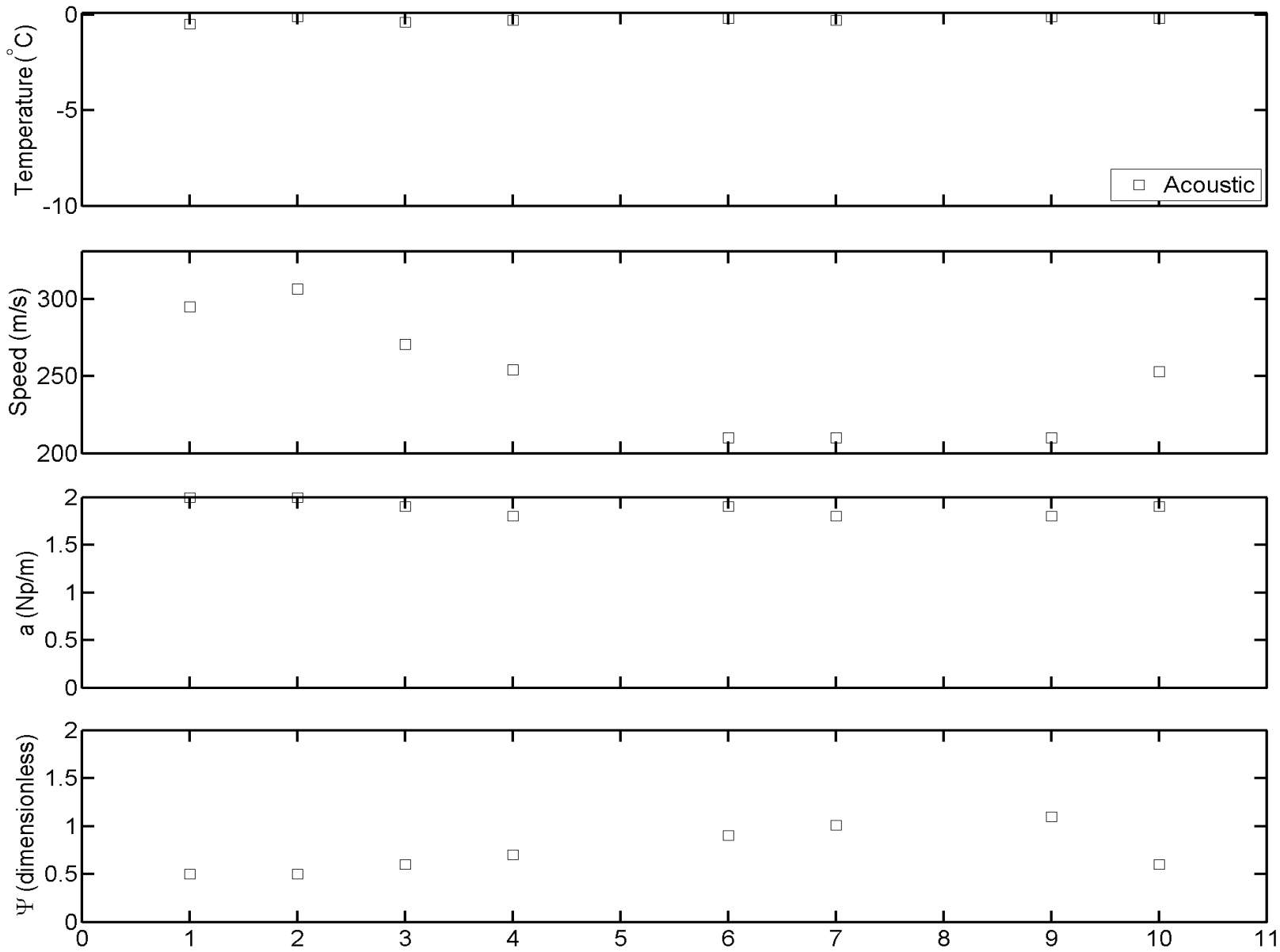

Figure B.14. Bow Lake (BL) Site transects showing average temperature, frequency-averaged speed and attenuation, and Ψ coefficient.

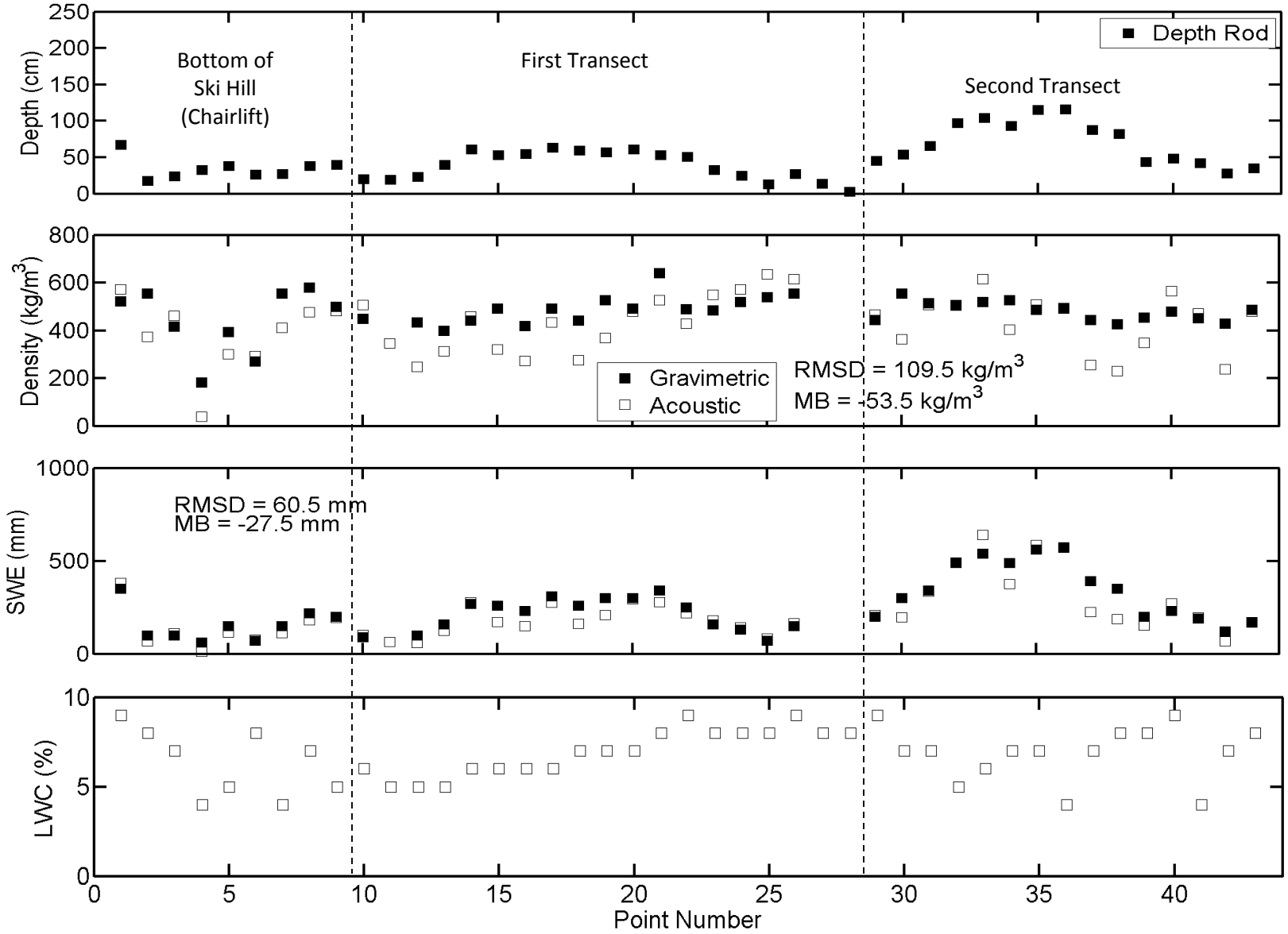

Figure B.15. Nakiska Ski Hills (NSH) Site transects showing depth, average density, SWE, and depth-averated liquid water content.

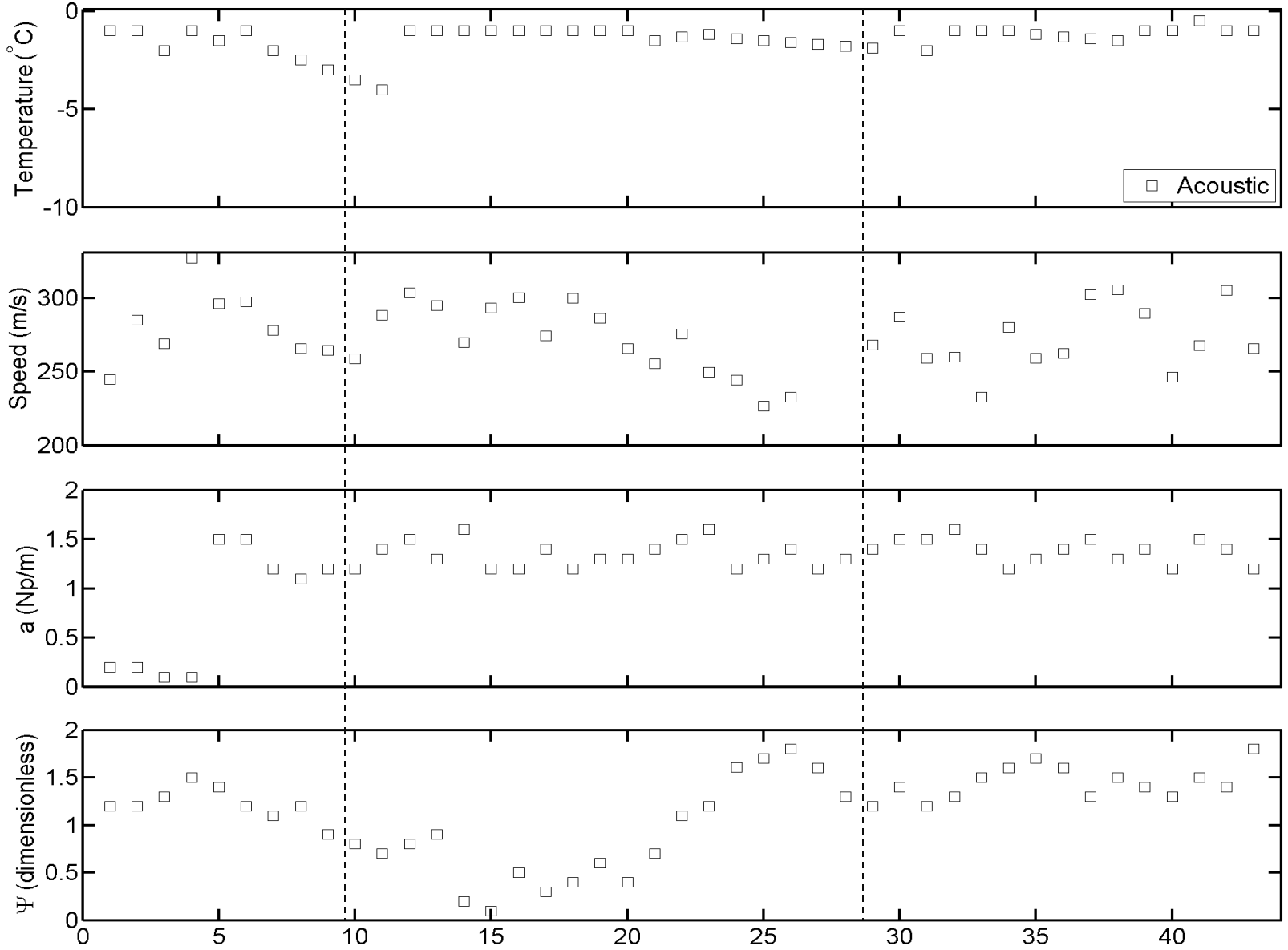

Figure B.16. Nakiska Ski Hills (NSH) Site transects showing average temperature, frequency-averaged speed and attenuation, and Ψ coefficient.

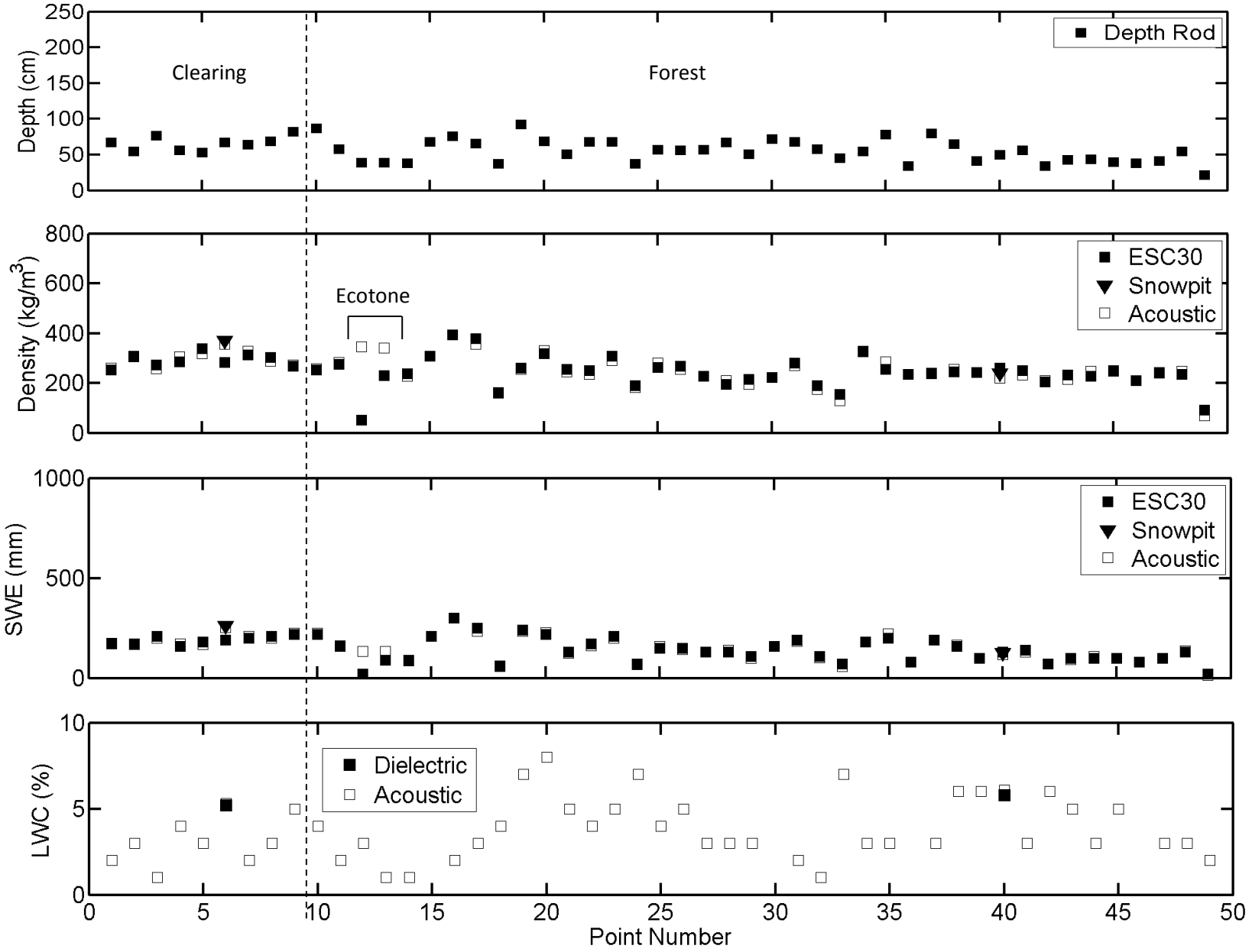

Figure B.17. Black Prince Cirque (BPC) Site transects showing depth, average density $\bar{\rho}$, SWE, and depth-averaged liquid water content.

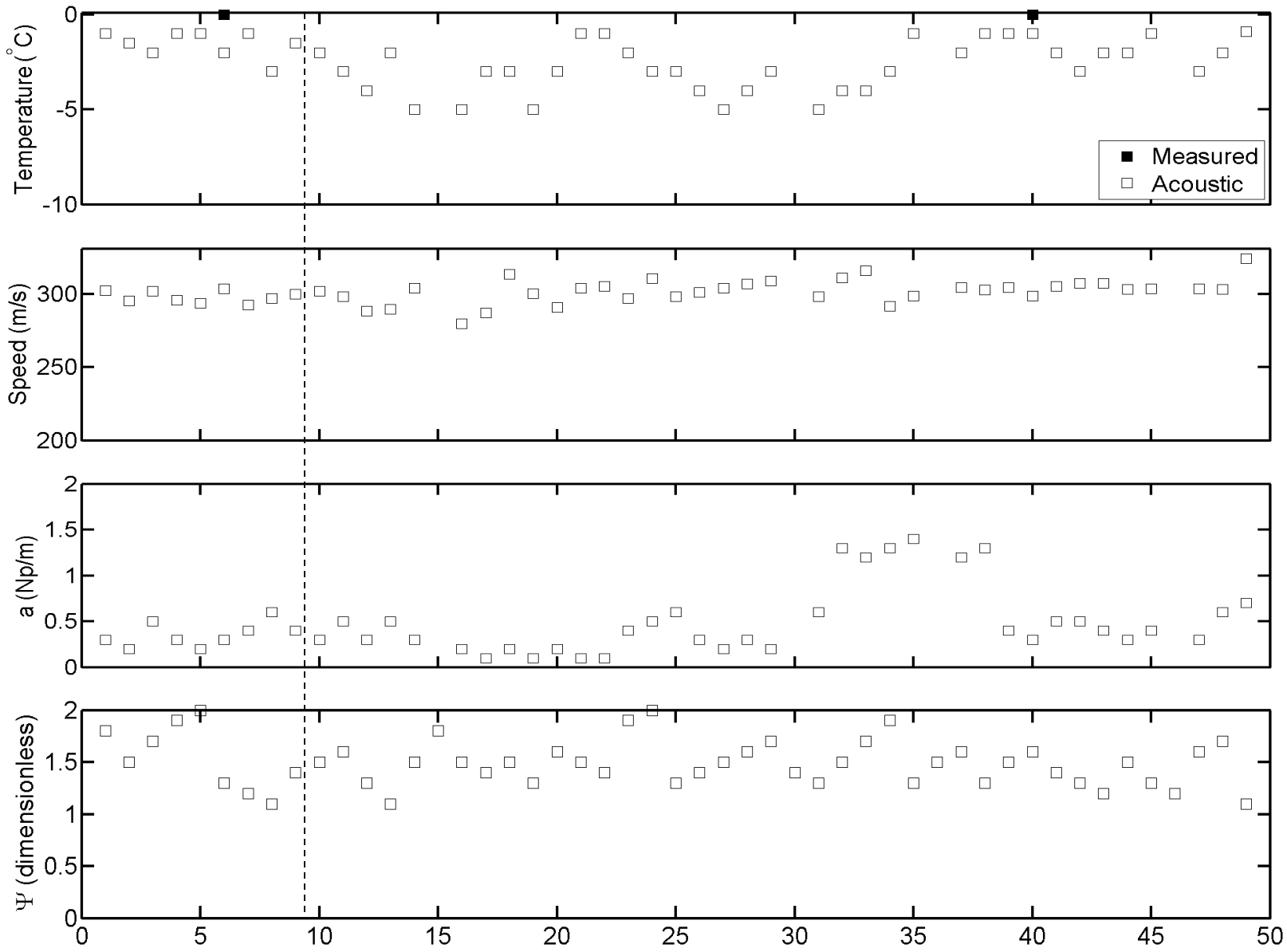

Figure B.18. Black Prince Cirque (BPC) Site transects showing average temperature, frequency-averaged speed and attenuation, and Ψ coefficient.

$\bar{\rho}$ **Comparison**	**Snowpit & Snowtube**	**ESC30 & SAS2**	**Snowpit & SAS2**
RMSD ($kg\ m^{-3}$)	62.6	50.1	18.2
MB ($kg\ m^{-3}$)	33.7	7.3	-18.0

SWE **Comparison**	**Snowpit & Snowtube**	**ESC30 & SAS2**	**Snowpit & SAS2**
RMSD (mm)	51.6	21.9	11.0
MB (mm)	35.5	3.6	-10.1

$\bar{\theta}_w$ **Comparison**	**Dielectric & Acoustic**
RMSD (%)	0.2
MB (%)	3.6

$\bar{T}$ **Comparison**	**Thermometer & Acoustic**
RMSD (°C)	1.6
MB (°C)	-1.5

Table B.5. Comparisons between snowpit, ESC30, and acoustic measurements of $\bar{\rho}$, SWE, $\bar{\theta}_w$ and $\bar{T}$ for the BPC site.

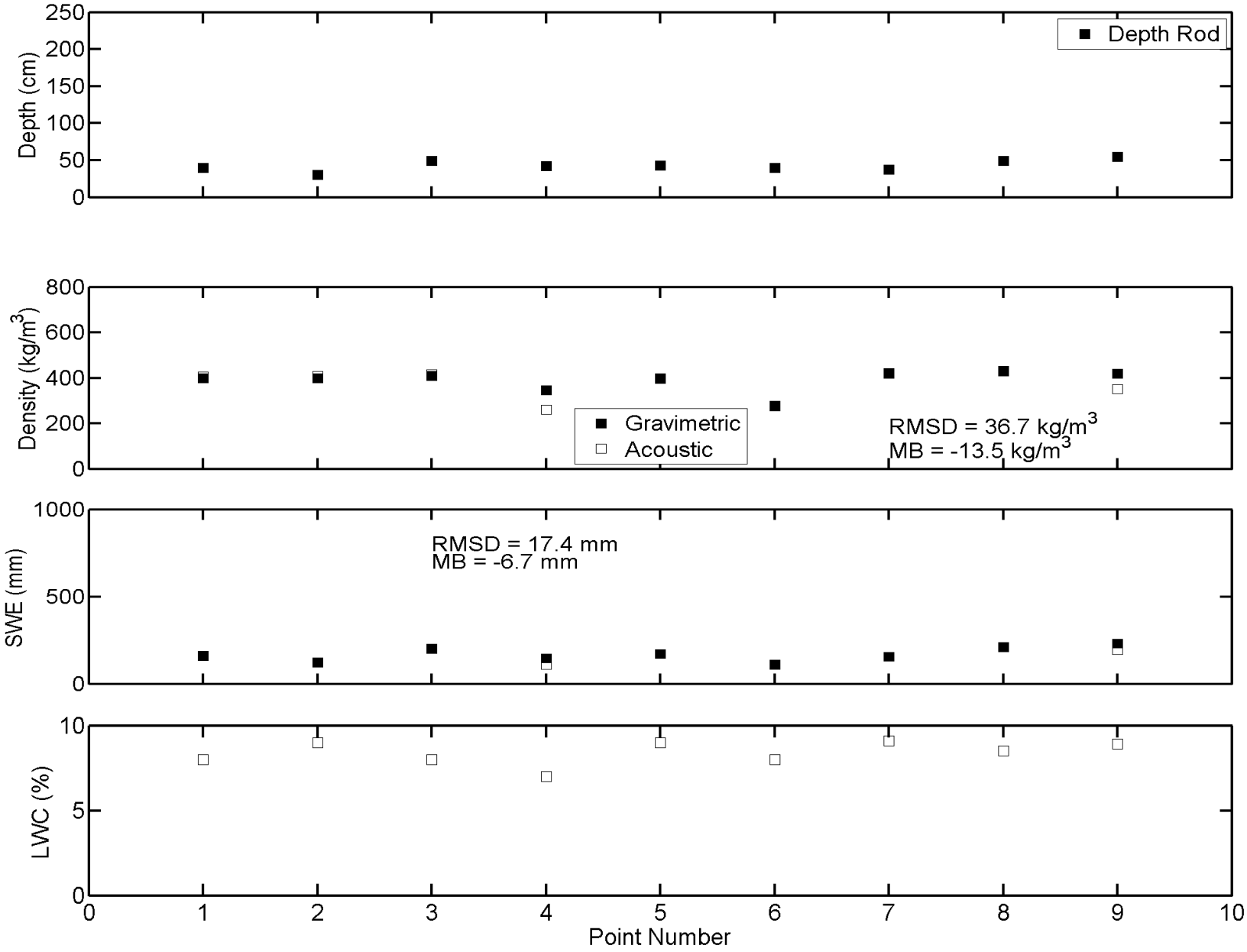

Figure B.19. Icefields Parkway Forest (IPF) Site transects showing depth, average density, SWE, and depth-averaged liquid water content.

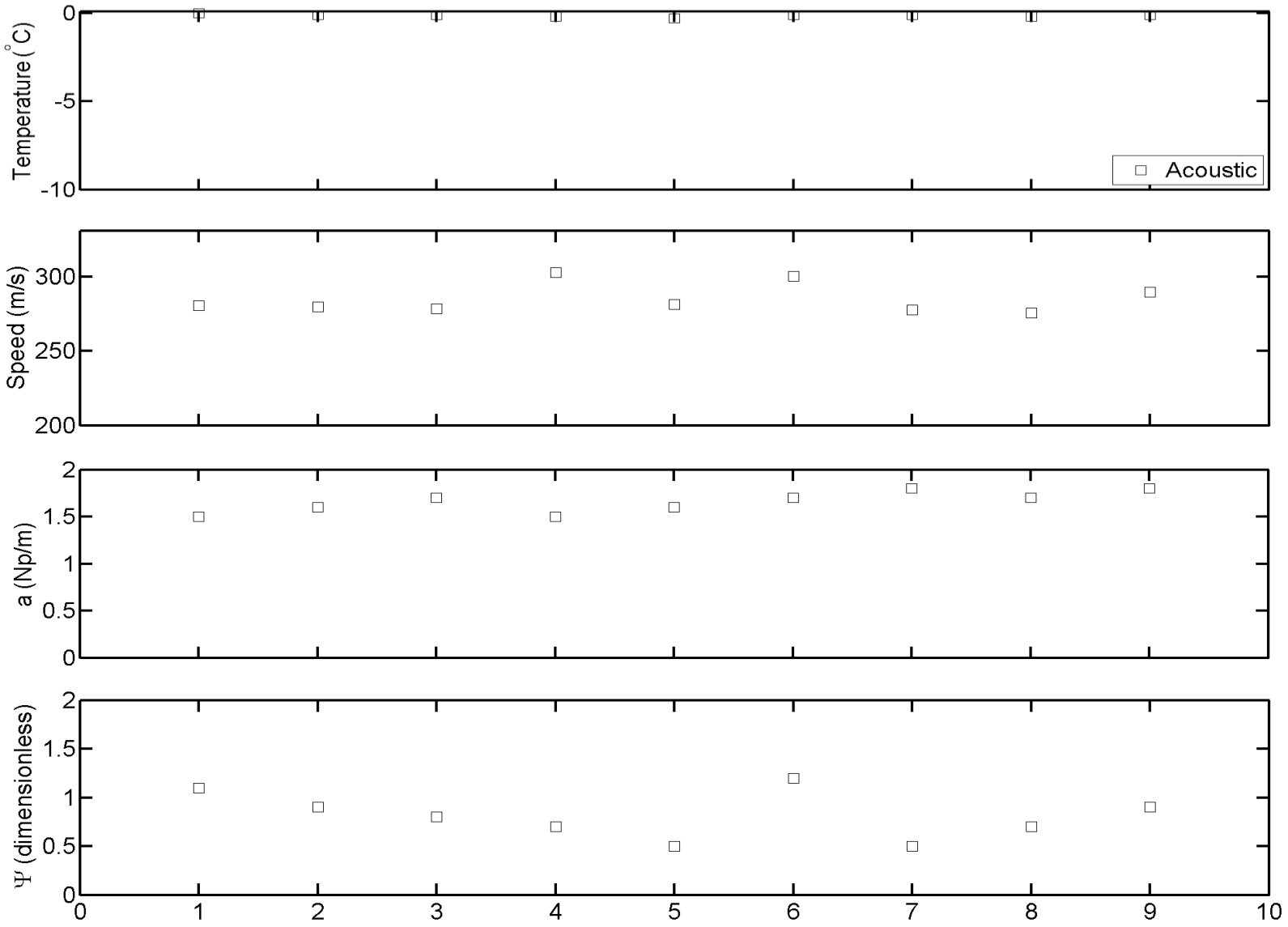

Figure B.20. Icefields Parkway Forest (IPF) Site transects showing average temperature, frequency-averaged speed and attenuation and Ψ coefficient.